國立中央大學天文研究所
鹿林天文台年報

2016

No.14

國立中央大學天文研究所 編

目錄

研究論文

工作報告

新聞報導

研究論文

A&A 593, A91 (2016)
DOI: 10.1051/0004-6361/201628447

Astronomy & Astrophysics

Long-term multi-wavelength variability and correlation study of Markarian 421 from 2007 to 2009⋆

M. L. Ahnen[1], S. Ansoldi[2], L. A. Antonelli[3], P. Antoranz[4], A. Babic[5], B. Banerjee[6], P. Bangale[7], U. Barres de Almeida[7,24], J. A. Barrio[8], J. Becerra González[9,25], W. Bednarek[10], E. Bernardini[11,26], B. Biasuzzi[2], A. Biland[1], O. Blanch[12], S. Bonnefoy[8], G. Bonnoli[3], F. Borracci[7], T. Bretz[13,27], S. Buson[14], A. Carosi[3], A. Chatterjee[6], R. Clavero[9], P. Colin[7], E. Colombo[9], J. L. Contreras[8], J. Cortina[12], S. Covino[3], P. Da Vela[4], F. Dazzi[7], A. De Angelis[14], B. De Lotto[2], E. de Oña Wilhelmi[15], F. Di Pierro[3], A. Domínguez[8], D. Dominis Prester[5], D. Dorner[13], M. Doro[14], S. Einecke[16], D. Eisenacher Glawion[13], D. Elsaesser[16], A. Fernández-Barral[12], D. Fidalgo[8], M. V. Fonseca[8], L. Font[17], K. Frantzen[16], C. Fruck[7], D. Galindo[18], R. J. García López[9], M. Garczarczyk[11], D. Garrido Terrats[17], M. Gaug[17], P. Giammaria[3], N. Godinović[5], A. González Muñoz[12], D. Gora[11], D. Guberman[12], D. Hadasch[19], A. Hahn[7], Y. Hanabata[19], M. Hayashida[19], J. Herrera[9], J. Hose[7], D. Hrupec[5], G. Hughes[1], W. Idec[10], K. Kodani[19], Y. Konno[19], H. Kubo[19], J. Kushida[19], A. La Barbera[3], D. Lelas[5], E. Lindfors[20], S. Lombardi[3], F. Longo[2], M. López[8], R. López-Coto[12], P. Majumdar[6], M. Makariev[21], K. Mallot[11], G. Maneva[21], M. Manganaro[9,⋆⋆], K. Mannheim[13], L. Maraschi[3], B. Marcote[18], M. Mariotti[14], M. Martínez[12], D. Mazin[7,28], U. Menzel[7], J. M. Miranda[4], R. Mirzoyan[7], A. Moralejo[12], E. Moretti[7], D. Nakajima[19], V. Neustroev[20], A. Niedzwiecki[10], M. Nievas Rosillo[8], K. Nilsson[20,29], K. Nishijima[19], K. Noda[7], L. Nogués[12], R. Orito[19], A. Overkemping[16,⋆⋆], S. Paiano[14], J. Palacio[12], M. Palatiello[2], D. Paneque[7], R. Paoletti[4], J. M. Paredes[18], X. Paredes-Fortuny[18], G. Pedaletti[11], L. Perri[3], M. Persic[2,30], J. Poutanen[20], P. G. Prada Moroni[22], E. Prandini[1,31], I. Puljak[5], W. Rhode[16], M. Ribó[18], J. Rico[12], J. Rodriguez Garcia[7], T. Saito[19], K. Satalecka[11], C. Schultz[14], T. Schweizer[7], S. N. Shore[22], A. Sillanpää[20], J. Sitarek[10], I. Snidaric[5], D. Sobczynska[10], A. Stamerra[3], T. Steinbring[13], M. Strzys[7], L. Takalo[20], H. Takami[19], F. Tavecchio[3], P. Temnikov[21], T. Terzić[5], D. Tescaro[14,⋆⋆], M. Teshima[7,28], J. Thaele[16], D. F. Torres[23], T. Toyama[7], A. Treves[2], V. Verguilov[21], I. Vovk[7], J. E. Ward[12], M. Will[9], M. H. Wu[15], R. Zanin[18] (The MAGIC Collaboration),
D. A. Blinov[32,33], W. P. Chen[34], N. V. Efimova[35], E. Forné[36], T. S. Grishina[32], T. Hovatta[37], B. Jordan[38], G. N. Kimeridze[39] E. N. Kopatskaya[32], E. Koptelova[34], O. M. Kurtanidze[39,40], S. O. Kurtanidze[39], A. Lähteenmäki[37,41], V. M. Larionov[32,35], E. G. Larionova[32], L. V. Larionova[32], R. Ligustri[42], H. C. Lin[34], B. McBreen[43], D. A. Morozova[32], M. G. Nikolashvili[39], C. M. Raiteri[44], J. A. Ros[36], A. C. Sadun[45], L. A. Sigua[39], M. Tornikoski[37], I. S. Troitsky[32], and M. Villata[44]

(Affiliations can be found after the references)

Received 7 March 2016 / Accepted 23 May 2016

ABSTRACT

Aims. We study the multi-band variability and correlations of the TeV blazar Mrk 421 on year timescales, which can bring additional insight on the processes responsible for its broadband emission.

Methods. We observed Mrk 421 in the very high energy (VHE) γ-ray range with the Cherenkov telescope MAGIC-I from March 2007 to June 2009 for a total of 96 h of effective time after quality cuts. The VHE flux variability is quantified using several methods, including the Bayesian Block algorithm, which is applied to data from Cherenkov telescopes here for the first time. The 2.3 yr long MAGIC light curve is complemented with data from the *Swift*/BAT and RXTE/ASM satellites and the KVA, GASP-WEBT, OVRO, and Metsähovi telescopes from February 2007 to July 2009, allowing for an excellent characterisation of the multi-band variability and correlations over year timescales.

Results. Mrk 421 was found in different γ-ray emission states during the 2.3 yr long observation period: The flux above 400 GeV spans from the minimum nightly value of $(1.3 \pm 0.4) \times 10^{-11}$ cm^{-2} s^{-1} to the maximum flux, that is about 24 times higher, at $(3.1 \pm 0.1) \times 10^{-10}$ cm^{-2} s^{-1}. Flares and different levels of variability in the γ-ray light curve could be identified with the Bayesian Block algorithm. The same behaviour of a quiet and active emission was found in the X-ray light curves measured by *Swift*/BAT and the RXTE/ASM, with a direct correlation in time. The behaviour of the optical light curve of GASP-WEBT and the radio light curves by OVRO and Metsähovi are different as they show no coincident features with the higher energetic light curves and a less variable emission. Overall, the fractional variability increases with energy. The comparable variability in the X-ray and VHE bands and their direct correlation during both high- and low-activity periods spanning many months show that the electron populations radiating the X-ray and γ-ray photons are either the same, as expected in the synchrotron-self-Compton mechanism, or at least strongly correlated, as expected in electromagnetic cascades.

Key words. astroparticle physics – BL Lacertae objects: individual: Markarian 421 – radiation mechanisms: non-thermal

⋆ The complete data set shown in Fig. 2 and the data points shown in Figs. 3 and 4 are only available at the CDS via anonymous ftp to cdsarc.u-strasbg.fr (130.79.128.5) or via http://cdsarc.u-strasbg.fr/viz-bin/qcat?J/A+A/593/A91

⋆⋆ Corresponding authors: Ann-Kristin Overkemping, e-mail: ann-kristin.overkemping@tu-dortmund.de; Marina Manganaro, e-mail: manganaro@iac.es; Diego Tescaro, e-mail: diego.tescaro@gmail.com

1. Introduction

Markarian 421 (Mrk 421) is a high-frequency peaked BL Lac object (HBL) at a redshift of $z = 0.030$ (Piner et al. 1999). It was the first extragalactic TeV emitter to be detected (Punch et al. 1992).

Blazars are active galactic nuclei (AGN) where the jet is aligned to our line-of-sight. This means that it is possible to observe very high energy (VHE) γ-rays that are produced inside the jets and relativistically beamed in our direction. Additionally, AGN emit radiation over the whole electromagnetic spectrum, from radio wavelengths to VHE γ-rays.

Blazars feature a spectral energy distribution (SED) with a two-bump structure. The low energy component is due to the synchrotron radiation caused by electrons of the relativistic beam, while the high energy peaked bump is attributed to other interactions. This could be the Compton scattering of less energetic photons by the same electron population in leptonic scenarios or these photons could be produced inside hadronic interactions of, for example, protons in the jet. In HBL objects as Mrk 421, the Synchrotron bump covers the energy range from radio to X-ray wavelengths while the peak can be found between UV and X-ray wavelengths. The second bump extends from low-energy γ-rays to VHE γ-rays.

A characteristic feature of blazars, and of Mrk 421 in particular, is that they show states of high activity in which the emitted electromagnetic radiation can increase by more than one order of magnitude on timescales ranging from years down to minutes. During high states blazars often show significant spectral flux changes, and up to some extent, correlated flux variations in the low- and high-energy bumps. This blazar variability is an extraordinary opportunity to break degeneracies between the various emission models. Different models produce flux variations (at a given energy band) with particles of different energies, cooling times, and cross sections for different processes, and thus are in principle distinguishable. It is also important to note that the blazar emission zone is unresolved for all instruments (with perhaps the exception of radio Very Long Baseline Array (VLBA) interferometric observations), and hence variability is the only way of probing its structure. Therefore, while "snapshot" multiwavelength (MWL) spectra provide us with clues on the emission mechanisms and physical parameters inside relativistic jets, detailed studies of time variability bring us additional information on the emission mechanisms and on the structure and the dynamics of the jet itself.

Mrk 421 has shown periods of large X-ray and γ-ray activity of various timescales, as reported previously in various publications (e.g. Gaidos et al. 1996; Cui 2004; Tluczykont et al. 2010). Mrk 421 has been the target of several past MWL campaigns, with the correlation between X-rays and TeV γ-rays as one of the key features under investigation. The details in the correlation between these two bands in Mrk 421 is crucial because it relates to the energy regions where most of the power is emitted (approximately the peaks of the two SED bumps), and hence the regions of the SED which can best distinguish between different theoretical scenarios.

A direct correlation between X-rays and TeV γ-rays has been reported multiple times during flaring activity (Macomb et al. 1995; Buckley et al. 1996; Fossati et al. 2004, 2008; Albert et al. 2007; Bartoli et al. 2011; Donnarumma et al. 2009; Abdo et al. 2011; Acciari et al. 2011; Cao & Wang 2013; Aleksić et al. 2015b). Recently, Aleksić et al. (2015a) and Baloković et al. (2016) also reported the existence of this correlation during low activity. Błażejowski et al. (2005) and Horan et al. (2009) were able to constrain the correlation to time differences below 1.5 days. These results are in agreement with the synchrotron-self-Compton (SSC) model, where the photons from both X-ray and γ-ray energies are produced by the same electron population. Other authors reported orphan flares in TeV γ-rays without an X-ray counterpart, which were observed in Mrk 421 during a MWL campaign in 2003 and 2004 (Błażejowski et al. 2005), unable to be explained by the SSC model. In Acciari et al. (2009) a correlation between TeV and X-rays is not found, and a possible hadronic origin of the emission is discussed. However, this correlation study relates to short observations (two half-day long observations) with very low variability. The X-ray emission was accurately characterized with continuous XMM observations, and flux variations at the level of 10% could be significantly resolved. Yet the TeV γ-ray measurements covered only a small fraction of the XMM observations, and had relatively large error bars. Therefore, the presented X-ray/TeV correlation results in Acciari et al. (2009) were not conclusive, and show very clearly the importance of having long, well sampled and sensitive TeV γ-ray observations to perform this kind of study.

Other energy bands are not evidently correlated with X-rays and TeV γ-rays. Macomb et al. (1995), Albert et al. (2007), Cao & Wang (2013) report a missing correlation of the optical and UV emission to the X-ray and TeV γ-ray emission. Confirming the trend of a strong correlation between X-rays and VHE, the work of Baloković et al. (2016) also reports a lack of correlation between optical/UV and X-rays, and moreover ascribes the observed broadband variability features during low activity to in situ electron acceleration in multiple compact regions. In Horan et al. (2009) a correlation with a time lag between the optical and the TeV γ-ray light curves is found, once with the optical features leading the TeV features and once vice versa, but the likelihood of having observed the optical leading and lagging the TeV features by chance is 20% and 60% respectively. In Aleksić et al. (2015a) an anti-correlation between the optical and UV light curves with the X-ray light curves is reported, but with the possibility that it might have been found by chance, proposing a dedicated correlation analysis over many years to properly characterize the temporal evolution of the optical and X-ray/TeV γ-ray bands.

Evidence of a correlation between radio and γ-ray activity was reported in Katarzyński et al. (2003), where the study of a single radio outburst with a X-ray and TeV γ-ray counterpart in February−March 2001 is presented. The author models a scenario in which the acceleration of electrons in the middle part of the jet describes well the temporal evolution of such a multispectral flare.

In the more recent work of Lico et al. (2014) a marginally significant correlation between radio and GeV γ-rays (without time lag) is reported. This study used observations spanning many months from 2011, when Mrk 421 did not show any flaring activity, hence suggesting a co-location of the radio and γ-ray emission of Mrk 421 during typical (low) activity.

A different result is derived from the outstanding radio activity observed in September 2012, where Mrk 421 showed a particularly symmetric flare profile, with the highest radio flux measured in three decades, as reported in Max-Moerbeck et al. (2014) and Hovatta et al. (2015). Both works assume that this giant radio flare is physically connected to a large γ-ray flaring activity measured by *Fermi*-LAT about one month before, and Max-Moerbeck et al. (2014) uses this time difference to locate the origin of the γ-ray emission upstream of the radio emission.

Because of the above-mentioned complexity and sometimes controversy in the multi-band flux variations and correlations observed during relatively short (weeks to months) campaigns, we need very long (multi-year) campaigns to put things into context. In this paper we report an extensive study of the multi-band flux variability of Mrk 421 during the 2.3 yr long period that spans from February 2007 to July 2009. We adopted the methodology reported in Aleksić et al. (2015a), which had been applied in a much shorter multi-instrument data set.

There are several publications that report studies with the VHE γ-ray emission of Mrk 421 during the above-mentioned 2.3 yr long period; yet they typically relate to smaller temporal intervals. For instance, Aleksić et al. (2012) reported MAGIC observations of a high active state performed from December 2007 to June 2008, and Abdo et al. (2011) and Aleksić et al. (2015a) reported results related to observations from a 4.5 month long time interval from January to June 2009. A very interesting study using Whipple 10 m observations performed from December 1995 to May 2009 was reported in Acciari et al. (2014), which allowed study of the duty cycle and evaluation of the VHE emission and its correlation with the X-ray emission. The study that we report in this paper relates to a time period that is (almost) contained in Acciari et al. (2014), but it provides a large number of improvements such as the larger sensitivity of MAGIC with respect to Whipple 10 m, which allows us to resolve the VHE flux with smaller uncertainties, and hence to study the variability and its correlation on shorter timescales (two days). Moreover, in this paper we apply a more sophisticated treatment to quantify variability and correlations (adopted from Aleksić et al. 2015a), and we extend the study to extensive light curves collected at radio, optical and hard X-rays (above 15 keV), hence giving a more complete overall picture of the year-long multi-band flux variability of Mrk 421 than that given in Acciari et al. (2014).

The paper is organized as follows. Section 2 describes the MAGIC observations, as well as the analysis and results obtained. Section 3 describes the application of the Bayesian Block algorithm to the MAGIC data, and the resulting quantification of the flux variability and identification of several VHE flares. The Bayesian Block is a well established methodology, but this is the first time that it is applied to VHE data. Section 4 describes the extensive observations of Mrk 421 performed at radio, optical and X-rays, and in Sects. 5 and 6 we report the quantification of the multi-band variability and its correlations. Finally, in Sects. 7 and 8 we summarise and discuss the results presented.

2. MAGIC observations of Mrk 421

2.1. The MAGIC telescopes

The Major Atmospheric Gamma-ray Imaging Cherenkov (MAGIC) telescopes are a system of two Cherenkov telescopes with a mirror diameter of 17 m each. They are situated at the ORM (Observatory Roque de los Muchachos) on the Canary Island of La Palma at a height of 2200 m above sea level.

In 2004 the MAGIC-I telescope was commissioned and started its observations in single telescope mode. The performance during the stand-alone operation of MAGIC-I was presented in Albert et al. (2008) and Aliu et al. (2009). Stereoscopic data were taken after the second telescope, MAGIC-II, was commissioned in 2009, and a major upgrade of the MAGIC telescopes was performed in 2012 (Aleksić et al. 2016a,b).

2.2. Observations and data analysis

Mrk 421, one of the strongest and brightest extragalactic sources, is observed by MAGIC on a regular basis. The source is observable from late November to June from the MAGIC latitude. In this analysis we examined data of Mrk 421 from MAGIC-I in single-telescope operation from 8th March 2007 (MJD – modified Julian date – 54 167) to 15th June 2009 (MJD 54 997), a time span of over two years. The overall amount of good quality data taken in wobble mode (Fomin et al. 1994) are 95.6 h distributed over 95 observation nights. The data cover a zenith angle range from 9° to 45°. Data with too-bright sky conditions and bad weather conditions were excluded. The data analysis was carried out using the standard MAGIC analysis chain MARS (MAGIC Analysis and Reconstruction Software; Zanin et al. 2013). During the selected time span an integral sensitivity as low as 1.6% of the Crab Nebula flux is reached and the energy resolution is ~20% (Aliu et al. 2009).

2.3. Measured VHE γ-ray flux

The light curve of Mrk 421 measured by MAGIC-I is binned nightly and is shown in both Fig. 1 and in the top panel of Fig. 2.

The light curve is naturally divided into three observation cycles due to the observability gaps of Mrk 421 from the end of June to the end of November each year with the MAGIC telescopes. Data from February 2007 to August 2007 will be called Period 1, data from September 2007 to the beginning of September 2008 will be called Period 2, and data from beginning of September 2008 to July 2009 will be called Period 3. In Fig. 2 these three periods are indicated. The light curve shows different levels of source flux and variability in these three time spans. In Period 1 and in Period 3 the flux is clearly at a lower level than in Period 2.

During Period 1 the average flux of the six data points is at a level of (0.38 ± 0.03) Crab units (CU)[1]. The flux is variable with variations up to a factor of two around the average flux. During Period 2 the flux is at a high average level of (1.38 ± 0.02) CU and it seldomly falls below 1 CU. The light curve shows a high variability with flux variations of about a factor of three around the average. The flux varies between the lowest value of (0.4 ± 0.1) CU on 17th December 2007 and the maximum value of (3.8 ± 0.1) CU on 31st March 2008 (MJD 54 556). During Period 3 the average VHE γ-ray flux is (0.61 ± 0.01) CU with variations of up to a factor of approximately two.

The time-averaged fluxes detected by MAGIC for the three identified observation periods are comparable to the ones measured by the Whipple 10 m telescope for the seasons 2006−2007, 2007−2008, and 2008−2009 respectively, which were reported in Acciari et al. (2014). The Whipple telescope detected a flux of (0.28 ± 0.02) CU for the 2006−2007 data, which is at a comparable level with the (0.38 ± 0.03) CU for Period 1 of the MAGIC data (here we note that the Whipple observations cover a larger time span, which started in 2006). Then an average flux of (1.46 ± 0.09) CU is reported by Whipple in 2007−2008, similar to the value of (1.38 ± 0.02) CU for Period 2, confirming the higher flux state. For the 2008−2009 season, the Whipple flux was (0.55 ± 0.03) CU, which is comparable to the average flux of (0.61 ± 0.01) CU in Period 3 measured by MAGIC.

In summary, during the three observation periods covered in this paper, Mrk 421 showed three clearly distinct VHE flux

[1] A Crab unit is defined here as a flux of 8.08×10^{-11} cm^{-2} s^{-1} in the energy range from 400 GeV to 50 TeV (Albert et al. 2008).

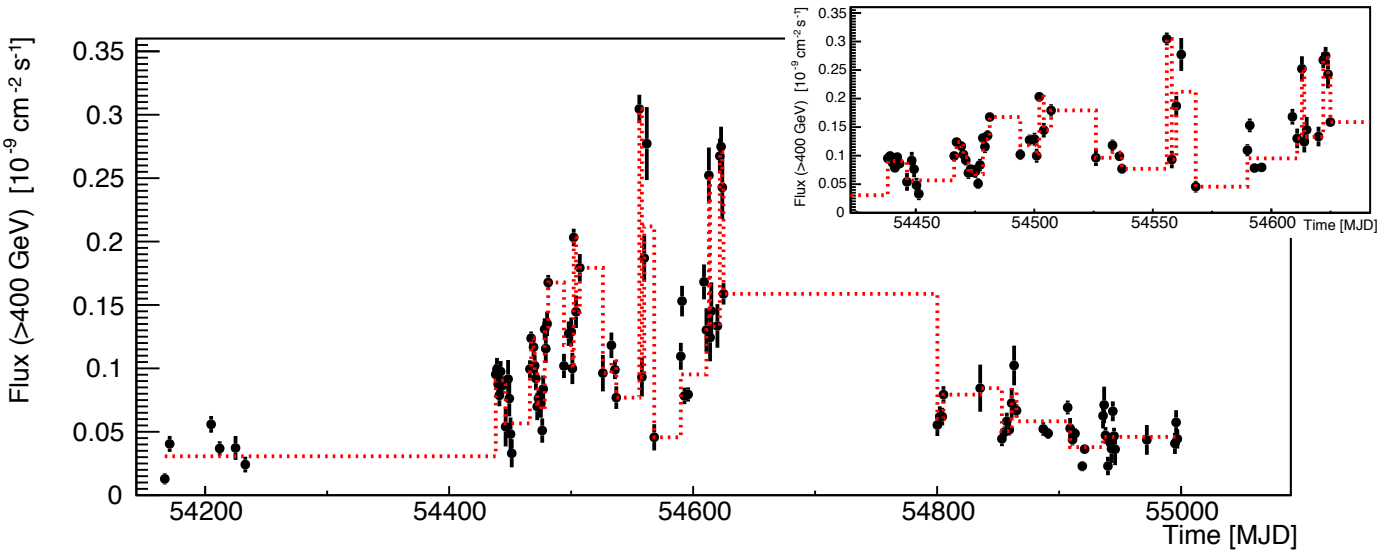

Fig. 1. Bayesian Blocks representation of the MAGIC light curve (black dots) from March 2007 to June 2009. The red dotted line defines the different identified blocks. The inlay shows a magnified version for the time range from December 2007 to June 2008, the high active Period 2. The long flat lines with no sampling between a data point and a new block do not guarantee a stable flux.

levels, with different apparent levels of variability. A quantitative evaluation of the VHE flux variability in these three periods is reported in Sects. 3 and 5, following the prescriptions given in Scargle (1998), Scargle et al. (2013) and Aleksić et al. (2015c).

3. Bayesian Blocks

We applied the Bayesian Block algorithm (Scargle 1998; Scargle et al. 2013) to the TeV light curve of Mrk 421. The algorithm generates a block-wise constant representation of a sequential data series by identifying statistically significant variations, and is suitable for characterizing local variability in astronomical light curves, even when not evenly sampled.

The optimal segmentation (defined by its change points) maximizes the goodness-of-fit with a certain model for the data lying in a block. The method requires a prior probability distribution parameter ($ncp_{\rm prior}$) for the number of changing points ($N_{\rm cp}$), a kind of smoothing parameter derived from the assumption that $N_{\rm cp} \ll N$, the number of measurements. A false-positive rate (p_0) is associated to the choice $ncp_{\rm prior}$.

The false-positive rate was chosen to be $p_0 = 0.01$, leading to a $ncp_{\rm prior} = 3.92$. We obtained the 39 blocks representation for 95 data points shown as a red dotted line in Fig. 1 on top of the flux points measured by MAGIC (black dots). The height of each block is the weighted average of all integral fluxes belonging to it.

An advantage of the Bayesian Block algorithm is that it is able to identify significant changes in data series independently of variations in gaps or exposure. Therefore, no information on true or important flux changes is lost, as can happen when applying other techniques where the data series is binned in predefined temporal intervals.

This is the first time that the Bayesian Block algorithm has been applied to a VHE γ-ray light curve. We use the results to estimate the variability level of the light curve in the different observation periods and to define flares. To quantify the variability for each period, we can simply determine the ratio of resulting number of blocks and the number of data points. A higher ratio implies a higher flux variability. All six data points from Period 1 belong to the same initial block. This ratio of 1/6 indicates a low variability during this period. The lack of additional blocks during this period may also be related to the very low number of data points. The high activity in Period 2 is evident by the 30 blocks detected for 56 data points during this time period by the algorithm (see inlay of Fig. 1). The resulting ratio of 30/56, which is slightly above 0.5, shows that the light curve is substantially more variable than Period 1. In Period 3 we have an eight-block representation for 33 data points, which is a ratio of ~0.24. This lower variability of the light curve during this period shows a milder activity of the AGN than in Period 2. An additional discussion of the variability will be given in Sect. 5.

It is of great interest to identify flaring activities in light curves, but the definition of a flare is somewhat arbitrary and, since blazars vary on timescales from years down to minutes, a definition is strongly biased by the prejudice of the temporal bins used to produce the light curves. It is easy to miss flaring activities in light curves with too-large temporal bins (if the variability occurs on small timescales) or in light curves with too-small temporal bins (if the flux values are dominated by statistical uncertainties). In this context, the Bayesian Block algorithm benefits from a more suitable temporal split (according to the true variability), and hence it can be used as a very efficient method to find flares. In the following, VHE γ-ray flares are defined as a flux rise of at least a factor of two. This comparison is based on the block heights, that is the weighted average flux of all data points in one block. A flare can include several rising steps in a row, which add up to a local maximum in flux. Subsequently, the flux decreases to a lower flux, which can happen on a daily or longer timescale. By using this flux-doubling threshold we have been able to identify several flares, which are reported in Table 1.

We estimate the flux-doubling times using the height difference between consecutive blocks and the time between the last data point of a given block and the starting point of the next block, which is a conservative measure of the rise time between blocks. In the case of several consecutive flux rises among continuous blocks, the flux-doubling time reported in Table 1 considers the rise as a single increase from minimum to maximum. It can be seen that the flux doubles its value on different timescales. The flux-doubling can occur during just one night, for example for the block starting on MJD 54 502, but it can also take many

Table 1. Dates, factor of flux increase, and flux-doubling times of flares found by the Bayesian block algorithm for the MAGIC light curve.

MJD	Increase	Flux-doubling time [days]	Notes
54 438	3.0 ± 0.3	139*	The flux rise follows the low flux in the beginning of 2007
54 467	2.2 ± 0.3	15	Two subsequent rises
54 481	2.5 ± 0.3	3	Two subsequent rises
54 502	2.0 ± 0.3	1	Flux rise in just one night
54 556	4.0 ± 0.6	10	Rise to the overall maximum flux value. The last given data point before this block was taken 19 days before
54 560	2.3 ± 0.5	2	
54 613	5.5 ± 1.7	20	The rise to the maximum takes place in three single steps. The first rise of a factor of 2.1 follows an observation 21 days before. The following block has a length of 19 days. Subsequently, the flux rises by a factor of 1.4 in just two days and by a factor of 1.9 during the same time interval
54 622	2.0 ± 0.2	2	

Notes. The given MJD identifies the first day of the highest block. See definition of VHE flare in the text. (*) Includes an observation gap of about half a year.

days. Additionally, it should be noted that it cannot be ruled out that the flux might fall between two measurements. All determined flux-doubling times are subject to this possibility. For the first entry in the table the flux-doubling time of 139 days is not meaningful because the time interval includes the long observation gap from May to December 2007 where the source behaviour in γ-rays is unknown. Therefore, the flux-doubling times reported in Table 1 should be considered as upper limits to the actual time needed to double the flux. That is, the actual flux-doubling times could be shorter than the ones reported.

The flares identified using the Bayesian Block algorithm are marked in Fig. 2 by vertical dotted lines so that it is possible to compare these positions with features in the light curves in the other wavelengths.

4. Observations at X-ray, optical and radio wavelengths

To study the variability and correlation between the TeV γ-ray data and other wavebands, data from several other instruments were considered. In the X-ray range data from *Swift*/BAT and RXTE/ASM were selected. The optical data shown here is from the GASP-WEBT consortium (which includes data from the KVA telescope located at the ORM close to MAGIC). Data from the Metsähovi and OVRO telescopes are used in the radio range.

4.1. Hard X-ray observations with Swift/BAT

The Burst Alert Telescope (BAT) on board the *Swift* satellite observes Mrk 421 in the hard X-ray regime, from 15 to 50 keV (Krimm et al. 2013). The *Swift*/BAT transient monitor results are provided by the *Swift*/BAT team[2]. Considering only averaged daily rates with a rate to rate error ratio greater than two, and additionally discarding six measurements with negative rates (on MJD 54 288, 54 476, 54 638, 54 750, 54 914, and 54 981), results in a total of 821 h of data distributed over 168 nightly flux measurements between 23rd February 2007 (MJD 54 154) and 17th June 2009 (MJD 54 999).

The *Swift*/BAT light curve of Mrk 421 is shown in Fig. 2. The overall hard X-ray flux behaviour is comparable to that of the MAGIC light curve, with a higher activity in Period 2 and several features that appear to be coincident, such as the peak structure around MJD 54 560.

4.2. Soft X-ray observations with RXTE/ASM

The all-sky monitor (ASM) was an instrument on board the RXTE satellite. It observed Mrk 421 in the energy range from 2 to 10 keV (Levine et al. 1996).

The results shown here are provided by the ASM/RXTE teams at MIT and at the RXTE SOF and GOF at NASA's GSFC[3]. Only averaged daily count rates, each consisting of several so-called observation dwells of 90 s length, with a rate to rate error ratio greater than two are considered for the following studies. Additionally, two negative rates, on MJD 54 371 and 54 914, are discarded. This results in a total of 532 daily flux measurements with a total observation length of 260 h between 10th February 2007 (MJD 54 141) and 16th June 2009 (MJD 54 998).

The RXTE/ASM light curve of Mrk 421 is shown in Fig. 2. The soft X-ray flux shows a similar behaviour to that of the hard X-rays and VHE γ-rays, which includes several overall flux levels and peak structures that are present also in the *Swift*/BAT and MAGIC light curves.

4.3. Optical observations

The optical data in the *R*-band shown here were recorded by the KVA (Kungliga Vetenskapsakademien) telescope and a collection of telescopes, which work together in the GASP-WEBT (Whole Earth Blazar Telescope)[4] consortium (Villata et al. 2008). The KVA telescope is situated at the ORM on La Palma close to the MAGIC telescopes. Photometric observations in the *R*-band are made with a 35 cm telescope. Observations are carried out in the same time intervals as MAGIC observations. Optical observations of Mrk 421 by the KVA telescope started in 2002, and show a variable optical light curve (Takalo et al. 2008).

[2] http://swift.gsfc.nasa.gov/results/transients/weak/Mrk421.lc.txt

[3] xte.mit.edu/asmlc/ASM.html

[4] http://www.oato.inaf.it/blazars/webt/

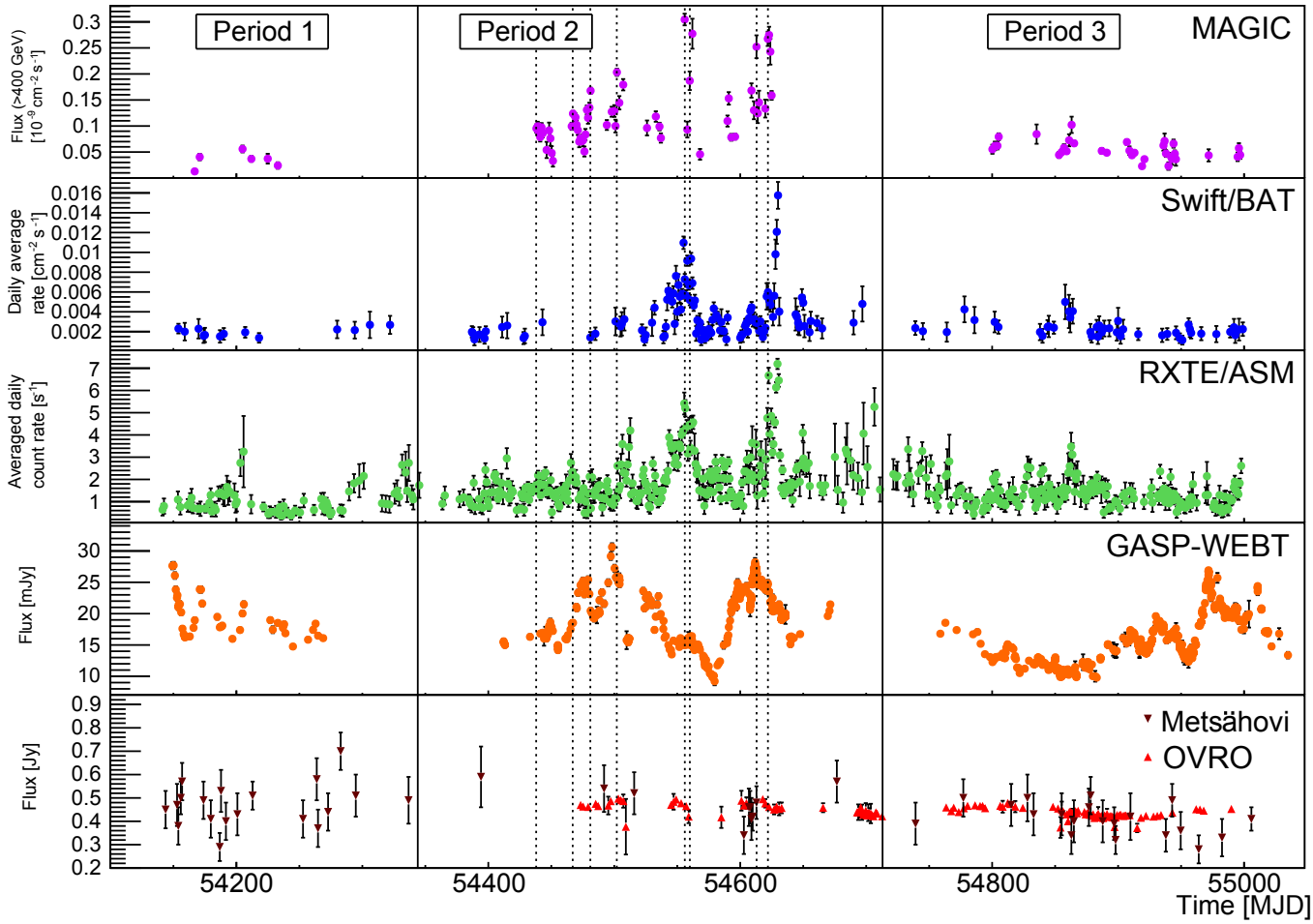

Fig. 2. Light curves of MAGIC, *Swift*/BAT, RXTE/ASM, GASP-WEBT, Metsähovi and OVRO *from top to bottom* in the time range from February 2007 to July 2009. The vertical dotted black lines denote the position of the TeV γ-ray flares as identified with the Bayesian Block algorithm (see Sect. 3). The vertical black lines mark the division between the three time periods (Period 1, Period 2, Period 3).

Mrk 421 is regularly monitored by telecopes of GASP-WEBT, and KVA in particular. The optical data reported in this paper relate to the period from 18th February 2007 (MJD 54 149) to 23rd July 2009 (MJD 55 035), which were recorded by the following instruments: Abastumani, Castelgrande, Crimean, L'Ampolla, Lulin, KVA, New Mexico Skies (now called iTelescopes), Sabadell, St. Petersburg, Talmassons, Torino, and Tuorla observatories. It should be mentioned that the flux measurements are corrected for the contribution of the host galaxy (see Nilsson et al. 2007) as well as for galactic extinction (Schlafly & Finkbeiner 2011).

The GASP-WEBT light curve shown in Fig. 2 includes a total of 815 observations distributed over 353 nights. When comparing the optical light curve to the γ-ray and X-ray light curves it is important to note that the optical light curve cannot be separated into different activity phases as the other light curves can be. The flux varies by the same amount throughout the whole observation length of more than two years. It can be seen that the features in the GASP-WEBT light curve are longer than and not coincident with those of the MAGIC, RXTE/ASM and *Swift*/BAT light curves.

4.4. Radio observations with Metsähovi

Radio data at 37 GHz are recorded by the 13.7 m telescope at the Metsähovi Radio Observatory in Finland (Teräsranta et al. 1998).

Considering only data points with a flux to error ratio greater than four of the Metsähovi light curve, leaves 49 nightly flux measurements between 13th February 2007 (MJD 54 144) and 24th June 2009 (MJD 55 006). The light curve is shown in Fig. 2. In comparison to the VHE γ-ray, the X-ray and the optical light curves mentioned above, the overall radio flux measured by Metsähovi is rather stable, yet with a slight decrease in Period 3.

4.5. Radio observations with OVRO

The Owens Valley Radio Observatory (OVRO), located in the USA, operates a 40 m radio telescope measuring at 15 GHz. It started observations in January 2008 and therefore does not cover the whole time span of MAGIC observations[5] (Richards et al. 2011).

In the available data set, often two observations were made during one day, which were only separated by ~2 min. These data points were averaged, which results in a total of 119 data points. The light curve with data points between 8th January 2008 (MJD 54 473) and 8th June 2009 (MJD 54 990) is shown in Fig. 2. As it occurs with the Metsähovi light curve, the flux is rather stable, with a small decrease in Period 3.

[5] www.astro.caltech.edu/ovroblazars/data/data.php

5. Multi-band flux variability

In order to quantify the variability in the emission of Mrk 421, the fractional variability $F_{\rm var}$, as it is given in Eq. (10) in Vaughan et al. (2003), is used. It is calculated using

$$F_{\rm var} = \sqrt{\frac{S^2 - \overline{\sigma_{\rm err}^2}}{\bar{x}^2}}, \quad (1)$$

and represents the normalized excess variance. S is the standard deviation and $\overline{\sigma_{\rm err}^2}$ the mean square error of the flux measurements. $\bar{x}$ stands for the average flux. The uncertainty of $F_{\rm var}$ is given by Eq. (2) in Aleksić et al. (2015c), after Poutanen et al. (2008):

$$\Delta F_{\rm var} = \sqrt{F_{\rm var}^2 + {\rm err}(\sigma_{\rm NXS}^2)} - F_{\rm var}, \quad (2)$$

where ${\rm err}(\sigma_{\rm NXS}^2)$ is given by Eq. (11) of Vaughan et al. (2003):

$${\rm err}(\sigma_{\rm NXS}^2) = \sqrt{\left(\sqrt{\frac{2}{N}} \cdot \frac{\overline{\sigma_{\rm err}^2}}{\bar{x}^2}\right)^2 + \left(\sqrt{\frac{\overline{\sigma_{\rm err}^2}}{N}} \cdot \frac{2F_{\rm var}}{\bar{x}}\right)^2}. \quad (3)$$

Here, N is the number of data points in a light curve. Note from Eq. (1) that $F_{\rm var}$ is not defined (and hence cannot be used) when the excess variance is negative, which can occur in the absence of variability, or when the instrument sensitivity is not good enough to detect it (i.e. large flux uncertainties).

$F_{\rm var}$ is calculated for all the light curves shown in Fig. 2 and the results are shown in Fig. 3 with open markers. For MAGIC, *Swift*/BAT, RXTE/ASM, Metsähovi and OVRO, the shown light curves feature one data point per night. For GASP-WEBT, the light curve contains nights with more than one data point. For the calculation of $F_{\rm var}$, the multiple GASP-WEBT optical fluxes related to single days were averaged, thus obtaining a single value.

In order to improve the direct comparison of the variability determined for the various energy bands, we also computed $F_{\rm var}$ using only the multi-instrument observations that are strictly simultaneous to those performed by MAGIC. These $F_{\rm var}$ values are depicted by the filled markers in Fig. 3, and remove potential biases due to the somewhat different temporal coverage of the various instruments.

The overall behaviour of the fractional variability shows a rising tendency with increasing frequency. Considering only the $F_{\rm var}$ values determined with simultaneous multi-instrument observations (filled markers in Fig. 3), the highest variability occurs in the VHE γ-ray band measured by MAGIC ($F_{\rm var} = 0.64 \pm 0.01$), although it is quite similar to the variability measured in the soft X-ray band ($F_{\rm var} = 0.50 \pm 0.01$) and hard X-ray band ($F_{\rm var} = 0.54 + \pm 0.02$) by RXTE/ASM and *Swift*/BAT respectively.

As mentioned in the previous sections (e.g. see Fig. 2), the overall flux levels and source activity appear different for the three different observation periods. Figure 4 reports the multi-band fractional variability determined separately for Periods 1, 2 and 3. The main trend observed in the 2.3 yr long time span reported in Fig. 3 is also reproduced when splitting the data in the three different periods: $F_{\rm var}$ always increases with energy, with the highest variability occurring in the X-ray and VHE γ-ray bands. The *Swift*/BAT light curve with one-day temporal bins reported in Fig. 2 has large statistical uncertainties, that, because of the relatively low activity and low variability of Mrk 421 during Periods 1 and 3, yielded a negative excess variance, hence preventing the calculation of the fractional variability for these two periods. On the other hand, the RXTE/ASM light curve with one-day temporal bins reported in Fig. 2 have somewhat smaller uncertainties and a better temporal coverage than that of *Swift*/BAT, which permitted the quantification of the fractional variability in the soft X-ray energy band for the three temporal periods considered.

In Fig. 4 it can also be seen that the variability for the MAGIC light curve is higher for Period 2 than in Periods 1 and 3 as it was already shown by the quantification of the variability with the results of the Bayesian Block algorithm (see Sect. 3). Due to the lower average flux in Period 1 compared to Period 3, the fractional variability in Period 1 is higher than in Period 3.

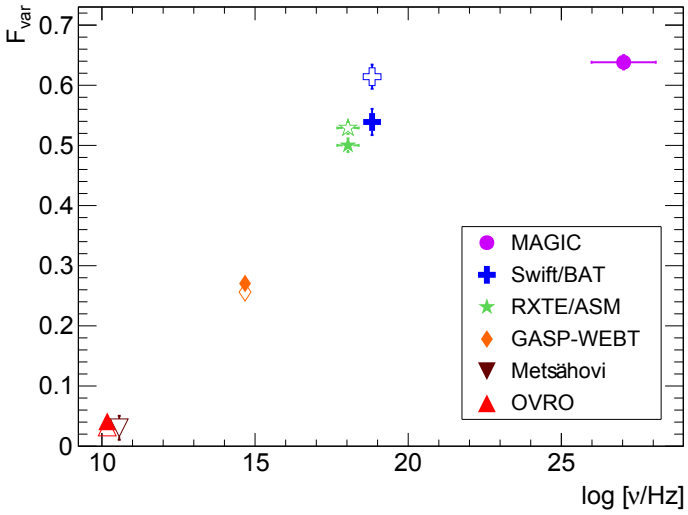

Fig. 3. Fractional variability ($F_{\rm var}$) as a function of the frequency for the 2.3 yr long time range from February 2007 to July 2009. The fractional variability was computed in two different ways: using all the flux measurements from the light curves reported in Fig. 2 (depicted with open markers), and using only those observations simultaneous to the VHE γ-ray measurements from MAGIC (depicted with filled markers). Vertical bars denote 1σ uncertainties and horizontal bars indicate the width of each energy bin.

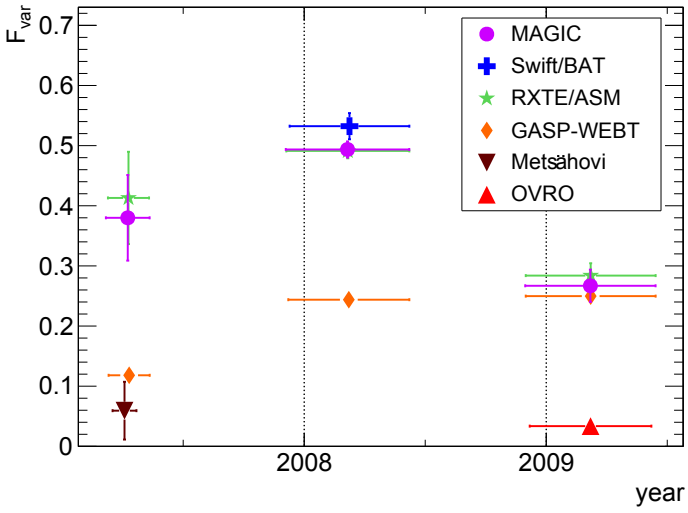

Fig. 4. Multi-instrument fractional variability ($F_{\rm var}$) for the three periods defined in Fig. 2. The fractional variability was computed using only those observations simultaneous to the VHE γ-ray measurements from MAGIC. Vertical bars denote 1σ uncertainties and horizontal bars indicate the covered time span of each instrument.

It is worth noticing that the fractional variability in the optical band is comparable to that at X-rays and VHE γ-rays during Period 3, which did not happen during Periods 1 and 2. Inspecting the light curves reported in Fig. 2, one can see that the timescales involved in the reported variabilities are very different. While the X-ray and VHE γ-ray light curves show day-long flux variations on the top of a rather stable flux level, the optical flux shows many-day-long flux variations on the top of a flux level that increases by about a factor of two throughout Period 3. Therefore, despite the very comparable $F_{\rm var}$ values during Period 3, the emission in the optical band is probably not related to that in the X-ray and VHE γ-ray bands.

These results are consistent with results from previous publications. This includes the rising fractional variability of Mrk 421 from optical to X-ray energies in 2001 (Giebels et al. 2007) and the same increase from optical to X-ray energies in March 2010 during a flare with a comparable variability of the VHE and the X-ray light curves (Aleksić et al. 2015b). These results are complemented by Aleksić et al. (2015a) and Baloković et al. (2016), which presented multi-wavelength data during the relatively low activity observed from January to June 2009 and from January to March 2013 respectively. These include results from the *Fermi*-LAT closing the gap between the X-ray and TeV γ-ray energy bands. They report a low flux in radio energies, rising to a maximum in the X-ray energy band. For GeV γ-rays measured by the *Fermi*-LAT the variability drops to a level comparable to the optical and UV wave band. The variability in the TeV γ-ray light curves increases to a level comparable to X-rays, which is consistent with the result from this study, that uses a much larger time span.

6. Multi-band correlations

To quantify the correlation of two light curves, the discrete correlation function (DCF), which was introduced by Edelson & Krolik (1988), is used here. A study of the correlations of the MAGIC light curve with light curves of other wavelengths has already been carried out for Mrk 421 for the first half of 2009 in Aleksić et al. (2015a). In that publication a method to determine confidence intervals for the resulting correlation is described in detail. Here, a short introduction to the method will be given. For more detailed information on that method the reader is referred to the cited publication and references therein.

The errors of the DCF values as stated by Edelson & Krolik (1988) might not be appropriate when the individual light-curve data points are correlated red-noise data (Uttley et al. 2003). Red-noise data are characterized by a power spectral density per unit of bandwidth proportional to $1/f^2$, where f is the frequency (Chatterjee et al. 2012). Since this is not the case for the given light curves, a Monte Carlo based approach is applied here to determine confidence intervals for the DCF values. Therefore, 1000 light curves are simulated for each telescope which feature the same sampling pattern and comparable exposure times as the original light curve. In addition, the power spectral density (PSD) should be as similar as possible to the PSD of the original light curve. Therefore, the light curves are simulated with PSDs following a power law with spectral indices in a range from -1.0 to -2.9 in steps of 0.1. The light curves with the PSD which match the PSD of the original light curve best, are determined using the PSRESP method (Chatterjee et al. 2008).

The DCF itself is calculated for sets of original light curves. With the calculated DCF of 1000 simulated light curves of one telescope and the original light curve of a second telescope, finally the confidence bands can be determined. Here, the confidence limits are determined as the 1%, 5%, 95% and 99% quantiles of the 1000 resulting DCFs.

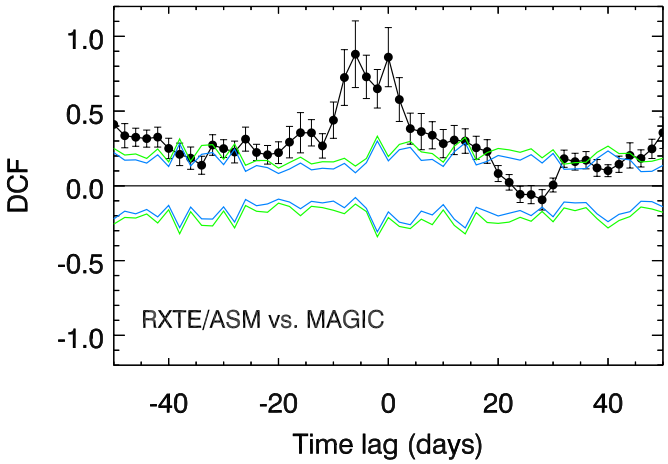

Fig. 5. Discrete correlation function for the light curves of RXTE/ASM and MAGIC for the 2.3 yr long period (Period 1, 2 and 3). Time lags from -50 to $+50$ days in steps of two days are considered. Black dots represent the DCF values with the error bars calculated as in Edelson & Krolik (1988). The green (blue) lines represent the 99% and 1% (95% and 5%) confidence limits for random correlations resulting from the dedicated Monte Carlo analysis described in Sect. 6.

In the following plots, the black dots and error bars are the DCF and its error calculated after Edelson & Krolik (1988). The blue and green lines represent the confidence limits of 95% and 5% and of 99% and 1% respectively determined with DCFs of the 1000 simulated light curves of the first telescope and the original light curve of the second telescope. A value above the 99% confidence limit is considered as a significant correlation, a significant anti-correlation is given for a value below the 1% limit.

A binning of two days is chosen in this case. The reason for this is the unequal binning of the light curves which might lead to shifts in the correlations by one day when the time difference in the two light curves is larger than half a day. Time lags between -50 and $+50$ days are examined. The time lag Δt is defined as the time difference of the second light curve to the first light curve (Instrument$_1$ vs. Instrument$_2$).

In the following subsections we report the results from our study on the correlation between the optical, X-ray and VHE γ-ray bands. The radio bands do not show significant variability and hence the radio fluxes cannot be correlated to the fluxes in the other bands.

6.1. RXTE/ASM and MAGIC

The RXTE/ASM and MAGIC cross-correlations were examined at first for the whole time range from February 2007 to June 2009. This is reported in Fig. 5.

There is positive and significant correlation for the entire range of time lags considered, that is from -50 to $+50$ days. The main cause of this positive correlation is the substantially larger flux level in Period 2, compared with that in Periods 1 and 3. If the light curves are shifted by a time lag smaller than the duration of these periods (e.g. 50 days), the pairing of VHE γ-ray fluxes and X-ray fluxes occurs always (for all time lags) within the observations from the same period, and hence one gets high VHE flux values related to high X-ray flux values, that is all from Period 2, and low VHE flux values matched with low X-ray flux

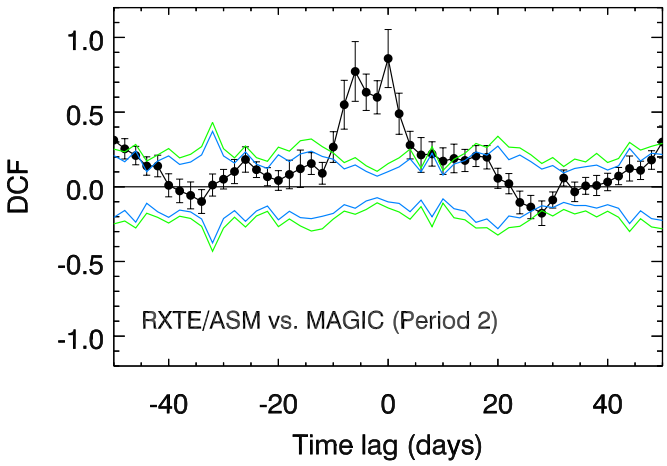

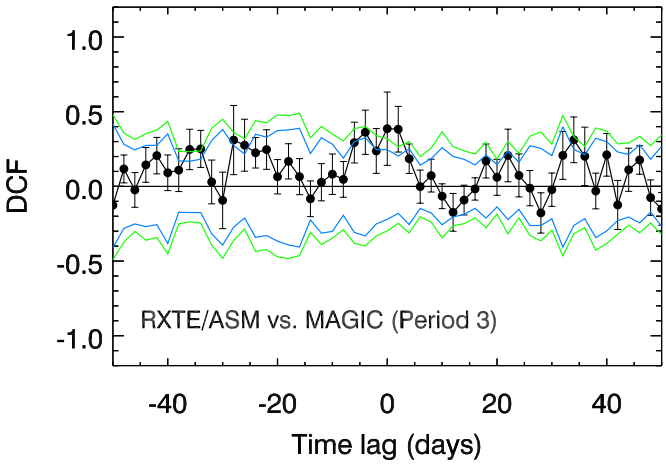

Fig. 6. Discrete correlation function for the light curves of RXTE/ASM and MAGIC for Period 2 (*top*) and for Period 3 (*bottom*). The description of data points and contours are given in the caption of Fig. 5.

values, that is all from Periods 1 and 3. And this effect naturally produces a positive correlation.

To remove the effect of the substantially different flux levels between the different periods, as well as to test the influence of the different states of activity and flux strength reported in the previous sections, the DCF is determined separately for Periods 2 and 3. The MAGIC light curve in the quiet Period 1 contains only six data points and is therefore not included in this study. The results are shown in Fig. 6. We note that there is still an overall positive correlation for both Periods 2 and 3, however the DCF values are typically within the 95% confidence contours. This positive (but not significant) correlation for all time lags is due to the fact that the two light curves considered here have the same overall trends: in Period 2 the VHE γ-ray and the X-ray light curves show an overall flux increase throughout the entire period, whereas in Period 3 they both show an overall decrease.

The quiet Period 3 shows a marginally significant correlation around a time lag of zero, while the active Period 2 shows a prominent correlation, with some structure around a time lag of zero. The DCF structure depicted in the top panel of Fig. 6 resembles that in Fig. 5, which indicates that the correlations in the high-activity Period 2 dominate the DCF values reported in Fig. 5, that relate to the full 2.3 yr time interval. In both

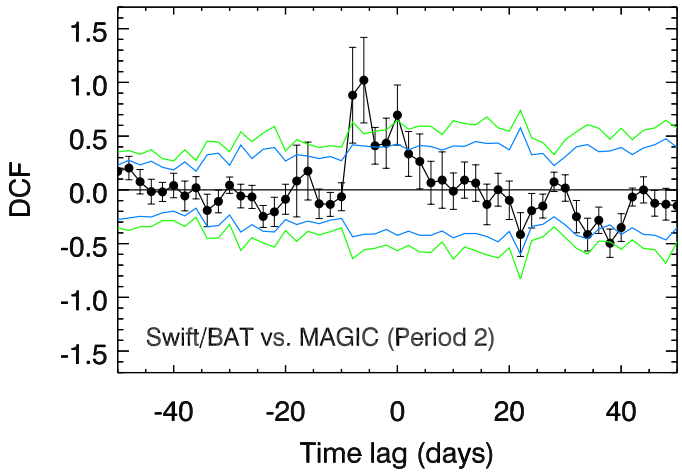

Fig. 7. Discrete correlation function for the light curves of *Swift*/BAT and MAGIC for Period 2. The description of data points and contours are given in the caption of Fig. 5.

cases, one finds a peak at $\Delta t = 0$ and $\Delta t = -6$ days. The first peak is due to the direct correlation dominated by simultaneous prominent features in both light curves (i.e. flares on MJD 54 556 and 54 622). On the other hand, the DCF peak at -6 days is dominated by the remarkable three-day long X-ray flaring activity around MJD 54 630, which is the highest flux value in the RXTE/ASM light curve. There is no counterpart in the VHE γ-ray light curve because MAGIC did not observe around that date, but this prominent X-ray flaring activity is matched with the large VHE flaring activity around MJD 54 622 for time lags of around -6 days. The relatively broad structure of positive DCF values, extending from -10 days to $+6$ days, is dominated by the remarkable and asymmetric flaring activity in the X-ray light curve in a broad region around MJD 54 556, which is coincident with the relatively short VHE flare at the same location.

6.2. *Swift*/BAT and MAGIC

The sensitivity and temporal coverage of *Swift*/BAT is somewhat lower than that of RXTE/ASM, which reduces the accuracy with which one can study the correlation between the hard X-ray band above 15 keV and the VHE γ-rays. For Period 3, we could only find a marginally significant correlation dominated by the somewhat higher X-ray and VHE flux values in the MJD range from 54 858 to 54 864. In Fig. 7 the correlation results of the *Swift*/BAT and the MAGIC light curves in the high-activity Period 2 are shown. When considering this period, we find DCF values above the 95% confidence level for time lags between -8 days and $+2$ days, with two peaks above the 99% confidence level for the time lags of 0, and also -8 and -6 days. The explanation of these two peaks is essentially the same as was given for the correlations between RXTE/ASM and MAGIC reported in Sect. 6.1. The peak at $\Delta t = 0$ is dominated by several features appearing simultaneously in both light curves, the peak at -6 to -8 days is dominated by the large three-day long X-ray activity around MJD 54 630 (where we do not have MAGIC observations), and the broad and somewhat asymmetric structure in the DCF plot is dominated by the large and broad and asymmetric X-ray flaring around MJD 54 556.

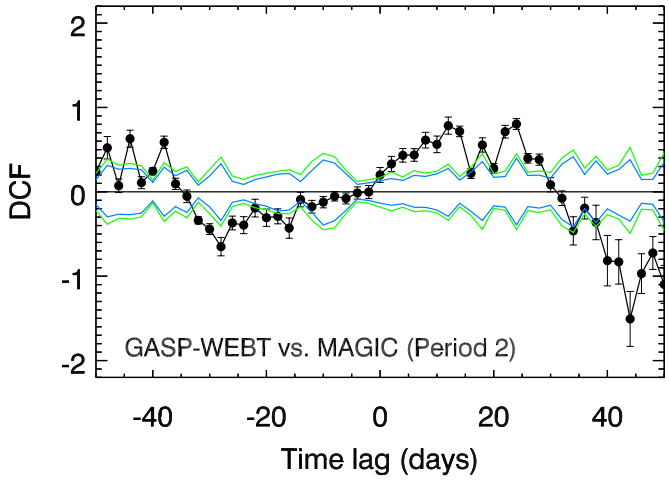

Fig. 8. Discrete correlation function for the light curves of GASP-WEBT and MAGIC for Period 2. The description of data points and contours are given in the caption of Fig. 5.

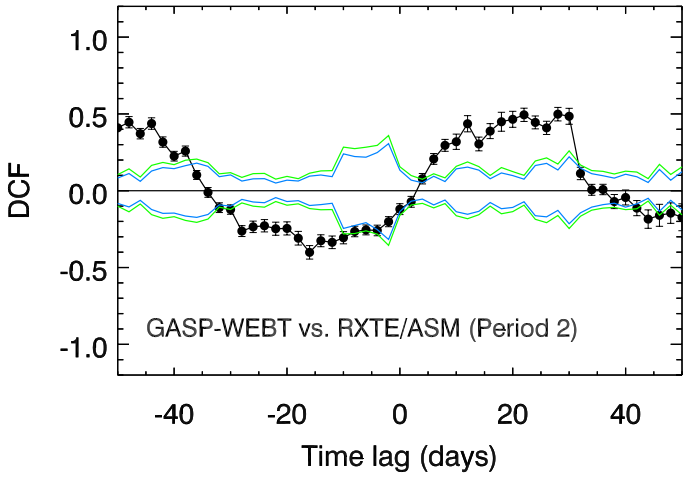

Fig. 9. Discrete correlation function for the light curves of GASP-WEBT and RXTE/ASM for Period 2. The description of data points and contours are given in the caption of Fig. 5.

6.3. GASP-WEBT and MAGIC

The correlation between the GASP-WEBT and MAGIC light curve for the high-activity Period 2 is shown in Fig. 8. There is a positive correlation for time lags between 0 and +28 days, as well as around −44 days, and a negative correlation for time lags around −28 and around +44 days. This alternation of correlation and anti-correlation is caused by the fact that the variability in the optical and VHE emission is dominated by two to three prominent features. And hence the alternating presence of rises and drops in flux in both light curves creates these features in the DCF. For instance, when shifting the optical light curve by e.g. +24 days or −44 days, minima and maxima in the two light curves become aligned yielding a significant correlation, while when the optical light curve is shifted by −28 or +44 days, the minima in one light curve are aligned with maxima in the other light curve, hence yielding a significant anti-correlation. Although the reported correlations for some time lags are significant from the statistical point of view, they are based on the alignment or misalignment of only two to three prominent and relatively broad features, and these prominent features are not necessarily related to each other.

In the quiet Period 3, we find an overall anti-correlation during the entire range of time lags proved. This result is produced by the overall flux decrease in the VHE light curve and the overall flux increase in the optical light curve throughout the entire Period 3. The same result was reported and discussed in Aleksić et al. (2015a).

6.4. GASP-WEBT and RXTE/ASM

The DCF results of GASP-WEBT and RXTE/ASM in Period 2 are shown in Fig. 9. A correlation is seen for positive time lags between +6 and +30 days, as well as for negative time lags between −50 and −38 days. Anti-correlations are seen between −28 and −10 days and between +44 and +50 days. These results are comparable to the results between GASP-WEBT and MAGIC. This again shows the alternation of rises and drops in flux produced by the fact that the variability in the optical and X-ray emission is dominated by only two to three prominent features. When shifting the optical light curve by the time lags, for which correlations are found, maxima in both light curves are aligned. When shifting the light curve by the time lags, for which anti-correlations are found, minima in the optical light curve are aligned with maxima in the X-ray light curves. Again, these correlations and anti-correlations might have been found by chance.

In Period 1 no correlations nor anti-correlations are seen for this pair of instruments. However, in Period 3 the GASP-WEBT light curve shows an overall anti-correlation with the RXTE/ASM light curve, which occurs due to the overall slow decrease of the X-ray rate and the flux increase in the optical light curve. This result is comparable to the overall anti-correlation for the X-ray and TeV γ-ray light curves discussed in Aleksić et al. (2015a), which used a part of the data set used in this paper.

7. Summary of results

i) Between March 2007 and June 2009, MAGIC-I accumulated 96 h of VHE γ-ray data of the blazar Mrk 421: the VHE flux varied around the typical flux baseline of about 0.5 CU, with the highest flux of about 3.8 CU occurring during the active state in 2008.

ii) For the first time the Bayesian Block algorithm was applied to the VHE γ-ray light curve from a Cherenkov telescope to identify different flux emission states, as well as to quantify the variability and to search for flaring activity.

iii) The MAGIC γ-ray light curve was compared to light curves of other wavebands, including the hard and soft X-ray wavebands from *Swift*BAT and RXTE/ASM, the optical *R*-band from GASP-WEBT, and two radio wavebands from Metsähovi and OVRO.

iv) The VHE and X-ray light curves resemble each other, showing a number of few-day long structures, while the optical and radio light curves show smaller flux variations and occurring on longer timescales.

v) The fractional variability is low for radio and optical wavebands, and high for the X-ray and VHE γ-ray bands during both low and high activity.

vi) The discrete correlation function shows a direct relation between the two X-ray bands and the VHE γ-ray band, while no correlation was found between the optical and the X-ray and VHE bands.

8. Discussion and conclusions

We have peformed a comprehensive variability and correlation study with 2.3 yr of multi-band data from Mrk 421. The measured variability as a function of energy, with the highest variability in the X-ray and VHE bands, and the observed direct X-ray-to-VHE correlation, both occuring comparably during high- and low-activity, suggests that the processes that dominate the flux variability in Mrk 421 are similar for the different activity levels. The pattern characterized by a high variability in the X-ray and γ-ray emission, accompanied by a low variability in the optical and radio emission, occurs in both quiescent and excited states, qualifying this behaviour as typical of Mrk 421. The low variability and different timescales observed both in the radio and optical emission may be explained by different emission regions, or by cooler electrons in the jet at a later time. Additionally, the correlation between the X-ray and the VHE γ-ray emission extending over many months suggests that the broadband emission of Mrk 421 is predominantly produced by the same particles, for example via the SSC process. Alternatively, the X-rays and γ-rays could both result from the same radiation process (e.g. synchrotron radiation), but from two different electron populations varying together most of the time, but not necessarily always. This is the case in hadronic scenarios where the X-ray and γ-ray photons result from the synchrotron radiation of electrons in subsequent and therefore coupled cascade generations (Mannheim 1993). The cascade generations are driven by the pair production in photon-photon scatterings involving low-energy photon fields, which can vary themselves, thereby modulating the variations of flux of the primary photo-mesons at the top of the cascades.

Acknowledgements. We would like to thank the Instituto de Astrofísica de Canarias for the excellent working conditions at the Observatorio del Roque de los Muchachos in La Palma. The financial support of the German BMBF and MPG, the Italian INFN and INAF, the Swiss National Fund SNF, the ERDF under the Spanish MINECO (FPA2012-39502), and the Japanese JSPS and MEXT is gratefully acknowledged. This work was also supported by the Centro de Excelencia Severo Ochoa SEV-2012-0234, CPAN CSD2007-00042, and MultiDark CSD2009-00064 projects of the Spanish Consolider-Ingenio 2010 programme, by grant 268740 of the Academy of Finland, by the Croatian Science Foundation (HrZZ) Project 09/176 and the University of Rijeka Project 13.12.1.3.02, by the DFG Collaborative Research Centers SFB823/C4 and SFB876/C3, and by the Polish MNiSzW grant 745/N-HESS-MAGIC/2010/0. The public data archives of *Swift*/BAT and RXTE/ASM are acknowledged. We thank the OVRO telescope for making its results available for the public. The OVRO 40 m monitoring program is supported in part by NASA grants NNX08AW31G and NNX11A043G, and NFS grants AST-0808050 and AST-1109911. We also thank the KVA and Metsähovi telescopes for making their light curves available. M. Villata organized the optical-to-radio observations by GASP-WEBT as the president of the collaboration. The Metsähovi team acknowledges the support from the Academy of Finland to our observing projects (numbers 212656, 210338, 121148, and others). St. Petersburg University team acknowledges support from Russian RFBR grant 15-02-00949 and St. Petersburg University research grant 6.38.335.2015. The Abastumani Observatory team acknowledges financial support by the Shota Rustaveli National Science Foundation under contract FR/577/6-320/13.

References

Abdo, A. A., Ackermann, M., Ajello, M., et al. 2011, ApJ, 736, 131
Acciari, V. A., Aliu, E., Aune, T., et al. 2009, ApJ, 703, 169
Acciari, V. A., Aliu, E., Arlen, T., et al. 2011, ApJ, 738, 25
Acciari, V. A., Arlen, T., Aune, T., et al. 2014, Astropart. Phys., 54, 1
Albert, J., Aliu, E., Anderhub, H., et al. 2007, ApJ, 663, 125
Albert, J., Aliu, E., Anderhub, H., et al. 2008, ApJ, 674, 1037
Aleksić, J., Alvarez, E. A., Antonelli, L. A., et al. 2012, A&A, 542, A100
Aleksić, J., Ansoldi, S., Antonelli, L. A., et al. 2015a, A&A, 576, A126
Aleksić, J., Ansoldi, S., Antonelli, L. A., et al. 2015b, A&A, 578, A22
Aleksić, J., Ansoldi, S., Antonelli, L. A., et al. 2015c, A&A, 573, A50
Aleksić, J., Ansoldi, S., Antonelli, L. A., et al. 2016a, Astropart. Phys., 72, 61
Aleksić, J., Ansoldi, S., Antonelli, L. A., et al. 2016b, Astropart. Phys., 72, 76
Aliu, E., Anderhub, H., Antonelli, L. A., et al. 2009, Astropart. Phys., 30, 293
Baloković, M., Paneque, D., Madejski, G., et al. 2016, ApJ, 819, 156
Bartoli, B., Bernardini, P., Bi, X. J., et al. 2011, ApJ, 734, 110
Błażejowski, M., Blaylock, G., Bond, I. H., et al. 2005, ApJ, 630, 130
Buckley, J. H., Akerlof, C. W., Biller, S., et al. 1996, ApJ, 472, L9
Cao, G., & Wang, J. 2013, PASJ, 65, 109
Chatterjee, R., Jorstad, S. G., Marscher, A. P., et al. 2008, ApJ, 689, 79
Chatterjee, R., Bailyn, C. D., Bonning, E. W., et al. 2012, ApJ, 749, 191
Cui, W. 2004, ApJ, 605, 662
Donnarumma, I., Vittorini, V., Vercellone, S., et al. 2009, ApJ, 691, L13
Edelson, R. A., & Krolik, J. H. 1988, ApJ, 333, 646
Fomin, V. P., Stepanian, A. A., Lamb, R. C., et al. 1994, Astropart. Phys., 2, 137
Fossati, G., Buckley, J., Edelson, R. A., Horns, D., & Jordan, M. 2004, New Astron., 48, 419
Fossati, G., Buckley, J. H., Bond, I. H., et al. 2008, ApJ, 677, 906
Gaidos, J. A., Akerlof, C. W., Biller, S., et al. 1996, Nature, 383, 319
Giebels, B., Dubus, G., & Khélifi, B. 2007, A&A, 462, 29
Horan, D., Acciari, V. A., Bradbury, S. M., et al. 2009, ApJ, 695, 596
Hovatta, T., Petropoulou, M., Richards, J. L., et al. 2015, MNRAS, 448, 3121
Katarzyński, K., Sol, H., & Kus, A. 2003, A&A, 410, 101
Krimm, H. A., Holland, S. T., Corbet, R. H. D., et al. 2013, ApJS, 209, 14
Levine, A. M., Bradt, H., Cui, W., et al. 1996, ApJ, 469, L33
Lico, R., Giroletti, M., Orienti, M., et al. 2014, A&A, 571, A54
Macomb, D. J., Akerlof, C. W., Aller, H. D., et al. 1995, ApJ, 449, L99
Mannheim, K. 1993, A&A, 269, 67
Max-Moerbeck, W., Hovatta, T., Richards, J. L., et al. 2014, MNRAS, 445, 428
Nilsson, K., Pasanen, M., Takalo, L. O., et al. 2007, A&A, 475, 199
Piner, B. G., Unwin, S. C., Wehrle, A. E., et al. 1999, ApJ, 525, 176
Poutanen, J., Zdziarski, A. A., & Ibragimov, A. 2008, MNRAS, 389, 1427
Punch, M., Akerlof, C. W., Cawley, M. F., et al. 1992, Nature, 358, 477
Richards, J. L., Max-Moerbeck, W., Pavlidou, V., et al. 2011, ApJS, 194, 29
Scargle, J. D. 1998, ApJ, 504, 405
Scargle, J. D., Norris, J. P., Jackson, B., & Chiang, J. 2013, ApJ, 764, 167
Schlafly, E. F., & Finkbeiner, D. P. 2011, ApJ, 737, 103
Takalo, L. O., Nilsson, K., Lindfors, E., et al. 2008, in AIP Conf. Ser. 1085, eds. F. A. Aharonian, W. Hofmann, & F. Rieger, 705
Teräsranta, H., Tornikoski, M., Mujunen, A., et al. 1998, A&AS, 132, 305
Tluczykont, M., Bernardini, E., Satalecka, K., et al. 2010, A&A, 524, A48
Uttley, P., Edelson, R., McHardy, I. M., Peterson, B. M., & Markowitz, A. 2003, ApJ, 584, L53
Vaughan, S., Edelson, R., Warwick, R. S., & Uttley, P. 2003, MNRAS, 345, 1271
Villata, M., Raiteri, C. M., Larionov, V. M., et al. 2008, A&A, 481, L79
Zanin, R., Carmona, E., Sitarek, J., et al. 2013, in Proc. 33rd International Cosmic Ray Conference (Rio de Janeiro, Brazil)

[1] ETH Zurich, 8093 Zurich, Switzerland
[2] Università di Udine, and INFN Trieste, 33100 Udine, Italy
[3] INAF National Institute for Astrophysics, 00136 Rome, Italy
[4] Università di Siena, and INFN Pisa, 53100 Siena, Italy
[5] Croatian MAGIC Consortium, Rudjer Boskovic Institute, University of Rijeka, University of Split and University of Zagreb, Croatia
[6] Saha Institute of Nuclear Physics, 1/AF Bidhannagar, Salt Lake, Sector-1, 700064 Kolkata, India
[7] Max-Planck-Institut für Physik, 80805 München, Germany
[8] Universidad Complutense, 28040 Madrid, Spain
[9] Inst. de Astrofísica de Canarias, 38200 La Laguna; Universidad de La Laguna, Dpto. Astrofísica, 38206 La Laguna, Tenerife, Spain
[10] University of Łódź, 90236 Lodz, Poland
[11] Deutsches Elektronen-Synchrotron (DESY), 15738 Zeuthen, Germany
[12] Institut de Fisica d'Altes Energies (IFAE), The Barcelona Institute of Science and Technology, Campus UAB, 08193 Bellaterra (Barcelona), Spain
[13] Universität Würzburg, 97074 Würzburg, Germany
[14] Università di Padova and INFN, 35131 Padova, Italy
[15] Institute for Space Sciences (CSIC/IEEC), 08193 Barcelona, Spain
[16] Technische Universität Dortmund, 44221 Dortmund, Germany
[17] Unitat de Física de les Radiacions, Departament de Física, and CERES-IEEC, Universitat Autònoma de Barcelona, 08193 Bellaterra, Spain
[18] Universitat de Barcelona, ICC, IEEC-UB, 08028 Barcelona, Spain
[19] Japanese MAGIC Consortium, ICRR, The University of Tokyo, Department of Physics and Hakubi Center, Kyoto University, Tokai University, The University of Tokushima, KEK, Japan

[20] Finnish MAGIC Consortium, Tuorla Observatory, University of Turku and Astronomy Division, University of Oulu, 90014 Oulu, Finland
[21] Inst. for Nucl. Research and Nucl. Energy, 1784 Sofia, Bulgaria
[22] Università di Pisa, and INFN Pisa, 56126 Pisa, Italy
[23] ICREA and Institute for Space Sciences (CSIC/IEEC), 08193 Barcelona, Spain
[24] Centro Brasileiro de Pesquisas Físicas (CBPF/MCTI), R. Dr. Xavier Sigaud, 150 – Urca, 22290-180 Rio de Janeiro, Brazil
[25] NASA Goddard Space Flight Center, Greenbelt, MD 20771; and Department of Physics and Department of Astronomy, University of Maryland, College Park, MD 20742, USA
[26] Humboldt University of Berlin, Institut für Physik Newtonstr. 15, 12489 Berlin, Germany
[27] École polytechnique fédérale de Lausanne (EPFL), Lausanne, Switzerland
[28] Japanese MAGIC Consortium, Kyoto, Japan
[29] Finnish Centre for Astronomy with ESO (FINCA), Turku, Finland
[30] INAF-Trieste, 34143 Trieste, Italy
[31] ISDC – Science Data Center for Astrophysics, 1290 Versoix (Geneva), Switzerland
[32] Astron. Inst., St.-Petersburg State Univ., 198504 St. Petersbourg, Russia
[33] University of Crete, Heraklion, Greece
[34] Graduate Institute of Astronomy, National Central University, 300 Zhongda Rd, 32001 Zhongli, Taoyuan, Taiwan
[35] Pulkovo Observatory, 196140 St.-Petersburg, Russia
[36] Agrupació Astronòmica de Sabadell, 08206 Sabadell, Barcelona, Spain
[37] Aalto University Metsähovi Radio Observatory, Metsähovintie 114, 02540 Kylmälä, Finland
[38] School of Cosmic Physics, Dublin Institute For Advanced Studies, Dublin 2, Ireland
[39] Abastumani Observatory, Mt. Kanobili, 0301 Abastumani, Georgia
[40] Engelhardt Astronomical Observatory, Kazan Federal University, Tatarstan, Russia
[41] Aalto University Department of Radio Science and Engineering, PO BOX 13000, 00076 Aalto, Finland
[42] Circolo Astrofili Talmassons, via Cadorna, 57, 33030 Talmassons, Italy
[43] School of Physics, University College Dublin, Belfield, Dublin 4, Ireland
[44] INAF–Osservatorio Astrofisico di Torino, 10025 Pino Torinese (TO), Italy
[45] Department of Physics, University of Colorado, Denver, CO 80217-3364, USA

The Astronomical Journal, 151:170 (8pp), 2016 June doi:10.3847/0004-6256/151/6/170

DISCOVERY OF AN X-RAY-EMITTING CONTACT BINARY SYSTEM 2MASS J11201034−2201340

Chin-Ping Hu[1,2], Ting-Chang Yang[2], Yi Chou[2], L. Liu[3], S.-B. Qian[3], C. Y. Hui[4], Albert K. H. Kong[5], L. C. C. Lin[6], P. H. T. Tam[7], K. L. Li[8], Chow-Choong Ngeow[2], W. P. Chen[2], and Wing-Huen Ip[2]
[1] Department of Physics, University of Hong Kong, Pokfulam Road, Hong Kong; cphu@hku.hk
[2] Graduate Institute of Astronomy, National Central University, Jhongli 32001, Taiwan; yichou@astro.ncu.edu.tw
[3] Yunnan Observatories, Chinese Academy of Sciences, P.O. Box 110, 650011 Kunming, China
[4] Department of Astronomy and Space Science, Chungnam National University, Daejeon, Korea
[5] Institute of Astronomy and Department of Physics, National Tsing Hua University, Hsinchu, Taiwan
[6] Institute of Astronomy and Astrophysics, Academia Sinica, Taiwan
[7] Institute of Astronomy and Space Science, Sun Yat-Sen University, Guangzhou 510275, China
[8] Department of Physics and Astronomy, Michigan State University, East Lansing, MI 48824-2320, USA
Received 2015 December 2; accepted 2016 April 17; published 2016 June 1

ABSTRACT

We report the detection of orbital modulation, a model solution, and the X-ray properties of a newly discovered contact binary, Two Micron All Sky Survey (2MASS) J11201034−2201340. We serendipitously found this X-ray point source outside the error ellipse when searching for possible X-ray counterparts of γ-ray millisecond pulsars among the unidentified objects detected by the *Fermi Gamma-ray Space Telescope*. The optical counterpart of the X-ray source (unrelated to the γ-ray source) was then identified using archival databases. The long-term Catalina Real-Time Transient Survey detected a precise signal with a period of $P = 0.28876208(56)$ days. A follow-up observation made by the Super Light Telescope of Lulin Observatory revealed the binary nature of the object. Utilizing archived photometric data of multi-band surveys, we construct the spectral energy distribution (SED), which is well fit by a K2V spectral template. The fitting result of the orbital profile using the Wilson–Devinney code suggests that 2MASS J11201034-2201340 is a short-period A-type contact binary and the more massive component has a cool spot. The X-ray emission was first noted in observations made by *Swift*, and then further confirmed and characterized by an *XMM-Newton* observation. The X-ray spectrum can be described by a power law or thermal Bremsstrahlung. Unfortunately, we could not observe significant X-ray orbital modulation. Finally, according to the SED, this system is estimated to be 690 pc from Earth with a calculated X-ray intensity of $(0.7 - 1.5) \times 10^{30}$ erg s^{-1}, which is in the expected range of an X-ray emitting contact binary.

Key words: binaries: close – binaries: eclipsing – stars: individual (2MASS J11201034-2201340) – X-rays: stars

1. INTRODUCTION

A W UMa-type system is a contact binary system where both components share a common envelope and are typical main-sequence stars with similar surface temperatures. Astronomers have been aware of the optical variability of prototypical W UMa-type systems for more than a century (Müller & Kempf 1903). To date, thousands of known W UMa-type variables have been found. The spectral type of this kind of system usually ranges from A to K, with a period that ranges from 0.2 to 1.4 days and variability amplitudes typically less than 1 mag. Contact binaries can be further classified into two major types: A and W (Binnendijk 1970). The primary minimum in the folded light curve of an A-type contact binary is caused by the less massive component transiting the more massive one; otherwise, the contact binary is a W-type. In general, an A-type system has a relatively longer orbital period ($P \gtrsim 0.3$ day), a lower mass ratio ($q \lesssim 0.3$), and an earlier spectral type (typically from A to G). On the other hand, a W-type system usually has a later spectral type. A- and W-type contact binaries are possibly related with respect to their evolution. For example, Hilditch et al. (1988) suggested that a W-type system evolves to an A-type system; however, Gazeas & Niarchos (2006) proposed an opposite evolutionary track.

W UMa-type systems are expected to have high chromospheric activity and coronal emission; hence, some systems are strong X-ray emitters, e.g., VW Cep (Carroll et al. 1980; Huenemoerder et al. 2006). The strength of the X-ray emission is related to the binary orbital period and the spectral type (Stępień et al. 2001; Chen et al. 2006). Chromospheric activity is related to the presence of cool spots, which cause asymmetry, known as the O'Connell effect (O'Connell 1951; Wilsey & Beaky 2009), in the orbital profile. In addition, the variability of the Hα equivalent width along with the orbital phase is an indication of chromospheric activity (Kaszas et al. 1998). A detailed investigation of the X-ray timing and spectral variability, as occurred with the brightest contact binary VW Cep (Huenemoerder et al. 2006), can reveal the position and geometry of the corona.

We present the detection of the contact binary 2MASS J11201034−2201340 in the X-ray, optical, and infrared bands in Section 2. Section 3 presents the results of optical band analysis, including the determination of the orbital period and the spectral energy distribution (SED). We also present the photometric solution to determine the basic physical parameters of this system, utilizing orbital profile fitting. Section 4 presents X-ray timing and spectral behaviors determined from the results of X-ray data analysis, e.g., the non-detection of orbital modulation and the non-thermal spectral nature. We also estimate X-ray intensity and discuss the relationship between X-ray and optical luminosities. Finally, we summarize our results and future aspects in Section 5.

2. SOURCE DETECTION

2.1. Swift Observations

After the detection of 1FGL J1119.9−2205 (also named 2FGL J1120.0−2204 and 3FGL J1119.9−2204), the *Swift XRT*

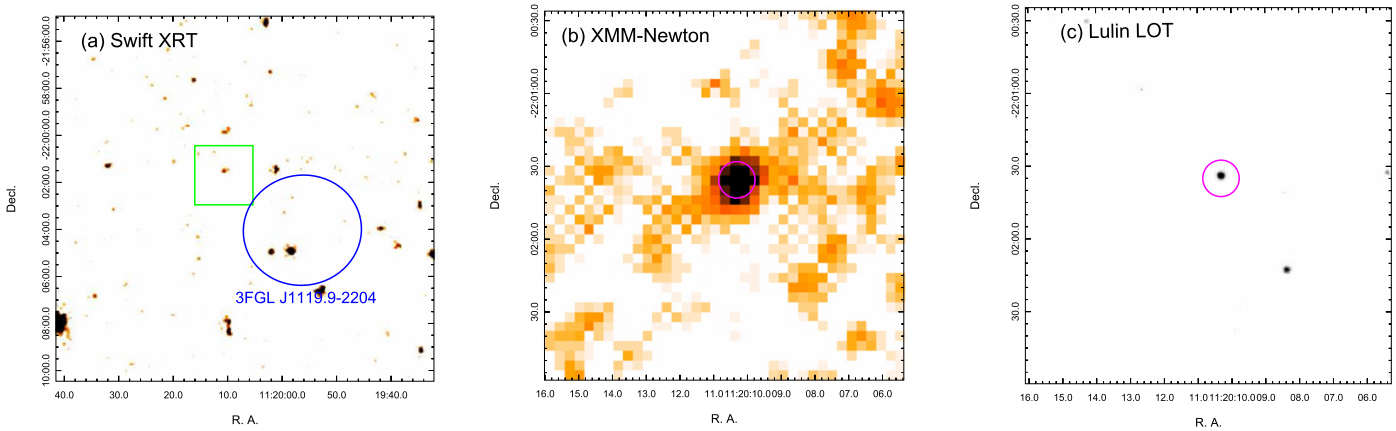

Figure 1. (a) *Swift* image of the field containing 2MASS J11201034−2201340 and 3FGL J1119.9−2204. This image is smoothed with a Gaussian kernel of $\sigma = 3''$ to enhance the visibility of faint sources. The blue circle encompasses the 95% error ellipse of 3FGL J1119.9−2204 and the green box is the region of the cropped *XMM-Newton* and Lulin LOT r'-band images in the center and right panels, respectively. (b) Enlarged view of the *XMM-Newton* image. The center of the cyan circle is located at the *XMM-Newton* determined position, with coordinates R.A. = $11^{h}20^{m}10^{s}.32$ and decl. = $-22°01'35''.6$ and the diameter of the circle is the *XMM-Newton* half-energy width. (c) The r'-band image of the same field in the center panel taken by the LOT.

took 27 exposures of this field for a total exposure time of ∼67 ks between 2010 and 2013. Hui et al. (2015) studied all of the *Swift* observational data and found two millisecond pulsar candidates within the 95% error ellipse of 3FGL J1119.9−2204. On the other hand, several uncataloged X-ray point sources outside the error ellipse were also detected, but their properties were not further investigated. 2MASS J11201034−2201340, which has relatively faint X-ray emission, is one of the outliers unrelated to the γ-ray source 3FGL J1119.9−2204.

The energy range of *XRT* is 0.2–10 keV, the pixel scale is $2''.36$, and the FWHM of the point-spread function (PSF) is roughly $7''$ in 1.5 keV (or a half-power diameter of $18''$). All the data, including two target IDs (41371 and 49351), were used to determine the X-ray positions of the point sources. We extracted photon events and X-ray images from the standard products of all the *XRT* observations using *xselect* version 2.4. The point sources were detected using the *detect* task of the multi-mission X-ray image analysis program *XIMAGE*, for which the signal-to-noise threshold was set to 3.0. The position and corresponding uncertainty were determined using the *xrtcentroid* task. We found an X-ray point source located at R.A. = $11^{h}20^{m}10^{s}.65$ and decl. = $-22°01'30''.7$ with a 90% uncertainty of $\sim 7''.6$. Figure 1(a) is the *Swift* image of the field containing 2MASS J11201034−2201340 and 3FGL J1119.9−2204.

2.2. XMM-Newton Observation

2FGL J1120.0−2204 was observed by the *XMM-Newton* observatory on 2014 June 14 for a total exposure time of ∼70 ks (ObsID 0742930101). All three detectors of the European Photon Imaging Camera (EPIC) were used in this observation. The MOS1 and MOS2 detectors were operated in full-frame mode with a timing resolution of 2.6 s and an on-axis PSF FWHM of $6''$ (half-energy width $13''.6$). The pn detector was operated in timing mode with an extreme timing resolution of 0.03 ms. In this mode, all X-ray photons are compressed in one dimension. However, this observation was performed to investigate the timing properties of the millisecond pulsar candidate 2FGL J1120.0-2204. The pn data were useless because the target is far from the aim point of the observation. The optical/UV monitor also was used in this observation but our target was outside the field of view and the optical/UV monitor data were unavailable. We applied the pipeline task *emproc* of the XMM Science Analysis Software (XMMSAS version 15.0.0) program to the MOS data using the latest instrumental calibration database. Events with patterns <12 were adopted in this research, and the flaring background was filtered out when the entire count rate was >3.5 counts s^{-1}. We performed source detection using the maximum likelihood fitting with the aid of the XMMSAS task *edetect_chain* and the signal-to-noise threshold set to 4σ.

We found a source located at R.A. = $11^{h}20^{m}10^{s}.32$ and decl. = $-22°01'35''.6$ with a 90% uncertainty of $2''$. The detection likelihood is 34.5, which corresponds to a 8σ significance level. This source is likely a point source because the likelihood of source extent is not determined. Figure 1(b) shows the *XMM-Newton* image of the region containing 2MASS J11201034−2201340 where a point source is clearly seen.

2.3. Optical and Infrared Counterparts

The field around the X-ray source was surveyed in the optical and infrared bands by USNO-B-1.0, the Two Micron All Sky Survey (2MASS), and the *Wide-field Infrared Survey Explorer* (*WISE*). All three catalogs are well organized by the the NASA/IPAC Infrared Science Archive (IRSA). Each catalog has only one source that is within the PSF of the *XMM-Newton*: USNO-B1.0 0679−0311979 at R.A. = $11^{h}20^{m}10^{s}.36$ and decl. = $-22°01'34''.14$, 2MASS J11201034−2201340 at R.A. = $11^{h}20^{m}10^{s}.35$ and decl. = $-22°01'34''.04$, and WISE J112010.35−220134.1 at R.A. = $11^{h}20^{m}10^{s}.35$ and decl. = $-22°01'34''.16$. 2MASS J11201034−2201340 is $5''.3$ from the *Swift* determined X-ray source and $1''.5$ from the position determined by *XMM-Newton*. Hence, 2MASS J11201034−2201340 is likely to be the optical counterpart of the X-ray source because the angular separation between the optical and X-ray positions reside well within the uncertainties of *Swift* and *XMM-Newton*.

We also observed the field with the Lulin One-Meter Telescope (LOT), located at Central Taiwan, using the ALTA U42 CCD with SDSS r'-band and g'-band filters. This configuration has a pixel scale of $0''.32$ and a limiting

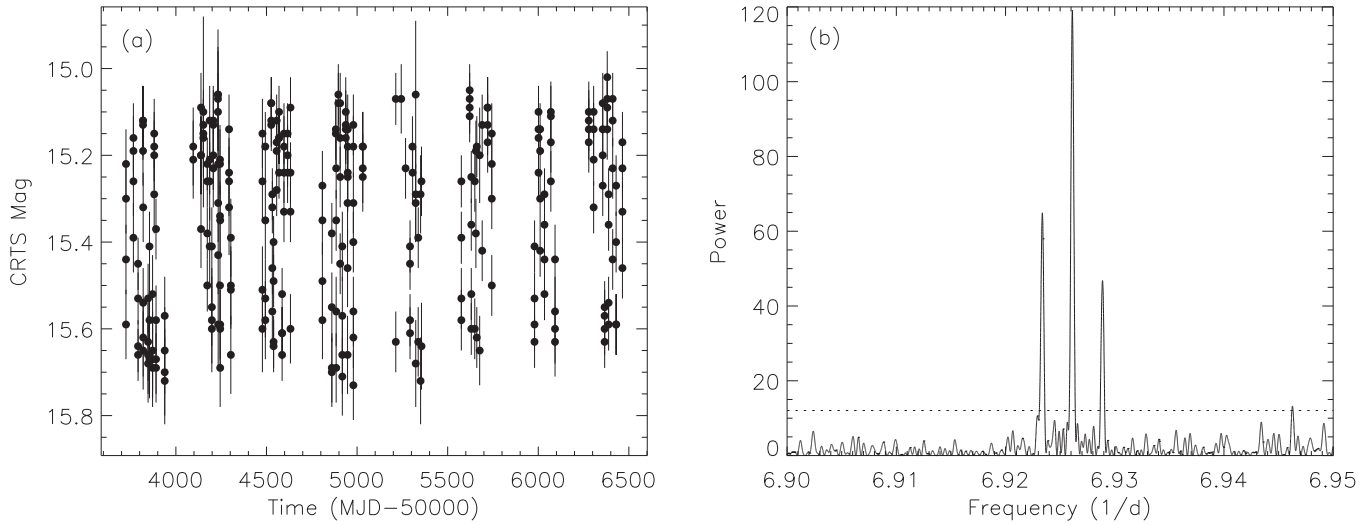

Figure 2. CRTS light curve (a) and the corresponding Lomb–Scargle power spectrum (b) of 2MASS J11201034−2201340. A significant peak located at $f = 6.926$ 1/day and its two associated 1 year aliases are clearly seen. The 3σ white noise level is indicated by the dashed line.

magnitude of ∼19.5 at the detection level of 5 σ. Figure 1(c) shows the cropped r'-band image. Only one source is detected in the region of the PSF of *XMM-Newton*.

3. DETAILED OPTICAL INVESTIGATION

3.1. Timing Analysis

To investigate the temporal variation of 2MASS J11201034 −2201340, we first collected the multi-epoch photometric data obtained by the Catalina Real-Time Transient Survey (CRTS) to search for periodicity. The CRTS data set contains the observations made by the Siding Springs Survey 0.5 m Schmidt telescope (218 exposures) and by the Catalina Sky Survey 0.7 m Schmidt telescope (76 exposures). We found a significant periodicity with a period of 0.144 day by applying the Lomb–Scargle periodogram (Scargle 1982; Horne & Baliunas 1986). Figure 2 shows the light curve from the CRTS and the power spectrum. One-year aliases due to the observational window function also were detected in the power spectrum.

To check the robustness of the detected result and the possibility that the true periodicity is twice the detected value, we observed the field using the *R* and *V* bands of the 0.4 m Super Light Telescope (SLT) at the Lulin Observatory on 2015 April 24–27. The SLT was equipped with an Andor iKon-L 936 CCD with a field of view of 28 × 28′ and a pixel scale of 0.″82. The exposure time for each frame was 5 minute, and the observation lasted ∼5 hr on April 24, 27, and 2.2 hr on April 26. The *R* band had 117 exposures and the *V* band had 115. For comparing the phase alignment of the CRTS data, the SLT data, and the data from other wavelengths, the observation times were corrected from the Earth to the solar barycenter. The CCD reduction package of the *Image Reduction and Analysis Facility* was used for standard image reduction, including bias, dark current, and flat-field corrections. We then compared the instrumental magnitude of 2MASS J11201034−2201340 with that of four comparison stars in the same field to obtain differential photometric data. The light curves clearly showed variability on a timescale of several hours. After folding both the light curves and the $B - V$ color curve using 0.144 and 0.288 day, respectively, we found that the color seemed to vary with a period of 0.288 day (see Figure 3). The true period of $0.28876208 \pm 5.6 \times 10^{-7}$ day is twice that detected by the Lomb–Scargle periodogram from the CRTS light curve. The uncertainty was estimated by a combination of the limited time span and photon statistical error. The uncertainty caused by limited time span and the strength of the signal was estimated using Equation (3) in Levine et al. (2011) and the statistical error was estimated using a 10^4 times Monte Carlo simulation.

From the archived multiepoch photometry data of *WISE* observations of this field, we found 52 *W1*-band (3.4 μm) and 42 *W2*-band (4.6 μm) significant detections and folded them with the best-determined periodicity. Figure 3 shows that there is still modulation and it is coherent in the mid-infrared bands.

3.2. Spectral Energy Distribution

We further investigated the physical properties of this system using currently available broadband SED data. For the optical band, we used the photometric *B*-, *R*-, and *I*-band data in the USNO-B 1.0 catalog, where $B1 = 16.4$, $B2 = 16.03$, $R1 = 14.36$, $R2 = 14.96$, and $I = 14.55$. To describe the spectral behavior of a contact binary system, it is better to use one of the flux minimum in the folded light curve that has all of the photons from the primary component. However, the amount of current data is insufficient because only one or two measurements were made for individual bands. Therefore, we took the average of the detected magnitudes for the *B* and *R* bands, for which there were two measurements, and applied a typical photometric uncertainty of 0.3 mag (Monet et al. 2003). The near-infrared data were from 2MASS in the *J*, *H*, and *Ks* bands, where $J = 13.875 \pm 0.03$, $H = 13.354 \pm 0.03$, and $Ks = 13.276 \pm 0.04$. The mid-infrared data were from *WISE* in the *W1* and *W2* bands, where $W1 = 13.286 \pm 0.025$ and $W2 = 13.331 \pm 0.031$.

The SLT did not observe standard stars, and so calibration in the *V* and *R* bands was not possible. Instead, to estimate the apparent magnitude of 2MASS J11201034−2201340, we used the cataloged star TYC 6090-207-1, which is a bright star with a coordinate of R.A. = $11^h19^m56^s.983$ and decl. = −22°04′ 43.″94 and magnitudes of $B = 13.09 \pm 0.26$ and a $V = 12.20 \pm 0.16$ (Høg et al. 2000). By scaling of the brightness of 2MASS J11201034−2201340 and TYC 6090-

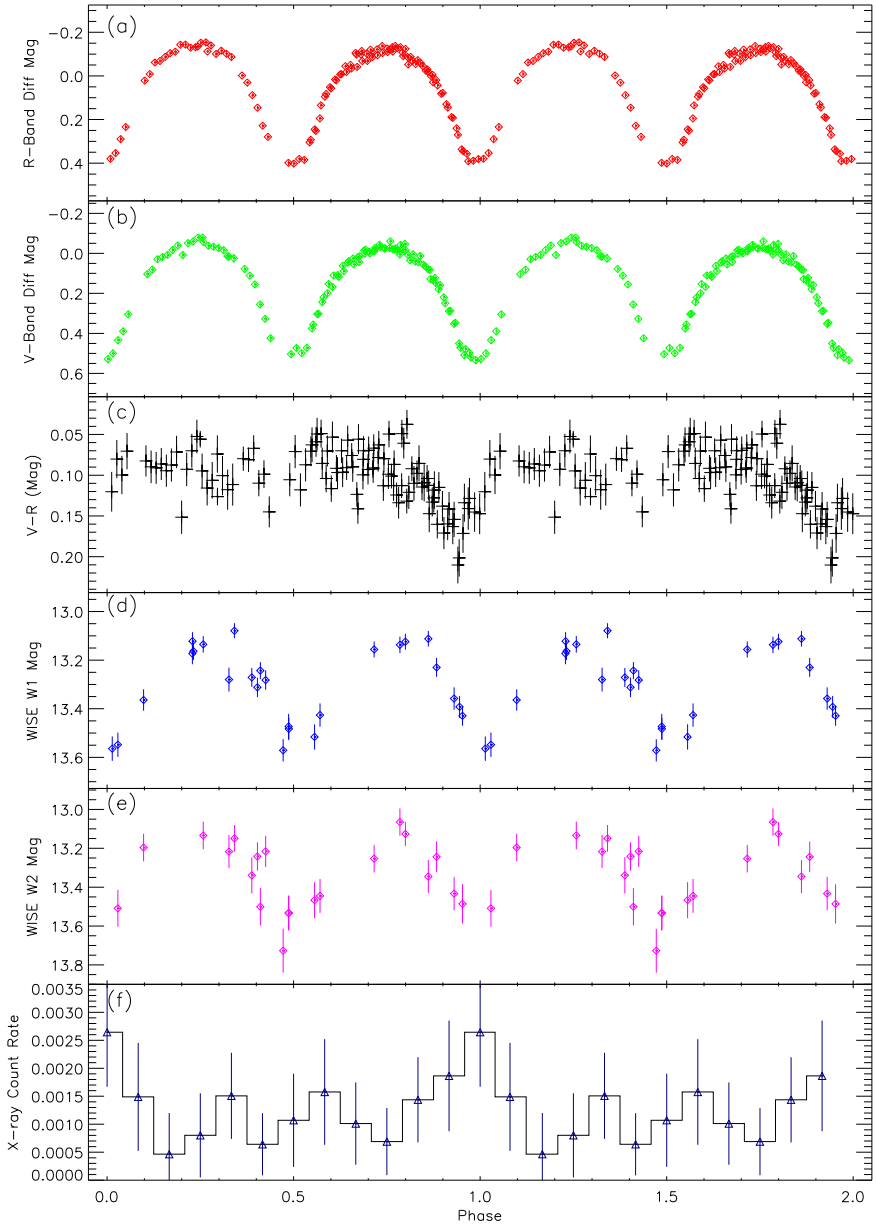

Figure 3. Multi-band light and color curves of 2MASS JJ11201034−2201340 folded according to a period of 0.288 day. (a) and (b) Folded *R*-band and *V*-band light curves obtained by SLT, (c) $V - R$ color variability, (d) and (e) folded *W1*-band and *W2*-band light curves obtained by *WISE*, and (f) folded X-ray light curve obtained by *XMM-Newton* with energy of 0.2–10 keV.

207-1, we estimated the *V*-band magnitude of 2MASS J11201034−2201340 as 15.37 ± 0.16.

Before constructing the SED, the measured magnitudes underwent extinction correction using the online Galactic dust extinction tool provided by IRSA. We assumed that the relationship between the extinction (A_V) and reddening ($E(B-V)$) is $A_V = 3.1E(B-V)$ (Güver & Özel 2009). We estimated the extinction for individual bands according to the latest measurements provided by Schlafly & Finkbeiner (2011). Figure 4 shows the constructed SED of 2MASS J11201034−2201340. We compared the SED with various stellar spectral templates presented in Pickles (1998) and found that our SED fit that of a K2V star that has a typical surface temperature of 4960 K. This indicates that the major component of 2MASS J11201034−2201340 is a late-type star.

3.3. Photometric Solution

To determine the physical nature of this contact binary system using the available data, we fit the observed *V*-band and *R*-band light curves using the Wilson–Devinney code (Wilson & Devinney 1971; Wilson 1979, 1990, 1994) to obtain a photometric solution. The surface temperature of the more massive star (T_1) was fixed at 4960 K as suggested by the SED fitting. The gravity darkening parameters were fixed at $g_1 = g_2 = 0.32$, according to the prediction made by Lucy (1967), and the bolometric albedos were fixed at $A_1 = A_2 = 0.5$ (Ruciński 1969) on the basis of the assumption that both components have convective envelopes. The limb-darkening coefficients for bolometric and individual bands ($x_{1\mathrm{bol}}$, $x_{2\mathrm{bol}}$, $y_{1\mathrm{bol}}$, $y_{2\mathrm{bol}}$, x_{1V}, x_{2V}, y_{1V}, y_{2V}, x_{1R}, x_{2R}, y_{1R}, and y_{2R}) were estimated using the values provided by van Hamme (1993; see Table 1). The remaining free parameters were the

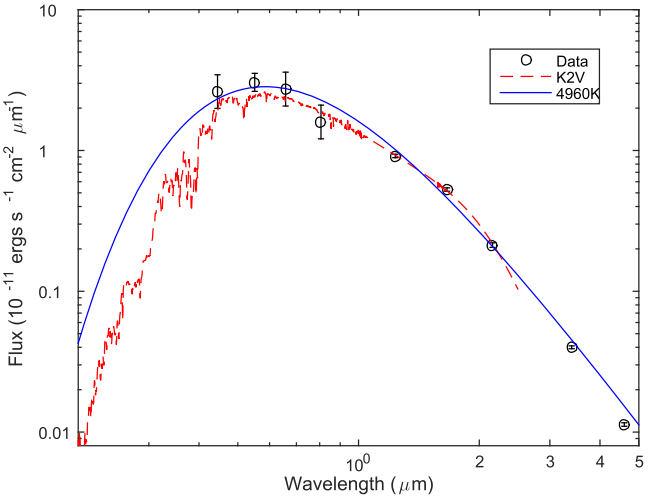

Figure 4. Spectral energy distribution of 2MASS J11201034−2201340. The data points were obtained from the USNO-B 1.0 catalog, the 2MASS catalog, and the *WISE* All-Sky Point Source catalog. The red dashed line is the best-fit K2V spectral template and the blue line is the corresponding blackbody radiation spectrum.

mass ratio (q), the inclination angle of the orbital plane (i), the surface temperature of the less massive component (T_2), the phase shift of the V and R bands, the dimensionless potential of the more massive star ($\Omega_1 = \Omega_2$), and the relative luminosity (L_1 and L_2) of each star in the V and R bands.

Because the spectral mass ratio could not be determined using the radial velocity method, we searched for a proper initial guessing value before fitting the light curves. We estimated the sum of the weighted square deviations (Σ) with respect to different trial values of q, ranging between 0.1 and 6. A minimum of Σ was clearly seen at $q = 0.3$, so we chose that as the initial q values for the fitting. Moreover, the profile seemed to be asymmetric, so we introduced a cool (dark) spot in the fitting to compare against the model without a cool spot. The cool spot model included three additional parameters: the colatitude (θ), longitude (ψ), and radius (Ω) of the spot. The best-fit parameters are given in Table 1 and the model light curves are shown in Figure 5.

The result of the fitting indicates that 2MASS J11201034 −2201340 is a short-period A-type contact binary with a nearly edge-on orbital plane. It is necessary that there be a cool spot on the more massive component to explain the O'Connell effect. In this scenario, the best-fit mass ratio is $q = 0.317$ and a fill-out factor is estimated to be $f = 14.8\%$, which suggests a low degree of over contact. From the averaged value of the phase shift, we proposed a linear ephemeris for the primary minimum defined as

$$T_{\rm primary} = \mathrm{MJD\ (TDB)}\ 53791.3984(1) + 0.28876208(56) \times N,$$

where N is the number of cycle count.

The magnitude of the secondary minimum (phase ∼0.5), which is not much different from that of the primary in the folded light curve, indicates that the less massive star is completely obscured and only the more massive star contributes to the flux. The V-band magnitude of the secondary minimum is estimated as 15.75 ± 0.16 in this measurement. Therefore, the distance can be roughly estimated as 690 ± 50 pc after considering the extinction and assuming that the more massive component is a K2V star.

Table 1
Photometric Solutions for 2MASS J11201034−2201340

Parameters	Photometric Elements Without Cool Spot	Errors	Photometric Elements Cool Spot Solutions	Errors
$g_1 = g_2$	0.32	assumed	0.32	assumed
$A_1 = A_2$	0.50	assumed	0.50	assumed
$x_{1\rm bol}$, $x_{2\rm bol}$	0.299, 0.299	assumed	0.299, 0.299	assumed
$y_{1\rm bol}$, $y_{2\rm bol}$	0.396, 0.396	assumed	0.396, 0.396	assumed
x_{1V}, x_{2V}	0.581, 0.581	assumed	0.581, 0.581	assumed
y_{1V}, y_{2V}	0.249, 0.249	assumed	0.249, 0.249	assumed
x_{1R}, x_{2R}	0.356, 0.356	assumed	0.356, 0.356	assumed
y_{1R}, y_{2R}	0.413, 0.413	assumed	0.413, 0.413	assumed
T_1	4960K	fixed	4960K	fixed
Phase Shift	−0.0153	±0.0005	−0.0155	±0.0004
q	0.291	±0.006	0.317	±0.004
$\Omega_1 = \Omega_2$	2.4253	±0.0126	2.4735	±0.0111
$\Omega_{\rm in}$	2.4464	⋯	2.5026	⋯
$\Omega_{\rm out}$	2.2645	⋯	2.3060	⋯
T_2	5125 K	±20 K	5124 K	±16 K
i	89.°4	±3.3	88.°5	±2.7
$L_1/(L_1 + L_2)(V)$	0.7180	±0.0051	0.7019	±0.0046
$L_1/(L_1 + L_2)(R)$	0.7259	±0.0045	0.7100	±0.0042
θ (°)	⋯	⋯	86.5	±2.6
ψ (°)	⋯	⋯	92.2	±4.7
Ω(°)	⋯	⋯	11.9	±1.2
T_s/T_*	⋯	⋯	0.80	±0.09
f	11.6%	±6.9%	14.8%	±5.7%

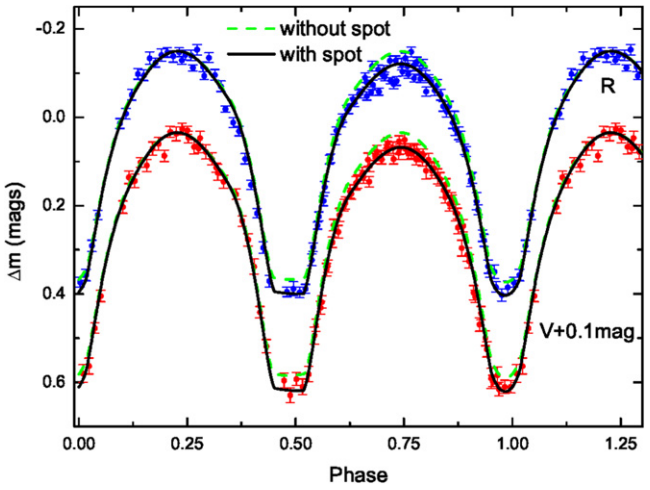

Figure 5. Observed folded R-band light curve (blue), folded V-band light curve (red) with a shift of 0.1 mag, and the corresponding best-fit contact binary model estimated using the Wilson–Devinney code. The green dashed line is the best-fit model without a cool spot and the black line is the best-fit model with a cool spot.

4. RESULTS FROM X-RAY OBSERVATIONS

4.1. X-Ray Profile and Spectrum

Investigation of the timing and spectral properties of the X-ray emission from 2MASS J11201034−2201340 detected

by *XMM-Newton* will add to our understanding of the nature of this system. After filtering out the flaring background, the effective exposure time was ~57 ks. We extracted 238 X-ray photons from a 20 arcsec radius circular region centered at the detected centroid of 2MASS J11201034−2201340 (see Figure 1). Because the effective exposure time encompassed only approximately two orbital cycles of 2MASS J11201034 −2201340, we needed to carefully examine background variability. We selected 10 backgrounds with the same area in the source-free region on the same chip and found that the background counts were ~150. Therefore, only ~90 X-ray photons that originated from the source were available for use in a marginal investigation of the timing and spectral analysis. First, we individually folded the source and all the backgrounds according to the best period determined in the optical band. Then, we obtained a mean folded light curve by averaging all the folded background light curves to obtain the fluctuation of the background in the phase domain. The clean folded light curve shown in Figure 3(f) was obtained by subtracting the background profile from the folded source light curve. Another way to compute the background contribution is by weighting a larger source-free region, e.g., a circle with an 80 arcsec radius or a large annulus around the source. Both methods yield similar results. The folded light curve showed no detection of significant X-ray variability. We used different bin sizes and applied the χ^2 test to the folded profile and found that the detection significance in all cases was $<1\sigma$. The lack of detection of variability means that the geometry of the X-ray emission area may differ from that of the optical area.

The high-energy emission mechanism can be investigated by X-ray spectral analysis, despite the small number of X-ray photons. The source selection criterion was the same as that for the X-ray timing analysis above, while we used an 80 arcsec radius circle around a source-free region to estimate the background spectrum. The response matrix was created using the XMMSAS task *rmfgen* and the ancillary response file was created using *arfgen*. The X-ray photons were further grouped to have at least 15 counts per spectral bin. No pile-up issue was addressed for this faint source.

The X-ray spectral fitting was achieved using `XSPEC v12.9.0`. The X-ray emission from a contact binary system may come from a hot coronal plasma and may be represented with a thermal or non-thermal model. We tried two typical spectral models: non-thermal power law (`XSPEC` model `powerlaw`), and the thermal Bremsstrahlung (`XSPEC` model `bremss`) to fit the X-ray spectrum. The spectral fitting was calculated within the energy range 0.2–10 keV. We first set the $N_{\rm H}$ to be a free parameter and yielded a best-fit value of 2.7×10^{-20} cm^{-2}, which is not very far from 3.65×10^{-20} cm^{-2} derived from Leiden/Argentine/Bonn (LAB) Survey (Kalberla et al. 2005). However, the uncertainty is 5×10^{-21} cm^{-2}, which is too large to well constrain the $N_{\rm H}$ value. Therefore, we fixed the $N_{\rm H}$ value at the galactic one of 3.65×10^{-20} cm^{-2} in the following analysis. The power-law model yielded an acceptable fitting with a photon index of 2.4 ± 0.5 and a $\chi^2_\nu = 1.09$. The uncertainties of spectral parameters are estimated within the 90% confidence interval. On the other hand, the thermal Bremsstrahlung model result in an equally good fitting with a slightly larger χ^2_ν of 1.15 and a plasma temperature of $kT = 0.8^{+1.4}_{-0.3}$ keV. Both of the single component model can describe the X-ray spectrum of 2MASS J11201034−2201340 very well and no additional components are required. The best-fit parameters for the two models are given in Table 2, and the spectral data and corresponding best-fit models are shown in Figure 6. The X-ray flux in the 0.3–10 keV energy range was estimated as $1.7^{+0.9}_{-0.5} \times 10^{-14}$ erg cm^{-2} s^{-1}.

Table 2
The Best-fit Parameters of two Different Models for the X-ray Spectrum of 2MASS J11201034−2201340 Obtained with *XMM-Newton*

	Power Law	Bremsstrahlung
Γ	2.4 ± 0.5	...
kT (eV)	...	$0.8^{+1.4}_{-0.3}$
Normalization	$4.2^{+1.2}_{-1.3} \times 10^{-6}$	$1.1^{+1.0}_{-0.6} \times 10^{-6}$
χ^2_ν (dof)	1.09(12)	1.15 (12)

4.2. Indications from X-Ray Emission

Because the fitting of the optical folded light curve suggested the presence of a cool spot, the existence of X-ray emission suggests chromospheric activity. The result of the X-ray spectral fitting also suggests a possible non-thermal or thermal Bremsstrahlung origin for the X-ray emission. However, the X-ray orbital profile shows no significant variations, but this may be due to an insufficient number of X-ray photons. Considering the stability of star spots, it is possible that their position and size in these two observations are quite different. To investigate the origin of the X-ray emission and its connection to the star spot, simultaneous X-ray and optical observations using an *X-ray telescope* with a large effective area are necessary.

Although only ~ 30X-ray photons were detected in all the *Swift* observations, we were able to estimate a crude X-ray spectrum and the corresponding X-ray flux by using the online tool provided by UK *Swift* Science Data Centre. The flux of X-rays between 0.3 and 10 keV determined by *Swift* was $1.0^{+0.6}_{-0.5} \times 10^{-14}$ erg cm^{-2} s^{-1}, which is consistent with the value obtained by a single *XMM-Newton* observation ($1.7^{+0.9}_{-0.5} \times 10^{-14}$ erg cm^{-2} s^{-1}). This may indicate that no significant X-ray flare was detected during the *Swift* observations.

Using the distance estimated from the SED, the X-ray intensity was estimated to be $(0.7 - 1.5) \times 10^{30}$ erg s^{-1}. Factoring in the relationship between the X-ray intensity and the orbital period (Chen et al. 2006), 2MASS J11201034 −2201340 is within a reasonable range on the X-ray intensity versus orbital period plot (see Figure 7). Stępień et al. (2001) categorized W UMa-type stars into hot $[(B-V)_0 \leqslant 0.6]$ and cool $[(B-V)_0 > 0.6]$ groups. The X-ray flux seems to positively correlate with the color index for the hot group, whereas it reaches a constant value after $(B-V)_0 > 0.6$. Judging from the SED fitting, 2MASS J11201034−2201340 is likely to be in the cool group. The ratio of the X-ray and bolometric fluxes, $\log(L_x/L_{\rm bol})$, is roughly estimated to be between −3 and −3.3, which is reasonably close to the value presented in Stępień et al. (2001). Accurate multi-band photometric observations and standard star calibration are required to investigate the nature of this system in detail.

5. SUMMARY

While searching for the X-ray and optical counterparts of millisecond pulsar candidates, we serendipitously detected the

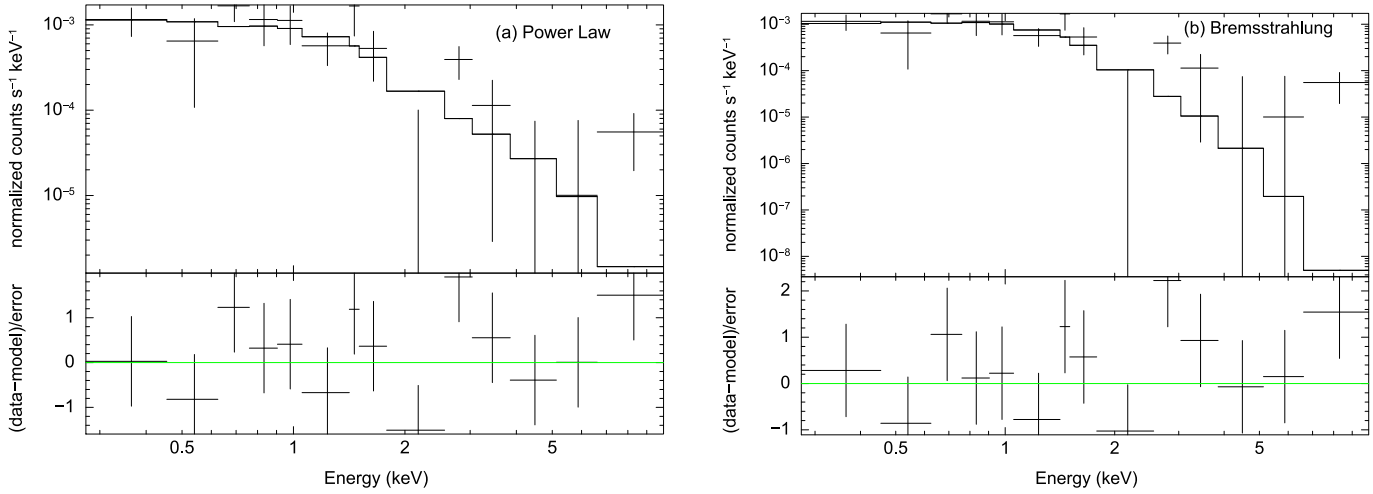

Figure 6. (a) X-ray spectral data (crosses) and the best-fit power-law model (steps) of 2MASS J11201034−2201340 obtained with *XMM-Newton*. The lower panel shows the deviation of each data point from the best-fit model. (b) The same as (a) for the thermal Bremsstrahlung model.

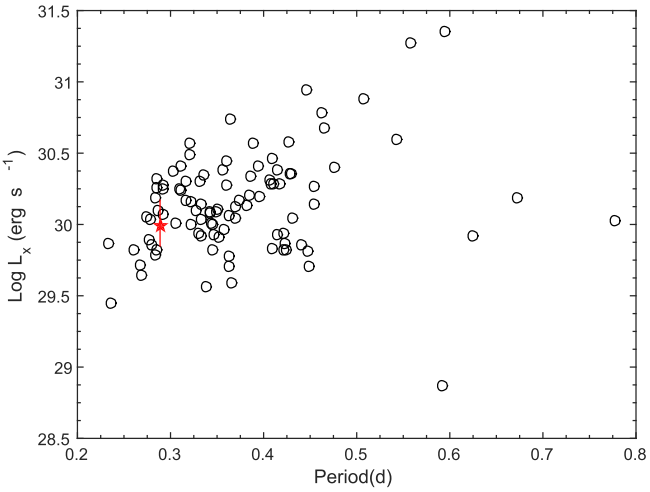

Figure 7. Relation between the X-ray luminosity and orbital period for contact binaries. The red star denotes 2MASS J11201034−2201340 and the open circles are historical data adopted from Chen et al. (2006).

modulation of the uncataloged X-ray-emitting contact binary 2MASS J11201034−2201340. We presented a multi-wavelength investigation of the object because it is detectable from infrared to X-ray bands. We first detected 2MASS J11201034−2201340 after we combined all of the *Swift* observations of 2FGL J1120.0−2204. The exact X-ray position was further confirmed by an *XMM-Newton* observation. For the optical band, the long-term CRTS light curve and SLT color measurements confirmed that the orbital period of this system is 0.288 day, which is between the values for A-type and W-type contact binaries. Photometric measurement data in the USNO-B 1.0, 2MASS, and *WISE* catalogs indicate that the broadband SED of 2MASS J11201034−2201340 is that of a K-type star. We used the Wilson–Devinney code to fit the orbital profile in the *R*- and *V*-band follow-up light curves observed by the SLT and showed that this system is an A-type contact binary with a mass ratio of ∼0.3. Furthermore, we proposed a cool spot to explain the asymmetric orbital profile. In addition to the optical periodicity, the X-ray emission hints at the X-ray origin of this object. Although the number of X-ray photons was insufficient to obtain a significant X-ray orbital profile, the X-ray spectrum is likely to be nonthermal, and thus can be linked to chromospheric activity and star spots. The X-ray flux, orbital period, and color index of 2MASS J11201034−2201340 all point to it being a typical contact binary. Additional multi-band observations with standard star calibrations and long-time-baseline monitoring should conclusively determine the physical properties of this object in detail.

This work made use of the data collected by *XMM-Newton*, an ESA science mission with instruments and contributions directly funded by ESA Member States and the USA (NASA). The *Swift* data was supplied by the UK *Swift* Science Data Centre at the University of Leicester. The orbital ephemeris is obtained using the data collected by the CRTS survey, which is supported by the U.S. National Science Foundation under grants AST-0909182. The LOT and SLT are maintained by the Graduate Institute of Astronomy, National Central University. The near-infrared data is collected by the 2MASS, which is a joint project of the University of Massachusetts and the Infrared Processing and Analysis Center/California Institute of Technology, funded by the NASA and the National Science Foundation. The mid-infrared data was provided by the *WISE*, which is a joint project of the University of California, Los Angeles, and the Jet Propulsion Laboratory/California Institute of Technology, funded by NASA.

C.-P.H. is supported by the NSC 101-2119-M008-007-MY3 grant from the Ministry of Science and Technology (MOST) of Taiwan and an ECS grant of Hong Kong Government under HKU 709713P. T.-C.Y. and W.-H.I. are supported by the MOST grant NSC 101-2119-M008-007-MY3 and MOST 104-2119-M-008-024. Y.C. is supported by the MOST grant NSC 102-2112-M-008-020-MY3. L.L. and S.-B.Q. is supported by the Science Foundation of Yunnan Province (2012HC011) and the Chinese Natural Science Foundation (No.11133007 and No. 11325315). C.Y.H. is supported by the National Research Foundation of Korea through grant 2014R1A1A2058590. A.K.H.K. is supported by the MOST grant 103-2628-M-007-003-MY3. P.H.T. is supported by the One Hundred Talents Program of the Sun Yat-Sen University. C.-C.N. is supported by the MOST grant NSC 101-2112-M-008-017-MY3 and 104-2112-M-008-012-MY3. W.P.C. is supported by the MOST grants 103-2112-M-008-024-MY3.

REFERENCES

Binnendijk, L. 1970, VA, 12, 217
Carroll, R. W., Cruddace, R. G., Friedman, H., et al. 1980, ApJL, 235, L77
Chen, W. P., Sanchawala, K., & Chiu, M. C. 2006, AJ, 131, 990
Gazeas, K. D., & Niarchos, P. G. 2006, MNRAS, 370, L29
Güver, T., & Özel, F. 2009, MNRAS, 400, 2050
Hilditch, R. W., King, D. J., & McFarlane, T. M. 1988, MNRAS, 231, 341
Høg, E., Fabricius, C., Makarov, V. V., et al. 2000, A&A, 355, L27
Horne, J. H., & Baliunas, S. L. 1986, ApJ, 302, 757
Huenemoerder, D. P., Testa, P., & Buzasi, D. L. 2006, ApJ, 650, 1119
Hui, C. Y., Park, S. M., Hu, C. P., et al. 2015, ApJ, 809, 68
Kalberla, P. M. W., Burton, W. B., Hartmann, D., et al. 2005, A&A, 440, 775
Kaszas, G., Vinko, J., Szatmary, K., et al. 1998, A&A, 331, 231
Levine, A. M., Bradt, H. V., Chakrabarty, D., Corbet, R. H. D., & Harris, R. J. 2011, ApJS, 196, 6
Lucy, L. B. 1967, ZAp, 65, 89
Monet, D. G., Levine, S. E., Canzian, B., et al. 2003, AJ, 125, 984
Müller, G., & Kempf, P. 1903, AN, 161, 141
O'Connell, D. J. K. 1951, PRCO, 2, 85
Pickles, A. J. 1998, PASP, 110, 863
Ruciński, S. M. 1969, AcA, 19, 245
Scargle, J. D. 1982, ApJ, 263, 835
Schlafly, E. F., & Finkbeiner, D. P. 2011, ApJ, 737, 103
Stępień, K., Schmitt, J. H. M. M., & Voges, W. 2001, A&A, 370, 157
van Hamme, W. 1993, AJ, 106, 2096
Wilsey, N. J., & Beaky, M. M. 2009, in Society for Astronomical Sciences Annual Symp. 28 (Rancho Cucamonga, CA: Society for Astronomical Sciences), 107
Wilson, R. E. 1979, ApJ, 234, 1054
Wilson, R. E. 1990, ApJ, 356, 613
Wilson, R. E. 1994, PASP, 106, 921
Wilson, R. E., & Devinney, E. J. 1971, ApJ, 166, 605

The Astrophysical Journal, 819:156 (30pp), 2016 March 10 doi:10.3847/0004-637X/819/2/156

MULTIWAVELENGTH STUDY OF QUIESCENT STATES OF Mrk 421 WITH UNPRECEDENTED HARD X-RAY COVERAGE PROVIDED BY *NuSTAR* IN 2013

M. Baloković[1], D. Paneque[2], G. Madejski[3], A. Furniss[4], J. Chiang[3],
M. Ajello[5], D. M. Alexander[6], D. Barret[7,8], R. D. Blandford[3], S. E. Boggs[9], F. E. Christensen[10], W. W. Craig[9,11],
K. Forster[1], P. Giommi[12], B. Grefenstette[1], C. Hailey[13], F. A. Harrison[1], A. Hornstrup[10], T. Kitaguchi[14,15], J. E. Koglin[3],
K. K. Madsen[1], P. H. Mao[1], H. Miyasaka[1], K. Mori[16], M. Perri[12,17], M. J. Pivovaroff[9], S. Puccetti[12,17], V. Rana[1],
D. Stern[18], G. Tagliaferri[19], C. M. Urry[20], N. J. Westergaard[10], W. W. Zhang[21], A. Zoglauer[9]
(The NuSTAR Team),
S. Archambault[22], A. Archer[23], A. Barnacka[24], W. Benbow[25], R. Bird[26], J. H. Buckley[23], V. Bugaev[23], M. Cerruti[25],
X. Chen[27,28], L. Ciupik[29], M. P. Connolly[30], W. Cui[31], H. J. Dickinson[32], J. Dumm[33], J. D. Eisch[32], A. Falcone[34], Q. Feng[31],
J. P. Finley[31], H. Fleischhack[28], L. Fortson[33], S. Griffin[22], S. T. Griffiths[35], J. Grube[29], G. Gyuk[29], M. Huetten[28],
N. Håkansson[27], J. Holder[36], T. B. Humensky[37], C. A. Johnson[37], P. Kaaret[35], M. Kertzman[38], Y. Khassen[26], D. Kieda[39],
M. Krause[28], F. Krennrich[32], M. J. Lang[30], G. Maier[28], S. McArthur[40], K. Meagher[41], P. Moriarty[30], T. Nelson[33],
D. Nieto[13], R. A. Ong[42], N. Park[40], M. Pohl[27,28], A. Popkow[42], E. Pueschel[26], P. T. Reynolds[43], G. T. Richards[41],
E. Roache[25], M. Santander[44], G. H. Sembroski[31], K. Shahinyan[33], A. W. Smith[21,45], D. Staszak[22], I. Telezhinsky[27,28],
N. W. Todd[23], J. V. Tucci[31], J. Tyler[22], S. Vincent[28], A. Weinstein[32], A. Wilhelm[27,28], D. A. Williams[37], B. Zitzer[46]
(The VERITAS Collaboration),
M. L. Ahnen[47], S. Ansoldi[48], L. A. Antonelli[49], P. Antoranz[50], A. Babic[51], B. Banerjee[52], P. Bangale[2],
U. Barres de Almeida[2,53], J. A. Barrio[54], J. Becerra González[21,45,55], W. Bednarek[56], E. Bernardini[28,57], B. Biasuzzi[48],
A. Biland[47], O. Blanch[58], S. Bonnefoy[54], G. Bonnoli[49], F. Borracci[2], T. Bretz[59,60], E. Carmona[61], A. Carosi[49],
A. Chatterjee[52], R. Clavero[55], P. Colin[2], E. Colombo[55], J. L. Contreras[54], J. Cortina[58], S. Covino[49], P. Da Vela[50],
F. Dazzi[2], A. De Angelis[62], B. De Lotto[48], E. de Oña Wilhelmi[63], C. Delgado Mendez[61], F. Di Pierro[49],
D. Dominis Prester[51], D. Dorner[59], M. Doro[2,62], S. Einecke[64], D. Elsaesser[59], A. Fernández-Barral[58], D. Fidalgo[54],
M. V. Fonseca[54], L. Font[65], K. Frantzen[65], C. Fruck[2], D. Galindo[66], R. J. García López[55], M. Garczarczyk[28],
D. Garrido Terrats[65], M. Gaug[65], P. Giammaria[49], D. Glawion (Eisenacher)[59], N. Godinović[51], A. González Muñoz[58],
D. Guberman[58], A. Hahn[2], Y. Hanabata[67], M. Hayashida[67], J. Herrera[55], J. Hose[2], D. Hrupec[51], G. Hughes[47], W. Idec[56],
K. Kodani[67], Y. Konno[67], H. Kubo[67], J. Kushida[67], A. La Barbera[49], D. Lelas[51], E. Lindfors[68], S. Lombardi[49], F. Longo[48],
M. López[54], R. López-Coto[58], A. López-Oramas[58,69], E. Lorenz[2], P. Majumdar[52], M. Makariev[70], K. Mallot[28],
G. Maneva[70], M. Manganaro[55], K. Mannheim[59], L. Maraschi[49], B. Marcote[66], M. Mariotti[62], M. Martínez[58],
D. Mazin[2,67], U. Menzel[2], J. M. Miranda[50], R. Mirzoyan[2], A. Moralejo[58], E. Moretti[2], D. Nakajima[67], V. Neustroev[68],
A. Niedzwiecki[56], M. Nievas Rosillo[54], K. Nilsson[68,71], K. Nishijima[67], K. Noda[2], R. Orito[67], A. Overkemping[64],
S. Paiano[62], J. Palacio[58], M. Palatiello[48], R. Paoletti[50], J. M. Paredes[66], X. Paredes-Fortuny[66], M. Persic[48,72],
J. Poutanen[68], P. G. Prada Moroni[73], E. Prandini[47,74], I. Puljak[51], W. Rhode[64], M. Ribó[66], J. Rico[58], J. Rodriguez Garcia[2],
T. Saito[67], K. Satalecka[54], V. Scapin[54], C. Schultz[62], T. Schweizer[2], S. N. Shore[73], A. Sillanpää[68], J. Sitarek[56],
I. Snidaric[51], D. Sobczynska[56], A. Stamerra[49], T. Steinbring[59], M. Strzys[2], L. Takalo[68], H. Takami[67], F. Tavecchio[49],
P. Temnikov[70], T. Terzić[51], D. Tescaro[55], M. Teshima[2,67], J. Thaele[64], D. F. Torres[75], T. Toyama[2], A. Treves[76],
V. Verguilov[70], I. Vovk[2], J. E. Ward[58], M. Will[55], M. H. Wu[63], R. Zanin[66]
(The MAGIC Collaboration),
J. Perkins[21], F. Verrecchia[12,17], C. Leto[12,17], M. Böttcher[77],
M. Villata[78], C. M. Raiteri[78], J. A. Acosta-Pulido[79,80], R. Bachev[81], A. Berdyugin[82], D. A. Blinov[83,84,85],
M. I. Carnerero[78,79,80], W. P. Chen[86], P. Chinchilla[79,80], G. Damljanovic[87], C. Eswaraiah[86], T. S. Grishina[83],
S. Ibryamov[81], B. Jordan[88], S. G. Jorstad[83,89], M. Joshi[83], E. N. Kopatskaya[83], O. M. Kurtanidze[90,91,92],
S. O. Kurtanidze[90], E. G. Larionova[83], L. V. Larionova[83], V. M. Larionov[83,93], G. Latev[94], H. C. Lin[86], A. P. Marscher[89],
A. A. Mokrushina[83,93], D. A. Morozova[83], M. G. Nikolashvili[90], E. Semkov[81], P. S. Smith[95], A. Strigachev[81],
Yu. V. Troitskaya[83], I. S. Troitsky[83], O. Vince[87], J. Barnes[96], T. Güver[97], J. W. Moody[98], A. C. Sadun[99], S. Sun[100],
T. Hovatta[1,101], J. L. Richards[31], W. Max-Moerbeck[102], A. C. R. Readhead[1], A. Lähteenmäki[101,103], M. Tornikoski[101],
J. Tammi[101], V. Ramakrishnan[101], R. Reinthal[82], E. Angelakis[104], L. Fuhrmann[104], I. Myserlis[104], V. Karamanavis[104],
A. Sievers[105], H. Ungerechts[105], and J. A. Zensus[104]
[1] Cahill Center for Astronomy and Astrophysics, California Institute of Technology, Pasadena, CA 91125, USA; mislavb@astro.caltech.edu
[2] Max-Planck-Institut für Physik, D-80805 München, Germany; dpaneque@mppmu.mpg.de
[3] W. W. Hansen Experimental Physics Laboratory, Kavli Institute for Particle Astrophysics and Cosmology, Department of Physics and SLAC National Accelerator Laboratory, Stanford University, Stanford, CA 94305, USA; madejski@stanford.edu, jchiang@slac.stanford.edu
[4] Department of Physics, Stanford University, Stanford, CA 94305, USA; amy.furniss@gmail.com
[5] Department of Physics and Astronomy, Clemson University, Kinard Lab of Physics, Clemson, SC 29634-0978, USA
[6] Department of Physics, Durham University, Durham DH1 3LE, UK
[7] Université de Toulouse, UPS—OMP, IRAP, Toulouse, France
[8] CNRS, Institut de Recherche en Astrophysique et Planétologie, 9 Av. colonel Roche, BP 44346, F-31028 Toulouse Cedex 4, France

[9] Space Science Laboratory, University of California, Berkeley, CA 94720, USA
[10] DTU Space, National Space Institute, Technical University of Denmark, Elektrovej 327, DK-2800 Lyngby, Denmark
[11] Lawrence Livermore National Laboratory, Livermore, CA 94550, USA
[12] ASI Science Data Center, Via del Politecnico snc I-00133, Roma, Italy
[13] Physics Department, Columbia University, New York, NY 10027, USA
[14] Department of Physical Science, Hiroshima University, Higashi-Hiroshima, Hiroshima 739-8526, Japan
[15] Core of Research for the Energetic Universe, Hiroshima University, Higashi-Hiroshima, Hiroshima 739-8526, Japan
[16] Columbia Astrophysics Laboratory, Columbia University, New York, NY 10027, USA
[17] INAF—Osservatorio Astronomico di Roma, via di Frascati 33, I-00040 Monteporzio, Italy
[18] Jet Propulsion Laboratory, California Institute of Technology, Pasadena, CA 91109, USA
[19] INAF—Osservatorio Astronomico di Brera, Via E, Bianchi 46, I-23807 Merate, Italy
[20] Yale Center for Astronomy and Astrophysics, Physics Department, Yale University, P.O. Box 208120, New Haven, CT 06520-8120, USA
[21] NASA Goddard Space Flight Center, Greenbelt, MD 20771, USA
[22] Physics Department, McGill University, Montreal, QC H3A 2T8, Canada
[23] Department of Physics, Washington University, St. Louis, MO 63130, USA
[24] Harvard-Smithsonian Center for Astrophysics, 60 Garden Street, Cambridge, MA 02138, USA
[25] Fred Lawrence Whipple Observatory, Harvard-Smithsonian Center for Astrophysics, Amado, AZ 85645, USA
[26] School of Physics, University College Dublin, Belfield, Dublin 4, Ireland
[27] Institute of Physics and Astronomy, University of Potsdam, D-14476 Potsdam-Golm, Germany
[28] Deutsches Elektronen-Synchrotron (DESY), Platanenallee 6, D-15738 Zeuthen, Germany
[29] Astronomy Department, Adler Planetarium and Astronomy Museum, Chicago, IL 60605, USA
[30] School of Physics, National University of Ireland Galway, University Road, Galway, Ireland
[31] Department of Physics and Astronomy, Purdue University, West Lafayette, IN 47907, USA
[32] Department of Physics and Astronomy, Iowa State University, Ames, IA 50011, USA
[33] School of Physics and Astronomy, University of Minnesota, Minneapolis, MN 55455, USA
[34] Department of Astronomy and Astrophysics, 525 Davey Lab, Pennsylvania State University, University Park, PA 16802, USA
[35] Department of Physics and Astronomy, University of Iowa, Van Allen Hall, Iowa City, IA 52242, USA
[36] Department of Physics and Astronomy and the Bartol Research Institute, University of Delaware, Newark, DE 19716, USA
[37] Santa Cruz Institute for Particle Physics and Department of Physics, University of California, Santa Cruz, CA 95064, USA
[38] Department of Physics and Astronomy, DePauw University, Greencastle, IN 46135-0037, USA
[39] Department of Physics and Astronomy, University of Utah, Salt Lake City, UT 84112, USA
[40] Enrico Fermi Institute, University of Chicago, Chicago, IL 60637, USA
[41] School of Physics and Center for Relativistic Astrophysics, Georgia Institute of Technology, 837 State Street NW, Atlanta, GA 30332-0430, USA
[42] Department of Physics and Astronomy, University of California, Los Angeles, CA 90095, USA
[43] Department of Applied Science, Cork Institute of Technology, Bishopstown, Cork, Ireland
[44] Department of Physics and Astronomy, Barnard College, Columbia University, NY 10027, USA
[45] University of Maryland, College Park, MD 20742, USA
[46] Argonne National Laboratory, 9700 S. Cass Avenue, Argonne, IL 60439, USA
[47] ETH Zurich, CH-8093 Zurich, Switzerland
[48] Università di Udine, and INFN Trieste, I-33100 Udine, Italy
[49] INAF National Institute for Astrophysics, I-00136 Rome, Italy
[50] Università di Siena, and INFN Pisa, I-53100 Siena, Italy
[51] Croatian MAGIC Consortium, Rudjer Boskovic Institute, University of Rijeka and University of Split, HR-10000 Zagreb, Croatia
[52] Saha Institute of Nuclear Physics, 1\AF Bidhannagar, Salt Lake, Sector-1, Kolkata 700064, India
[53] Centro Brasileiro de Pesquisas Físicas (CBPF\MCTI), R. Dr. Xavier Sigaud, 150—Urca, Rio de Janeiro—RJ, 22290-180, Brazil
[54] Universidad Complutense, E-28040 Madrid, Spain
[55] Inst. de Astrofísica de Canarias, E-38200 La Laguna, Tenerife, Spain; Universidad de La Laguna, Dpto. Astrofísica, E-38206 La Laguna, Tenerife, Spain
[56] University of Łódź, PL-90236 Lodz, Poland
[57] Humboldt University of Berlin, Istitut für Physik Newtonstr. 15, D-12489 Berlin, Germany
[58] IFAE, Campus UAB, E-08193 Bellaterra, Spain
[59] Universität Würzburg, D-97074 Würzburg, Germany
[60] Ecole polytechnique fédérale de Lausanne (EPFL), Lausanne, Switzerland
[61] Centro de Investigaciones Energéticas, Medioambientales y Tecnológicas, E-28040 Madrid, Spain
[62] Università di Padova and INFN, I-35131 Padova, Italy
[63] Institute for Space Sciences (CSIC\IEEC), E-08193 Barcelona, Spain
[64] Technische Universität Dortmund, D-44221 Dortmund, Germany
[65] Unitat de Física de les Radiacions, Departament de Física, and CERES-IEEC, Universitat Autònoma de Barcelona, E-08193 Bellaterra, Spain
[66] Universitat de Barcelona, ICC, IEEC-UB, E-08028 Barcelona, Spain
[67] Japanese MAGIC Consortium, ICRR, The University of Tokyo, Department of Physics and Hakubi Center, Kyoto University, Tokai University, The University of Tokushima, KEK, Japan
[68] Finnish MAGIC Consortium, Tuorla Observatory, University of Turku and Department of Physics, University of Oulu, Finland
[69] Laboratoire AIM, Service d'Astrophysique, DSM\IRFU, CEA\Saclay F-91191 Gif-sur-Yvette Cedex, France
[70] Inst. for Nucl. Research and Nucl. Energy, BG-1784 Sofia, Bulgaria
[71] Finnish Centre for Astronomy with ESO (FINCA), Turku, Finland
[72] INAF—Osservatorio Astronomico di Trieste, Trieste, Italy
[73] Università di Pisa, and INFN Pisa, I-56126 Pisa, Italy
[74] ISDC—Science Data Center for Astrophysics, 1290, Versoix (Geneva), Switzerland
[75] ICREA and Institute for Space Sciences (CSIC\IEEC), E-08193 Barcelona, Spain
[76] Università dell'Insubria and INFN Milano Bicocca, Como, I-22100 Como, Italy
[77] Centre for Space Research, Private Bag X6001, North-West University, Potchefstroom Campus, Potchefstroom, 2520, South Africa
[78] INAF—Osservatorio Astrofisico di Torino, I-10025 Pino Torinese (TO), Italy
[79] Instituto de Astrofisica de Canarias (IAC), La Laguna, Tenerife, Spain
[80] Departamento de Astrofisica, Universidad de La Laguna, La Laguna, Tenerife, Spain
[81] Institute of Astronomy, Bulgarian Academy of Sciences, 72 Tsarigradsko shosse Blvd., 1784 Sofia, Bulgaria
[82] Tuorla Observatory, Department of Physics and Astronomy, Väisäläntie 20, FI-21500 Piikkiö, Finland
[83] Astronomical Institute, St. Petersburg State University, Universitetskij Pr. 28, Petrodvorets, 198504 St. Petersburg, Russia

[84] Department of Physics and Institute for Plasma Physics, University of Crete, 71003, Heraklion, Greece
[85] Foundation for Research and Technology—Hellas, IESL, Voutes, 71110 Heraklion, Greece
[86] Graduate Institute of Astronomy, National Central University, 300 Zhongda Road, Zhongli 32001, Taiwan
[87] Astronomical Observatory, Volgina 7, 11060 Belgrade, Serbia
[88] School of Cosmic Physics, Dublin Institute For Advanced Studies, Ireland
[89] Institute for Astrophysical Research, Boston University, 725 Commonwealth Avenue, Boston, MA 02215, USA
[90] Abastumani Observatory, Mt. Kanobili, 0301 Abastumani, Georgia
[91] Engelhardt Astronomical Observatory, Kazan Federal University, Tatarstan, Russia
[92] Center for Astrophysics, Guangzhou University, Guangzhou 510006, China
[93] Pulkovo Observatory, St.-Petersburg, Russia
[94] Institute of Astronomy and NAO, Sofia, Bulgaria
[95] Steward Observatory, University of Arizona, 933 N. Cherry Ave., Tucson, AZ 85721, USA
[96] Department of Physics, Salt Lake Community College, Salt Lake City, UT 84070 USA
[97] Istanbul University, Science Faculty, Department of Astronomy and Space Sciences, Beyazıt, 34119, Istanbul, Turkey
[98] Department of Physics and Astronomy, Brigham Young University, Provo, UT 84602, USA
[99] Department of Physics, University of Colorado Denver, Denver, Colorado, CO 80217-3364, USA
[100] Center for Field Theory and Particle Physics and Department of Physics, Fudan University, 200433 Shanghai, China
[101] Aalto University, Metsähovi Radio Observatory, Metsähovintie 114, FI-02540 Kylmälä, Finland
[102] National Radio Astronomy Observatory, P.O. Box 0, Socorro, NM 87801, USA
[103] Aalto University Department of Radio Science and Engineering, P.O. BOX 13000, FI-00076 Aalto, Finland
[104] Max-Planck-Institut für Radioastronomie, Auf dem Hügel 69, D-53121 Bonn, Germany
[105] Instituto de Radio Astronomia Milimétrica, Avenida Divina Pastora 7, Local 20, 18012 Granada, Spain
Received 2015 September 24; accepted 2015 December 5; published 2016 March 9

ABSTRACT

We present coordinated multiwavelength observations of the bright, nearby BL Lacertae object Mrk 421 taken in 2013 January–March, involving GASP-WEBT, *Swift*, *NuSTAR*, *Fermi*-LAT, MAGIC, VERITAS, and other collaborations and instruments, providing data from radio to very high energy (VHE) γ-ray bands. *NuSTAR* yielded previously unattainable sensitivity in the 3–79 keV range, revealing that the spectrum softens when the source is dimmer until the X-ray spectral shape saturates into a steep $\Gamma \approx 3$ power law, with no evidence for an exponential cutoff or additional hard components up to ∼80 keV. For the first time, we observed both the synchrotron and the inverse-Compton peaks of the spectral energy distribution (SED) simultaneously shifted to frequencies below the typical quiescent state by an order of magnitude. The fractional variability as a function of photon energy shows a double-bump structure that relates to the two bumps of the broadband SED. In each bump, the variability increases with energy, which, in the framework of the synchrotron self-Compton model, implies that the electrons with higher energies are more variable. The measured multi band variability, the significant X-ray-to-VHE correlation down to some of the lowest fluxes ever observed in both bands, the lack of correlation between optical/UV and X-ray flux, the low degree of polarization and its significant (random) variations, the short estimated electron cooling time, and the significantly longer variability timescale observed in the *NuSTAR* light curves point toward in situ electron acceleration and suggest that there are multiple compact regions contributing to the broadband emission of Mrk 421 during low-activity states.

Key words: BL Lacertae objects: individual (Markarian 421) – galaxies: active – gamma rays: general – radiation mechanisms: nonthermal – X-rays: galaxies

1. INTRODUCTION

Markarian 421 (Mrk 421 hereafter) is a nearby active galaxy with a featureless optical spectrum devoid of prominent emission or absorption lines, strongly polarized variable optical and radio flux, and compact (milliarcsecond-scale) radio emission. As such, it is classified as a BL Lacertae (BL Lac) type. Its spectral energy distribution (SED) is well described by a characteristic two-peak shape (for a review, see, e.g., Urry & Padovani 1995; Ulrich et al. 1997). In the more general context of blazars, Mrk 421 belongs to a subclass of the so-called high-energy-peaked BL Lac (HBL) objects, relatively low luminosity sources with both peaks located at relatively high energies (respectively at ∼1 keV and ∼100 GeV). Mrk 421 is among the closest and most comprehensively studied objects of the HBL class and is also the first extragalactic source detected in the very high energy (VHE) γ-ray band ($E > 100$ GeV; Punch et al. 1992).

The observed properties of Mrk 421, as well as other similar blazars, are best explained as arising from a relativistic jet seen at a small angle to our line of sight (Urry & Padovani 1995). The nonthermal and polarized continuum observed from the radio band to the soft X-ray band suggests that this part of the SED is due to a distribution of relativistic electrons radiating via the synchrotron process. The radiation in the γ-ray band is likely due to inverse-Compton scattering by energetic electrons responsible for the synchrotron radiation, as confirmed by simultaneous, correlated variations in the low- and high-energy SED components (e.g., Giebels et al. 2007; Fossati et al. 2008; Aleksić et al. 2015b). The seed photons are most likely the synchrotron photons internal to the jet. Such "synchrotron self-Compton" (SSC) models, developed by many authors (for early examples see, e.g., Jones et al. 1974; Ghisellini et al. 1985; Marscher & Gear 1985), have been successfully invoked to describe the full SED of HBL objects (e.g., Ulrich et al. 1997; Fossati et al. 2008; Tavecchio et al. 2010).

The range of measured flux of Mrk 421 spans up to two orders of magnitude in some spectral bands, with flares occurring on very short timescales (a day or less; e.g., Gaidos et al. 1996; Tanihata et al. 2003; Fossati et al. 2008). Possibly the best bands to study such variability are the X-ray and VHE γ-ray bands: in the context of the SSC model, they represent radiation from the most energetic electrons, which have the

shortest timescales for radiative losses. The cross-correlation of time series measured in various bands provides additional clues to the radiative processes, the acceleration and energy distribution of radiating particles, and the structure and intrinsic power of the relativistic jet. The relative temporal variability in different spectral bands, from radio through VHE γ-rays, provides an important handle on the location of the energy dissipation with respect to the central black hole (Sikora et al. 2009; Janiak et al. 2012). In the context of a specific model for the radiation, the underlying particle distributions may be determined more or less directly from the observed multiwavelength SEDs. Particle-acceleration mechanisms can then be constrained by the shape of those particle distributions. Diffusive shock acceleration, an example of a first-order Fermi (Fermi I) process, is generally associated with single power-law distributions (e.g., Blandford & Eichler 1987; Jones & Ellison 1991). In contrast, log-parabolic distributions are produced in models of stochastic acceleration (e.g., Massaro et al. 2004; Tramacere et al. 2011), which can be considered equivalent to a second-order Fermi (Fermi II) process.

Mrk 421 and other HBL-type blazars have been extensively studied in the soft X-ray band (e.g., Makino et al. 1987; Takahashi et al. 1996; Ravasio et al. 2004; Tramacere et al. 2007b, 2009), revealing a range of spectral slopes in various quiescent and flaring states. Less is known about the hard X-ray ($\gtrsim$10 keV) properties of blazar jet emission: the data are far fewer and available mostly for flaring episodes, or averaged over relatively long timescales (e.g., Guainazzi et al. 1999; Giebels et al. 2007; Fossati et al. 2008; Ushio et al. 2009; Abdo et al. 2011). This energy band probes the most energetic and fastest-varying tail of the distribution of synchrotron-radiating particles and therefore represents an important diagnostic of the content of the jet and the processes responsible for the acceleration of particles to the highest energies. The inverse-Compton component increases with energy and could potentially contribute significantly to the hard X-ray band. If so, it would also provide a strong constraint on the low-energy part of the electron distribution, which is a significant, if not dominant, part of the total kinetic power of the jet.

Mrk 421 observations were part of the *Nuclear Spectroscopic Telescope Array* (*NuSTAR*; Harrison et al. 2013) blazar program, aimed at advancing our understanding of astrophysical jets. The multiwavelength campaign focused on Mrk 421 was carried out between 2012 December and 2013 May, with three to four pointings per month, designed to maximize strictly simultaneous overlap with observations by the VHE γ-ray facilities VERITAS and MAGIC. We also secured nearly simultaneous soft X-ray, optical, and UV observations from the *Swift* satellite. The γ-ray data from *Fermi*-LAT, which observes Mrk 421 every 3 hr, was also used together with all the coordinated multiwavelength data. Mrk 421 varied in flux throughout the campaign, with a relatively low flux in the X-ray and VHE bands at the beginning, increasing to a major flare toward the end of the campaign. In this paper, we present part of the data collected during the first 3 months of the campaign, with particular emphasis on the detailed shape of the X-ray spectrum, its variability, and the correlated variability observed in VHE γ-rays. We also report briefly on the observations of Mrk 421 prior to the start of the campaign, in 2012 July, when the object was used for calibration purposes during the in-orbit verification phase of *NuSTAR*. During this period, Mrk 421 emission was broadly consistent with previously observed quiescent states, which we define here to be characterized by relatively low flux at all frequencies and by the absence of significant flaring (see, e.g., Abdo et al. 2011). The flaring period of the 2013 campaign will be covered in a separate publication.

The outline of the paper is as follows. In Section 2 we describe the multiwavelength observations and data used in this paper. We dedicate Section 3 to a detailed characterization of the hard X-ray spectrum of Mrk 421 with *NuSTAR*. The results of the multiwavelength campaign in 2013 January–March are presented in Section 4. Discussion of the empirical results and modeling of the broadband properties are given in Section 5, and in Section 6 we summarize the main results. We adopt a distance of 141 Mpc to Mrk 421, calculated from its measured redshift $z = 0.0308$ (based on absorption lines in the spectrum of the host galaxy; Ulrich et al. 1975) and the cosmological parameters recently refined by the Planck Collaboration (Ade et al. 2014): $h_0 = 0.67$, $\Omega_\Lambda = 0.685$.

2. OBSERVATIONS AND DATA ANALYSIS

2.1. Radio

The Owens Valley Radio Observatory (OVRO) 40 m telescope was used for observation at 15 GHz, as a part of a long-term blazar monitoring program. Additional observations were scheduled at times of coordinated observations with X-ray and VHE γ-ray observatories. The data were reduced using standard processing and calibration techniques described in detail in Richards et al. (2011). Radio observations of Mrk 421 between 2.64 and 142 GHz have been obtained within the framework of the F-GAMMA program (Fuhrmann et al. 2007, 2014; Angelakis et al. 2010), a γ-ray blazar monitoring program related to the *Fermi Gamma-ray Space Telescope*. Observations with the Effelsberg 100 m and Pico Veleta 30 m telescopes are performed roughly once per month. The Effelsberg measurements are conducted with heterodyne receivers at 2.64, 4.85, 8.35, 10.45, 14.60, 23.05, and 32.0 GHz, while the Pico Veleta telescope is used with the EMIR receiver to provide the high-frequency (86.2 and 142.3 GHz) flux measurements. Standard data processing and calibration were performed as described in Angelakis et al. (2008, 2015). The Metsähovi Radio Observatory 14 m telescope also participated in this multi-instrument campaign, providing observations of Mrk 421 at 37 GHz every few days. Details of the observing strategy and data reduction for this monitoring program can be found in Teräsranta et al. (1998).

2.2. Optical

The coverage at optical frequencies was provided by various telescopes around the world within the GASP-WEBT program (e.g., Villata et al. 2008, 2009). In particular, the following observatories contributed to this campaign: Teide (IAC80), Crimean, Lowell (Perkins telescope), Roque de los Muchachos (KVA and Liverpool telescopes), Abastumani, Pulkovo, St. Petersburg, Belogradchik, Rozhen (50/70 cm, 60 cm, and 200 cm telescopes), Vidojevica, and Lulin. Additionally, many observations were performed with iTelescopes, Bradford Robotic Telescope, ROVOR, and the TUBITAK National Observatory. In this paper, we use only *R*-band photometry. The calibration stars reported in Villata et al. (1998) were used for calibration, and the Galactic extinction was corrected with

the reddening corrections given in Schlafly & Finkbeiner (2011). The flux from the host galaxy was estimated using the *R*-band flux from Nilsson et al. (2007) for the apertures of 5″ and 7.″5 used by various instruments. We applied an offset of −5 mJy to the fluxes from ROVOR in order to achieve better agreement with the light curves from the other instruments. This difference may be related to the specific spectral response of the filters used, or the different analysis procedures that were employed. Additionally, a point-wise fluctuation of 2% on the measured flux was added in quadrature to the statistical uncertainties in order to account for potential day-to-day differences in observations with any of the instruments.

Polarization measurements are utilized from four observatories: Lowell (Perkins telescope), St. Petersburg, Crimean, and Steward (Bok telescope). The polarization measurements from Lowell and St. Petersburg observatories are derived from *R*-band imaging polarimetry. The measurements from Steward Observatory are derived from spectropolarimetry between 4000 and 7550 Å with a resolution of ∼15 Å. The reported values are constructed from the median Q/I and U/I in the 5000–7000 Å band. The effective wavelength of this bandpass is not too different from the Kron-Cousins *R* band, and the wavelength dependence in the polarization of Mrk 421 seen in the spectropolarimetry during this period is not strong enough to significantly affect the variability analysis of the measurements from various telescopes. The observing and data-processing procedures for the polarization measurements are described in Larionov et al. (2008), Smith et al. (2009), and Jorstad et al. (2010).

2.3. Swift UVOT and XRT

Swift observations with the UV/Optical Telescope (UVOT; Roming et al. 2005) were performed only with the UV filters (namely, W1, M2, and W2). Observations with the optical filters were not needed because we had organized extensive coverage with ground-based optical telescopes, which have better sensitivity and angular resolution than *Swift*-UVOT. We performed aperture photometry for all filters in all the observations using the standard UVOT software distributed within the HEAsoft package (version 6.10) and the calibration included in the latest release of the CALDB. Counts were extracted from an aperture of 5″ radius for all filters and converted to fluxes using the standard zero points from Breeveld et al. (2011). The fluxes were then dereddened using the value of $E(B-V) = 0.014$ (Schlegel et al. 1998; Schlafly & Finkbeiner 2011) with $A_\lambda/E(B-V)$ ratios calculated using the mean Galactic interstellar extinction curve from Fitzpatrick (1999). No variability was detected within single exposures in any filter. The results of the processing were carefully verified, checking for possible contaminations from nearby objects within source apertures and from objects falling within background apertures. In almost all observations, Mrk 421 is on the "ghost wings" (Li et al. 2006) from the nearby star 51 UMa, so we estimated the background from two circular apertures of 16″ radius off the source but on the wings, excluding stray light and support structure shadows.

The complete list of *Swift* X-ray Telescope (XRT; Burrows et al. 2005) and UVOT observations used here is given in Table 1. The observations were organized to be taken simultaneously with (or as close as possible to) the MAGIC/VERITAS and *NuSTAR* observations, following the fruitful monitoring campaign practice since 2009. *Swift* observed the source 33 times in 2013 up to the end of March. All *Swift*-XRT observations were carried out using the Windowed Timing (WT) readout mode. The data set was processed with the XRTDAS software package (version 2.9.0) developed at ASDC and distributed with the HEASoft package (version 6.13). Event files were calibrated and cleaned with standard filtering criteria with the `xrtpipeline` task using the latest calibration files available in the *Swift* CALDB. The average spectrum was extracted from the summed cleaned event file. Events for the spectral analysis were selected within a circle of 20 pixel (≃46″) radius, which encloses about 80% of the PSF, centered on the source position. The background was extracted from a nearby circular region of 40 pixel radius. The ancillary response files (ARFs) were generated with the `xrtmkarf` task applying corrections for PSF losses and CCD defects using the cumulative exposure map. The latest response matrices (version 14) available in the *Swift* CALDB were used.

Before the spectral fitting, the 0.3–10 keV source spectra were binned using the `grppha` task to ensure a minimum of 20 counts per bin. Spectra were modeled in `Xspec` (version 12.8.0) using power-law and log-parabolic models, identical to the modeling presented in detail in Section 3.2. The models include photoelectric absorption by a fixed column density estimated to be $N_{\rm H} = 1.92 \times 10^{20}\,{\rm cm}^{-2}$ (Kalberla et al. 2005). The log-parabolic model was found to fit the data better in each observation (though statistical improvement is marginal in some cases) and was therefore used to compute fluxes in various subbands. Spectral parameters are provided for each observation in Table 2.

2.4. NuSTAR

NuSTAR (Harrison et al. 2013) is a focusing hard X-ray telescope operating in the band from 3 to 79 keV. It is the first X-ray observatory to extend the sensitivity beyond the ≃10 keV cutoff shared by virtually every current focusing X-ray satellite. The inherently low background associated with concentrating target X-rays enables *NuSTAR* to achieve approximately a 100-fold improvement in sensitivity over the collimated and coded-mask instruments that operate, or have operated, in the same bandpass. All observations are conducted in parallel with two coaligned, independent telescopes called FPMA and FPMB (for Focal Plane Module A and B).

The *NuSTAR* primary mission includes monitoring of several types of blazars; Mrk 421 has been selected for this program as a representative of the high-peaked BL Lac (HBL) class. In order to maximize the strictly simultaneous overlap of observations by *NuSTAR* and ground-based VHE γ-ray observatories during the 5-month campaign, three observations per month were scheduled according to visibility of Mrk 421 at the MAGIC and VERITAS sites. A typical *NuSTAR* observation spanned 10 hr, resulting in 15–20 ks of source exposure after accounting for orbital modulation of visibility and filtering out South Atlantic Anomaly crossings where the background radiation is high. In addition to those observations, Mrk 421 was observed as a bright calibration target in 2012 July and early 2013 January. The total exposure time over 88 orbits of *NuSTAR* observations in this period is ≃250 ks. A list of all *NuSTAR* observations considered in this paper is given in Table 3. Analysis of the remainder of the campaign data will be presented elsewhere.

The raw data have been reduced using the NuSTARDAS software version 1.3.1, as a part of the HEAsoft package version 6.12. The spectra of Mrk 421 were extracted from a

Table 1
Summary of the *Swift* Observations of Mrk 421 (2013 January–March)

Sequence ID	Start Date	Start Time	Number of Orbits	Exposure[a] (ks)		UV Flux Density[b] (mJy)			Count Rate[c] (s^{-1})
	(UTC)	(MJD)		UVOT	XRT	W1	M1	W2	
00080050001	2013 Jan 02	56294.7961	2	1.6	1.8	26.8 ± 0.9	27.0 ± 0.9	…	12.6 ± 0.1
00035014024	2013 Jan 04	56296.9370	1	1.0	1.0	23.6 ± 0.8	23.7 ± 0.8	20.4 ± 0.7	18.8 ± 0.2
00035014025	2013 Jan 08	56300.1523	1	0.8	0.8	21.1 ± 0.7	20.3 ± 0.7	17.6 ± 0.6	7.8 ± 0.1
00035014026	2013 Jan 10	56302.1557	2	1.1	1.7	22.5 ± 0.7	23.1 ± 0.8	19.7 ± 0.7	9.1 ± 0.1
00035014028	2013 Jan 10	56302.3418	2	0.8	1.3	22.7 ± 0.8	22.3 ± 0.7	19.2 ± 0.6	9.0 ± 0.1
00035014027	2013 Jan 10	56302.4752	1	1.3	1.3	22.1 ± 0.7	22.1 ± 0.7	18.8 ± 0.6	8.33 ± 0.09
00035014029	2013 Jan 10	56302.6764	3	2.9	3.8	21.5 ± 0.7	21.3 ± 0.7	18.3 ± 0.6	9.52 ± 0.06
00035014031	2013 Jan 10	56302.9601	1	0.7	0.7	21.3 ± 0.7	20.9 ± 0.7	18.1 ± 0.6	11.0 ± 0.2
00035014032	2013 Jan 12	56304.4790	1	1.1	1.1	18.7 ± 0.6	18.5 ± 0.6	16.1 ± 0.5	14.1 ± 0.1
00035014034	2013 Jan 15	56307.0928	3	3.8	4.0	17.2 ± 0.6	17.4 ± 0.6	15.0 ± 0.5	22.4 ± 0.1
00035014033	2013 Jan 15	56307.3519	5	5.0	6.3	17.7 ± 0.6	17.8 ± 0.6	15.4 ± 0.5	22.59 ± 0.08
00035014035	2013 Jan 18	56310.1675	1	1.0	1.0	18.9 ± 0.6	18.7 ± 0.6	16.1 ± 0.5	8.9 ± 0.1
00080050002	2013 Jan 20	56312.2389	7	3.9	8.8	19.6 ± 0.6	19.4 ± 0.6	16.4 ± 0.6	9.17 ± 0.04
00035014036	2013 Jan 22	56314.5070	1	1.1	1.1	21.7 ± 0.7	21.7 ± 0.7	19.2 ± 0.6	10.5 ± 0.1
00035014038	2013 Jan 25	56317.3009	3	0.6	7.8	15.7 ± 0.5	15.4 ± 0.6	13.4 ± 0.4	11.4 ± 0.2
00035014039	2013 Jan 28	56320.3057	1	1.0	1.0	13.7 ± 0.5	13.7 ± 0.5	12.0 ± 0.4	17.6 ± 0.2
00035014040	2013 Feb 01	56324.6601	1	1.1	1.1	13.3 ± 0.4	13.3 ± 0.4	11.7 ± 0.4	28.5 ± 0.2
00035014041	2013 Feb 04	56327.1409	2	0.3	0.8	15.3 ± 0.6	15.0 ± 0.6	13.4 ± 0.5	28.7 ± 0.3
00080050003	2013 Feb 06	56329.0586	6	2.1	9.5	14.5 ± 0.5	14.4 ± 0.5	12.8 ± 0.4	21.54 ± 0.05
00035014043	2013 Feb 10	56333.1279	1	1.0	1.0	13.2 ± 0.4	13.0 ± 0.4	11.3 ± 0.4	21.1 ± 0.2
00080050005	2013 Feb 12	56335.0700	6	2.6	6.3	17.4 ± 0.6	17.7 ± 0.6	15.7 ± 0.5	22.82 ± 0.08
00035014044	2013 Feb 15	56338.0045	1	1.0	0.8	18.1 ± 0.6	18.2 ± 0.6	15.8 ± 0.5	8.9 ± 0.6
00080050006	2013 Feb 17	56340.0047	7	2.9	9.2	18.1 ± 0.6	18.7 ± 0.6	16.1 ± 0.5	13.18 ± 0.05
00035014045	2013 Feb 19	56342.1393	2	0.6	1.1	16.0 ± 0.5	15.7 ± 0.6	13.4 ± 0.4	12.2 ± 0.2
00035014046	2013 Feb 23	56346.3481	1	1.0	1.0	19.6 ± 0.7	19.9 ± 0.7	17.5 ± 0.6	15.0 ± 0.2
00035014047	2013 Feb 27	56350.3573	1	1.1	1.1	19.6 ± 0.7	19.2 ± 0.6	17.0 ± 0.6	12.3 ± 0.1
00035014048	2013 Mar 01	56352.3675	1	1.1	1.0	19.4 ± 0.6	19.2 ± 0.6	16.5 ± 0.5	16.9 ± 0.1
00080050007	2013 Mar 04	56355.9845	1	1.0	1.0	23.8 ± 0.9	24.9 ± 0.8	21.2 ± 0.7	33.8 ± 0.3
00080050009	2013 Mar 05	56356.0538	5	2.5	3.9	24.0 ± 0.8	24.2 ± 0.8	21.0 ± 0.7	30.4 ± 0.1
00035014049	2013 Mar 07	56358.3190	1	0.9	0.6	27.0 ± 0.9	27.9 ± 0.9	25.3 ± 0.9	25.5 ± 0.3
00080050011	2013 Mar 12	56363.0045	7	6.1	8.3	25.6 ± 0.9	25.8 ± 0.9	22.0 ± 0.7	17.2 ± 0.8
00035014051	2013 Mar 15	56366.2540	1	0.8	0.8	20.5 ± 0.7	20.7 ± 0.7	18.0 ± 0.6	23.43 ± 0.06
00080050013	2013 Mar 17	56368.0609	6	7.7	8.9	22.5 ± 0.7	22.5 ± 0.7	19.5 ± 0.6	19.6 ± 0.3
00035014052	2013 Mar 18	56369.0665	1	1.0	1.0	21.1 ± 0.7	21.3 ± 0.7	18.6 ± 0.6	21.95 ± 0.07
00035014053	2013 Mar 19	56370.0675	1	1.0	1.0	20.7 ± 0.7	21.1 ± 0.7	19.2 ± 0.6	30.3 ± 0.2
00035014054	2013 Mar 23	56374.2797	1	0.9	1.0	20.7 ± 0.7	20.7 ± 0.7	18.5 ± 0.6	58.0 ± 0.3

Notes.
[a] For *Swift*-XRT, sum of all good time intervals after standard filtering; for *Swift*-UVOT, the total integration time, summed over all bands.
[b] Extinction-corrected flux in *Swift*-UVOT filters (see text for details).
[c] *Swift*-XRT source count rate in the 0.3–10 keV band averaged over the exposure time. Background has been subtracted, and PSF and pileup corrections have been applied. The uncertainty is quoted at 68% significance (1σ).

circular region of 100″ radius centered on the peak of the distribution of cleaned events. Background spectra were extracted from a region encompassing the same detector on which the source was focused, excluding the circular region from which the source counts were extracted. As the background generally differs between different detectors and may be variable on few-orbit timescales, extraction from a region of maximal area on the same detector where the source is present provides the best background estimate over the *NuSTAR* band. Nevertheless, other background extractions have been attempted and no significant differences have been observed in the results.

The response files were generated using the standard `nupipeline` and `nuproducts` scripts and the calibration files from CALDB version 20131223. All flux values reported in this paper have been corrected for the finite extraction aperture by the processing software. The dominant background component above 25 keV is the internal detector background. With good background characterization, the data may be used for spectral modeling up to the high-energy end of the *NuSTAR* band at 79 keV. The spectra of all *NuSTAR* observations of Mrk 421 are above the background level at least up to 25 keV and up to ≈40 keV in observations at high flux. For this reason, we quote count rates only up to 30 keV in the remainder of the paper. Three faint serendipitous sources have been found in the *NuSTAR* field of view (detected only in the deep co-added image using all observations presented in G. B. Lansbury et al., in preparation); however, they do not represent a contamination problem owing to the overwhelming brightness of Mrk 421 in all epochs.

Table 2
Models Fitted to the *Swift*-XRT Spectra of Each Observation

	Power Law		Log-parabola ($E_* = 1$ keV)			Time-averaged Flux[a]		
Start Time (MJD)	Γ	χ^2/dof	α	β	χ^2/dof	0.3–3 keV	3–7 keV	2–10 keV
56294.7906	2.86 ± 0.03	254/199	2.85 ± 0.03	0.23 ± 0.09	233/198	20.0 ± 0.5	2.7 ± 0.2	5.6 ± 0.4
56296.9370	2.68 ± 0.02	281/227	2.64 ± 0.02	0.28 ± 0.07	235/226	27.0 ± 0.3	4.8 ± 0.2	9.9 ± 0.6
56300.1523	2.75 ± 0.04	171/144	2.74 ± 0.04	0.1 ± 0.1	168/143	10.0 ± 0.4	1.8 ± 0.1	3.6 ± 0.3
56302.1557	2.80 ± 0.03	219/198	2.79 ± 0.03	0.16 ± 0.09	208/197	13.0 ± 0.2	2.0 ± 0.2	4.1 ± 0.3
56302.3418	2.82 ± 0.03	199/183	2.79 ± 0.03	0.2 ± 0.1	187/182	14.0 ± 0.2	2.1 ± 0.2	4.3 ± 0.3
56302.4751	2.89 ± 0.03	175/172	2.87 ± 0.03	0.3 ± 0.1	159/171	13.0 ± 0.4	1.5 ± 0.1	3.3 ± 0.2
56302.6764	2.74 ± 0.02	335/275	2.71 ± 0.02	0.19 ± 0.06	304/274	14.0 ± 0.2	2.4 ± 0.1	5.0 ± 0.2
56302.9601	2.75 ± 0.04	139/155	2.73 ± 0.04	0.2 ± 0.1	132/154	15.0 ± 0.2	2.5 ± 0.3	5.1 ± 0.2
56304.4790	2.60 ± 0.02	252/218	2.56 ± 0.03	0.26 ± 0.08	219/217	21.0 ± 0.6	4.2 ± 0.2	8.4 ± 0.3
56307.0928	2.49 ± 0.01	500/394	2.45 ± 0.01	0.22 ± 0.03	385/393	33.0 ± 0.2	8.3 ± 0.4	16.0 ± 0.4
56307.3519	2.60 ± 0.01	728/431	2.56 ± 0.01	0.26 ± 0.03	477/430	33.0 ± 0.2	6.6 ± 0.2	13.0 ± 0.3
56310.1675	2.85 ± 0.03	198/161	2.83 ± 0.04	0.3 ± 0.1	180/160	12.0 ± 0.3	1.6 ± 0.1	3.5 ± 0.3
56312.2389	2.72 ± 0.01	403/351	2.69 ± 0.01	0.17 ± 0.04	350/350	14.0 ± 0.1	2.5 ± 0.1	5.1 ± 0.1
56314.5070	2.69 ± 0.03	232/197	2.68 ± 0.03	0.07 ± 0.10	229/196	16.0 ± 0.3	3.2 ± 0.2	6.4 ± 0.3
56317.3009	2.71 ± 0.03	165/171	2.69 ± 0.04	0.2 ± 0.1	158/170	17.0 ± 0.3	3.0 ± 0.3	6.2 ± 0.4
56320.3057	2.58 ± 0.02	278/216	2.53 ± 0.03	0.31 ± 0.08	238/215	25.0 ± 0.6	5.1 ± 0.3	10.0 ± 0.5
56324.6601	2.35 ± 0.02	302/261	2.31 ± 0.03	0.21 ± 0.06	270/260	49.0 ± 0.7	15.0 ± 0.5	30 ± 1
56327.1409	2.51 ± 0.02	307/250	2.45 ± 0.02	0.33 ± 0.07	231/249	40.0 ± 0.5	9.1 ± 0.3	18.0 ± 0.9
56329.0586	2.39 ± 0.01	1123/530	2.33 ± 0.01	0.24 ± 0.02	687/529	31.0 ± 0.1	9.0 ± 0.1	18.0 ± 0.3
56333.1279	2.41 ± 0.02	307/256	2.37 ± 0.02	0.21 ± 0.06	277/255	31.0 ± 0.6	8.8 ± 0.4	17.0 ± 0.6
56335.0700	2.51 ± 0.01	528/444	2.49 ± 0.01	0.10 ± 0.03	496/443	34.0 ± 0.3	8.9 ± 0.1	18.0 ± 0.2
56338.0045	2.76 ± 0.03	172/169	2.74 ± 0.04	0.2 ± 0.1	166/168	17.0 ± 0.3	2.8 ± 0.3	5.8 ± 0.6
56340.0047	2.61 ± 0.01	586/419	2.58 ± 0.01	0.17 ± 0.03	493/418	20.0 ± 0.1	4.2 ± 0.1	8.4 ± 0.2
56342.1393	2.53 ± 0.03	243/187	2.51 ± 0.04	0.1 ± 0.1	236/186	19.0 ± 0.3	4.5 ± 0.5	9.0 ± 0.3
56346.3481	2.75 ± 0.03	223/196	2.72 ± 0.03	0.27 ± 0.09	198/195	21.0 ± 0.6	3.3 ± 0.2	6.9 ± 0.4
56350.3573	2.60 ± 0.03	221/196	2.57 ± 0.03	0.20 ± 0.09	206/195	18.0 ± 0.4	3.8 ± 0.3	7.6 ± 0.5
56352.3675	2.46 ± 0.02	269/243	2.44 ± 0.03	0.14 ± 0.07	256/242	24.0 ± 0.5	6.5 ± 0.4	13.0 ± 0.8
56355.9845	2.52 ± 0.02	279/256	2.48 ± 0.02	0.21 ± 0.07	249/255	55.0 ± 0.8	13.0 ± 0.6	26.0 ± 0.6
56356.0538	2.55 ± 0.01	692/444	2.52 ± 0.01	0.21 ± 0.03	518/443	45.0 ± 0.4	10.0 ± 0.2	20.0 ± 0.4
56358.3190	2.39 ± 0.03	230/213	2.41 ± 0.03	−0.07 ± 0.08	228/212	48 ± 1	17 ± 1	33 ± 2
56363.0045	2.57 ± 0.01	837/476	2.53 ± 0.01	0.24 ± 0.02	517/475	34.0 ± 0.2	7.3 ± 0.1	15.0 ± 0.2
56366.2540	2.40 ± 0.02	230/245	2.38 ± 0.03	0.12 ± 0.07	222/244	27.0 ± 0.3	8.4 ± 0.4	16.0 ± 0.9
56368.0609	2.40 ± 0.01	758/516	2.37 ± 0.01	0.14 ± 0.02	643/515	34.0 ± 0.2	10.0 ± 0.2	20.0 ± 0.2
56369.0665	2.37 ± 0.02	352/301	2.33 ± 0.02	0.19 ± 0.05	315/300	44.0 ± 0.5	14.0 ± 0.6	27.0 ± 0.8
56370.0675	2.36 ± 0.02	323/308	2.34 ± 0.02	0.09 ± 0.05	313/307	43.0 ± 0.6	14.0 ± 0.4	28.0 ± 0.8
56374.2797	2.14 ± 0.01	539/425	2.08 ± 0.02	0.18 ± 0.03	457/424	78.0 ± 0.7	35.0 ± 0.6	68 ± 2

Note.
[a] Flux calculated from the best-fit model, in units of 10^{-11} erg s^{-1} cm^{-2}.

2.5. *Fermi*-LAT

The Large Area Telescope (LAT) on board the *Fermi* satellite is a pair-conversion telescope with energy coverage from 20 MeV to >300 GeV. LAT has a ∼2.4 sr field of view and provides all-sky monitoring coverage on a ∼3 hr timescale (Atwood et al. 2009). For the analyses presented in this paper, we have selected `Source` class events with energies in the range 0.1–300 GeV and within 15° of the position of Mrk 421. In order to greatly reduce contamination from Earth limb photons, we have excluded events at zenith angles >100° and any events collected when the spacecraft rocking angle was >52°. The data were analyzed using the `P7REP_SOURCE_V15` instrument-response functions and the standard unbinned-likelihood software provided with version 09-33-00 of the *Fermi* Science Tools.[106]

The analyses considered data in day-long and week-long intervals contemporaneous with the *NuSTAR* observation windows. The likelihood model used for all intervals included the sources from the second *Fermi*-LAT catalog (Nolan et al. 2012) located within a 15° region of interest centered on Mrk 421, as well as the standard Galactic diffuse, isotropic, and residual instrumental background emission models provided by the Fermi Science Support Center.[107] For all epochs, the spectrum of Mrk 421 was fitted with a power-law model, with both the flux normalization and photon index being left as free parameters in the likelihood fit. We summarize the spectral parameters for four selected epochs (discussed in detail in Section 5) in Table 4. The systematic uncertainty on the flux is estimated as approximately 5% at 560 MeV and under 10% at 10 GeV and above (Ackermann et al. 2012). As variability in the *Fermi*-LAT band

[106] http://fermi.gsfc.nasa.gov/ssc/data/analysis/

[107] http://fermi.gsfc.nasa.gov/ssc/data/access/lat/BackgroundModels.html

Table 3
Summary of the *NuSTAR* Observations of Mrk 421 (2013 January–March)

Sequence ID	Start Date (UTC)	Start Time (MJD)	Number of Orbits	Duration (ks)	Exposure[a] (ks)	Count Rate[b] (s^{-1}) FPMA	Count Rate[b] (s^{-1}) FPMB
10002015001	2012 Jul 07	56115.1353	14	81.0	42.0	3.71 ± 0.01	3.84 ± 0.01
10002016001	2012 Jul 08	56116.0732	8	46.2	25.4	4.18 ± 0.01	4.45 ± 0.01
60002023002	2013 Jan 02	56294.7778	3	15.6	9.2	1.162 ± 0.009	1.155 ± 0.008
60002023004	2013 Jan 10	56302.0533	8	44.6	22.6	0.785 ± 0.007	0.751 ± 0.006
60002023006	2013 Jan 15	56307.0386	8	45.9	22.4	2.79 ± 0.01	2.74 ± 0.01
60002023008	2013 Jan 20	56312.0980	8	45.2	24.9	0.923 ± 0.006	0.899 ± 0.006
60002023010	2013 Feb 06	56329.0116	8	42.2	19.3	3.52 ± 0.01	3.55 ± 0.01
60002023012	2013 Feb 12	56335.0106	6	35.4	14.8	4.39 ± 0.02	4.43 ± 0.02
60002023014	2013 Feb 17	56339.9828	7	41.7	17.4	1.50 ± 0.01	1.54 ± 0.01
60002023016	2013 Mar 04	56355.9631	6	35.0	17.3	4.11 ± 0.02	4.13 ± 0.02
60002023018	2013 Mar 11	56362.9690	6	31.9	17.5	3.04 ± 0.01	3.02 ± 0.01
60002023020	2013 Mar 17	56368.0210	6	35.1	16.6	4.33 ± 0.02	4.38 ± 0.02

Notes.
[a] Livetime-corrected sum of all good time intervals composing the observation.
[b] PSF-corrected source count rate and its uncertainty in the 3–30 keV band averaged over the exposure time.

was not significant, these epochs may be considered representative of the entire 2013 January–March period.

2.6. MAGIC

MAGIC is a system of two 17 m diameter imaging air-Cherenkov telescopes (IACTs) located at the Roque de los Muchachos Observatory on La Palma, one of the Canary Islands (28°46′ N, 17°53.′4 W at 2231 m above sea level). The hardware was substantially upgraded during 2011 and 2012 (Aleksić et al. 2016a), which yielded a performance characterized by a sensitivity of ≃0.7% of the Crab Nebula flux to detect a point-like source above 200 GeV at 5σ in 50 hr of observation. Equivalently, a 1 hr integration yields a detection of a source with approximately 5% Crab flux. The angular resolution is $\lesssim 0.^{\circ}07$ (68% containment, >200 GeV), and the energy resolution is 16%. The systematic uncertainties in the spectral measurements for a Crab-like point source were estimated to be 11% in the normalization factor (at ≃200 GeV) and 0.15 in the power-law slope. The systematic uncertainty in the absolute energy determination is estimated to be 15%. Further details about the performance of the MAGIC telescopes after the hardware upgrade in 2011–2012 can be found in Aleksić et al. (2016b).

After data-quality selection, Mrk 421 was observed with MAGIC for a total of 10.8 hr between 2013 January 8 and 2013 March 18. Most of these observations (8 hr in total) were strictly simultaneous with the *NuSTAR* observations. They were performed in the "false-source tracking" mode (Fomin et al. 1994), where the target source position has an offset of $0.^{\circ}4$ from the camera center, so that both signal and background data are taken simultaneously. Those data were analyzed following the standard procedure described in Aleksić et al. (2016b), using the MAGIC Analysis and Reconstruction Software (MARS; Moralejo et al. 2009). The analysis cuts to extract γ-ray signals from the hadronic background were optimized on the Crab Nebula data and dedicated Monte Carlo simulations of γ-ray-induced showers.

The significance of the source detection, calculated using Equation (17) from Li & Ma (1983), varied between 8.3σ (MJD 56310) and 38.3σ (MJD 56335). Observed intranight variability is not statistically significant, so we used data integrated over complete observations for the spectral analysis. Spectra were modeled with a power-law function with a normalization energy of 300 GeV. The normalization energy was chosen to be 300 GeV for both MAGIC and VERITAS, in order to facilitate a direct comparison of the VHE spectral results. For observations in which the spectrum is not well described by a power-law model (MJD 56302, 56335, and 56363), we additionally fit a log-parabolic model. A summary of the observations and the spectral modeling is given in Table 5. All uncertainties quoted in the table and in the rest of the paper are statistical only.

2.7. VERITAS

The Very Energetic Radiation Imaging Telescope Array System (VERITAS) is an array of four 12 m diameter IACTs located in southern Arizona (Weekes et al. 2002; Holder et al. 2006) designed to detect emission from astrophysical objects in the energy range from ∼100 GeV to greater than 30 TeV. A source with 1% of the Crab Nebula flux can be detected in ≃25 hr of observations; equivalently, a source with approximately 5% Crab flux can be detected in a 1 hr integration. VERITAS has an energy resolution of ≃15% and an angular resolution (68% containment) of $\sim 0.^{\circ}1$ per event at 1 TeV. The uncertainty on the VERITAS energy calibration is approximately 20%. The systematic uncertainty on reconstructed spectral indices is estimated at 0.2, independent of the source spectral index, according to studies of Madhavan (2013). Details of the sensitivity of the system after the recent hardware upgrade can be found on the VERITAS Web site.[108]

VERITAS observations of Mrk 421 were carried out under good weather conditions during the period of the *NuSTAR* campaign, resulting in a total, quality-selected exposure time of 15.5 hr during the period 2013 January 10 to 2013 March 17, almost all of which is strictly simultaneous with *NuSTAR* exposures. These observations were taken at $0.^{\circ}5$ offset in each of four cardinal directions from the position of Mrk 421 to enable simultaneous background estimation using

[108] http://veritas.sao.arizona.edu/specifications

Table 4
Spectral Parameters of the *Fermi*-LAT Observations of Mrk 421 for Four Selected Epochs in 2013 January–March

Start Time (MJD)	Stop Time (MJD)	Photon Flux[a] (10^{-7} s^{-1} cm^{-2})	Photon Index	Energy Flux[a] (10^{2} eV s^{-1} cm^{-2})
56112.1500	56119.6000	2.3 ± 0.4	1.74 ± 0.09	3.4 ± 0.8
56291.7900	56298.5200	2.1 ± 0.5	1.8 ± 0.1	2.9 ± 0.8
56298.5200	56304.8200	1.5 ± 0.4	1.6 ± 0.1	3.1 ± 0.9
56304.8200	56309.8400	2.6 ± 0.6	1.9 ± 0.1	3 ± 1

Note.
[a] Fluxes in the 0.1–100 GeV band.

the "false-source tracking" method (Fomin et al. 1994). Detected events are parameterized by the principal moments of the elliptical images of the Cherenkov shower in each camera (Hillas 1985). Cosmic-ray background rejection is carried out by discarding events based on a set of selection cuts that have been optimized a priori using VERITAS observations of the blazar 1ES 1218+304 (photon index 3.0) and the Crab Nebula (photon index 2.5). The results were verified using two independent analysis packages (Cogan 2008; Daniel 2008).

The significance of the source detection was calculated using Equation (17) from Li & Ma (1983) and was found to vary between 18.7σ (on MJD 56302) and 40.4σ (on MJD 56368). No significant intranight variability was detected. Since the observations spanned several hours during each night, the energy threshold varied owing to the range of zenith angles observed. Fluxes are therefore quoted at a commonly reached minimum energy of 200 GeV. We modeled the spectra with a power-law function with a normalization energy of 300 GeV. For four observations (MJD 56302, 56356, 56363, and 56368), the spectrum is better described with a log-parabolic model, while for the other observations this model does not provide a significantly better fit than the simpler power-law model. A summary of the observations, VHE flux, and spectral parameters with their statistical uncertainties is given in Table 6.

3. CHARACTERIZATION OF THE HARD X-RAY SPECTRUM OF MRK 421 WITH *NuSTAR*

3.1. Flux and Hardness Ratio Variability

Figure 1 shows the background-subtracted X-ray light curves extracted from the *NuSTAR* observations of Mrk 421 listed in Table 3. The split into subbands at 7 keV is based on the spectral analysis and justified in later sections. The count rate above 30 keV is dominated by the background on short timescales and is therefore not shown here. The differences in count rates between observations, as well as the range covered in each particular observation, are entirely dominated by the intrinsic variability of the target. For example, the calibration observation taken in 2012 July (the top panel of Figure 1) includes a possible "flare" in which the count rate increased by a factor of 2.5 over a 12 hr period and dropped by almost a factor of two in 3 hr. Several observations in 2013 have shown a steadily decreasing count rate over the course of $\simeq$12 hr. We did not observe any sharp increases followed by exponential decay typical of flaring events, although we cannot exclude the possibility that the observed count rate decreases are due to such events. All of the observed increases in the count rate (e.g., 2012 July 7 and 8, 2013 February 6, as well as 2013 March 5 and 17 on a shorter timescale) appear rather symmetric with respect to subsequent decreases. The campaign observations up to the end of 2013 March have predominantly covered relatively low flux states of Mrk 421, even though the lowest and the highest observed fluxes span almost an order of magnitude.

The observed count rates are not consistent with a constant flux during any of the observations. However, the dominant variations in the count rate can be described as smooth on a timescale of several hours. If a simple exponential decay fit, $R(t) \propto e^{-t/\tau_{\rm var}}$, is performed on the observations that show significant downward trends (2012 July 8, 2013 January 15, February 12 and 17, March 5 and 12), the typical decay timescale ($\tau_{\rm var}$) is found to be between 6 and 12 hr. These rough fits are not meant to describe the light curves fully, but only to provide an estimate of the timescale on which the flux changes significantly. For the remainder of the paper we use $\tau_{\rm var} = 9 \pm 3$ hr as our best estimate of this timescale.

In order to characterize the variability on shorter timescales ($\Delta t \ll \tau_{\rm var}$), we consider the data in individual *NuSTAR* orbits as this represents a natural, albeit still arbitrary, way of partitioning the data. The *NuSTAR* orbits are approximately 90 minutes long and contain roughly 50 minutes of source exposure. We treat each orbit independently and fit two simple light-curve models to the observed count rates: a constant flux during the orbit, $R(t) =$ constant, and a linear trend in time, i.e., $R(t) \propto t$. The upper panel of Figure 2 provides an example of both models fitted to the 2012 July data binned into 10-minute time bins, so that each orbit is divided into 5–7 bins per focal-plane module.[109] The lower panel of Figure 2 shows the results of this fitting procedure performed on all 88 orbits.

We find that the flux during the majority of orbits is better described by a linear trend than by a constant-flux model. Linear trends account for most of the orbit-to-orbit variability and approximate smooth variations on super-orbital timescales of $\tau_{\rm var} \approx 9$ hr. In 10-minute bins, for example, the variability amplitude typically does not exceed the observed count-rate uncertainty of 3%. Based on the mildly overpopulated tail of the reduced-χ^2 distribution for the linear-trend fits, we estimate that up to 20% of orbits show excess variance beyond the simple linear trend. Subtracting that trend and comparing the residual scatter to the median rate uncertainty within each orbit, $(\sigma_R)_{\rm orb}$, gives a distribution slightly skewed toward values greater than unity (see lower right panel of Figure 2). This is consistent with intrinsic suborbital variability on a $\sim$10-minute timescale in $\lesssim$20% of orbits, while for the majority of the observations the short-timescale variability can be constrained to have a $\lesssim$5% amplitude. These results are independent of the exact choice of the bin size and hold for any subhour binning.

[109] Because these data were taken in the calibration phase of the mission in suboptimal pointing conditions, a systematic uncertainty of 4% was added to the light curve to reflect the total uncertainty in the true count rate.

Table 5
Summary of the MAGIC Observations of Mrk 421 (2013 January–March)

Start Time (MJD)	Exposure (minutes)	Zenith Angle (deg)	σ[a]	Model Fit[b,c] F_0	Model Fit[b,c] Γ or α	Model Fit[b,c] β	Model Fit[b,c] χ^2/dof	Flux $>$ 200 GeV[c] (10^{-11} s^{-1} cm^{-2})
56302.1365	122	9–23	16.5	1.7 ± 0.1	2.87 ± 0.07	…	19.7 / 16	…
				1.9 ± 0.1	3.2 ± 0.2	0.8 ± 0.3	9.7 / 15	5.7 ± 0.4
56307.2556	39	21–29	14.9	3.0 ± 0.2	2.48 ± 0.09	…	18.8 / 15	10.4 ± 0.9
56310.2441	54	20–31	8.3	1.3 ± 0.2	2.8 ± 0.1	…	11.6 / 14	3.7 ± 0.5
56312.1718	119	9–33	11.5	1.3 ± 0.1	2.9 ± 0.1	…	8.8 / 20	3.9 ± 0.4
56316.2417	29	24–30	10.9	2.4 ± 0.2	2.3 ± 0.1	…	21.5 / 17	8.1 ± 0.9
56327.0731	25	16–22	25.7	8.6 ± 0.4	2.27 ± 0.05	…	20.5 / 19	34 ± 2
56333.1147	29	9–10	15.8	4.4 ± 0.3	2.34 ± 0.09	…	15.5 / 15	16 ± 1
56335.0795	116	9–24	38.3	5.7 ± 0.2	2.52 ± 0.03	…	25.9 / 19	…
				6.4 ± 0.3	2.53 ± 0.04	0.33 ± 0.09	9.6 / 18	20.5 ± 0.7
56340.1722	29	23–36	13.5	3.0 ± 0.3	2.4 ± 0.1	…	18.7 / 14	10 ± 1
56362.0826	29	15–21	20.1	6.0 ± 0.4	2.36 ± 0.07	…	22.1 / 19	20.7 ± 1.4
56363.1066	56	23–33	29.1	5.8 ± 0.2	2.56 ± 0.04	…	34.0 / 20	…
				6.8 ± 0.4	2.59 ± 0.06	0.56 ± 0.06	18.6 / 19	20 ± 1

Notes.
[a] Detection significance, computed according to Equation (17) from Li & Ma (1983) using data above 200 GeV integrated over the exposure time.
[b] A power-law model of the form $dN/dE = F_0\,(E/E')^{-\Gamma}$, $E' = 300$ GeV, is fitted to each observation. A log-parabolic model fit of the form $dN/dE = F_0\,(E/E')^{-\alpha-\beta\log(E/E')}$ is shown for observations in which it provides a better description of the spectrum than the power-law model. The normalization constant, F_0, is in units of 10^{-10} s^{-1} cm^{-2} TeV^{-1}.
[c] Quoted uncertainties are statistical.

Table 6
Summary of the VERITAS Observations of Mrk 421 (2013 January–March)

Start Time (MJD)	Exposure (minutes)	Zenith Angle (deg)	σ[a]	Model Fit[b,c] F_0	Model Fit[b,c] Γ or α	Model Fit[b,c] β	Model Fit[b,c] χ^2/dof	Flux $>$ 200 GeV[c] (10^{-11} s^{-1} cm^{-2})
56302.3411	131	9–33	18.7	1.7 ± 0.2	3.2 ± 0.2	…	10.2 / 5	…
				1.8 ± 0.2	3.3 ± 0.2	1.1 ± 0.7	7.9 / 4	5.2 ± 0.6
56307.3487	170	8–28	34.5	3.6 ± 0.2	3.1 ± 0.1	…	15.7 / 9	12.2 ± 0.7
56312.3762	197	6–31	32.6	1.5 ± 0.1	3.2 ± 0.2	…	4.9 / 5	5.0 ± 0.4
56329.2864	49	7–28	25.2	4.5 ± 0.5	2.7 ± 0.2	…	8.2 / 5	17 ± 2
56340.3344	89	7–23	22.7	2.5 ± 0.2	3.2 ± 0.2	…	5.1 / 5	8.5 ± 0.8
56356.2352	43	6–21	33.6	6.0 ± 0.5	3.0 ± 0.1	…	10.4 / 8	…
				6.3 ± 0.5	3.0 ± 0.1	0.6 ± 0.4	8.2 / 7	20 ± 2
56363.2355	127	7–17	39.2	3.5 ± 0.2	3.5 ± 0.1	…	16.7 / 6	…
				4.1 ± 0.3	3.9 ± 0.1	1.9 ± 0.4	5.6 / 5	10.9 ± 0.8
56368.1885	123	9–26	40.4	4.3 ± 0.3	3.2 ± 0.1	…	9.2 / 9	…
				4.3 ± 0.3	3.2 ± 0.1	0.7 ± 0.3	4.6 / 8	13 ± 1

Notes.
[a] Detection significance, computed according to Equation (17) from Li & Ma (1983) using data above 200 GeV integrated over the exposure time.
[b] A power-law model of the form $dN/dE = F_0\,(E/E')^{-\Gamma}$, $E' = 300$ GeV, is fitted to each observation. A log-parabolic model fit of the form $dN/dE = F_0\,(E/E')^{-\alpha-\beta\log(E/E')}$ is shown for observations in which it provides a better description of the spectrum than the power-law model. The normalization constant, F_0, is in units of 10^{-10} s^{-1} cm^{-2} TeV^{-1}.
[c] Quoted uncertainties are statistical.

Based on a separate analysis of the low- and high-flux data alone, we do not find significant evidence for a change in variability characteristics with flux.

The hardness of the spectrum, defined here as the ratio of count rates in the hard 7–30 keV and in the soft 3–7 keV bands, changes over the course of the observations. In Figure 3 we show the general trend of the spectrum hardening when the count rate is higher. Although the observed range of hardness ratios is relatively large at any specific count rate, the overall trend is clearly present in the binned data shown with thick black lines. There are no apparent circular patterns observed in the count rate versus hardness ratio plane, as previously seen in soft X-ray observations during bright flaring periods (e.g., Takahashi et al. 1996; Ravasio et al. 2004; Tramacere et al. 2009). We note, however, that the circular patterns might not be observable in the *NuSTAR* data presented here simply

because the observations predominantly covered instances of declining flux, whereas the patterns arise from differences in the rising and the declining phases of a flare. The apparent symmetric features observed on 2012 July 7/8, 2013 February 6, and 2013 March 17 do not display enough contrast in flux and hardness ratio to show well-defined circular patterns.

3.2. Observation-averaged Spectroscopy

We first model the *NuSTAR* spectra for each observation separately, before examining the clear intra-observation spectral variability in Section 3.3 (see Figures 2 and 3, and Baloković et al. 2013a). All observation-averaged spectra are shown in Figure 4. For spectral analysis we use spectra grouped to a minimum of 20 photons per bin and perform the modeling in `Xspec` (version 12.8.0). The simplest model for a featureless blazar spectrum is a power-law function:

$$F(E) \propto E^{-\Gamma}, \tag{1}$$

where Γ is the photon index. The `Xspec` model is formulated as `phabs(zpow)`, where the `phabs` component accounts for the Galactic absorption with fixed hydrogen column density of $N_{\rm H} = 1.92 \times 10^{20}$ cm^{-2} (Kalberla et al. 2005). We first fit each of the 12 observation-averaged spectra with a power-law model and find that this model fits the observations with lower mean flux better than the ones where the mean flux is high (see Table 7). This is likely due to the fact that the higher-flux spectra are somewhat more curved than lower-flux ones, although the curvature is not immediately obvious to the eye, i.e., in Figure 4. The fits confirm that the effective photon index decreases with increasing flux, as suggested by the observed harder-when-brighter behavior shown in Figure 3.

The fitting results imply that a power-law model with $\Gamma \approx 3$ describes the data well for observations with the lowest flux observed in the campaign. The poorer fit of the power-law model for the high-flux observation data may be due to intrinsic curvature, or it may be simply an effect of superposition of different curved or broken-power-law spectra. The latter effect can certainly be expected to be present since the hardness does vary with the flux and the source exhibited significant variability during most of the observations (see Figure 1). We address this issue by examining spectra on a shorter timescale in Section 3.3. In order to better characterize the observation-averaged spectra, we replace the power-law model with two other simple models that allow extra degrees of freedom. The first one is a broken-power-law model, `bknpow`:

$$\begin{aligned} F(E) &\propto E^{-\Gamma_1},\ E < E_b; \\ F(E) &\propto E^{-\Gamma_2},\ E > E_b. \end{aligned} \tag{2}$$

This model provides better fits to highest-flux spectra. However, the broken-power-law form is degenerate at low flux and degrades into the simpler power-law shape discussed above for observations of low mean flux (i.e., the photon indices converge to a single value and E_b becomes unconstrained). Both photon indices depend on the flux, but the dependence of Γ_2 seems to be weaker. The break energy seems to be largely independent of flux and relatively poorly constrained to the range roughly between 5 and 10 keV.

The third `Xspec` model we use is a simple log-parabolic shape, `logpar`:

$$f(E) \propto (E/E_*)^{-\alpha-\beta\log(E/E_*)}. \tag{3}$$

In this model, α and β are free parameters, while E_* is the so-called pivot energy (fixed parameter) at which α equals the local power-law photon index. The β parameter describes deviation of the spectral slope away from E_*. In our analysis we fix the value of E_* to 5 keV, so that α closely approximates the photon index in the 3–7 keV band. This model fits all observations well and also hints at spectral trends outlined earlier. The log-parabolic model does not provide statistically better fits than the broken-power-law model; in most cases they fit equally well (see Table 7). However, the log-parabolic is often used for modeling blazar spectra in the literature and does not contain a rather unphysical sharp break in the spectrum. All relevant parameters of the fits to the observation-averaged spectra are summarized in Table 7. We note that for the *NuSTAR* observation on 2013 January 2 (MJD 56294), the best-fit parabolic model has marginally significant negative curvature, $\beta = -0.2 \pm 0.1$. As this is the shortest of all *NuSTAR* observations and the same effect is not observed in any of the other spectra, while negative curvature is a physically possible scenario, it is likely that this anomalous result arises from the fact that the high-energy background is not sufficiently well sampled in such a short exposure.

3.3. Time-resolved Spectroscopy

We next consider spectra integrated over time intervals shorter than the complete *NuSTAR* observations. Separating the data into individual orbits represents the most natural although still arbitrary way of partitioning. Any particular orbit has a smaller spread in flux compared to a complete observation, since variability amplitude is significantly lower—we have established in Section 3.1 that the dominant flux variations occur on a super-orbital timescale of $\tau_{\rm var} \approx 9$ hr. The shorter exposures significantly reduce the statistical quality but still allow for a basic spectral analysis, such as the one presented in the preceding section, to be performed on spectra from single orbits. The average orbit exposure is 2.8 ks, and the total number of source counts per orbit is between 2000 and 20,000 per focal-plane module.

As with the observation-averaged spectra, we fit power-law, broken-power-law, and log-parabolic models using `Xspec`. We again find that the broken-power-law model parameter E_b (the break energy) is poorly constrained in general, so we fix it at 7 keV for the remainder of this analysis. Choosing a different value in the interval between 5 and 10 keV does not significantly alter any results; however, break energies outside of that interval cause one of the photon indices to become poorly constrained in a considerable number of orbits. Similarly, the curvature parameter of the log-parabolic model (β) is poorly constrained for the lowest-flux data, likely owing to both the lack of intrinsic curvature and relatively poor photon statistics. In a similar manner to the observation-averaged spectral modeling, the log-parabolic model does not necessarily provide statistically better fits than the broken power-law model. We use it because it provides a smooth spectrum over the modeled energy range, and in order to facilitate comparison to other work in the literature.

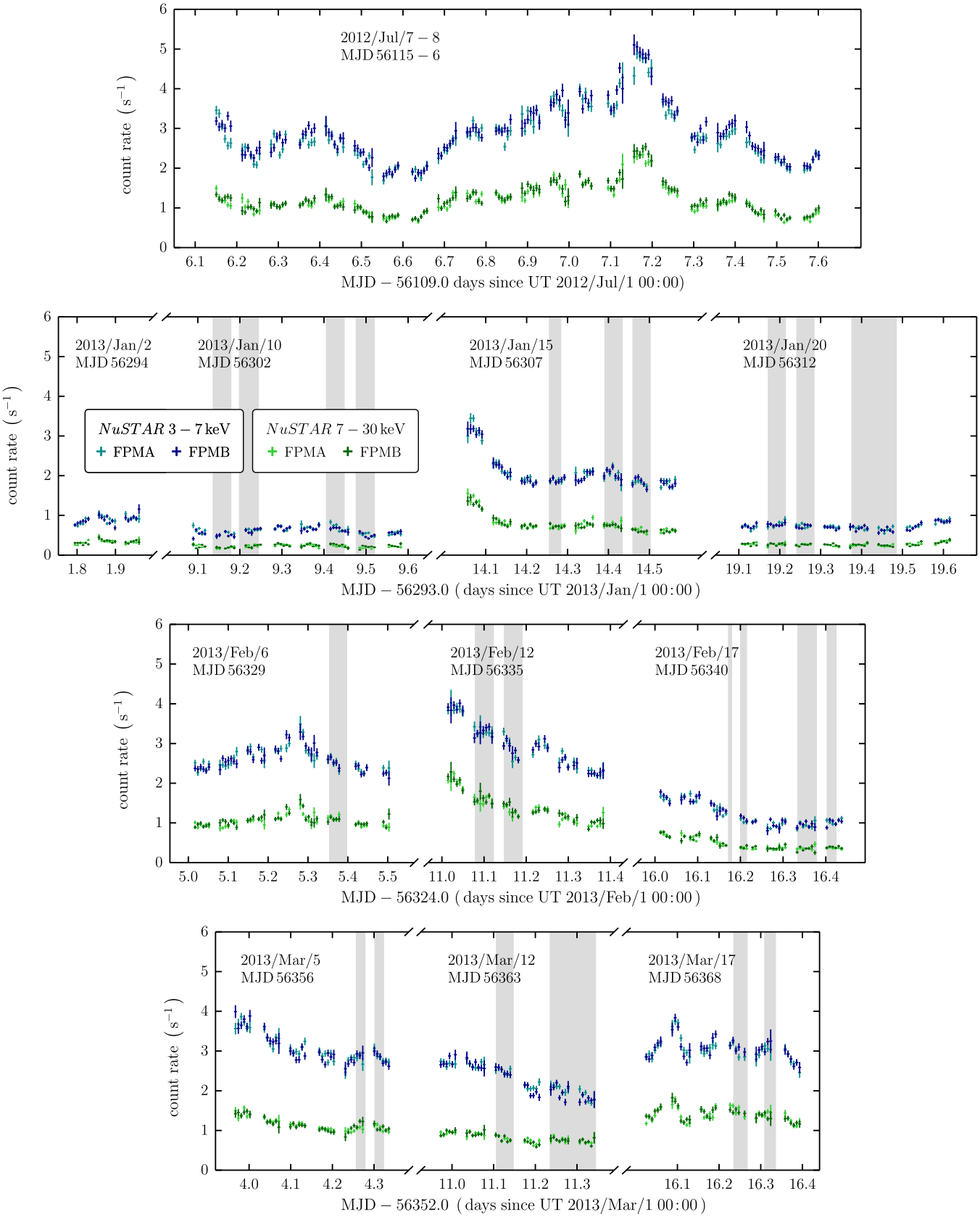

Figure 1. Count rates for *NuSTAR* in the 3–7 keV (blue) and 7–30 keV (green) bands. The legend given in the second panel from the top applies to all panels; for both bands FPMA count rates are plotted with a lighter color. The data are binned into 10-minute bins. The time axis of each row starts with the first day of the month, and the UTC and MJD dates are printed above the light curves for each particular observation. Note that the data shown in the top panel represent two contiguous observations (broken up near MJD 56115.15). The intervals shaded in gray show times for which simultaneous data from MAGIC and VERITAS are presented in this paper. Both the horizontal and the vertical scales are equal in all panels.

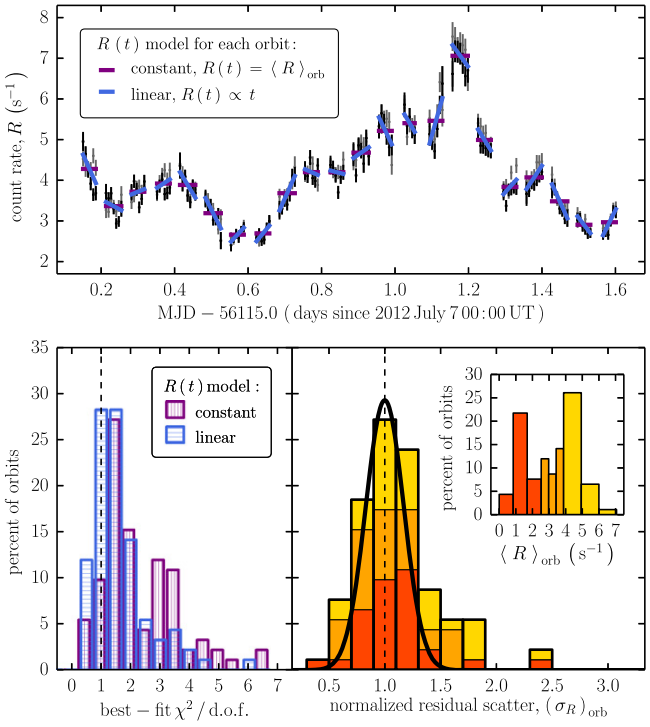

Figure 2. Upper panel shows the light curve of the 2012 July observation (FPMA in black, FPMB in gray) shown as an example for the count rate modeling; the two models fitted to each orbit of data are represented by purple (constant model) and blue lines (linear model). In the lower panels, the colored histograms on the left-hand side (colors matching the upper panel) show the distributions of reduced χ^2 for the two models fitted to every *NuSTAR* orbit up to the end of 2013 March. The number of degrees of freedom (dof) in each fit varies slightly owing to the different duration of the orbits, but it is typically around 10. The right panel shows the distribution of the residual scatter after subtraction of the best-fit linear trend from the observed count rates in each orbit, in units of the median rate uncertainty within the orbit, $(\sigma_R)_{\rm orb}$. The colors reflect the mean count rate of the orbit: the lowest-rate third in red, the mid-rate third in orange, and the highest-rate third in yellow, distributed as shown in the inset. The residual scatter distribution is slightly skewed to values greater than unity, indicating that $\lesssim$20% of orbits show excess variability on suborbital timescales. A Gaussian of approximately matching width is overplotted with a thick black line simply to highlight the asymmetry of the observed distribution.

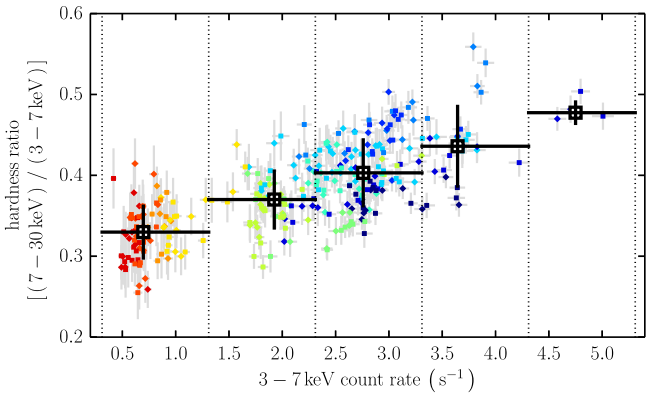

Figure 3. Hardness ratio (defined as the ratio of the number of counts in the 7–30 keV band to that in the 3–7 keV band) as a function of the count rate in individual 30-minute bins of *NuSTAR* data is shown with colored symbols: FPMA are plotted with squares, and FPMB with diamonds. The colors distingush different observations and match those in Figure 4. The thick black error bars and symbols show median count rate and hardness ratio in bins (1 count s^{-1} width), delimited by the vertical dotted lines. The vertical error bars denote standard deviation within each bin.

With less smearing over different spectral states of the source, the spectral variability is more clearly revealed by this analysis. As shown with the gray data points in Figure 5 (one for each *NuSTAR* orbit), for any of the three models statistically significant spectral changes occur as the X-ray flux varies. The spectrum becomes harder as the flux increases. Most of the change happens below $\simeq$7 keV, as shown by the substantial variations in the parameters Γ_1 and α, compared to the lower-amplitude variations in Γ_2 and β. In all cases the trends are consistent with the well-established harder-when-brighter behavior, also evident in the more basic representation using hardness ratios in Figure 3. Since for orbits with the lowest count rate the uncertainties on the spectral parameters are relatively large, in the following section we verify that the same spectral variability trends persist for data with higher signal-to-noise ratio (S/N).

3.4. Flux-resolved Spectroscopy

In order to verify that the spectral parameter trends we identify in the time-resolved spectra are not spuriously produced by relatively low photon statistics at the low-flux and high-energy ends, we proceed to examine stacked single-orbit spectra of similar flux. Stacking provides the highest possible S/N in well-defined flux bins and allows us to use the data up to 70 keV—where the signal is fainter by a factor of a few than the *NuSTAR* detector background. We combine spectra for each focal-plane module separately due to intrinsic differences in response matrices. Spectra from both modules are fitted simultaneously in `Xspec`, just like the observation-averaged and the single-orbit ones. Note that this procedure implicitly assumes that the source behaves self-consistently, in the sense that a particular flux level corresponds to a unique spectral shape within the data-taking time interval. The validity of this assumption is further discussed in Section 5.

We first stack the spectra of three complete observations (2013 January 2, 10, and 20), since Mrk 421 displayed a nearly constant low flux during all three (see Figure 1). The combined spectrum is very similar to the spectra from any of the constituent observations but has significantly higher S/N. It can be statistically well described as a simple power law with $\Gamma = 3.05 \pm 0.02$ from 3 to 70 keV ($\chi^2_r = 1.05$). For completeness, modeling with a broken-power-law model gives the break energy at 6 ± 3 keV, and low- and high-energy photon indices both formally consistent with the Γ value found for the simpler power-law model. Furthermore, the curvature parameter of the log-parabolic model is consistent with zero ($\beta = 0.01 \pm 0.04$), and $\alpha \approx \Gamma$. These fitting results lead us to conclude that in the lowest-flux state observed in 2013 the hard X-ray spectrum follows a steep power law with $\Gamma \approx 3$. Extrapolating below 3 keV for the sake of comparison with the literature, we derive a 2–10 keV flux of $(3.5 \pm 0.2) \times 10^{-11}$ erg s^{-1} cm^{-2} for the $\Gamma = 3$ power-law model normalized to the lowest observed orbital flux (orbit #6 of the 2013 January 20 observation). A state of such low X-ray flux has not yet been described in the published literature,[110] making the results of this analysis new and unique.

We combine the spectra of all 88 orbits according to their 3–7 keV flux in order to obtain higher S/N for the flux states covered in the data set. The choice of flux bins shown with

[110] To the best of our knowledge, the lowest published 2–10 keV flux thus far was $(4.1 \pm 0.2) \times 10^{-11}$ erg s^{-1} cm^{-2} (1997 May; Massaro et al. 2004).

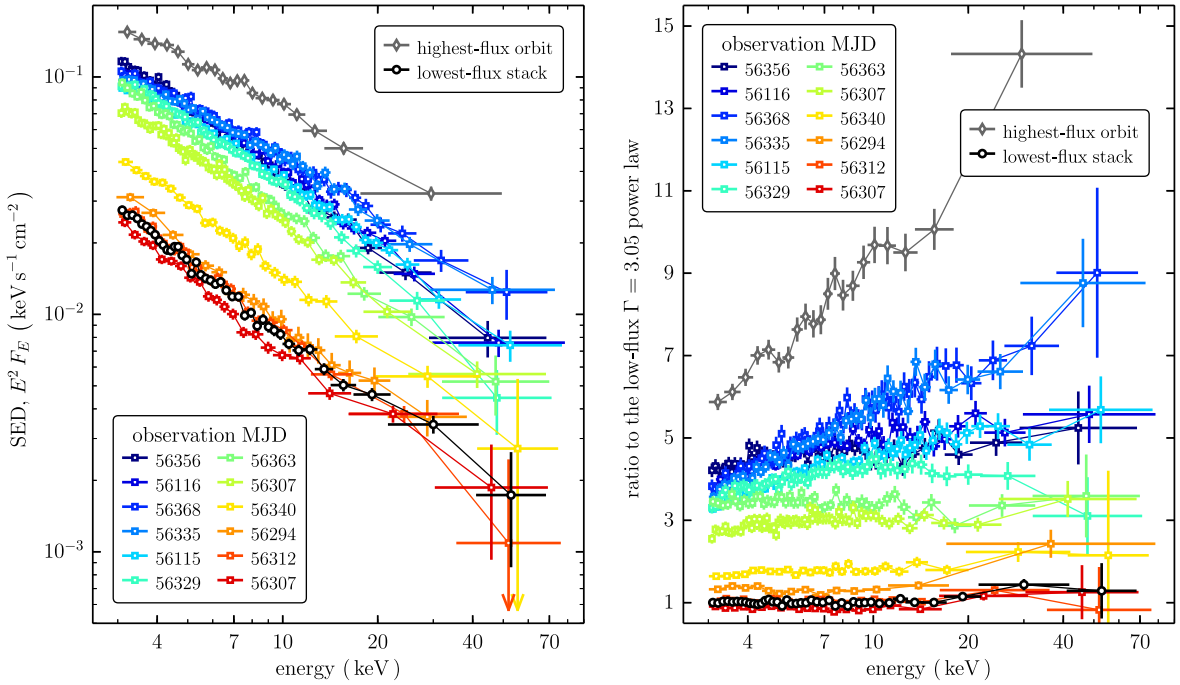

Figure 4. Unfolded *NuSTAR* spectra of Mrk 421 in each of the 12 observations. Colors are arranged by the 3–7 keV flux. Also shown are spectra of the single highest-flux orbit (gray symbols) and the stack of three lowest-flux observations (black symbols). Modules FPMA and FPMB have been combined for clearer display, and the bin midpoints for each spectrum are shown connected with lines of the same color to guide the eye. The left panel shows the unfolded spectra in the νF_ν representation, while the right panel shows the same spectra plotted as a ratio to the best-fit model for the lowest-flux stacked spectrum (a power law with $\Gamma = 3.05$). Note that the vertical scale is logarithmic in the left and linear in the right panel.

black symbols in Figure 5 is such that relatively uniform uncertainty in spectral parameters is achieved across the flux range; this condition requires stacking of ∼10 orbits of data on the faint end, while a single orbit is sufficient at the bright end. The results, however, are largely independent of the exact choice of which orbits to combine into a particular flux bin. Fitting the stacked spectra with the same simple spectral models as before reveals spectral trends much more clearly than for observation-averaged or time-separated spectra, as shown by black symbols in Figure 5. The spectra of the lowest-flux stack and the highest-flux orbit are displayed in Figure 4 for comparison with the observation-averaged spectra. The analysis performed here describes the spectral changes happening between those two extremes as a smooth function of the X-ray flux.

For each of the parameters of the power-law, broken-power-law, and log-parabolic models we parameterize their dependence on the X-ray flux as

$$X(F_{3-7\,\mathrm{keV}}) = s \log(F_{3-7\,\mathrm{keV}}/F_0) + X_0, \quad (4)$$

where X stands for any of the spectral parameters (Γ, Γ_1, E_b, Γ_2, α, β), s is the slope of the relation, $F_{3-7\,\mathrm{keV}}$ is the 3–7 keV flux, F_0 is a reference flux in erg s^{-1} (chosen to be the median flux of our data set, $\log F_0 = -10.1$), and X_0 is the vertical offset (parameter value at the reference flux). We find that in all cases this linear function adequately describes the general trends. Since we find that the break energy of the broken power-law model (E_b) is independent of flux within its large uncertainties, we keep it fixed at 7 keV while fitting for the trends in the Γ_1 and Γ_2 parameters. For Γ_2, the high-energy photon index of the broken-power-law model, the best-fit slope is small but different from zero at the 2σ level. For the rest of the spectral parameters, the trends are statistically more significant. Figure 5 shows the best-fit $X(F_{3-7\,\mathrm{keV}})$ relations superimposed on the time- and flux-resolved fitting results, clearly matching the trends that the former analysis hinted at. We list the best-fit linear trend parameters s and X_0, with their 1σ uncertainties, in Table 8.

Finally, we briefly return to the broken power-law model fits only to make a comparison to the previously observed spectral variability during flares. The *RXTE* 2–20 keV data analyzed by Giebels et al. (2007) overlap in the 2–10 keV flux only for the highest-flux single-orbit data presented here and extend almost a decade above that. These authors showed that the break energy is essentially independent of flux and $\langle E_b \rangle = 5.9 \pm 1.1$ keV (68% confidence interval), which is consistent with the median value of approximately 7 keV found from our nondegenerate fits of the broken-power-law model. The photon indices were found to vary with flux up to approximately 10^{-9} erg s^{-1} cm^{-2}, above which they saturate at $\Gamma_1 \approx 2.2$ and $\Gamma \approx 2.5$. The data presented here smoothly connect to those trends (see Figure 6), extending them toward the faint end. Whereas the low-energy photon index (Γ_1 or Γ_L) continues to increase with decreasing flux, reaching $\Gamma \approx 3$ at $\lesssim 10^{-10}$ erg s^{-1} cm^{-2}, the high-energy one (Γ_2 or Γ_H) essentially levels off to the same $\Gamma \approx 3$ at a factor of a few higher flux. A naive extrapolation of the Giebels et al. (2007) trends is therefore not supported by the new *NuSTAR* observations. Our analysis reveals a clear low-flux saturation effect that none of the previous studies could have constrained owing to lack of sensitivity.

Table 7
Models Fitted to the *NuSTAR* Spectra of Each Observation

	Power Law		Broken Power Law				Log-parabola ($E_* = 5$ keV)			Time-averaged Flux[b]		
Start Time (MJD)	Γ	χ^2/dof	Γ_1	E_b[a]	Γ_2	χ^2/dof	α	β	χ^2/dof	3–7 keV	2–10 keV	7–30 keV
56115.1353	2.82 ± 0.01[c]	1085/949	2.74 ± 0.02	$7.0^{+0.8}_{-0.6}$	2.92 ± 0.03	922/947	2.76 ± 0.01	0.21 ± 0.03	906/948	9.47 ± 0.03	18.8 ± 0.1	6.48 ± 0.03
56116.0732	2.87 ± 0.01[c]	1126/833	2.78 ± 0.03	$7.0^{+1.0}_{-0.7}$	2.98 ± 0.04	978/831	2.99 ± 0.01	0.24 ± 0.04	967/832	11.08 ± 0.03	22.1 ± 0.1	7.16 ± 0.04
56294.7778	3.10 ± 0.04	415/390	$3.19^{+0.07}_{-0.05}$	$7.6^{+1.1}_{-1.4}$	2.9 ± 0.1	399/388	3.16 ± 0.05	-0.2 ± 0.1	403/389	2.87 ± 0.05	6.4 ± 0.1	1.57 ± 0.04
56302.0533	3.07 ± 0.03	512/506	3.08 ± 0.04	7.5 (f)	3.04 ± 0.07	511/505	3.07 ± 0.04	0.0 ± 0.1	512/505	1.91 ± 0.02	4.10 ± 0.05	1.05 ± 0.01
56307.0386	3.02 ± 0.01	865/710	2.89 ± 0.03	$6.4^{+0.8}_{-1.3}$	$3.13^{+0.06}_{-0.04}$	742/708	2.92 ± 0.02	0.28 ± 0.05	741/710	6.43 ± 0.03	13.0 ± 0.1	3.55 ± 0.02
56312.0980	3.05 ± 0.02	571/543	$2.9^{+0.1}_{-0.4}$	$4.6^{+1.3}_{-0.9}$	$3.09^{+0.04}_{-0.03}$	568/541	3.03 ± 0.03	0.1 ± 0.1	572/542	2.26 ± 0.02	4.71 ± 0.05	1.22 ± 0.01
56329.0116	2.93 ± 0.01	925/724	2.80 ± 0.02	$7.5^{+0.5}_{-0.4}$	3.13 ± 0.04	709/722	2.82 ± 0.02	0.39 ± 0.05	709/723	8.27 ± 0.05	16.3 ± 0.1	4.94 ± 0.04
56335.0106	2.73 ± 0.01	839/742	2.66 ± 0.02	$10.2^{+1.5}_{-1.1}$	$2.92^{+0.8}_{-0.06}$	738/740	2.64 ± 0.02	0.21 ± 0.05	742/741	9.25 ± 0.05	18.1 ± 0.1	7.00 ± 0.06
56339.9828	3.02 ± 0.02	577/559	2.95 ± 0.03	7.5 (f)	3.09 ± 0.05	559/558	2.96 ± 0.03	0.14 ± 0.09	558/558	3.83 ± 0.03	7.9 ± 0.1	2.14 ± 0.03
56355.9631	3.01 ± 0.01	823/701	$2.91^{+0.03}_{-0.04}$	$6.3^{+0.9}_{-0.6}$	3.09 ± 0.04	751/699	2.94 ± 0.02	0.22 ± 0.05	751/700	9.74 ± 0.04	19.9 ± 0.1	5.45 ± 0.05
56362.9690	3.10 ± 0.01	640/640	$3.01^{+0.05}_{-0.15}$	$5.8^{+3.1}_{-1.6}$	$3.16^{+0.16}_{-0.03}$	603/638	3.04 ± 0.02	0.19 ± 0.06	600/639	7.49 ± 0.05	15.6 ± 0.1	3.80 ± 0.04
56368.0210	2.75 ± 0.01	848/760	2.67 ± 0.02	$8.8^{+0.9}_{-1.3}$	2.91 ± 0.05	756/758	2.68 ± 0.02	0.24 ± 0.05	749/759	9.51 ± 0.05	18.6 ± 0.1	6.93 ± 0.05

Notes.
[a] Energy (in keV) at which the model sharply changes slope from Γ_1 to Γ_2. For some observations this parameter is unbound, so we fix it to 7.5 keV and mark with (f).
[b] Flux calculated from the best-fit model, in units of 10^{-11} erg s^{-1} cm^{-2}. Note that the 2–10 keV band requires some extrapolation below the *NuSTAR* bandpass, but we provide it here for easier comparison with the literature.
[c] Formal statistical uncertainty is 0.008; however, the *NuSTAR* bandpass calibration is limited to 0.01 (Madsen et al. 2015), so we round up the values assuming this lowest uncertainty limit for these cases.

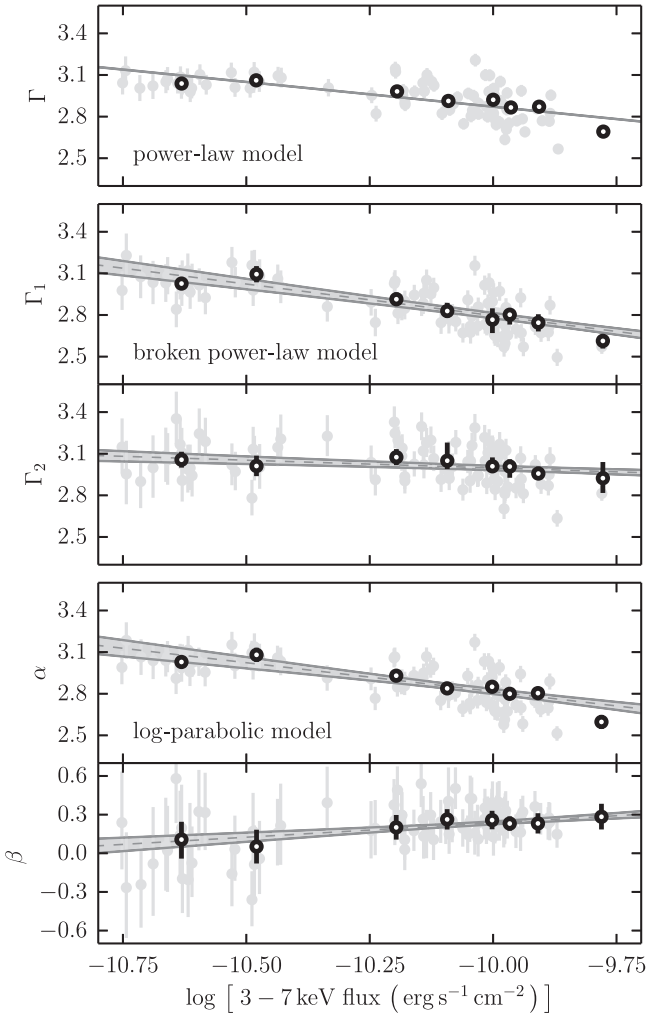

Figure 5. Trends in the hard X-ray spectral parameters as functions of flux for three simple spectral models revealed by time- and flux-resolved analyses of the *NuSTAR* data. The values fitted to high-S/N stacked spectra separated by flux (see text for an explanation) are shown with black-lined open circles. A linear function is fitted to each of the trends, and the uncertainty region is shaded in gray. Parameters of the fitted linear trends are given in Table 8. The filled gray circles in the background show spectral modeling results for spectra of 88 individual orbits.

Table 8
Best-fit Linear Relations Parameterized in Equation (4) for Describing the Change of Spectral Parameters with the X-Ray Flux. The Uncertainties are Quoted at the 1σ Level

Model	Parameter, X	Slope, s	Zero Point, X_0
`pow`	Γ	-0.32 ± 0.07	2.88 ± 0.02
`bknpow`	Γ_1	-0.46 ± 0.07	2.80 ± 0.02
`bknpow`	E_b [a]	1 ± 9	7 ± 2
`bknpow`	Γ_2	-0.11 ± 0.05	3.00 ± 0.01
`logpar`	α	-0.42 ± 0.07	2.82 ± 0.02
`logpar`	β	0.22 ± 0.06	0.24 ± 0.01

Note.
[a] Owing to poor constraint on this parameter, it is kept fixed at 7 keV while quantifying the trends in the Γ_1 and Γ_2 parameters.

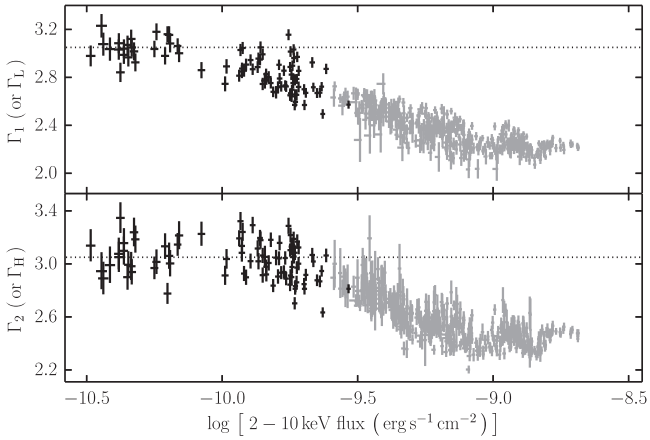

Figure 6. Comparison of the spectral trends revealed in our data (black symbols) with the ones published by Giebels et al. (2007; gray symbols). For this set of fits to the *NuSTAR* data the break energy (E_b) was kept fixed at 7 keV. The uncertainties are given at the 68% confidence level in order to match the previous results. Note the smoothness of the trends covering nearly two orders of magnitude and the apparent saturation effects at each end. The dotted lines are median photon indices for 2–10 keV flux below 10^{-10} erg s^{-1} cm^{-2}, representing the apparent low-flux saturation values.

4. RESULTS FROM THE MULTIWAVELENGTH OBSERVATIONS

4.1. Multiwavelength Variability

The majority of observations performed in 2013 January through March were coordinated between the participating observatories so as to maximize the strictly simultaneous overlap in the X-ray and VHE bands. In particular, nine 10–12 hr long observations performed by *NuSTAR* were accompanied with *Swift* pointings at the beginning, middle, and end, and the ground-based Cherenkov-telescope arrays MAGIC and VERITAS covered roughly half of the *NuSTAR* exposure each. Approximately 50 hr of simultaneous observations with *NuSTAR* and either MAGIC or VERITAS resulted in total exposure of 23.5 hr (the remainder being lost owing to poor weather conditions and quality cuts). Figure 7 shows the multiwavelength light curves and highlights the dates of *NuSTAR* observations taken simultaneously with MAGIC and VERITAS observations with vertical lines. A zoomed-in view of the VHE γ-ray observation times is shown overlaid on the expanded *NuSTAR* light curves in Figure 1.

The VHE flux varied between approximately 0.1 and 2 Crab units, reaching substantially lower and higher than the long-term average of 0.446 ± 0.008 Crab (Acciari et al. 2014), which is considered typical for a nonflaring state of Mrk 421 (Aleksić et al. 2015b). In Figure 7 we show typical fluxes for *Fermi*-LAT, *Swift*-XRT, and OVRO bands, represented by medians of the long-term monitoring data that are publicly available. The *Fermi*-LAT light curve reveals elevated flux with respect to the median, as do the optical and UV data when compared to historical values. Modest soft X-ray flux is apparent from *Swift*-XRT data in comparison with the long-baseline median (Baloković et al. 2013a; Stroh & Falcone 2013) and the intense flaring episodes covered in the literature (e.g., Acciari et al. 2009; Tramacere et al. 2009; Aleksić et al. 2012). Count rates of $\lesssim 10$ s^{-1} in the 0.3–10 keV band are up to a factor of $\simeq 2$

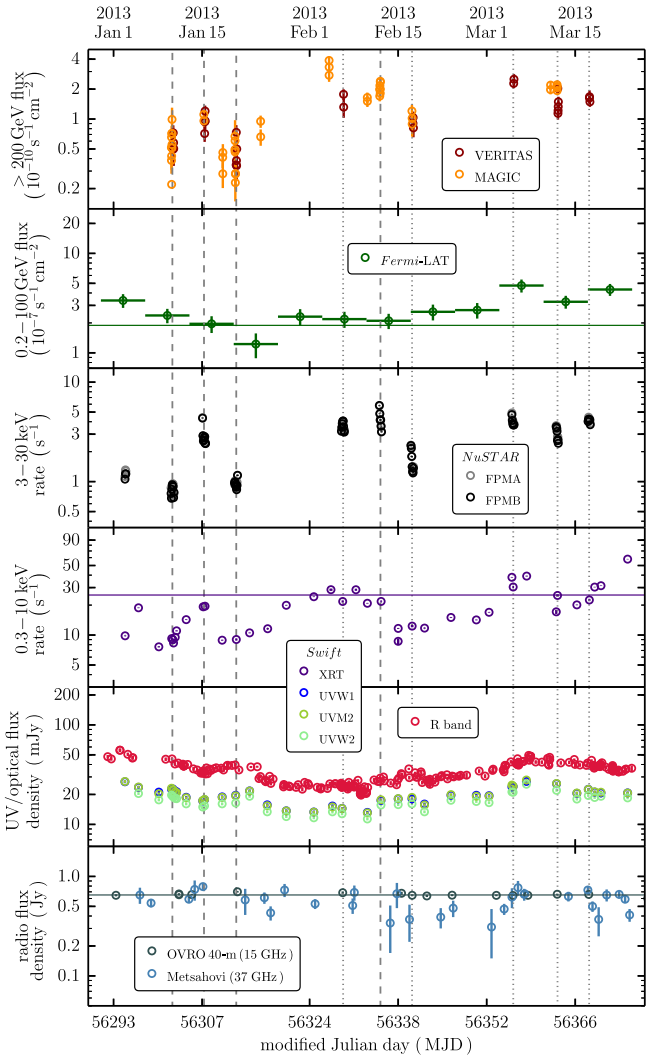

Figure 7. Light curves for Mrk 421 from MAGIC, VERITAS (both above 200 GeV, binned in ∼30-minute intervals), *Fermi*-LAT (0.2–100 GeV, binned weekly), *NuSTAR* (3–30 keV, binned by orbit), *Swift*-XRT (0.3–10 keV, complete observations), *Swift*-UVOT (UVW1, UVM2, and UVW2 bands, complete observations), ground-based optical observatories (R band, intranight cadence), OVRO, and Metsähovi (15 and 37 GHz, both with 3–4-day cadence). The host-galaxy contribution in the R band has been subtracted out according to Nilsson et al. (2007). The dynamic range in all panels is 40. Vertical and horizontal error bars show statistical uncertainties and the bin width, respectively, although some of the error bars are too small to be visible in this plot. The vertical lines mark midpoints of the coordinated *NuSTAR* and VHE observations: dashed lines mark the epochs for which we discuss SED snapshots in Section 4.4, while the rest are shown with dotted lines. The horizontal lines in some panels show the long-term median values (see text for details).

lower than those observed in quiescent periods during multi-wavelength campaigns in 2009 (Aleksić et al. 2015b) and 2010 March (Aleksić et al. 2015c). The radio flux was only slightly elevated above the values that have remained steady for the past 30 years, apart from the exceptional radio flare observed in 2012 October (see Section 4.5 for more details).

Remarkably well correlated flux variability in the X-ray and VHE bands on a timescale of about a week is already apparent from Figure 7 and will be discussed in more detail in Section 4.2.1. The fluxes in the UV and *Fermi*-LAT bands (to the extent allowed by the limited photon statistics) are consistent with a slow increase in flux between January and March but do not show a clear short-term flux correlation.

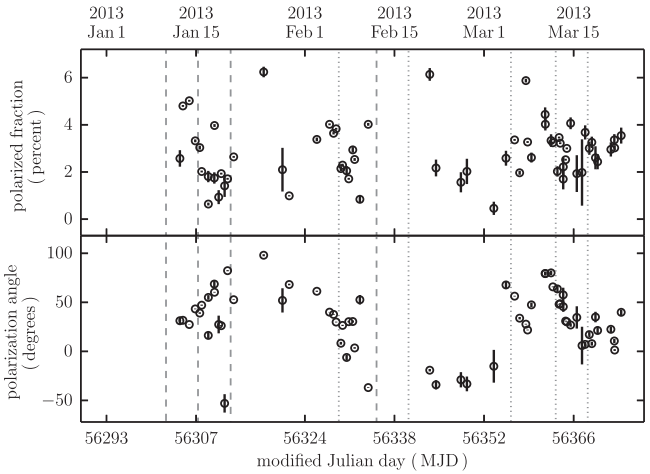

Figure 8. Optical polarization of Mrk 421 between 2013 January and March. The degree of polarization is shown in the upper panel, and the position angle of polarization is shown in the lower panel. Measurement uncertainties are based on photon statistics and are often smaller than the data points plotted. As in Figure 7, the vertical lines mark midpoints of the coordinated *NuSTAR* and VHE observations: dashed lines mark the epochs for which we discuss SED snapshots in Section 4.4, while the rest are shown with dotted lines.

Further details regarding these bands are presented in Section 4.2.2. The activity observed in the first 3 months of 2013 can be generally described as low. Note in particular that on January 10 and 20, Mrk 421 showed a remarkably low X-ray and VHE flux in comparison to the historical X-ray and VHE fluxes reported in Stroh & Falcone (2013) and Acciari et al. (2014), respectively. Optical polarization, shown in Figure 8, showed random and statistically significant variations around the average polarized fraction of 3%, and the polarization angle also varied significantly without any obvious coherent structure.

A general trend observed in the 2013 campaign is a gradual rise in broadband emission between January and March by a factor of $\lesssim$10, depending on the band. This was followed by an intense flaring period in 2013 April (not shown in Figure 7), rivaling the brightest flares ever observed for Mrk 421 (Baloković et al. 2013b; Cortina et al. 2013; Paneque et al. 2013; Pian et al. 2014). Analysis of the campaign data from the flaring period and more detailed analysis of the multiwavelength variability properties will be presented in separate publications. In the following sections, we focus on quantifying short-timescale and time-averaged correlations between different spectral bands and on the basic modeling of the Mrk 421 SED in the low-activity state that has not previously been characterized in any detail, except very recently in Aleksić et al. (2015b).

The variability across the electromagnetic spectrum can be described using the fractional variability distribution. Fractional variability, $F_{\rm var}$, is mathematically defined in Vaughan et al. (2003), and its uncertainty is calculated following the prescription from Poutanen et al. (2008), as described in Aleksić et al. (2015a). It can be intuitively understood as a measure of the variability amplitude, with uncertainty primarily driven by the uncertainty in the flux measurements and the number of measurements performed. While the systematic uncertainties on the absolute flux measurements[111] do not

[111] Estimated to be 20% in the VHE band and around 10% in the optical, X-ray, and GeV bands—see Section 2 for details.

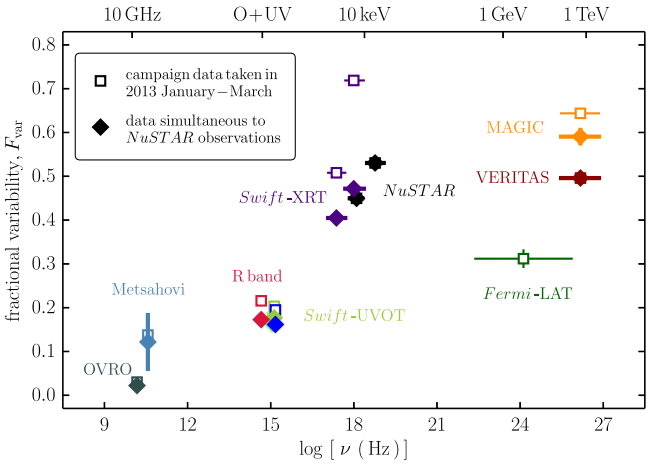

Figure 9. Fractional variability amplitude, $F_{\rm var}$, as a function of frequency for the period 2013 January–March. The vertical error bars depict the statistical uncertainty, while the horizontal error bars show the energy band covered (with the markers placed in the center of the segments). We show $F_{\rm var}$ computed in two ways: using the complete light curves acquired in the campaign (open symbols), and using only the data taken within narrow windows centered on the coordinated *NuSTAR* and VHE observations (filled symbols). Note that the points overlap where only the coordinated observations are available. The *Fermi*-LAT point is based on the weekly binned light curve shown in Figure 7.

directly add to the uncertainty in $F_{\rm var}$, it is important to stress that different observing sampling and, more importantly, different instrument sensitivity do influence $F_{\rm var}$ and its uncertainty: a densely sampled light curve with very small temporal bins and small error bars might allow us to see flux variations that are hidden otherwise, and hence we might obtain a larger $F_{\rm var}$. Some practical issues of its application in the context of multiwavelength campaigns are elaborated in Aleksić et al. (2014, 2015b, 2015c).

In this paper we explore two cases, as shown in Figure 9. First, we use the full January–March data set reported in Figure 7 (which has different cadence and different number of observations in each band), and second, we use only data collected simultaneously, in narrow windows centered on observations coordinated between *NuSTAR* and VHE telescopes. In the latter case the fluxes are averaged over the complete *NuSTAR*, *Swift,* and VHE observations, effectively smoothing over any variability on shorter timescales. The optical and radio fluxes are taken from single measurements closest in time to the coordinated observations. In the former case, however, we sample shorter timescales and during a longer time span, which allows us to detect somewhat higher variability, as one can infer by comparing the *Swift* and MAGIC observations reported by the open/filled markers in Figure 9. $F_{\rm var}$ for *Fermi*-LAT is calculated from the weekly binned light curve shown in Figure 7; the relatively low GeV γ-ray flux observed by *Fermi*-LAT precludes us from using significantly shorter time bins, or dividing the *Fermi*-LAT band into subbands as we do for *Swift*-XRT and *NuSTAR*. Figure 9 shows that $F_{\rm var}$ determined from our campaign rises significantly from the radio toward the X-ray band (consistent with Giebels et al. 2007), decreases over the *Fermi*-LAT band (consistent with Abdo et al. 2011), and then rises again in the VHE band. This double-bump structure relates to the two bumps in the broadband SED shape of Mrk 421 and has been recently reported for both low activity (Aleksić et al. 2015b) and high activity (Aleksić et al. 2015c). The less variable energy bands (radio, optical/UV, and GeV γ-ray bands) relate to the rising segments of the SED bumps, while the most variable energy bands (X-rays and VHE γ-ray bands) relate to the falling segments of the SED bumps.

4.2. Correlations between Spectral Bands

4.2.1. X-Ray versus VHE γ-Ray Band

The existence of a correlation between the X-ray and VHE fluxes is well established on certain timescales and in certain activity states of Mrk 421: claims of correlated variability stem from long-term monitoring of fluxes in these bands that include high-activity states (Bartoli et al. 2011; Acciari et al. 2014), as well as observations of particular flaring events that probe correlated variability on timescales as short as 1 hr (Giebels et al. 2007; Fossati et al. 2008; Acciari et al. 2009). The detection of such a correlation in a low state was reported for the first time in Aleksić et al. (2015b), using the X-ray (*Swift*-XRT, *RXTE*-PCA) and VHE (MAGIC, VERITAS) data obtained during the 4.5-month multiwavelength campaign in 2009, when Mrk 421 did not show any flaring activity and varied around its typical *Swift*-XRT 0.3–10 keV count rates of $\sim$25 $\rm s^{-1}$ and VHE flux of 0.5 Crab. In this section, we confirm the flux–flux correlation in the X-ray and VHE bands with higher confidence, during a period of even lower activity. We also study the characteristics of such a correlation in different X-ray bands using the strictly simultaneous *Swift*, *NuSTAR*, MAGIC, and VERITAS observations.[112] We summarize the results in Figure 10 for three nonoverlapping X-ray bands. The flux in each band was calculated from the best-fit broadband model (power-law, or log-parabolic where needed; see Section 3).

In the following, we use the discrete correlation function (DCF) and the associated uncertainty as defined in Edelson & Krolik (1988). We carried out the correlation analysis on two timescales: a $\sim$1 hr timescale, using strictly simultaneous observations, and a $\lesssim$1-day timescale, using data averaged over complete 6–10 hr observations (i.e., averaged over one night of observations with each of the VHE observatories). Figure 1 shows the exact overlap of the *NuSTAR* and VHE observations. For both timescales and for all three X-ray bands we find significant correlations between fluxes in log–log space: DCF $\gtrsim$ 0.9 in all cases, with typical uncertainty of 0.1–0.2. The DCF is therefore inconsistent with zero with a minimum significance of 3.5σ (nightly averaged fluxes, 7–30 keV band) and maximum significance of 15σ (simultaneous data, 3–7 keV band). As a sanity check, we also compute Pearson's correlation coefficients and find $>5\sigma$ significance in all cases. The strongest correlation, at 14σ, is again found for the 3–7 keV band and strictly simultaneous data shown in the upper middle panel of Figure 10. Note that we compute the correlation coefficients and DCF values using the logarithm of flux: because of greater dynamic range, the true flux–flux correlations are even more significant.

The similar slope of the $\log F_{\rm X\text{-}ray} - \log F_{\rm VHE}$ correlation on both timescales may indicate that the correlation is mainly driven by flux variability on a timescale of several days, i.e.,

[112] The MAGIC and VERITAS observations reported in this paper were performed after the extensive hardware upgrades performed on these two facilities in 2011 and 2012. They are therefore much more sensitive than the ones performed in 2009, which allows for a significant detection of lower flux in a single night of observation.

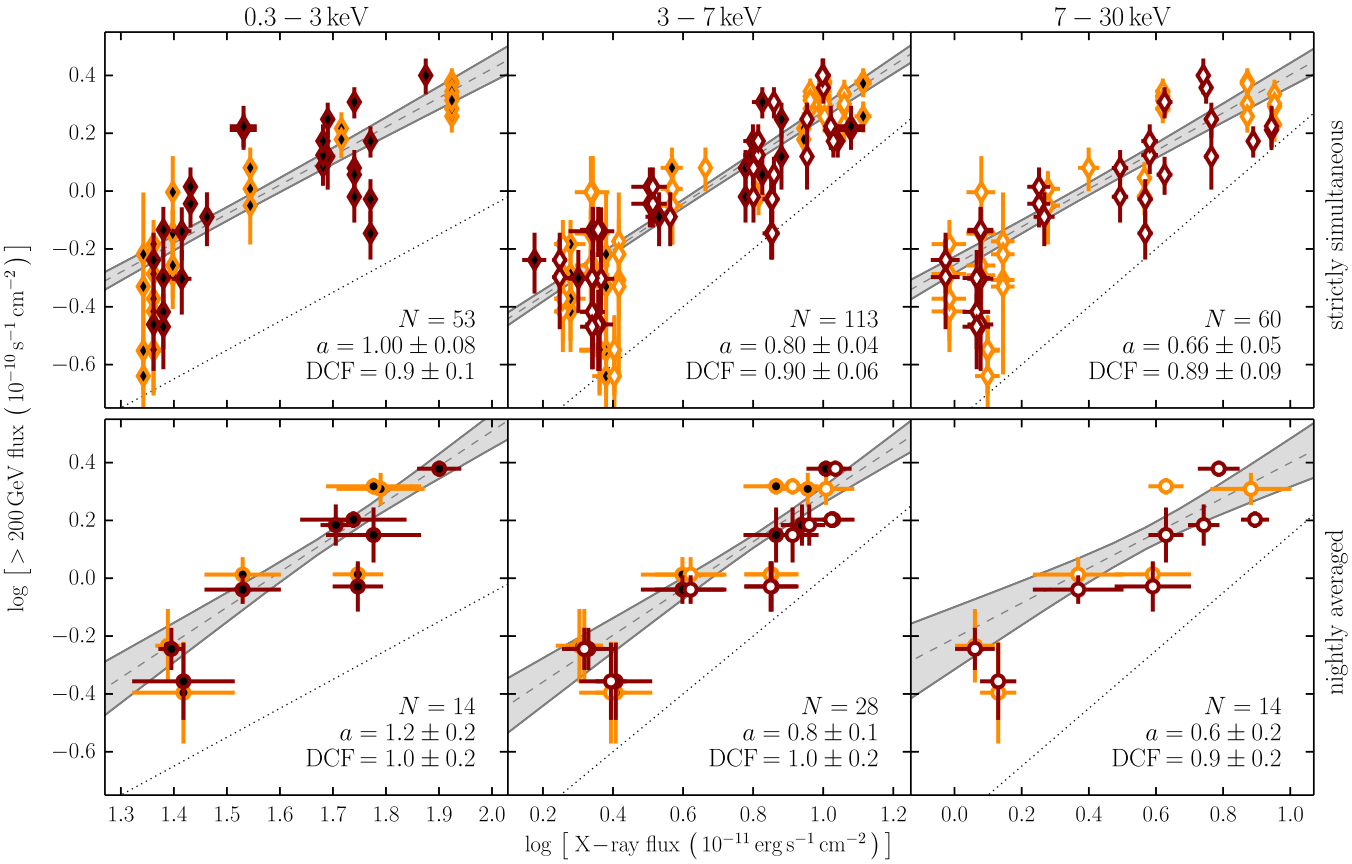

Figure 10. Flux–flux correlation between the X-ray and VHE (>200 GeV) flux in three different X-ray bands: *Swift*-XRT 0.3–3 keV in the left panel, *Swift*-XRT and *NuSTAR* 3–7 keV in the middle, and *NuSTAR* 7–30 keV in the right panel. *Swift*-XRT and *NuSTAR* measurements are shown with black-filled and white-filled symbols, respectively. Orange symbols mark MAGIC measurements, while dark red symbols mark VERITAS. In the upper panels we show only the data taken essentially simultaneously (within 1.5 hr). The lower panels show data averaged over the nights of simultaneous observations with X-ray and VHE instruments. The *N*, *a*, and DCF values given in each panel are the number of data points considered, the slope of the log–log relation, and the discrete correlation function. The best-fit linear relation (dashed gray line) and its uncertainty region are shown with gray shading. The thin dotted line of slope unity is shown in all panels for comparison.

between different observations, rather than within single observations spanning several hours. The statistical significance of the correlation on the ∼daily timescale is lower, owing both to the smaller number of data points and to the fact that flux variance is larger because of the presence of strong variability on shorter timescales. For a chosen X-ray band, the best-fit slopes of the relation (a; listed in Figure 10) are statistically consistent with a single value. This is in good agreement with our finding that the dominant X-ray flux variability timescale is $\tau_{\rm var} \approx 9$ hr (see Section 3.1). It could also be indicative of a lag between the bands, which is longer than the binning of the data taken strictly simultaneously; however, such an analysis is outside of the scope of this paper. Results of Aleksić et al. (2015b) point to absence of any lags between the X-ray and VHE bands in a nonflaring state of Mrk 421 in 2009.

An interesting result stems from our ability to broaden the search for the correlation over a very wide band in X-rays, enabled by the simultaneous *Swift* and *NuSTAR* coverage. As shown in the upper three panels of Figure 10, the slope of the relation systematically shifts from 1.00 ± 0.08 for the soft 0.3–3 keV band, to 0.80 ± 0.04 for the 3–7 keV band, and to 0.66 ± 0.05 for the hard 7–30 keV band. The same behavior is seen in the nightly averaged data, with somewhat lower significance. The persistence of this trend on both timescales and in all observatory combinations counters the possibility of a systematic bias related to those choices. We interpret it as an indication that the soft X-ray band scales more directly with the VHE flux (which is dominated by *soft* γ-ray photons on the low-energy end of the VHE band) owing to the emission being produced by the same population of relativistic electrons. The greater relative increase in the hard X-ray flux with respect to the soft band is consistent with both the spectral hardening already revealed by our analysis (see Section 3.4) and the fractional variability distribution determined from our data (Figure 9). Our interpretation would imply that the hard X-ray band scales more directly with the higher-energy VHE flux (e.g., >1 TeV), which we cannot quantify well with the current data.

We find no significant correlation of the simultaneously observed spectral slopes in the hard X-ray and VHE bands. Remarkably, on two dates when the observed X-ray flux was lowest, January 10 and 20 (MJD 56302 and 56312, respectively), steep spectra with $\Gamma \approx 3$ were observed by *NuSTAR* and both VHE observatories. Other simultaneous observations yield $\Gamma > 2.6$ in the 3–30 keV band and $\Gamma > 2.4$ in the VHE band, with an average photon index of approximately 3 in both bands. In comparison to the previously published results, we note that the observed steepness of the X-ray and VHE spectra presented here is atypical for Mrk 421. In a more typical low state, such as that observed in the 2009 campaign (Abdo et al. 2011), a photon index of ≃2.5 has been

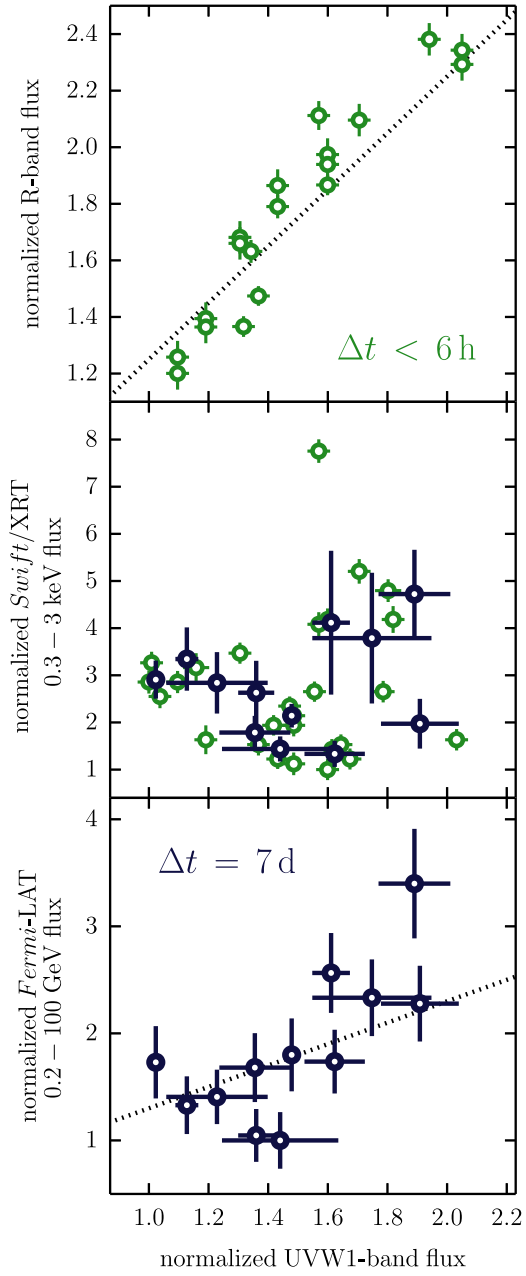

Figure 11. Flux–flux correlations between the UV band (*Swift*-UVOT filter UVW1) and the optical (R band; top), soft X-ray (*Swift*-XRT 0.3–3 keV; middle), and GeV γ-ray (*Fermi*-LAT 0.2–100 GeV; bottom) bands. The green data points are based on flux measurements that are coincident within 6 hr. The blue data points are derived by averaging over 7-day intervals, i.e., integration times used for determination of the flux in the *Fermi*-LAT band. In the top and bottom panels we overplot the slope of one-to-one proportionality (not a fit) with a black dotted line. Note that the vertical scale is linear in all panels, but has a different dynamic range in each one.

observed in both bands. Here we compare our *NuSTAR* spectral slopes to that of the *RXTE* spectrum (2–20 keV) integrated over several months. Care should be taken in comparing with previously published results, because direct slope measurements in the 3–30 keV band were not available before, especially on short timescales. While the simultaneously observed steep slopes add support to the connection between X-ray and VHE bands, higher-quality data for the quiescent states are clearly needed in order to quantify it further.

4.2.2. UV/Optical versus Other Bands

Despite the low flux observed in the X-ray and γ-ray bands, the range of the UV/optical flux was higher than in some flaring episodes reported in the past (e.g., Aleksić et al. 2012). In this section we present flux correlation analyses with respect to the UV band, as represented by measurements using *Swift*-UVOT. The choice of band UVW1 ($\lambda_{\rm eff} = 2120$ Å) for this work is arbitrary; results do not change for either of the other two filters, as all of them sample the flux on the opposite side of the extremely variable synchrotron SED peak from the X-ray band. In Figure 11 we show the correlations between the UV and optical, soft X-ray and GeV γ-ray bands, each normalized to the lowest flux observed in the 2013 campaign. As in previous sections, we use the DCF and the associated uncertainty to quantify the correlation significance.

A strong correlation is expected between the UV and optical fluxes and is confirmed by the data presented here. Previous work hinted at a possible correlation of the optical flux and the X-ray flux, but over a very narrow dynamic range and with low significance (Lichti et al. 2008). The states of Mrk 421 observed in early 2013 are not consistent with that result, indicating perhaps that a physically different regime was probed. We examine two different timescales in more detail here: for the UV and X-ray measurements taken within 6 hr of each other the DCF is 0.2 ± 0.2, while for weekly averaged values it is 0.3 ± 0.4, i.e., consistent with zero in both cases. Note that the X-ray data require averaging in the latter case, and that the uncertainty in flux is dominated by intrinsic variability. Given the established difference in the variability characteristics (see Figure 9), the lack of a significant correlation, especially on the shorter timescale, is not unexpected.

The most interesting correlation in terms of constraints on physical models is the one between the UV (and hence the optical, given their essentially 1-to-1 correspondence) and the *Fermi*-LAT band (0.2–100 GeV), shown in the bottom panel of Figure 11. In the framework of the SSC model, emission in these bands is due to electrons of roughly the same energy. Since the *Fermi*-LAT light curve had to be derived in ≈1-week bins owing to the low photon counts (see Section 2.5), we average the UV flux over the same time periods in order to cross-correlate them. Overall, the DCF is 0.8 ± 0.3, revealing a possible correlation with a 2.7σ significance. In order to examine its robustness against contributions from the outlying data points, we perform the following test: we first remove the highest-flux *Fermi*-LAT data point and find that it does not change the DCF, and then we remove the lowest-flux *Swift*-UVOT data point, which increases the DCF to 0.9 ± 0.4 but lowers the significance. We therefore estimate the correlation significance to be $\simeq 2.5\sigma$ based on the data presented here. Existence of a real correlation between UV and γ-ray bands cannot be confirmed with the current data, but this may be possible with the Mrk 421 observations at higher γ-ray flux, such as those taken during our multiwavelength campaign in 2013 April.

4.3. The Peak of the Synchrotron SED Component

Previous work on modeling the Mrk 421 SED established that the lower-energy peak of the SED, likely arising from synchrotron processes, is usually located at frequencies between $\sim 10^{17}$ and $\sim 10^{18}$ Hz. The peak itself is therefore

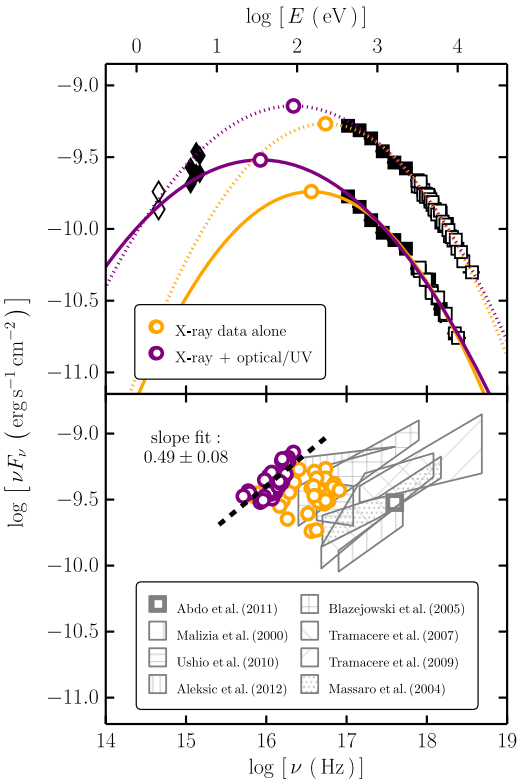

Figure 12. Upper panel shows examples of approximate localization of the synchrotron SED component peak for two orbits of simultaneous observations with *Swift* and *NuSTAR*. The *Swift* data are shown as black filled symbols (diamonds for the UVOT and squares for the XRT), and the *NuSTAR* data are shown as black open squares. Open diamonds represent *R*-band data. For each of the epochs we show a log-parabolic curve fit to X-ray data alone (yellow) and all data (purple). For each curve, we mark the SED peak with an open circle of matching color. In the lower panel we show results of the SED peak localization based on data from strictly simultaneous *Swift* and *NuSTAR* orbits. The colored data points show $\nu_{\rm syn.\ peak}$ and $(\nu F_\nu)_{\rm syn.\ peak}$, i.e., the frequency of the SED peak and the flux at the peak. The assumption of the log-parabolic model connecting the UV/optical and X-ray data (purple empty circles) reveals a proportionality between $\log(\nu F_\nu)_{\rm syn.\ peak}$ and $\log \nu_{\rm syn.\ peak}$; the dashed black line shows a linear fit best describing that relation. The other method (using only X-ray data) does not show a similar relation. In comparison with the observations published previously, shown here with different hatched gray regions, in 2013 January–March we observed a state in which the peak occurred at atypically low energy and high flux.

often directly observable in the *Swift*-XRT band, as in other similar HBL sources (e.g., Tramacere et al. 2007a; Furniss et al. 2015). Its location in frequency space can be estimated from the UV/optical and X-ray data, using a reasonable smooth interpolation or extrapolation model (e.g., Massaro et al. 2004; Błażejowski et al. 2005; Tramacere et al. 2009; Ushio et al. 2010). For the analysis presented here, we use 30 pairs of *Swift*-XRT and *NuSTAR* spectra assembled from data taken simultaneously, together with UV data taken within the same *Swift* observation and *R*-band data taken within 24 hr. Since optical variability is significantly lower, especially on short timescales, the nonsimultaneity of the optical flux measurements is not a serious concern. We employ the two most commonly used methods from the literature to localize the synchrotron SED peak. In the top panel of Figure 12 we show examples of both methods applied to two representative sets of data. The two methods are (i) fitting a log-parabolic model to the X-ray data alone, using `Xspec` model `logpar` described by Equation (3), and extrapolating to lower energies; and (ii) fitting a log-parabolic model to both optical/UV and X-ray data.

The X-ray-based extrapolation underestimates the UV/optical flux by more than an order of magnitude in nearly all cases. The peak frequencies predicted by this method uniformly cover the frequency range from 10^{16} to 10^{17} Hz and a factor of $\simeq$3 in peak flux. Interpretation of this simplistic parameterization of the SED would imply that it should consist of two superimposed components in order to match the observed UV/optical flux. However, log-parabolic fits that additionally include the *R*-band and UVOT fluxes provide a simpler solution that matches the data well on both sides of the SED peak. This is demonstrated by the two examples shown in Figure 12. Both methods are somewhat sensitive to the systematic uncertainties in the cross-normalization between the instruments and to the exact values of the line-of-sight column density and extinction corrections. We conservatively estimate that the combination of these effects results in a factor of $\simeq$2 uncertainty in the synchrotron peak frequency ($\nu_{\rm syn.\ peak}$), which dominates any statistical uncertainty from the fits. For this reason we do not show the uncertainties for individual $\nu_{\rm syn.\ peak}$ estimates in Figure 12.

Both methods consistently show the peak at an atypically low frequency ($\nu_{\rm syn.\ peak} < 10^{17}$ Hz), with peak flux comparable to high-activity states (see lower panel of Figure 12 and references listed there). The scatter is found to be larger for the fits using only the X-ray data, which can be easily understood since the curvature is subtle in all but the lowest-energy bins of the *Swift*-XRT band and the parabola has no constraint at energies below the peak. The optical/UV data provide the leverage to constrain the parabolic curves significantly better. We find an interesting trend using the second method: the flux at the SED peak is approximately proportional to the square root of the peak frequency. This is highlighted with a linear fit shown in the lower panel of Figure 12. The best-fit slope of the relation parameterized as $\log(\nu F_\nu)_{\rm syn.\ peak} \propto b \log(\nu_{\rm syn.\ peak})$ is $b = 0.49 \pm 0.08 \approx 0.5$. The dynamic range over which the relation holds, assuming that this parameterization is valid at all, is unknown. It is clear from the comparison with the peak localization taken from the literature (listed in the lower panel of Figure 12) that the relation is not universal, although its slope is broadly consistent with the slopes of previously identified relations of the same kind. Given the fact that the simple method used to derive it is purely phenomenological and sensitive to systematic uncertainties, we refrain from quantifying and interpreting this correlation further.

For all observations presented here $\nu_{\rm syn.\ peak} < 10^{17}$ Hz, essentially independent of the choice of model. If only a single peak is assumed to exist, our data unambiguously imply that the synchrotron peak frequency was well below the *Swift*-XRT band (<0.3 keV) during this period of very low X-ray activity. This is atypical for Mrk 421 based on the previously published data. We found that, for the states of lowest X-ray activity, our data show a peak frequency as low as $\nu_{\rm syn.\ peak} \lesssim 10^{16}$ Hz, estimated with a (symmetric) log-parabolic function fitted to both optical/UV and X-ray (*Swift*-XRT and *NuSTAR*) data. A peak frequency as low as $\sim 10^{16}$ Hz has been reported in Ushio et al. (2010), but only when using a specific model that led to a very asymmetric parameterization of the synchrotron bump. When using a symmetric function (comparable to a log-parabola), the fit to the same observational data

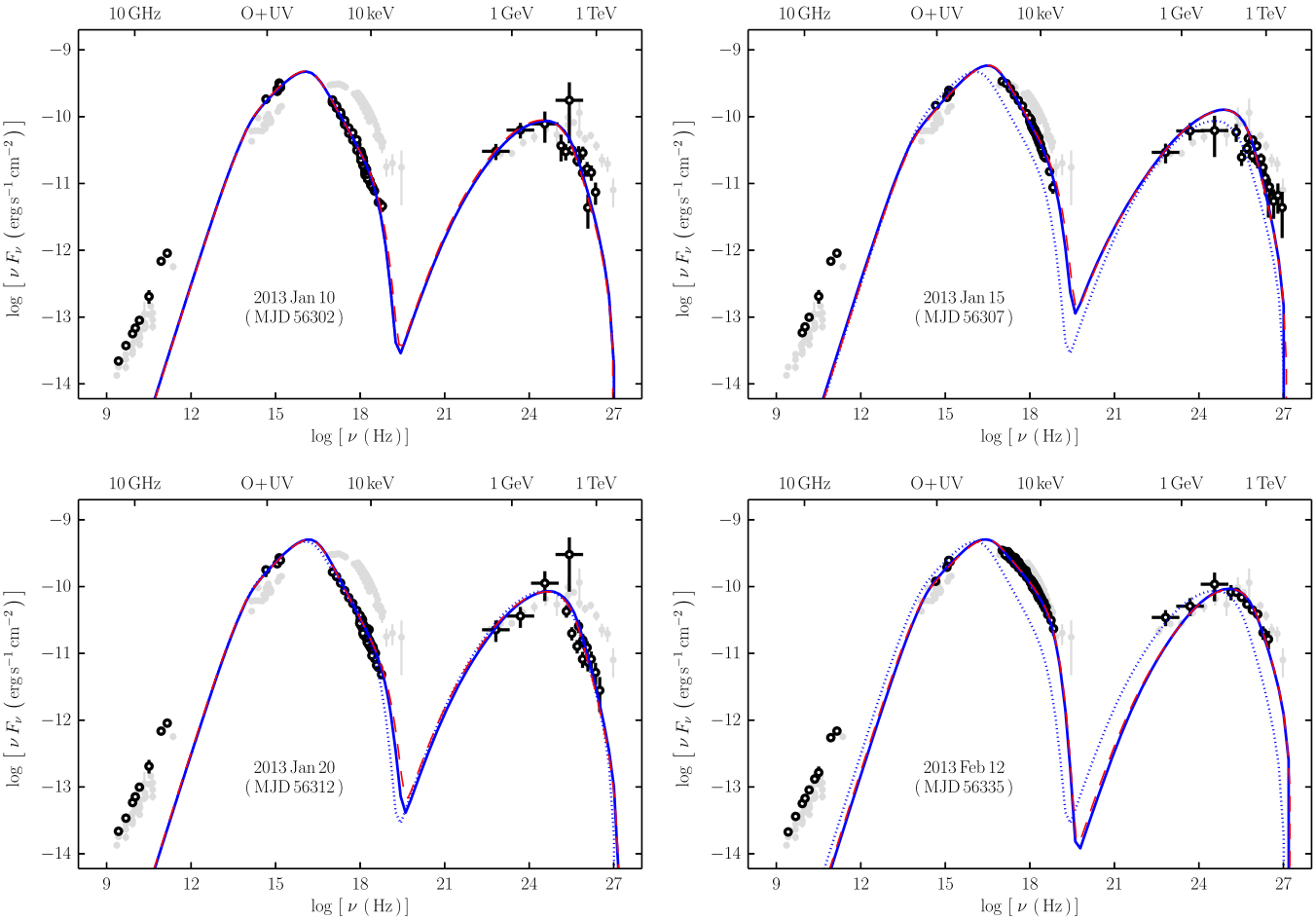

Figure 13. SED snapshots for four selected epochs during the campaign, assembled using simultaneous data from *Swift*-UVOT, *Swift*-XRT, *NuSTAR*, *Fermi*-LAT, MAGIC, and VERITAS. Most of the data were acquired over a period shorter than 12 hr in each case; the exceptions are the *Fermi*-LAT data and part of the radio data, which were accumulated over roughly 1-week time intervals. The two left panels show low-state SEDs, while the two on the right show elevated states (not flaring, but among the highest presented in this paper). The gray symbols in the background of each panel show the SED of Mrk 421 from Abdo et al. (2011) averaged over a quiescent 4.5-month period. The solid blue lines show a simple one-zone SSC model discussed in Section 5.3. To aid comparison, the model curve from the first panel is reproduced in the other panels with a blue dotted line. The dashed red lines show SED models with a time-averaged electron distribution discussed in Section 5.3 for comparison with previously published results.

reported in Ushio et al. (2010) led to a peak frequency of $\sim 10^{17}$ Hz, which is typical for Mrk 421.

Blazars are classified by the frequency of the peak of the synchrotron emission as LBLs, IBLs, and HBLs (for low-, intermediate-, and high-$\nu_{\rm syn.\ peak}$ BL Lacs) if $\nu_{\rm syn.\ peak}$ is below 10^{14} Hz, in the range 10^{14}–10^{15} Hz, or above 10^{15} Hz, respectively. The data presented here show that Mrk 421, which is one of the archetypal TeV HBLs, with a synchrotron peak position well above that of the typical HBL, changed its broadband emission in such a way that it almost became an IBL. This effect may also happen to other HBLs that have not been as extensively observed as Mrk 421 and suggests that the SED classification may denote a temporary characteristic of blazars, rather than a permanent one.

4.4. Broadband SED at Different Epochs

For a better understanding of the empirically observed correlations, we need to consider the complete broadband spectrum. SED snapshots for four selected epochs (marked with dashed vertical lines in Figure 7) are shown in Figure 13. They were selected to show a state of exceptionally low X-ray and VHE flux (January 10 and 20; see Section 4.2.1), in contrast to higher, though not flaring, states (January 15, February 12, for example). In all SED plots we also show data accumulated over 4.5 months in the 2009 multiwavelength campaign (Abdo et al. 2011), which is currently the best-characterized quiescent broadband SED available for Mrk 421 in the literature. For the two epochs of very low X-ray flux, we show for the first time states in which both the synchrotron and inverse-Compton SED peaks are shifted to *lower* energies by almost an order of magnitude compared to the typical quiescent SED. The accessibility of the low-activity state shows the large scientific potential brought by the improvements in the X-ray and VHE instrumentation in the past several years with the launch of *NuSTAR* and upgrades to the MAGIC and VERITAS telescopes.

We note that the empirical SEDs from the 2013 campaign shown here represent $\lesssim$12 hr of observation in the X-ray and VHE bands, rather than integrations over a time period of weeks or even months. We match the simultaneous UV, X-ray, and VHE data to optical data taken within at most 2 days, radio data taken within at most 2 weeks, and *Fermi* data integrated over time intervals of 6–10 days centered on the time of the

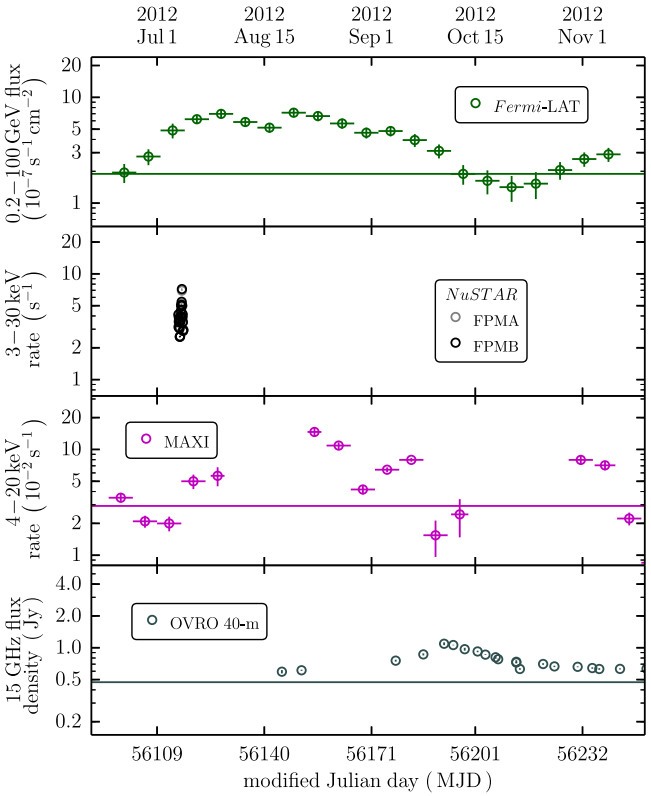

Figure 14. Light curves for Mrk 421 around the γ-ray flare detected by *Fermi*-LAT in 2012, from *Fermi*-LAT (0.2–100 GeV, binned weekly), *NuSTAR* (3–30 keV, binned by orbit; see the top panel of Figure 1 for greater time resolution), MAXI (4–20 keV, weekly bins), and OVRO (15 GHz, ∼weekly–daily cadence). Vertical and horizontal error bars show statistical uncertainties and the bin width, respectively, although some of the error bars are too small to be visible in this plot. The colored horizontal lines show the long-term median flux calculated from publicly available monitoring data. The dynamic range in all panels is 40, as in Figure 7, so that the two figures are directly comparable.

coordinated X-ray and VHE observations. Mrk 421 is a point-like and unresolved source for single-dish radio instruments, which means that the data shown in Figure 13 include emission from spatial scales larger than the jet itself and therefore should be considered as upper limits for the SSC models of jet emission. We further discuss the SED in the context of the SSC model in Sections 5.3 and 5.4.

4.5. Brief Summary of the Flaring Activity in 2012

In addition to the coordinated multiwavelength campaign conducted in 2013, Mrk 421 was observed independently with several instruments in 2012 July–September, including *NuSTAR*, *Fermi,* and OVRO. In 2012 July, the flux in the *Fermi*-LAT band increased above the median level and peaked twice over the following 2 months (see Figure 14). The first peak was reported on July 16 by the *Fermi*-LAT Collaboration (D'Ammando et al. 2012) and, within the same day, by the ARGO-YBJ collaboration (Bartoli et al. 2012). The daily flux seen by *Fermi*-LAT increased to $(1.4 \pm 0.2) \times 10^{-6}$ s^{-1}cm^{-2}, a factor of $\simeq$8 above the average flux reported in the second *Fermi*-LAT catalog (2FGL; Nolan et al. 2012). Light curves from several observatories monitoring Mrk 421 in 2012 July–September are shown in Figure 14 in order to provide a timeline for this flaring event.

An observation of Mrk 421 was performed by *NuSTAR* on 2012 July 7 and 8, shortly before the start of flaring activity in the γ-ray band. The observation[113] was not originally intended for scientific usage, as the pointing was suboptimal at this early point in the mission (less than a month after launch). However, it represents both the longest and the most variable *NuSTAR* observation considered in this paper (see Figure 1) and thus represents an important part of the *NuSTAR* data presented here. The available X-ray and γ-ray data are clearly too sparse to allow for associations to be inferred between any specific features in the light curves. There is indication from the MAXI public monitoring data[114] that the X-ray flux in the 4–20 keV band increased further after the *NuSTAR* observation, peaking between 2 and 5 weeks later (see Figure 14). The *NuSTAR* observation therefore makes it possible to investigate the hard X-ray spectrum of Mrk 421 at the time when its γ-ray activity was rapidly increasing.

A unique feature of this event is the well-defined rapid radio flare observed at 15 GHz from OVRO (Hovatta et al. 2012, 2015). Approximately 70 days after the first peak of the γ-ray flare, Mrk 421 reached a flux density of 1.11 ± 0.03 Jy, approximately 2.5 times its median flux density. Note that in Figure 14 we show the light curves on a logarithmic scale with a fixed dynamic range in order to facilitate direct comparison with Figure 7; on a linear plot both the γ-ray and the radio flare appear strikingly peaked. Based on the statistical properties of *Fermi*-LAT and OVRO 15 GHz light curves, Max-Moerbeck et al. (2014) have shown that the γ-ray and the radio flare are likely causally related. During most of the flaring activity in 2012, Mrk 421 was very close to the Sun on the sky, which resulted in relatively poor multiwavelength coverage. We therefore do not attempt a more comprehensive analysis of the sparse data available for this epoch. Hovatta et al. (2015) present the radio and γ-ray data, as well as a physical model for the flaring activity, for both the 2012 flare and the flare observed during the multiwavelength campaign in 2013 April. As the latter event has been covered with numerous instruments (e.g., Baloković et al. 2013b; Cortina et al. 2013; Paneque et al. 2013; Pian et al. 2014), we defer a comprehensive analysis of this period to a separate publication.

5. DISCUSSION

5.1. Spectral Variability in the X-Ray Band

The good temporal coverage of the *NuSTAR* data reveals a typical variability timescale of $\tau_{\rm var} \approx 9 \pm 3$ hr. Significant variability is clearly detectable even in the low-flux states, which is the case for several epochs in early 2013. We find no evidence for strong intrahour variability; on timescales as short as ∼10 minutes the variability amplitude is $\lesssim$5%, approximately an order of magnitude lower than the typical flux change over a 10 hr observation. This can be inferred from the fact that in the light curves shown in Figure 1 only a small fraction of adjacent bins differ in count rate by more than 3σ. We summarize this more formally in Figure 2. In contrast to some previous studies (e.g., Takahashi et al. 1996), we observed no clear time-dependent circular patterns in the count rate–hardness plane. The reason for this may be that most of the observations seem to have covered periods of decreasing flux,

[113] The observation consists of two contiguous segments, sequence IDs 10002015001 and 10002016001; see Table 3.
[114] http://maxi.riken.jp/top/

with no well-defined flare-like events except for a few "mini-flares" of modest $\lesssim$40% amplitude.

We find that the X-ray spectrum of Mrk 421 cannot generally be described as a simple power law, but instead it gradually steepens between 0.3 and ~70 keV. For most of the *Swift* and *NuSTAR* observations in the 2013 January–March period, we find that the spectra in both bands are better described when a curvature term is added to the basic power law, as in the log-parabolic model available in `Xspec`. Using this model, we find significant curvature at the highest observed fluxes—still notably lower than in any flaring states—gradually vanishing as flux decreases (see Figure 5). This has a simple explanation because the X-ray band samples the Mrk 421 SED close to the synchrotron peak: when the X-ray flux is low and the SED peak shifts to lower energy (away from the *NuSTAR* band), the hard X-ray spectra can be well described by a power law. This behavior is consistent with the steady increase of fractional variability with energy through the X-ray band, as shown in Figure 9. The high sensitivity of *NuSTAR* reveals that the hard X-ray spectrum does not exhibit an exponential cutoff, and it is well described by a power law with a photon index $\Gamma \approx 3$, even during the epochs related to the lowest X-ray fluxes. The *NuSTAR* data also show no signature of spectral hardening up to ~80 keV, meaning that the onset of the inverse-Compton bump must be at even higher energies.

5.2. Correlated Variability in the X-Ray and VHE Spectral Bands

The data gathered in the 2013 multiwavelength campaign contribute some unique details to the rich library of blazar phenomena revealed by Mrk 421. The object is highly variable on a wide range of timescales and fluxes, with the fractional variability amplitude highest at the high-energy ends of the synchrotron and inverse-Compton SED bumps (see Figure 9). The well-matched coverage in the X-ray and VHE bands reveals that the steep spectral slope observed in the X-ray band at very low flux occurs simultaneously in time with an atypically steep slope observed in the VHE band. For the first time we observed a simultaneous shift of both the synchrotron and the inverse-Compton SED peaks to lower energies in comparison to the typical quiescent state (see Figure 13), constrained primarily by the X-ray and VHE data. The measurements in those bands do not support the existence of high-energy cutoffs up to $\simeq$80 keV and $\simeq$1 TeV. All of this indicates that the energies of radiating particles must be very high (up to $\gamma \sim 10^6$; see Section 5.3 below) even when the source is in such a low state.

In Section 4.2.1 we have shown that the X-ray and VHE fluxes are correlated at $>3\sigma$ significance. Parameterizing the correlation as $\log(F_{\text{X-ray}}) = a \log(F_{\text{VHE}}) + b$, the correlation is found to be approximately linear ($a \approx 1$) on both half-hour and half-day timescales. This is consistent with most previous results considering similar spectral bands: $a = 1.7 \pm 0.3$ (Tanihata et al. 2004), $a \approx 1$ (Fossati et al. 2008, for averaged and nonflaring periods; also Aleksić et al. 2015b), $a = 1$ (Acciari et al. 2014; assumed linear), etc. We emphasize the importance of distinguishing between (i) a correlation of count rates versus a correlation of fluxes, since the conversion between them is nonlinear owing to spectral variability, and (ii) a general correlation versus a correlation associated with isolated flares, since those could potentially be produced by different physical mechanisms (as argued by, e.g., Katarzyński et al. 2005). Indeed, for isolated flaring periods Fossati et al. (2008) and Giebels et al. (2007) find $a \approx 2$ and $a = 2.9 \pm 0.6$, respectively. Care should be taken with direct comparison of the results in the literature, since the chosen spectral bands are not always the same, and we have shown in Section 4.2.1 that the slope does depend on the band choice as a consequence of the spectral variability.

We note that in the simplest, one-zone SSC model, one expects a close correlation between the X-ray and VHE fluxes. However, if the scattering takes place exclusively in the Thomson regime, the inverse-Compton flux should obey a quadratic ($a = 2$) relationship, since increasing both the number of electrons and the seed photon flux results in a quadratic increase in the scattering rate. Since we detect a linear relationship, this would argue that the scattering cross section is diminished, possibly because the scattering takes place in the less efficient Klein–Nishina regime. For example, a quadratic relation has recently been observed in a similar HBL object, Mrk 501 (Furniss et al. 2015). It has been shown previously (e.g., Katarzyński et al. 2005) that this implication is valid only if the normalization of the entire electron distribution is changed to produce flux variations. For changes in other parameters of the electron distribution, or in physical conditions within the emission region, this is no longer strictly correct. The linearity of the flux–flux correlation itself does not uniquely indicate Klein–Nishina effects; we therefore combine the broadband SED modeling and variability properties in the following section, in order to further investigate this issue.

5.3. Interpretation within the Framework of a Single-zone SSC Model

In the framework of an SSC model, if the peak energies of the synchrotron and inverse-Compton SED are resolved, then along with constraints from temporal variability and an estimate of the bulk Doppler factor of the emitting material, fairly general and robust estimates can be made of the characteristic particle energies, the magnetic field strength, and the overall size of the emitting region. An estimate for the characteristic electron Lorentz factor (γ_c, measured in the comoving frame of the emitting plasma) is given roughly by the square root of the ratio of the energies of the synchrotron and inverse-Compton peaks. The radiation at the peaks is dominated by electrons of intermediate energy, where the Klein–Nishina reduction in the scattering cross section is not expected to be significant. From the SEDs shown in Figure 13, we estimate $\nu_{\text{syn. peak}} \simeq 10^{16}$ Hz and $\nu_{\text{IC peak}} \simeq 10^{25}$ Hz. It then follows that $\gamma_c \sim (\nu_{\text{IC peak}}/\nu_{\text{syn. peak}})^{1/2} \sim 3 \times 10^4$. Assuming a bulk Doppler factor of $\delta \sim 25$, we can also estimate the magnetic field strength in the plasma comoving frame: $B = 4\pi\nu_{\text{syn. peak}} m_e c/(3e\delta\gamma_c^2) \simeq 0.1$ G. Finally, an upper limit for the size of the emitting region in the comoving frame is given by the observed variability timescale, $\tau_{\text{var}} \approx 9$ hr, and the bulk Doppler factor δ: $R \lesssim c\tau_{\text{var}}\delta \simeq 2 \times 10^{16}$ cm.

We can constrain the properties of the jet emission region more precisely by directly modeling the multiwavelength SED data shown in Figure 13 with a standard one-zone SSC model. Specifically, we apply an equilibrium version of the SSC model from Böttcher & Chiang (2002), fully described in Böttcher et al. (2013). This model has already been used to represent Mrk 421 in two different states (Acciari et al. 2009). In this model, the emission originates from a spherical region with radius R, containing relativistic electrons that propagate down

Table 9
Model Parameters for the Equilibrium SSC Model for Four Selected Epochs

Parameter	Jan 10	Jan 15	Jan 20	Feb 12
$\gamma_{\rm min}$ (10^4)	2.2	3.5	2.4	5.0
$\gamma_{\rm max}$ (10^5)	4.0	4.8	5.8	6.8
q	3.5	3.5	3.6	3.0
η	35	35	35	35
B (G)	0.17	0.25	0.16	0.10
Γ	25	25	25	25
R (10^{16} cm)	0.9	0.55	1.0	1.4
θ (deg)	2.29	2.29	2.29	2.29
τ (hr)	3.4	2.1	3.8	5.3
L_e (10^{43} erg s^{-1})	3.0	2.6	3.0	3.3
$\epsilon = L_B/L_e$	0.18	0.25	0.20	0.14

Note. The electron energy distribution parameters listed here refer to the electrons injected into the emission region, and the equilibrium distribution is calculated self-consistently within the model, as described in Section 5.3. Model SED curves are shown in Figure 13.

Table 10
Model Parameters for the Snapshot SSC Model for Four Selected Epochs

Parameter	Jan 10	Jan 15	Jan 20	Feb 12
$\gamma_{\rm min}$ (10^3)	2.0	1.3	1.7	3.0
$\gamma_{\rm brk}$ (10^4)	2.5	3.7	3.0	5.2
$\gamma_{\rm max}$ (10^5)	4.0	4.8	5.8	6.8
p_l	2.0	2.0	2.0	2.0
p_h	4.5	4.5	4.6	4.0
B (G)	0.21	0.28	0.19	0.10
Γ	25	25	25	25
R (10^{16} cm)	0.93	0.60	1.04	1.69
θ (deg)	2.29	2.29	2.29	2.29
τ (hr)	3.4	2.2	3.9	6.3
L_e (10^{43} erg s^{-1})	3.3	2.9	3.3	4.1
$\epsilon = L_B/L_e$	0.51	0.47	0.56	0.33

Note. The electron energy distribution parameters listed here refer to the distribution directly responsible for the SSC emission. This simplified model is described in Section 5.3 and used for comparison with the literature. Model SED curves are shown in Figure 13.

the jet with a bulk Lorentz factor Γ. In order to decrease the number of free parameters, we assume a value $\Gamma = 25$ with the jet axis aligned near the line of sight with the critical angle $\theta = 1/\Gamma = 0.04$ rad $= 2.^\circ29$, which makes the Doppler factor equal to the jet Lorentz factor ($\delta = \Gamma$). This simplifying choice is often used in the literature when direct measurements are not available (see, e.g., Abdo et al. 2011 and the discussion therein). A Doppler factor of 25 is higher than the value inferred from VLBA measurements of the blob movement by Piner et al. (2010). This is a common situation in VHE blazars, often referred to as the "bulk Lorentz factor crisis," and requires that the radio and VHE emissions are produced in regions with different Lorentz factors (Georganopoulos & Kazanas 2003; Ghisellini et al. 2005; Henri & Saugé 2006). High Doppler factors ($\gtrsim$10) are required to explain previously reported rapid variations in the VHE band (Gaidos et al. 1996; Celotti et al. 1998; Galante 2011) and are typically used in theoretical scenarios to describe the broadband emission of VHE blazars. Relativistic leptons are injected according to a power-law distribution $dn/d\gamma \propto \gamma^{-q}$ between $\gamma_{\rm min}$ and $\gamma_{\rm max}$. These particles lose energy through synchrotron and inverse-Compton radiation, leading to an equilibrium between particle injection, radiative cooling, and particle escape. The particle escape is characterized with an escape efficiency factor η, defined so that $\tau_{\rm esc} = \eta R/c$ is the escape time. This results in a particle distribution that propagates along the jet with power L_e. Synchrotron emission results from the interaction of particles with a magnetic field B, generating a Poynting-flux luminosity of L_B. L_e and L_B allow the calculation of the equipartition parameter L_B/L_e. Various other blazars have been represented with this model, with the resulting model parameters summarized in Aliu et al. (2013). In application to the broadband data, the intrinsic source VHE flux from the SSC model is absorbed by the Franceschini et al. (2008) model describing the extragalactic photon field. In Table 9, we list the relevant model parameters that reproduce the observed SED of Mrk 421 for the four selected epochs in 2013.

Since the injected particle distribution in our SSC model follows a single power law, the observed spectral shapes in the GeV and VHE bands imply certain constraints on the model parameters. In the 0.1–100 GeV band, the observed spectra have photon indices in the range $\Gamma \sim 1.6$–1.7, while, by contrast, the VHE spectra have photon indices of $\Gamma \sim 2.3$–3.5 (see Tables 5 and 6). These indices imply spectral breaks of $\Delta\Gamma \sim 0.6$–1.9, which are moderately to significantly larger than the "cooling" break of $\Gamma = 0.5$ that arises from incomplete (or "weak") synchrotron cooling of an injected power-law distribution of electrons. In the strong-cooling regime, i.e., where the synchrotron cooling timescale is shorter than the particle-escape time, the cooled electron distribution has a break at the lower bound of the injected power law, $\gamma_b = \gamma_{\rm min}$, and has power-law shapes $dn/d\gamma \propto \gamma^{-2}$ for $\gamma < \gamma_b$ and $dn/d\gamma \propto \gamma^{-(q+1)}$ for $\gamma > \gamma_b$. For the parameters shown in Table 9, this particle distribution implies a synchrotron spectrum with a peak at $\nu_{\rm syn.\ peak} \simeq (1\text{–}2) \times 10^{16}$ Hz and spectral shapes $F_\nu \propto \nu^{-1/2}$ ($dN/dE \propto E^{-1.5}$) for $\nu < \nu_{\rm syn.\ peak}$ and $F_\nu \propto \nu^{-q/2}$ ($dN/dE \propto E^{-(2.6-3.2)}$) for $\nu > \nu_{\rm syn.\ peak}$ (see Table 7 and Figure 13). For $\gamma_{\rm min} = 3 \times 10^4$ and $B = 0.2$ G, a synchrotron cooling timescale of $\tau_{\rm syn} = 4 \times 10^5$ s is obtained in the comoving frame of the emitting plasma; this is slightly larger than the nominal (i.e., in the absence of any scattering) escape time of $\tau_{\rm esc,\ nom} = R/c = 3 \times 10^5$ s. The escape efficiency factor, $\eta = 35$, ensures that the cooled electron distribution extends to sufficiently low energies to model both the optical/UV points and the *Fermi*-LAT data down to 0.1 GeV. The Larmor radius of the lowest-energy electrons in the modeled magnetic field is small enough that the electrons have sufficient time to cool within the emission region before escaping.

Past SED modeling of HBL-type blazars has often used SSC calculations that have electron distributions assumed to persist in the specified state for the entire duration of the observation. For example, for a given variability timescale, a single, time-averaged, multiply broken power-law electron distribution is used by Abdo et al. (2011) to model the multiwavelength data obtained for Mrk 421 over a 4.5-month period in early 2009. By contrast, the SED calculations we have performed in this paper attempt to model specific flaring or quiescent periods for which most of the data (optical, X-ray, and VHE) were obtained within 12 hr intervals. Our modeling assumes that an initial power-law electron spectrum is injected into the emission region, and we compute the resulting quasi-equilibrium particle distribution for those epochs given the radiative and particle escape timescales. Since the 2009 observations could contain a large number of similarly short

flaring and quiescent episodes with a range of physical properties, it would be inappropriate to attempt to model those data with the procedure we have used here. However, as we have indicated above, it should be possible to obtain equivalent time-averaged SED models that have multiply broken power-law electron distributions and that we can compare directly to the Abdo et al. (2011) results.

We have performed such modeling, and in Table 10, we give the parameters for the same four selected epochs appearing in Table 9. The SEDs produced by the two models can be matched very well, as shown in Figure 13 with the blue and dashed red lines. As we noted above, the equivalent time-averaged electron distributions can be represented via a broken power law with a break at $\langle\gamma\rangle_{\rm brk} \simeq \gamma_{\rm min}$ and index $p_l = 2.0$ below $\langle\gamma\rangle_{\rm brk}$ and index $p_h = q + 1$ above the break.

As Abdo et al. (2011) demonstrate and as we discuss above, for data that resolve the shapes of both the synchrotron and self-Compton components of the SED, the model parameters in these sorts of leptonic time-averged models are largely determined once either the variability timescale or the Doppler factor is constrained or set. Therefore, when comparing the current model parameters to those of Abdo et al. (2011), we consider just their $\delta = 21$ results. In terms of the shape of the underlying particle distributions, the value of $p_l = 2.0$ we find is comparable to their value of $p_1 = 2.2$, and our values of $p_h = 4.0$–4.6 are similar to their high-energy index of $p_3 = 4.7$. While this does not uniquely imply that the same energy-loss mechanisms and acceleration processes are at work in both cases, the consistency is encouraging. The Abdo et al. (2011) modeling does require an additional medium-energy power-law component that is dictated by their generally broader SED peaks (see the gray points in Figure 13). In the context of the quasi-equilibrium modeling, this would arise from a distribution of physical parameters in shorter flaring and quiescent episodes that are averaged over the 4.5-month observation time.

Several physical parameters in the current modeling do differ substantially from those of Abdo et al. (2011). The characteristic electron Lorentz factors are about an order of magnitude lower ($\langle\gamma\rangle_{\rm brk} = (2.5$–$5.2) \times 10^4$ vs. $\gamma_{\rm brk2} = 3.9 \times 10^5$), while the inferred emitting region radius is about a factor of 3–10 smaller ($R = (0.6$–$1.7) \times 10^{16}$ cm vs. 5.2×10^{16} cm), the inferred magnetic field is substantially higher ($B = 0.10$–0.28 vs. 0.038), and the resulting jet powers differ by a factor of three to four. As a consequence, the current modeling yields equipartition parameters that are much closer to unity, in the range $\epsilon = 0.33$–0.56 vs. $\epsilon = 0.1$ for the Abdo et al. (2011) result. Given the overall similarity in the size and shape of the synchrotron and SSC components among all five data sets (i.e., the four 2013 epochs and the 2009 data shown in Figure 13), the differences in model parameters can be understood as being driven mostly by the combination of the order-of-magnitude larger characteristic electron Lorentz factor and the order-of-magnitude higher peak synchrotron frequency required by the Abdo et al. (2011) data and modeling. Since $\nu_{\rm syn} \propto B\gamma^2$, the order-of-magnitude higher magnetic fields in the current modeling are readily understood, and those in turn largely account for the equipartition parameters being substantially closer to unity. We note that other authors, such as Aleksić et al. (2015c), have inferred SSC model parameters that are below equipartition by much more than an order of magnitude. However, Aleksić et al. (2015c) considered a flaring state of Mrk 421 that had much higher synchroton peak frequencies, as well as substanially higher fluxes at all wavelengths. Accordingly, their much larger disparity in the partitioning of the jet power compared to the current results is not surprising and roughly fits in with the preceding discussion.

Studying broadband emission of Mrk 421 at different epochs, Mankuzhiyil et al. (2011) found that there were no substantial shifts in the location of the peaks of the synchrotron and the inverse-Compton bumps. They concluded that the variability in the blazar emission was dominated by changes in the parameters related to the environment, namely, the emission-region size, the Lorentz (Doppler) factor, and the magnetic field. The observational results presented here, with substantially broader energy coverage and better instrumental sensitivity due to the advent of new γ-ray and X-ray instruments, differ from those presented in Mankuzhiyil et al. (2011). We show that, besides changes in the magnetic field, the distortions in the broadband emission of Mrk 421 also require changes in the electron energy distribution, which may be due to variations in the mechanism accelerating the electrons to high energies.

Having modeled the broadband SEDs with single-zone SSC calculations, we can test the hypothesis that the VHE emission occurs in the Klein–Nishina regime. The SED modeling yields injected electron Lorentz factors in the range $\sim 3 \times 10^4$ to $\sim 6 \times 10^5$. Assuming that the target synchrotron photons for inverse-Compton scattering have energies around the synchrotron peak at $\nu_{\rm syn.\ peak} \sim 10^{16}$ Hz, the parameter governing the transition between Thomson and Klein-Nishina regimes is $4\,h\nu_{\rm syn.\ peak}\gamma/m_e c^2$ (Blumenthal & Gould 1970), which in the observer frame becomes $4\,h\nu_{\rm syn.\ peak}\gamma/\delta m_e c^2$.

When considering photons from the synchrotron peak position ($E = h\nu_{\rm syn.\ peak} \sim 40$ eV, i.e., about one order of magnitude lower than the typical position of the synchrotron peak in Mrk 421), we obtain $4\,h\nu_{\rm syn.\ peak}\gamma/\delta m_e c^2 \simeq 0.4$–$8$, indicating that the inverse-Compton scattering of photons with energy $h\nu_{\rm syn.\ peak}$ takes place, at least partially, in the Klein–Nishina regime. The X-ray energies probed with *Swift*-XRT are roughly one order of magnitude above $h\nu_{\rm syn.\ peak}$, far above the range where Thomson scattering is relevant, and consistent with the linear ($a \simeq 1$) relationship between the soft X-ray and VHE flux.

5.4. Toward a Multi-zone Emission Scenario

The electrons responsible for the broadband emission of Mrk 421 lose energy mostly owing to synchrotron cooling, as one can infer from the dominance of the synchrotron bump over the inverse-Compton bump shown in the SEDs from Figure 13. Note that the inefficiency of cooling via the Compton channel is independently implied from the observed slope of the X-ray–VHE flux correlation. The observed variability timescale (measured in a stationary observer's frame) due to synchrotron cooling alone is given by $\tau_{\rm syn} = 1.2 \times 10^3 B^{-3/2} E^{-1/2} \delta^{-1/2}$ s, where E is the photon energy in keV and B is the comoving frame magnetic field strength in G. Taking $E \approx 10$ keV as the energy typical for the *NuSTAR* band, assuming $B \approx 0.2$ G, as found from our SED modeling, and $\delta = 25$ as before, we arrive at $\tau_{\rm syn}$ of $\sim 10^3$ s.[115] This is more than an order of magnitude shorter than the

[115] Note that the longer synchrotron cooling timescale discussed in Section 5.3 refers to emission at much lower energies, below the synchrotron peak of the SED.

variability timescale $\tau_{\rm var} \approx 9$ hr measured in the observer's frame, as we can derive from the *NuSTAR* light curves. Since the synchrotron cooling timescales are so short, this requires that the electron acceleration must be happening locally, very close to where the emission takes place.

Considering the disparity between the variability timescale and the synchrotron cooling timescale, along with the similarity of the increases and decreases in flux during the *NuSTAR* observations (Figure 1), it seems unlikely that the output is dominated by a single shocked region as a site of particle acceleration, such as is often argued to be the case in flaring episodes. Instead, we can interpret the flux changes as a geometrical effect due to a spatially extended region containing multiple particle-acceleration zones contributing comparably to the overall SED. Observation of variability due to geometrical effects of a spatially extended region would lack sharp flux increases in the X-ray band, which might result from sudden particle-acceleration events, because the sharp flux increases and decreases from the different regions (even if partially connected) would not occur at exactly the same time. In this scenario, the shortest variability timescales, comparable to the electron cooling timescales, would be produced only when a single region dominates the overall emission, which is expected to occur during flaring episodes, but not during the relatively low activity reported in this paper. As described in Section 3.1, the observed increases appear at least as smooth and as slow as the observed decreases, consistent with this picture.

One may argue that the X-ray flux variability reported in Section 3.1 is not due to the acceleration/cooling of electrons, but rather produced by variations in the parameters related to the environment (e.g., B, R) or the Dopper factor δ (e.g., due to a change in the viewing angle). In that case, the smooth and relatively slow changes observed in the *NuSTAR* light curves would not be related to the short electron cooling timescales derived above, but rather to the variations in the above-mentioned parameters. However, such a theoretical scenario is strongly disfavored by the fractional variability as a function of energy reported in Figure 9, as well as by the lack of correlation between optical and X-ray fluxes reported in Figure 11, while there is a correlation between optical and GeV γ-ray fluxes, as well as X-ray and VHE fluxes, reported in Figures 10 and 11, respectively. The only possibility for the parameters R, B, or δ to dominate the measured flux variations would be to have, at least, two distinct emission regions, one dominating the optical and GeV γ-ray bands, and the other dominating the X-ray and VHE bands. Therefore, despite the success of the one-zone SSC scenario in describing the broadband SED (see Section 5.3), we argue that the observed multiwavelength variability and correlations point toward an emission region composed of several distinct zones and dominated by changes in the electron energy distribution. The increase in the fractional variability with energy for both SED bumps and the harder-when-brighter trend that is clearly observed in the X-ray spectra measured with *NuSTAR* (which is the segment of the broadband SED reconstructed with the highest accuracy) indicate that the changes in the electron energy distribution are generally chromatic,[116] with strongest variability in the highest-energy electrons. However, the saturation of the X-ray spectral shape at the lowest and highest X-ray fluxes (see Section 3.4 and Figure 6) suggests that at the times of lowest and highest activity, the variations in the electron energy distribution become achromatic, at least for those electron energies responsible for the X-ray emission. It is possible that at those times the variability is not dominated by acceleration and cooling of the electrons, but rather by variations in the physical parameters of the environment in which particle acceleration occurs. For the periods of very low activity, a possibility would be that the radiation is being produced within a larger region by particles accelerated by Fermi II processes (e.g., stochastic acceleration on magnetic turbulence), as suggested, for instance, by Massaro et al. (2004) and Ushio et al. (2009).

The magnetic field implies a size constraint for the acceleration zones, since electrons cannot attain energies corresponding to a gyroradius significantly larger than the characteristic size of a zone. The *NuSTAR* data imply no cutoff in the synchrotron SED up to ~80 keV, so we can estimate the electron gyroradius $R_{\rm G}$ corresponding to that photon energy using $B = 0.2$ G and the maximal $\gamma \sim 10^6$. Since $R_{\rm G} = \gamma m_{\rm e} c^2 e^{-1} B^{-1}$, we have $R_{\rm G} \lesssim 10^{11}$ cm, which is much smaller than the inferred emission-region size of 10^{16} cm. Given the large difference of five orders of magnitude between the gyroradius for the highest-energy electrons and the size of the overall emitting region, the electrons cannot travel far from their acceleration site without losing a substantial fraction of their energy, and hence the particle acceleration and the emission need to be essentially co-spatial. We therefore conclude that the set of physical parameters discussed here offers a self-consistent picture in which the observed properties of Mrk 421 in a nonflaring state are consistent with compact zones of particle acceleration distributed within a significantly larger volume that produces the total emission. While detailed characterization of the acceleration process is outside the scope of the paper, one possible scenario involves magnetic reconnection and "mini-jets" formed within a larger emission volume, as suggested, for instance, by Nalewajko et al. (2011) and developed further by Nalewajko et al. (2015). For a recent summary of arguments in favor of magnetic reconnection for powering blazar jets, the reader is referred to Sironi et al. (2015).

Regardless of the exact acceleration mechanism, emitting regions composed of multiple zones, e.g, as in the model proposed by Marscher (2014), would be consistent with other behavior observed in blazars, such as the increase in the degree of polarization of the synchrotron radiation when the polarization electric vector rotates, or curvature in the SED arising from nonuniform particle acceleration and energy losses. In a low-activity state, where no single zone dominates the output, the addition of polarization vectors from individual zones would result in a low overall level of polarization with random fluctuations in both the polarization degree and angle. Our optical polarization measurements, shown in Figure 8, are consistent with that prediction. While multizone scenarios have previously been considered for flaring states (e.g., Massaro et al. 2004; Ushio et al. 2009; Cao & Wang 2013; Aleksić et al. 2015c), it has usually been assumed that the quiescent state can be well described by a simpler single-zone SSC model (e.g., Abdo et al. 2011). The observations presented here, however, show that, even in this state of very low activity, the emission region may have a more complex structure than previously assumed.

[116] In the sense of larger relative increase at higher energies.

6. SUMMARY AND CONCLUSIONS

We have observed the blazar Mrk 421 in an intensive multiwavelength campaign in 2013, including GASP-WEBT, *Swift*, *Fermi*-LAT, MAGIC, VERITAS, and, for the first time, the new high-sensitivity hard X-ray instrument *NuSTAR*. In this paper we present part of the data from the campaign between the beginning of January and the end of 2013 March, with the focus on the unprecedented coverage of the X-ray part of the broadband spectrum. Another successful aspect of the campaign is the achieved goal of strictly simultaneous observations in the X-ray and VHE γ-ray bands, in order to constrain the correlated variability. During the data-taking period presented in this work, Mrk 421 exhibited relatively low activity, including the lowest flux state ever investigated with high temporal and broadband spectral coverage.

The rich data set yields a number of important empirical results, which we summarize below.

1. During the first 3 months of 2013, the X-ray and VHE γ-ray activity of Mrk 421 was among the lowest ever observed.
2. *NuSTAR* performed half-day-long observations of Mrk 421, which showed that this source varies predominantly on timescales of several hours, with multiple instances of exponentially varying flux on timescales of 6–12 hr. Mrk 421 also exhibited smaller-amplitude, intrahour variations at the $\lesssim$5% level. However, only $\lesssim$20% of the X-ray data show any appreciable intrahour variability. Within the dynamic range of our observations, we find no differences in the variability pattern or timescales between the lower and higher flux states.
3. We find a systematic model-independent hardening of the X-ray spectrum with increasing X-ray flux. As the X-ray activity decreases, the curvature in the X-ray spectrum decreases and the spectral shape becomes softer. At 2–10 keV fluxes $\lesssim 10^{-10}$ erg s^{-1} cm^{-2}, the spectral curvature completely disappears, and the spectral shape saturates into a steep $\Gamma \approx 3$ power law, with no evidence for an exponential cutoff or additional hard components up to $\simeq$80 keV.
4. For two epochs of extremely low X-ray and VHE flux, in a regime not previously reported in the literature, we observed atypically steep spectral slopes with $\Gamma \approx 3$ in both X-ray and VHE bands. Using a simple steady-state one-zone SSC scenario, we find that in these two epochs the peaks of both the synchrotron and inverse-Compton components of the SED shifted toward lower frequencies by more than an order of magnitude compared to their positions in the typical low states of Mrk 421 observed previously. The peak of the synchrotron bump of Mrk 421 shifted from ~0.5–1 keV to ~0.04 keV, which implies that HBLs can move toward becoming IBLs, leading to the conclusion that the SED classification based on the peak of the synchrotron bump may denote only a temporary rather than permanent characteristic of blazars.
5. A clear double-bump structure is found in the fractional variability distribution, computed from radio to VHE γ-ray energies. This double-bump structure relates to the two peaks in the broadband SED shape of Mrk 421 and has been recently reported (with less resolution) for both low-activity (Aleksić et al. 2015b) and high-activity states (Aleksić et al. 2015c). The less variable energy bands (radio, optical/UV, and GeV γ-rays) relate to the segments of the SED rising up toward the peaks as a function of photon energy, while the most variable energy bands (X-rays and VHE γ-rays) sample the SED above the peaks, where it steeply declines with photon energy.
6. We find a tight X-ray–VHE flux correlation in three nonoverlapping X-ray bands between 0.3 and 30 keV, with significantly different scaling. These results are consistent with an SSC scenario in which the X-ray and VHE radiations are produced by the same relativistic electrons, and the scattering of X-ray photons to VHE energies (~TeV) occurs in the less-efficient Klein–Nishina regime. From broadband SED modeling with a single-zone SSC model for four epochs, and assuming a constant Doppler factor of 25, we infer a magnetic field $B \sim 0.2$ G and electron Lorentz factors as large as $\gamma \gtrsim 6 \times 10^5$. These parameter values, which are typical for describing the broadband SED of HBLs, further support the claim that, in the context of the SSC model, the inverse-Compton scattering responsible for the VHE emission takes place in the Klein–Nishina regime.
7. There is tentative evidence for an optical/UV–GeV flux correlation, which is consistent with the emission in these two bands being produced by the same lower-energy electrons within the SSC framework.
8. No correlation is found between fluxes in the optical/UV and the soft X-ray bands on either short or long timescales. However, we do find that a simple parameterization of the SED around the synchrotron peak with a log-parabolic function leads to a correlation between the peak flux and the frequency at which it occurs over a limited frequency range.
9. The reported increase in the fractional variability with energy (for each of the two SED bumps) and the hardening of the X-ray spectra with increasing flux suggest that the variability in the emission of Mrk 421 is produced by chromatic changes in the electron energy distribution, with the highest-energy electrons varying the most. The saturation of the X-ray spectral shape at the extremely high and low X-ray fluxes indicates that, for these periods of outstanding activity, the flux variability is instead dominated by other processes that lead to achromatic variations in the X-ray emission.
10. The lifetimes of relativistic electrons due to synchrotron losses are estimated to be $\tau_{\rm syn} \lesssim 10^3$ s, which are substantially shorter than the $\sim 3 \times 10^4$ s that dominate the large-amplitude variations in the *NuSTAR* light curves. Together with the fractional variability distribution and the multiwavelength correlations observed in this campaign, this observation suggests that the broadband emission of Mrk 421 during low activity is produced by multiple emission regions.
11. The electron cooling times of $\tau_{\rm syn} \lesssim 10^3$ s are also shorter than the emission-region crossing time ($\gtrsim 10^4$ s), which points toward in situ electron acceleration. While particle acceleration in shocks is not excluded by our data, the gyroradii of the most energetic electrons (those radiating in the upper part of the *NuSTAR* band, or the upper part of the VHE band) are $\lesssim 10^{11}$ cm, which is shorter than the cooling (energy-loss) timescales inferred from our modeling. This is suggestive of an electron-acceleration

process occurring in relatively compact zones within a larger emission volume.

We thank the anonymous referee for constructive suggestions that helped improve and clarify the paper.

M.B. acknowledges support from the International Fulbright Science and Technology Award, and from NASA Headquarters under the NASA Earth and Space Science Fellowship Program, grant NNX14AQ07H. This research was supported in part by the Department of Energy Contract DE-AC02-76SF00515 to the SLAC National Accelerator Center. G.M. and A.F. acknowledge the support via NASA grant NNX13AO97G. D.B. acknowledges support from the French Space Agency (CNES) for financial support.

This work was supported under NASA Contract No. NNG08FD60C and made use of data from the *NuSTAR* mission, a project led by the California Institute of Technology, managed by the Jet Propulsion Laboratory, and funded by the National Aeronautics and Space Administration. We thank the *NuSTAR* Operations, Software, and Calibration teams for support with the execution and analysis of these observations. This research has made use of the *NuSTAR* Data Analysis Software (NuSTARDAS) jointly developed by the ASI Science Data Center (ASDC, Italy) and the California Institute of Technology (USA).

VERITAS is supported by grants from the U.S. Department of Energy Office of Science, the U.S. National Science Foundation, and the Smithsonian Institution, by NSERC in Canada, and by STFC in the U.K. We acknowledge the excellent work of the technical support staff at the Fred Lawrence Whipple Observatory and at the collaborating institutions in the construction and operation of the instrument. The VERITAS Collaboration is grateful to Trevor Weekes for his seminal contributions and leadership in the field of VHE gamma-ray astrophysics, which made this study possible.

The MAGIC Collaboration would like to thank the Instituto de Astrofísica de Canarias for the excellent working conditions at the Observatorio del Roque de los Muchachos in La Palma. The financial support of the German BMBF and MPG, the Italian INFN and INAF, the Swiss National Fund SNF, the ERDF under the Spanish MINECO, and the Japanese JSPS and MEXT is gratefully acknowledged. This work was also supported by the Centro de Excelencia Severo Ochoa SEV-2012-0234, CPAN CSD2007-00042, and MultiDark CSD2009-00064 projects of the Spanish Consolider-Ingenio 2010 programme, by grant 268740 of the Academy of Finland, by the Croatian Science Foundation (HrZZ) Project 09/176 and the University of Rijeka Project 13.12.1.3.02, by the DFG Collaborative Research Centers SFB823/C4 and SFB876/C3, and by the Polish MNiSzW grant 745/N-HESS-MAGIC/2010/0.

The *Fermi*-LAT Collaboration acknowledges generous ongoing support from a number of agencies and institutes that have supported both the development and the operation of the LAT, as well as scientific data analysis. These include the National Aeronautics and Space Administration and the Department of Energy in the United States, the Commissariat à l'Energie Atomique and the Centre National de la Recherche Scientifique/Institut National de Physique Nucléaire et de Physique des Particules in France, the Agenzia Spaziale Italiana and the Istituto Nazionale di Fisica Nucleare in Italy, the Ministry of Education, Culture, Sports, Science and Technology (MEXT), High Energy Accelerator Research Organization (KEK), and Japan Aerospace Exploration Agency (JAXA) in Japan, and the K. A. Wallenberg Foundation, the Swedish Research Council, and the Swedish National Space Board in Sweden. Additional support for science analysis during the operations phase is gratefully acknowledged from the Istituto Nazionale di Astrofisica in Italy and the Centre National d'Études Spatiales in France.

This research has made use of the XRT Data Analysis Software (XRTDAS) developed under the responsibility of the ASI Science Data Center (ASDC), Italy.

The St. Petersburg University team acknowledges support from Russian RFBR grant 15-02-00949 and St. Petersburg University research grant 6.38.335.2015.

The work of M.B. is supported by the South African Research Chairs Initiative (SARChI) of the Department of Science and Technology and the National Research Foundation of South Africa. Any opinion, finding, and conclusion or recommendation expressed in this material is that of the authors and the NRF does not accept any liability in this regard.

The IAC team acknowledges the support from the group of support astronomers and telescope operators of the Observatorio del Teide.

G.D. and O.V. gratefully acknowledge the observing grant support from the Institute of Astronomy and Rozhen National Astronomical Observatory, Bulgaria Academy of Sciences. This work is a part of the Projects No. 176011 (Dynamics and kinematics of celestial bodies and systems), No. 176004 (Stellar physics), and No. 176021 (Visible and invisible matter in nearby galaxies: theory and observations) supported by the Ministry of Education, Science, and Technological Development of the Republic of Serbia.

This research was partially supported by the Scientific Research Fund of the Bulgarian Ministry of Education and Sciences under grant DO 02-137 (BIn-13/09).

The Abastumani team acknowledges financial support of the project FR/638/6-320/12 by the Shota Rustaveli National Science Foundation under contract 31/77.

T.G. acknowledges support from Istanbul University (Project numbers 49429 and 48285), Bilim Akademisi (BAGEP program), and TUBITAK (project numbers 13AT100-431, 13AT100-466, and 13AT60-430).

The Boston University effort was supported in part by NASA grants NNX12AO90G and NNX14AQ58G.

Data from the Steward Observatory spectropolarimetric monitoring project were used in this paper. This program is supported by Fermi Guest Investigator grants NNX08AW56G, NNX09AU10G, NNX12AO93G, and NNX15AU81G.

The OVRO 40 m monitoring program is supported in part by NASA grants NNX08AW31G and NNX11A043G and NSF grants AST-0808050 and AST-1109911.

The Metsähovi team acknowledges the support from the Academy of Finland to our observing projects (numbers 212656, 210338, 121148, and others).

This research has made use of NASA's Astrophysics Data System and of Astropy, a community-developed core Python package for astronomy (Astropy Collaboration 2013).

Facilities: NuSTAR, MAGIC, VERITAS, *Fermi*, *Swift*.

REFERENCES

Abdo, A. A., Ackermann, M., Ajello, M., et al. 2011, ApJ, 736, 131
Acciari, V. A., Aliu, E., Aune, T., et al. 2009, ApJ, 703, 169
Acciari, V. A., Aliu, E., Arlen, T., et al. 2011, ApJ, 738, 25

Acciari, V. A., Arlen, T., Aune, T., et al. 2014, APh, 54, 1
Ackermann, M., Ajello, M., Albert, A., et al. 2012, ApJS, 203, 4
Ade, P. A. R., Aghanim, N., Armitage-Caplan, C., et al. 2014, A&A, 571, 16
Aleksić, J., Alvarez, E. A., Antonelli, L. A., et al. 2012, A&A, 542, 100
Aleksić, J., Ansoldi, S., Antonelli, L. A., et al. 2014, A&A, 572, A121
Aleksić, J., Ansoldi, S., Antonelli, L. A., et al. 2015a, A&A, 573, 50
Aleksić, J., Ansoldi, S., Antonelli, L. A., et al. 2015b, A&A, 576, 126
Aleksić, J., Ansoldi, S., Antonelli, L. A., et al. 2015c, A&A, 578, 22
Aleksić, J., Ansoldi, S., Antonelli, L. A., et al. 2016a, APh, 72, 61
Aleksić, J., Ansoldi, S., Antonelli, L. A., et al. 2016b, APh, 72, 75
Aliu, E., Archambault, S., Arlen, T., et al. 2013, ApJ, 779, 92
Angelakis, E., Fuhrmann, L., Marchili, N., et al. 2008, MmSAI, 79, 1042
Angelakis, E., Fuhrmann, L., Marchili, N., et al. 2015, A&A, 575, 55
Angelakis, E., Fuhrmann, L., Nestoras, I., et al. 2010, in Proc. Workshop Fermi Meets Jansky, AGN in Radio and Gamma-Rays, ed. T. Savolainen et al. (Bonn), arXiv:1006.5610
Astropy Collaboration 2013, A&A, 558, 33
Atwood, W. B., Abdo, A. A., Ackermann, M., et al. 2009, ApJ, 697, 1071
Baars, J. W. M., Genzel, R., Paulini-Toth, I. I. K., & Witzel, A. 1977, A&A, 61, 99
Baloković, M., Ajello, M., Blandford, R. D., et al. 2013a, EPJWC, 61, 04013
Baloković, M., Furniss, A., Madejski, G., & Harrison, F. A. 2013b, ATel, 4974, 1
Bartoli, B., Bernardini, P., Bi, X. J., et al. 2011, ApJ, 734, 110
Bartoli, B., Bernardini, P., Bi, X. J., et al. 2012, ATel, 4272, 1
Blandford, R. D., & Eichler, D. 1987, PhR, 154, 1
Blasi, M. G., Lico, R., Giroletti, M., et al. 2013, A&A, 559, 75
Błażejowski, M., Blaylock, G., Bond, I. H., et al. 2005, ApJ, 630, 130
Blumenthal, G. R., & Gould, R. J. 1970, RvMP, 42, 237
Böttcher, M., & Chiang, J. 2002, ApJ, 581, 127
Böttcher, M., Reimer, A., Sweeney, K., & Prakash, A. 2013, ApJ, 768, 54
Breeveld, A. A., Landsman, W., Holland, S. T., et al. 2011, in AIP Conf. Proc. 1358, Gamma Ray Bursts 2010, ed. J. E. McEnery, J. L. Racusin, & N. Gehrels (Melville, NY: AIP), 373
Burrows, D. N., Hill, J. E., Nousek, J. A., et al. 2005, SSRv, 120, 165
Cao, G., & Wang, J. 2013, PASJ, 65, 109
Celotti, A., Fabian, A. C., & Rees, M. J. 1998, MNRAS, 293, 239
Cogan, P. 2008, ICRC, 3, 1385
Cortina, J., et al. 2013, ATel, 4976, 1
D'Ammando, F., et al. 2012, ATel, 4261, 1
Daniel, M. 2008, ICRC, 3, 1325
Edelson, R. A., & Krolik, J. H. 1988, ApJ, 333, 646
Fitzpatrick, E. L. 1999, PASP, 111, 63
Fomin, V. P., Stepanian, A. A., Lamb, R., et al. 1994, APh, 2, 137
Fossati, G., Buckley, J. H., Bond, I. H., et al. 2008, ApJ, 677, 906
Franceschini, A., Rodighiero, G., & Vaccari, M. 2008, A&A, 487, 837
Fuhrmann, L., Larsson, S., Chiang, J., et al. 2014, MNRAS, 441, 1899
Fuhrmann, L., Zensus, J. A., Krichbaum, T. P., Angelakis, E., & Readhead, A. C. S. 2007, in AIP Conf. Ser. 921, The First GLAST Symposium, ed. S. Ritz, P. Michelson, & C. A. Meegan (Melville, NY: AIP), 249
Furniss, A., Koda, N., Madejski, G., et al. 2015, ApJ, 812, 65
Gaidos, J. A., Akerlof, C. W., Biller, S., et al. 1996, Natur, 383, 319
Galante, N. 2011, ICRC, 8, 63
Georganopoulos, M., & Kazanas, D. 2003, ApJL, 594, L27
Ghisellini, G., Maraschi, L., & Treves, A. 1985, A&A, 146, 204
Ghisellini, G., Tavecchio, F., & Chiaberge, M. 2005, A&A, 432, 401
Giebels, B., Dubus, G., & Khélifi, B. 2007, A&A, 462, 29
Guainazzi, M., Vacanti, G., Malizia, A., et al. 1999, A&A, 342, 124
Harrison, F. A., Craig, W. W., Christensen, F. E., et al. 2013, ApJ, 770, 103
Henri, G., & Saugé, L. 2006, ApJ, 640, 185
Hillas, A. M. 1985, ICRC, 3, 445
Holder, J., Atkins, R. W., Badran, H. M., et al. 2006, APh, 25, 391
Hovatta, T., et al. 2012, ATel, 4451, 1
Hovatta, T., Petropoulou, M., Richards, J. L., et al. 2015, MNRAS, 448, 3121
Janiak, M., Sikora, M., Nalewajko, K., et al. 2012, ApJ, 760, 129
Jones, F. C., & Ellison, D. C. 1991, SSRv, 58, 259
Jones, F. C., O'Dell, S. L., & Stein, W. A. 1974, ApJ, 188, 353
Jorstad, S. G., Marscher, A. P., Larionov, V. M., et al. 2010, ApJ, 715, 362
Kalberla, P. M. W., Burton, W. B., Hartmann, D., et al. 2005, A&A, 440, 775
Katarzyński, K., Ghisellini, G., Tavecchio, F., et al. 2005, A&A, 433, 479
Landau, R., Golisch, B., Jones, T. J., et al. 1986, ApJ, 308, 78
Larionov, V. M., Jorstad, S. G., Marscher, A. P., et al. 2008, A&A, 492, 389
Li, T., & Ma, Y. 1983, ApJ, 272, 317
Li, W., Jha, S., Filippenko, A. V., et al. 2006, PASP, 118, 37
Lichti, G. G., Bottacini, E., Ajello, M., et al. 2008, A&A, 486, 721
Lister, M. L., Aller, M. F., Aller, H. D., et al. 2013, AJ, 146, 120
Madhavan, A. 2013, PhD thesis, Iowa State Univ.
Madsen, K. K., Harrison, F. A., Markwardt, C. B., et al. 2015, ApJS, 220, 8
Makino, F., Tanaka, Y., Matsuoka, M., et al. 1987, ApJ, 313, 662
Malizia, A., Capalbi, M., Fiore, F., et al. 2000, MNRAS, 312, 123
Mankuzhiyil, N., Ansoldi, S., Persic, M., & Tavecchio, F. 2011, ApJ, 733, 14
Marscher, A. P. 2014, ApJ, 780, 87
Marscher, A. P., & Gear, W. K. 1985, ApJ, 198, 114
Marscher, A. P., Jorstad, S. G., D'Arcangelo, F. D., et al. 2008, Natur, 452, 966
Massaro, E., Perri, M., Giommi, P., & Nesci, R. 2004, A&A, 413, 489
Max-Moerbeck, W., Hovatta, T., Richards, J. L., et al. 2014, MNRAS, 445, 428
Moralejo, A., Gaug, M., Carmona, E., et al. 2009, arXiv:0907.0943
Nalewajko, K., Giannios, D., Begelman, M. C., et al. 2011, MNRAS, 413, 333
Nalewajko, K., Uzdensky, D. A., Cerutti, B., Werner, G. R., & Begelman, M. C. 2015, ApJ, 815, 101
Nilsson, K., Pasanen, M., Takalo, L. O., et al. 2007, A&A, 475, 199
Nolan, P. L., Abdo, A. A., Ackermann, M., et al. 2012, ApJS, 199, 31
Paneque, D., D'Ammando, F., Orienti, M., et al. 2013, ATel, 4977, 1
Pian, E., Türler, M., Fiocchi, M., et al. 2014, A&A, 570, 77
Piner, B. G., Pant, N., & Edwards, P. G. 2010, ApJ, 723, 1150
Poutanen, J., Zdziarski, A. A., & Ibragimov, A. 2008, MNRAS, 389, 1427
Punch, M., Akerlof, C. W., Cawley, M. F., et al. 1992, Natur, 358, 477
Ravasio, M., Tagliaferri, G., Ghisellini, G., & Tavecchio, F. 2004, A&A, 424, 841
Richards, J. L., Hovatta, T., Lister, M. I., et al. 2013, EPJWC, 61, 04010
Richards, J. L., Max-Moerbeck, W., Pavlidou, V., et al. 2011, ApJS, 194, 29
Roming, P. W. A., Kennedy, T. E., Mason, K. O., et al. 2005, SSRv, 120, 95
Schlafly, E. F., & Finkbeiner, D. P. 2011, ApJ, 737, 103
Schlegel, D. J., Finkbeiner, D. P., & Davis, M. 1998, ApJ, 500, 525
Sikora, M., Stawarz, Ł., Moderski, R., et al. 2009, ApJ, 704, 38
Sironi, L., Petropoulou, M., & Giannios, D. 2015, MNRAS, 450, 183
Smith, P. S., Montiel, E., Rightley, S., et al. 2009, in Fermi Symp. eConf Proc. C091122, arXiv:0912.3621
Stroh, M. C., & Falcone, A. D. 2013, ApJS, 207, 28
Takahashi, T., Tashiro, M., Madejski, G. M., et al. 1996, ApJ, 470, 89
Tanihata, C., Kataoka, J., Takahashi, T., & Madejski, G. M. 2004, ApJ, 601, 759
Tanihata, C., Takahashi, T., Kataoka, J., & Madejski, G. M. 2003, ApJ, 584, 153
Tavecchio, F., Ghisellini, G., Ghirlanda, G., et al. 2010, MNRAS, 401, 1570
Teräsranta, H., Tornikoski, M., Mujunen, A., et al. 1998, A&AS, 132, 305
Tramacere, A., Giommi, P., Massaro, E., et al. 2007a, A&A, 467, 501
Tramacere, A., Giommi, P., Perri, M., et al. 2009, A&A, 501, 879
Tramacere, A., Massaro, F., & Cavaliere, A. 2007b, A&A, 466, 521
Tramacere, A., Massaro, E., & Taylor, A. M. 2011, ApJ, 739, 66
Ulrich, M. H., Kinman, T. D., Lynds, C. R., et al. 1975, ApJ, 198, 261
Ulrich, M.-H., Maraschi, L., & Urry, C. M. 1997, ARA&A, 35, 445
Urry, C. M., & Padovani, P. 1995, PASP, 107, 803
Ushio, M., Stawarz, Ł., Takahashi, T., et al. 2010, ApJ, 724, 1509
Ushio, M., Tanaka, T., Madejski, G., et al. 2009, ApJ, 699, 1964
Vaughan, S., Edelson, R., Warwick, R. S., & Uttley, P. 2003, MNRAS, 345, 1271
Villata, M., Raiteri, C. M., Gurwell, M. A., et al. 2009, A&A, 504, L9
Villata, M., Raiteri, C. M., Lanteri, L., Sobrito, G., & Cavallone, M. 1998, A&AS, 130, 305
Villata, M., Raiteri, C. M., Larionov, V. M., et al. 2008, A&A, 481, L79
Weekes, T. C., Badran, H., Biller, S. D., et al. 2002, APh, 17, 221

The Astrophysical Journal, 833:143 (7pp), 2016 December 20 doi:10.3847/1538-4357/833/2/143

DISCOVERY OF A REDBACK MILLISECOND PULSAR CANDIDATE: 3FGL J0212.1+5320

Kwan-Lok Li[1], Albert K. H. Kong[2], Xian Hou[2,3,4], Jirong Mao[3,4], Jay Strader[1], Laura Chomiuk[1], and Evangelia Tremou[1]
[1] Department of Physics and Astronomy, Michigan State University, East Lansing, MI 48824, USA; liliray@pa.msu.edu (KLL)
[2] Institute of Astronomy and Department of Physics, National Tsing Hua University, Hsinchu 30013, Taiwan
[3] Yunnan Observatories, Chinese Academy of Sciences, Kunming, 650216, China
[4] Key Laboratory for the Structure and Evolution of Celestial Objects, Chinese Academy of Sciences, Kunming, 650216, China
Received 2016 August 19; revised 2016 October 17; accepted 2016 October 24; published 2016 December 13

ABSTRACT

We present a multiwavelength study of the unidentified *Fermi* object, 3FGL J0212.1+5320. Within the 95% error ellipse, *Chandra* detects a bright X-ray source (i.e., $F_{0.5-7\,\mathrm{keV}} = 1.4 \times 10^{-12}\,\mathrm{erg\,cm^{-2}\,s^{-1}}$) that has a low-mass optical counterpart ($M \lesssim 0.4\,M_{\odot}$ and $T \sim 6000$ K). A clear ellipsoidal modulation is shown in optical/infrared at 20.87 hr. The gamma-ray properties of 3FGL J0212.1+5320 are all consistent with that of a millisecond pulsar (MSP), suggesting that it is a γ-ray redback (RB) MSP binary with a low-mass companion filling $\gtrapprox$64% of the Roche lobe. If confirmed, it will be an RB binary with one of the longest orbital periods known. Spectroscopic data taken in 2015 from the Lijiang observatory show no evidence of strong emission lines, revealing that the accretion is currently inactive (the rotation-powered pulsar state). This is consistent with the low X-ray luminosities ($L_X \approx 10^{32}\,\mathrm{erg\,s^{-1}}$) and the possible X-ray modulation seen by *Chandra* and *Swift*. Considering that the X-ray luminosity and the high X-ray-to-γ-ray flux ratio (8%) are both comparable to those of the two known γ-ray transitional MSPs, we suspect that 3FGL J0212.1+5320 could be a potential target to search for future transition to the accretion active state.

Key words: binaries: close – gamma-rays: stars – pulsars: general – X-rays: binaries

1. INTRODUCTION

Progenitors of millisecond pulsars (MSPs), though not yet fully understood, are believed to be neutron stars in low-mass X-ray binaries (LMXBs). According to the recycling scenario (Alpar et al. 1982), the neutron stars are spun up through accretion from the late-type companions (if any) to ultimately evolve into MSPs. Through the so-called LMXB Case A channel (Tauris 2011), a compact binary (i.e., orbital period <1 day) consisting of an MSP and a very low-mass companion (which was stripped by the neutron star and/or partially "evaporated" by the energetic pulsar wind/γ-rays; Chen et al. 2013) remains at the very end phase of such an evolution, known as black widow (BW; companion mass: $<0.1M_{\odot}$) or redback (RB; companion mass: ~0.1–0.4 $M_{\odot}$) binaries. A few RBs, known as transitional MSPs (tMSPs), have already shown remarkable transition(s) between the LMXB state and the radio pulsar state in optical, X-rays, and/or γ-rays (i.e., M28I, Papitto et al. 2013; PSR J1023+0038, Archibald et al. 2009; Patruno et al. 2014; PSR J1227−4853, Roy et al. 2015), clearly indicating the close relationship between LMXBs and radio MSPs. BW/RBs are interesting objects, not to mention the fascinating theoretical interpretation of multiwavelength observations for individual studies (e.g., the keV-to-GeV emission models of PSR J1023+0038 in different states; Li et al. 2014; Papitto & Torres 2015). They also provide crucial information on the long-term accretion history. In particular, BWs are the key to uncovering how the companions are finally eliminated, after which isolated MSPs are formed (van den Heuvel & van Paradijs 1988).

As MSPs are powerful γ-ray sources with strong GeV magnetospheric radiations (e.g., from the outer gap, the slot gap, or the polar cap; Ruderman & Sutherland 1975; Cheng et al. 1986; Muslimov & Harding 2003) and/or the inverse-Compton γ-ray emissions of the pulsar wind nebulae when the accretion is active (Li et al. 2014; Takata et al. 2014), many of them should have been detected by *Fermi*-LAT as a class of unidentified *Fermi* object (UFO), the second-largest population detected by *Fermi*-LAT (Acero et al. 2015). Although not all the UFOs are MSPs (in fact, many of them are thought to be active galactic nuclei, the largest source class in the catalog), good BW/RB candidates can be selected based on the γ-ray spectral curvatures and the γ-ray variabilities (Kong et al. 2012, 2014; Ray et al. 2012; Hui et al. 2015b) and their pulsar natures confirmed by detecting the radio/γ-ray pulsations. Thanks to the *Fermi* Pulsar Search Consortium, a great success has been achieved in discovering new pulsars through "blind" searches for coherent pulsations in radio and γ-rays (Ray et al. 2012), and the known BW and RB populations have been greatly extended in recent years.

Alternatively, multiwavelength studies of UFOs are the secondary way to search for BW/RB MSP candidates. In most of the cases, X-ray follow-ups are the key to narrowing down the source location, allowing identification of the optical counterparts. Once the optical counterpart is identified, time-series optical observations can test the BW/RB identity by searching for the orbital modulation on timescales of hours produced by pulsar irradiation on the companion and/or ellipsoidal variation. Through this multiwavelength technique, several UFOs, for example, 2FGL J1311.7−3429/PSR J1311−3430 (Pletsch et al. 2012), 1FGL J1417.7−4407/PSR J1417−4402 (not a canonical BW/RB system; Strader et al. 2015; Camilo et al. 2016), and 1FGL J2339.7−0531/PSR J2339−0533 (Kong et al. 2012; Pletsch & Clark 2015), have been identified as MSP binaries, and some of them have been confirmed by the detection of millisecond radio/γ-ray pulsations, proving the validity of the method.

In this paper, we report the discovery of a γ-ray-emitting RB candidate, 3FGL J0212.1+5320. In the following sections, we

Table 1
X/γ-Ray Properties of Some Known RBs in the Pulsar State and 3FGL J0212.1+5320

Name	Spectral Curvature[a] (γ-ray; σ)	Variability[b] (γ-ray)	$F_{0.1-100\,\mathrm{GeV}}$ (10^{-11} erg cm^{-2} s^{-1})	Γ_X	$F_{0.5-7\,\mathrm{keV}}$ (10^{-13} erg cm^{-2} s^{-1})	F_X/F_γ
(Generic γ-ray-emitting RBs)						
PSR J2129−0429	3.7	60.3	1.1	1.3	0.11	0.10%
PSR J2339−0533	8.7	40.1	3.0	1.4	1.4	0.48%
PSR J1628−3205	5.5	50.5	1.2	(no X-ray detection)		<1.1%
PSR J1048+2339	2.5	49.7	0.7	(no X-ray detection)		<1.9%
(Prospective tMSP Candidates in the Pulsar State)						
PSR J2215+5135	6.8	56.9	1.4	1.8	1.0	0.74%
PSR J1723−2837	3.3	55.7	1.8	0.9	24	13%
(*Fermi*-detected tMSPs in the Pulsar State)						
PSR J1227−4853	...	...	0.4	1.2	4.6	13%
PSR J1023+0038	...	...	0.1	0.9	4.7	37%
(Our Target)						
3FGL J0212.1+5320	6.3	51.5	1.7	1.3	14	7.9%

Notes.
[a] 3FGL curvature index: significance of the fit improvement between power law and either LogParabola or PLExpCutoff spectrum type.
[b] 3FGL variability index: a value greater than 72.44 indicates that there is a less than 1% chance of being a steady source.
References. 3FGL (Acero et al. 2015); Tam et al. (2010); Kong et al. (2012); Linares (2014); Hui et al. (2015a); Xing & Wang (2015); Deneva et al. (2016).

present multiwavelength studies using the optical imaging/spectroscopic data from the Lijiang (Fan et al. 2015), Lulin, and Michigan State University (MSU) observatories; the *Chandra* X-ray data; and the *Fermi*-LAT third source catalog (3FGL; Acero et al. 2015). Discussions will be given in the last section.

2. THE GAMMA-RAY PROPERTIES IN 3FGL

3FGL J0212.1+5320 is an unidentified bright γ-ray source (i.e., $F_\gamma = (1.71 \pm 0.16) \times 10^{-11}\,\mathrm{erg\,cm^{-2}\,s^{-1}}$ in 0.1–100 GeV, which is in the top 15% among the sources in 3FGL; Acero et al. 2015) that was first detected by *Fermi*-LAT in γ-rays in the *Fermi*-LAT first source catalog (1FGL; Abdo et al. 2010). It also later appears in 3FGL with a detection significance of 25σ.

Based on the second *Fermi*-LAT pulsar catalog (Abdo et al. 2013), the γ-ray properties of pulsars can be characterized by a low source variability and a curved γ-ray spectral shape. Although they are not necessary conditions, 3FGL J0212.1+5320 fulfills both of the criteria (Table 1), suggesting its possible pulsar nature in γ-rays. Similar to many other γ-ray pulsars that have seen stability in γ-rays over years (Abdo et al. 2010), 3FGL J0212.1+5320 can also be considered as a steady source with a small 3FGL variability index of 51.47 (i.e., for a source with a variability index larger than 72.44, there is a less than 1% chance of being a steady source; Acero et al. 2015). In addition, the γ-ray spectrum of 3FGL J0212.1+5320 is probably more than a single power law, but rather with an extra curvature component (e.g., an exponential cutoff) as the spectral curve significance is 6.3σ in 3FGL, which is also another common feature among the pulsars detected in 3FGL (Acero et al. 2015). In fact, Saz Parkinson et al. (2016) and Mirabal et al. (2016) have found that 3FGL J0212.1+5320 is a strong MSP candidate, using statistical and machine-learning techniques.

3. *SWIFT* AND *CHANDRA* X-RAY OBSERVATIONS

As one of the survey targets in the *Swift*/XRT survey of *Fermi* unassociated sources (Stroh & Falcone 2013), 3FGL J0212.1+5320 has been observed twice by *Swift*/XRT in 2010 October (the observations are separated by 3 days with a total exposure time of 4.5 ks). Within the 95% 3FGL error ellipse, a bright X-ray counterpart was detected and listed as 1SXPS J021210.6+532136 in the *Swift*/XRT point-source catalog (1SXPS; Evans et al. 2014). According to 1SXPS, the source is located at $\alpha\,(\mathrm{J2000}) = 02^h12^m10^s.62$, $\delta\,(\mathrm{J2000}) = +53°21'36''.8$ (90% positional uncertainty: $3''.8$) with a mean count rate of $(2.26 \pm 0.26) \times 10^{-2}\,\mathrm{counts\,s^{-1}}$. A moderate flux variability is seen between the two observations from $(2.61 \pm 0.32) \times 10^{-2}\,\mathrm{counts\,s^{-1}}$ to $(1.31 \pm 0.41) \times 10^{-2}\,\mathrm{counts\,s^{-1}}$ in 3 days (equivalent to a 2.9σ change). The X-ray spectrum could be described by an absorbed power law of $N_H = 1.4^{+2.8}_{-1.4} \times 10^{21}\,\mathrm{cm^{-2}}$ (the Galactic column density $N_H = 1.5 \times 10^{21}\,\mathrm{cm^{-2}}$; Kalberla et al. 2005) and $\Gamma_X = 1.0^{+0.5}_{-0.4}$ with an unabsorbed flux of $F_{0.3-10\,\mathrm{keV}} = 1.6^{+0.5}_{-0.3} \times 10^{-12}\,\mathrm{erg\,cm^{-2}\,s^{-1}}$ (*W-stat* = 57.98 and $\chi^2 = 63.02$; dof = 78). Alternatively, the spectrum could be fitted with an APEC thermal plasma model, but with an extremely high and poorly constrained plasma temperature (i.e., $kT \sim 100$ keV). As the best-fit temperature is just too high to be physical, we do not further consider the APEC model in the following analyses.

Chandra has also observed the field of view once with ACIS for 30 ks in 2013 August (Obs ID: 14814; PI: Saz Parkinson), and 1SXPS J021210.6+532136 is clearly detected at $\alpha\,(\mathrm{J2000}) = 02^h12^m10^s.50$, $\delta\,(\mathrm{J2000}) = +53°21'38''.9$ (90% positional uncertainty: $0''.8$) with a net count rate of $(9.03 \pm 0.17) \times 10^{-2}\,\mathrm{counts\,s^{-1}}$ (0.5–7 keV). With a total number of

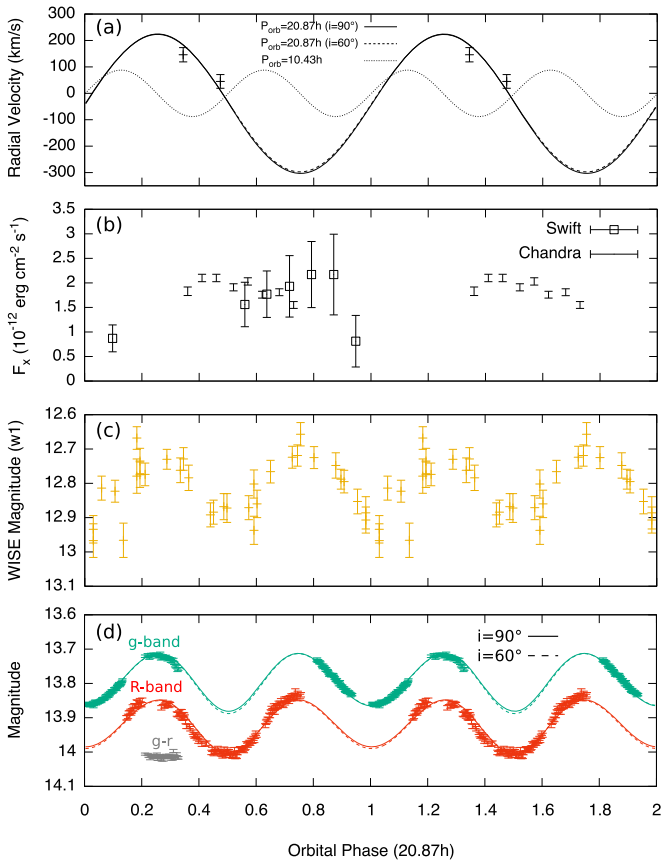

Figure 1. Several physical quantities vs. orbital phase ($P_{\rm orb} = 20.8698$ hr), including (a) the radial velocities with the ELC models at 20.87 hr (solid line for $i = 90°$ and dashed line for $i = 60°$) and a 10.43 hr model curve (with an arbitrary amplitude; dotted line) projected on the 20.87 hr orbital phase for comparison, (b) the X-ray flux (the *Swift* data are only shown in the first cycle for a clear view of the *Chandra* data in the second cycle), (c) the *WISE* $w1$-band data, and (d) the g- and R-band data tentatively calibrated with the UCAC4 Catalog (Zacharias et al. 2013) and the extinction of $A_v = 0.4992$ mag (Schlafly & Finkbeiner 2011) with the ELC models and the (g–r) with an arbitrary offset. Two cycles are shown for clarity.

2685 photon counts, we binned the data to have at least 20 counts per bin and fitted the binned spectrum with an absorbed power law. The best-fit parameters are $N_{\rm H} = (1.4 \pm 0.5) \times 10^{21}\,{\rm cm}^{-2}$, $\Gamma_{\rm X} = 1.3 \pm 0.1$, and $F_{0.5-7\,{\rm keV}} = (1.35 \pm 0.06) \times 10^{-12}\,{\rm erg\,cm^{-2}\,s^{-1}}$ (or $F_{0.3-10\,{\rm keV}} = (1.89 \pm 0.08) \times 10^{-12}\,{\rm erg\,cm^{-2}\,s^{-1}}$; $\chi^2 = 98.78$ and dof $= 105$), which are all consistent with those extracted from the *Swift*/XRT data and the *Chandra* spectral fitting by Saz Parkinson et al. (2016). To examine the short-term variability seen by *Swift*/XRT, we extracted a 4000 s bin light curve with the *Chandra*/ACIS data, and a flux variability on an hourly timescale is clearly shown (Figure 1). To quantify the variability significance, we computed the χ^2 value of the eight data bins with a flat light-curve model, which is $\chi^2 = 24.39$ (dof $= 7$), indicating that there is only a 0.1% chance that the variability is produced by random fluctuation.

4. OPTICAL DATA

At the *Chandra* X-ray position, we found a bright optical counterpart ($R = 14.23$ mag) in the USNO-B1.0 catalog (Monet et al. 2003), USNO-B1.0 1433-0078846, with an offset of $0\farcs2$. The same source is also detected in the Two Micron All Sky Survey (2MASS; Skrutskie et al. 2006) and *WISE* (Wright et al. 2010) catalogs. Using the multi-epoch photometry table of *WISE*,[5] a variability of 0.2–0.3 mag is clearly seen in the $w1$-band data of 33 epochs taken in 2010 February and August. The modulation is likely periodic with a period of ∼10–20 hr (see Figure 1(c) for the modulation, although the phase light curve was folded at 20.87 hr).

4.1. Imaging from the MSU and Lulin Observatories

A monitoring campaign with the 0.6 m telescope in the MSU observatory and the 1 m telescope in the Lulin Observatory was carried out from 2015 October to 2016 January to investigate the ∼10–20 hr modulation seen in *WISE*. We observed the source for three consecutive nights from October 10 to 12 with the 0.6 m telescope in the R band (200/300 s for each frame, depending on the weather) and with the 1 m telescope in the SDSS r and g bands for three other nights (i.e., November 8/9 and January 9; only g-band images were taken on the first two nights, and both r- and g-band images were taken by turns on the last night; 60/120 s for the r/g-band images, respectively).

4.2. Spectroscopy from the Lijiang Observatory

Two 1200 s medium-resolution optical spectra (5750–8800 Å) were taken on 2015 November 4 and 5 with the 2.4 m telescope at the Lijiang observatory. After (i) the standard reduction processes with the IRAF package ONEDSPEC, (ii) a flux calibration with the standard star BD +28° 4211 (Oke 1990), and (iii) an extinction correction with $A_v = 0.4992$ mag (Schlafly & Finkbeiner 2011; which is roughly consistent with the $N_{\rm H}$ value estimated by *Chandra*) and the Cardelli extinction law (Cardelli et al. 1989), the calibrated data show spectral shapes comparable to that of a low-mass star (Figure 2) without any accretion features. After matching the data with the synthetic spectra from the Munari online library[6] (Munari et al. 2005; a solar metallicity of [M/H] = 0 and a typical RB rotational broadening of $V = 100\,{\rm km\,s^{-1}}$ are assumed), we found that the spectra can be best described by $T = 5750$ K and $\log g = 4.5$ (Figure 2), of which the stellar properties are very close to the $M \approx 0.4\,M_\odot$ low-mass companion of the RB PSR J2129−0429 (Bellm et al. 2016). Therefore, we tentatively assume the secondary star of 3FGL J0212.1+5320 to be around $M \sim 0.4\,M_\odot$.

5. DETAILED TIMING ANALYSES

5.1. Orbital Period Determination

After applying the standard data reduction procedures by IRAF on the optical imaging data and removing some bad frames due to bad tracking or bad weather, we used a differential photometry technique to study the optical modulation, which shows a clear sinusoidal shape in all bands (Figure 1(d)). We fitted all the data (including the *WISE* data; all are heliocentric corrected) simultaneously with sinusoidal functions with common period and phases, but different amplitudes and baselines for each data set. The best-fit period is 10.43479(7) hr (corresponding to the pulsar irradiation case) or 20.8698(1) hr (the ellipsoidal variation case) with the flux minimum epoch at HJD 2,457,305.5551(4) (the phase zero of Figure 1 and the following timing analyses). It is worth noting

[5] http://irsa.ipac.caltech.edu/Missions/wise.html
[6] http://archives.pd.astro.it/2500-10500/

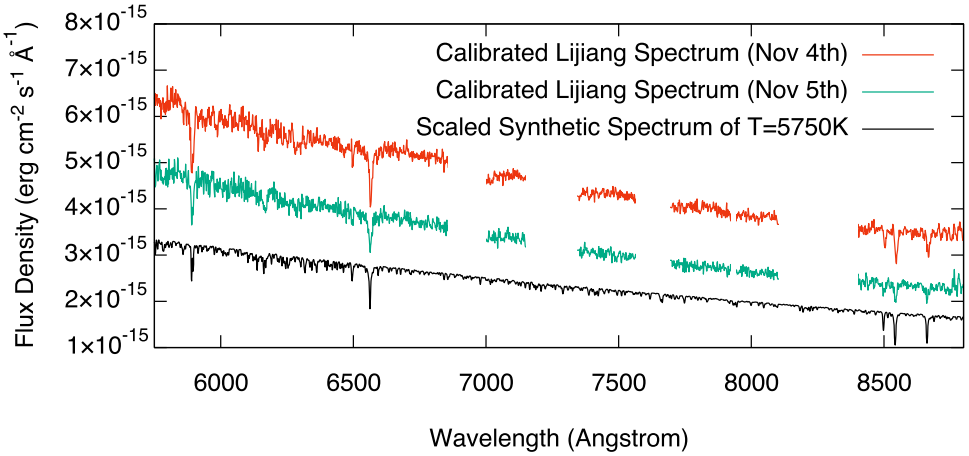

Figure 2. From top to bottom, the curves are the two Lijiang spectra of USNO-B1.0 1433-0078846 taken on November 4 and 5, and the model spectrum of $T = 5750$ K from the Munari synthetic spectral library. There are four gaps present on the Lijiang spectra due to the removal of the telluric lines.

that the data used span over 5 yr of time (i.e., from 2010 to 2015), which leads to a very high accuracy of the best-fit period. The best-fit amplitudes of the bands are roughly consistent with each other within a largest offset of 0.02 mag (i.e., $a_{w1} = 0.09 \pm 0.02$ mag, $a_R = 0.0845 \pm 0.0009$ mag, $a_g = 0.0731 \pm 0.0004$ mag, and $a_r = 0.092 \pm 0.007$). In particular, the simultaneous r- and g-band data taken by Lulin on January 9 do not show any clear color evolving trend during the phase interval of $\phi_{10} = 0.42$–0.66 at $P = 10.43$ hr (or $\phi_{20} = 0.21$–0.33 at $P = 20.87$ hr; Figure 1(d)), suggesting that there is likely no strong orbital color variability. This indicates that the pulsar irradiation effect on the companion is very limited and thus the modulation is probably caused by ellipsoidal variation.

5.2. Radial Velocity (RV) Measurement

Following the method described in Bellm et al. (2016), we first removed the telluric lines of the Lijiang spectra by omitting bands of 6860–7000 Å, 7570–7700 Å, 7150–7350 Å, and 8100–8400 Å. Using the `RVSAO` Package of `IRAF`, we used the task `xcsao` to calculate the barycentric-corrected RVs by cross-correlating the spectral data with the $T = 5750$ K synthetic spectrum (all the spectra involved are automatically normalized during the cross-correlation process). Both the spectra were found to be redshifted with RVs of $136 \pm 19\,\mathrm{km\,s^{-1}}$ (November 4) and $31 \pm 17\,\mathrm{km\,s^{-1}}$ (November 5). By applying the 20.87 hr (or 10.43 hr) ephemeris, the orbital phases of the RVs are $\phi_{20} = 0.34$ (or $\phi_{10} = 0.69$) and $\phi_{20} = 0.47$ (or $\phi_{10} = 0.95$), respectively. For the pulsar irradiation case (i.e., the orbital period is 10.43 hr), the companion should be moving from behind the pulsar to the front in the orbital interval of $\phi_{10} = 0.5$–1 (i.e., $\phi_{20} = 0.25$–0.5 in Figure 1(a)), during which the lowest RV occurs at $\phi_{10} = 0.75$ (i.e., $\phi_{20} = 0.375$). Therefore, the RV at $\phi_{10} = 0.95$ (i.e., $\phi_{20} = 0.47$) should be higher than that at $\phi_{10} = 0.69$ (i.e., $\phi_{20} = 0.34$). However, the result shows differently, indicating the invalidity of the irradiation case (see Figure 1(a) for a more clear demonstration). On the contrary, the observed RVs can be naturally explained in the case of ellipsoidal variation if the orbital phase zero is defined as the inferior conjunction (i.e., the companion is between the pulsar and the observer; Figure 1(a)).

5.3. Eclipsing Light Curve (ELC) Fitting

We used the ELC code (Version 3; Orosz & Hauschildt 2000) to model the optical light curves (i.e., R and g bands) obtained from the MSU and Lulin observatories for a deeper understanding of the interacting binary. For the R-band data, we omitted the short r-band light curve (i.e., 2.4 hr) obtained from Lulin to prevent extra systematic uncertainties originating from the cross-calibrations between different filter systems (i.e., r and R bands) and instruments. As ELC is capable of fitting RV, we also considered the two RVs to have a better constraint on the fitting result, despite the limited data quantity/quality. We also allowed a tiny phase shift between the phase-folded light curves and the models to further calibrate for the epoch of the inferior conjunction (i.e., the phase zero of the ELC models).

By (i) using the orbital period of $P_{\rm orb} = 20.8698$ hr, (ii) assuming that the effective temperature of the companion is $T_{\rm eff} = 5750$ K (it was not well determined because the ELC fit is insensitive to the companion temperature as ELC fits the normalized light curves) and the mass of the secondary star is $m_2 \sim 0.4\,M_\odot$ (by setting $m_2 = 0.3$–$0.5\,M_\odot$), (iii) disabling the radiation heating effect, (iv) adopting the linear limb-darkening law (van Hamme 1993) with a coefficient of $\kappa = 0.6483$ (Sing 2010), and (v) setting a circular orbit (i.e., $e = 0$), we fitted the light curves by varying four binary parameters, which are the binary inclination (i), the mass ratio ($q = m_1/m_2$, where m_1 is the pulsar mass), the orbital separation (a), and the Roche lobe filling factor (β, the ratio of the volume-averaged radii of the companion star and the Roche lobe; Joss & Rappaport 1984). With the built-in optimizer `gridELC`, we searched for the best-fit solution by minimizing the χ^2 value, and the least reduced chi-square of $\chi^2_\nu = 3.1$ (dof = 344) was found at $i = 90°$, $q = 6.8$, $a = 4.6R_\odot$, and $\beta = 0.64$ ($m_1 = 1.5\,M_\odot$ and $m_2 = 0.2\,M_\odot$ are inferred). It is not a good fit statistically, and the extreme inclination at the upper bound may imply that the fit did not converge.[7] In addition, we found that the data can be fitted fairly well even if a fixed inclination angle of a different value is used (see the similarity between the best-fit models at different inclinations in Figure 1(d)). Therefore, instead of

[7] We once considered turning on the radiation heating effect to improve the fit. However, the flux overestimation in the valley at $\phi \sim 0.5$ is the main cause of the bad fitting. The radiation heating effect will even increase the predicted flux there to worsen the fit.

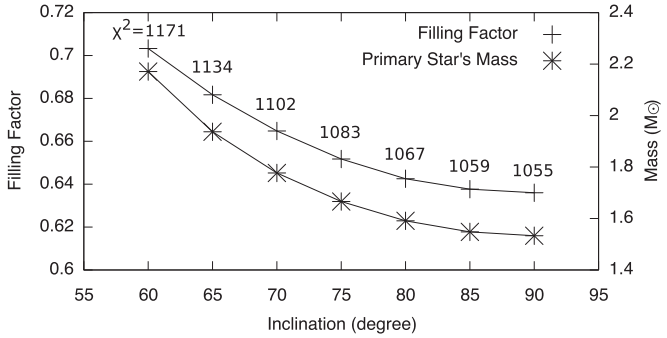

Figure 3. The above two curves show the best-fit filling factors of the secondary star and the inferred masses of the primary star vs. the binary inclinations from 60° to 90° with the corresponding best-fit χ^2 values.

estimating the parameter uncertainties, we obtain and discuss the best-fit parameter sets at different inclinations from $i = 90°$ to $i = 60°$ with a step size of 5°. To elaborate the choice of $i = 60°$, it was chosen based on the χ^2 values of the RVs on the ELC fits ($\chi^2_{\rm RV}$). Despite the complexity of the optical emission revealed by the bad ELC fit, the RV data in principle would not be affected, making $\chi^2_{\rm RV}$ a useful indicator to test the model validity. In this case, we chose a criterion of $\chi^2_{\rm RV} < 3.84$ (95% c.l. for dof = 1) to reject all other steps of $i < 60°$ with large $\chi^2_{\rm RV}$. We note that the selection heavily depends on the weighting on the RV data in the ELC fit (i.e., no weighting applied here) and therefore the rejection does not imply that the inclination has to be $i > 60°$. The selection simply indicates that the unweighted best-fit models with $i < 60°$ are inconsistent with the RV data, and thus no discussion will be given on those fits.

Figure 3 shows the best-fit Roche lobe filling factors and the inferred pulsar masses for $i = 60°$–90°. As expected, the best-fit filling factor decreases with the inclination (from 0.70 to 0.64). All the best-fit results lead the primary star's mass to the range of $m_1 = 1.5$–$2.2\,M_\odot$ (and $m_2 \approx 0.2\,M_\odot$), which is consistent with that of a pulsar. Certainly, the errors of the best-fit pulsar masses could be large (e.g., the uncertain companion mass as one of the major sources of error). Also, we found that the ELC fits are not robust. For instance, if we remove the constraints on the RV curve (i.e., the two Lijiang data points) and the companion mass (i.e., $m_2 = 0.3$–$0.5\,M_\odot$), the best-fit solution of $i = 90°$ changes to $q = 7.7$, $a = 5.0R_\odot$, and $\beta = 0.63$, with which $m_1 = 2.0\,M_\odot$ and $m_2 = 0.3\,M_\odot$ are inferred (see Figure 3). Even two RV data points and a weak constraint on the companion mass are sufficient to significantly affect the fitting result. Therefore, we conclude that the best-fit parameters and the inferred masses are merely indicative. Detailed modeling (e.g., by adding hot/cool spots on the companion) and high-quality photometry sets and spectroscopic data of a complete orbit are required to place a further constraint on the pulsar mass. More imaging and spectroscopic observations are being planned to probe the system in the near future.

5.4. Possible X-Ray Orbital Modulation

As mentioned in Section 3, there is a significant variability seen in both *Swift*/XRT and *Chandra* data, which is possibly induced by the X-ray orbital modulation. We thus folded the light curve with the 20.87 hr timing solution after converting the *Chandra* X-ray flux into the *Swift*/XRT band (i.e., 0.3–10 keV) and performing a barycentric correction to the data. Although the folded X-ray light curve does not cover a full orbital cycle, the X-ray variation is likely periodic with an X-ray minimum around the inferior conjunction (Figure 1(b)). A similar phenomenon has been previously seen in the RB PSR J1023+0038 (Bogdanov et al. 2011; Li et al. 2014; Tendulkar et al. 2014). From the *Chandra* data bins, the X-ray maximum occurs around the superior conjunction (i.e., $\phi_{20} \sim 0.5$; observer-pulsar-companion), although the *Swift* data favor the flux maximum around $\phi_{20} > 0.5$.

6. DISCUSSION AND CONCLUSION

We presented a multiwavelength study of 3FGL J0212.1+5320 and found that an RB MSP binary as its physical nature can naturally explain the entire data set. The X/γ-ray spectral properties and the hourly timescale orbital period are very similar to that of many known RBs (Table 1), revealing the first hint of 3FGL J0212.1+5320 as an RB candidate. The inferred primary star's masses from the best-fit ELC models are 1.5–2.2 $M_\odot$, which are consistent with that of a neutron star, though they are only indicative estimates. An hourly variability is seen in the *Swift*/*Chandra* joint light curve, and it could be an orbital modulation, although uncertainly. If the modulation is genuine, it could be caused by an intrabinary shock emission, through Doppler boosting with a pulsar-wrapping shock geometry (Li et al. 2014) or partial occultation by the companion (Bogdanov et al. 2011). All the observational evidence is pointing to the conclusion of 3FGL J0212.1+5320 as a newly discovered RB system.

A bright optical counterpart (could be one of the brightest known for RBs) has been identified with a clear orbital modulation at 20.87 hr. We do not see an obvious nonuniform radiation heating contributing to the orbital modulation, and therefore the companion is probably not completely tidally locked. This may imply that 3FGL J0212.1+5320 is a very young MSP system. According to Zahn (1977), the synchronization timescale of such a close binary is approximately $t_{\rm sync} \sim 10^4((1 + q_i)/2)^2(P_i/1\ {\rm day})^4$ yr (Equation (6.1) of Zahn 1977), where q_i and P_i are the initial mass ratio and orbital period, respectively.[8] Assuming an initial mass ratio of $q_i = 2.8$ (i.e., $m_{1,i} = 1.4\,M_\odot$ and $m_{2,i} = 0.5\,M_\odot$),[9] $P_i \approx 13$ days gives $t_{\rm sync} \gtrsim 10^9$ yr and $P_i \approx 4$ days gives $t_{\rm sync} \gtrsim 10^7$ yr. We took the calculated timescales for 3FGL J0212.1+5320 as lower limits because the orbital widening by the ablation from the pulsar (Chen et al. 2013), which would extend the synchronization process, was not considered in Zahn's work. In the case of $t_{\rm sync} \gtrsim 10^7$ yr, the initial orbital period is actually close to the estimated value of PSR J2129−0429 (i.e., $P_i \approx 2.5$ days; Bellm et al. 2016), which has a long orbital period of $P = 15.2$ hr, comparable to 3FGL J0212.1+5320's. Obviously, a young age of 3FGL J0212.1+5320 (i.e., on the order of 10 Myr) would be a self-consistent explanation for the data. In fact, ∼10 Myr old MSPs are rare but not impossible. For example, PSR J1823−3021A, one of the youngest MSPs known, has a characteristic age of 25 Myr (Freire et al. 2011). Searching for the radio/X-/γ-ray pulsations of 3FGL J0212.1+5320 and computing the

[8] The equation presented here is slightly different from the one in Zahn (1977) because of the different definitions of the mass ratios.

[9] The initial masses are both poorly known due to the highly uncertain accretion and ablation processes, and thus the values are merely estimated within reasonable ranges.

characteristic age would be useful for investigating the speculation.

Despite no heating effect seen, it is still highly likely that the companion is uniformly irradiated by the X/γ-rays from the pulsar, resulting in a higher surface temperature than a $\sim 0.4\,M_{\odot}$ star should have. As the companion mass is no longer the only dominant factor to determine the surface temperature, the assumption of $m_2 \sim 0.4\,M_{\odot}$ (see Section 4.2) could be overestimated. Considering the fact that all the fitting results indicate a lighter m_2, $m_2 \lesssim 0.4\,M_{\odot}$ would be more reasonable.

As the companion has a temperature close to that of the Sun, it is convenient to use the solar R-band absolute magnitude (i.e., $R = 4.42$ mag; Binney & Merrifield 1998) to infer the distance of 3FGL J0212.1+5320. From the ELC model fits, the size of the companion is about $R_c \approx 1\,R_{\odot}$. After a proper scaling, the inferred distance is about $d \approx 0.8$ kpc, leading to an X-ray luminosity of $L_{\rm X} \approx 10^{32}\,{\rm erg\,s^{-1}}$, which is relatively high among the known X-ray RBs in the *pulsar state* (when radio pulsations can be detected and $L_X \sim 10^{31} - 4 \times 10^{32}\,{\rm erg\,s^{-1}}$; Linares 2014). Since a high X-ray luminosity (i.e., $L_{\rm X} \gtrapprox 10^{32}\,{\rm erg\,s^{-1}}$) in the pulsar state is a common feature of all three known tMSPs (i.e., PSR J1023+0038, PSR J1227−4853, and M28I), it has been suggested by Linares (2014) that $L_{\rm X} \gtrapprox 10^{32}$ is possibly a consequence of a stronger interaction between the pulsar and the companion, and therefore the higher X-ray luminosity could be a signature of an RB binary developing a strong accretion for the transition. One possibility is that the companion of a pre-transition (to the LMXB state) system has a stronger wind (i.e., a stronger inflow to the pulsar; see Takata et al. 2014; Li et al. 2014, for the interpretation of a varying stellar wind as the transition trigger for PSR J1023+0038), which powers a stronger intrabinary shock X-ray emission. Based on the X-ray luminosity, two bright systems, PSR J2215+5135 ($L_{\rm X} = 1.3 \times 10^{32}\,{\rm erg\,s^{-1}}$) and PSR J1723-2837 ($L_{\rm X} = 2.4 \times 10^{32}\,{\rm erg\,s^{-1}}$; see Table 1 for their γ/X-ray properties), have been suggested by Linares (2014) to be potential targets for state transitions in the near future. 3FGL J0212.1+5320 could be the third member of the group. In addition, we also examined the X-ray-to-γ-ray flux ratios of some known RBs and found that the flux ratios of the tMSPs (i.e., $\gg$1%) are significantly larger than that of the "normal" RBs (i.e., $\lesssim$1%). 3FGL J0212.1+5320 has a ratio of 7.9% that is consistent with the tMSP ones. One of the two prospective tMSP candidates, PSR J1723−2837, also has a large ratio of 13% (Table 1).

Certainly, the speculation is not mature and should not be taken conclusively. However, it is still worth paying attention to the X-ray activity of 3FGL J0212.1+5320 for any future transition. Even if it is not exhibiting any transition in the near future, 3FGL J0212.1+5320 could be one of the brightest RBs in X-rays and certainly is one of the best sources for studying the X-ray emissions of RBs.

No previous attempt of a radio pulsation blind search for 3FGL J0212.1+5320 has been found in the literature (Ransom et al. 2011; Guillemot et al. 2012; Camilo et al. 2015). In fact, the system is likely radio-faint as no radio counterpart can be found in the 1.4 GHz NRAO/VLA Sky Survey, of which the detection limit is ~2.5 mJy (Condon et al. 1998; note that most of the radio MSPs found by targeting *Fermi*-LAT sources have flux densities much lower than 2.5 mJy at 1.4 GHz; Ray et al. 2012). Nevertheless, a GBT observation is being planned for searching for radio coherent pulsations. Hopefully, this extreme RB MSP (i.e., high X-ray luminosity, bright optical companion, long orbital period, and potentially young age) can be confirmed soon.

After the submission of this paper, we became aware of a similar work by Linares et al. (2016), in which results including the measured orbital period, the RV curve of the companion, the *Chandra* spectral analysis, and the RB MSP nature interpretation are consistent with ours. In particular, they have sampled a much better RV curve, which would be very helpful in searching the radio/γ-ray pulsations in the future.

Support for this work was partially provided by the National Aeronautics and Space Administration through Chandra Award Number DD5-16078X issued by the Chandra X-ray Observatory Center, which is operated by the Smithsonian Astrophysical Observatory for and on behalf of the National Aeronautics Space Administration under contract NAS8-03060. Support from NASA grant NNX15AU83G is gratefully acknowledged. A.K.H.K. and X.H. are supported by the Ministry of Science and Technology of Taiwan through grant nos. 103-2628-M-007-003-MY3 and 104-2811-M-007-059. X.H. is also supported by the National Natural Science Foundation of China through grant no. 11503078. J.M. is supported by the Hundred Talent Program of Chinese Academy of Sciences, the Key Research Program of Chinese Academy of Sciences (grant No. KJZD-EW-M06), and the Introducing Oversea Talent Plan of Yunnan Province. J.S. acknowledges support from a Packard Fellowship. The Lulin Observatory is operated by the Graduate Institute of Astronomy in National Central University, Taiwan. We acknowledge the support of the staff of the Lijiang 2.4 m telescope. Funding for the telescope has been provided by the Chinese Academy of Sciences and the People's Government of Yunnan Province. The scientific results reported in this article are based in part on data obtained from the *Chandra* Data Archive. We acknowledge the use of public data from the *Swift* data archive. This publication makes use of data products from the *Wide-field Infrared Survey Explorer*, which is a joint project of the University of California, Los Angeles, and the Jet Propulsion Laboratory/California Institute of Technology, funded by the National Aeronautics and Space Administration.

REFERENCES

Abdo, A. A., Ackermann, M., Ajello, M., et al. 2010, ApJS, 188, 405
Abdo, A. A., Ajello, M., Allafort, A., et al. 2013, ApJS, 208, 17
Acero, F., Ackermann, M., Ajello, M., et al. 2015, ApJS, 218, 23
Alpar, M. A., Cheng, A. F., Ruderman, M. A., & Shaham, J. 1982, Natur, 300, 728
Archibald, A. M., Stairs, I. H., Ransom, S. M., et al. 2009, Sci, 324, 1411
Bellm, E. C., Kaplan, D. L., Breton, R. P., et al. 2016, ApJ, 816, 74
Binney, J., & Merrifield, M. 1998, Galactic Astronomy (Princeton, NJ: Princeton Univ. Press)
Bogdanov, S., Archibald, A. M., Hessels, J. W. T., et al. 2011, ApJ, 742, 97
Camilo, F., Kerr, M., Ray, P. S., et al. 2015, ApJ, 810, 85
Camilo, F., Reynolds, J. E., Ransom, S. M., et al. 2016, ApJ, 820, 6
Cardelli, J. A., Clayton, G. C., & Mathis, J. S. 1989, ApJ, 345, 245
Chen, H.-L., Chen, X., Tauris, T. M., & Han, Z. 2013, ApJ, 775, 27
Cheng, K. S., Ho, C., & Ruderman, M. 1986, ApJ, 300, 500
Condon, J. J., Cotton, W. D., Greisen, E. W., et al. 1998, AJ, 115, 1693
Deneva, J. S., Ray, P. S., Camilo, F., et al. 2016, ApJ, 823, 105
Evans, P. A., Osborne, J. P., Beardmore, A. P., et al. 2014, ApJS, 210, 8
Fan, Y.-F., Bai, J.-M., Zhang, J.-J., et al. 2015, RAA, 15, 918
Freire, P. C. C., Abdo, A. A., Ajello, M., et al. 2011, Sci, 334, 1107
Guillemot, L., Freire, P. C. C., Cognard, I., et al. 2012, MNRAS, 422, 1294
Hui, C. Y., Hu, C. P., Park, S. M., et al. 2015a, ApJL, 801, L27

Hui, C. Y., Park, S. M., Hu, C. P., et al. 2015b, ApJ, 809, 68
Joss, P. C., & Rappaport, S. A. 1984, ARA&A, 22, 537
Kalberla, P. M. W., Burton, W. B., Hartmann, D., et al. 2005, A&A, 440, 775
Kong, A. K. H., Huang, R. H. H., Cheng, K. S., et al. 2012, ApJL, 747, L3
Kong, A. K. H., Jin, R., Yen, T.-C., et al. 2014, ApJL, 794, L22
Li, K. L., Kong, A. K. H., Takata, J., et al. 2014, ApJ, 797, 111
Linares, M. 2014, ApJ, 795, 72
Linares, M., Miles-Páez, P., Rodríguez-Gil, P., et al. 2016, MNRAS, arXiv:1609.02232
Mirabal, N., Charles, E., Ferrara, E. C., et al. 2016, ApJ, 825, 69
Monet, D. G., Levine, S. E., Canzian, B., et al. 2003, AJ, 125, 984
Munari, U., Sordo, R., Castelli, F., & Zwitter, T. 2005, A&A, 442, 1127
Muslimov, A. G., & Harding, A. K. 2003, ApJ, 588, 430
Oke, J. B. 1990, AJ, 99, 1621
Orosz, J. A., & Hauschildt, P. H. 2000, A&A, 364, 265
Papitto, A., Ferrigno, C., Bozzo, E., et al. 2013, Natur, 501, 517
Papitto, A., & Torres, D. F. 2015, ApJ, 807, 33
Patruno, A., Archibald, A. M., Hessels, J. W. T., et al. 2014, ApJL, 781, L3
Pletsch, H. J., & Clark, C. J. 2015, ApJ, 807, 18
Pletsch, H. J., Guillemot, L., Fehrmann, H., et al. 2012, Sci, 338, 1314
Ransom, S. M., Ray, P. S., Camilo, F., et al. 2011, ApJL, 727, L16
Ray, P. S., Abdo, A. A., Parent, D., et al. 2012, in 2011 Fermi Symp., ed. A. Morselli (arXiv:1205.3089)
Roy, J., Ray, P. S., Bhattacharyya, B., et al. 2015, ApJL, 800, L12
Ruderman, M. A., & Sutherland, P. G. 1975, ApJ, 196, 51
Saz Parkinson, P. M., Xu, H., Yu, P. L. H., et al. 2016, ApJ, 820, 8
Schlafly, E. F., & Finkbeiner, D. P. 2011, ApJ, 737, 103
Sing, D. K. 2010, A&A, 510, A21
Skrutskie, M. F., Cutri, R. M., Stiening, R., et al. 2006, AJ, 131, 1163
Strader, J., Chomiuk, L., Cheung, C. C., et al. 2015, ApJL, 804, L12
Stroh, M. C., & Falcone, A. D. 2013, ApJS, 207, 28
Takata, J., Li, K. L., Leung, G. C. K., et al. 2014, ApJ, 785, 131
Tam, P. H. T., Hui, C. Y., Huang, R. H. H., et al. 2010, ApJL, 724, L207
Tauris, T. M. 2011, in ASP Conf. Ser. 447, Evolution of Compact Binaries, ed. L. Schmidtobreick, M. R. Schreiber, & C. Tappert (San Francisco, CA: ASP), 285
Tendulkar, S. P., Yang, C., An, H., et al. 2014, ApJ, 791, 77
van den Heuvel, E. P. J., & van Paradijs, J. 1988, Natur, 334, 227
van Hamme, W. 1993, AJ, 106, 2096
Wright, E. L., Eisenhardt, P. R. M., Mainzer, A. K., et al. 2010, AJ, 140, 1868
Xing, Y., & Wang, Z. 2015, ApJ, 808, 17
Zacharias, N., Finch, C. T., Girard, T. M., et al. 2013, AJ, 145, 44
Zahn, J.-P. 1977, A&A, 57, 383

[Previous | Next | ADS]

Rapid optical decay of the neutron star transient MAXI J0556-332

ATel #8530; ***Ruolan Jin, Albert K. H. Kong (National Tsing Hua University, Taiwan)***
*on **11 Jan 2016; 11:37 UT***
Credential Certification: Albert Kong (akong@phys.nthu.edu.tw)

Subjects: Optical, X-ray, Binary, Neutron Star, Transient

Referred to by ATel #: 8854

We observed the neutron star X-ray transient MAXI J0556-332 currently in outburst with the 1m telescope at the Lulin Observatory in Taiwan. The observations were taken on 2016 January 9 (MJD 57396.66) and 10 (MJD 57397.67) with the SDSS g and r-band filters. The source is clearly seen in all images with exposure time ranging from 180s to 300s. By comparing with several comparison stars in the AAVSO Photometric All-Sky Survey (APASS), we obtained g = 18.74 +/- 0.06 and r = 19.10 +/- 0.06 on January 9, and g = 18.73 +/- 0.17 on January 10 (with thin cloud). On January 7, the source was at V = 17.41 and R = 17.7 (ATel #8517). This strongly suggests that the source is now about 1 magnitude fainter. A Swift/UVOT observation with the uvw2 filter was taken simultaneously with our Lulin observation on January 10. MAXI J0556-332 is detected with a significance of 16 sigma. The uvw2-band magnitude (in AB system) is 19.07 +/- 0.07 (stat) +/- 0.03 (sys).

We checked the recent MAXI/GSC data and the source also shows a slight decrease in X-ray flux back to the level at the start of the X-ray outburst on January 6 (ATel #8513). Both optical and X-ray observations indicate that the outburst of MAXI J0556-332 may start to decay, or the source is undergoing a more complicated evolution. Multi-wavelength observations are encouraged.

The Lulin Observatory is operated by the Graduate Institute of Astronomy in National Central University, Taiwan.

Related
8854 X-ray fading and optical/X-ray flaring in the current faint outburst of MAXI J0556-332
8530 Rapid optical decay of the neutron star transient MAXI J0556-332
8517 Optical Faulkes Telescope monitoring of MAXI J0556-332 caught its rise into outburst
8513 MAXI/GSC detection of renewed activity of the neutron star X-ray binary MAXI J0556-332
4524 Re-brightening of MAXI J0556-332, a transient NS X-ray binary, detected by MAXI/GSC
3650 MAXI J0556-332 is a transient neutron-star Z source
3349 Discovery of a strong emission line at 0.5 keV in MAXI J0556-332 with the RGS on XMM-Newton
3328 Past optical (in)activity of MAXI J0556-332
3327 Rebrightening of MAXI J0556-332
3119 Radio detection of MAXI J0556-332 with the ATCA
3116 Optical observations of MAXI J0556-332 and an indication of a probable neutron star primary
3112 Changes in the timing properties of MAXI J0556-332
3110 Eclipse-like Absorption in MAXI J0556-332
3106 RXTE Observes MAXI J0556-332
3104 Optical Identification and Spectroscopy of the X-ray Transient MAXI J0556-332
3103 MAXI J0556-332: Swift/XRT localization
3102 MAXI/GSC detects a new X-ray transient MAXI J0556-332

[Telegram Index]

R. E. Rutledge, Editor-in-Chief rrutledge@astronomerstelegram.org
Derek Fox, Editor dfox@astronomerstelegram.org
Mansi M. Kasliwal, Co-Editor mansi@astronomerstelegram.org

Icarus 269 (2016) 15–22

Contents lists available at ScienceDirect

Icarus

journal homepage: www.elsevier.com/locate/icarus

Lightcurves of the Karin family asteroids

Fumi Yoshida[a], Takashi Ito[a,*], Budi Dermawan[b], Tsuko Nakamura[c], Shigeru Takahashi[d], Mansur A. Ibrahimov[e], Renu Malhotra[f], Wing-Huen Ip[g], Wen-Ping Chen[g], Yu Sawabe[h], Masashige Haji[h], Ryoko Saito[h], Masanori Hirai[h]

[a] National Astronomical Observatory, Osawa 2-21-1, Mitaka, Tokyo, Japan
[b] Department of Astronomy, Bandung Institute of Technology, Jalan Ganesha 10, Bandung 40132, Indonesia
[c] Teikyo-Heisei University, 2-51-4 Higashi–Ikebukuro, Toshima, Tokyo 170-8445, Japan
[d] Nobeyama Radio Observatory, Nobeyama 462-2, Minami-Maki-Mura, Nagano 384-1305, Japan
[e] Ulugh Beg Astronomical Institute, 33 Astronomical Street, Tashkent 700052, Uzbekistan
[f] Lunar & Planetary Laboratory, The University of Arizona, 1629 E. University Boulevard, Tucson, AZ 85721-0092, USA
[g] Institute of Astronomy, National Central University, Jhongda Road 300, Jhongli, Taoyuan 32001, Taiwan
[h] Fukuoka University of Education, Akama-Bunkyo-machi 1-1, Munakata, Fukuoka 811-4192, Japan

ARTICLE INFO

Article history:
Received 12 May 2012
Revised 25 November 2015
Accepted 6 January 2016
Available online 15 January 2016

Keywords:
Asteroids
Photometry
Rotation

ABSTRACT

The Karin family is a young asteroid family formed by an asteroid breakup 5.8 Myr ago. Since the members of this family probably have not experienced significant orbital or collisional evolution yet, it is possible that they still preserve properties of the original family-forming event in terms of their spin state. We carried out a series of photometric observations of the Karin family asteroids, and here we report on the analysis of the lightcurves including the rotation period of eleven members. The mean rotation rate of the Karin family members turned out to be much lower than those of near-Earth asteroids or small main belt asteroids (diameter $D < 12$ km), and even lower than that of large main belt asteroids ($D > 130$ km). We investigated a correlation between the peak-to-trough variation and the rotation period of the eleven Karin family asteroids, and found a possible trend that elongated members have lower spin rates, and less elongated members have higher spin rates. However, this trend has to be confirmed by another series of future observations.

1. Introduction

Asteroid families are remnants of catastrophic disruption and reaccumulation events between small bodies in the Solar System (e.g. Michel et al., 2003). Each member of an asteroid family has the potential to provide us with clues about the family-formation events that created them. However, since asteroid families are generally old (~Gyr), it is quite likely that the family members have undergone significant orbital, collisional, and spin-state evolution that masks properties of the original family-forming events.

A sophisticated numerical technique devised by Nesvorný et al. (2002) changed the above situation. Using their method, they detected three young asteroid families in the main belt: the Karin family (~5.8 Myr old), the Iannini family (~5 Myr old), and the Veritas family (~8 Myr old). These families are remarkably younger than previously known asteroid families, and more and more younger asteroid clusters have been recognized since then (e.g. Nesvorný and Vokrouhlický, 2006; Vokrouhlický and Nesvorný, 2008; 2009). With these discoveries in hand, we find many aspects of the study of young asteroid families interesting: their spin period distribution, their shape distribution, and possible detection of non-principal axis rotation.

We expect that the young family members preserve some properties of the original family-forming event in their spin period distribution. Although there are several laboratory experimental studies on the spin period distribution of collisional fragments (e.g. Fujiwara et al., 1989; Nakamura and Fujiwara, 1991; Kadono et al., 2009), it is hard to directly apply their results to real collisions between Small Solar System Bodies (SSSBs) in the gravity-dominant regime. Thus, observations of spin rates of the young asteroid family members can be unique opportunities to collect information on large-scale collisions.

As for the asteroid spin rate distribution, it is now widely known that the Yarkovsky–O'Keefe–Radzievskii–Paddack (YORP) effect may spin up or spin down 10-km-sized asteroids on a 10^8 yr timescale, and smaller asteroids could spin up/down even faster (e.g. Rubincam, 2000; Bottke et al., 2006). However, as the ages

* Corresponding author. Tel.: +81422343454; fax: +81422343840.
E-mail addresses: fumi.yoshida@nao.ac.jp (F. Yoshida), tito@cfca.nao.ac.jp (T. Ito).

http://dx.doi.org/10.1016/j.icarus.2016.01.004
0019-1035/

of the young asteroid families are substantially shorter than the timescale of the YORP effect, each family member perhaps statistically retains its initial spin status just after the family-formation event. In old asteroid families, such as the Koronis family, the YORP effect has changed the initial spin rate since the family-formation events (e.g. Slivan, 2002; Slivan et al., 2003; Vokrouhlický and Čapek, 2002; Vokrouhlický et al., 2003). Comparisons between the spin rate distribution of old and young asteroid families can serve as a help in the timescale estimate of the YORP effect. Actually the YORP effect is very sensitive to small-scale topography of asteroids (e.g. Statler, 2009). However, with the current observational data that we have in hand, we have not reached a detailed quantitative estimate of how seriously the YORP effect has influenced the dynamics of the Karin family members. Gaining a deeper understanding of these dynamics remains an aim of future inquiry.

In addition to the spin rate statistics, the shape distribution of the young asteroid family members is important for understanding the fragmentation and reaccumulation process of SSSBs in comparison with laboratory collisional experiments. It may help us understand the dynamical process of fragmentation and reaccumulation of asteroids, such as how angular momentum is distributed to each of the remnants. Also, it is possible to get an estimate of the satellite/binary forming efficiency at asteroid disruption events.

The young asteroid families also draw our attention in terms of possible detection of non-principal axis rotation (sometimes called "tumbling motion"). The study of a celestial body's non-principal axis rotation gives us important insights into energy dissipation and excitation processes, as well as internal structure of the body. Non-principal axis rotation could be excited by collisions of small projectiles, but it will be damped quickly unless the excitation continues. This is the main reason why the non-principal axis rotation of SSSBs has been confirmed only for a few tens of lightcurves (e.g. Harris, 1994; Pravec and Harris, 2000; Paolicchi et al., 2002; Mueller et al., 2002; Warner et al., 2009; Oey et al., 2012; Pravec et al., 2014). However, the age of the young family asteroids is quite young, and we may be able to observe their non-principal axis rotation before it has totally decayed.

Based on the motivations mentioned above, we began a series of photometric observations of the young asteroid families in November 2002. In this paper we focus on the current result of our lightcurve observation of the Karin family asteroids through the *R*-band imaging that we had carried out until May 2004, and summarize the result for eleven Karin family members whose rotation period we determined. Note that throughout the present paper we assume that the lightcurve variations are due to shapes of asteroids, not due to albedo features.

2. Observations

During the period from November 2002 to May 2004, we observed and determined the rotational periods of eleven Karin family members, including the largest member, (832) Karin. Table 1 shows the list of the observatories, the telescopes, and field of views of the instruments that we used for our observations.

We used the *R*-filter for our lightcurve observations because it is widely known that brightness of the reflected light in optical wavelengths from most asteroids becomes the highest in the *R*-band among the Johnson–Cousins *UBVRI* filters. In our observations all the telescopes were driven at the sidereal tracking rate, and the exposure time was limited by the moving rate of asteroids as well as by seeing during the observing nights. As typical main belt asteroids (MBAs) having the semimajor axis $a = 2.8$ AU move at the speed of ~0.55″/min at its opposition, and as the typical seeing size at the observatories was from 1.0″ to 3.0″, we chose a single exposure time of two to eight minutes so that an asteroid has an appearance of a point source. Generally, we continued the *R*-band imaging for a particular asteroid throughout a night except when we took images of standard stars: an "asteroid per night" strategy.

Table 1
Observatories and instruments. E is the elevation of the observatory (m), D_t is the diameter of the telescope mirror that we used (m), and FOV denotes the field of view of the imaging system that we used for our purpose. The full observatory names and the telescope names are as follows: Steward: the 2.3 m telescope ("Bok") at the Steward Observatory (Kitt Peak, Arizona, USA). Vatican: the 1.8 m telescope ("VATT") at the Vatican Observatory (Mt. Graham, Arizona, USA). Maidanak: the 1.5 m telescope ("AZT") at Maidanak Observatory (Uzbekistan). Lulin: the 1 m telescope at the Lulin Observatory (Taiwan). Kiso: the 1 m telescope at the Kiso Observatory (Nagano, Japan). Fukuoka: the 0.4 m telescope at the Fukuoka University of Education (Fukuoka, Japan).

Name	Longitude	Latitude	E	D_t	FOV
Steward	111°36′01.6″W	31°57′46.5″N	2071	2.29	4.5′ × 4.5′
Vatican	109°53′31.25″W	32°42′04.69″N	3191	1.8	6.8′ × 6.8′
Maidanak	66°53′47.08″E	38°40′23.95″N	2593	1.5	8.5′ × 3.5′
Lulin	120°52′25″E	23°28′07″N	2862	1.0	11.5′ × 11.2′
Kiso	137°37′42.2″E	35°47′38.7″N	1130	1.05	50′ × 50′
Fukuoka	130°35′44.7″E	33°48′45.3″N	70	0.40	5.75′ × 4.36′

We used the Landolt standard stars (Landolt, 1992) for the purpose of calibration. Before and/or after each of the observing nights, we took dome flats or twilight sky flats for flat-fielding. After the observation, we applied a standard data reduction procedure against the data: bias subtraction and flat division. Table 2 is the summary of our observational details.

3. Analysis and results

To construct composite lightcurves of asteroids from the observational data, we followed a sequence proposed by Harris and Lupishko (1989). The actual procedure is described in our previous publications (Dermawan et al., 2002; 2011; Yoshida et al., 2004). Principally, it is an iterative repetition of frequency analysis and fitting to Fourier series. We employed two different algorithms to examine periodicities in the lightcurve data: Lomb's Spectral Analysis (LSA, Lomb, 1976) and the WindowCLEAN Analysis (WCA, Roberts et al., 1987). WCA incorporates a discrete Fourier transform as well as the CLEAN algorithm (Högbom, 1974), and (Mueller et al., 2002) adopted WCA when they detected multiple rotational periodicities of asteroid (4179) Toutatis. When the frequency analysis is done, we fit the lightcurve with a Fourier series. We have to be particularly careful when we combine lightcurves derived from several observing runs because they generally have different lightcurve-mean magnitudes. See Section 3.1 for details of how we combined the lightcurves obtained from multiple observing runs.

Once we have obtained the lightcurve of an asteroid, we estimate the peak-to-trough variation of its lightcurve. To compare the amplitudes (A) of the lightcurves of the Karin family members taken at different solar phase angles (α) with each other as well as with other solar system bodies, we used the empirical relationship by Zappalà et al. (1990) that normalizes the amplitudes to a solar phase angle of 0 degree. Zappalà et al. (1990) gives $A(\alpha) = A(0)(1 + m\alpha)$, and it empirically determines the parameter $m = 0.030$ for S-type asteroids, which the Karin family members are classified as. However, we have to note that these amplitudes can be only used in a statistical sense, because, except for (832) Karin, these asteroids' spin obliquities are not known.

3.1. Procedure for combining lightcurves

In this subsection we describe how we dealt with the standard stars in our observation and how we combined lightcurves of asteroids obtained from different observing nights, making a single lightcurve for each asteroid.

Table 2
Aspect data of observed asteroids. Date of observations (mid-time of the observing night) in UT, ecliptic longitude λ (deg), ecliptic latitude β (deg), solar phase angle α (deg), and abbreviated codes of the observatories (S: Steward, V: Vatican, M: Maidanak, L: Lulin, K: Kiso, and F: Fukuoka), and the sky condition at the observational night (P: photometric, NP: non-photometric).

Date (UT)	λ	β	α	obs.	cond.
(832) Karin					
2003–08–22.64	330.7	1.6	0.85	F	P
2003–08–23.64	330.5	1.6	0.61	F	P
2003–09–03.63	328.2	1.6	4.70	F	P
2003–09–04.63	328.0	1.6	5.13	F	P
2003–09–05.63	327.8	1.6	5.54	K	NP
2003–09–26.19	324.8	1.5	13.36	V	P
2003–09–27.19	324.7	1.5	13.68	V	P
2003–09–28.17	324.6	1.5	13.99	V	P
2003–09–29.17	334.5	1.5	14.30	V	P
(7719) 1997 GT_{36}					
2003–10–14.16	315.5	0.9	18.39	S	P
2003–10–15.15	315.6	0.9	18.53	S	P
2003–10–16.14	315.6	0.9	18.66	S	P
2003–10–17.14	315.7	0.8	18.79	S	P
(10783) 1991 RB_9					
2004–03–24.50	236.6	1.7	14.94	S	P
2004–03–26.46	236.0	1.8	14.51	S	NP
2004–03–27.43	235.9	1.8	14.30	S	NP
2004–05–07.66	229.9	2.3	1.12	L	NP
2004–05–09.76	229.4	2.3	0.76	L	P
2004–05–10.68	229.2	2.3	0.83	L	P
2004–05–11.81	229.0	2.3	1.09	M	NP
2004–05–13.81	228.6	2.3	1.74	M	NP
(11728) Einer					
2003–05–08.44	251.9	3.0	8.57	V	P
2003–05–09.44	251.7	3.0	8.20	V	P
2003–06–29.62	242.3	2.1	11.97	L	P
2003–06–30.53	242.2	2.1	12.26	L	P
(13765) Nansmith					
2003–09–29.46	47.2	1.3	14.20	V	P
2003–10–15.38	45.1	1.4	8.53	S	P
2003–10–16.37	45.0	1.4	8.14	S	P
2003–10–17.37	44.8	1.4	7.73	S	P
2003–10–23.46	38.5	0.9	5.10	K	NP
2003–10–24.34	38.7	0.9	4.67	K	P
2003–10–26.42	39.2	0.9	3.80	K	NP
2003–10–27.43	39.4	0.9	3.36	K	NP
(16706) Svojsik					
2003–05–08.23	187.4	2.5	12.33	V	P
2003–05–09.30	187.3	2.5	12.63	V	P
(28271) 1999 CK_{16}					
2002–11–17.69	64.7	−1.2	4.48	L	P
2002–12–01.71	64.6	−1.3	1.71	L	NP
2002–12–04.63	64.0	−1.3	2.95	L	P
2002–12–05.58	63.8	−1.3	3.36	L	P
2004–03–24.29	161.1	−1.3	7.81	S	P
2004–03–26.27	161.0	−1.2	8.56	S	NP
2004–03–27.22	160.6	−1.3	8.90	S	NP
(40921) 1999 TR_{171}					
2003–07–20.71	300.5	−3.1	1.62	L	NP
2003–07–21.69	300.3	−3.1	1.37	L	NP
(43032) 1999 VR_{26}					
2003–08–01.89	342. 8	−4.3	12.14	M	P
2003–08–02.90	342.7	−4.3	11.79	M	P
2003–08–03.89	342.5	−4.3	11.44	M	P
2003–08–04.86	342.4	−4.3	11.10	M	P
2003–09–22.25	333.3	−4.2	9.32	V	P
2003–09–27.24	332.6	−4.1	11.12	V	P
2003–09–28.18	332.5	−4.1	11.44	V	P
2003–09–29.17	332.4	−4.1	11.78	V	P
(69880) 1998 SQ_{81}					
2003–09–22.44	20.4	−1.7	7.72	V	P
2003–09–26.47	19.6	−1.8	6.10	V	P
2003–09–27.41	19.5	−1.8	5.71	V	P
2003–09–28.45	19.3	−1.8	5.28	V	P
2003–09–29.34	19.1	−1.9	4.90	V	P
2003–10–14.33	15.9	−2.0	1.84	S	P
(71031) 1999 XE_{68}					
2003–09–01.87	353.2	−2.3	5.05	M	P
2003–09–02.86	353.0	−2.4	4.66	M	P
2003–09–03.85	352.8	−2.4	4.27	M	P
2003–09–26.34	348.1	−2.6	5.21	V	P
2003–09–28.27	347.7	−2.7	5.96	V	P

(*continued on next page*)

(*continued*)

3.1.1. Observation of the Landolt standard stars

We took the following procedures when observing Landolt standard stars.

(1) On photometric nights. Before and/or after the observation of each asteroid, we take images of the Landolt standard stars at several different airmasses. We determine the atmospheric extinction coefficients of the night based on this dataset.

(2) On non-photometric nights. While we take images of asteroids, we take images of one or two Landolt standard stars, once or twice if possible, at the same airmasses at which we observed the asteroids.

3.1.2. Combining lightcurves I. (With clear maxima and minima)

When all the observations are done, we measure the brightness of asteroids by IRAF. Eventually we combine all the lightcurves from different observing nights into a single composite lightcurve for each asteroid.

(1) Measuring field stars. When we measure the brightness of an asteroid by IRAF, we also measure the brightness of five or six field stars that exist on the same image as the asteroid. Here we should note that all the field stars that we choose must be included in the USNO–A2.0 catalogue[1]. Although we are aware that the brightness magnitude of the stars catalogued in the USNO–A2.0 catalog contains a certain degree of error, here we do not take care of the errors.

(2) Elimination of anomalous field stars. We draw lightcurves of each of the field stars, and confirm that none of those we have chosen is a variable star. Also, if any of the chosen field stars is located on an image frame with a serious problem such as caused by camera shutter problems or cosmic ray contamination, we discard the entire image itself from the analysis.

(3) Choosing the brightest field star. When we have found several field stars whose brightness does not vary with time, we select the brightest one among them as a comparison star for the asteroid's relative photometry. This is because errors in relative photometry are smaller when we choose a brighter star as a comparison star.

(4) Relative photometry of asteroids. Using the selected field stars as comparison stars, we carry out relative photometry work for each asteroid. As a result, we obtain lightcurves in relative magnitude for each of the observation nights for each of the asteroids.

(5) Determination of lightcurve-mean magnitudes. We determine lightcurve-mean magnitude of each asteroid from the lightcurves in relative magnitude. We get the lightcurve-mean magnitudes in the process of fitting each of the lightcurves with Fourier series. When we see maximum and minimum in lightcurves, determination of lightcurve-mean magnitude is straightforward.

[1] http://tdc-www.harvard.edu/catalogs/ua2.html.

Table 3
Major observational results. P is the rotation period (hours), $A(0)$ is the reduced peak-to-trough variation, α is the solar phase angle during our observation (deg), QC is the quality code of the period results, and the panel designation in Fig. 1. For (28271) 1999CK_{16}, $*$ denotes the observation result in 2002, and † denotes the observation result in 2004. The $\pm$ errors in P are derived from the stepsize of the CLEAN analysis.

Asteroid	P	$A(0)$	α	QC	Fig. 1
(832) Karin	$18.348^{+0.037}_{-0.037}$	0.56 ± 0.02	0.6–14.3	2	a
(7719) 1997 GT_{36}	$29.555^{+1.231}_{-1.137}$	0.31 ± 0.02	18.4–18.8	2	b
(10783) 1991 RB_9	$7.334^{+0.005}_{-0.004}$	0.26 ± 0.02	0.8–14.9	3	c
(11728) Einer	$13.622^{+0.150}_{-0.140}$	0.14 ± 0.01	8.6–12.3	2	d
(13765) Nansmith	$10.526^{+0.014}_{-0.014}$	0.06 ± 0.02	7.7–17.7	2	e
(16706) Svojsik	$5.866^{+0.120}_{-0.120}$	0.09 ± 0.04	12.3–13.2	1	f
(28271)* 1999 CK_{16}	$5.635^{+0.005}_{-0.010}$	0.07 ± 0.04	1.7–4.5	2	g
(28271)† 1999 CK_{16}	$5.645^{+0.043}_{-0.043}$	0.17 ± 0.02	7.8–8.9	2	h
(40921) 1999 TR_{171}	$6.662^{+0.346}_{-0.158}$	0.35 ± 0.02	1.4–1.6	2	i
(43032) 1999 VR_{26}	$32.890^{+0.078}_{-0.077}$	0.60 ± 0.06	9.3–12.1	2	j
(69880) 1998 SQ_{81}	$7.675^{+0.010}_{-0.014}$	0.08 ± 0.01	1.8–7.7	2	k
(71031) 1999 XE_{68}	$20.187^{+0.064}_{-0.064}$	0.39 ± 0.04	4.3–6.0	2	l

(6) Combining lightcurves based on the lightcurve means. When several observing nights are (nearly) consecutively distributed, we combine the lightcurves of each asteroid from all the observing nights, based on the lightcurve-mean magnitude that we have determined in Section 3.1.2 (5).

(7) Frequency analysis. For each asteroid, we carry out frequency analysis of the combined lightcurves produced in Section 3.1.2 (6) and get necessary quantities such as rotation period.

3.1.3. Combining lightcurves II. (Without clear maxima or minima)

When we do not see any maxima or minima in lightcurves of asteroids, determination of lightcurve-mean magnitude is not straightforward. This happens when the spin period of an asteroid is as long as, or longer than, the observational period—observation length of a night does not reach the spin period of an asteroid. In this case we utilize the observational data of the Landolt standard stars that we have prepared in Sections 3.1.1 (1) and 3.1.1 (2), and carry out the following procedures, instead of Sections 3.1.2 (5) and 3.1.2 (6), to combine several lightcurves of an asteroid into a single one. Note that we carry out the procedure described in this subsection only when the observation night is photometric. Observational data from non-photometric nights without clear maxima or minima is not used, and is just discarded.

(1) Calibration of the field star brightness. Using the Landolt standard stars, we calibrate the brightness of the field stars that we selected. Then we calculate the apparent brightness magnitude of the asteroid using the calibrated brightness of the field stars.

(2) Combining lightcurves based on the lightcurve means. Based on the magnitude of each of the asteroids estimated in Sections 3.1.3 (1), we combine their lightcurves from different nights into a single lightcurve.

(3) Frequency analysis. For each asteroid, we carry out frequency analysis of the combined lightcurves produced in Sections 3.1.3 (2), and get necessary quantities such as rotation period.

3.2. Lightcurves

Fig. 1 shows all the lightcurves that we obtained in the series of observations. Table 3 summarizes rotation period P, reduced peak-to-trough variation $A(0)$, solar phase angle α during the observation period, and the period quality code (Lagerkvist et al., 1989). As for the rotation period P, we chose the most reliable peak value from the periodicity analysis results by LSA or WCA (mostly by WCA for the lightcurves presented in the present paper). We regard that the LSA analysis as compensating for vulnerabilities of WCA and justifying our result even when the lightcurve data contains large temporal gaps. Note that we checked out phase plots for the peaks of other periods, although we did not show them in the present paper.

Since Fig. 1 and Tables 2 and 3 describe most of our results, we just give supplementary information for three of the objects as follows:

(832) Karin. The results of our lightcurve observation of this asteroid are already published (Yoshida et al. (2004) for the observation in 2003, and Ito and Yoshida (2007) for the observation in 2004). Since our 2004 observation was mainly for multi-color photometry of this asteroid, here we just present our 2003 observation result from Yoshida et al. (2004).

(28271) 1999 CK_{16}. We observed this asteroid twice at two different oppositions: from November to December 2002 and in March 2004. The rotation periods that were derived from both the observations are close to each other. The lightcurve amplitudes taken in 2002 (Fig. 1(g)) and 2004 (Fig. 1(h)) are different because geometric configurations between the asteroid, observer, and the Sun were different.

(11728) Einer. The rotation period derived for this asteroid is from the most prominent peak obtained from the period analysis. However, note that other period values might also be possible due to potential aliasing.

4. Discussions

The spin period distribution of asteroids is often compared with the Maxwellian distribution (e.g. Binzel et al., 1989). Unfortunately, the number of our lightcurve samples is still far from being sufficient for such a detailed statistical discussion. Here, let us just compare the mean value of the rotation rate $1/P$ of the eleven Karin family asteroids that we observed with those of near-Earth asteroids (NEAs), small MBAs ($D < 12$ km), and large MBAs ($D > 130$ km). According to Table 2 of Binzel et al. (2002, p. 265), the mean values of the rotation rate of NEAs, small MBAs, and large MBAs are 4.80 ± 0.29 rev/day, 4.34 ± 0.23 rev/day, and 2.90 ± 0.12 rev/day, respectively. On the other hand, from our present work, the mean rotation rate of the Karin family asteroids turned out to be ~2.40 rev/day, or ~2.51 rev/day excluding (832) Karin (we used the period value obtained in 2004 for (28271) 1999CK_{16}). Therefore, the mean rotation rate of the Karin family members is much lower than those of the NEAs and the small MBAs, and even lower than that of the large MBAs. This may be quite an interesting fact, considering the widely believed hypothesis that most of the small MBAs are collisional remnants.

According to Table 2 of Binzel et al. (2002, p. 265), the reduced peak-to-trough variation of the NEAs, the small MBAs, and the large MBAs is 0.29, 0.28, and 0.19, respectively. Meanwhile, the average reduced peak-to-trough variation of the Karin family members is 0.24–0.27[2] . The average value excluding (832) Karin, 0.24–0.25, is closer to that of the small MBA group with $D < 12$ km, rather than that of the large MBAs. This is consistent with our conventional knowledge that asteroid remnants, such as small MBAs or young family asteroids, are more likely to have an elongated

[2] It is ~0.26 if we choose the value 0.07 for (28721) 1999 CK_{16}, ~0.24 if we exclude (832) Karin and choose the value 0.07 for (28721) 1999 CK_{16}, ~0.27 if we choose the value 0.17 for (28721) 1999 CK_{16}, and ~0.25 if we exclude (832) Karin and choose the value 0.17 for (28721) 1999 CK_{16}.

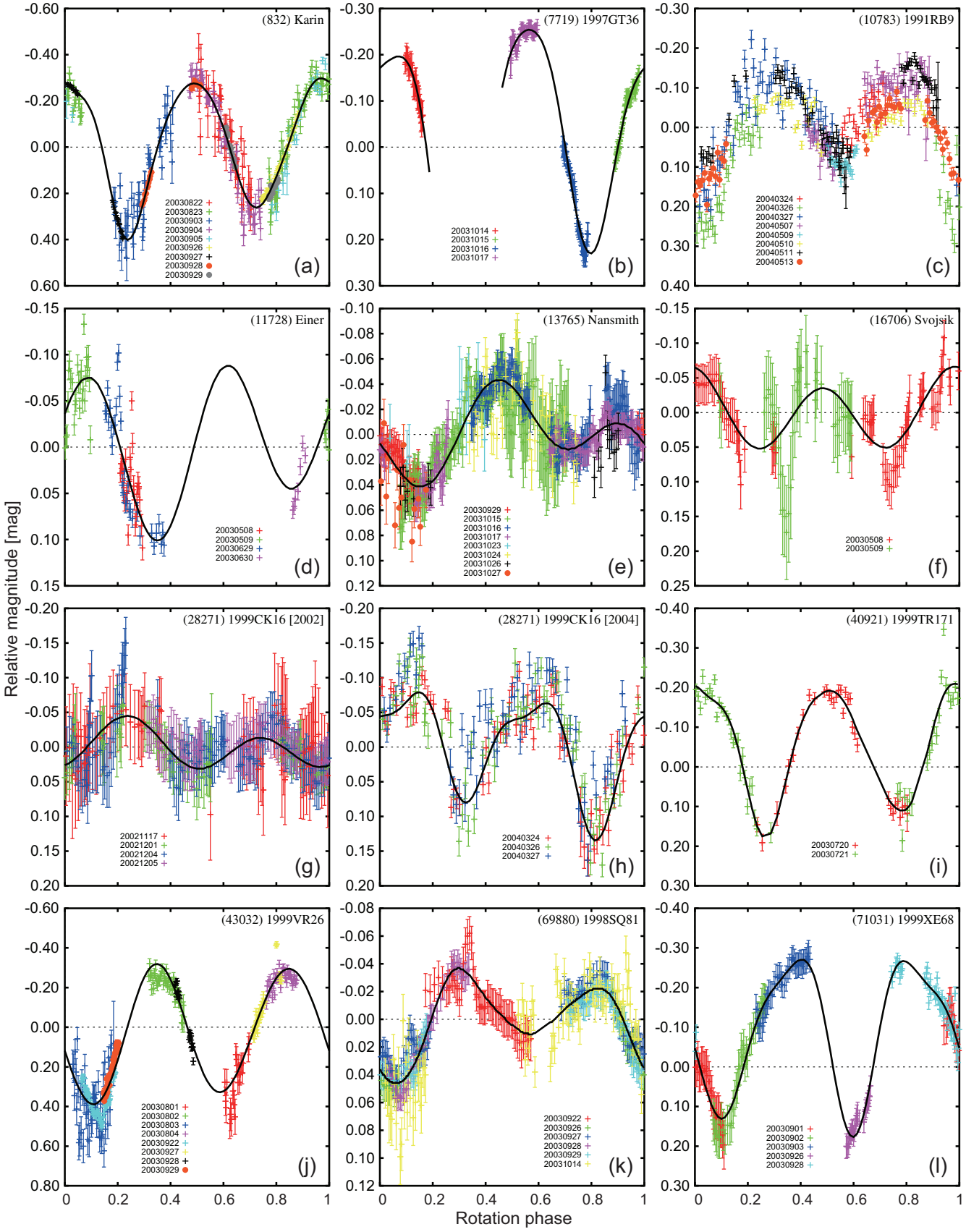

Fig. 1. Results of the lightcurve analysis of eleven Karin family asteroids. (a) (832) Karin, (b) (7719) 1997 GT_{36}. (c) (10783) 1991 RB_9, (d) (11728) Einer (e) (13765) Nansmith. (f) (16706) Svojsik, (g) (28271) 1999 CK_{16} (observed in 2002), (h) (28271) 1999 CK_{16} (observed in 2004), (i) (40921) 1999 TR_{171}, (j) (43032) 1999 VR_{26}, (k) (69880) 1998 SQ_{81}, and (l) (71031) 1999 XE_{68}. The vertical axis denotes the relative magnitude referred to a field star at each observing night. Note that the lightcurve of (832) Karin in (a) is a quoted one from Yoshida et al. (2004).

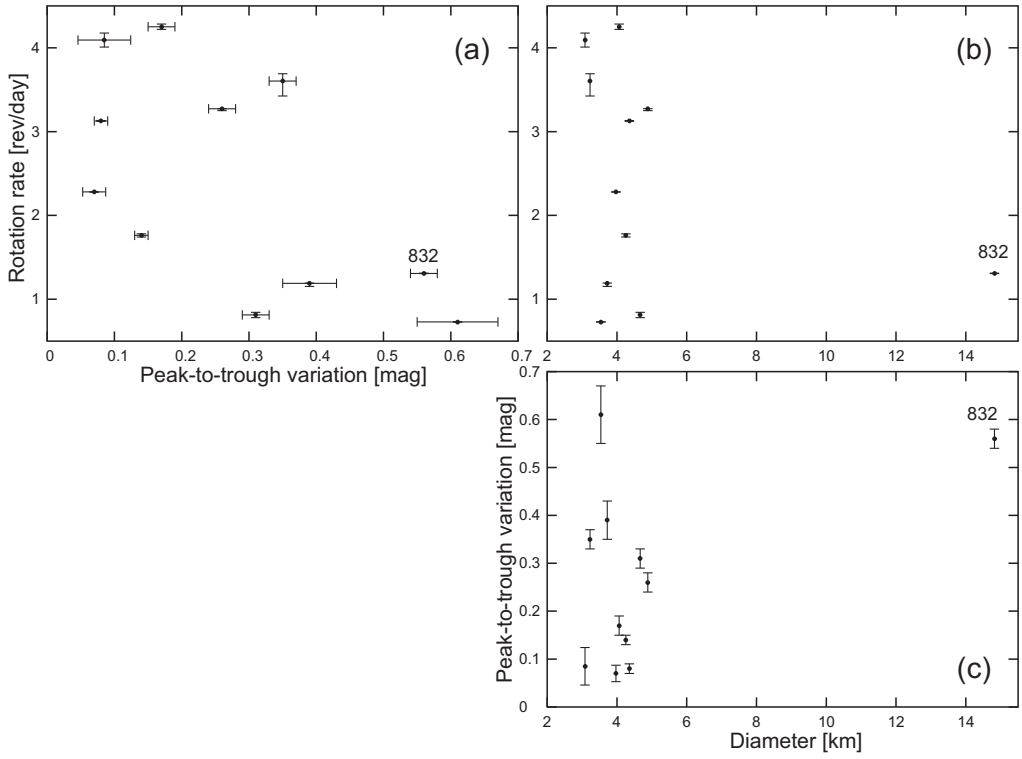

Fig. 2. Relation between the rotation rate 1/*P*, diameter *D*, and the reduced peak-to-trough variation *A*(0) of the eleven Karin family asteroids that we observed. (a) *A*(0) and 1/*P*, (b) *D* and 1/*P*, and (c) *D* and *A*(0). The largest member, (832) Karin, is denoted as "832". Note that as for (28271) 1999 CK_{16} we used its values obtained from our 2004 observation, as its *A*(0) value in 2004 is larger than its value in 2002, being closer to their maximum.

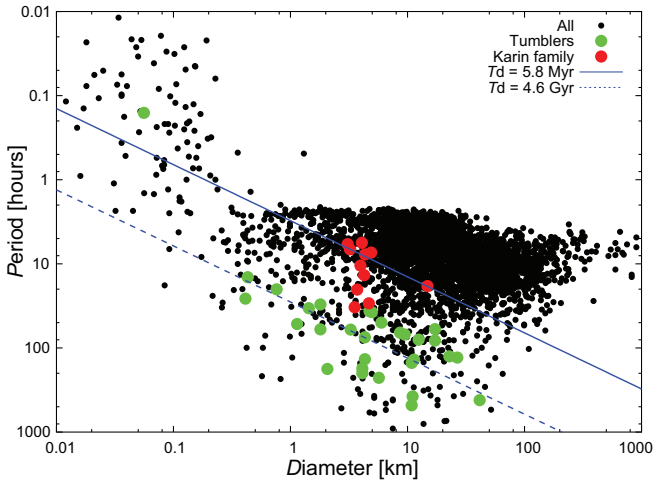

Fig. 3. Relation between the rotation period *P* (hours) and diameter *D* (km) of 3,745 known asteroids (filled black circles) including 31 tumblers (filled green circles) and the eleven Karin family asteroids (filled red circles). The diagonal blue lines show the theoretical (*D*, *P*) relation of asteroids when their damping timescale $T_d = 5.8$ Myr (the upper solid blue line) and when their damping timescale $T_d = 4.6$ Gyr (the lower dashed blue line) calculated by Eq. (1). (For interpretation of the references to color in this figure legend, the reader is referred to the web version of this article).

(and irregular) shape than a spherical shape compared with large asteroids that can be parent bodies of asteroid families.

We summarized our main result of the spin period *P* and the peak-to-trough variation magnitude *A*(0) of the eleven Karin family members in Fig. 2 (we are aware that we have ignored the effect of asteroids' obliquity in this figure, because we have no information on it so far). In Fig. 2(a) that shows the relation between *A*(0) and 1/*P*, you may see a slight trend from the top left to the bottom right, which tells us that elongated asteroids have a lower spin rate, and those less elongated asteroids have a higher spin rate. A similar trend has been recognized in fast-rotating sub-km-size MBAs (Dermawan et al., 2011; Nakamura et al., 2011). However, we are aware that the number of our present lightcurve samples is not large enough to reach a definite conclusion on our conjecture. In other words, Fig. 2(a) may be just a scatter plot from the fact that the number of objects is not large enough for rigorously statistical discussions. Whether the "trend" really exists depends on how many more lightcurve samples of the Karin family members we can obtain from now on.

At the end of this paper, we would like to consider the possibility that some of the Karin family members still possess non-principal axis rotation. From the result that we have presented in the previous sections, we plotted the rotation period of the eleven Karin family asteroids on a diagram that shows the relation between rotation period *P* and diameter *D* in Fig. 3. For this figure, we estimated the diameter of the Karin family members from its absolute magnitude *H* using the relationship $\log_{10} D = 3.1295 - 0.5 \log_{10} p - 0.2H$ where *p* is the albedo of an asteroid (Bowell and Lumme, 1979). We used the absolute magnitude values of the asteroids listed on the Lowell asteroid orbital elements database[3]. We assumed the albedo value of $p = 0.21$ for the S-type asteroids (cf. Yoshida and Nakamura, 2007; Strom et al., 2015)[4].

[3] ftp://ftp.lowell.edu/pub/elgb/astorb.html.

[4] The value $p = 0.21$ is the mean albedo calculated from the catalog of asteroid albedo and taxonomic types in PSI PDS database, http://sbn.psi.edu/pds/resource/albedo.html. The albedo value can be dependent on asteroid size, but we are not sure how strongly or weakly dependent it is. For example, recent survey observations have revealed the albedo dependence on asteroid size for each of the taxonomic types (e.g. Usui et al., 2013). In Usui et al.'s (2013) Fig. 5(b) for S-type asteroids, we may (or may not) see some skewed albedo distribution in the diameter range of $D < 10$km, but we are not sure about the quantitative analysis result in a smaller range. Another thing is that the range of *D* of the asteroids that we

For comparison , we also plotted the (*D, P*) relation of 3,745 known asteroids listed on the PSI PDS lightcurve database whose rotational periods are known to a certain reliability[5]. For these asteroids, we applied the mean albedo of $p = 0.081$ following Ryan and Woodward (2010) to all the asteroids, assuming their absolute magnitude H listed in the Lowell asteroid orbital elements database mentioned above. Also, among these asteroids we highlighted 31 possible tumblers[6] in green so that we can compare their (*D, P*) relation with that of the Karin family asteroids.

Theoretically, the damping timescale of the non-principal axis rotation of a celestial body T_d (Gyr) can be expressed in its relationship between P (hours) and D (km) as in the following equation by Harris (1994), a reconsideration of a theory by Burns and Safronov (1973):

$$P \sim 17 D^{\frac{2}{3}} T_d^{\frac{1}{3}}. \quad (1)$$

Smaller and slower rotators have longer damping timescales of the non-principal axis rotation. In Fig. 3 we drew two damping timescales of non-principal axis rotation using diagonal lines calculated by Eq. (1). The upper solid blue line in Fig. 3 indicates the (*D, P*) relation of asteroids when their damping timescale $T_d = 5.8$ Myr, equivalent to the age of the Karin family. The lower dashed blue line in Fig. 3 indicates that of asteroids when their damping timescale $T_d = 4.6$ Gyr, almost equivalent to the age of the solar system. You can see from Fig. 3 that many of the Karin members we observed are located below the upper solid line for $T_d = 5.8$ Myr, indicating that they can still maintain the non-principal axis rotation, if there is any, since their damping timescale T_d is possibly longer than their age, 5.8 Myr. Although in the present analysis we did not detect clues on the non-principal axis rotation of the Karin family members, several members with relatively long rotational periods such as (7719) 1997 GT_{36}, (43032) 1999 VR_{26}, or (71031) 1999 XE_{68} are still candidates as tumbling asteroids.

We greatly appreciate the effort and courtesy extended by all the people who helped us during our observations at the Vatican Observatory's "VATT" (the Alice P. Lennon Telescope and the Thomas J. Bannan Astrophysics Facility). We thank Elizabeth Green, Paula White, Ed Olszewski, and Andy Odell for allowing our use of the Steward 90-inch "Bok" telescope. FY is deeply thankful to Tom Gehrels who recommended that we use the VATT and the Bok telescopes in Arizona, and particularly for his encouragement of our observing activity and his enormous contribution to asteroid studies. Without his warmth, help, and thoughtful suggestions, we could not have carried out our observations there at all. The staff members at the Maidanak Observatory greatly helped us during our stay and observing activity. The authors thank the two anonymous referees for suggesting directions that significantly improved the quality of this paper. FY also has benefited from stimulating enlightenment by Murier Yoshida. Detailed and constructive review by Yolande McLean has considerably improved the English presentation of this paper. Some part of the data analysis was performed at the National Astronomical Observatory of Japan's Astronomy Data Center (ADC) and Center for Computational Astrophysics (CfCA). This study is supported by the JSPS Kakenhi grant (16740259/2004–2005, 18540426/2006–2008, 18540427/2006–2008, 21540442/2009–2011, 25400458/2013–2015, 25400238/2013–2015), the JSPS program for Asia–Africa academic platform (2009–2011), the JSPS bilateral open partnership joint research project (2014–2015), the Sumitomo Foundation research funding (030755/2003–2004), and the Heiwa Nakajima Foundation research funding for Asian studies (2009).

observed this time is rather narrow (see Fig. 2(c)) except (832) Karin, and we can expect that the albedos for these asteroids are not so different from each other, even if there is a dependency of albedo on size. Therefore, in the present paper, we used the average albedo.

[5] http://sbn.psi.edu/pds/resource/lc.html as of April 30, 2012 (V12.0). Among the lightcurve datafile data/lc_summary.tab, we selected the asteroids only with the lightcurve reliability of 2, 2+, 3 or higher.

[6] Among all the lightcurve data in data/lc_summary.tab, we selected the asteroids having the credible tumbling flag T or T+.

References

Binzel, R.P., Farinella, P., Zappalà, V., et al., 1989. Asteroid rotation rates: Distributions and statistics. In: Binzel, R.P., Gehrels, T., Matthews, M.S. (Eds.), Asteroids II. The University of Arizona Press, Tucson, Arizona, pp. 416–441.
Binzel, R.P., Lupishko, D.F., Di Martino, M., et al., 2002. Physical properties of near-Earth objects. In: Bottke, W.F., Cellino, A., Paolicchi, P., Binzel, R.P. (Eds.), Asteroids III. The University of Arizona Press, Tucson, Arizona, pp. 255–271.
Bottke, W.F., Nesvorný, D., Rubincam, D.P., et al., 2006. The yarkovsky and YORP effects: Implications for asteroid dynamics. Annu. Rev. Earth Planet. Sci. 34, 157–191.
Bowell, E., Lumme, K., 1979. Colorimetry and magnitudes of asteroids. In: Gehrels, T. (Ed.), Asteroids. The University of Arizona Press, Tucson, Arizona, pp. 132–169.
Burns, J.A., Safronov, V.S., 1973. Asteroid nutation angles. Mon. Not. R. Astron. Soc. 165, 403–411.
Dermawan, B., Nakamura, T., Fukushima, H., et al., 2002. CCD photometry of the MUSES-c mission target: Asteroid (25143) 1998 SF36. Publ. Astron. Soc. Japan 54, 635–640.
Dermawan, B., Nakamura, T., Yoshida, F., 2011. Subaru lightcurve observations of sub-km-sized main-belt asteroids. Publ. Astron. Soc. Japan 63, S555–S576.
Fujiwara, A., Cerroni, P., Davis, D.R., et al., 1989. Experiments and scaling laws for catastrophic collisions. In: Binzel, R.P., Gehrels, T., Matthews, M. (Eds.), Asteroids II. The University of Arizona Press, Tucson, Arizona, pp. 240–265.
Harris, A.W., 1994. Tumbling asteroids. Icarus 107, 209–211.
Harris, A.W., Lupishko, D.F., 1989. Photometric lightcurve observations and reduction techniques. In: Binzel, R.P., Gehrels, T., Matthews, M.S. (Eds.), Asteroids II. The University of Arizona Press, Tucson, Arizona, pp. 39–53.
Högbom, J.A., 1974. Aperture synthesis with a non-regular distribution of interferometer baselines. Astron. Astrophys. Suppl. Ser. 14, 417–426.
Ito, T., Yoshida, F., 2007. Color variation of a very young asteroid, karin. Publ. Astron. Soc. Japan 59, 269–275.
Kadono, T., Arakawa, M., Ito, T., et al., 2009. Spin rates of fast-rotating asteroids and fragments in impact disruption. Icarus 200, 694–697.
Lagerkvist, C.I., Harris, A.W., Zappalá, V., 1989. Asteroid lightcurve parameters. In: Binzel, R.P., Gehrels, T., Matthews, M.S. (Eds.), Asteroids II. The University of Arizona Press, Tucson, Arizona, pp. 1162–1179.
Landolt, A.U., 1992. UBVRI photometric standard stars in the magnitude range 11.5–16.0 around the celestial equator. Astron. J. 104, 340–371,436–491.
Lomb, N.R., 1976. Least-squares frequency analysis of unequally spaced data. Astrophys. Space Sci. 39, 447–462.
Michel, P., Benz, W., Richardson, D.C., 2003. Disruption of fragmented parent bodies as the origin of asteroid families. Nature 421, 608–611.
Mueller, B.E.A., Samarasinha, N.H., Michael, M.J.S., 2002. The diagnosis of complex rotation in the lightcurve of 4179 toutatis and potential applications to other asteroids and bare cometary nuclei. Icarus 158, 205–311.
Nakamura, A., Fujiwara, A., 1991. Velocity distribution of fragments formed in a simulated collisional disruption. Icarus 92, 132–146.
Nakamura, T., Dermawan, B., Yoshida, F., 2011. Sphericity preference in shapes of sub-km-sized fast-rotating main-belt asteroids. Publ. Astron. Soc. Japan 63, S577–S584.
Nesvorný, D., Bottke, W.F., Dones, L., et al., 2002. The recent breakup of an asteroid in the main-belt region. Nature 417, 720–722.
Nesvorný, D., Vokrouhlický, D., 2006. New candidates for recent asteroid breakups. Astron. J. 132, 1950–1958.
Oey, J., Pilcher, F., Benishek, V., et al., 2012. Photometric analysis of the very long period and tumbling asteroid 1278 kenya. Minor Planet Bull. 39, 86–88.
Paolicchi, P., Burns, J.A., Weidenschiling, S.J., 2002. Side effects of collisions: spin rate changes, tumbling rotation states, and binary asteroids. In: Bottke, W.F., Cellino, A., Paolicchi, P., Binzel, R.P. (Eds.), Asteroids III. The University of Arizona Press, Tucson, Arizona, pp. 517–526.
Pravec, P., Harris, A.W., 2000. Fast and slow rotation of asteroids. Icarus 148, 12–20.
Pravec, P., Scheirich, P., Ďurech, J., et al., 2014. The tumbling spin state of (99942) apophis. Icarus 233, 48–60.
Roberts, D.H., Lehar, J., Dreher, J.W., 1987. Time series analysis with CLEAN i. derivation of a spectrum. Astron. J. 93, 968–989.
Rubincam, D.P., 2000. Radiative spin-up and spin-down of small asteroids. Icarus 148, 2–11.
Ryan, E.R., Woodward, C.E., 2010. Rectified asteroid albedos and diameters from IRAS and MSX photometry catalogs. Astron. J. 140, 933–943.
Slivan, S.M., 2002. Spin vector alignment of koronis family asteroids. Nature 419, 49–51.
Slivan, S.M., Binzel, R.P., Crespo da Silva, L.D., et al., 2003. Spin vectors in the Koronis family: Comprehensive results from two independent analyses of 213 rotation lightcurves. Icarus 162, 285–307.
Statler, T.S., 2009. Extreme sensitivity of the YORP effect to small-scale topography. Icarus 202, 502–513.

Strom, R.G., Malhotra, R., Xiao, Z., et al., 2015. The inner solar system cratering record and the evolution of impactor populations. Res. Astron. Astrophys. 15, 407–434.
Usui, F., Kasuga, T., Hasegawa, S., et al., 2013. Albedo properties of main belt asteroids based on the all-sky survey of the infrared astronomical satellite *akari*. Astrophys. J. 762, 56.
Vokrouhlický, D., Nesvorný, D., 2008. Pairs of asteroids probably of a common origin. Astron. J. 136, 280–290.
Vokrouhlický, D., Nesvorný, D., 2009. The common roots of asteroids (6070) rheinland and (54827) 2001 NQ8. Astron. J. 137, 111–117.
Vokrouhlický, D., Nesvorný, D., Bottke, W.F., 2003. The vector alignments of asteroid spins by thermal torques. Nature 425, 147–151.
Vokrouhlický, D., Čapek, D., 2002. YORP-induced long-term evolution of the spin state of small asteroids and meteoroids: Rubincam's approximation. Icarus 159, 449–467.
Warner, B.D., Harris, A.W., Pravec, P., 2009. The asteroid lightcurve database. Icarus 202, 134–146.
Yoshida, F., Dermawan, B., Ito, T., et al., 2004. Photometric observations of a very young family-member asteroid (832) karin. Publ. Astron. Soc. Japan 56, 1105–1113.
Yoshida, F., Nakamura, T., 2007. Subaru main belt asteroid survey (SMBAS) — size and color distributions of small main-belt asteroids. Planet. Space Sci. 55, 1113–1125.
Zappalà, V., Cellino, A., Barucci, A.M., et al., 1990. An analysis of the amplitude-phase relationship among asteroids. Astron. Astrophys. 231, 548–560.

Monthly Notices
of the
ROYAL ASTRONOMICAL SOCIETY

MNRAS **461,** 3047–3056 (2016)
Advance Access publication 2016 June 24

doi:10.1093/mnras/stw1516

Exceptional outburst of the blazar CTA 102 in 2012: the GASP–WEBT campaign and its extension

V. M. Larionov,[1,2]★ M. Villata,[3]★ C. M. Raiteri,[3]★ S. G. Jorstad,[1,4] A. P. Marscher,[4] I. Agudo,[5] P. S. Smith,[6] J. A. Acosta-Pulido,[7,8] M. J. Árévalo,[7,8] A. A. Arkharov,[2] R. Bachev,[9] D. A. Blinov,[1,10,11] G. Borisov,[9,12] G. A. Borman,[13] V. Bozhilov,[14] A. Bueno,[7,8] M. I. Carnerero,[3,7,8] D. Carosati,[15,16] C. Casadio,[5] W. P. Chen,[17] D. P. Clemens,[4] A. Di Paola,[18] Sh. A. Ehgamberdiev,[19] J. L. Gómez,[5] P. A. González-Morales,[7,8] A. Griñón-Marín,[7,8] T. S. Grishina,[1] V. A. Hagen-Thorn,[1] S. Ibryamov,[9] R. Itoh,[20] M. Joshi,[4] E. N. Kopatskaya,[1] E. Koptelova,[17] C. Lázaro,[7,8] E. G. Larionova,[1] L. V. Larionova,[1] A. Manilla-Robles,[7,8] Y. Metodieva,[14] Yu. V. Milanova,[1] D. O. Mirzaqulov,[19] S. N. Molina,[5] D. A. Morozova,[1] S. V. Nazarov,[13] E. Ovcharov,[14] S. Peneva,[9] J. A. Ros,[21] A. C. Sadun,[22] S. S. Savchenko,[1] E. Semkov,[9] S. G. Sergeev,[13] A. Strigachev,[9] Yu. V. Troitskaya[1] and I. S. Troitsky[1]

Affiliations are listed at the end of the paper

Accepted 2016 June 21. Received 2016 June 17; in original form 2016 April 21

ABSTRACT

After several years of quiescence, the blazar CTA 102 underwent an exceptional outburst in 2012 September–October. The flare was tracked from γ-ray to near-infrared (NIR) frequencies, including *Fermi* and *Swift* data as well as photometric and polarimetric data from several observatories. An intensive Glast-Agile support programme of the Whole Earth Blazar Telescope (GASP–WEBT) collaboration campaign in optical and NIR bands, with an addition of previously unpublished archival data and extension through fall 2015, allows comparison of this outburst with the previous activity period of this blazar in 2004–2005. We find remarkable similarity between the optical and γ-ray behaviour of CTA 102 during the outburst, with a time lag between the two light curves of $\approx$1 h, indicative of cospatiality of the optical and γ-ray emission regions. The relation between the γ-ray and optical fluxes is consistent with the synchrotron self-Compton (SSC) mechanism, with a quadratic dependence of the SSC γ-ray flux on the synchrotron optical flux evident in the post-outburst stage. However, the γ-ray/optical relationship is linear during the outburst; we attribute this to changes in the Doppler factor. A strong harder-when-brighter spectral dependence is seen both the in γ-ray and optical non-thermal emission. This hardening can be explained by convexity of the UV–NIR spectrum that moves to higher frequencies owing to an increased Doppler shift as the viewing angle decreases during the outburst stage. The overall pattern of Stokes parameter variations agrees with a model of a radiating blob or shock wave that moves along a helical path down the jet.

Key words: methods: observational – techniques: photometric – techniques: polarimetric – galaxies: active – quasars: individual: CTA 102.

1 INTRODUCTION

The blazar CTA 102 (4C +11.69, 2FGL J2232.4+1143, $z = 1.037$) is a luminous, well-studied quasar. Like other blazars, it is believed that its jet is oriented close to our line of sight, which causes strong

★ E-mail: v.larionov@spbu.ru (VML); villata@oato.inaf.it (MV); raiteri@oato.inaf.it (CMR)

relativistic beaming of the jet's emission and violent variability at all wavelengths. CTA 102 was first identified as a quasar by Sandage & Wyndham (1965) and belongs to the optically violently variable (Angel & Stockman 1980), as well as the high polarized quasar, subclasses (Moore & Stockman 1981).

On long time-scales, the blazar exhibits rather modest variability at optical bands. Moderate-amplitude fluctuations around the average magnitude of $B = 17.7$ mag over a 14 yr range (about 65 observations between 1973 and 1987) were reported by Pica et al. (1988). An overall amplitude $\Delta R = 0.88$ mag was observed by Villata et al. (2001) in 1994–1997. However, occasional sharp flares have also been observed in CTA 102. Variations as high as $\Delta B = 1.07$ mag in 2 d (Pica et al. 1988) and $\Delta V = 1.13$ mag in 3 d (Katajainen et al. 2000) were observed in 1978 and 1996, respectively. The previously reported historical maximum for the object, $R \approx 14.5$ mag, was reached on 2004 October 4 during a short-term event accompanied by prominent intra-night variability (Osterman Meyer et al. 2009). Between that episode and 2012, only moderate variability has been seen in the light curve of this blazar (see Fig. 1).

CTA 102 was discovered to be a γ-ray emitter early in the *Compton Gamma Ray Observatory* (*CGRO*; EGRET detector) mission at a level of $(2.4 \pm 0.5) \times 10^{-7}$ photons cm^{-2} s^{-1} ($E > 100$ MeV; Nolan et al. 1993). It was also detected in the 10–30 MeV energy range by the COMPTEL instrument of *CGRO* (Blom et al. 1995). Since the blazar usually exists in a quiescent state, the average γ-ray flux is rather low, $(2.9 \pm 0.2) \times 10^{-9}$ photons cm^{-2} s^{-1} ($1 < E < 100$ GeV) according to the 2FGL catalogue based on data from the Large Area Telescope (LAT) of the *Fermi* Gamma-ray Space Telescope (Nolan et al. 2012). Therefore, accurate relative timing of flux variations in γ-ray and optical bands is only possible during large outbursts. Similar events may serve as a crucial test for models localizing the γ-ray emission in blazars (e.g. Marscher & Jorstad 2010). This type of cross-correlation analysis, performed for several other blazars, has recently shown that γ-ray and optical flares are usually coincident (e.g. Raiteri et al. 2012, 2013) and associated with the passage of a new superluminal knot through the 43 GHz radio core (e.g. Marscher et al. 2010; Agudo et al. 2011). Casadio et al. (2015) studied the evolution of the parsec-scale jet in CTA 102 with ultra-high angular resolution through a sequence of 80 total and polarized intensity Very Long Baseline Array (VLBA) images at 43 GHz, covering the time span from 2007 June to 2014 June. They have shown that a flare seen both in γ and optical bands took place $\gtrsim$12 pc from the black hole, and suggested the synchrotron self-Compton (SSC) process as the source of the γ-ray emission.

In this paper, we analyse the largest outburst of CTA 102 to date at optical and γ-ray bands (Larionov, Blinov & Jorstad 2012). A preliminary analysis of our data collected through fall 2012 is reported in Larionov et al. (2013a); in the present paper, we extend the data set-up to the end of 2015. In Section 2, we describe our observational data and their reduction; in Section 3.1 we analyse the colour variability of CTA 102 and evolution of its spectral energy distribution (SED); Section 3.2 deals with γ–optical correlations. Optical spectra are discussed in Section 3.3. The polarimetric behaviour of this blazar and a model describing its temporal evolution are presented in Section 4. The final conclusions are summarized in Section 5.

2 OBSERVATIONS AND DATA REDUCTION

2.1 Optical and near-infrared photometry

The Glast-Agile support programme of the Whole Earth Blazar Telescope (GASP–WEBT; see e.g. Villata et al. 2008, 2009) observations in 2008–2013 were performed in the *R* band at the following observatories: Belogradchik, Calar Alto, Crimean Astrophysical, Lowell (Perkins telescope), Lulin, Mount Maidanak, New Mexico Skies (iTelescopes), Roque de los Muchachos (Liverpool Telescope), Rozhen, Sabadell, Skinakas, St. Petersburg, Teide (IAC80), and Tijarafe. *BVI* photometric data are from St. Petersburg and Lowell observatories. The *V*- and *R*-band light curves are complemented by data taken at Steward Observatory under a monitoring programme in support of the *Fermi* mission. Near-infrared (NIR, *JHK*) data are from the Perkins Telescope, AZT-24 (Campo Imperatore), and Teide (TCS). We also use *B*- and *R*- Mt. Maidanak data during the 2004 outburst. After the nominal end of the GASP campaign, we continued monitoring CTA 102 in optical–NIR bands (Crimean Astrophysical Observatory, Lowell Observatory, St. Petersburg University, Steward Observatory, Campo Imperatore observing station of Rome Observatory) in order to track the post-outburst behaviour. We used photometric sequences in optical bands

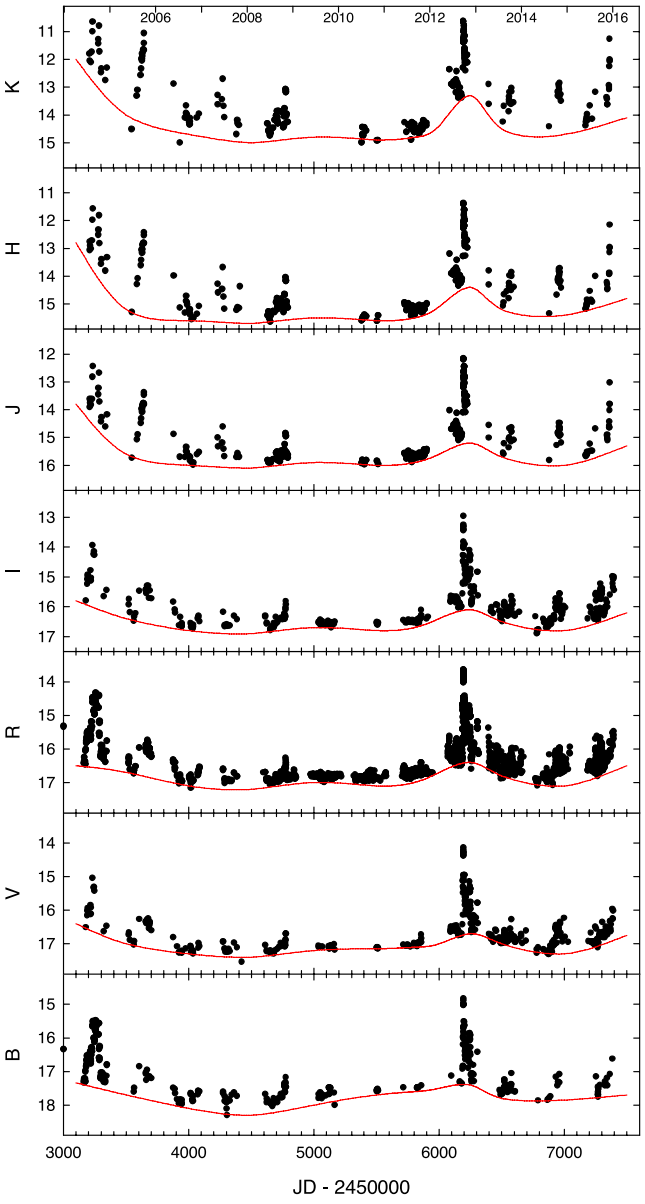

Figure 1. Optical and NIR light curves of CTA 102 over the time interval 2004–2015. Spline curves correspond to lower envelopes for variations in each colour band. Hereafter, we denote TJD=JD−2450000.0.

<71>

reported in Raiteri et al. (1998) and, in NIR bands, those given on the AZT-24 webpage.[1]

We corrected the optical and NIR data for Galactic extinction using values reported in the NASA Extragalactic Database[2] for each filter (Schlafly & Finkbeiner 2011). The magnitude-to-flux transformations were calculated with coefficients determined by Mead et al. (1990).

The optical and NIR light curves of CTA 102 during the 2004–2015 time interval are shown in Fig. 1; spline curves correspond to lower envelopes of variations in each colour band. We note that during both the 2004 and 2012 outbursts the amplitudes of long-term (marked with splines) and short-term (individual data points) variations increase with wavelength, as is common in flat-spectrum radio quasars.

2.2 Optical polarimetry

We use polarimetric data collected at St. Petersburg University (Crimea and St. Petersburg), Lowell (Perkins), Steward, and Calar Alto observatories, supplementing these with data from the Kanata telescope (Itoh et al. 2013). Instrumental polarization was derived from measurements of stars located near the object under the assumption that their radiation is intrinsically unpolarized. The Galactic latitude of CTA102 is -38° and $A_V = 0.16$ mag, so that interstellar polarization (ISP) in its direction is less than 0.6 per cent. To correct for ISP, the mean relative Stokes parameters of nearby stars were subtracted from the relative Stokes parameters of the object. This removes the instrumental polarization as well. The fractional polarization has been corrected for statistical bias, according to Wardle & Kronberg (1974). Fig. 2 presents the flux and polarization behaviour of CTA 102 for 2005–2015. We supplement this plot with a panel showing the γ-ray light curve from the *Fermi* LAT in order to demonstrate that the most prominent γ-ray activity ever recorded for this source was observed during the 2012 September–October optical outburst. In Fig. 3, we present a blow-up of the most active interval of the 2012 outburst. From visual inspection of these figures, it is apparent that during the entire time range covered by *Fermi* observations up to the 2012 season, CTA 102 remained inactive at both γ-ray and optical bands; the degree of polarization was mostly $\leq$10 per cent, while the electric-vector position angle (EVPA) showed marked variations over the range $[-200^\circ, 400^\circ]$. We resolve the $\pm 180^\circ$ ambiguity by adding/subtracting 180° each time that the subsequent value of the EVPA is $>90^\circ$ less/more than the preceding one. Occasional clockwise rotations of the polarization vector by up to $\sim 700^\circ$ are apparent. The onset of the activity in the 2012 season was accompanied by a violent increase of optical polarization activity. The degree of polarization exceeded 20 per cent at some epochs, during which the position angle varied over the range 150°–300°.

2.3 γ-ray observations

The γ-ray data were obtained with the *Fermi* (LAT), which observes the entire sky every 3 h at energies of 20 MeV–300 GeV (Atwood et al. 2009). We analysed the LAT data in the energy range 0.1–200 GeV using the unbinned likelihood analysis of the standard *Fermi* analysis software package Science Tools v9r33p0 and instrument response function `P8R2_SOURCE_V6`. Source class photons

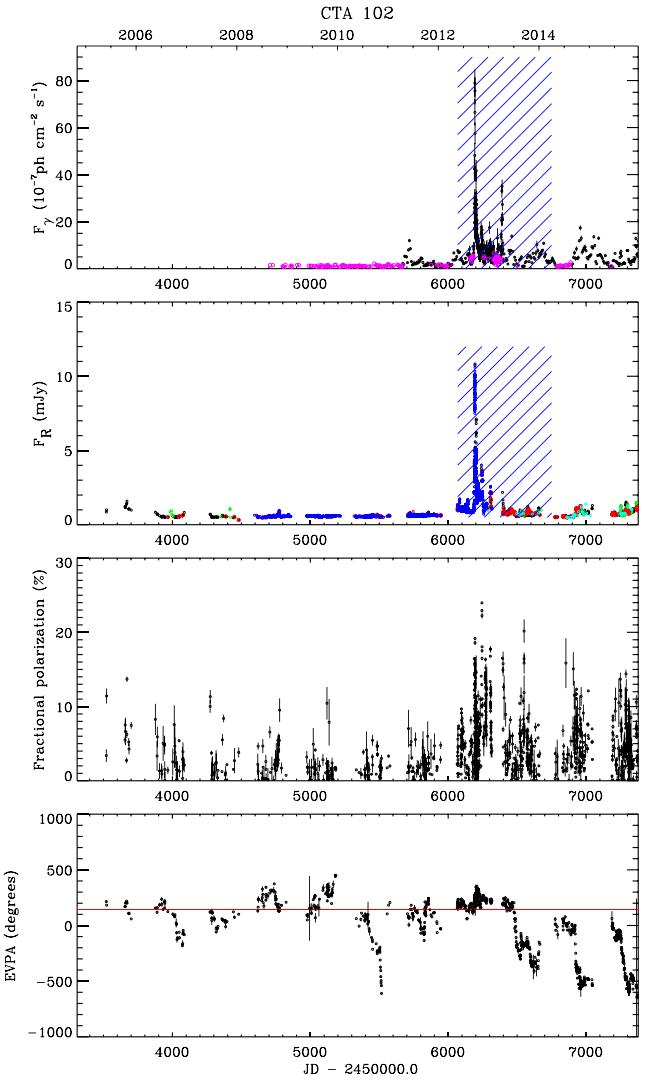

Figure 2. From top to bottom: γ-ray and optical flux evolution, optical fractional polarization, and position angle of polarization of CTA 102 over the time interval 2005–2015. Magenta points in the γ-ray light curve indicate upper limits; blue symbols in the optical panel denote GASP data. Shaded areas in two upper panels mark the outburst time interval, as discussed in Section 3.2. The red line in the EVPA panel corresponds to the mean direction of mm-wave radio jet.

(`evclass=128` and `evtype=3`) were selected within a 15° region of interest centred on the blazar. Cuts in the satellite zenith angle ($<100^\circ$) and rocking angle ($<52^\circ$) were used to exclude the Earth limb background. The diffuse emission from the Galaxy was modelled using spatial model `gll_iem_v06`. The extragalactic diffuse and residual instrumental backgrounds were included in the fit as an isotropic spectral template `iso_source_v05`. The background model[3] includes all sources from the 3FGL catalogue within 15° of the blazar. Photon fluxes of sources beyond 10° from the blazar and spectral shapes of all targets were fixed to their values reported in the 3FGL catalogue. The source is considered to be detected if the test statistic TS provided by the analysis exceeds 10, which corresponds to approximately a 3σ detection level (Nolan

[1] http://www.astro.spbu.ru/staff/vlar/NIRthumbs/cta102.html
[2] http://ned.ipac.caltech.edu/
[3] http://fermi.gsfc.nasa.gov/ssc/data/access/lat/4yr_catalog/gll_psc_v16.xml

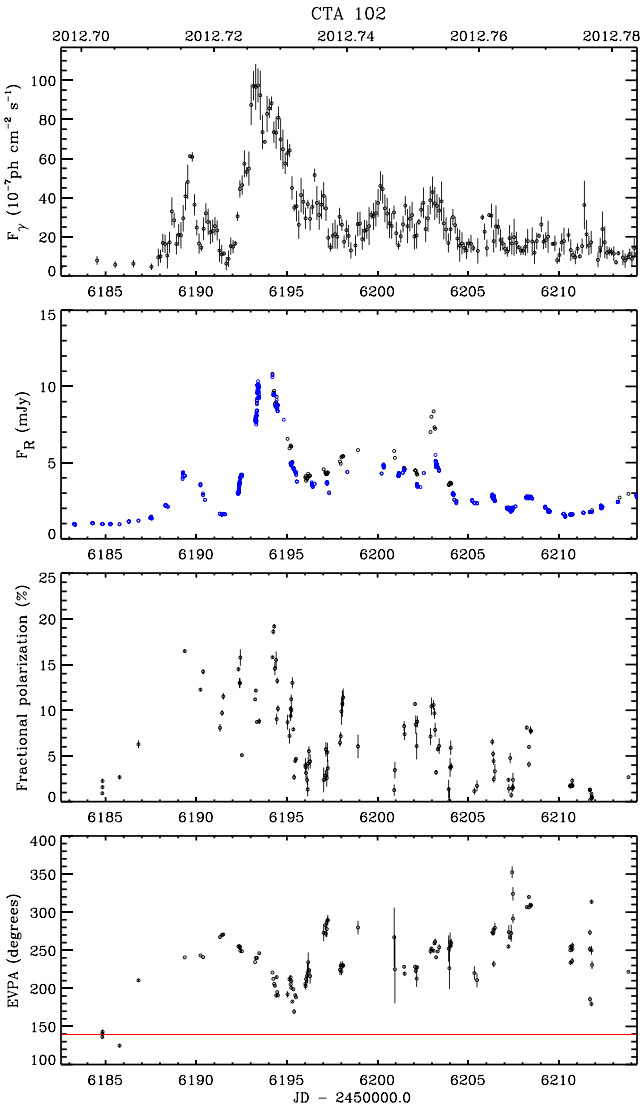

Figure 3. Blow-up of Fig. 2 during the 2012 September–October flare.

et al. 2012). The systematic uncertainties in the effective LAT area do not exceed 10 per cent in the energy range we use (Ackermann et al. 2012). This makes them insignificant with respect to the statistical errors, which dominate over the short time-scales analysed in this paper. Moreover, our analysis is based on the relative flux variations. Because of this, the systematic uncertainties are not taken into account.

Different time bins $t_{\rm int}$, from 12 h to 7 d, were used, depending on the flux density of the object. This maximizes the availability of detections at temporal resolutions that are as short as possible.

2.4 *Swift* observations

2.4.1 *Optical and ultraviolet data*

Swift Ultraviolet/Optical telescope (UVOT) observations were performed in the optical *v*, *b*, and *u* bands, as well as in the UV filters *uvw*1, *uvm*2, and *uvw*2. We reduced the data with HEASOFT package version 6.10, with the 20101130 release of the *Swift*/UVOTA CALDB. Multiple exposures in the same filter at the same epoch were summed with `uvotimsum`, and then aperture photometry was performed with the task `uvotsource`. We used an aperture radius of 5 arcsec centred on the source, and background from an annulus between 25 and 35 arcsec radii. To take the spectral shape of CTA 102 into account, we re-calibrated the effective wavelengths and count-to-flux conversion factors as explained in Raiteri et al. (2010), using a power-law fit to the average source spectrum. This also produced a better agreement between the ground-based and space data than when using the Breeveld et al. (2011) calibrations. Galactic extinction was calculated by convolving the Cardelli, Clayton & Mathis (1989) mean extinction laws with the filter effective areas and source flux. All of the derived parameters are given in Table 1.

Table 1. *Swift* calibrations used for CTA 102 analysis.

Bandpass	*v*	*b*	*u*	*uw*1	*um*2	*uw*2
λ, Å	5427	4353	3470	2595	2250	2066
A_λ, mag	0.24	0.32	0.38	0.54	0.67	0.64
conv. factors	2.603	1.468	1.649	4.420	8.372	5.997

Notes. Units of count rate to flux conversion factors are 10^{-16} erg cm^{-2} s^{-1} Å^{-1}.

2.4.2 *X-ray data*

The X-ray data were obtained over a photon energy range of 0.3–10 keV by the *Swift* X-ray Telescope (XRT). We reduced the data using HEASOFT package version 6.11. The standard `xrtpipeline` task was used to calibrate and clean the events. We selected events with grades 0–12 in `pc` mode and 0–2 in `wt` mode. An ancillary response file was created with a point spread function correction using the `xrtmkarf` task, and the data were rebinned with the `grppha` task to ensure a minimum of 10 photons in every newly defined channel. We fit the spectra with the spectral analysis tool XSPEC using a power-law model with minimum χ^2 value and fixing the hydrogen column density ($N_{\rm H} = 5.04 \times 10^{20}$ cm^{-2}) according to the measurements of Dickey & Lockman (1990). We used Cash statistics along with Monte Carlo spectral simulations to estimate the goodness of fit at a confidence level of 90 per cent. If the parameters failed a goodness-of-fit test, we rebinned the data with a minimum of 20 photons in each spectral channel and repeated the model-fit procedure. If the new model still did not satisfy a goodness-of-fit test, we rejected the data; this occurred only in two cases.

3 RESULTS

3.1 Colour evolution

The question of whether a blazar's radiation becomes redder or bluer when it brightens is a topic of numerous papers. It is commonly agreed that the relative contributions of the big blue bump (BBB) and Doppler-boosted synchrotron radiation from the jet are different between quiescence and outbursts, and that this leads to variability of the SED. The situation is even more complicated in the cases like CTA 102, where broad emission lines contaminate the wide photometric bands (e.g. the Mg II λ2800 Å line is redshifted to λ5700 Å). A straightforward way to isolate the contribution of the component of radiation that is variable on the shortest time-scales (presumably, synchrotron radiation) has been suggested by Hagen-Thorn (see e.g. Hagen-Thorn et al. 2008, and references therein). The method is based on plots of (quasi-)simultaneous flux densities in different colour bands and the construction of the relative continuum spectrum based on the slopes of the sets of flux–flux relations thus obtained.

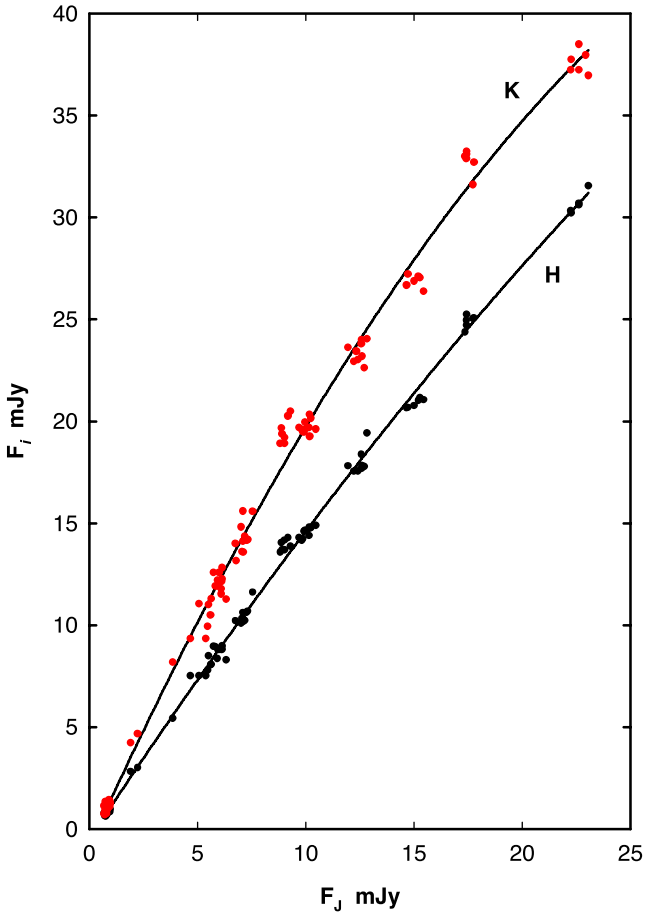

Figure 4. Flux–flux relations between the NIR J band and the H (black circles) and K (red circles) bands over the time interval 2008–2012. Lines are second-order polynomial fits.

An example of such an approach is given in Fig. 4, where the flux densities in the H and K bands are plotted against the J-band flux density. The lack of linearity between variations in corresponding bands means that the low- and high-flux behaviours could reflect variability of different sources of radiation (e.g. the ambient jet in low states and a shock in high states). Alternatively, if the same component is responsible for all of the variability patterns, the parameters of this component change significantly in a manner that depends on the brightness of the source. In Fig. 5, we plot relative SEDs of the variable component in CTA 102 in quiescence and during the 2012 outburst from *Swift* UV to NIR bands, showing marked hardening of the SED during the high state, together with substantial curvature (convexity) of the spectrum. Since the logarithmic spectral shapes are far from linear, we are not able to determine a single power-law slope α (in the sense $F_\nu \propto \nu^{-\alpha}$) for the entire optical–NIR range. As a value that characterizes these slopes, we select the tangent to the spectrum at the central R-band frequency. For the quiescent stage, we obtain $\alpha_R = 1.78 \pm 0.05$, and for the outburst $\alpha_R = 1.50 \pm 0.03$. We emphasize that these values refer to the *variable* component only, not to the entire flux. Meanwhile, if we look at the evolution of the *total* flux optical SED, we see the opposite: $\alpha_R = 0.4 \pm 0.1$ during quiescence and $\alpha_R = 1.4 \pm 0.1$ for the outburst. The closeness of the latter value to that obtained for the variable source is caused by the fact that, during the outburst state, the relative contribution of intrinsically blue underlying

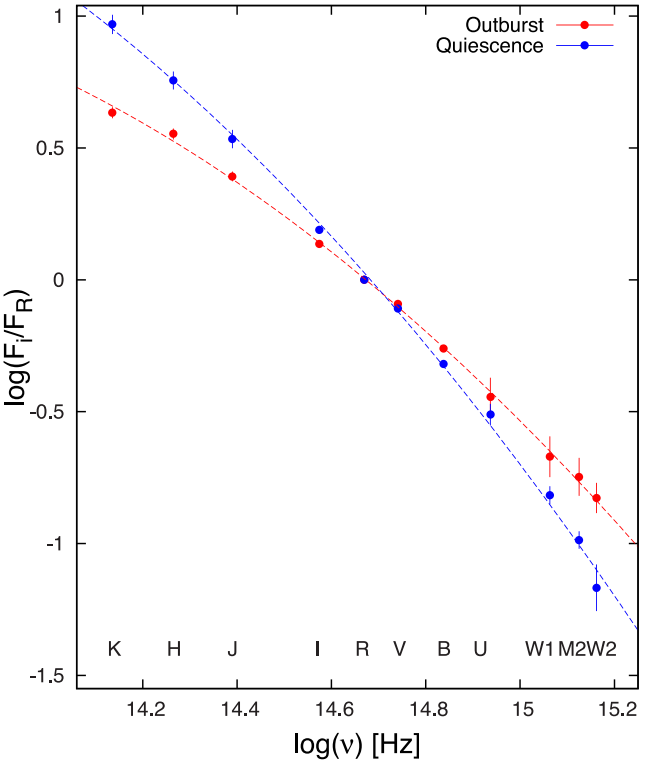

Figure 5. Relative continuum spectra of the *variable* component in CTA 102 during quiescence (blue) and the 2012 flare (red) from NIR to UV.

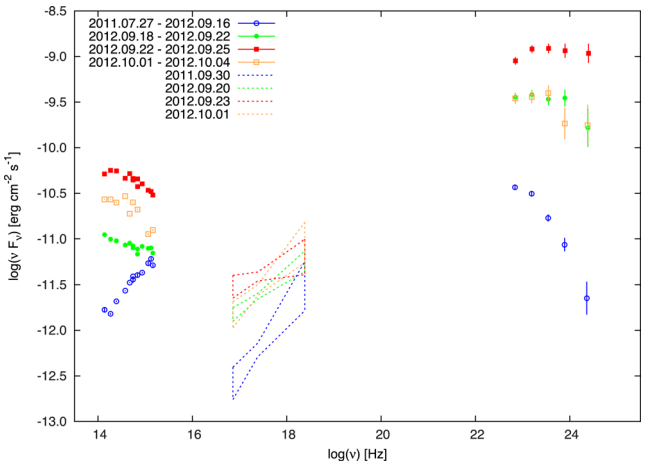

Figure 6. (Quasi-)simultaneous SEDs of CTA 102 from NIR to γ-ray bands.

components (BBB+ Mg II line emission) becomes small compared to the synchrotron radiation of the variable source.

Simultaneous spectral hardening in the γ-ray region during the outburst is also apparent in Fig. 6. Notice that in this figure we plot total flux densities, in contrast to Fig. 5.

We hypothesize, as suggested in Larionov, Villata & Raiteri (2010) for the case of BL Lac, that this spectral hardening of the variable optical and γ-ray components is mostly caused by a change of the viewing angle of the emitting zone, which shifts in frequency the synchrotron spectrum due to increased Doppler boosting. Some (or all) of the hardening could also result from the population of emitting electrons becoming enriched with a high-energy extension during the outburst compared to the quiescent state.

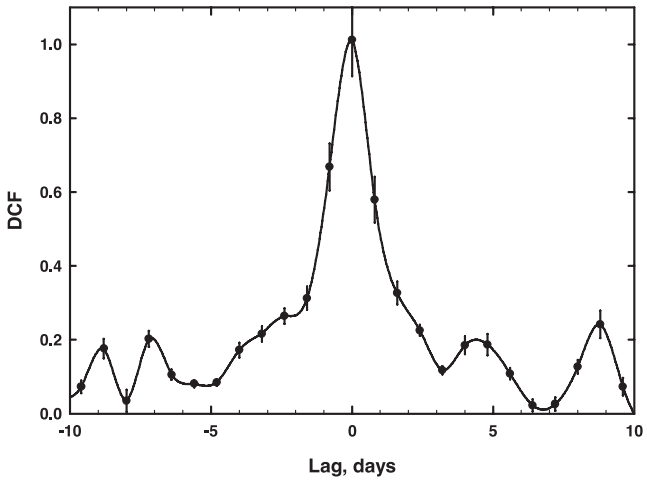

Figure 7. DCF between optical and γ-ray light curves of CTA 102. Negative delays correspond to γ-ray lagging behind optical variations. The zero delay at the peak of the DCF indicates cospatiality of the active regions.

3.2 γ-ray–optical correlations

We have calculated the discrete correlation function (DCF; Edelson & Krolik 1988; Hufnagel & Bregman 1992) between the optical and γ-ray flux variations of CTA 102 during 2012. The results, given in Fig. 7, clearly demonstrate that there is no time delay between the variations in the two energy bands within the accuracy of the DCF method. The value of the lag between optical and γ-ray variations, based on the DCF centroid position, is $-0\overset{d}{.}05 \pm 0\overset{d}{.}02$. One may note that there are secondary 'humps' at ≈4.5 and ≈9 d. We surmise that these are caused by recurring optical and γ-ray sub-flares during the 2012 outburst (see Section 4.1 and Fig. 14).

This lack of delay allows us to compare directly the optical and γ-ray flux densities. To do this, we (1) bin the *R*-band optical data so that the mid-point and size of each optical bin correspond to the mid-point and size of the respective γ-ray bin, and (2) subtract from the binned optical data a tentative value of the flux of (quasi-)permanent emission components (BBB + QSO-like emission with a prominent Mg II line). Combined, this amounts to $\log(\nu F_\nu) = -11.5$ in the *R* band, which is similar to the value obtained for CTA 102 in Raiteri et al. (2014), corresponding to as much as 50 per cent of the total quiescent flux. Fig. 8 demonstrates clear differences during the various stages of CTA 102 activity. The onset of γ-ray activity (TJD 5700–5943, blue circles in Fig. 8) corresponds to a rather stable optical level. During the outburst stage (TJD 6069–6678, red circles), we see a relation between γ-ray and optical fluxes of the form $F_\gamma \propto F_{\rm opt}^{1.12\pm0.04}$, while in the post-outburst stage, TJD 6776–7231 (green circles), $F_\gamma \propto F_{\rm opt}^{2.21\pm0.32}$.

We assume that the variable optical emission is mostly synchrotron radiation from the jet, while the γ-ray emission is from inverse Compton (IC) scattering of optical/IR photons by the jet's relativistic electrons. The origin of the seed photons may be external to the jet, e.g. hot dust continuum or broad-line emission (external Compton or EC model), or synchrotron photons from the jet (SSC model). In the EC model, we expect the respective fluxes to vary as $F_C \propto F_{\rm sync}$, since only the relativistic electron population is in common, while in the SSC model $F_C \propto F_{\rm sync}^2$, since both the relativistic electrons and emission radiated by them are involved in the high-energy photon production. Here, $F_{\rm sync}$ is the flux of the synchrotron radiation and F_C is that of the IC emission. These dependences will be altered slightly by the different optical and γ-ray

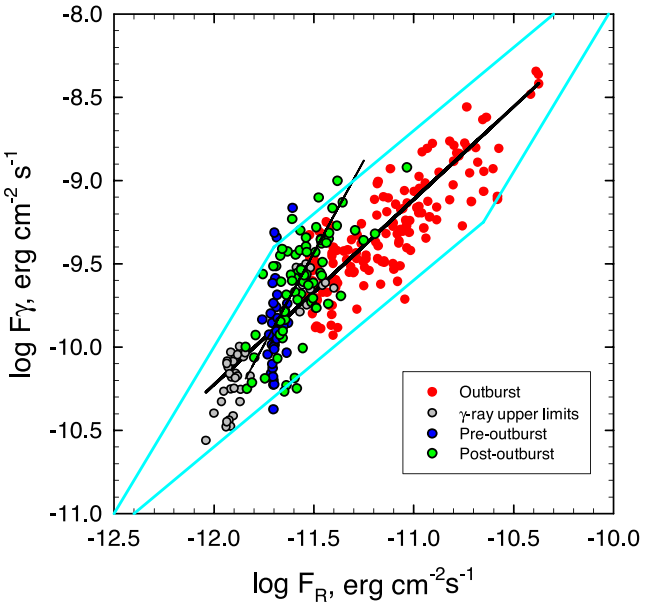

Figure 8. γ-ray–optical flux–flux diagram. Slopes of the linear (on a logarithmic scale) fits are 1.12 ± 0.04 (outburst stage) and 2.21 ± 0.32 (post-outburst stage). Almost all data points lie inside the parallelogram, whose sides have slopes of 1 and 2 (see the text).

K-corrections at times when the optical and γ-ray spectral indices are not the same.

A competing explanation of the near-unity slope between optical and γ-ray fluxes, besides the EC model, is that their variability is mostly caused by variations of Doppler factor resulting from changes in the viewing angle. This can occur if the entire jet changes its direction (wobbles or precesses), or if different parts of the jet cross-section with various velocity vectors relative to the mean become periodically or sporadically bright as time passes. Under this scenario, the post-outburst stage with presumably small variations in viewing angle produces SSC-like variability that was hidden during the height of the outburst under higher amplitude Doppler-boosted variations of geometrical origin.

Thus, the data distribution in Fig. 8 can be explained as due to two concurrent effects, with slopes of ∼1 (Doppler factor variations) and ∼2 (intrinsic SSC dependence), so that the data mostly lie inside a circumscribed parallelogram with sides having the above slopes. The relative lengths of these sides depend on the relative dominance of the two effects, and the best-fitting slope of the entire distribution can vary from ∼1 to 2. The best-fitting slope of 1.12 during the outburst would indicate almost complete dominance of the Doppler factor variations, while the best fit found for the post-outburst stage implies an essentially constant Doppler factor during that period. Another advantage of this model is that it can explain the polarimetric variability in CTA 102 (see Section 4.1).

3.3 Optical spectra

We analyse the optical spectroscopic behaviour of CTA 102 using the data taken at Steward Observatory of the University of Arizona for the 'Ground-based Observational Support of the *Fermi* Gamma-ray Space Telescope' programme[4] at the 2.3 m Bok telescope and 1.54 m Kuiper telescope from 2008 to 2015. All of these spectra

[4] http://james.as.arizona.edu/~psmith/Fermi/

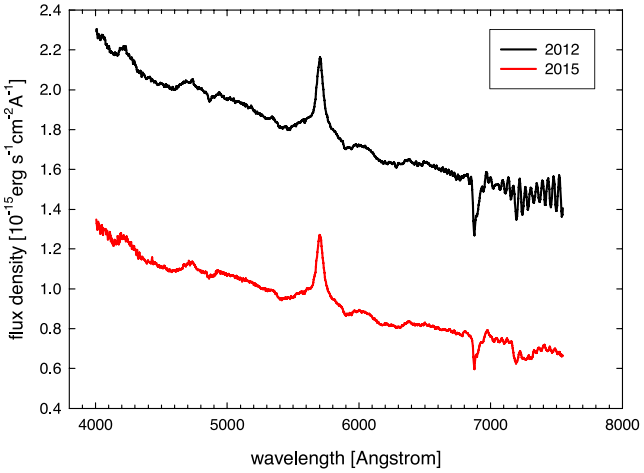

Figure 9. Averaged spectra of CTA 102 during the 2012 and 2015 observing seasons. Absorption features longwards of λ6800 Å are of telluric origin.

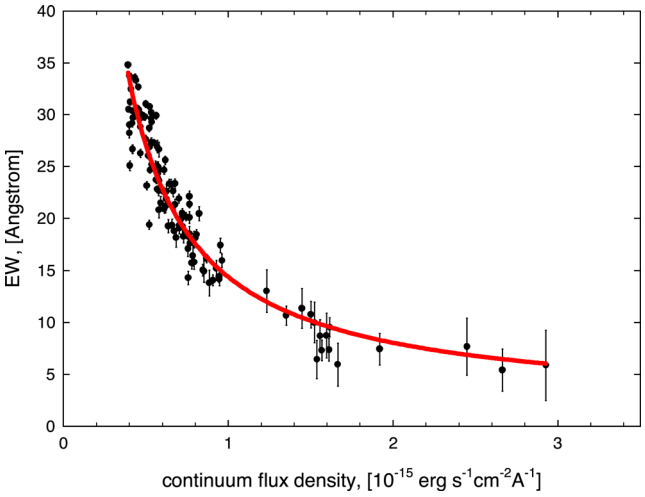

Figure 10. EW of Mg II line versus continuum flux over the time interval 2009–2015. The red curve corresponds to the expected EW if the line flux remains constant.

contain a prominent Mg II λ2800 Å broad emission line redshifted to λ5700 Å. Fig. 9 displays averaged spectra for the 2012 and 2015 observing seasons. We use 133 spectra spread over the time interval 2009–2015 to check whether there is any correlation between continuum (mostly synchrotron) flux density variations and changes in the Mg II line flux.

We evaluate the line parameters (the equivalent width, EW, and the line full width at half-maximum, FWHM), fitting the line profile with a single Gaussian function superposed on a featureless continuum. The results are presented in Fig. 10, where EW is plotted against the continuum flux density; the inverse proportionality of these two quantities indicates that the line flux is stable. The red curve corresponds to the expected EW if the line flux remains constant. These results imply that enhanced activity of the jet has little or no effect on the broad-line region (BLR), where one expects most or all of the Mg II emission to originate.

We note that similar results have been obtained for other blazars, e.g. 3C 454.3 (Raiteri et al. 2008) and OJ 248 (Carnerero et al. 2015). However, some cases of correlated broad-line flux variability connected to γ-ray variability have indeed been reported by León-Tavares et al. (2013), Isler et al. (2013), and Isler et al. (2015).

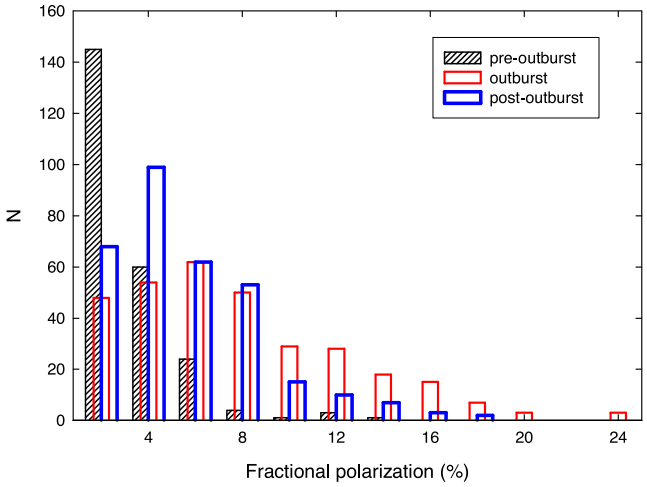

Figure 11. Histograms of fractional polarization before (black shaded), during (red), and after (blue) the 2012 outburst.

We measure the Mg II line FWHM, from which one can derive the velocity of the gas clouds in the BLR, and obtain $v_{\rm FWHM} = 2100 \pm 250\,{\rm km\,s^{-1}}$. This value is a lower limit to the actual velocity range of the broad-line clouds, since it depends on the geometry and orientation of the BLR (see e.g. Wills & Brotherton 1995). In fact, because the line of sight to a blazar is probably nearly perpendicular to the accretion disc, the de-projected velocity range is likely to be a factor of $\gtrsim$2 higher than the FWHM given above.

4 DISCUSSION

4.1 Polarimetric behaviour and helical jet model

Our polarimetric data obtained during 2008–2015 allow one to see remarkable changes in the behaviour of CTA 102 that were probably triggered by (or, at least, coincided with) the prominent outburst of 2012. Fig. 11 shows histograms of the polarization degree (PD) before, during, and after the flare. This highlights the increased range of PD variations already seen in Fig. 2. A natural reason for this change is a decrease in the viewing angle of the jet, as already suggested by Casadio et al. (2015) based on analysis of the superluminal apparent motion of knots in VLBA images. However, if we consider the range of values of viewing angles found in that paper (from 3.°9 before the 2012 outburst to 1.°2 after it) and compare the values of PD expected within the moving shock model for polarization variations (see e.g. Fig. 12 and also Larionov et al. 2013b; Raiteri et al. 2013), we find that we would expect to see the opposite: a decrease in PD during the outburst. A positive correlation between the photometric flux and PD may be obtained if the bulk Lorentz factor of the emitting plasma is much higher, e.g. $\Gamma \approx 30$ (dashed line in Fig. 12). In this case, a decrease in viewing angle would increase PD (see also equations 1– 3 in Larionov et al. 2013b). However, such a high value is difficult to reconcile with that found by Casadio et al. (2015), $\Gamma = 17.3$.

Yet another possible reason for this apparent contradiction could be the difference in sizes between the parts of jet responsible for the flaring optical radiation and the centroid of the radio 'core'. In this case, the source of the polarized optical flux could have a mean velocity vector that is less well aligned with the line of sight than that of the radio emission region. This explanation is supported by very different time-scales of variability in optical (few days) and

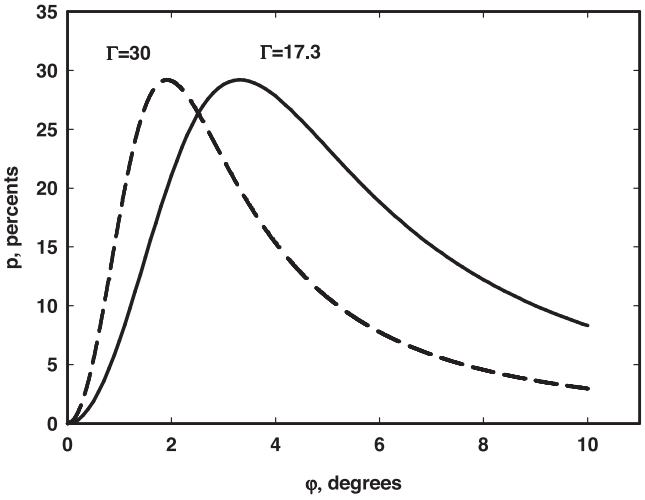

Figure 12. Behaviour of fractional polarization versus viewing angle for plasma compression ratio $\eta = 1.5$, Lorentz factor $\Gamma = 17.3$ (solid line), and $\Gamma = 30$ (dashed line), in the moving shock model.

radio (months) wavelengths and, correspondingly, different sizes of the emission regions (see also Casadio et al. 2015).

Fig. 13 shows the distribution of the absolute Stokes parameters of CTA 102 during both quiescence and different stages of the 2012 activity. We notice that the cluster of (Q, U) points obtained before and after the outburst (more than 300 data points, marked as black circles) is located near the origin of the coordinates. All of the data points are tightly packed around this location, which corresponds to a very low level of polarized flux during quiescence (see also Figs 2 and 11). The onset of the outburst was accompanied by a definite loop-like rotation in the plane of the Stokes parameters, while the fading stage of the outburst included less ordered drifts, misplaced relative to the pre-outburst position. This latter feature may reflect the change in orientation of the jet itself, while the clockwise rotation could arise from spiral movement of the radiating blob through the jet.

As in the case of S5 0716+71 (Larionov et al. 2013b), we propose a model of a relativistic shock moving down a helical jet, or along helical magnetic field lines, to explain these rotations. The main parameters that determine the visible behaviour of the outburst are (1) jet viewing angle θ; (2) pitch angle ζ of the spiral motion and helical field; (3) parameters of polarization of the undisturbed jet; (4) bulk Lorentz factor Γ of the shocked plasma; (5) scaling factor of the exponential rise of the outburst τ; (6) factor k, responsible for different time-scales of the rise and decline of the outburst; (7) period of the shock's spiral revolution in the observer's frame $P_{\rm obs}$; (8) the same period in the source frame; (9) radius of spiral; (10) shocked plasma compression η = ratio of post-shock to pre-shock density; and (11) spectral index of the emitting plasma α.

Some of these parameters can be obtained, or at least constrained, directly from observations. For example, the Lorentz factor Γ during the 2012 outburst is close to 17, according to Casadio et al. (2015); the average level of polarization during quiescence is of the order of 1 per cent (see Fig. 11); the value of $P_{\rm obs} \approx 4\overset{\rm d}{.}7$ is obtained from repeating optical (and γ-ray) sub-flares during the outburst; the mean value of the slope of the synchrotron spectrum is $\alpha = 1.50$, which we obtain from our photometric data (see Section 5 and Fig. 5).

Using relations 1–9 from Larionov et al. (2013b), we obtain the values of the model parameters that are given in Table 2. To

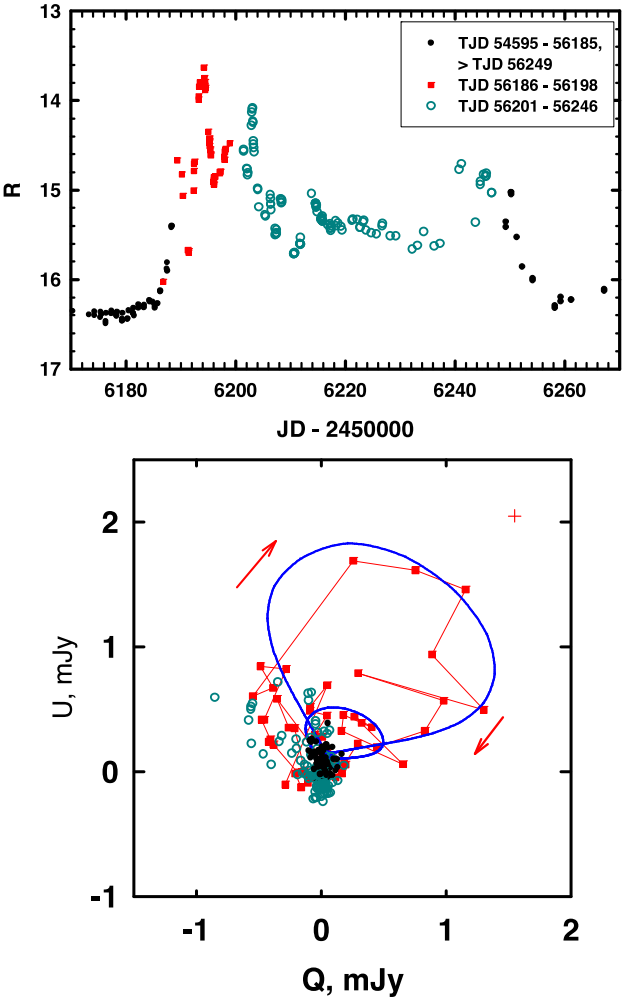

Figure 13. Bottom panel: absolute Stokes parameters Q and U of the optical polarization of CTA 102. The typical errors in the Stokes parameters are shown by the red cross. The blue curve corresponds to the path of the vector of polarization according to our model (see the text). The top panel presents the R-band light curve, with intervals of time colour-coded in the same way as in the plot of Stokes parameters.

Table 2. Model parameters for the photometric and polarimetric behaviour of CTA 102 in 2012 September.

θ°	ζ°	$p_{\rm jet}$	Γ	τ	k	$P_{\rm obs}$	$P_{\rm src}$	r	η	α
(1)	(2)	(3)	(4)	(5)	(6)	(7)	(8)	(9)	(10)	(11)
2.65	0.9	1	18.2	0.75	1.83	4.7	2.35	0.0018	1.35	1.50

Notes. Units: $p_{\rm jet}$ in per cent, r in parsecs, $P_{\rm obs}$ in days, $P_{\rm src}$ in years. τ and k in fractions of $P_{\rm src}$.

confront the model with observational results, we plot both together in Figs 13 and 14. Since our model only takes into account smooth variability caused by a radiating blob moving along a helical path in the jet and neglects the effects caused by turbulence that is probably present, we are able to reproduce only the basic variability pattern. In particular, we see a series of decaying flares after the main outburst (and the precursor preceding it). Nevertheless, the agreement of the model with the Q versus U evolution in Fig. 13 is quite good. The model evolution of the degree of polarization corresponds to an upper envelope to the observational data. This is as expected, since turbulence adds superposed polarization vectors at random

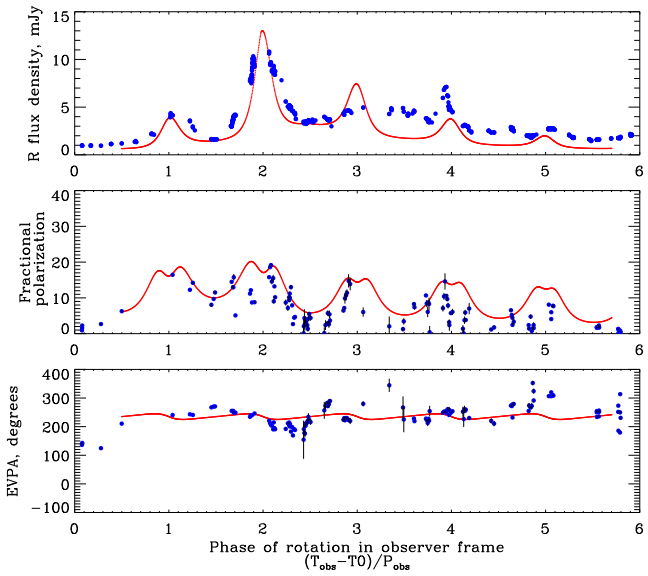

Figure 14. Comparison of optical photometric and polarimetric data during the giant outburst of CTA 102 in 2012, with our model fit.

position angles, which often partially cancel the polarization from the ordered component of the magnetic field.

We note that our finding of clockwise rotation of the polarization vector is supported by the detection of negative circular polarization in the 15 GHz radio emission of CTA 102 by Gabuzda et al. (2008), who used the observation as evidence for a helical magnetic field. In addition, inspection of the EVPA behaviour in Fig. 2 allows one to see at least three episodes of clockwise rotation with amplitude exceeding 700° (TJD 5500, 6500, 7250) and no cases of anticlockwise rotations of similar length. Thus, this appears to be a persistent feature of the blazar, in agreement with an ordered, helical component of the magnetic field.

4.2 Weakness of spectral variations

The Mg II emission line flux is, at most, weakly variable over the course of our observations despite marked changes in the optical synchrotron flux. We consider this to be a consequence of two factors: (1) the part of jet where the outburst occurred is located parsecs outside of the BLR (see Casadio et al. 2015), and (2) the ultra-high amplitude of the 2012 outburst might have been determined to major extent by a change in the viewing angle. The number of ionizing photons traversing the BLR would not significantly change during such a re-orientation of the jet.

4.3 Implication of variable Doppler factor

We have used our photometric and polarimetric data centred on the 2012 outburst to assess the main geometric parameters that govern the overall pattern of Stokes parameter variations within a model of a radiating blob or shock wave that moves along a helical path down the jet. The changes in the viewing angle caused by helical motion imply strong changes in the Doppler factor, from $\delta \approx 28$, when the emission region is closest to our line of sight, to $\delta \approx 16$ when it is farthest. The larger value is similar to $\delta_{\rm var} \approx 30$ obtained by Casadio et al. (2015) based on VLBA data.

Our long-term study of the polarimetric behaviour of CTA 102 allows us to identify at least three episodes of sustained clockwise rotations and no similar episodes of anticlockwise rotation. This repeated behaviour suggests that the cause of the rotations is geometrical rather than the result of random walks related to a disordered magnetic field (although some shorter, apparently random rotations occur as well; Kiehlmann et al. 2016).

As is shown in Figs 2 and 11, the mean level of polarization of CTA 102 substantially increased shortly before the onset of the 2012 outburst, and did not revert to the pre-outburst level until fall 2015. This supports the hypothesis that secular variations of the viewing angle of the jet led to both enhanced photometric activity and corresponding changes in the linear polarization. We can expect that flaring activity in this blazar will be more pronounced than in previous years as long as the jet remains closely aligned with our line of sight. Indeed, as reported by Carrasco et al. (2016), Balonek (2016), and Becerra, Carpenter & Cutini (2016), at the end of 2016 January a new high-amplitude outburst occurred at γ-ray, optical, and NIR bands (see also http://vo.astro.spbu.ru/sites/default/files/optic/cta102R.png). Unfortunately, this happened when the object was difficult to observe owing to proximity to the sun in the sky, so this expected effect cannot yet be verified in detail.

5 CONCLUSIONS

During the GASP/WEBT campaign, we obtained densely sampled optical photometric and polarimetric data around the period of unprecedented optical and γ-ray activity of CTA 102, and combined optical data with contemporaneous observations throughout the γ-ray to NIR frequency range. We find detailed correspondence of optical and γ-ray events, which confirms cospatiality of the synchrotron and IC emission sites. The relation between optical and γ-ray flux during the height of the outburst is roughly linear. This is as expected from either the EC process for the high-energy emission or from variable Doppler boosting acting as the main factor controlling the overall pattern of variability at both energy ranges. However, the Doppler boosting caused by changed viewing angle of the emission region is a preferred explanation for the variability of the total flux and polarization parameters. In contrast, during the decay the relation between the fluxes is, within the uncertainties, consistent with the $F_\gamma \propto F_{\rm opt}^2$ law expected from the SSC mechanism. Presumably, any changes in viewing angle during the decline were too minor to have a dominant effect on the variations in flux.

We have determined the SED of the variable component of synchrotron emission during both quiescence and the stages of outburst, and found appreciable hardening of the SED during the outburst. This hardening could be explained by convexity of the UV–NIR spectrum (see Fig. 5) that moved to higher frequencies owing to an increased Doppler shift as the viewing angle decreased. This effect could have been amplified by an increase in the number of high-energy electrons. The same spectral hardening is apparent in the γ-ray part of the spectrum.

As we can judge from our data, the change of viewing angle that led to enhanced activity in CTA 102 starting in 2012 may have resulted in a higher duty cycle of activity. When the viewing angle is smaller, the Doppler factor is more sensitive to changes in that angle; hence, variations caused by a non-constant viewing angle will be more pronounced and occur over shorter time intervals.

ACKNOWLEDGEMENTS

The radio-to-optical data collected by the GASP–WEBT collaboration are stored in the GASP–WEBT archive; for questions regarding their availability, please contact the WEBT

president, Massimo Villata (villata@oato.inaf.it). The St. Petersburg University team acknowledges support from Russian RFBR grant 15-02-00949, and St. Petersburg University research grants 6.38.335.2015 and 6.42.1113.2016. The research at Boston University was funded in part by NASA Fermi Guest Investigator grants NNX08AV65G, NNX10AO59G, NNX10AU15G, NNX11AO37G, NNX11AQ03G, and NNX14AQ58G. The research at Steward Observatory was funded in part by NASA Fermi Guest Investigator grants NNX09AU10G and NNX12AO93G. Acquisition of the MAPCAT data at Calar Alto is performed at the IAA-CSIC and is supported by the Spanish Ministry of Economy and Competitiveness (MINECO) grant AYA2013-40825-P. IA acknowledges support by a Ramón y Cajal grant of the MINECO. AZT-24 observations are made within an agreement between Pulkovo, Rome and Teramo observatories. The PRISM camera at Lowell Observatory was developed by K. Janes et al. at BU and Lowell Observatory, with funding from the NSF, BU, and Lowell Observatory. This research was conducted in part using the Mimir instrument, jointly developed at Boston University and Lowell Observatory and supported by NASA, NSF, and the W. M. Keck Foundation. Calar Alto Observatory is jointly operated by the Max-Planck-Institut für Astronomie and the Instituto de Astrofísica de Andalucía-CSIC. This research was partially supported by the Scientific Research Fund of the Bulgarian Ministry of Education and Sciences under grant DO 02-137 (BIn-13/09). The Maidanak Observatory team acknowledges support from Uzbekistan Academy of Sciences grant F2-FA-F027. Skinakas Observatory is a collaborative project of the University of Crete, the Foundation for Research and Technology – Hellas, and the Max-Planck-Institut für Extraterrestrische Physik. This paper is partly based on observations made with the IAC80 and TCS telescopes operated by the Instituto de Astrofisica de Canarias in the Spanish Observatorio del Teide on the island of Tenerife.

REFERENCES

Ackermann M. et al., 2012, ApJS, 203, 4
Agudo I. et al., 2011, ApJ, 726, L13
Angel J. R. P., Stockman H. S., 1980, ARA&A, 18, 321
Atwood W. B. et al., 2009, ApJ, 697, 1071
Balonek T., 2016, Astron. Telegram, 8598
Becerra J., Carpenter B., Cutini S., 2016, Astron. Telegram, 8722
Blom J. J. et al., 1995, A&A, 295, 330
Breeveld A. A., Landsman W., Holland S. T., Roming P., Kuin N. P. M., Page M. J., 2011, in McEnery J. E., Racusin J. L., Gehrels N., eds, AIP Conf. Ser. Vol. 1358, Gamma Ray Bursts 2010. Am. Inst. Phys., New York, p. 373
Cardelli J. A., Clayton G. C., Mathis J. S., 1989, ApJ, 345, 245
Carnerero M. I. et al., 2015, MNRAS, 450, 2677
Carrasco L., Recillas E., Miramon J., Porras A., Chavushyan V., Carraminana A., 2016, Astron. Telegram, 8590
Casadio C. et al., 2015, ApJ, 813, 51
Dickey J. M., Lockman F. J., 1990, ARA&A, 28, 215
Edelson R. A., Krolik J. H., 1988, ApJ, 333, 646
Gabuzda D. C., Vitrishchak V. M., Mahmud M., O'Sullivan S. P., 2008, MNRAS, 384, 1003
Hagen-Thorn V. A., Larionov V. M., Jorstad S. G., Arkharov A. A., Hagen-Thorn E. I., Efimova N. V., Larionova L. V., Marscher A. P., 2008, ApJ, 672, 40
Hufnagel B. R., Bregman J. N., 1992, ApJ, 386, 473
Isler J. C. et al., 2013, ApJ, 779, 100
Isler J. C. et al., 2015, ApJ, 804, 7
Itoh R. et al., 2013, ApJ, 768, L24
Katajainen S. et al., 2000, A&AS, 143, 357
Kiehlmann S. et al., 2016, A&A, 590, A10
Larionov V. M., Villata M., Raiteri C. M., 2010, A&A, 510, A93
Larionov V., Blinov D., Jorstad S., 2012, Astron. Telegram, 4397
Larionov V. M. et al., 2013a, EPJ Web Conf., 61, 04019
Larionov V. M. et al., 2013b, ApJ, 768, 40
León-Tavares J. et al., 2013, ApJ, 763, L36
Marscher A. P., Jorstad S. G., 2010, in Savolainen T., Ros E., Porcas R. W., Zensus J. A., eds, Fermi Meets Jansky – AGN in Radio and Gamma Rays. Max-Planck-Institut f. Radioastronomie, Bonn, p. 171
Marscher A. P. et al., 2010, ApJ, 710, L126
Mead A. R. G., Ballard K. R., Brand P. W. J. L., Hough J. H., Brindle C., Bailey J. A., 1990, A&AS, 83, 183
Moore R. L., Stockman H. S., 1981, ApJ, 243, 60
Nolan P. L. et al., 1993, ApJ, 414, 82
Nolan P. L. et al., 2012, ApJS, 199, 31
Osterman Meyer A., Miller H. R., Marshall K., Ryle W. T., Aller H., Aller M., Balonek T., 2009, AJ, 138, 1902
Pica A. J., Smith A. G., Webb J. R., Leacock R. J., Clements S., Gombola P. P., 1988, AJ, 96, 1215
Raiteri C. M., Villata M., Lanteri L., Cavallone M., Sobrito G., 1998, A&AS, 130, 495
Raiteri C. M. et al., 2008, A&A, 491, 755
Raiteri C. M. et al., 2010, A&A, 524, A43
Raiteri C. M. et al., 2012, A&A, 545, A48
Raiteri C. M. et al., 2013, MNRAS, 436, 1530
Raiteri C. M. et al., 2014, MNRAS, 442, 629
Sandage A., Wyndham J. D., 1965, ApJ, 141, 328
Schlafly E. F., Finkbeiner D. P., 2011, ApJ, 737, 103
Villata M., Raiteri C. M., Sobrito G., de Francesco G., Lanteri L., Cavallone M., 2001, Astrophys. Lett. Commun., 40, 123
Villata M. et al., 2008, A&A, 481, L79
Villata M. et al., 2009, A&A, 504, L9
Wardle J. F. C., Kronberg P. P., 1974, ApJ, 194, 249
Wills B. J., Brotherton M. S., 1995, ApJ, 448, L81

[1]*Astronomical Institute, St.-Petersburg State University, 198504 St.-Petersburg, Russia*
[2]*Pulkovo Observatory, 196140 St.-Petersburg, Russia*
[3]*INAF, Osservatorio Astrofisico di Torino, via Osservatorio 20, I-10025 Pino Torinese, Italy*
[4]*Institute for Astrophysical Research, Boston University, Boston, MA, 22015 USA*
[5]*Instituto de Astrofisíca de Andalucía, CSIC, E-18080 Granada, Spain*
[6]*Steward Observatory, University of Arizona, Tucson, AZ 85721, USA*
[7]*Instituto de Astrofisica de Canarias (IAC), La Laguna, E-38200 Tenerife, Spain*
[8]*Departamento de Astrofisica, Universidad de La Laguna, La Laguna, Tenerife, Spain*
[9]*Institute of Astronomy, Bulgarian Academy of Sciences, BG-1784 Sofia, Bulgaria*
[10]*Department of Physics and Institute for Plasma Physics, University of Crete, GR-71003 Heraklion, Greece*
[11]*Foundation for Research and Technology – Hellas, IESL, Voutes, GR-7110 Heraklion, Greece*
[12]*Armagh Observatory, UK*
[13]*Crimean Astrophysical Observatory, P/O Nauchny, 298409, Russia*
[14]*Department of Astronomy, Faculty of Physics, Sofia University, BG-1164 Sofia, Bulgaria*
[15]*EPT Observatories, Tijarafe, E-38780 La Palma, Spain*
[16]*INAF, TNG Fundacion Galileo Galilei, E-38712 La Palma, Spain*
[17]*Graduate Inst. of Astronomy, National Central Univ., Jhongli, Taiwan*
[18]*INAF, Osservatorio Astronomico di Roma, I-00040 Monte Porzio Catone, Italy*
[19]*Maidanak Observatory of the Ulugh Beg Astronomical Institute, Uzbekistan*
[20]*Department of Physical Sciences, Hiroshima University, Japan*
[21]*Agrupació Astronòmica de Sabadell, Spain*
[22]*Department of Physics, University of Colorado, Denver, CO 80217-3364, USA*

This paper has been typeset from a TEX/LATEX file prepared by the author.

Monthly Notices of the ROYAL ASTRONOMICAL SOCIETY

MNRAS **462,** 2396–2417 (2016) doi:10.1093/mnras/stw1797
Advance Access publication 2016 July 28

Long-term photometry of IC 348 with the Young Exoplanet Transit Initiative network

D. J. Fritzewski,[1,2★] M. Kitze,[1] M. Mugrauer,[1] R. Neuhäuser,[1] C. Adam,[1] C. Briceño,[3] S. Buder,[1,4] T. Butterley,[5] W.-P. Chen,[6] B. Dinçel,[1,7] V. S. Dhillon,[8,9] R. Errmann,[1,10] Z. Garai,[11] H. F. W. Gilbert,[1] C. Ginski,[1,12] J. Greif,[1] L. K. Hardy,[8] J. Hernández,[13,14] P. C. Huang,[6] A. Kellerer,[15] E. Kundra,[11] S. P. Littlefair,[8] M. Mallonn,[2] C. Marka,[1,16] A. Pannicke,[1] T. Pribulla,[11] St. Raetz,[1,17] J. G. Schmidt,[1,18] T. O. B. Schmidt,[1,19] M. Seeliger,[1] R. W. Wilson[5] and V. Wolf[1]

Affiliations are listed at the end of the paper

Accepted 2016 July 20. Received 2016 July 20; in original form 2016 June 28

ABSTRACT

We present long-term photometric observations of the young open cluster IC 348 with a baseline time-scale of 2.4 yr. Our study was conducted with several telescopes from the Young Exoplanet Transit Initiative (YETI) network in the Bessel *R* band to find periodic variability of young stars. We identified 87 stars in IC 348 to be periodically variable; 33 of them were unreported before. Additionally, we detected 61 periodic non-members of which 41 are new discoveries. Our wide field of view was the key to those numerous newly found variable stars. The distribution of rotation periods in IC 348 has always been of special interest. We investigate it further with our newly detected periods but we cannot find a statistically significant bimodality. We also report the detection of a close eclipsing binary in IC 348 composed of a low-mass stellar component ($M \gtrsim 0.09\,\mathrm{M}_\odot$) and a K0 pre-main-sequence star ($M \approx 2.7\,\mathrm{M}_\odot$). Furthermore, we discovered three detached binaries among the background stars in our field of view and confirmed the period of a fourth one.

Key words: techniques: photometric – binaries: eclipsing – starspots – stars: variables: general – stars: variables: T Tauri, Herbig Ae/Be – open clusters and associations: individual: IC 348.

1 INTRODUCTION

The transit technique for finding planetary candidates is applied in several ground-based (e.g. Bakos et al. 2004; Nutzman & Charbonneau 2008) and space-based surveys (e.g. Bordé, Rouan & Léger 2003; Ricker et al. 2014). This work is part of a project within the ground-based Young Exoplanet Transit Initiative (YETI; Neuhäuser et al. 2011). We used the data obtained by this survey to search for general periodic variation in the young open cluster IC 348. For an overview on the current state of YETI we refer the reader to the recent work of Garai et al. (2016).

In this paper we focus on the young (2 Myr; Luhman et al. 2003), nearby (316 pc; Herbig 1998), and compact ($D \sim 20$ arcmin; Luhman et al. 2003) open cluster IC 348. It is an intensely studied region of ongoing star formation. The T Tauri stars (TTS) found therein by Herbig (1954) played an important role in the exploration of star formation (Herbig 1998). The theory that TTS are young was strengthened and later confirmed through colour measurements and theoretical evolutionary models with the help of those TTS.

It is well known that IC 348 is younger than 10 Myr but its age and the age spread are still under debate. Luhman et al. (1998) found an age spread from 0.5 to 10 Myr from the photometric scatter in the colour–magnitude diagram (CMD). A similar wide age spread was assumed in the Orion nebula cluster (ONC) but it was shown by Jeffries et al. (2011) that observational and physical effects give rise to the observed luminosity dispersion. Because of the observed colour spread in IC 348 Bell et al. (2013) argue for an age of 6 Myr for IC 348 while Luhman et al. (2003) adopted a median age of 2 Myr which we use in this work.

The stellar content of IC 348 was researched with the photometric studies by Herbig (1998) and Luhman et al. (1998). With the help of the proper motion measurements from Scholz et al. (1999) and additional photometric and spectroscopic data Luhman et al. (2003)

★ E-mail: dfritzewski@aip.de

Table 1. Overview of the YETI telescopes used for this work. FoV stands for field of view. In Stará Lesná two 0.6-m telescopes have been used with different detectors. The table is sorted by the number of obtained frames.

Observatory	Telescope	Longitude (°)	Latitude (°)	FoV (arcmin^2)	# Frames	CCD detector	Pixel scale (arcsec pixel^{-1})
Jena[a]	0.6 m Schmidt	11.48416 E	50.92888 N	52.8 × 52.8	10 808	e2v 42-10	1.547
Jena[b]	0.25 m Cassegrain	11.48416 E	50.92888 N	21.0 × 20.4	2390	e2v 47-10	1.193
Stará Lesná	0.6 m Cassegrain	20.29081 E	49.15207 N	14 × 14	1957	FLI ML3048	0.410
				16.9 × 16.9		MI G4-9000	0.333
pt5m, La Palma[c]	0.5 m mod. Dall–Kirkham	17.88188 W	28.76058 N	10.2 × 6.9	1050	KAF-3200ME	0.280
Lulin	1 m Cassegrain	120.87297 E	23.46908 N	11.5 × 11.2	614	e2v 36-40	0.515
Tenagra	0.8 m Ritchey–Chrétien	110.98475 W	31.55571 N	14.8 × 14.8	584		0.867
Saitama	0.55 m Ritchey–Chrétien	139.60561 E	35.86225 N	12.8 × 12.4	218	ML4710-1	0.727
Swarthmore	0.6 m Ritchey-Chrétien	75.35605 W	39.90702 N	26 × 26	195	Apogee U16M	0.381
Llano del Hato	1 m Cassegrain–Coudé	70.87094 W	8.78794 N	18.5 × 18.5	30	e2v 42-40	0.542

[a]Mugrauer & Berthold (2010); [b]Mugrauer (2016); [c]Hardy et al. (2015).

compiled a membership catalogue of IC 348, including spectral classification for most of its members. This catalogue has recently been extended by Luhman, Esplin & Loutrel (2016) to include 478 members. The membership criterion was based on proper motion, position on the CMD, and spectral features and classification.

Using CCD detectors, photometric time series of different durations and with different fields of view (FoV), but all in the *I* band, have been obtained and published. The first time series of its kind of IC 348 was published by Herbst, Maley & Williams (2000b) with a baseline time-scale of 4 months. The FoV was 10.2 × 10.2 arcmin^2 and the authors found 19 periodic variable stars near the centre of the cluster. With more data from the same survey, Cohen, Herbst & Williams (2004) were able to detect 28 periodic variables. Finally, with a baseline of 7 yr, Nordhagen et al. (2006a) found 12 additional periodic stars in the same FoV. An independent study with deeper photometry was published by Littlefair et al. (2005) and found 32 new periodic variables in IC 348. The most extensive study so far has been conducted by Cieza & Baliber (2006). The authors used a wider FoV (46.2 × 46.2 arcmin^2) and were able to discover 75 additional periodic variables. Moreover, they combined and analysed all previous studies and counted a total of 106 periodic stars among the members of IC 348 when applying the membership of Luhman et al. (2016).

The evolution of angular momentum in young stars is a topic of recent research (e.g. Tanveer Karim et al. 2016) and the distribution of rotation periods is a stepping stone to its understanding. Since the discovery of a bimodal period distribution for stars with $M > 0.25\,M_{\odot}$ in the 1 Myr old ONC by Attridge & Herbst (1992) other open clusters are compared to this young cluster. IC 348 is slightly older and the previous time series studies came to the conclusion that the period distributions of both clusters look alike. The distribution consists of fast rotators with periods of ∼2 d and slow rotators with periods of ∼8 d. With more rotational periods for the members of IC 348 we can investigate the distribution in more detail.

In this study, carried out within the YETI network we used an even wider FoV (52.8 × 52.8 arcmin^2) than any previous studies. With this FoV we can find variabilities in IC 348 and its vicinity. Moreover, we used several telescopes located all over the world to achieve a better phase coverage of our time series.

The paper starts with an overview of our observations and the data reduction workflow (Section 2). Thereafter, we present the results (Section 3), starting with variables in IC 348, followed by further results on field stars. In the discussion (Section 4) we compare our results with previous studies.

Table 2. Observational seasons and number of nights with successful observations.

Season	Date	Number of nights
1	2012 Aug. 8–2013 Mar. 15	57
2	2013 Aug. 1–2014 Feb. 4	41
3	2014 Sep. 16–2015 Jan. 18	27

2 OBSERVATIONS AND DATA REDUCTION

2.1 Observations

IC 348 was observed between 2012 August 22 and 2015 January 18 in 125 telescopic nights over three seasons. Observations were carried out by nine telescopes through the YETI network, with a distributed longitudinal coverage (Table 1). The University Observatory Jena alone contributed 88 nights. Details on all observations can be found in Table 2. To achieve a good phase coverage 3-week-long YETI campaigns were performed in which IC 348 was observed from the participating observatories on every clear night. Therefore continuous coverage of IC 348 could be achieved at some nights through combined observations. Overall, the distributed observations resulted in a better phase coverage of the data. In Fig. 1 we compare the phase coverage of YETI data to Jena data alone and the advantage of YETI is clearly visible. For easier interpretation of Fig. 1 we show the deviation of the curves in addition to the data. The combined light curves, compiled from all telescopes, have better phase coverage in the range of 10–25 d (25 percentage points) and for periods of the multiple of 1 d (up to 35 percentage points). The better phase coverage for multiple periods of 1 d reduces the 1 d alias period significantly when searching for periods.

In Jena the open cluster was observed with the 0.6-m Schmidt telescope. We used the Schmidt-Teleskop-Kamera (STK; Mugrauer & Berthold 2010) with its Bessel *R* filter and exposed for 50 s. The exposure times at other telescopes differed because of different apertures, smaller FoV, and other detectors. Additional *BVI* images were acquired on some nights at the University Observatory Jena. Further observations were carried out with the 0.25-m Cassegrain telescope equipped with the Cassegrain-Teleskop-Kamera-II (CTK-II; Mugrauer 2016) at the University Observatory Jena. For those observations we used Bessel *V* and *I* filters and exposed for 180 s.

In addition to the Jena telescopes we observed with the pt5m telescope on La Palma (Hardy et al. 2015), the 1-m Cassegrain at the LOT observatory in Lulin, the 1-m Cassegrain-Coudé in Llano del Hato, the two 0.6-m Cassegrain in Stará Lesná, and the

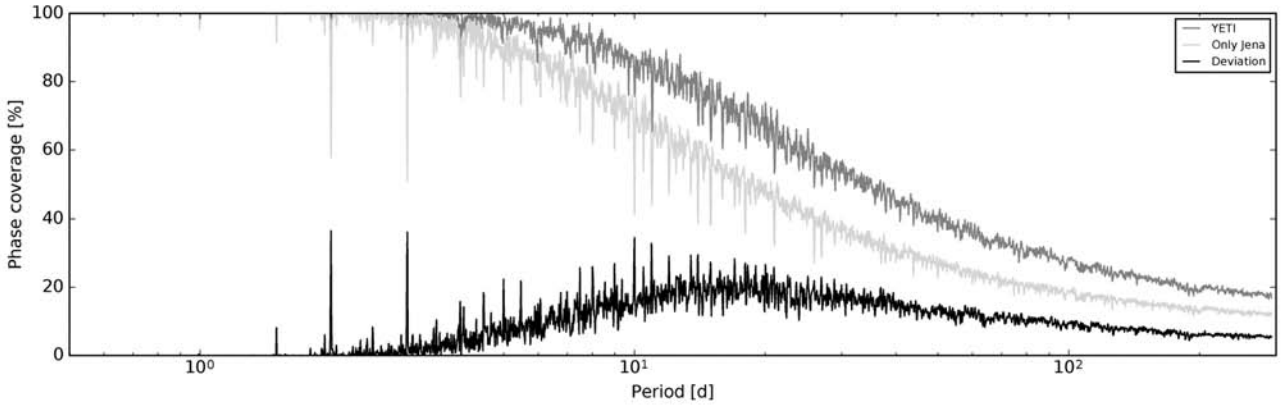

Figure 1. Phase coverage of the data for a single star. The dark grey line includes all YETI observations while the light grey line gives the phase coverage for the observations from the University Observatory Jena. In black the difference of both curves is shown for easier interpretation. The better phase coverage for periods of the multiple of 1 d is clearly visible (spikes), as well as the big advantage for periods in the range of 10–25 d.

Ritchey–Chrétien telescopes of Saitama University, Swarthmore College, and Tenagra observatory. The locations, diameters, and detectors of all telescopes used can be found in Table 1.

Most data were gathered with the STK operated at the Jena 0.6-m Schmidt telescope, therefore the stars which were analysed are all in the FoV of this telescope. Additionally, the STK exhibits the widest FoV of all instruments used. Some telescopes obtained images with deeper photometry. We decided not to use the additional fainter stars from those frames. The sparse coverage of the light curve would not have given insight to the time-scale we are interested in.

The STK is equipped with a 2048 × 2048 pixels e2v CCD detector with a FoV of 52.8 × 52.8 arcmin^2 (Mugrauer & Berthold 2010). The centre of IC 348 was positioned slightly off the centre of the detector to north-east to allow simultaneous observations with the CTK-II (centred at $\alpha = 3^{\rm h}\,45^{\rm m}\,20^{\rm s}$, $\delta = +32^\circ\,4'\,50''$). From this FoV the 1001 brightest stars have been analysed independent of their membership status down to a limiting magnitude of $R = (18.7 \pm 0.3)$ mag. Within our sample 137 stars are members of IC 348 according to Luhman et al. (2016). Further stars are either unidentified members, background or foreground stars.

All other telescopes used for this observation have a smaller FoV. Therefore, they included a tighter area around IC 348 or covered the whole region with various pointings, which implies that not all stars of our selection have been observed by all telescopes.

The FoV of the STK is shown in Fig. 2 as a composite image of *B*, *V*, and *R* observations. It is dominated by the bright star Atik (o Per). The open cluster IC 348 lies south of it and is surrounded by a reflection nebula. In this frame we marked our observed stars according to their properties.

2.2 Data reduction and photometry

For every night, in addition to the science frames, darks and flats were obtained. Whenever possible we acquired sky flats, otherwise the nightly dome flats were used. Some telescopes included the bias in an overscan region while others produced dedicated bias frames. From those images a standard reduction with dark, bias, and flat-field correction was performed with IRAF.

For every telescopic pointing the data were extracted separately from the reduced images with aperture photometry followed by differential photometry. For the differential photometry we used an implementation of the algorithm presented by Broeg, Fernández & Neuhäuser (2005), based on the IRAF task PHOT as described in detail in Errmann et al. (2014). This algorithm calculates an artificial star for comparison from all stars in the FoV, weighted according to the standard deviation of the differential light curves. From this procedure we obtained a light curve for each pointing on each night.

In Fig. 3 the mean photometric precision of one night is shown. The winter night of 2014 December 8 is exemplary and represents the normal conditions achieved at the University Observatory Jena. For example for a 16 mag star a photometric precision of 0.03 mag is reached.

After combining the data for each telescope, by adjusting the flux level from night to night, we had to collate all observations of each star obtained with different telescopes. For this step we first searched for periodic variations in the light curves from the Jena observations using the algorithms presented in Section 2.3. Thereafter, we used the periods to produce phase-folded light curves. Because of the tighter sampling in the phase domain the data from other telescopes can easily be incorporated into the light curve. This was done by adjusting the flux of the observations to the flux of the data with similar phases. The very good phase coverage of the Jena data was mandatory for this method.

With only a few nights of multiband photometry we decided to anchor our photometry to Trullols & Jordi (1997). We used the night of 2014 December 8 for the transformation and all magnitudes used in the current work are based on this system.

2.3 Algorithms used to find periodic variabilities

The main goal of this work was to find new periodic photometric variables in IC 348 and to confirm and improve ephemerides of already known variable stars in this cluster. Therefore we applied three different algorithms to detect periodicities in the data. All algorithms have in common that they use a grid of fixed periods as their input. We employed the same grid for all algorithms to gain comparable results.

This period grid had a range from $P_{\rm min} = 0.04$ d (∼1 h) to $P_{\rm max} = T/3 = 293$ d (where T is our observational time base). We used such a wide range because at least one long-periodic eclipse is known in IC 348 (Nordhagen et al. 2006b) and more might be discovered. We chose our lower limit to include short-term variability but not stellar pulsations. The upper limit was guided by the decision to include at least three cycles. To save computation time

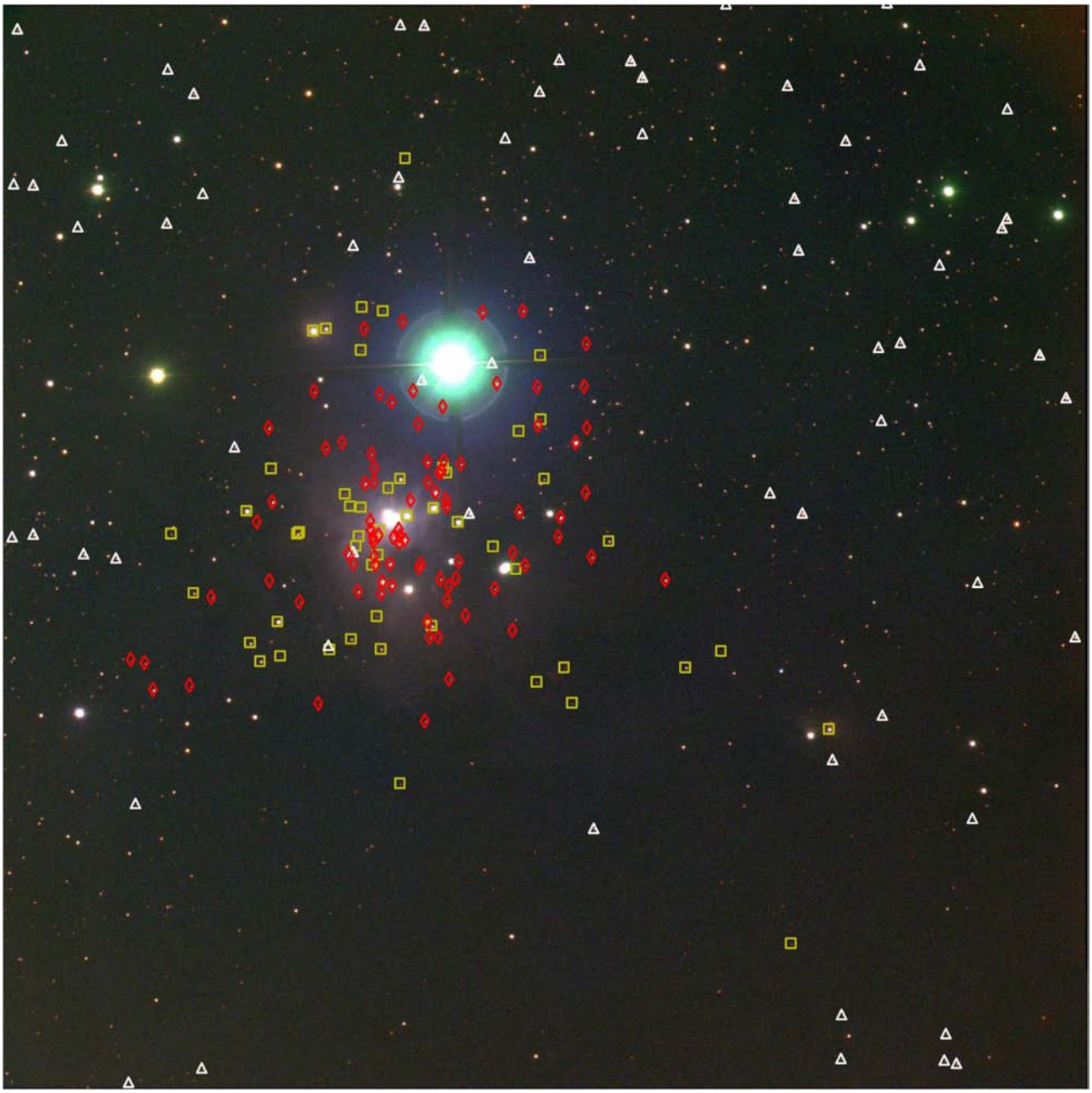

Figure 2. *BVR* image of IC 348 as observed from Jena with STK on 2014 December 8 with an integration time of 50 s in each band. The full STK FoV with a size of 52.8 × 52.8 arcmin^2 is shown. North is up and east to the left. The open cluster IC 348 is located around and within the reflection nebula south of the bright star Atik (o Per). Periodically variable members of IC 348 are marked with a (red) diamond, while all other members detected in this image are marked with a (yellow) square. Non-members for which we found a period are marked with a (white) triangle.

we used an exponentially spaced grid with $n \sim 38\,000$ points. The resolution of the grid is for the lower limit 1 s, for a period of 1 d, 20 s and for the upper limit of 293 d, 1.6 h.

The first algorithm we used is the widely applied generalized Lomb–Scargle (GLS) periodogram by Zechmeister & Kürster (2009). From the periodogram we obtained the spectral power density as a measurement of the certainty of the periodic variations. Although the algorithm is fast and convenient for finding periods it has some drawbacks. It favours signals with sinusoidal shape which can lead to incorrect best-fitting values for non-sinusoidal-shaped light curves like transits, occultations, or eclipsing binaries.

As a second algorithm the minimal string-length algorithm by Dworetsky (1983) was used. Unlike the GLS a string-length algorithm can find periodic variabilities of all shapes with the same sensitivity. In this algorithm the sum of the distances of succeeding points in the phase-folded representation is measured. Because of lower phase coverage for long periods this method is biased towards longer periods. To correct this effect a sum of a second-order polynomial and an exponential decay was fitted to the output of the algorithm. From the normalized and detrended results we were able to find the best period.

Our third algorithm was the Gregory–Loredo Bayesian signal detection as presented in Gregory & Loredo (1992) and Gregory

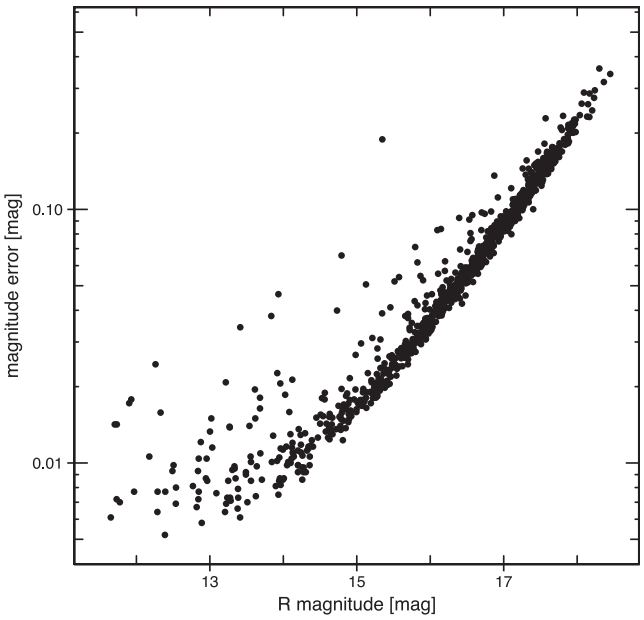

Figure 3. Photometric precision for the night of 2014 December 8 for the observations at the University Observatory Jena. This figure includes all 1001 selected stars from the FoV. In that night we also gathered *BVI* photometry of IC 348 with the STK.

(1999). This method uses different step functions to calculate the likelihood for a given period based on Bayesian statistics. It is unbiased towards shape and sampling of the light curve because the step function can adopt arbitrary shapes. We used the assumption of independent Gaussian errors and directly applied the formulation given by Gregory (1999).

Each algorithm returned a best period leading to three different values after one run of the algorithms. To find the best period automatically we applied an additional program. Therein we set as an initial selection criterion that two of the three algorithms find the same period within an error range of 10 per cent. Afterwards an additional run of the period search was conducted within that 10 per cent range of the best period. Now a match within 1 per cent was required and we used a tighter spacing of the grid. With this criterion we were able to use the maxima of the periodograms independently of their power density and were able to detect variabilities with low signal-to-noise ratio. To exclude false detection all phase-folded light curves were examined manually and non-periodic were removed.

3 RESULTS

In this section we first present the results for the member stars of IC 348 and later findings for non-members. The membership is according to Luhman et al. (2016).

If a star has a commonly used name we use this name to identify it in this section and give other identifiers as a footnote. Otherwise we use our internal numbering. The abbreviations used in this section are as following: LRL refers to Luhman et al. (1998) (and subsequent publications), HMW to Herbst et al. (2000b), CB to Cieza & Baliber (2006), and FKM to this work. When no distinct identifier is known we give the Two Micron All Sky Survey (2MASS) name but continue using our identifier.

3.1 Periodic variables in IC 348

With the above mentioned method we were able to identify 87 photometric periodic stars in IC 348. Of those stars 33 have not been reported as periodic before. Including all previous studies (overview of Cieza & Baliber 2006) the total number of periodic variables in IC 348 is now 139 out of 478 members. The reasons for non-detections of previously known periodic variables are discussed in Section 4.1. Most of the stars are rotating young stars that show spot-induced variability, although some periodic variabilities are due to occultations of protoplanetary discs or accretion. The results are summarized in Table A1 and the phase-folded light curves are shown in Fig. A1. In the following paragraphs we will present only some notable variables.

3.1.1 V695 Persei

V695 Per[1] has one of the largest peak-to-peak amplitudes in our observations with 1.2 mag. The phase-folded light curve (Fig. 4) resembles a typical occultation which was explained by Barsunova, Grinin & Sergeev (2013) as an AA Tauri-like system. The protoplanetary disc follows a Keplerian motion with a period of (7.55 $\pm$ 0.08) d. For the third season we observed a change in the light curve. Some data points seem to be outlier to the previously observed shape of the light curve. This is shown in the third panel of Fig. 4. The outliers might be explained with a reconfiguration of the protoplanetary disc or the magnetic field. As a result the disc could be warped in a different way which leads to a change of the phase of the occultation. Alternatively an additional occultation might take place and the two effects overlap. Further monitoring of this star can help to constrain the reasons.

3.1.2 V718 Persei

The unusual photometric periodicity of the star V718 Per[2] was discovered by Cohen, Herbst & Williams (2003) and analysed in depth thereafter (Nordhagen et al. 2006b; Grinin et al. 2008). It is periodically occulted by a part of its protoplanetary disc. The occultation has a period of (4.7 $\pm$ 0.1) yr (Nordhagen et al. 2006b) while the eclipse lasts for 3.5 yr. In our data, spanning 2.4 yr, we were able to see the decrease of brightness of 0.9 mag (Fig. 5). This observation shows that V178 Per is a rather stable system. IC 348 was monitored from Van Vleck Observatory from 1991 (Nordhagen et al. 2006b): the system was therefore observed in a stable configuration for 24 yr now.

3.1.3 A close stellar companion to LRL 47

As well as the modulation of the flux due to starspots with a period of (4.91 $\pm$ 0.05) d, the light curve of LRL 47[3] showed an additional feature. In the three observing seasons four short dips were found (see Fig. 6). All of them show the typical V-shape of a grazing transit.

LRL 47 is known to be active in X-ray (Preibisch, Zinnecker & Herbig 1996; Preibisch & Zinnecker 2001, 2002; Stelzer et al. 2012; Flaherty et al. 2014) like a lot of young stars are (Neuhäuser 1997). Lada et al. (2006) found no evidence of a circumstellar disc around

[1] FKM 570, LRL 99, HMW 73, CB 49.
[2] FKM 123, HMW 15, LRL 35.
[3] FKM 71.

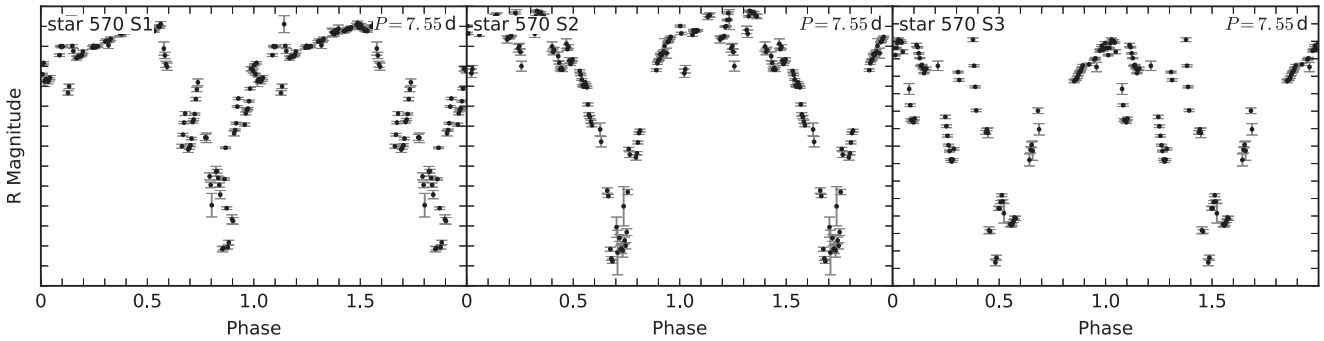

Figure 4. Phase-folded light curves of the AA Tauri-like star V695 Per for all three observing seasons. While the first two seasons are phased adequately the observations from the third season show some variability in the phase. The data have been binned and the spacing is 0.1 mag for all tick marks on the magnitude axis.

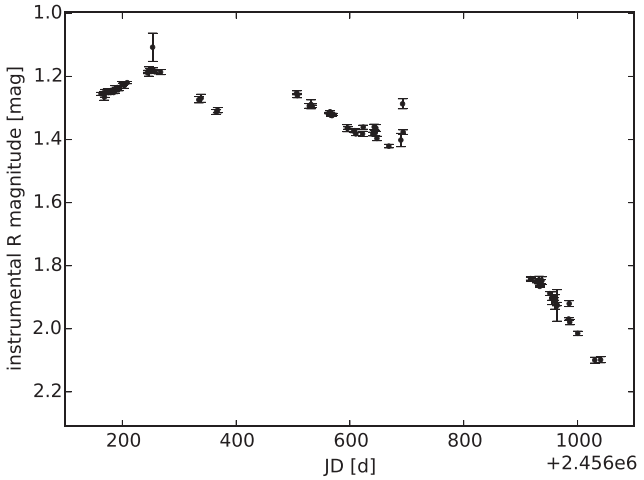

Figure 5. The full light curve of V718 Per shows the strong decrease of brightness due to the long-periodic occultation of the star. The data have been binned to one data point per night.

it. Dahm (2008) and Currie & Kenyon (2009) later confirmed this result. The non-existence of a disc is not unusual for stars in IC 348. Lada et al. (2006) found a disc fraction of (50 ± 6) per cent and Cieza et al. (2007) state that discs might disappear as soon as 1 Myr after the stellar formation, building planets within this time. This star might have had a circumstellar disc which has already vanished. In addition to the non-existence of a disc, Duchêne, Bouvier & Simon (1999) were able to exclude a stellar companion to this star with a detection limit of 3 mag at 0.5 arcsec (i.e. 158 au).

The transits were observed at Jena, Tenagra, and Lulin observatories. Hence, we have three independent observations, an observational effect can therefore be excluded. These observations show again the power of the YETI network. With only a single telescope we would have missed most of the events. From the University Observatory Jena only the first event was visible and was observed. Unfortunately the *V* and *I* band observations carried out with the CTK-II mounted to the second telescope at the University Observatory Jena are not accurate enough to gain additional colour information of the transit.

The properties for the four transits are given in Table 3. The transit mid-points has been obtained with JKTEBOP (Etzel 1981; Popper & Etzel 1981; Southworth, Maxted & Smalley 2004). Also with JKTEBOP we determined a period of (5.123874 ± 0.000063) d from

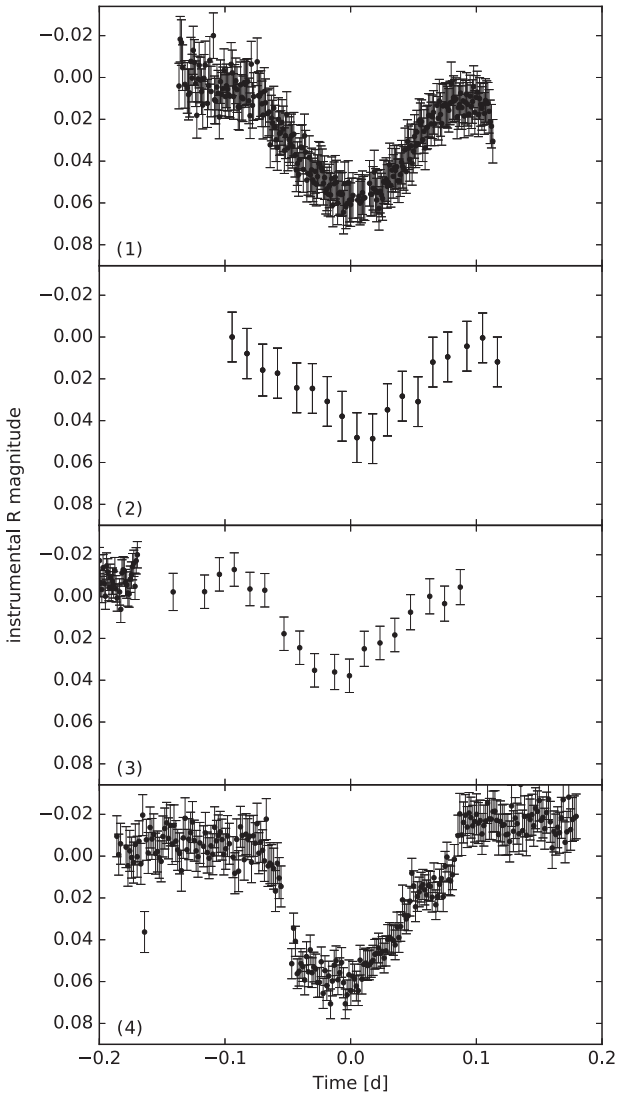

Figure 6. The light curves of the four observed transits of LRL 47 (star 71). Each is centred on the transit mid-point (see Table 3) and scaled the same for better comparison. The Tenagra telescope (2 and 3) has observed with a lower sampling than the other two telescopes (Jena/STK panel 1 and Lulin panel 4) therefore the data are sparse. In panel 3 the advantage of the YETI network is visible. The observations from two telescopes are included in this light curve. All information on the transits are listed in Table 3, including depth, duration, telescope, and time.

Table 3. Parameters of the observed transits of LRL 47. MJD_{mid} gives the midpoint of the transit as modified JD (MJD = JD − 245 6000 d). The epoch is the orbital cycle number relative to the first observation.

Number	Depth (mag)	MJD_{mid} (d)	Epoch	Telescope
1	0.05	188.5105 ± 0.0016	0	Jena
2	0.05	203.8714 ± 0.0149	3	Tenagra
3	0.04	244.8718 ± 0.0097	11	Tenagra
4	0.07	962.2088 ± 0.0030	151	Lulin

those four transits. This period is close to the rotational period of (4.91 ± 0.05) d but is feasible for a close companion.

According to Luhman et al. (2003) LRL 47 is a K0 ± 2 star. From the isochrones of Siess, Dufour & Forestini (2000) we can find for the spectral type K0 a mass of $M_P = 2.7\,M_\odot$ and a radius of $R_P = 4.14\,R_\odot$ at the age of 2 Myr. This age is not necessarily the true age of this star. Luhman et al. (1998) gave an age spread from 0.5 to 10 Myr for IC 348 which is under debate (see Section 1). Therefore the primary's radius can be overestimated by a factor of 2. Nevertheless, we continue with the median age of 2 Myr to find an estimation of the companion's properties.

Using JKTEBOP again for fitting the data did not lead to a satisfactory result. The reason for this is the grazing nature of the transit and our lack of additional information on the system. To get an idea of what kind the transiting object is, we assumed a Keplerian orbit and a non-grazing transit. With these assumptions we can calculate lower boundaries for the companion's radius and mass.

First, we calculated the inclination and radius from our supposed values for the primary and the measured parameters of the transit. Thereafter we derived the mass for the companion from the low-mass isochrones of Baraffe et al. (2015). After an iterative process we concluded on an inclination of $i \lesssim 75\overset{\circ}{.}4$, a radius of $R_C \gtrsim 0.87\,R_\odot$, and a mass of $M_C \gtrsim 0.09\,M_\odot$. Here we give no uncertainties because they would strongly underestimate the true errors. As said above those values are only lower (upper) boundaries for the mass and radius (and inclination). Because of the grazing of the transit we cannot be sure about the true radii ratio and therefore the derived values. From those lower boundaries we can conclude that this star might have a close stellar companion which might be near the hydrogen burning limit.

The four light curves show two slightly different shapes (Fig. 6). The first two occurrences of the transit have a symmetric V-shape. In contrast, the latter two have a steep decrease of flux at the beginning and a slower increase after the minimum. Even though two different shapes are observed we are not looking at a secondary and a primary transit. Except the first transit all have an odd orbital cycle number which rules out the double period. A secondary transit is not visible in the data of phase 0.5. This constrains the mass ratio to $\frac{M_C}{M_P} \ll 1$. The different shapes of the transit can be explained with active regions and starspots on the stellar surface.

Independent of the mass, this short period means that the companion has a small semimajor axis in the range of 0.08–0.1 au. Therefore it is close to the primary and could not have been detected by direct imaging even using adaptive optics on a 4-m class telescope (Duchêne et al. 1999).

To constrain the mass of the companion candidate radial velocity measurements of the primary with $R = 13.5$ mag are necessary.

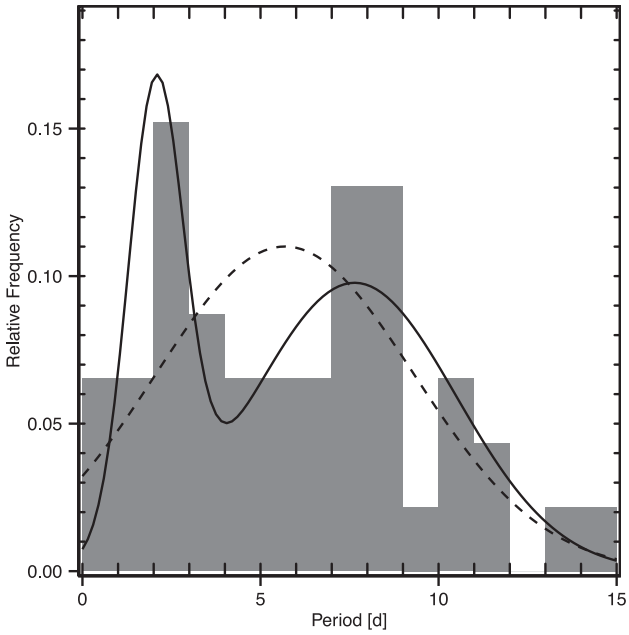

Figure 7. Period distribution of the rotation periods for high-mass stars in IC 348 (grey bars). Overlaid are a simple Gaussian model (dashed line) and a bimodal mixture model of two different Gaussians (solid line).

3.1.4 Period distribution

The distribution of the rotation periods has been an interest to all previous time series studies of IC 348. It has always been compared to the slightly younger ONC for which Herbst et al. (2000a) discovered a bimodal period distribution. The bimodal distribution is present for more massive stars which was defined by Herbst et al. (2000a) as $M > 0.25\,M_\odot$ or spectral type (SpT) earlier than M2 (Cohen et al. 2004) for young stars.

The comparison always gave the impression that the period distribution is similar to the period distribution of the ONC. Hence, it is bimodal with peaks for periods of about 2 and 8 d. Despite the similarities a Kolmogorov–Smirnov test could not confirm that the two distributions (ONC and IC 348) are the same (Cohen et al. 2004; Littlefair et al. 2005). Furthermore, Littlefair et al. (2005) used the Hartigan dip test (Hartigan 1985; Hartigan & Hartigan 1985) and found that the bimodality in IC 348 is not statistically significant. Using the R (R Core Team 2015) implementation of the dip test (Maechler 2015) we find that the extended set of rotation periods now available has no statistically significant bimodality.

In addition to the dip test we applied two Gaussian models (Fig. 7) to the data. At first we used the MASS package in R (Venables & Ripley 2002) to fit a unimodal Gaussian to the data. The second model is a mixture model of two different Gaussians. To find the parameters we applied the MIXTOOLS package for R (Benaglia et al. 2009). Both models were compared to the empirical cumulative distribution function (eCDF) of the data (Fig. 8). An F-test yields a p-value of 1.1×10^{-9}, which is the probability that the null hypothesis is true. In this case the null hypothesis is the unimodal distribution. Including all data from Cieza & Baliber (2006) the F-test yields an even smaller p-value.

We conclude that a bimodal Gaussian distribution fits more likely the data than a unimodal Gaussian distribution. Since the dip test, in contrast, favours the unimodal model the bimodality of the rotation period distribution in IC 348 is still an open issue.

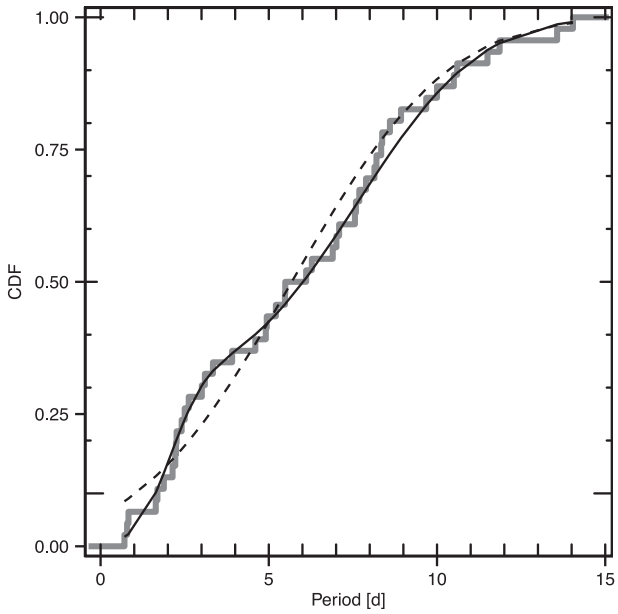

Figure 8. Cumulative distribution function (CDF) of our data. The mixture model is fitting very well. The colours and line types are the same as in Fig. 7.

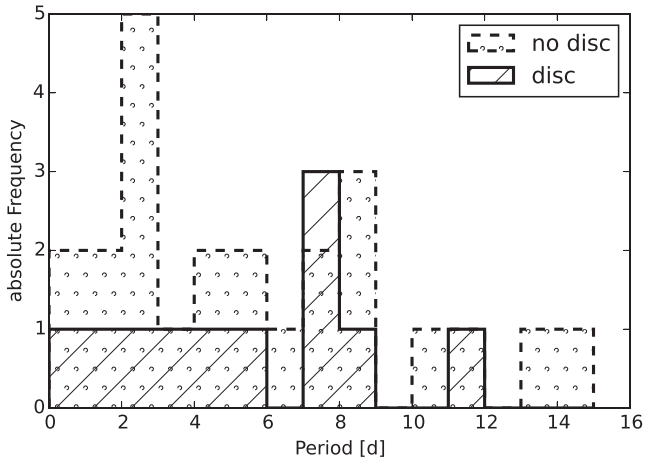

Figure 9. The period distribution of stars with $M > 0.25\,M_{\odot}$ separated by the existence of discs. Few discs are observed around those more massive stars in the cluster and we cannot make a statement about influence of the disc on the stellar rotation.

Separating the rotation periods for stars with and without discs using the data from Lada et al. (2006) is also inconclusive. The low numbers of stars with discs shows a peak for the slow rotators (Fig. 9) but with only two more stars than in the other bins. Among the stars without an observed disc indicator more fast rotators can be found. Nevertheless, slow rotators are among those stars, too. For the histogram in Fig. 9 we used only stars which are in the group of $M > 0.25\,M_{\odot}$. Cieza & Baliber (2006) also found no evidence that the slow rotors preferably have discs. Even with the additional periods the statistics are still inconclusive.

For an additional regrouping we used all members with observed periods and an Hα emission from Luhman et al. (2003). Within this sample we classified all stars with an Hα equivalent width greater than 10 Å as classical T Tauri stars (cTTS) and all other as weak-lined T Tauri stars (wTTS; Herbig 1998).[4] Stars without an Hα equivalent width measurement were excluded from the sample. In Fig. 10 we show the histogram of all rotation periods separated into the two groups. Because of the small amount of cTTS in our sample we have not applied statistical tests to these data. From Fig. 10 we can clearly see that wTTS are among slow and fast rotators. The same result was found in a much larger sample from Orion by Tanveer Karim et al. (2016), too. The few cTTS are distributed over the whole range of periods and we cannot find any difference between the two groups.

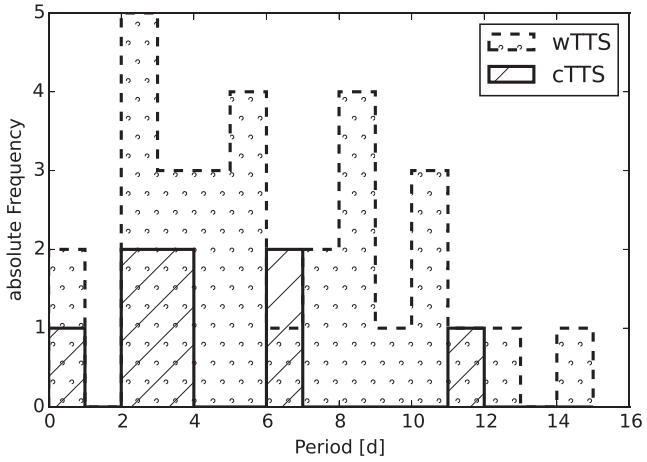

Figure 10. The period distribution of TTS separated by cTTS and wTTS. Few cTTS are in our sample, but wTTS can be found in nearly all period bins.

3.2 UX Orionis-type stars in IC 348

V909 Per,[5] V712 Per,[6] and V719 Per[7] have all been classified as UX Orionis-type stars (UXOr) by Barsunova et al. (2015). Those stars are surrounded by clumpy material in their protoplanetary disc. These clumps occult the star which leads to sudden decrease of the flux with few periodicity. From the visual inspection of the light curves we can confirm their results. For V909 Per we show the full light curve in Fig. 11. In our light curves we were able to identify the same deep sudden drops as Barsunova et al. (2015). GM Cephei is a similar star which has previously been monitored by YETI (Chen et al. 2012).

While obtaining *BVRI* photometry V719 Per was covered by its disc and is therefore the faintest star in our sample $R = (18.73 \pm 0.33)$ mag. Additionally, it has a colour of $(V - R) = (2.8 \pm 0.6)$ mag and is one of the reddest stars examined. This observation seems to disagree with the properties of UXOr variables which are expected to become bluer when eclipsed. Barsunova et al. (2015) showed that V719 Per appears bluer near the photometric minimum but redder all other times during the eclipse. Our observations were obtained in the first phase of the occultation and therefore the star appeared redder.

[4] Using the more detailed, spectral type-dependent classification of Barrado y Navascués & Martín (2003) would not change our results and we decided to use a single critical value to distinguish between the two groups.
[5] FKM 78, LRL 5, HMW 20.
[6] FKM 140, LRL 37, HMW 23, CB 102.
[7] FKM 365, LRL 75, HMW 56, CB 123.

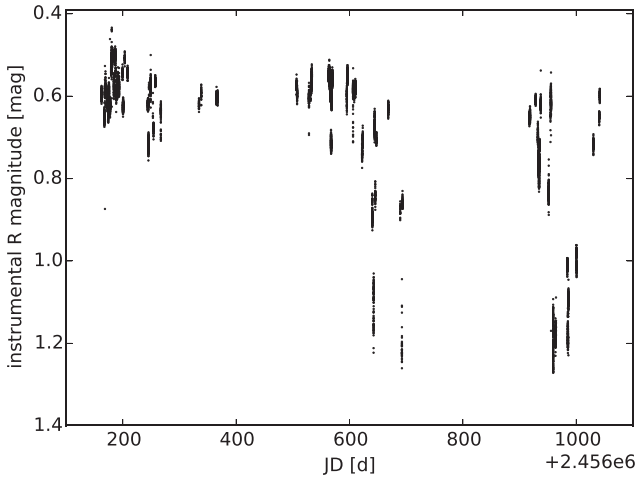

Figure 11. The UX Orionis-type star V909 Per shows sharp, sudden, non-periodic decreases of the flux. This figure includes all observations of this star.

Table 4. Periods, brightness, and colours of the four non-member eclipsing binaries found in the data. The magnitudes of the stars 974 and 975 are from Scholz et al. (1999).

ID	Period (d)	R (mag)	$(V-R)$ (mag)
213	0.4340 ± 0.0015	15.02 ± 0.02	0.95 ± 0.21
777	0.4882 ± 0.0015	17.26 ± 0.10	0.93 ± 0.30
974	0.422 ± 0.002	15.41 ± 0.02	0.98 ± 0.21
975	0.446 ± 0.002	15.72 ± 0.02	0.92 ± 0.21

3.3 Non-member variable stars

Within this data set we found four detached eclipsing binaries which are background stars to IC 348. They have the identifiers 213 (2MASS J03455377+3226418), 777 (CSS J034539.4+314252), 974 (CB 6), and 975 (CB 17). Only 777 is a previously known binary. The stars 975 and 974 were studied by Cieza & Baliber (2006), though incorrect periods were stated and the binarity was not mentioned. Therefore, we can conclude that the binarity of this system was unknown before. Of those four stars all but 213 might be W UMa-type binaries. The minima of 213 have rather different depths, therefore, it might be a different type of detached binary.

With our data we found for 777 a period of (0.4882 ± 0.0015) d which is consistent with the value of 0.48825 d given by Drake et al. (2014). The periods of all four binaries are listed in Table 4 and all four phase-folded light curves are presented Fig. 12.

Among the field stars the star 55 (NSVS J0343111+321746) is a quasi-periodic variable. Woźniak et al. (2004) found a period of 300 d for this star and classified it as a *SR*+*L* AGB star. The period cannot be confirmed because we limited our search range to 293 d. Nevertheless, this star shows clearly a quasi-periodic variability as visible from the light curve in Fig. 13. The classification as a *SR*+*L* AGB star can be confirmed.

3.4 Stability of periods

Cohen et al. (2004) reported that they found not a single variable star in IC 348 with a coherent phase for more than one observational season. In contrast Rebull (2001) found ∼30 per cent of the stars in the similar aged flanking fields of ONC to be stable up to 1 yr.

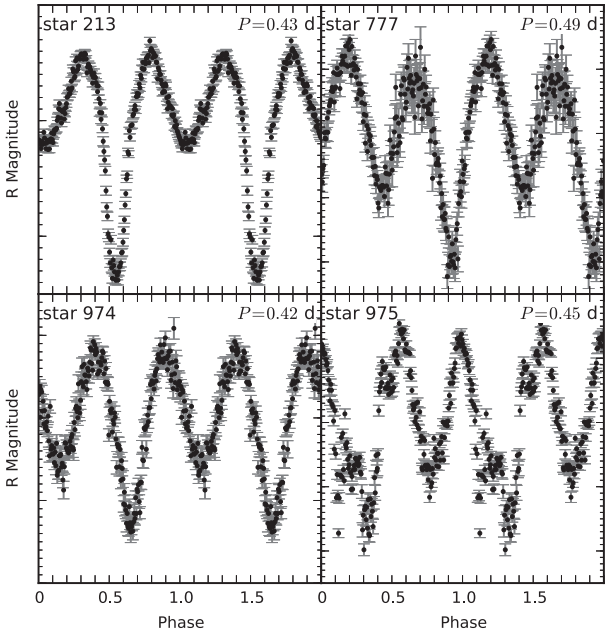

Figure 12. Phase-folded light curves of the four detached binaries in the FoV. Those stars are not members of IC 348. Further information is given in Table 4. The spacing is 0.01 mag for minor ticks and 0.1 mag for major ticks.

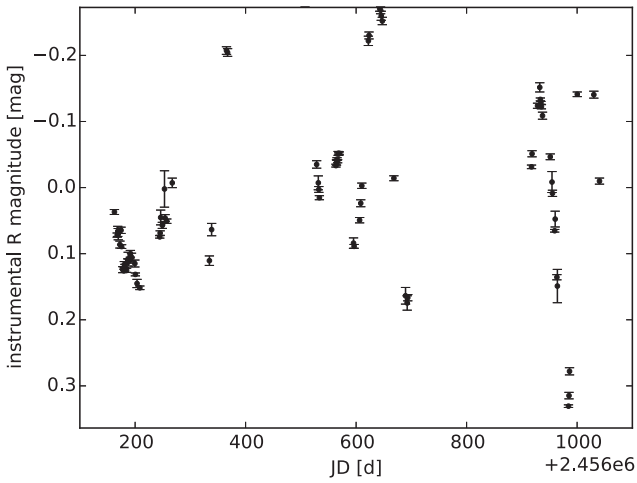

Figure 13. The full light curve of star 55 (NSVS J0343111+321746) shows quasi-periodic variability. The data have been binned to one data point per night.

In this study we can report coherent phases of the stars in IC 348. Overall 48 per cent of the members have a coherent phase over the range of 2.4 yr.

This behaviour can be seen in Fig. A1 where we show the phase-folded light curves of the photometric periodic IC 348 members. All stars which have a season number added to their name have not been observed in a coherent phase over all three seasons.

3.5 Colour–magnitude diagram

In Fig. 14 we present the CMD of the whole FoV as measured from our V and R images. The diagram has not been dereddened and presents the observed colours and magnitudes. In this figure we

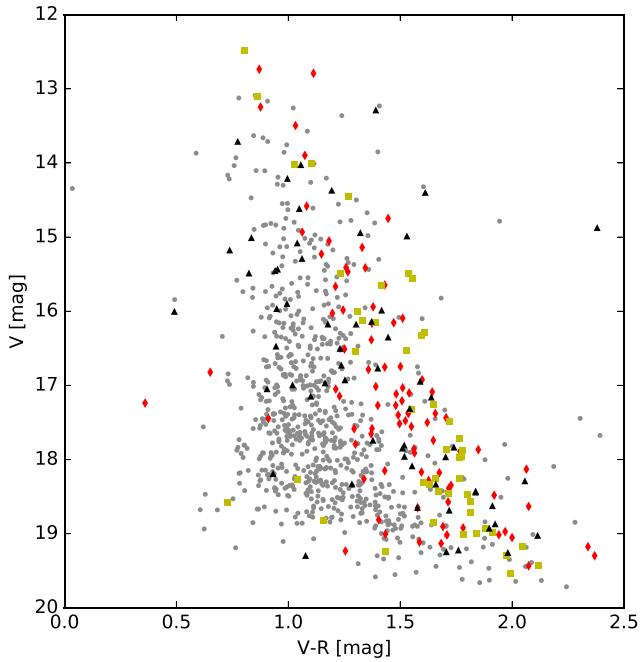

Figure 14. CMD of our FoV. The stars are marked with the same symbols as in Fig. 2 (except that the periodic non-members are marked in black instead of white) and the field stars are added with light grey circles. The cluster sequence is clearly visible. The overlap of the cluster sequence with other periodically variable stars is due to the extinction towards IC 348 (see text).

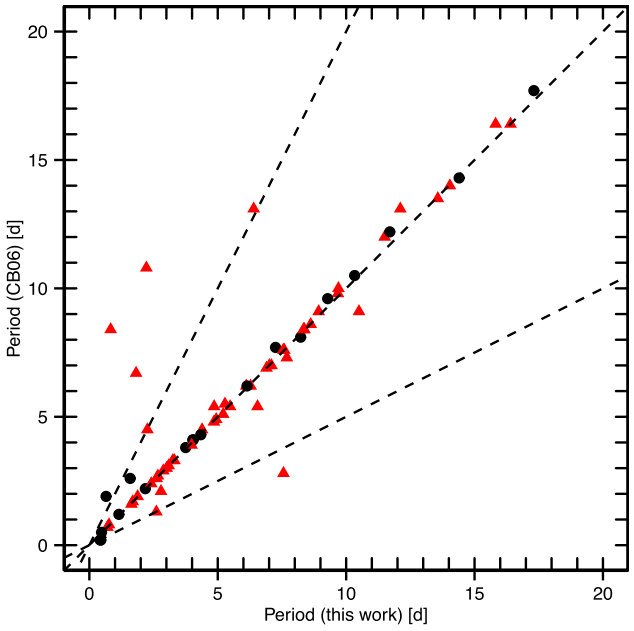

Figure 15. Comparison of our periods to the data of Cieza & Baliber (2006) (CB06). The (red) triangles represent members of IC 348 and (black) dots are field stars. The dotted lines correspond to the relations of 1:2, 1:1, and 2:1 (from top to bottom).

marked the periodic stars as well as the members of IC 348. The members form a well-defined cluster sequence. Some outliers are bluer than expected. Those stars are located close to the bright star Atik (o Per), which may explain the anomalous colour measurements.

In addition to the members on the cluster sequence a lot of photometric periodic stars, which are not members of the cluster, have similar positions in the CMD. Nevertheless most of those stars have sky positions which do not correspond to the position of IC 348 (Fig. 2). Those stars are reddened by the medium around IC 348 and are background stars. Only two stars on the cluster sequence have a sky position corresponding with IC 348. One of them, LRL 77 (80), has been classified by Luhman et al. (2003) as a foreground star from proper motion. Our period of $P = 15.3$ d confirms this classification. This period is too long for a typical member of the cluster. The other one star 607 ([PSZ 2003] J034450.0+320345; Preibisch, Stanke & Zinnecker 2003) is positioned on the southern outskirts of the cluster and we find a period of $P = 200$ d. In conclusion, none of the non-members near the sky position of the cluster and on the cluster sequence in the CMD is an unidentified member.

4 DISCUSSION

From the long-term photometry of the young open cluster IC 348 we found various periodic variable stars. For all periods given in Table A1 the systematic error is 1 per cent of the given period. This systematic error arises through the selection process of the best period. In our selection algorithm two periods are consistent if they differ by less than 1 per cent. Therefore, the true period can have an error of up to 1 per cent. For short periods the phase difference of small errors is percentually bigger than for long periods. Therefore, a short period can be determined more accurately. In contrast to this strong confinement from the periodogram rotating stars do not exhibit such a well-defined periodicity. Because of the evolution of starspots a measurement error is introduced. This error is hard to estimate because it arises from physical processes in the star, with unknown properties for this particular star. Measuring the period of a differentially rotating star can lead to results differing as much as 10 per cent (see Section 4.1). A 1 per cent error is therefore a reasonable estimate even for fast rotating stars.

The periodicity of binary stars can be determined with greater accuracy because the orbital period is not subject to phase changes. If it is possible from the periodograms we give smaller errors for those stars in Table A1.

4.1 Comparison with previous work

In the previous work of Cieza & Baliber (2006) all known periods have been merged into a single data set. From this base we can compare our results with the known periods. The comparison with Cieza & Baliber (2006) shows that our method is reliable. Only six periods found in both works differ strongly. When phase-folding our light curves with the period given by Cieza & Baliber (2006) we cannot see any coherent behaviour in the light curve. The periods given by Cieza & Baliber (2006) might suffer from beating with the sampling rate. A very special case is the star 968 (CB 62, LRL 72) for which the authors gave a period of 1 d which is very likely an alias period, since the observations were carried out in a few nights at one observatory. Our data with a better phase coverage show a periodicity of (44.6 ± 0.5) d.

For all other stars found in both studies the periods match well with the line of equality, or in some cases have a ratio of 1:2 or 2:1 (Fig. 15). Some periods differ by 0.3 d which can be explained

by differentially rotating stars and spot evolution (see Rebull 2001; Cieza & Baliber 2006).

For 24 stars for which Cieza & Baliber (2006) gave a period we were not able to find any periodic variability. Given the activity of the young stars this is not a surprising result. Several reasons can lead to a non-detection. On the one hand the star might have shown no periodic behaviour over the course of 3 yr. Some observed stars were periodic only in one out of three seasons and a lot of stars are not periodic at all, which does not mean that no starspots were present. The stars are still very variable, but no periodicity can be detected because of the number or the evolution of the starspots. For the stars which showed no periodic variability Jackson & Jeffries (2012) found in NGC 2516 no qualitative difference to stars which did. Therefore it is not unusual to miss rotational periods published before. For the same reason it was possible to find 25 new rotation periods although IC 348 is well researched. On the other hand the variability due to spots can easily be covered by other non-periodic behaviours. If the noise in terms of erratic behaviour of the light curve is too strong, even the best algorithms cannot find the underlying period in the light curve.

Cieza & Baliber (2006) stated the number of periodic stars in IC 348 to be 143. This included 37 stars not listed as members in Luhman et al. (2003). With the membership criterion of Cieza & Baliber (2006) (everything in the FoV of their study, including foreground and background objects) the number of stars in IC 348 which have shown some periodicity is around 200.

4.2 Further periodic variables in the field of view

The case of LRL 47 shows the importance of the long-term monitoring of young open clusters for finding companions. Although, the periodicity of the observed transit is 5.12 d it was observed only four times over three observing seasons. Other surveys have missed this event before and we were only able to calculate a period because we used observations distributed through YETI at observatories worldwide.

By analysing the whole FoV and not just the members of the cluster we were able to find additional periodic stars, including three unknown contact binaries. This shows there is additional scientific value in analysing all available data, and not just primary targets (in this case the stars associated with the cluster).

5 CONCLUSIONS

With long-term photometry from different telescopes world-wide we were able to identify 148 periodic variabilities in our FoV centred at IC 348. Because of the long time-scale and the wide FoV 74 of the periods are newly discovered. This includes 33 new periodic variables in IC 348. The total number of periodic stars among the members of IC 348 (counting only the stars of Luhman et al. 2016) rises with this study to 139. Discovering new periods in this well-studied cluster is possible due to the high variability of the starspots on these young stars. With a time base large enough it should be possible to determine rotational periods for most stars in young clusters. Photometric long-term studies are therefore viable sources of statistically significant data on the rotation of stars.

With the additional periods for the stars in IC 348 we were able to show that a bimodal Gaussian distribution fits the data more likely than a unimodal. Nevertheless, a dip test was inconclusive and we have no statistical evidence that the period distribution of the stars in IC 348 is bimodal. In addition we showed that for the stars of IC 348 the rotation period does not depend on the type of the TTS. wTTS and cTTS can both be found among fast and slow rotators. The same applies to stars with and without an observed disc indicator. Stars without a disc can also be found among the slow rotators.

For LRL 47 we found a close low-mass stellar companion. The companion has been observed in a grazing transit hence our analysis from single-band photometric data is not reliable. For further characterization of this system – including mass determination – radial velocity data are desirable.

Outside the cluster we discovered three previously unknown background detached binaries and were able to confirm the period of a fourth.

ACKNOWLEDGEMENTS

We would like to thank the anonymous referee for the helpful comments which improved and clarified the paper. We are grateful to D. Cohen and E. Jensen for obtaining valuable observations at the Peter van de Kamp Observatory, Swarthmore College, and Y. Oasa at Saitama University Observatory. We thank A. Dathe, A. Ide, D. Keeley, W. Pfau, S. Schönfeld, and L. Trepl for observing at the University Observatory Jena. Based on observations obtained with telescopes of the University Observatory Jena, which is operated by the Astrophysical Institute and University-Observatory of the Friedrich–Schiller University, and on observations obtained at the Llano del Hato National Astronomical Observatory of Venezuela, operated by the Centro de Investigaciones de Astronomía (CIDA) for the Ministerio del Poder Popular para la Ciencia y Tecnología. We would like to thank the Thuringian State (Thüringer Ministerium für Bildung, Wissenschaft und Kultur) in project number B 515-07010 for financial support. MK thanks RN and Professor R. Redmer in DFG projects NE 515/34-1 and 2 and RE 882/12-2, respectively, both in SPP 1385. CA thanks RN in DFG projects NE 515/35-1 and 2 in SPP 1385. TB and RWW are grateful to the Science and Technology Facilities Committee (STFC) for financial support (grant reference ST/J001236/1). BD thanks RN in DFG project C2 in SFB-TR 7. RE thanks RN in DFG projects NE 515/34-1 and 2 in SPP 1385. CG thanks MM in DFG project MU 2695/18-1. CM thanks K. Schreyer in DFG project SCHR 665/7-1. AP thanks RN in DFG project C2 in SFB-TR 7. SR thanks RN in DFG projects NE 515/33-1 and 2 in SPP 1385. SR is currently a Research Fellow at ESA/ESTEC. JGS thanks RN in DFG project B9 in SFB-TR 7. TOBS thanks Professor J. Schmitt in DFG RTG 1351 *Extrasolar Planets and their Host Stars*. This work was supported by grant VEGA 2/0143/14 of Slovak Academy of Sciences. IRAF is distributed by the National Optical Astronomy Observatories, which are operated by the Association of Universities for Research in Astronomy, Inc., under cooperative agreement with the National Science Foundation. This research has made use of NASA's Astrophysics Data System. This research has made use of the VizieR catalogue access tool and SIMBAD data base, both operated at CDS, Strasbourg, France. The original description of the VizieR service was published in A&AS, 143, 23. 'The SIMBAD astronomical data base' in A&AS, 143, 9 (Wenger et al.). This research has made use of TOPCAT (Taylor 2005) and ASTROMETRY.NET (Lang et al. 2010). This publication makes use of data products from the Two Micron All Sky Survey, which is a joint project of the University of Massachusetts and the Infrared Processing and Analysis Center/California Institute of Technology, funded by the National Aeronautics and Space Administration and the National Science Foundation.

REFERENCES

Attridge J. M., Herbst W., 1992, ApJ, 398, L61
Bakos G., Noyes R. W., Kovács G., Stanek K. Z., Sasselov D. D., Domsa I., 2004, PASP, 116, 266
Baraffe I., Homeier D., Allard F., Chabrier G., 2015, A&A, 577, A42
Barrado y Navascués D., Martín E. L., 2003, AJ, 126, 2997
Barsunova O. Y., Grinin V. P., Sergeev S. G., 2013, Astrophysics, 56, 395
Barsunova O. Y., Grinin V. P., Sergeev S. G., Semenov A. O., Shugarov S. Y., 2015, Astrophysics, 58, 193
Bell C. P. M., Naylor T., Mayne N. J., Jeffries R. D., Littlefair S. P., 2013, MNRAS, 434, 806
Benaglia T., Chauveau D., Hunter D. R., Young D., 2009, J. Stat. Software, 32, 1
Bordé P., Rouan D., Léger A., 2003, A&A, 405, 1137
Broeg C., Fernández M., Neuhäuser R., 2005, Astron. Nachr., 326, 134
Chen W. P. et al., 2012, ApJ, 751, 118
Cieza L., Baliber N., 2006, ApJ, 649, 862
Cieza L. et al., 2007, ApJ, 667, 308
Cohen R. E., Herbst W., Williams E. C., 2003, ApJ, 596, L243
Cohen R. E., Herbst W., Williams E. C., 2004, AJ, 127, 1602
Currie T., Kenyon S. J., 2009, AJ, 138, 703
Dahm S. E., 2008, AJ, 136, 521
Drake A. J. et al., 2014, ApJS, 213, 9
Duchêne G., Bouvier J., Simon T., 1999, A&A, 343, 831
Dworetsky M. M., 1983, MNRAS, 203, 917
Errmann R. et al., 2014, Astron. Nachr., 335, 345
Etzel P. B., 1981, in Carling E. B., Kopal Z., eds, Photometric and Spectroscopic Binary Systems. Reidel, Dordrecht, p. 111
Flaherty K. M. et al., 2014, ApJ, 793, 2
Garai Z. et al., 2016, Astron. Nachr., 337, 261
Gregory P. C., 1999, ApJ, 520, 361
Gregory P. C., Loredo T. J., 1992, ApJ, 398, 146
Grinin V. P., Stempels H. C., Gahm G. F., Sergeev S., Arkharov A., Barsunova O., Tambovtseva L., 2008, A&A, 489, 1233
Hardy L. K., Butterley T., Dhillon V. S., Littlefair S. P., Wilson R. W., 2015, MNRAS, 454, 4316
Hartigan P. M., 1985, J. R. Stat. Soc. Ser. C (Appl. Stat.), 34, 320
Hartigan J. A., Hartigan P. M., 1985, Ann. Stat., 13, 70
Herbig G. H., 1954, PASP, 66, 19
Herbig G. H., 1998, ApJ, 497, 736
Herbst W., Rhode K. L., Hillenbrand L. A., Curran G., 2000a, AJ, 119, 261
Herbst W., Maley J. A., Williams E. C., 2000b, AJ, 120, 349
Jackson R. J., Jeffries R. D., 2012, MNRAS, 423, 2966
Jeffries R. D., Littlefair S. P., Naylor T., Mayne N. J., 2011, MNRAS, 418, 1948
Lada C. J. et al., 2006, AJ, 131, 1574
Lang D., Hogg D. W., Mierle K., Blanton M., Roweis S., 2010, AJ, 139, 1782
Littlefair S. P., Naylor T., Burningham B., Jeffries R. D., 2005, MNRAS, 358, 341
Luhman K. L., Rieke G. H., Lada C. J., Lada E. A., 1998, ApJ, 508, 347
Luhman K. L., Stauffer J. R., Muench A. A., Rieke G. H., Lada E. A., Bouvier J., Lada C. J., 2003, ApJ, 593, 1093
Luhman K. L., Esplin T. L., Loutrel N. P., 2016, ApJ, preprint (arXiv:1605.08907)
Maechler M., 2015, diptest: Hartigan's Dip Test Statistic for Unimodality – Corrected (http://CRAN.R-project.org/package=diptest)
Mugrauer M., 2016, Astron. Nachr., 337, 226
Mugrauer M., Berthold T., 2010, Astron. Nachr., 331, 449
Neuhäuser R., 1997, Science, 276, 1363
Neuhäuser R. et al., 2011, Astron. Nachr., 332, 547
Nordhagen S., Herbst W., Rhode K. L., Williams E. C., 2006a, AJ, 132, 1555
Nordhagen S., Herbst W., Williams E. C., Semkov E., 2006b, ApJ, 646, L151
Nutzman P., Charbonneau D., 2008, PASP, 120, 317
Popper D. M., Etzel P. B., 1981, AJ, 86, 102
Preibisch T., Zinnecker H., 2001, AJ, 122, 866
Preibisch T., Zinnecker H., 2002, AJ, 123, 1613
Preibisch T., Zinnecker H., Herbig G. H., 1996, A&A, 310, 456
Preibisch T., Stanke T., Zinnecker H., 2003, A&A, 409, 147
R Core Team 2015, R: A Language and Environment for Statistical Computing. R Foundation for Statistical Computing, Vienna, Austria (http://www.R-project.org/)
Rebull L. M., 2001, AJ, 121, 1676
Ricker G. R. et al., 2014, Proc. SPIE, 9143, 914320
Scholz R.-D. et al., 1999, A&AS, 137, 305
Siess L., Dufour E., Forestini M., 2000, A&A, 358, 593
Southworth J., Maxted P. F. L., Smalley B., 2004, MNRAS, 351, 1277
Stelzer B., Preibisch T., Alexander F., Mucciarelli P., Flaccomio E., Micela G., Sciortino S., 2012, A&A, 537, A135
Tanveer Karim M. et al., 2016, AJ, preprint (arXiv:1605.04333)
Taylor M. B., 2005, in Shopbell P., Britton M., Ebert R., eds, ASP Conf. Ser. Vol. 347, Astronomical Data Analysis Software and Systems XIV. Astron. Soc. Pac., San Francisco, p. 29
Trullols E., Jordi C., 1997, A&A, 324, 549
Venables W. N., Ripley B. D., 2002, Modern Applied Statistics with S, 4th edn. Springer, New York (http://www.stats.ox.ac.uk/pub/MASS4)
Woźniak P. R., Williams S. J., Vestrand W. T., Gupta V., 2004, AJ, 128, 2965
Zechmeister M., Kürster M., 2009, A&A, 496, 577

APPENDIX: COMPLETE LIST OF RESULTS

In the appendix we present a table (Table A1) of our results for all periodically variable stars in the FoV and the phase-folded light curves for all periodically variable stars among the IC 348 members.

Table A1. Here we present all periods (members and non-members) found in our data. ID gives the number used in this paper. Identifier is a name from 2MASS or Preibisch et al. (2003). CB and LRL are the IDs of Cieza & Baliber (2006) and Luhman et al. (1998), respectively. Stars with an LRL ID in parenthesis are non-members of IC 348 according to Luhman et al. (2003), other stars with an LRL ID are members from Luhman et al. (2016). P states our period with the error ΔP while $P_{\rm CB}$ is the value given by Cieza & Baliber (2006). Amplitude gives the peak-to-peak amplitude of the periodic light curve in magnitudes. R and $(V-R)$ are in the Bessel system and have been measured from our data.

ID	RA (°)	Dec. (°)	Identifier	CB	LRL	P (d)	ΔP (d)	$P_{\rm CB}$ (d)	Amplitude (mag)	R (mag)	$(V-R)$ (mag)
25	56.1632	32.1552	2MASS J03443916+3209182	109	9	1.64	0.02	1.6	0.094	13.3	1.4
27	56.1539	32.1127	2MASS J03443694+3206453	95	6	1.69	0.02	1.7	0.072	11.7	1.1
30	55.9635	32.2193	2MASS J03435123+3213091		22	0.788	0.003		0.12	11.9	0.9
31	55.8851	32.5134	2MASS J03433241+3230477			0.78	0.01		0.019	11.9	1.4
36	56.1000	32.1834	2MASS J03442398+3211000		38	0.71	0.01		0.027	12.4	0.9
38	55.7496	32.1541	2MASS J03425992+3209144			45.5	0.5		0.21	12.5	2.4
49	55.5409	32.3859	2MASS J03420982+3223086			39.1	0.4		0.16	12.8	1.6
52	55.5155	32.2742	2MASS J03420373+3216269			0.1132	0.001		0.012	12.9	0.8
54	55.4924	32.2384	2MASS J03415816+3214179			4.13	0.04		0.10	13.0	1.1
60	55.8956	32.5271	2MASS J03433494+3231372			0.84	0.01		0.055	13.2	1.2
67	56.0684	32.1654	2MASS J03441642+3209552	45	53	3.01	0.03	3	0.15	13.2	1.0
71	55.9813	32.1590	2MASS J03435550+3209321		47	4.91	0.05		0.88	13.5	1.1
72	55.7439	32.4100	2MASS J03425852+3224359			32.7	0.3		0.15	13.5	1.5
80	56.1809	32.1382	2MASS J03444342+3208172		(77)	15.3	0.2		0.077	13.6	1.0
84	55.4940	32.0440	2MASS J03415855+3202379			11.51	0.12		0.088	13.6	1.3
87	56.1462	32.1270	2MASS J03443503+3207370	91	24 A	2.26	0.02	4.5	0.12	13.8	1.3
95	56.0209	32.1650	2MASS J03440499+3209537		56	21.5	0.2		0.063	13.9	1.2
98	56.2563	32.1810	2MASS J03450151+3210512	133	79	1.88	0.02	1.9	0.071	13.9	1.1
107	56.1452	32.1093	2MASS J03443487+3206337	89	48	5.48	0.05	5.4	0.15	14.2	1.3
109	55.7419	32.3678	2MASS J03425806+3222042			28.1	0.3		0.028	14.0	1.0
110	56.0369	32.2697	2MASS J03440885+3216105		44	7.89	0.08		0.053	14.1	1.3
112	56.3775	32.0322	2MASS J03453061+3201557		10 363	2.24	0.02		0.084	14.1	1.1
118	56.1186	32.1230	2MASS J03442847+3207224	76	66	7.01	0.07	7	0.17	14.2	1.3
125	56.1602	32.1266	2MASS J03443845+3207356	104	36	5.21	0.05	5.1	0.27	14.2	1.4
126	55.5462	32.3783	2MASS J03421109+3222418			11.0	0.1		0.05	14.2	1.1
139	56.4865	32.1620	2MASS J03455676+3209428			1.26	0.01		0.031	14.4	0.7
145	55.8836	32.1049	2MASS J03433205+3206172		94	5.49	0.05		0.18	14.5	1.2
147	56.1672	32.1928	2MASS J03444011+3211341		59	2.14	0.02		0.10	14.6	1.4
151	56.0007	32.3708	2MASS J03440015+3222144			12.15	0.12		0.028	14.5	0.9
154	56.2572	32.2411	2MASS J03450174+3214276	134	39	16.4	0.2	16.4	0.10	14.6	1.5
157	56.1066	32.2084	2MASS J03442557+3212299	68	64	8.37	0.08	8.4	0.47	14.8	1.4
158	56.4391	32.1445	2MASS J03454539+3208401			11.91	0.12		0.052	14.7	0.8
162	55.7459	32.5015	2MASS J03425901+3230053			21.0	0.2		0.054	14.6	1.4
163	56.1126	32.0789	2MASS J03442702+3204436	71	69	8.93	0.09	9.1	0.20	14.7	1.2
168	55.6818	31.9876	2MASS J03424360+3159150	10		2.18	0.02	2.2	0.094	14.8	1.4
174	56.1775	32.1055	2MASS J03444261+3206194	121	146	11.5	0.1	12	0.16	14.8	1.2
176	56.1558	32.1033	2MASS J03443740+3206118	97	82	6.28	0.06	6.2	0.095	15.0	1.4
184	56.3166	32.5146	2MASS J03451598+3230519	135		4.04	0.04	4.1	0.12	14.9	1.4
187	55.9618	31.9059	2MASS J03435084+3154210			4.04	0.04		0.12	14.9	1.3
190	56.4079	32.1403	2MASS J03453789+3208249			0.28	0.01		0.012	14.9	1.0
195	55.6255	31.7028	2MASS J03423010+3142104			29.9	0.3		0.088	15.0	1.2
213	56.4741	32.4451	2MASS J03455377+3226418			0.434	0.002		0.075	15.0	0.9
217	55.6693	32.2859	2MASS J03424056+3217101			3.34	0.03		0.085	15.3	1.2
223	55.9531	32.1260	2MASS J03434875+3207332	25	111	39.1	0.4	20.3	0.07	15.3	1.3
226	56.0091	32.3278	2MASS J03440216+3219399	35	118	6.11	0.06	6.2	0.35	15.2	1.5
245	56.3181	32.1056	2MASS J03451634+3206199		1933	28.5	0.3		1.9	15.8	1.5
246	56.3474	32.4104	2MASS J03452338+3224369			8.69	0.09		0.097	15.4	1.4
251	56.0746	32.2057	2MASS J03441791+3212203	46	93	4.39	0.04	4.5	0.16	15.3	1.4
252	55.9989	32.2342	2MASS J03435970+3214028	34	87	14.04	0.1	14	0.16	15.3	1.6
260	55.9643	32.5303	2MASS J03435141+3231486	28		3.75	0.04	3.8	0.13	15.4	1.6
262	56.0476	32.3279	2MASS J03441143+3219401	41	137	0.766	0.008	0.8	0.092	15.6	1.4
268	56.0469	32.1034	2MASS J03441125+3206121	40	105	10.5	0.1	9.1	0.22	15.5	1.5
277	55.9843	32.5050	2MASS J03435622+3230178	30		8.23	0.08	8.1	0.10	15.5	1.6
279	55.6486	32.2889	2MASS J03423566+3217198	7		1.15	0.02	1.2	0.035	15.5	0.9
280	56.1172	32.2667	2MASS J03442812+3216002	75	85	2.67	0.03	2.7	0.22	15.9	1.2
282	56.1162	32.1255	2MASS J03442787+3207316	74	86	6.55	0.07	5.4	0.084	15.6	1.5
292	55.7311	31.9535	2MASS J03425546+3157123	11		0.6508	0.001	1.9	0.12	15.5	1.2

Table A1 – *continued*

ID	RA (°)	Dec. (°)	Identifier	CB	LRL	P (d)	ΔP (d)	P_{CB} (d)	Amplitude (mag)	R (mag)	$(V-R)$ (mag)
296	56.1229	32.4403	2MASS J03442949+3226250			9.5	0.1		0.044	15.7	1.3
297	56.1605	32.1336	2MASS J03443854+3208006	105	58	7.69	0.08	7.3	0.20	15.7	1.7
304	56.0986	32.1130	2MASS J03442366+3206465	64	92	9.7	0.1	10	0.28	15.6	1.5
305	56.1605	32.2167	2MASS J03443838+3212597	103	144	13.5	0.1	13.5	0.27	15.8	1.5
317	55.9842	32.1434	2MASS J03435619+3208362		142	3.91	0.04		0.066	15.9	1.4
318	55.9495	32.2992	2MASS J03434788+3217567	24	126	9.68	0.1	9.8	0.16	15.7	1.5
327	56.3845	32.0542	2MASS J03453230+3203150	140	10 289	0.705	0.001	0.7	0.17	15.8	1.2
341	56.0901	32.1772	2MASS J03442161+3210376	58	41	7.56	0.08	2.8	1.3	16.6	2.1
346	56.0957	32.1993	2MASS J03442297+3211572		120	5.06	0.05		0.16	15.9	1.5
347	56.1188	31.9984	2MASS J03442851+3159539		68	26.9	0.3		0.22	15.8	1.5
348	56.1384	32.2581	2MASS J03443321+3215290		122	6.96	0.07		0.098	15.7	1.7
349	56.0930	32.2002	2MASS J03442232+3212007	61	100	0.83	0.01	8.4	0.099	16.1	1.6
353	55.6923	32.4549	2MASS J03424614+3227172			12.1	0.1		0.075	16.0	1.0
355	56.1111	32.0662	2MASS J03442663+3203583	69	62	3.09	0.03	3.1	0.16	16.0	1.8
357	56.2907	32.2268	2MASS J03450986+3213350			2.47	0.02		0.03	16.0	1.1
364	56.0170	32.1214	2MASS J03440410+3207170		174	10.0	0.1		0.20	16.3	1.6
366	56.5065	32.1606	2MASS J03460161+3209375			1.67	0.02		0.087	16.1	0.9
384	56.1064	32.1920	2MASS J03442555+3211307	67	60 B	4.86	0.05	5.4	0.36	16.3	1.6
386	55.7794	32.1718	2MASS J03430704+3210182	14		6.14	0.06	6.2	0.19	16.1	1.7
387	56.1859	32.1369	2MASS J03444458+3208125		103	25.7	0.3		0.89	17.0	2.0
391	56.0898	32.1716	2MASS J03442155+3210174	56	116	7.09	0.07	7	0.36	16.1	1.8
394	55.9558	32.1778	2MASS J03434939+3210398	27	147	6.4	0.06	13.1	0.19	16.2	1.4
407	56.2123	32.2693	2MASS J03445096+3216093	128	101	12.1	0.1	13.1	0.27	16.0	1.5
421	56.0929	32.0953	2MASS J03442228+3205427	60	61	11.9	0.1	30	0.50	16.5	1.3
441	55.7352	31.7106	2MASS J03425646+3142382			8.62	0.09		0.23	16.2	2.1
444	55.5361	32.4745	2MASS J03420867+3228276			2.84	0.03		0.14	16.3	1.7
465	56.0897	32.2528	2MASS J03442156+3215098		185	8.17	0.08		0.31	16.9	0.4
470	56.2338	32.0991	2MASS J03445611+3205564	131	188	3.31	0.03	3.3	0.087	16.3	1.3
476	56.3981	31.9406	2MASS J03453551+3156257	141		9.28	0.09	9.6	0.13	16.4	1.5
477	56.1691	32.3865	2MASS J03444061+3223110	114		4.03	0.04	4.1	0.14	16.3	1.5
502	56.1023	32.0659	2MASS J03442457+3203571	65	123	4.94	0.05	4.9	0.33	17.1	1.9
505	56.2034	32.2228	2MASS J03444881+3213218	127	178	6.9	0.07	6.9	0.25	16.5	1.7
509	56.1812	32.1286	2MASS J03444351+3207427		52	8.14	0.08		0.13	16.6	1.9
514	56.2198	32.0158	2MASS J03445274+3200565		1939	10.9	0.1		0.15	16.7	1.6
523	55.9983	32.2654	2MASS J03435953+3215551	33	155	7.59	0.08	7.6	0.33	16.7	1.4
525	56.3444	31.7239	2MASS J03452267+3143259			17.1	0.2		0.15	16.4	1.4
526	55.6077	32.3507	2MASS J03422585+3221022	2		17.3	0.2	17.7	0.22	16.5	1.6
543	55.6177	32.5133	2MASS J03422824+3230479	3		4.34	0.04	4.3	0.45	16.3	1.5
544	55.9534	32.2644	2MASS J03434881+3215515	26	162	2.88	0.03	2.9	0.18	16.9	1.7
565	55.5846	32.0920	2MASS J03422033+3205310	1		7.25	0.07	7.7	0.57	16.6	1.8
570	56.0802	32.1263	PSZ2003 J034419.2+320734	49	99 A	7.55	0.08	7.6	1.3	16.0	1.5
596	56.3977	32.0572	2MASS J03453545+3203259		10 284	1.57	0.02		0.26	16.6	1.6
607	56.2081	32.0628	2MASS J03444998+3203455			220	2		0.085	16.7	1.7
608	56.0906	32.2087	2MASS J03442176+3212312		180	3.26	0.03		0.08	16.7	1.7
611	56.1249	32.3230	2MASS J03442997+3219227		104	8.67	0.09		0.25	16.8	2.3
616	55.6342	31.7272	2MASS J03423219+3143382			12.2	0.1		0.21	16.7	1.9
617	55.6703	32.2264	2MASS J03424086+3213347	9		0.47375	0.00025	0.5	0.085	16.6	1.8
640	56.1495	32.2645	2MASS J03443588+3215533		181	7.7	0.08		0.17	16.6	1.7
670	56.3423	32.0345	2MASS J03452214+3202040		10 373	0.78	0.01		0.10	16.9	1.3
683	56.0756	32.0825	2MASS J03441816+3204570		31	3.34	0.03		0.14	17.4	2.1
696	55.6000	31.9005	2MASS J03422398+3154016			0.579	0.001		0.07	17.0	1.3
699	56.2718	32.1653	2MASS J03450521+3209544		177	4.95	0.05		0.16	17.1	1.6
701	56.3406	32.5352	2MASS J03452174+3232065			5.07	0.05		0.2	16.9	1.9
723	56.0283	32.1318	2MASS J03440678+3207540	37	156	2.61	0.03	1.3	0.13	17.1	2.0
735	55.8874	32.4675	2MASS J03433299+3228027	22		11.7	0.1	12.2	0.23	17.3	2.0
758	56.2620	32.1169	2MASS J03450285+3207006		150	2.39	0.02		0.14	17.3	1.7
774	56.3116	32.4332	2MASS J03451480+3225594			5.58	0.06		0.2	17.0	1.9
775	56.1584	32.1937	2MASS J03443800+3211370		193	2.39	0.02		0.25	17.4	1.4
777	56.4146	31.7148	2MASS J03453948+3142528			0.4882	0.0015		0.27	17.3	0.9
796	56.1134	32.2393	2MASS J03442724+3214209		132	4.4	0.04		1.2	17.2	1.7
798	56.4449	32.4804	2MASS J03454675+3228487	143		10.33	0.1	10.5	0.20	17	1.7
800	56.1874	32.2268	2MASS J03444495+3213364		112	20.0	0.2		0.20	17.1	1.8

Table A1 *– continued*

ID	RA (°)	Dec. (°)	Identifier	CB	LRL	P (d)	ΔP (d)	$P_{\rm CB}$ (d)	Amplitude (mag)	R (mag)	$(V-R)$ (mag)
807	55.6372	31.7057	2MASS J03423291+3142205			10.69	0.11		1.0	16.9	2.1
811	56.1616	32.3183	2MASS J03443878+3219056	108	208	4.85	0.05	4.8	0.20	16.9	2.4
829	56.0312	32.0691	2MASS J03440750+3204088		214	2.34	0.02		0.24	17.5	1.6
848	55.7330	31.7464	2MASS J03425593+3144463			2.46	0.02		0.12	17.1	1.6
849	56.1574	32.2050	2MASS J03443777+3212181	100	154	3.25	0.03	3.3	0.25	17.4	1.7
898	56.4328	32.4098	2MASS J03454385+3224350	142		14.4	0.1	14.3	0.30	17.5	1.8
927	56.4929	32.4466	2MASS J03455824+3226475			7.72	0.07		0.80	18.2	1.1
935	55.9526	32.2307	2MASS J03434862+3213507		261	0.638	0.006		0.30	18.0	1.3
941	56.0191	32.4684	2MASS J03440459+3228062			6.96	0.07		0.40	17.5	1.7
952	56.0834	32.1127	2MASS J03442001+3206455	50	210	8.62	0.09	8.6	0.45	17.6	1.4
955	56.1240	32.1777	2MASS J03442972+3210398		40	4.6	0.05		0.25	15.4	1.4
956	56.1363	32.1545	2MASS J03443276+3209157	82	88	5.28	0.05	5.5	0.33	16.2	0.7
957	56.1355	32.1490	2MASS J03443257+3208558	80	71	1.82	0.02	6.7	0.14	16.1	2.1
958	56.1311	32.1457	2MASS J03443153+3208449	78	29	2.22	0.02	10.8	0.069	12.8	1.1
959	56.1363	32.1438	2MASS J03443274+3208374	81	16	2.62	0.03	2.6	0.088	12.5	1.0
960	56.1611	32.1450	2MASS J03443871+3208420	107	23	2.41	0.02	2.4	0.12	15.4	1.6
961	56.1614	32.1489	2MASS J03443869+3208567	106	108	2.79	0.03	2.1	0.13	16.0	1.6
962	56.1558	32.1504	2MASS J03443741+3209009	99	83	8.34	0.08	8.4	0.43	16.5	0.9
964	56.1633	32.1623	2MASS J03443919+3209448	110	91	3.98	0.04	3.9	0.54	16.3	1.4
965	56.1416	32.1482	2MASS J03443398+3208541	86	65	15.8	0.2	16.4	0.21	14.7	1.5
967	56.0903	32.1070	2MASS J03442166+3206248	57	125	8.36	0.08	8.4	0.18		
968	56.0939	32.0314	2MASS J03442257+3201536	62	72	44.7	0.4	1	0.21	15.9	1.6
972	56.1083	32.2750	2MASS J03442595+3216306		(972)	7.56	0.08		0.032	14.2	0.8
973	56.0406	32.2868	2MASS J03440973+3217130			9.58	0.1		0.2	15.5	0.5
974	55.6466	32.5650	2MASS J03423520+3233544	6		0.422	0.002	0.2	0.25		
975	55.8014	32.5698	2MASS J03431233+3234114	17		0.446	0.002	0.20	0.35		
996	56.1153	32.5637	2MASS J03442766+3233495	73		1.59	0.02	2.6	0.094	15.8	1.5
998	56.0927	32.5625	2MASS J03442225+3233449			12.13	0.12		0.043	14.5	1.0
1001	56.4838	32.572	2MASS J03455608+3234190			11.88	0.12		0.13	15.8	1.2

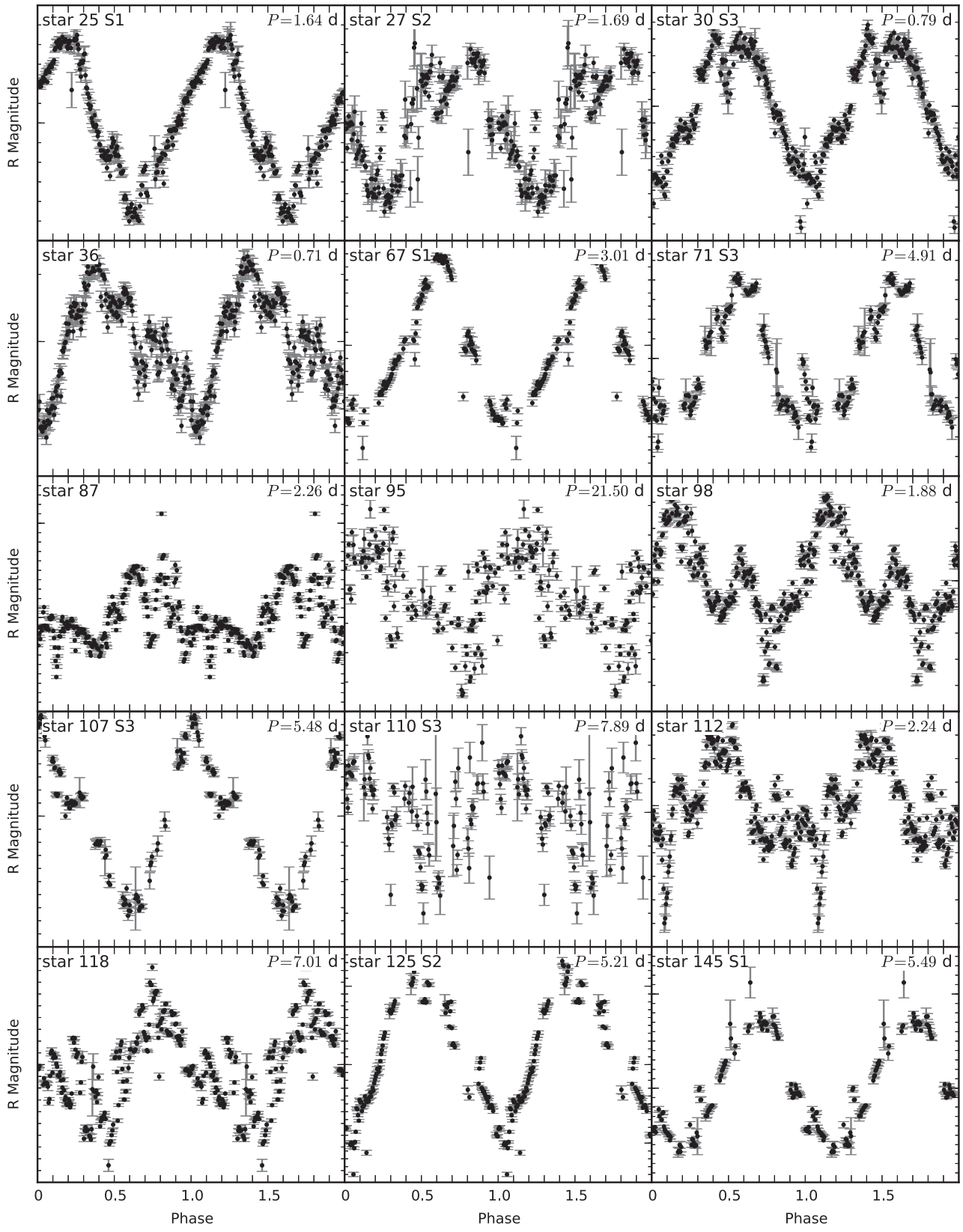

Figure A1. Phase-folded and binned (200 bins) light curves of all periodically variable IC 348 members. We present the double phase for easier visualization (data points in the phase between 1 and 2 are repeated from phase 0 to 1). For stars without a coherent phase over the full time span of the observations only one season is shown. This is indicated by S*n* added to the star number, where *n* is an integer from 1 to 3 (compare Table 2). The spacing is 0.01 mag for minor ticks and 0.1 mag for major ticks on the magnitude axis.

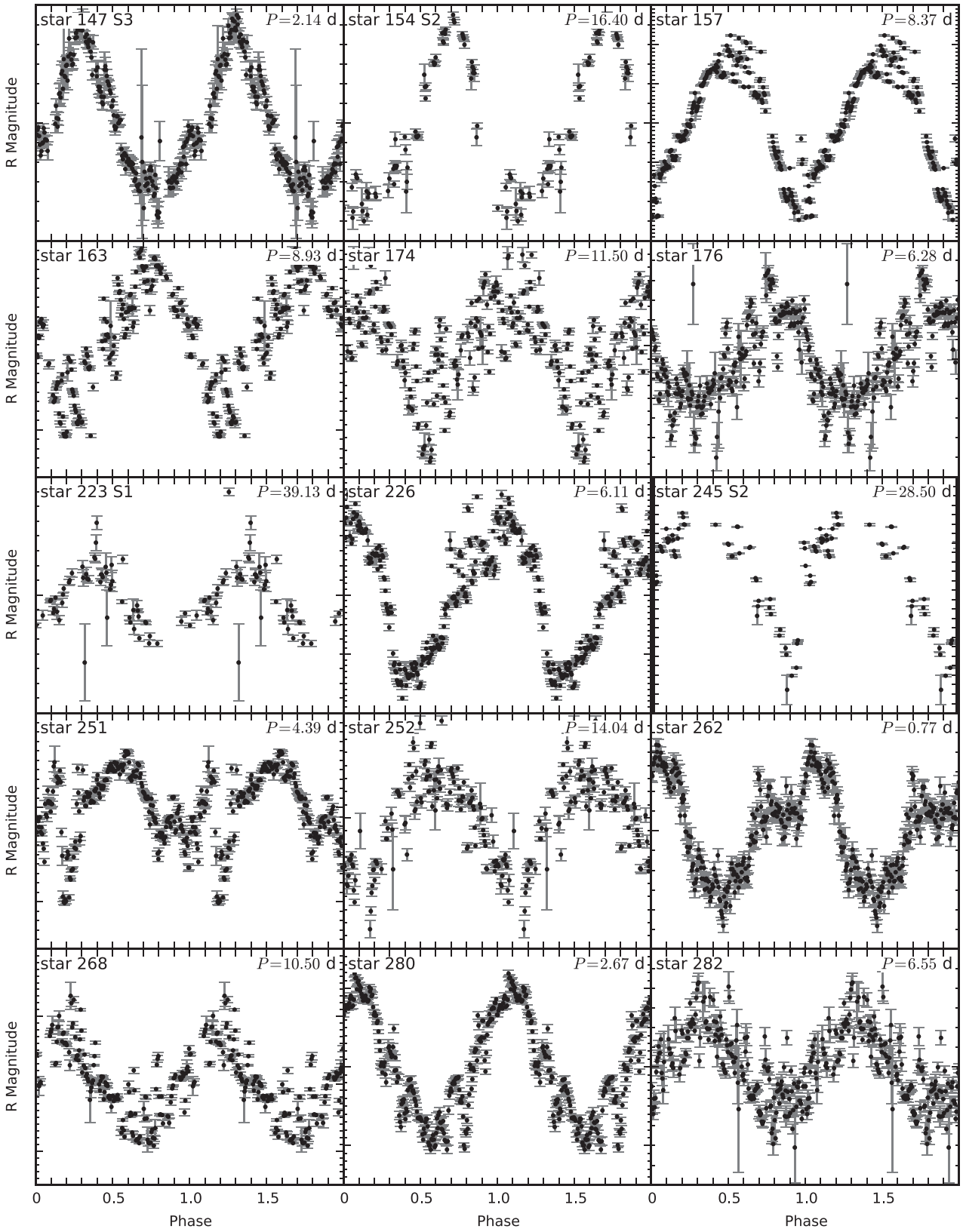

Figure A1 – *continued*

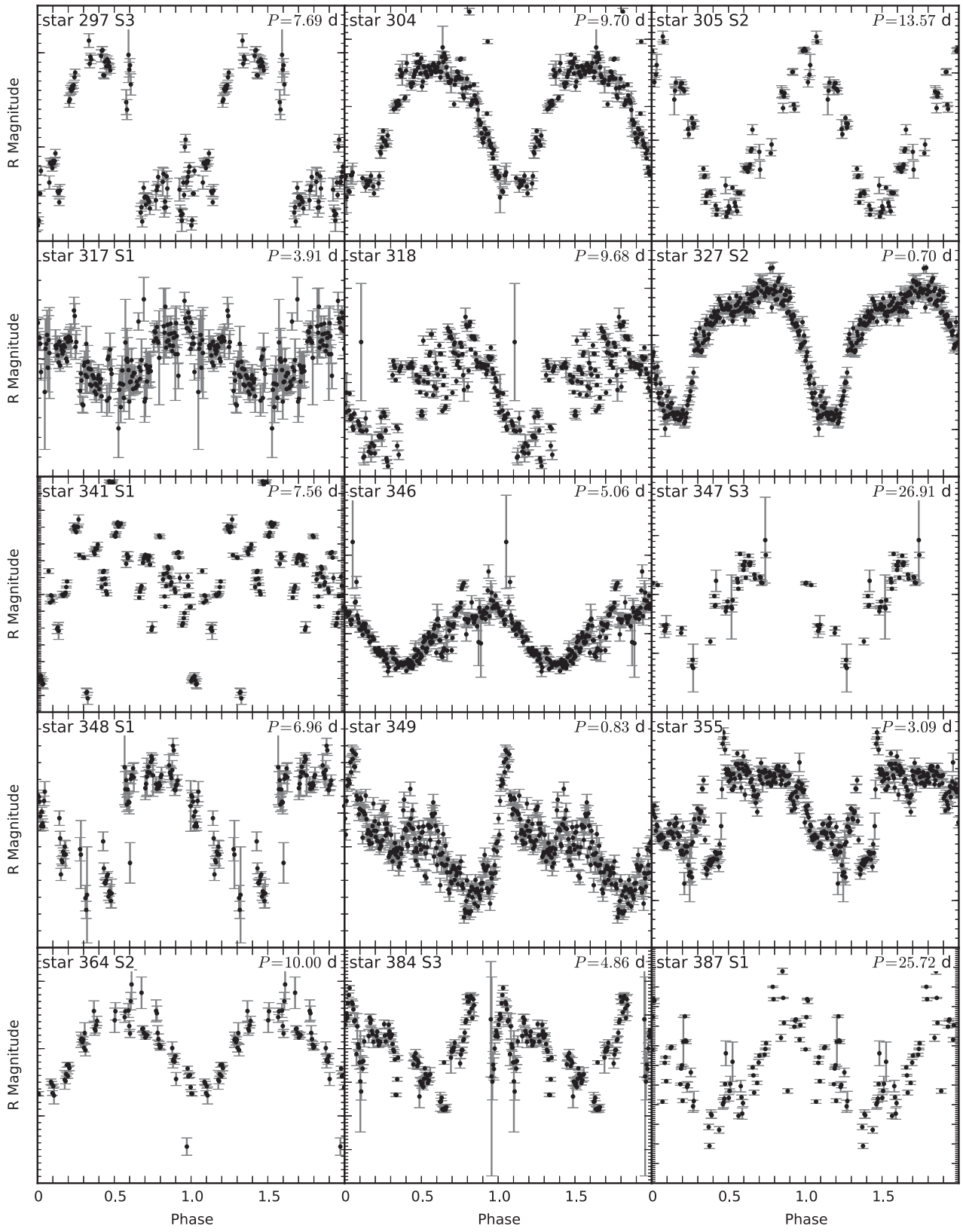

Figure A1 – *continued*

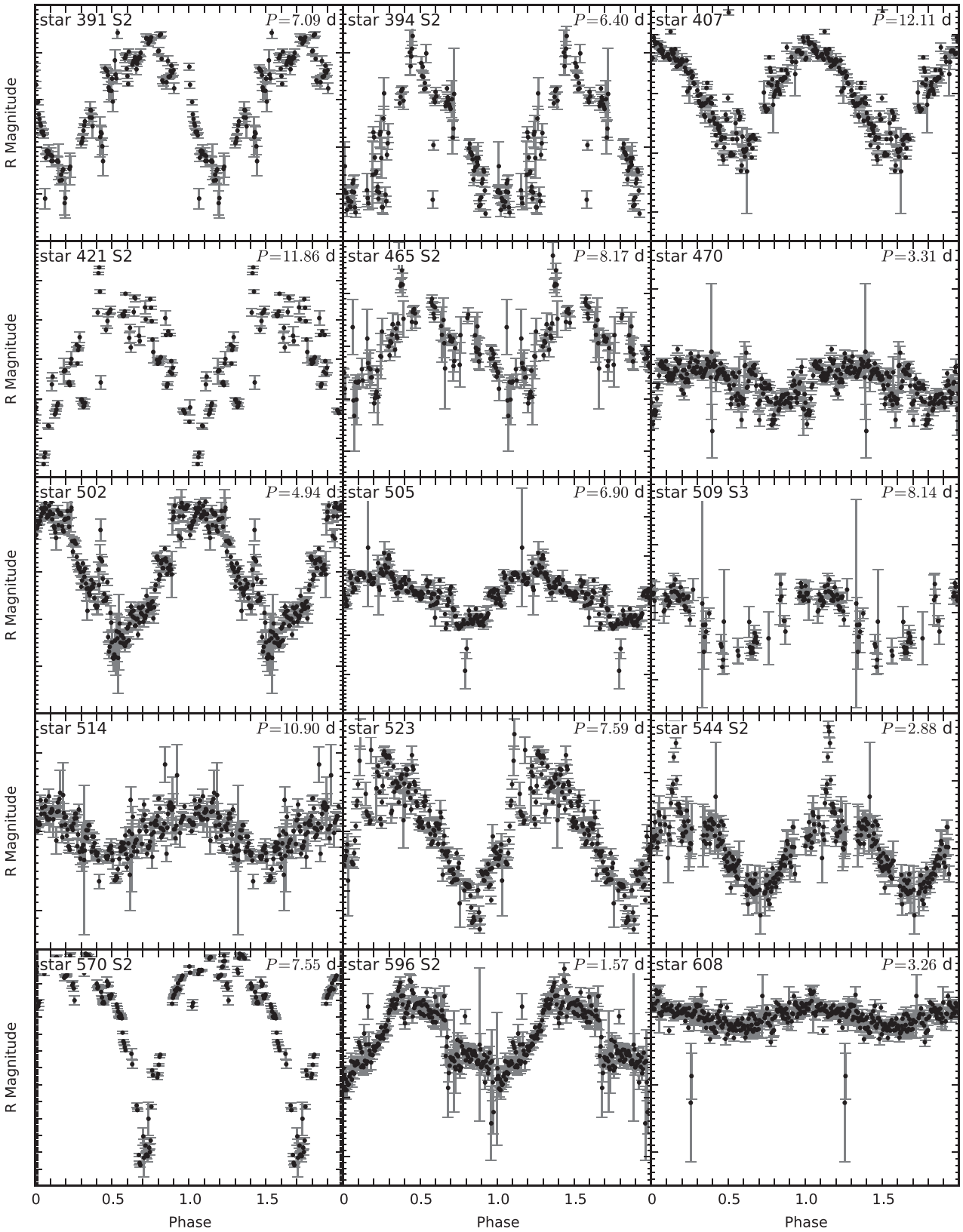

Figure A1 – *continued*

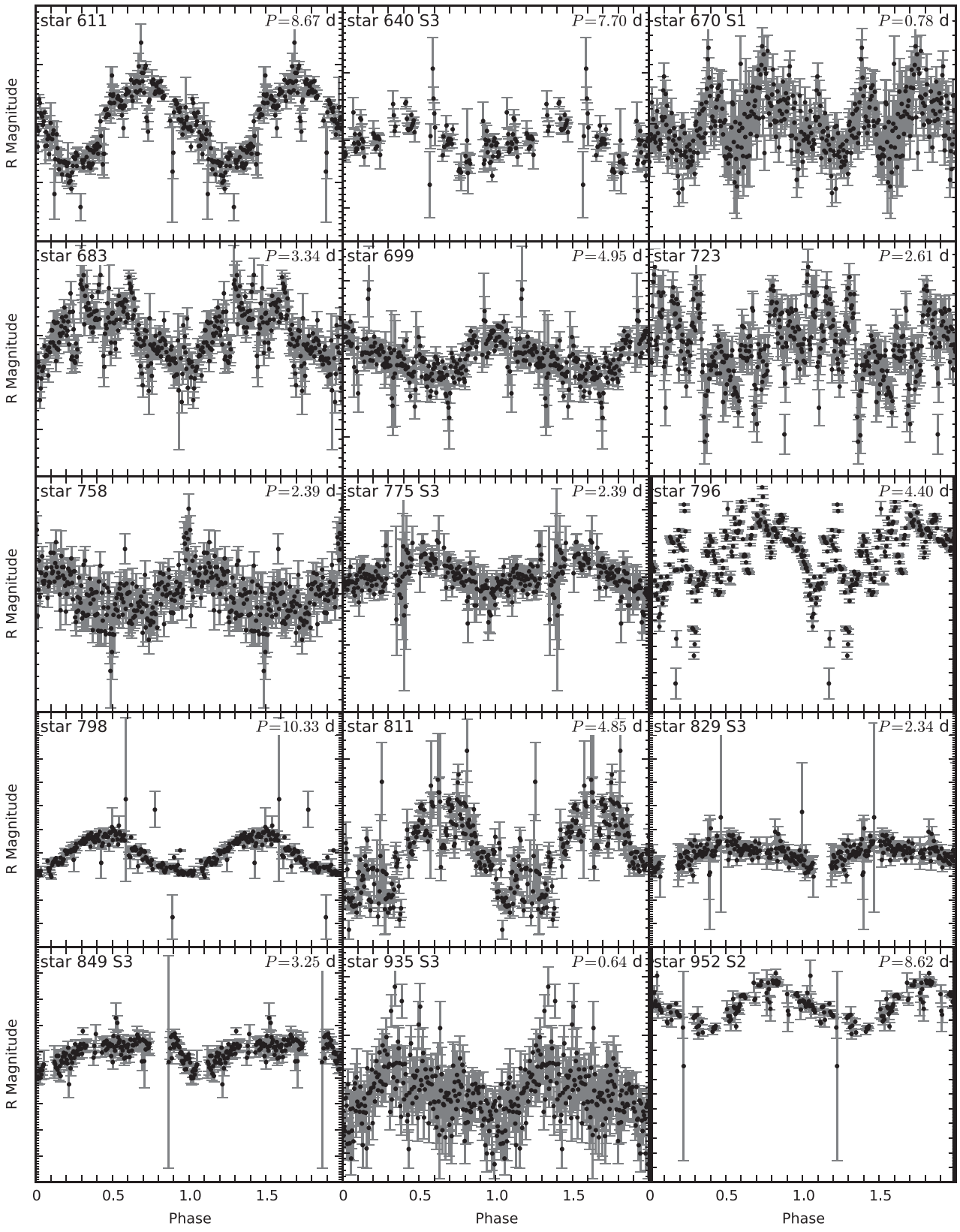

Figure A1 – *continued*

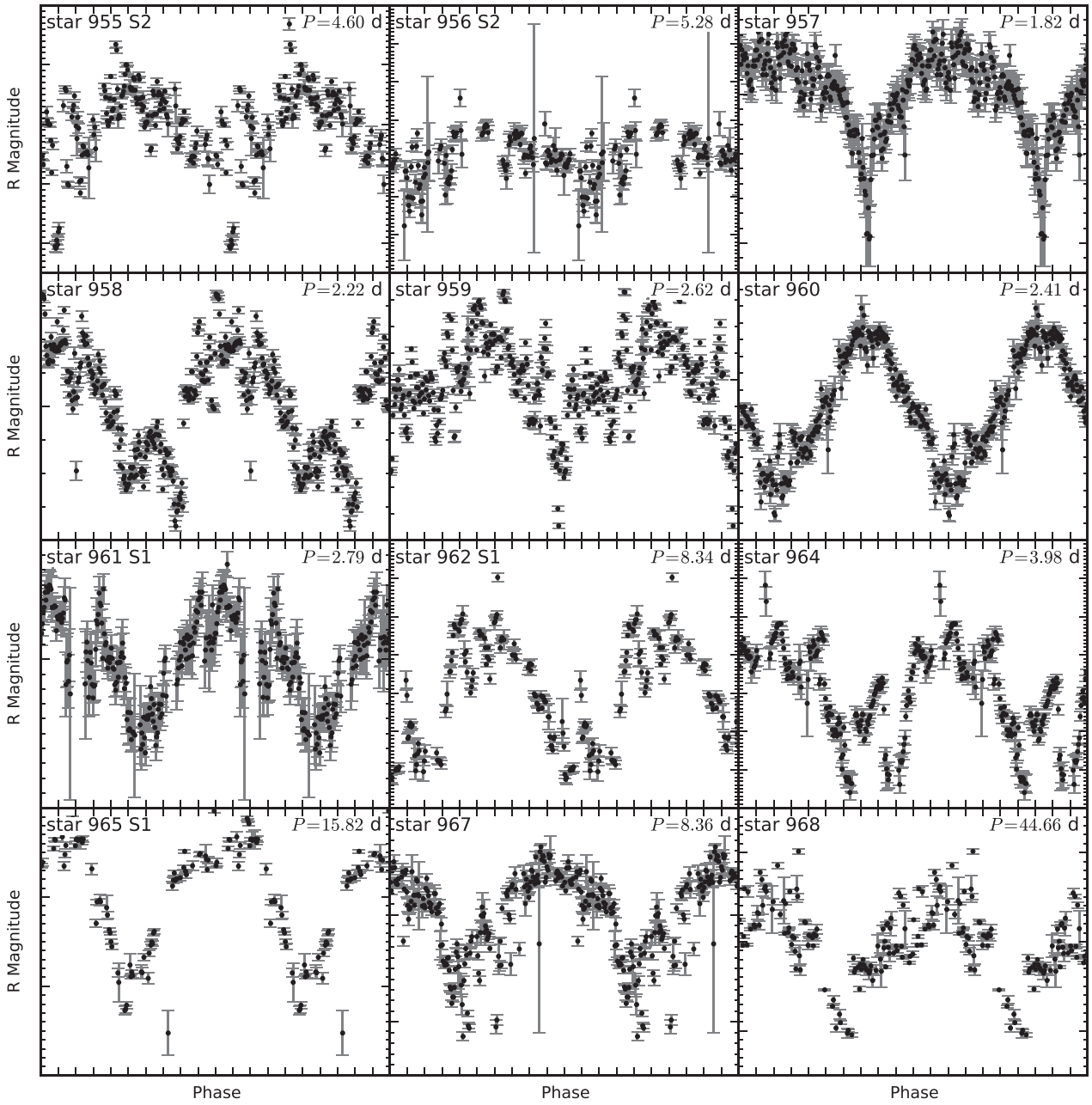

Figure A1 – *continued*

[1]*Astrophysikalisches Institut und Universitäts-Sternwarte Friedrich-Schiller-Universität Jena, Schillergässchen 2-3, D-07745 Jena, Germany*
[2]*Leibniz-Institut für Astrophysik (AIP), An der Sternwarte 16, D-14482 Potsdam, Germany*
[3]*Cerro Tololo Interamerican Observatory, Casilla Postal 603, La Serena 1700000, Chile*
[4]*Max-Planck-Institut für Astronomie, Königstuhl 17, D-69117 Heidelberg, Germany*
[5]*Centre for Advanced Instrumentation, Department of Physics, University of Durham, South Road, Durham DH1 3LE, UK*
[6]*Graduate Institute of Astronomy, National Central University, 300 Jhongda Road, Jhongli 32001, Taiwan*
[7]*Institut für Astronomie und Astrophysik Tübingen, Sand 1, D-72076 Tübingen, Germany*
[8]*Department of Physics and Astronomy, University of Sheffield, Sheffield S3 7RH, UK*
[9]*Instituto de Astrofísica de Canarias, E-38205 La Laguna, Tenerife, Spain*
[10]*Abbe School of Photonics, Max-Wien-Platz 1, D-07743 Jena, Germany*
[11]*Astronomical Institute, Slovak Academy of Sciences, 059 60 Tatranská Lomnica, Slovakia*
[12]*Leiden Observatory, Leiden University, PO Box 9513, NL-2300 RA Leiden, the Netherlands*
[13]*Centro de Investigaciones de Astronomía, Apdo. Postal 264, Mérida 5101-A, Venezuela*

[14]*Instituto de Astronomía, Universidad Nacional Autónoma de México, Unidad Académica en Ensenada, Ensenada 22860, Mexico*
[15]*Battcock Centre for Experimental Astrophysics, Cavendish Laboratory, Cambridge University, JJ Thompson Avenue, Cambridge CB3 0HE, UK*
[16]*Instituto Radioastronomía Milimétrica (IRAM), Avenida Divina Pastora 7, E-18012 Granada, Spain*
[17]*ESTEC – SCI-S ESA – European Space Agency, Keplerlaan 1, NL-2201 AZ Noordwijk, the Netherlands*
[18]*Theoretische Astrophysik, Universität Tübingen, Auf der Morgenstelle 10, D-72076 Tübingen, Germany*
[19]*Hamburger Sternwarte, Gojenbergsweg 112, D-21029 Hamburg, Germany*

This paper has been typeset from a TEX/LATEX file prepared by the author.

LETTER

doi:10.1038/nature16452

Repetitive patterns in rapid optical variations in the nearby black-hole binary V404 Cygni

Mariko Kimura[1], Keisuke Isogai[1], Taichi Kato[1], Yoshihiro Ueda[1], Satoshi Nakahira[2], Megumi Shidatsu[3], Teruaki Enoto[1,4], Takafumi Hori[1], Daisaku Nogami[1], Colin Littlefield[5], Ryoko Ishioka[6], Ying-Tung Chen[6], Sun-Kun King[6], Chih-Yi Wen[6], Shiang-Yu Wang[6], Matthew J. Lehner[6,7,8], Megan E. Schwamb[6], Jen-Hung Wang[6], Zhi-Wei Zhang[6], Charles Alcock[8], Tim Axelrod[9], Federica B. Bianco[10], Yong-Ik Byun[11], Wen-Ping Chen[12], Kem H. Cook[6], Dae-Won Kim[13], Typhoon Lee[6], Stuart L. Marshall[14], Elena P. Pavlenko[15], Oksana I. Antonyuk[15], Kirill A. Antonyuk[15], Nikolai V. Pit[15], Aleksei A. Sosnovskij[15], Julia V. Babina[15], Aleksei V. Baklanov[15], Alexei S. Pozanenko[16,17], Elena D. Mazaeva[16], Sergei E. Schmalz[18], Inna V. Reva[19], Sergei P. Belan[15], Raguli Ya. Inasaridze[20], Namkhai Tungalag[21], Alina A. Volnova[16], Igor E. Molotov[22], Enrique de Miguel[23,24], Kiyoshi Kasai[25], William L. Stein[26], Pavol A. Dubovsky[27], Seiichiro Kiyota[28], Ian Miller[29], Michael Richmond[30], William Goff[31], Maksim V. Andreev[32,33], Hiromitsu Takahashi[34], Naoto Kojiguchi[35], Yuki Sugiura[35], Nao Takeda[35], Eiji Yamada[35], Katsura Matsumoto[35], Nick James[36], Roger D. Pickard[37,38], Tamás Tordai[39], Yutaka Maeda[40], Javier Ruiz[41,42,43], Atsushi Miyashita[44], Lewis M. Cook[45], Akira Imada[46] & Makoto Uemura[47]

How black holes accrete surrounding matter is a fundamental yet unsolved question in astrophysics. It is generally believed that matter is absorbed into black holes via accretion disks, the state of which depends primarily on the mass-accretion rate. When this rate approaches the critical rate (the Eddington limit), thermal instability is supposed to occur in the inner disk, causing repetitive patterns of large-amplitude X-ray variability (oscillations) on timescales of minutes to hours[1]. In fact, such oscillations have been observed only in sources with a high mass-accretion rate, such as GRS 1915+105 (refs 2, 3). These large-amplitude, relatively slow timescale, phenomena are thought to have physical origins distinct from those of X-ray or optical variations with small amplitudes and fast timescales (less than about 10 seconds) often observed in other black-hole binaries—for example, XTE J1118+480 (ref. 4) and GX 339−4 (ref. 5). Here we report an extensive multi-colour optical photometric data set of V404 Cygni, an X-ray transient source[6] containing a black hole of nine solar masses[7] (and a companion star) at a distance of 2.4 kiloparsecs (ref. 8). Our data show that optical oscillations on timescales of 100 seconds to 2.5 hours can occur at mass-accretion rates more than ten times lower than previously thought[1]. This suggests that the accretion rate is not the critical parameter for inducing inner-disk instabilities. Instead, we propose that a long orbital period is a key condition for these large-amplitude oscillations, because the outer part of the large disk in binaries with long orbital periods will have surface densities too low to maintain sustained mass accretion to the inner part of the disk. The lack of sustained accretion—not the actual rate—would then be the critical factor causing large-amplitude oscillations in long-period systems.

V404 Cyg, which was originally discovered as a nova in 1938 and detected by the GINGA satellite in 1989[9], underwent an outburst in June 2015 after 26 years of dormancy. At 18:31:38 on June 15 (15.77197 Universal Time (UT)), Swift/Burst Alert Telescope (BAT) initially detected this outburst as a possible γ-ray burst[10]. The outburst was also detected by the Monitor of All-sky X-ray Image (MAXI) instrument on June 16.783 UT[11].

Following these detections, we started a world-wide photometric campaign (Extended Data Tables 1 and 2, Methods section 'Detailed methods of optical observations') partly within the Variable Star Network (VSNET) Collaboration, and collected extensive sets of multi-colour optical photometric data consisting of >85,000 points. Our data set also includes early observations with the Taiwanese–American Occultation Survey (TAOS) starting on June 15, 18:34:07 UT, 2 min 29 s after the Swift/BAT trigger[12] (see Extended Data Tables 1 and 2, and Methods section 'Detailed methods of optical observations' concerning

[1]Department of Astronomy, Graduate School of Science, Kyoto University, Oiwakecho, Kitashirakawa, Sakyo-ku, Kyoto 606-8502, Japan. [2]JEM Mission Operations and Integration Center, Human Spaceflight Technology Directorate, Japan Aerospace Exploration Agency, 2-1-1 Sengen, Tsukuba, Ibaraki 305-8505, Japan. [3]MAXI team, RIKEN, 2-1 Hirosawa, Wako, Saitama 351-0198, Japan. [4]The Hakubi Center for Advanced Research, Kyoto University, Kyoto 606-8302, Japan. [5]Astronomy Department, Wesleyan University, Middletown, Connecticut 06459, USA. [6]Institute of Astronomy and Astrophysics, Academia Sinica, 11F of Astronomy-Mathematics Building, AS/NTU No. 1, Section 4, Roosevelt Road, Taipei 10617, Taiwan. [7]Department of Physics and Astronomy, University of Pennsylvania, 209 South 33rd Street, Philadelphia, Pennsylvania 19125, USA. [8]Harvard-Smithsonian Center for Astrophysics, 60 Garden Street, Cambridge, Massachusetts 02138, USA. [9]Steward Observatory, University of Arizona, Tucson, Arizona 85721, USA. [10]Center for Cosmology and Particle Physics, New York University, 4 Washington Place, New York, New York 10003, USA. [11]Department of Astronomy and University Observatory, Yonsei University, Seoul 120-749, South Korea. [12]Institute of Astronomy and Department of Physics, National Central University, Chung-Li 32054, Taiwan. [13]Max Planck Institute for Astronomy, Königstuhl 17, 69117 Heidelberg, Germany. [14]Kavli Institute for Particle Astrophysics and Cosmology (KIPAC), Stanford University, 452 Lomita Mall, Stanford, California 94309, USA. [15]Crimean Astrophysical Observatory, 298409 Nauchny, Crimea. [16]Space Research Institute, Russian Academy of Sciences, 117997 Moscow, Russia. [17]National Research Nuclear University MEPhI (Moscow Engineering Physics Institute), Moscow, Russia. [18]Leibniz Institute for Astrophysics, Potsdam, Germany. [19]Fesenkov Astrophysical Institute, Almaty, Kazakhstan. [20]Kharadze Abastumani Astrophysical Observatory, Ilia State University, Tbilisi, Georgia. [21]Institute of Astronomy and Geophysics, Mongolian Academy of Sciences, Ulaanbaatar 13343, Mongolia. [22]Keldysh Institute of Applied Mathematics, Russian Academy of Sciences, Moscow, Russia. [23]Departamento de Física Aplicada, Facultad de Ciencias Experimentales, Universidad de Huelva, 21071 Huelva, Spain. [24]Center for Backyard Astrophysics, Observatorio del CIECEM, Parque Dunar, Matalascañas, 21760 Almonte, Huelva, Spain. [25]Baselstrasse 133D, CH-4132 Muttenz, Switzerland. [26]6025 Calle Paraiso, Las Cruces, New Mexico 88012, USA. [27]Vihorlat Observatory, Mierova 4, Humenne, Slovakia. [28]Variable Star Observers League in Japan (VSOLJ), 7-1 Kitahatsutomi, Kamagaya, Chiba 273-0126, Japan. [29]Furzehill House, Ilston, Swansea SA2 7LE, UK. [30]Physics Department, Rochester Institute of Technology, Rochester, New York 14623, USA. [31]American Association of Variable Star Observers (AAVSO), 13508 Monitor Lane, Sutter Creek, California 95685, USA. [32]Institute of Astronomy, Russian Academy of Sciences, 361605 Peak Terskol, Kabardino-Balkaria, Russia. [33]International Center for Astronomical, Medical and Ecological Research of National Academy of Sciences of Ukraine (NASU), 27 Akademika Zabolotnoho street, 03680 Kiev, Ukraine. [34]Department of Physical Science, School of Science, Hiroshima University, 1-3-1 Kagamiyama, Higashi-Hiroshima, Hiroshima 739-8526, Japan. [35]Osaka Kyoiku University, 4-698-1 Asahigaoka, Kashiwara, Osaka 582-8582, Japan. [36]1 Tavistock Road, Chelmsford, Essex CM1 6JL, UK. [37]The British Astronomical Association, Variable Star Section (BAA VSS), Burlington House, Piccadilly, London W1J 0DU, UK. [38]3 The Birches, Shobdon, Leominster, Herefordshire HR6 9NG, UK. [39]Polaris Observatory, Hungarian Astronomical Association, Laborc utca 2/c, 1037 Budapest, Hungary. [40]112-14 Kaminishiyama-machi, Nagasaki, Nagasaki 850-0006, Japan. [41]Observatorio de Cantabria, Carretera de Rocamundo sin número, Valderredible, Cantabria, Spain. [42]Instituto de Fisica de Cantabria (CSIC-UC), Avenida Los Castros sin número, E-39005 Santander, Cantabria, Spain. [43]Agrupacion Astronomica Cantabra, Apartado 573, 39080 Santander, Spain. [44]Seikei Meteorological Observatory, Seikei High School, Kichijoji-kitamachi 3-10-13, Musashino, Tokyo 180-8633, Japan. [45]Center for Backyard Astrophysics (Concord), 1730 Helix Court, Concord, California 94518, USA. [46]Kwasan and Hida Observatories, Kyoto University, Kitakazan-Ohmine-cho, Yamashina-ku, Kyoto 607-8471, Japan. [47]Hiroshima Astrophysical Science Center, Hiroshima University, Kagamiyama 1-3-1, Higashi-Hiroshima, Hiroshima 739-8526, Japan.

<102>

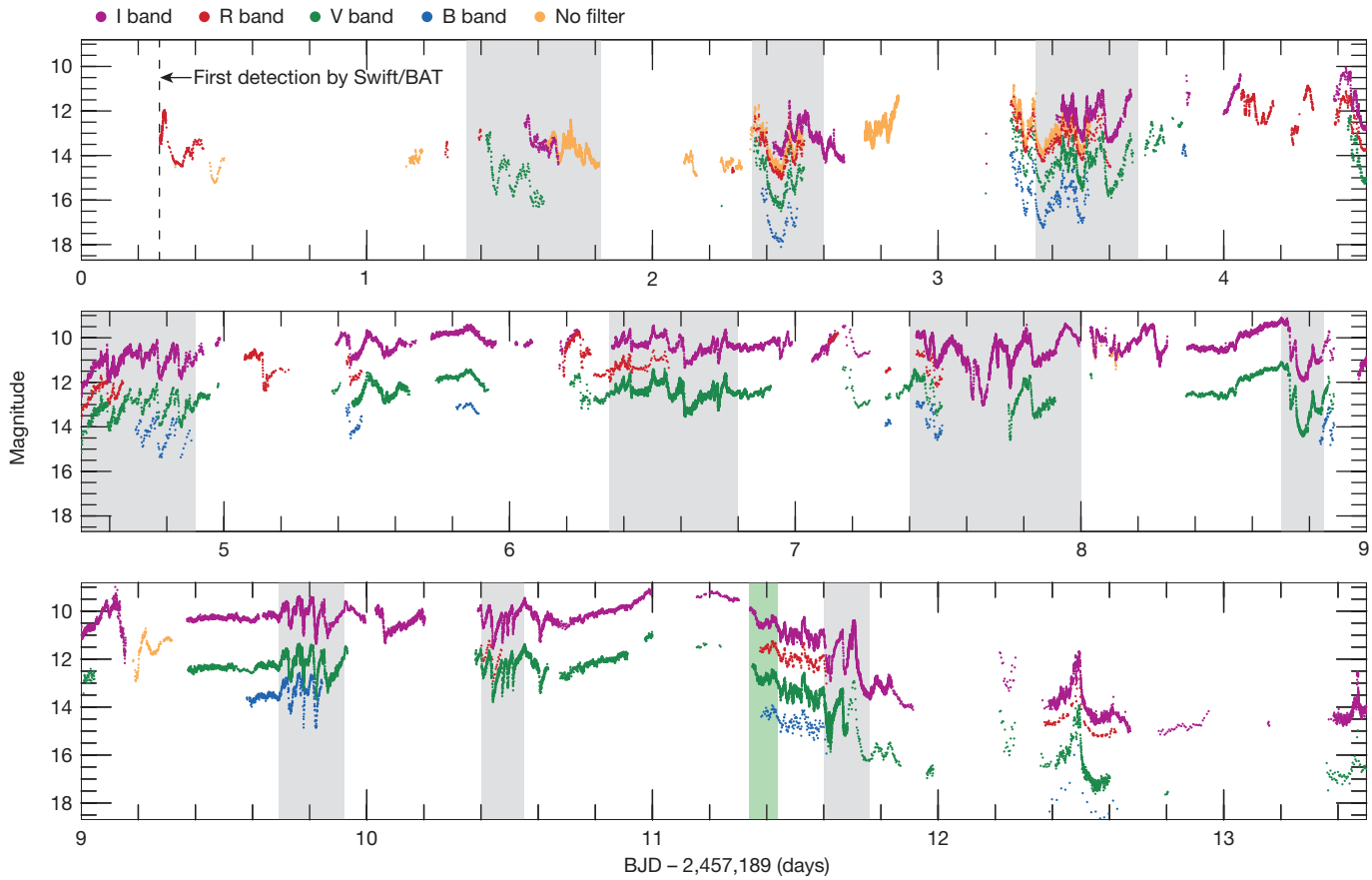

Figure 1 | Overall multi-colour light curves during the 2015 outburst of V404 Cyg. Shown are multi-colour light curves (B, V, R and I bands, and no filters) during BJD 2,457,189 to 2,457,202 (BJD 2,457,189 corresponds to 2015 June 15). It is clearly seen that dip-type oscillations (variations with recurrent sudden dips) were observed from the beginning to the end of the outburst. The horizontal axis shows BJD − 2,457,189. The significant periods of repetitive optical variations are indicated in grey and green shading for the 'dip-type' and 'heartbeat-type' oscillations, respectively.

the VSNET collaboration team and TAOS). Some weak activity started approximately 1,000 s before the Swift/BAT trigger[13]. The same activity above 80 keV was also detected by the active anti-coincidence shield (ACS) of the Spectrometer on INTEGRAL (SPI) telescope of the INTEGRAL observatory in the same time intervals (P. Minaev, personal communication).

Our observations immediately indicated that large-amplitude short-term variations on timescales of ~100 s to ~2.5 h were already present, starting less than three minutes after the Swift/BAT trigger. In Fig. 1 and Extended Data Fig. 1, we show the overall optical multi-colour light curves. The overall trend of the light curves can be divided into three stages: (1) gradual rise during BJD (Barycentric Julian Day) 2,457,189 to 2,457,194.5 (brightening by 1 mag d^{-1} on average); (2) the plateau during BJD 2,457,194.5 to 2,457,200.0; and (3) rapid fading during BJD 2,457,200.0 to 2,457,203.3 (fading on average by 2.5 mag d^{-1}). Short-term variations with amplitudes varying between 0.1 mag and 2.5 mag were observed throughout the outburst, and consisted of characteristic structures such as recurrent sudden dips from a peak (Fig. 1).

Moreover, fluctuations similar in shape to the unique X-ray variations of the enigmatic black-hole binary GRS 1915 + 105[2] are present in the optical light curve of V404 Cyg (Fig. 2). The patterns in the X-ray light curve of GRS 1915+105 have been classified into at least 12 categories on the basis of their flux and colour characteristics[3]. Repeating structures like these had not been observed in optical wavelengths before the 2015 outburst of V404 Cyg. The variations that we observed can be divided into two characteristic classes: (1) 'dip-type' oscillations (repetitions of a gradual rise followed by a sudden dip, sometimes with accompanying spikes on timescales of ~45 min to ~2.5 h; Fig. 2a–c); and (2) 'heartbeat-type' oscillations (rhythmic small spikes with short periods of ~5 min; Fig. 2d). Although rapid optical variations have been detected in the black-hole binary V4641 Sgr, those variations are stochastic with no indication of regular patterns[14]. The variations we found in V404 Cyg at optical wavelengths were regular and similar in shape to those in GRS 1915 + 105, although the interval between dips is about 5 times larger in V404 Cyg than in GRS 1915 + 105.

Using X-ray data from Swift/X-ray Telescope (XRT), we compared simultaneous optical and X-ray light curves (Fig. 3). When both X-ray and optical data showed strong short-term variations, the temporal correlations were generally good, although the X-ray flux variations are much larger than the optical ones. The good correlation indicates that both X-ray and optical observations recorded the same phenomena (see also Methods section 'Comparison with X-ray observations' and Extended Data Fig. 2). Spectral analyses of the simultaneous X-ray data (Methods section 'Origin of cyclic dips' and Extended Data Fig. 3) indicate that there was no tendency for increased absorption when the X-ray flux decreased, suggesting that these dips do not originate in absorption. In some epochs, we found evidence for heavy obscuration as found in the GINGA data during the 1989 outburst[15]; however this is not related to dip-type variations. We can thus infer that the short-term fluctuations directly reflect variations in radiation from the accretion disk or its associated structures. Detailed analyses of the typical simultaneous broad-band spectral energy distribution (SED) (Methods section 'SED modelling' and Extended Data Fig. 6) show that the majority of the optical flux is most likely to be produced by reprocessing of X-ray irradiation in the disk.

For GRS 1915 + 105, it has been proposed that the observed variability is caused by limit-cycle oscillations in the inner accretion disk due to Lightman–Eardley viscous instability[16], which can explain a slow rise in

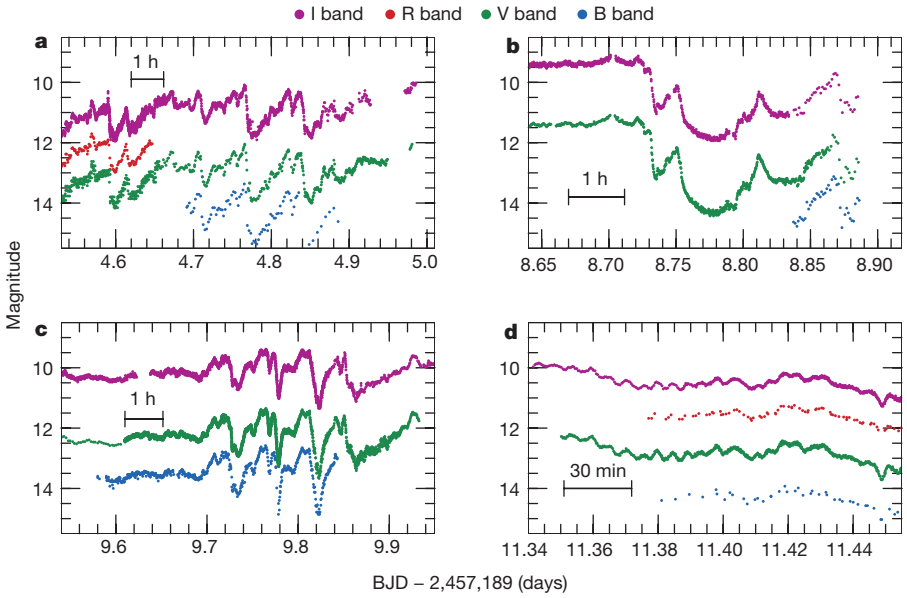

Figure 2 | Short-term and large-amplitude optical variations having repeating structures in the 2015 outburst of V404 Cyg. a–d, Variations with characteristic patterns during BJD 2,457,193.6 to 2,457,194.0 (**a**), BJD 2,457,197.7 to 2,457,198.0 (**b**), BJD 2,457,198.6 to 2,457,198.9 (**c**) and BJD 2,457,200.34 to 2,457,200.6 (**d**). In **a**, **b** and **c**, there are gradual rises with increasing amplitudes of fluctuations followed by dips, during which fluctuations disappear. These variations are sometimes accompanied by spikes. The interval between two dips ranges from ~45 min to ~2.5 h. **d**, Repetitive small oscillations with high coherence at intervals of ~5 min. The shapes of these oscillations resemble those of GRS 1915+105[3].

brightness (mass accumulation) followed by a sudden drop (accretion to the black hole). Such a model assumes that the black hole is accreting mass nearly at the Eddington rate, which is supported by observations of GRS 1915+105[17]. Similar types of X-ray variability have also been detected in the black-hole binary IGR J17091−3624 (ref. 18), whose Eddington rate is unknown because both the mass and the distance are uncertain.

In V404 Cyg, however, the accurate determination of the distance based on a parallax measurement[8] and the dynamical mass determination[7] enable us to conclude from our 2015 data that the black hole in this system was accreting at a much lower rate than the Eddington rate most of the time. During the period when GRS 1915+105-type variations in the optical light curves were recorded in V404 Cyg, its bolometric luminosity, averaged over an interval longer than the period of

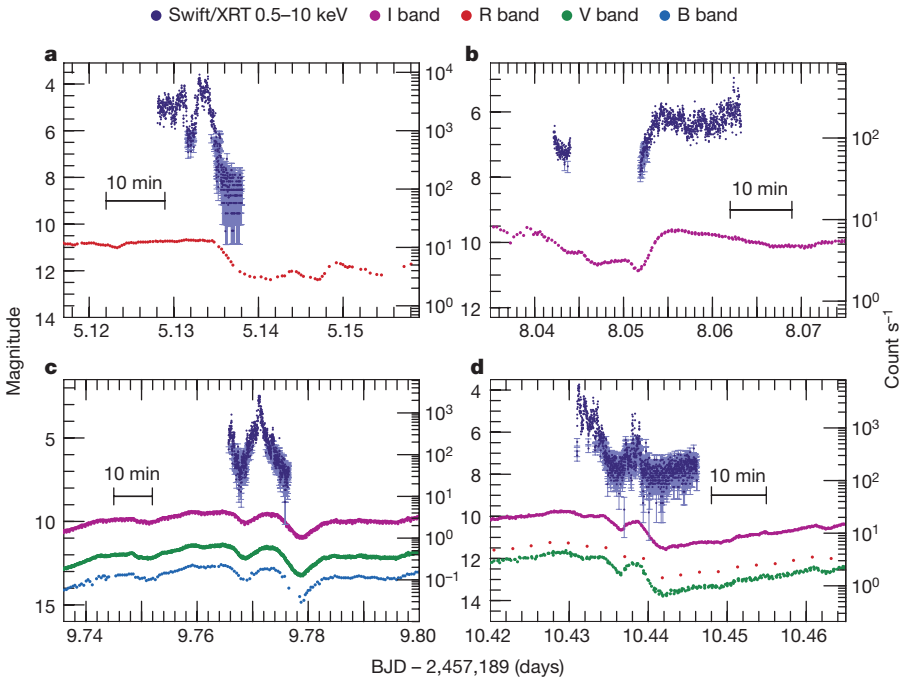

Figure 3 | Correlation between optical and X-ray fluctuations of V404 Cyg in the 2015 outburst. The times covered in each panel are BJD 2,457,194.126 to 2,457,194.140 (**a**), BJD 2,457,197.050 to 2,457,197.065 (**b**), BJD 2,457,198.760 to 2,457,198.780 (**c**) and BJD 2,457,199.430 to 2,457,199.450 (**d**). In each panel, the left-hand *y* axis shows magnitude in bands I, R, V and B, and the right-hand *y* axis shows counts per second in the Swift/XRT 0.5–10 keV band. Panels **a** and **b** cover the fading and rising phases, respectively; panels **c** and **d** show the correlations of short-term fluctuations. When both X-ray and optical light strongly varied, the correlation is generally good (though note in **a**, **c** and **d** that optical dips lag behind X-ray dips). Navy blue error bars, $\pm 1\sigma$. We plot points without errors when errors are smaller than or comparable to the plotting symbols.

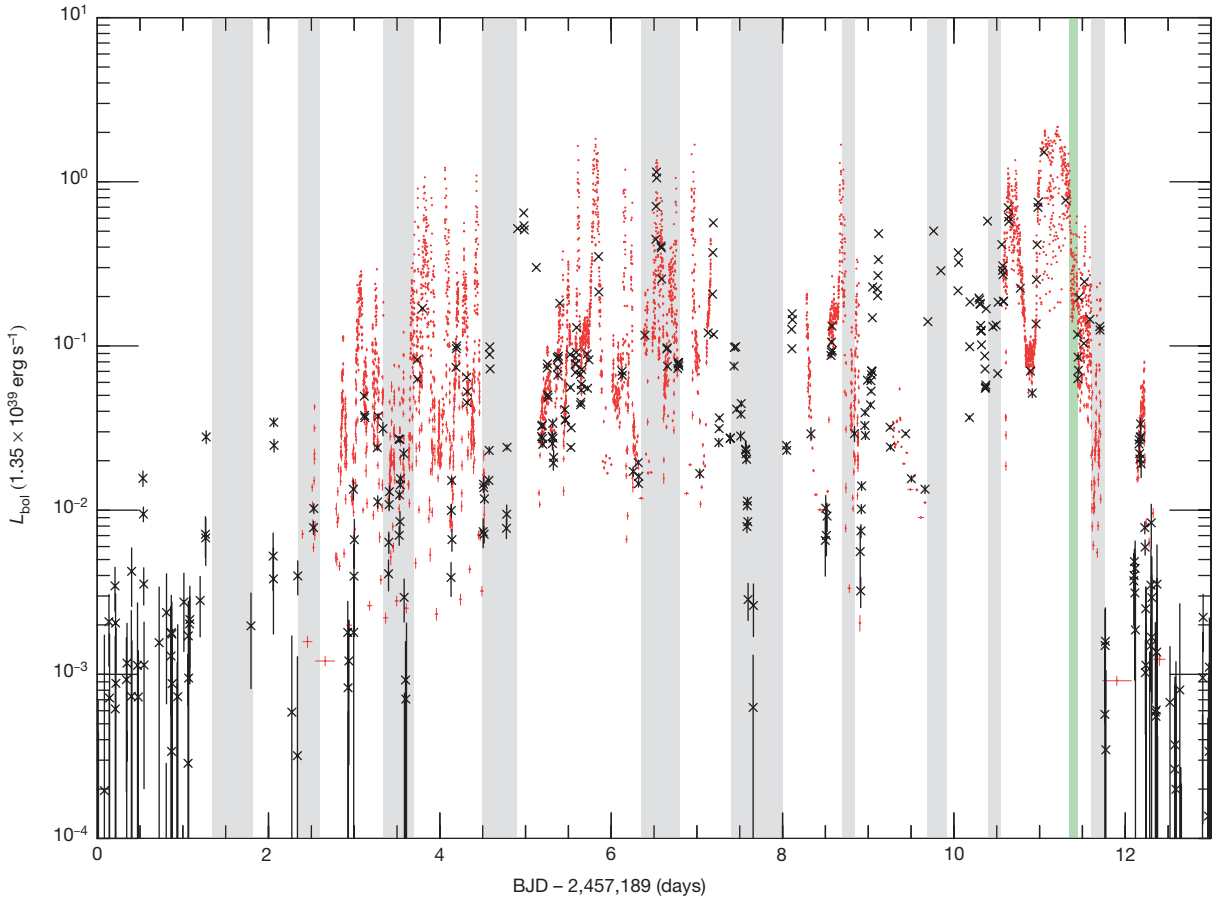

Figure 4 | The bolometric luminosity L_{bol} of V404 Cyg during the 2015 outburst. It is normalized to the Eddington luminosity assuming a black hole mass of $9M_{\odot}$. Black points, Swift/BAT survey data (15–50 keV); red points, from the public Target Opportunity release of INTEGRAL Imager on Board the Integral Satellite (IBIS)/CdTe array (ISGRI) monitoring (25–60 keV). Grey and green shadings represent respectively the periods of the 'dip-type oscillations' and the 'heartbeat-type oscillations'. Black and red error bars, $\pm 1\sigma$.

oscillation, spanned a wide range, from $\sim$0.01 L_{Edd} to $\sim$0.4 L_{Edd} (where L_{Edd} is the Eddington luminosity for a nine solar-mass, $M_{\odot}$, black hole), as estimated from the hard X-ray flux and SED (Fig. 4 and Methods section 'Time history of the bolometric luminosity'). Remarkably, the dip-type oscillations were observed at mean bolometric luminosity of $\sim$0.015 L_{Edd}, $\sim$0.07 L_{Edd} and $\sim$0.06 L_{Edd} during BJD 2,457,191.35 to 2,457,191.60, BJD 2,457,192.34 to 2,457,192.70, and BJD 2,457,200.60 to 2,457,200.76, respectively.

It is also worth noting that a typical dip similar to those seen in GRS 1915+105 was observed just 3 min after the first detection of this outburst (Extended Data Fig. 1b). This fact suggests that the accretion rate is not the critical parameter for inducing these oscillations. Our results imply that there is a novel type of disk instability that is different from the known dwarf-nova type[19] or the Lightman–Eardley type[16].

We point out that black-hole binaries showing large-amplitude, short-term variations either in X-ray or optical bands have long orbital periods (33.9 d in GRS 1915+105[20], $\sim$4 d in IGR J17091−3624[21], 6.5 d in V404 Cyg[22], and 2.8 d in V4641 Sgr[23]; see Methods section 'Objects showing violent short-term variations in outburst' and Extended Data Table 3 for a comparison of these objects), reinforcing the earlier suggestion of this link between violent oscillations and long orbital periods[24]. It has been proposed that the accretion disk in a system with a long orbital period suffers from instabilities in the disk's vertical structure, and hence the disk beyond this radius of instability may never build up[15,25]. Our SED modelling of this outburst, however, requires a disk having a large radius ($\gtrsim 1.7 \times 10^{12}$ cm), even considering the uncertainty of the interstellar reddening, to account for the ultraviolet flux particularly. This result implies that the disk extended up to distances close to the maximum achievable radius (Methods section 'SED modelling'). This radius is consistent with the short-term optical variations detected below 0.01 Hz (Extended Data Fig. 5 and Methods section 'Power spectra') and the time lag of $\sim$1 min between the X-ray and optical light curves (Fig. 3 and Extended Data Fig. 2) if we assume that the optical light mainly comes from reprocessed X-rays. We note that synchrotron emission has been proposed to be the origin of the short-term and large-amplitude fluctuations in the case of V4641 Sgr[14]. The optical polarization of V404 Cyg, however, did not show evidence of significant variations during the 2015 outburst[26,27]. This fact disfavours synchrotron emission as the origin of the short-term variations.

Outbursts of X-ray transients are thought to be triggered by the dwarf-nova-type instability: once the surface density at some radius reaches the critical density (Σ_{crit}) after continuous mass transfer from the secondary star, thermal instability occurs and the disk undergoes an outburst[19]. In systems with long orbital periods, it is difficult for surface densities in the outer disk to reach Σ_{crit}, which is roughly proportional to the radius[28]. As a result, thermal instability in the inner part of the disk occurs more easily and governs the outburst behaviour[29]. This is probably the reason why long-period systems behave differently from short-period 'classical' X-ray transients. In fact, our estimate of the disk mass (5×10^{25} g) accreted during the 2015 outburst is far smaller than the mass (2×10^{28} g) of a fully built-up disk in quiescence (Methods section 'Estimation of the disk mass and comparison with previous outbursts' and Extended Data Fig. 4). These values indicate that the surface density was well below the Σ_{crit} required to induce thermal instability in most parts of the disk at the onset of the present outburst. Once the X-ray outburst started in the inner region, hydrogen atoms in the outer part of the disk would have been ionized and 'passively'

maintained in the hot state as long as the X-ray illumination continued. This explains the large optical fluxes observed[28]. The rapid decay observed in the 2015 outburst of V404 Cyg may reflect the lack of the exponential decay in long-period systems as theoretically predicted[30]. Because the surface densities in the rest of the disk were too low to sustain the outburst by viscous diffusion[19], only the inner part of the disk was responsible for the dynamics of the present outburst, as inferred from the rapid fading from the outburst (Methods section 'Disk radius inferred from final fading rate'). We infer that, in outbursts of IGR J17091−3624[18,21] and the 1938 outburst of V404 Cyg (Methods section 'Estimation of the disk mass and comparison with previous outbursts' and Extended Data Fig. 4), the radius of the active disk is larger, which explains why the duration of those events is longer than that of the 2015 outburst of V404 Cyg.

Online Content Methods, along with any additional Extended Data display items and Source Data, are available in the online version of the paper; references unique to these sections appear only in the online paper.

Received 25 July; accepted 13 November 2015.

1. Janiuk, A. & Czerny, B. On different types of instabilities in black hole accretion discs: implications for X-ray binaries and active galactic nuclei. *Mon. Not. R. Astron. Soc.* **414,** 2186–2194 (2011).
2. Fender, R. P. & Belloni, T. GRS 1915+105 and the disc-jet coupling in accreting black hole systems. *Annu. Rev. Astron. Astrophys.* **42,** 317–364 (2004).
3. Belloni, T., Klein-Wolt, M., Méndez, M., van der Klis, M. & van Paradijs, J. A model-independent analysis of the variability of GRS 1915+105. *Astron. Astrophys. 355,* 271–290 (2000).
4. Hynes, R. I. *et al.* The remarkable rapid X-ray, ultraviolet, optical and infrared variability in the black hole XTE J1118+480. *Mon. Not. R. Astron. Soc.* **345,** 292–310 (2003).
5. Motch, C., Ilovaisky, S. A. & Chevalier, C. Discovery of fast optical activity in the X-ray source GX 339−4. *Astron. Astrophys.* **109,** L1–L4 (1982).
6. Tanaka, Y. & Shibazaki, N. X-ray novae. *Annu. Rev. Astron. Astrophys.* **34,** 607–644 (1996).
7. Khargharia, J., Froning, C. S. & Robinson, E. L. Near-infrared spectroscopy of low-mass X-ray binaries: accretion disk contamination and compact object mass determination in V404 Cyg and Cen X-4. *Astrophys. J.* **716,** 1105–1117 (2010).
8. Miller-Jones, J. C. A. *et al.* The first accurate parallax distance to a black hole. *Astrophys. J.* **706,** L230–L234 (2009).
9. Makino, F. GS 2023+338. *IAU Circ.* **4782** (1989).
10. Barthelmy, S. D. *et al.* Swift trigger 643949 is V404 Cyg. *GRB Coord. Netw. Circ.* **17929** (2015).
11. Negoro, H. *et al.* MAXI/GSC detection of a new outburst from the Galactic black hole candidate GS 2023+338 (V* V404 Cyg). *Astron. Telegr.* **7646** (2015).
12. Chen, Y. T. *et al.* TAOS early optical observations of V404 Cyg. *Astron. Telegr.* **7722** (2015).
13. Golenetskii, S. *et al.* Konus-Wind observation of Galactic transient V404 Cyg in outburst. *GRB Coord. Netw. Circ.* **17938** (2015).
14. Uemura, M. *et al.* Rapid optical fluctuations in the black hole binary V4641 Sagittarii. *Publ. Astron. Soc. Jpn* **54,** L79–L82 (2002).
15. Życki, P. T., Done, C. & Smith, D. A. The 1989 May outburst of the soft X-ray transient GS 2023+338 (V404 Cyg). *Mon. Not. R. Astron. Soc.* **309,** 561–575 (1999).
16. Belloni, T., Méndez, M., King, A. R., van der Klis, M. & van Paradijs, J. An unstable central disk in the superluminal black hole X-ray binary GRS 1915+105. *Astrophys. J.* **479,** L145–L148 (1997).
17. Neilsen, J., Remillard, R. A. & Lee, J. C. The physics of the "heartbeat" state of GRS 1915+105. *Astrophys. J.* **737,** 69–108 (2011).
18. Altamirano, D. *et al.* The faint "heartbeats" of IGR J17091−3624: an exceptional black hole candidate. *Astrophys. J.* **742,** L17–L23 (2011).
19. Osaki, Y. Dwarf-nova outbursts. *Publ. Astron. Soc. Pacif.* **108,** 39–60 (1996).
20. Steeghs, D. *et al.* The not-so-massive black hole in the microquasar GRS 1915+105. *Astrophys. J.* **768,** 185–191 (2013).
21. Janiuk, A., Grzedzielski, M., Capitanio, F. & Bianchi, S. Interplay between heartbeat oscillations and wind outflow in microquasar IGR J17091−3624. *Astron. Astrophys.* **574,** A92–A102 (2015).
22. Casares, J., Charles, P. A. & Naylor, T. A 6.5-day periodicity in the recurrent nova V404 Cygni implying the presence of a black hole. *Nature* **355,** 614–617 (1992).
23. Orosz, J. A. *et al.* A black hole in the superluminal source SAX J1819.3−2525 (V4641 Sgr). *Astrophys. J.* **555,** 489–503 (2001).
24. Bagnoli, T. & in't Zand, J. J. M. Discovery of GRS 1915+105 variability patterns in the rapid burster. *Mon. Not. R. Astron. Soc.* **450,** L52–L56 (2015).
25. Hameury, J.-M., Menou, K., Dubus, G., Lasota, J.-P. & Hure, J.-M. Accretion disc outbursts: a new version of an old model. *Mon. Not. R. Astron. Soc.* **298,** 1048–1060 (1998).
26. Panopoulou, G., Reig, P. & Blinov, D. Optical polarization of V404 Cyg. *Astron. Telegr.* **7674** (2015).
27. Itoh, R. *et al.* Optical and near-infrared polarimetry for V404 Cyg with 1.6m Pirka and 1.5m Kanata telescopes in Japan. *Astron. Telegr.* **7709** (2015).
28. Lasota, J.-P. The disc instability model of dwarf novae and low-mass X-ray binary transients. *New Astron. Rev.* **45,** 449–508 (2001).
29. Kim, S.-W., Wheeler, J. C. & Mineshige, S. Disk instability and outburst properties of the intermediate polar GK Persei. *Astrophys. J.* **384,** 269–283 (1992).
30. King, A. R. & Ritter, H. The light curves of soft X-ray transients. *Mon. Not. R. Astron. Soc.* **293,** L42–L48 (1998).

Supplementary Information is available in the online version of the paper.

Acknowledgements We acknowledge the variable star observations from the AAVSO International Database contributed by observers worldwide and used in this research. We also thank the INTEGRAL groups for making the products of the ToO data public online at the INTEGRAL Science Data Centre. Work at ASIAA was supported in part by the thematic research program AS-88-TP-A02. A.S.P., E.D.M. and A.A.V. are grateful to the Russian Science Foundation (grant 15-12-30016) for support. R.Ya.I. is grateful for partial support by the grant RUSTAVELI FR/379/6-300/14. We thank H. Maehara, H. Akazawa, K. Hirosawa and J. Lluis for their optical observations. This work was supported by the Grant-in-Aid "Initiative for High-Dimensional Data-Driven Science through Deepening of Sparse Modeling" from the Ministry of Education, Culture, Sports, Science and Technology (MEXT) of Japan (25120007 TK and 26400228 YU).

Author Contributions M.K. led the campaign, performed optical data analysis and compiled all optical data. K.I. and A.I. performed optical data analysis. T.K., Y.U., D.N. and M.U. contributed to science discussions. S.N., M.S., T.E., T.H. and H.T. performed X-ray data analysis. Other authors than those mentioned above performed optical observations. M.K., K.I., T.K., Y.U., S.N., T.E., M.S. and A.I. wrote the manuscript. T.K., Y.U. and D.N. supervised this project. M.K., K.I., T.K., Y.U., T.E., M.S., D.N., C.L., R.I., M.J.L., F.B.B., D.K., E.P.P., A.S.P., I.E.M., M.R., E.M., W.L.S., S.K., L.M.C., A.I. and M.U. improved the manuscript. All authors have read and approved the manuscript.

Author Information Reprints and permissions information is available at www.nature.com/reprints. The authors declare no competing financial interests. Readers are welcome to comment on the online version of the paper. Correspondence and requests for materials should be addressed to M.K. (mkimura@kusastro.kyoto-u.ac.jp).

METHODS

Detailed methods of optical observations. Immediately after the detection by Swift/BAT on June 15.77197 UT, the VSNET collaboration team[31] started a world-wide photometric campaign of V404 Cyg. There was also an independent detection by CCD (charge coupled device) photometry on June 16.169 UT[32]. Time-resolved CCD photometry was carried out at 27 sites using 36 telescopes with apertures of dozens of centimetres (Extended Data Table 2). We also used the public AAVSO data[33]. We corrected for bias and flat-fielding in the usual manner, and performed standard aperture photometry. The observers, except for TAOS[34], used standard filters (B, V, R_C, I_C; we write R and I for R_C and I_C in the main text and figures for brevity) and measured magnitudes of V404 Cyg relative to local comparison stars whose magnitudes were measured by A. Henden (sequence 15167RN) from the AAVSO Variable Star Database[35]. We applied small zero-point corrections to some observers' measurements. When filtered observations were unavailable, we used unfiltered data to construct the light curve. The exposure times were mostly 2–30 s, with some exceptional cases of 120 s in B band, giving typical time resolution of a few seconds. All of the observation times were converted to BJD.

Comparison with X-ray observations. For the Swift/XRT light curves (Fig. 3 and Extended Data Fig. 2), we extracted source events from a region with a 30-pixel radius centred on V404 Cyg. To avoid pile-up effects, we further excluded an inner circular region if the maximum count rate of the XRT raw light curves, binned in 10 s intervals, exceeded 200 counts s^{-1}. The inner radii are set to be 10 and 20 pixels at the maximum raw rate of 1,000 counts s^{-1} and 2,000 counts s^{-1}, respectively, and those for intermediate count rates were determined via linear interpolation between the two points. The presented light curves were corrected for photon losses due to this exclusion by using the xrtlccorr tool. In addition, from Fig. 3a, c and d, we can see a time delay in the start of a dip in optical light, relative to that in X-rays. The delay time was ~1 min, which is similar to the reported value of 0–50 s (ref. 36). This was determined by cross-correlating the U-band and X-ray (0.3–10 keV) light curves obtained with Swift/UltraViolet and Optical Telescope (UVOT) and Swift/XRT on UT 2015 June 21[36]. The observations were carried out when the source showed little rapid optical flickering and no extreme flares, and thus the nature of the lag may be different from that in our observations. We also note that the apparent difference between the Swift/UVOT and the ground-based times[36] is caused by the drift of the clock on board the satellite, to which we have applied the necessary corrections.

Origin of cyclic dips. In order to examine the possibility that absorption by gas in the line-of-sight causes the observed violent flux variations in the optical and X-ray bands (Fig. 3), we studied intensity-sliced X-ray spectra. A striking example is shown in Extended Data Fig. 3a. The period shown corresponds to that in Fig. 3a when both the X-ray and optical fluxes exhibited a sudden intensity drop towards the latter part of the period. We divided it into five intervals (T1 to T5; Extended Data Fig. 3a), and generated spectra through the tools xrtpipeline and xrtproducts in standard pipeline processing. We excluded the central 60-arcsecond strip from this Windowed Timing (WT) mode data, to avoid the heavy pile-up effect when the raw count rate exceeds ~150 counts s^{-1}. We compared the νF_ν spectra of the five intervals, where the spectra are fitted by a single power-law model multiplied by photoelectric absorption (phabs × pegpwrlw; in the standard X-ray spectral fitting package XSPEC). The absorbed X-ray flux ranges by two orders of magnitude, from 2.1×10^{-9} erg s^{-1} cm^{-2} in T5 to 3.0×10^{-7} erg s^{-1} cm^{-2} in T3. However, the best-fit column density and photon index were relatively stable over the five intervals, ~$(2–6) \times 10^{-21}$ cm^{-2} and ~1.0–1.5, respectively. Since the X-ray spectrum does not show a noticeable rise in column density when the X-ray flux sharply dropped, and since there is no stronger iron edge in the latter part of the observation, absorption cannot be the primary cause of the time variation in our data sets that cover the X-ray and optical bands simultaneously.

Objects showing violent short-term variations in outburst. In Extended Data Table 3 we show the list of X-ray binaries that have shown violent short-term variations either in X-rays or in optical wavelengths.

IGR J17091−3624 is known as the second black hole X-ray binary whose X-ray light curves showed a variety of patterns, resembling those of GRS 1915 + 105[18]. The variations observed in the 2011 outburst of this object were classified as ρ ('heartbeat'), ν (similar to class ρ but with secondary peak after the dips), α ('rounded-bumps'), β/λ (repetitive short-term oscillations after low-quiet period) and μ (ref. 18).

The Rapid Burster (RB or MXB 1730−335), a low-mass X-ray binary (LMXB) containing a neutron star (NS), was discovered by Small Astronomy Satellite (SAS-3) observations[37]. This object has been recently reported to show cyclic long X-ray bursts with periods of a few seconds resembling class ρ ('heartbeat') variations and those with periods of 100–200 s resembling class θ ("M"-shaped light curves) variations of GRS 1915 + 105[24]. The emission of the Rapid Burster did not reach the Eddington luminosity during these variations[38].

V4641 Sgr was originally discovered as a variable star[39] and was long confused with a different variable star, GM Sgr[40]. V4641 Sgr is famous for its short and bright outburst in 1999, which reached a optical magnitude of at least 8.8 mag (refs 41–44). V4641 Sgr showed short-term variations in optical wavelengths during the 2002, 2003 and 2004 outbursts[14,45–47]. It was the first case in which short-term and large-amplitude variations in the optical range during an outburst were detected. V4641 Sgr is classified as a LMXB, and has a long orbital period. Its mass-accretion rate is less than the Eddington rate (except for the 1999 outburst[44,48]). These properties are similar to those of V404 Cyg. However, while the short-term variations of V4641 Sgr seemed to be random, those of V404 Cyg showed repetitive patterns; this is the greatest difference between these two objects. There has been a suggestion that V4641 Sgr is a 'microblazar'[49] because the jets observed during the outburst in 1999 were proposed to have the largest bulk Lorentz factor among known galactic sources[43].

There are also other X-ray transients showing short-term optical variations (for example, XTE J1118+480 and GX 339−4). However, these two sources are quasi-periodic oscillations (QPOs), characterized by very short periods. The periods are much shorter than those of repetitive patterns (tens of seconds to a few hours) that we discuss in this Letter. Furthermore, the amplitudes of their variations are significantly smaller than those observed in V4641 Sgr[4,50] on timescales longer than tens of seconds.

Estimation of the disk mass and comparison with the previous outbursts. Following the method in ref. 15, we estimated the mass stored in the disk at the onset of the outburst. By integrating the X-ray light curve of Swift/BAT and assuming the spectral model *C* in table 1 in ref. 15, we obtained a value of 5.0×10^{25} g assuming a radiative efficiency of 10% and a distance of 2.4 ± 0.2 kpc (ref. 8). The mass during the 1989 outburst has been updated to 3.0×10^{25} g by using this updated distance. The stored mass in the 2015 outburst was approximately the same as that in the 1989 one. As discussed in ref. 15, these masses are far smaller than the mass of a fully built-up disk, estimated to be 2.0×10^{28} g, if these outbursts were starting at the outermost region.

We compare the published optical light curves of the 1989 and 1938 outbursts[51,52] with our data from the 2015 outburst (Extended Data Fig. 4). We can see that these outbursts have different durations. The 1938 outburst was apparently longer than the others, and it may have had different properties from the 1989 and 2015 ones. The fading rates of the 1989 and 2015 outbursts are significantly larger than those of classical X-ray transients[6], or of FRED (fast rise and exponential decline)-type outbursts, such as 0.028 mag d^{-1} in V518 Per = GRO J0422+32 (ref. 53) and 0.015 mag d^{-1} in V616 Mon = A0620−00 (ref. 54). This supports the hypothesis that the outbursts in 1989 and 2015 are different from typical outbursts of classical X-ray transients and that the stored disk mass was a factor of ~10^3 smaller in the 1989 and 2015 outbursts than the mass of a fully built up disk.

Power spectra. We performed power spectral analyses on BJD 2,457,193, BJD 2,457,196 and BJD 2,457,200. We used the continuous and regularly sampled high-cadence data set obtained by LCO (Extended Data Table 1) with exposure times of 5 s (on BJD 2,457,193) and 2 s (others). The durations of these observations are 1.4, 3.1 and 2.2 h, respectively. Considering the read-out times of 1 s, the Nyquist frequencies of these observations are 0.08 and 0.17 Hz, respectively. The power spectral densities (PSDs) were calculated using powspec software in the FTOOLS Xronos package on magnitude measurements. We did not apply de-trending of the light curve since the durations of the individual observations were shorter than the timescale of the global variation of the outburst. The power spectra are well expressed by a power law ($P \propto f^{-\Gamma}$) with an index Γ of 1.9 ± 0.1, 1.8 ± 0.1, and 2.3 ± 0.1 on BJD 2,457,193, 2,457,196 and 2,457,200, respectively (Extended Data Fig. 5). Interpretation of the physical origins on the basis of these variations is difficult, because a power law index of ~2 in the PSDs is often observed in natural phenomena. In this region ($f < 0.01$ Hz), the power originating in the optical variations of V404 Cyg is significantly higher than that of white noise estimated from the observations.

We next summarize the other reports on short-term variations of V404 Cyg during the present outburst. On BJD 2,457,191, this object was observed using the Argos photometer on the 2.1m Otto Struve Telescope at McDonald Observatory with an exposure time of 2 s[55]. They reported that the power spectrum was dominated by steep red noise. Observations on BJD 2,457,193 and BJD 2,457,194 were also performed using the ULTRACAM attached with the 4.2m William Herschel Telescope on La Palma observatory with a high time resolution (466.8 ms)[56]. They reported that the variations were dominated by timescales longer than tens of seconds. Although large amplitude flares (0.3–0.4 mag) on timescales shorter than 1 s were reported[57], these flares may be of different origin. For the variations with timescales longer than 100 s, our results agree with these reports[55,56].

Disk radius inferred from final fading rate. The timescale τ of heating/cooling waves in dwarf novae and X-ray transients[58] is a function of the mass of the central object (M_1) and radius (r) with the form $\tau \propto \alpha M_1^{-1/2} r^{3/2}$, where α is the viscosity

parameter[59]. Here, we estimate the disk radius of V404 Cyg assuming that the timescale of the final fading reflected a dwarf nova-type cooling wave. Using the Kepler data of V344 Lyr and V1504 Cyg, we measured a fading rate of 1.5 mag d^{-1} of the normal outbursts immediately preceding superoutbursts. During the outbursts in V344 Lyr and V1504 Cyg[60], the disk radius is expected to be very close to the 3:1 resonance radius. Adopting a typical mass of a white dwarf in a cataclysmic variable ($M_1 = 0.83 M_\odot$; ref. 61), we estimated the disk radius of V404 Cyg to be 7.8×10^{10} cm for a black hole mass of $9 M_\odot$. This is much smaller than the radius (1.2×10^{12} cm) expected for a fully built-up disk[15].

SED modelling. Extended Data Fig. 6a shows the multi-wavelength SED on BJD 2,457,199.431 to 2,457,199.446, when the source was simultaneously observed in the X-ray, ultraviolet (UV) and optical bands. The optical fluxes in the V and I_C bands are taken from our photometric data averaged over the period. Note that R_C-band data are also available but not used here, because of the contamination by the continuum strong Hα line[62–64].

The X-ray spectrum is extracted from simultaneous Swift/XRT data (ObsID 00031403058) which were taken in the WT mode. The data are processed through the pipeline processing tool xrtpipeline. The events detected within 20 pixels around the source position are removed to mitigate pile-up effects. The U-band flux is obtained from the Swift/UVOT images with the same ObsID as the XRT, through the standard tool uvot2pha provided by the Swift team. A circular region centred at the source position with a radius of 5 arcsec is adopted as the source extraction region of the UVOT data. The optical, UV and X-ray data are corrected for interstellar extinction/absorption by assuming A_V (interstellar extinction in the V band) = 4 (ref. 65) and using the extinction curve in ref. 66 and the N_H (hydrogen column density) versus $E(B-V)$ relation in ref. 67. Radio data are from the RATAN-600 observation performed in the same period[68].

The multi-wavelength SED can be reproduced with the diskir model[69,70], which accounts for the emission from the accretion disk, including the effects of Comptonization in the inner disk and reprocessing in the outer disk. We find that partial covering X-ray absorption (using the pcfabs model implemented in the spectral analysis software XSPEC) improves the quality of the fit significantly. The inner-disk temperature is estimated to be 0.12 ± 0.01 keV, and the electron temperature and photon index of the Comptonization component, the ratio between the luminosity of the Compton tail and disk blackbody (L_C/L_d), and the fraction of the bolometric flux thermalized in the outer disk (f_{out}), are 17.5 ± 0.8 keV, 1.78 ± 0.03, 1.17 ± 0.03, and $1.3^{+0.6}_{-0.8} \times 10^{-2}$, respectively (the errors in this section represent 90% confidence ranges for one parameter). The inner radius (R_{in}) is estimated to be $(1.5–5.4) \times 10^8$ cm, and the outer radius (R_{out}) is $(2.5 \pm 0.3) \times 10^{12}$ cm. The derived value of R_{out} is comparable to or even larger than the binary separation ($\sim 2.2 \times 10^{12}$ cm). However, it could be smaller due to uncertainties in interstellar/circumbinary extinction[71] and/or the contribution of jet emission. For instance, if A_V is 0.4 mag larger than the assumed value (4.0), R_{out} becomes $(1.9 \pm 0.2) \times 10^{12}$ cm. The maximum achievable radius of a stable disk for a q (mass ratio) = 0.06 object (Extended Data Table 3) is around $0.62A$ (radius of the 2:1 resonance) to $\sim 0.7A$ (tidal limit), where A is the binary separation[72]. Considering the uncertainties, the result of our analysis ($\gtrsim 0.77A$) is compatible with this maximum radius. Our result appears to favour a large A_v value. For the partial covering absorber, the best-fit value of the column density is $5.2^{+0.4}_{-0.5} \times 10^{23}$ cm^{-2} and that of the covering fraction is 64 ± 4%.

The radio SED can be approximated by a power-law with a photon index of ~ 1, as in other black hole binaries in the low/hard state[73]. This profile is likely to be generated by the optically-thick synchrotron emission from compact jets[74]. Because an optically-thick synchrotron spectrum often extends up to the millimetre to near-infrared bands[75–77], it may contribute to the optical fluxes, in particular at longer wavelengths. The blackbody emission from the companion, a K3III-type star[7] with a radius of $\sim 3 R_\odot$ and a temperature of $\sim$4,320 K, contributes to the SED negligibly.

Extended Data Figure 6b plots the simultaneous SED on BJD 2,457,191.519 to 2,457,191.524, which is $\sim$2 orders of magnitude fainter in the X-ray band than that shown in the left panel. The X-ray, UV and optical data are taken from the Swift data (ObsID 00031403038) and our photometric measurements in the same manner as described above. This SED can be reproduced with the irradiated disk model as well, with somewhat smaller photon index ($1.43^{+0.02}_{-0.03}$) and inner-disk temperature (<0.07 keV), and a larger f_{out} ($0.06^{+0.02}_{-0.05}$) than those on BJD 2,457,199.431 to 2,457,199.446.

Time history of the bolometric luminosity. The bolometric luminosity L_{bol} of V404 Cyg is evaluated based on the hard X-rays above $\sim$15 keV where the intrinsic spectrum is less affected by an absorption.

We processed the Swift/BAT archival survey data via batsurvey in the HEAsoft package to derive count rates with individual exposures of $\sim$300 s. Even within this short exposure, photon statistics are good during bright states (>0.05 counts s^{-1}). Assuming a Crab-like spectrum (1 Crab $\approx$ 0.039 counts s^{-1}), the BAT count rates R (counts s^{-1}) are then converted into 15–50 keV flux ($F_{15–50}$) and luminosity ($L_{15–50}$) using $F_{15–50} = 3.6 \times 10^{-7} R$ (erg s^{-1} cm^{-1}) and a fiducial distance of 2.4 kpc, respectively. In Fig. 4, we show L_{bol} after multiplying by a conversion factor $L_{bol}/L_{15–50} = 7$ determined from SED modelling (previous section). We find that this bolometric correction factor lies within the range 2.5–10 by fitting 19 X-ray(XRT)-optical simultaneous SED in different periods between BJD 2,457,192.019 and 2,457,201.011. Since the BAT survey data are rather sparse, in order to catch shorter-term variations, we further overlaid the INTEGRAL IBIS/ISGRI monitoring in the 25–60 keV band available at ref. 78, assuming a conversion parameter of 1 Crab rate to be 172.1 counts s^{-1} and a bolometric correction factor of $L_{bol}/L_{25–60} = 9.97$.

The luminosity was highly variable during the outburst, changing by five orders of magnitude. While V404 Cyg sometimes reaches the Eddington luminosity (L_{Edd}) at the peak of multiple sporadic flares, it also repeatedly dropped below 1–10% of L_{Edd} (Fig. 4). At earlier phases of this outburst, the characteristic oscillation already occurred during a lower luminosity state, as discussed in the main text.

Sample size. No statistical methods were used to predetermine sample size.

31. Kato, T. *et al.* Variable Star Network: world center for transient object astronomy and variable stars. *Publ. Astron. Soc. Jpn* **56,** S1–S54 (2004).
32. Muyllaert, E. V404 Cyg going into outburst!? *BAAVSS Alert* 4101 (2015); https://groups.yahoo.com/neo/groups/baavss-alert/conversations/messages/4101.
33. AAVSO American Association of Variable Star Observers. Download data. http://www.aavso.org/data-download/ (accessed 4 July 2015).
34. Lehner, M. J. *et al.* The Taiwanese-American Occultation Survey: the multi-telescope robotic observatory. *Publ. Astron. Soc. Pacif.* **121,** 138–152 (2009).
35. AAVSO American Association of Variable Star Observers. Variable star plotter. http://www.aavso.org/vsp (accessed 4 July 2015).
36. Gandhi, P. *et al.* Correlated optical and X-ray variability in V404 Cyg. *Astron. Telegr.* **7727** (2015).
37. Lewin, W. H. G. *et al.* The discovery of rapidly repetitive X-ray bursts from a new source in Scorpius. *Astrophys. J.* **207,** L95–L99 (1976).
38. Bagnoli, T., in't Zand, J. J. M., Galloway, D. K. & Watts, A. L. Indications for a slow rotator in the Rapid Burster from its thermonuclear bursting behaviour. *Mon. Not. R. Astron. Soc.* **431,** 1947–1955 (2013).
39. Goranskij, V. P. Variable stars in Sagittarius. *Astronomicheskii Tsirkulyar* **1024,** 3–4 (1978).
40. Samus, N. N. *et al.* V4641 Sagittarii and GM Sagittarii. *IAU Circ.* **7277** (1999).
41. Stubbings, R. *et al.* GM Sagittarii and SAX J1819.3−2525 = XTE J1819−254. *IAU Circ.* **7253** (1999).
42. Kato, T., Uemura, M., Stubbings, R., Watanabe, T. & Monard, B. Preoutburst activity of V4641 Sgr = SAX J1819.3−2525: possible existence of 2.5-day period. *Inform. Bull. Variable Stars* **4777** (1999).
43. Hjellming, R. M. *et al.* Light curves and radio structure of the 1999 September transient event in V4641 Sagittarii (=XTE J1819−254 = SAX J1819.3−2525). *Astrophys. J. 544,* 977–992 (2000).
44. Uemura, M. *et al.* The 1999 optical outburst of the fast X-ray nova, V4641 Sagittarii. *Publ. Astron. Soc. Jpn* **54,** 95–101 (2002).
45. Uemura, M. *et al.* Outburst and post-outburst active phase of the black hole X-ray binary, V4641 Sgr in 2002. *Publ. Astron. Soc. Jpn* **56,** S61–S75 (2004).
46. Uemura, M. *et al.* Optical observation of the 2003 outburst of a black hole X-ray binary, V4641 Sagittarii. *Publ. Astron. Soc. Jpn* **56,** 823–829 *(*2004).
47. Uemura, M. *et al.* Outburst of a black hole X-ray binary V4641 Sgr in 2004 July. *Inform. Bull. Variable Stars* **5626,** 1–4 (2005).
48. Revnivtsev, M., Sunyaev, R., Gilfanov, M. & Churazov, E. V4641 Sgr — a super-Eddington source enshrouded by an extended envelope. *Astron. Astrophys.* **385,** 904–908 (2002).
49. Mirabel, I. F. & Rodrguez, L. F. Sources of relativistic jets in the Galaxy. *Annu. Rev. Astron. Astrophys.* **37,** 409–443 (1999).
50. Imamura, J. N., Kristian, J., Middleditch, J. & Steiman-Cameron, T. Y. The 8 second optical quasi-periodic oscillations in GX 339−4. *Astron. Astrophys.* **365,** 312–316 (1990).
51. Casares, J., Charles, P. A., Jones, D. H. P., Rutten, R. G. M. & Callanan, P. J. Optical studies of V404 Cyg, the X-ray transient GS 2023+338. I — the 1989 outburst and decline. *Mon. Not. R. Astron. Soc.* **250,** 712–725 (1991).
52. Wagner, R. M. *et al.* Optical identification of the X-ray source GS 2023+338 as V404 Cygni. *Astrophys. J.* **378,** 293–297 (1991).
53. Chevalier, C. & Ilovaisky, S. A. CCD photometry of GRO J0422+32 during activity and quiescence. *Astron. Astrophys.* **297,** 103–114 (1995).
54. Whelan, J. A. J. *et al.* Spectroscopic observations of the X-ray nova A0620−00. *Mon. Not. R. Astron. Soc.* **180,** 657–673 (1977).
55. Hynes, R. I., Robinson, E. L. & Morales, J. Rapid optical photometry of V404 Cyg. *Astron. Telegr.* **7677** (2015).
56. Gandhi, P. *et al.* Sub-second multi-band optical timing of V404 Cyg with ULTRACAM. *Astron. Telegr.* **7686** (2015).
57. Hynes, R. I., Robinson, E. L. & Morales, J. Further rapid optical photometry of V404 Cyg. Astron. *Telegr.* **7710** (2015).
58. Cannizzo, J. K. On the relative rates of decay of the optical and soft X-ray fluxes in dwarf nova outbursts. *Astrophys. J.* **473,** L41–L44 (1996).
59. Meyer, F. Transition waves in accretion disks. *Astron. Astrophys.* **131,** 303–308 (1984).

60. Cannizzo, J. K., Smale, A. P., Wood, M. A., Still, M. D. & Howell, S. B. The Kepler light curves of V1504 Cygni and V344 Lyrae: a study of the outburst properties. *Astrophys. J.* **747,** 117–128 (2012).
61. Savoury, C. D. J.*et al.* Cataclysmic variables below the period gap: mass determinations of 14 eclipsing systems. *Mon. Not. R. Astron. Soc.* **415,** 2025–2041 (2011).
62. Munoz-Darias, T., Sanchez, D. M. & Casares, J. Optical spectroscopy of V404 Cyg: evolution of the P Cygni profiles. *Astron. Telegr.* **7669** (2015).
63. Caballero-Garcia, M. D., Castro-Tirado, A. J., Oates, S. & Jeong, S. Early optical spectroscopy follow-up of V404 Cyg with GTC/OSIRIS. *Astron. Telegr.* **7699** (2015).
64. Scarpaci, J., Maitra, D., Hynes, R. & Markoff, S. Multi-band optical observations of V404 Cygni and correlated spectral changes. *Astron. Telegr.* **7737** (2015).
65. Casares, J., Charles, P. A., Naylor, T. & Pavlenko, E. P. Optical studies of V404 Cygni the X-ray transient GS 2023+338 – part three – the secondary star and accretion disc. *Mon. Not. R. Astron. Soc.* **265,** 834–852 (1993).
66. Cardelli, J. A., Clayton, G. C. & Mathis, J. S. The relationship between infrared, optical, and ultraviolet extinction. *Astrophys. J.* **345,** 245–256 (1989).
67. Bohlin, R. C., Savage, B. D. & Drake, J. F. A survey of interstellar H I from Lα absorption measurements. II. *Astrophys. J.* **224,** 132–142 (1978).
68. Trushkin, S. A., Nizhelskij, N. A. & Tybulev, P. G. The inverted radio spectrum of the flare in V404 Cyg. *Astron. Telegr.* **7667** (2015).
69. Gies, D. R. *et al.* Stellar wind variations during the X-ray high and low states of Cygnus X-1. *Astrophys. J.* **678,** 1237–1247 (2008).
70. Kaptein, R. G. *et al.* Discovery of 1RXS J171824.2−402934 as an X-ray burster. *Astron. Astrophys.* **358,** L71–L74 (2000).
71. Hynes, R. I. *et al.* The quiescent spectral energy distribution of V404 Cyg. *Mon. Not. R. Astron. Soc.* **399,** 2239–2248 (2009).
72. Osaki, Y. & Meyer, F. Early humps in WZ Sge stars. *Astron. Astrophys.* **383,** 574–579 (2002).
73. Fender, R. P. Powerful jets from black hole X-ray binaries in low/hard X-ray states. *Mon. Not. R. Astron. Soc.* **322,** 31–42 (2001).
74. Blandford, R. D. & Königl, A. Relativistic jets as compact radio sources. *Astrophys. J.* **232,** 34–48 (1979).
75. Corbel, S. & Fender, R. P. Near-infrared synchrotron emission from the compact jet of GX 339−4. *Astrophys. J.* **573,** L35–L39 (2002).
76. Gandhi, P. *et al.* A variable mid-infrared synchrotron break associated with the compact jet in GX 339−4. *Astrophys. J.* **740,** L13–L19 (2011).
77. Russell, T. D. *et al.* The accretion-ejection coupling in the black hole candidate X-ray binary MAXI J1836−194. *Mon. Not. R. Astron. Soc.* **439,** 1390–1402 (2014).
78. INTEGRAL Science Data Centre. INTEGRAL data analysis. http://www.isdc.unige.ch/integral/analysis#QLAsources (8 August 2015).
79. Wang, J. H. *et al.* Early optical brightening in GRB 071010B. *Astrophys. J.* **679,** L5–L8 (2008).
80. Kloppenborg, B. K., Pieri, R., Eggenstein, H.-B., Maravelias, G. & Pearson, T. A demonstration of accurate wide-field *V*-band photometry using a consumer-grade DSLR camera. *J. Am. Assoc. Variable Star Obs.* **40,** 815–833 (2012).
81. Alcock, C. *et al.* TAOS: The Taiwanese-American Occultation Survey. *Earth Moon Planets* **92,** 459–464 (2003).
82. Zhang, Z.-W. *et al.* The TAOS project: results from seven years of survey data. *Astron. J.* **146,** 14–23 (2013).
83. Casares, J. & Charles, P. A. Optical studies of V404 Cyg, the X-ray transient GS 2023+338. IV. the rotation speed of the companion star. *Mon. Not. R. Astron. Soc.* **271,** L5–L9 (1994).
84. Wijnands, R., Yang, Y. J. & Altamirano, D. The enigmatic black hole candidate and X-ray transient IGR J17091−3624 in its quiescent state as seen with XMM-Newton. *Mon. Not. R. Astron. Soc.* **422,** L91–L95 (2012).
85. Reid, M. J. *et al.* A parallax distance to the microquasar GRS 1915+105 and a revised estimate of its black hole mass. *Astrophys. J.* **796,** 2–9 (2014).
86. Iyer, N., Nandi, A. & Mandal, S. Determination of the mass of IGR J17091−3624 from "spectro-temporal" variations during the onset phase of the 2011 outburst. *Astrophys. J.* **807,** 108–116 (2015).
87. Sala, G. *et al.* Constraints on the mass and radius of the accreting neutron star in the Rapid Burster. *Astrophys. J.* **752,** 158–164 (2012).
88. MacDonald, R. K. D. *et al.* The black hole binary V4641 Sagitarii: activity in quiescence and improved mass determinations. *Astrophys. J.* **784,** 2–20 (2014).
89. Fender, R. P. *et al.* MERLIN observations of relativistic ejections from GRS 1915+105. *Mon. Not. R. Astron. Soc.* **304,** 865–876 (1999).
90. King, A. L. *et al.* An extreme X-ray disk wind in the black hole candidate IGR J17091−3624. *Astrophys. J.* **746,** L20–L24 (2012).
91. Szkody, P. *et al.* V404 Cygni. *IAU Circ.* **4794** (1989).

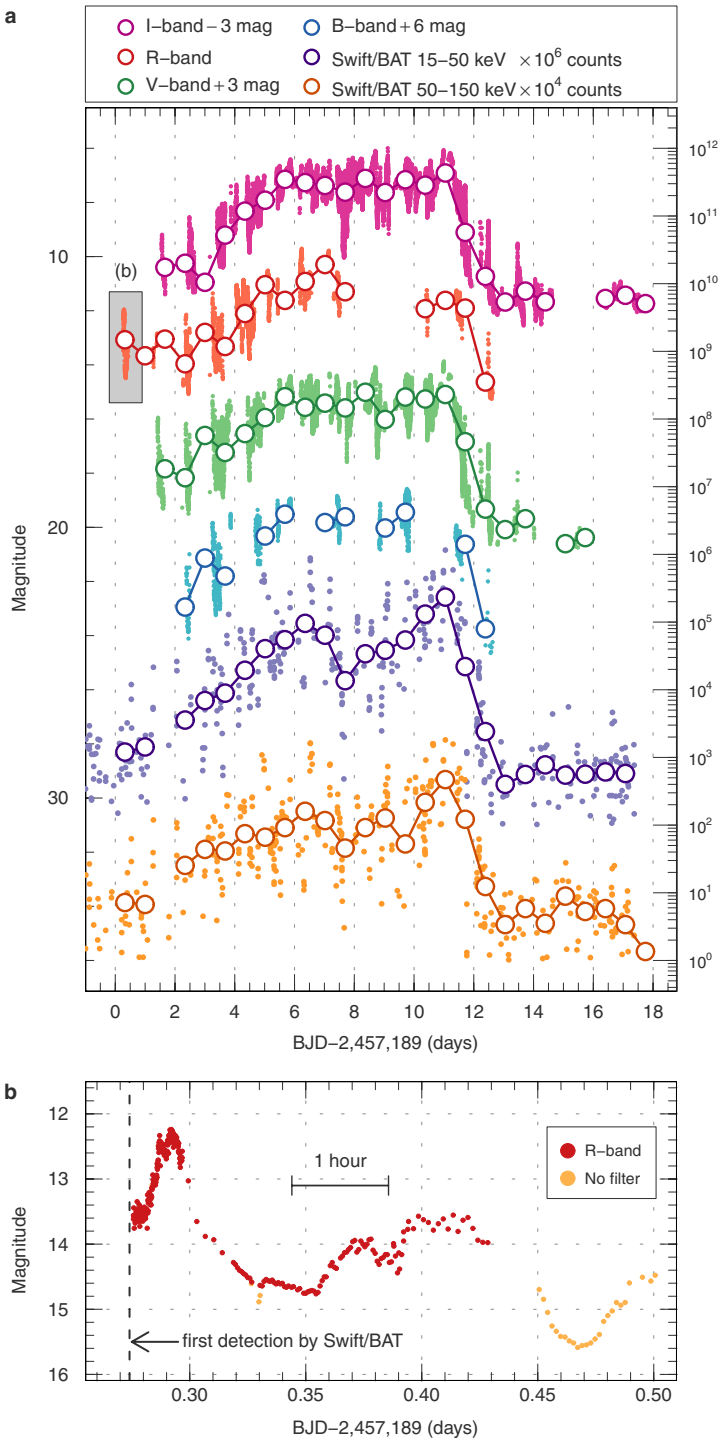

Extended Data Figure 1 | Optical and X-ray light curves of V404 Cyg during an outburst in 2015 June–July. a, Overall multi-colour light curves and Swift/BAT light curves. The plotted points are averaged for every 0.67 days. **b**, An enlarged view of the shaded box in **a** (the first detection of short-term variations). On BJD 2,457,203, the mean magnitude dropped below $V = 17.0$. Superimposed on this rapid fading, the amplitude of variations became progressively smaller and smaller. After BJD 2,457,205, the mean magnitude seemed to be constant, and the outburst virtually ended.

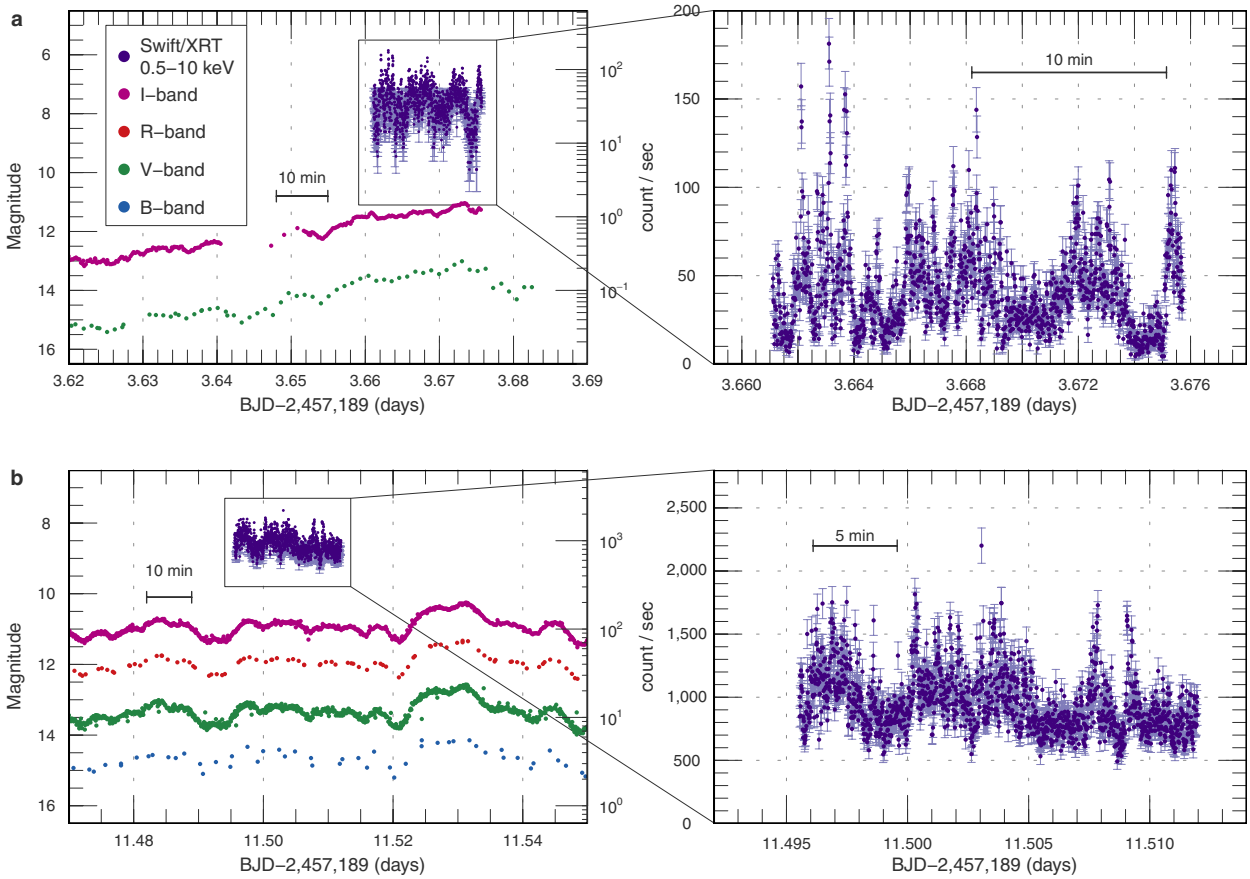

Extended Data Figure 2 | Additional examples of simultaneous optical and X-ray observations of V404 Cyg in the 2015 outburst. Data shown in Fig. 3 are excluded. **a**, **b**, Main panels, correlations on BJD 2,457,192 (a) and BJD 2,457,200 (b); right panels, Swift/XRT light curves on linear scales. Navy blue error bars, $\pm 1\sigma$.

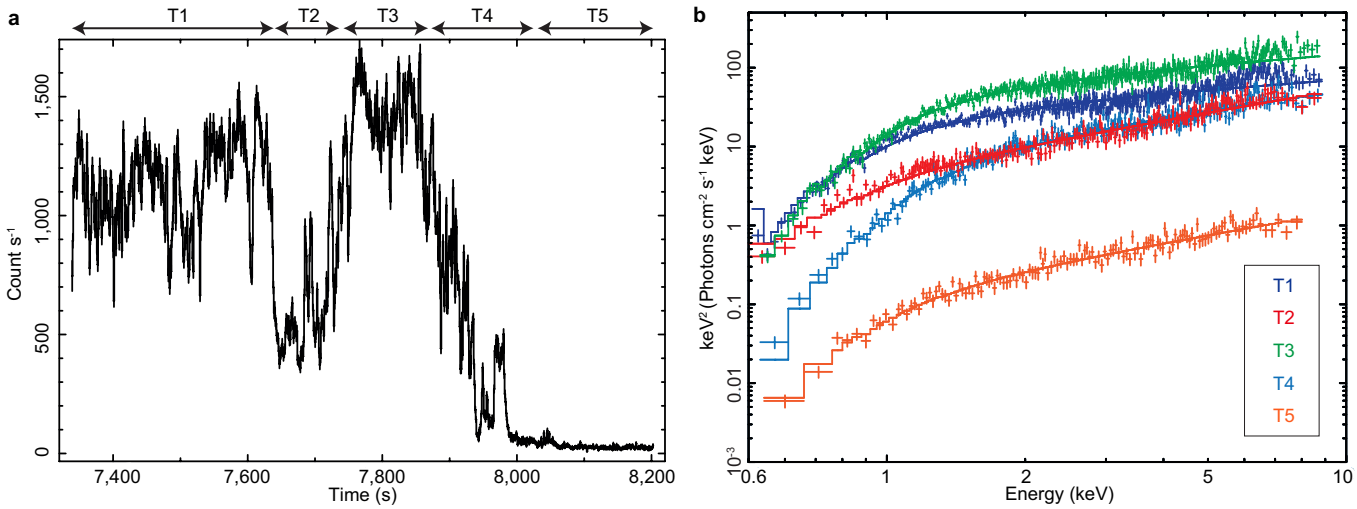

Extended Data Figure 3 | Example of the soft X-ray light curve and spectra during the dip-type oscillation in the 2015 outburst of V404 Cyg. a, The ~860-s-long Swift/XRT raw light curve (BJD 2,457,194.125–2,457,194.135, ObsID 00031403040) without pile-up correction, same as the X-ray data in Fig. 3a. **b**, Time-sliced soft X-ray spectra with pile-up correction, in the intervals of T1 to T5 determined in **a**. The exposures of individual spectra are ~100–300 s. Error bars, $\pm 1\sigma$.

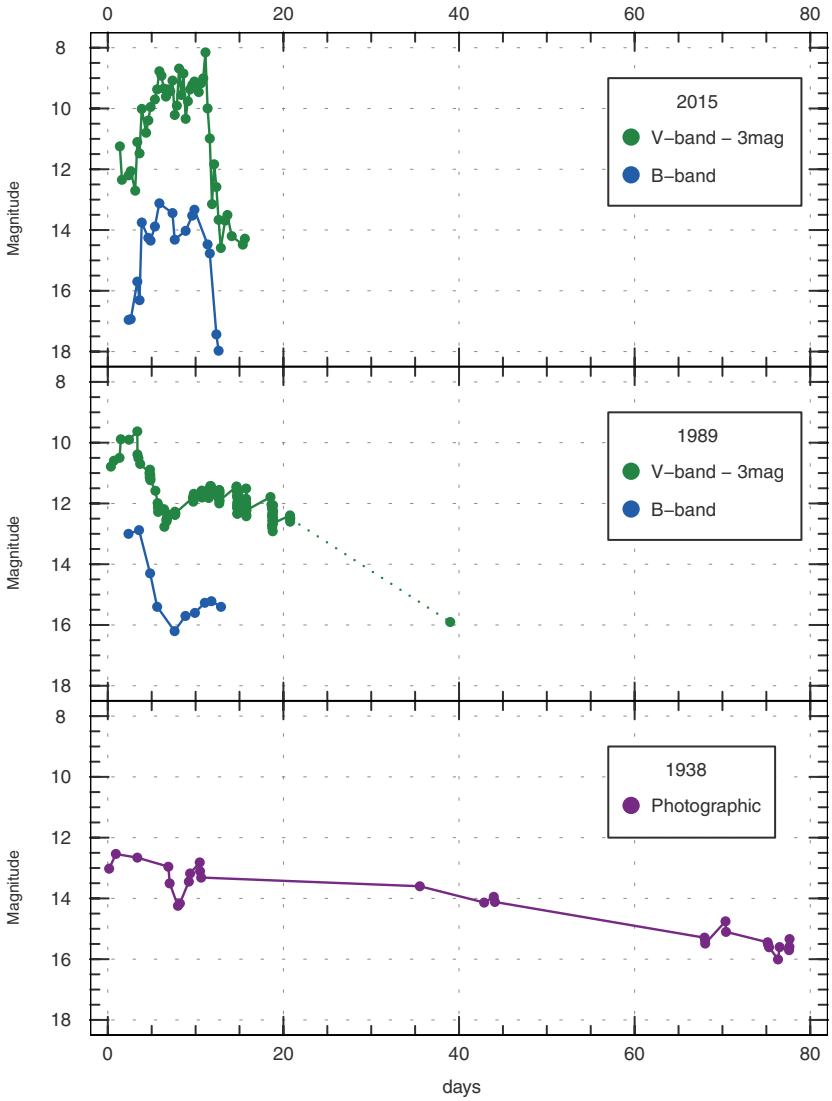

Extended Data Figure 4 | Comparison of the 1938, 1989 and 2015 outbursts of V404 Cyg. The horizontal axis represents days BJD − 2,429,186, BJD − 2,447,673 and BJD − 2,457,189, respectively. Photographic magnitudes are approximately the same as B band.

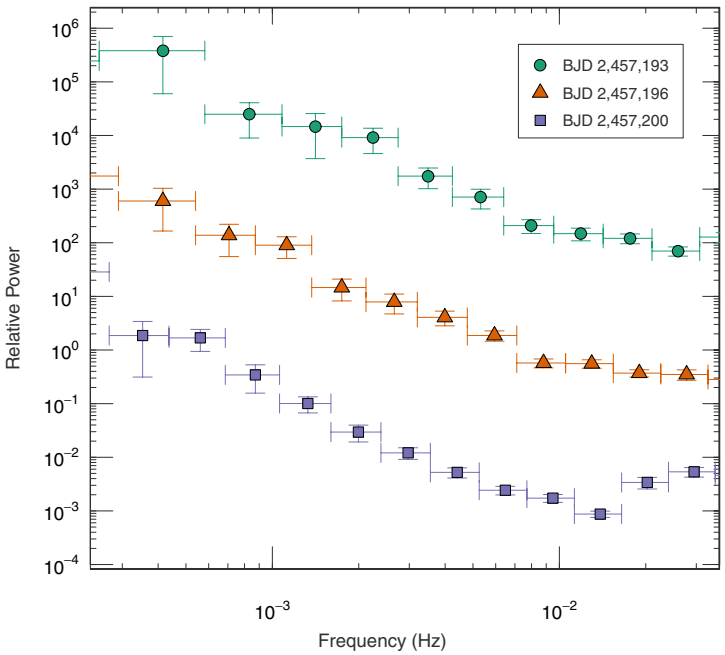

Extended Data Figure 5 | Power spectral densities of the early stage, the middle stage, and the later stage in the 2015 outburst of V404 Cyg. Power spectral densities of the fluctuations on BJD 2,457,193 (top, circles), BJD 2,457,196 (middle, triangles) and BJD 2,457,200 (bottom, rectangles). The abscissa and ordinate denote the frequency in Hz and the power in arbitrary units, respectively. For better visualization, the obtained spectrum is multiplied by 8×10^{-4} on BJD 2,457,196 and by 10^{-4} on BJD 2,457,200. $\pm 1\sigma$ error bars obtained from relevant χ^2 distributions of the power spectra.

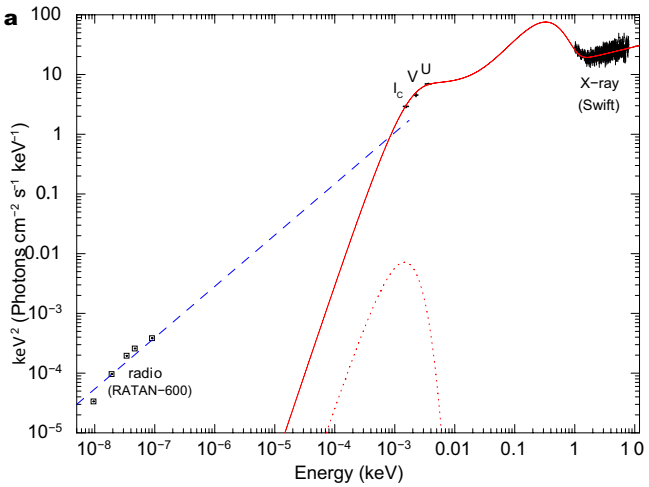

Extended Data Figure 6 | Simultaneous, extinction-corrected multi-wavelength SEDs of V404 Cyg. a, **b**, The intervals shown are BJD 2,457,199.431–2,457,199.446 (**a**) and BJD 2,457,191.519–2,457,191.524 (**b**). The optical (V and I_C) fluxes are averaged over the intervals; error bars, s.e. The X-ray, U- and UW2-band data are obtained with Swift; error bars, $\pm 1\sigma$. The radio fluxes (open squares) are compiled from the RATAN-600 results at BJD 2,457,199.433 (ref. 68). The red solid and dotted lines show the contribution of emissions from the irradiated disk with Comptonization and from the companion star, respectively. The blue dashed line approximates the radio SED, which is extended to the optical bands for illustrative purposes.

Extended Data Table 1 | A log of photometric observations of the 2015 outburst of V404 Cyg

Start*	End*	Mag†	Error‡	N§	Obs‖	Band¶
0.274	0.295	13.24	0.032	215	TAO	R
0.282	0.499	15.34	0.101	37	PZN	CR
0.386	0.426	15.18	0.036	86	PZN	R_C
0.386	0.426	14.31	0.040	20	CRI&PZN	R_C
1.137	1.192	14.92	0.024	61	PZN	CR
1.274	1.398	13.93	0.086	20	PZN	R_C
1.283	1.284	11.40	0.000	2	KW2	I_C
1.283	1.284	12.50	0.000	2	KW2	V
1.283	1.284	11.95	0.068	2	KW2	B
1.551	1.670	13.48	0.029	191	deM	I_C
1.627	1.810	14.98	0.009	2430	LCO	CR
2.109	2.517	15.07	0.024	224	PZN	CR
2.277	2.404	14.57	0.104	35	PZN	R_C
2.341	2.522	14.19	0.044	231	DPV	CR
2.354	2.529	15.41	0.056	158	DPV	V
2.354	2.529	14.12	0.049	158	DPV	R_C
2.380	2.505	17.19	0.075	61	Ter	B
2.380	2.505	15.52	0.072	61	Ter	V
2.381	2.506	14.33	0.062	61	Ter	R_C
2.406	2.524	14.65	0.024	354	Ter	CR
2.422	2.615	14.43	0.045	151	Kai	I_C
2.423	2.609	14.43	0.045	147	Kai	R_C
2.446	2.669	13.46	0.021	667	deM	I_C
2.742	2.859	13.91	0.009	2652	LCO	CR
3.801	3.341	12.55	0.048	1216	TAO	R
3.251	3.524	16.10	0.054	186	Ter	B
3.252	3.525	14.45	0.051	183	Ter	V
3.252	3.524	13.41	0.044	177	Ter	R_C
3.260	3.529	13.58	0.017	1278	Ter	CR
3.266	3.308	13.54	0.086	48	PZN	CR
3.271	3.307	13.64	0.091	40	PZN	R_C
3.410	3.489	15.80	0.095	38	CRI	B
3.411	3.488	14.36	0.071	37	CRI	V
3.411	3.488	13.17	0.062	37	CRI	R_C
3.411	3.489	12.01	0.058	37	CRI	I_C
3.419	3.588	14.48	0.048	189	RPc	V
3.428	3.553	14.52	0.056	128	Trt	V
3.430	3.519	12.25	0.023	597	IMi	I_C
3.435	3.673	12.47	0.020	1036	deM	I_C
3.525	3.650	12.64	0.075	37	COO	I_C
3.530	3.820	14.53	0.076	165	Kis	V
3.819	3.821	10.39	0.014	2	Kis	I_C
3.998	4.057	11.49	0.038	149	KU1	I_C
4.059	4.311	12.04	0.036	397	Mdy	R_C
4.187	4.316	11.88	0.022	169	TAO	R
4.435	4.673	11.66	0.021	1089	deM	I_C
4.546	4.649	13.41	0.041	82	Kis	V
4.579	4.637	11.32	0.008	1416	LCO	I_C
4.976	4.978	12.14	0.034	5	Kis	V
4.979	4.981	10.04	0.004	3	Kis	I_C
5.070	5.223	11.19	0.042	254	Mdy	R_C
5.426	5.481	12.75	0.054	36	CRI	B
5.427	5.481	13.96	0.057	36	CRI	V
5.427	5.480	11.66	0.048	35	CRI	R_C
5.427	5.480	10.57	0.044	36	CRI	I_C
5.448	5.633	10.45	0.010	840	deM	I_C
5.595	5.670	10.25	0.020	25	COO	I_C
5.724	5.954	9.85	0.007	920	SWI	I_C
5.745	5.911	11.69	0.011	346	GFB	V
5.923	5.949	10.32	0.013	24	COO	I_C
6.011	6.015	12.51	0.016	5	OKU	V
6.019	6.076	10.27	0.005	154	OKU	V
6.146	6.157	10.01	0.050	4	KW2	I_C
6.146	6.157	12.02	0.121	4	KW2	V
6.146	6.157	13.15	0.159	2	KW2	B
6.182	6.281	10.55	0.048	129	Aka	R_C
6.210	6.280	12.41	0.060	64	Aka	V
6.293	6.554	11.31	0.030	85	CRI	R_C
6.295	6.550	12.30	0.037	83	CRI	V
6.346	6.428	11.84	0.028	93	PZN	R_C
3.356	6.543	9.94	0.011	412	DPV	I_C
6.363	6.521	12.25	0.010	572	Trt	V
6.369	6.406	10.09	0.008	334	DPV	I_C
6.430	6.615	12.38	0.022	418	RJV	V
6.584	6.827	12.65	0.005	5910	LCO	V
6.592	6.861	10.54	0.012	794	RIT	I_C
6.717	6.944	10.36	0.007	942	SWI	I_C
6.745	6.912	12.35	0.010	347	GFB	V
6.919	6.950	10.35	0.076	24	COO	I_C
7.056	7.057	13.27	0.010	3	Kis	V
7.057	7.137	10.55	0.019	295	Kis	V
7.115	7.147	10.01	0.018	45	Aka	R_C
7.144	7.150	9.87	0.016	18	KW2	I_C
7.144	7.150	11.76	0.068	18	KW2	V
7.144	7.150	13.44	0.184	2	KW2	B
7.313	7.512	13.79	0.063	67	CRI	B
7.314	7.511	12.54	0.065	67	CRI	V
7.314	7.512	11.45	0.060	66	CRI	R_C
7.315	7.511	10.36	0.061	65	CRI	I_C
7.422	7.588	10.52	0.011	1501	IMi	I_C
7.427	7.670	11.35	0.035	1104	deM	I_C
7.675	7.802	10.81	0.012	1961	LCO	I_C
7.707	7.945	10.70	0.019	1003	SWI	I_C
7.744	7.907	12.98	0.036	350	GFB	V
8.030	8.300	10.22	0.020	535	KU1	I_C
8.032	8.035	11.69	0.036	5	OKU	V
8.038	8.297	10.27	0.016	1022	OKU	I_C
8.038	8.128	12.03	0.040	81	Ioh	CR
8.152	8.214	12.41	0.028	103	Wnm	cG
8.360	8.543	9.95	0.015	68	CRI	I_C
8.394	8.619	10.41	0.011	623	Kai	I_C
8.419	8.671	10.17	0.012	1129	deM	I_C
8.709	8.859	13.42	0.036	413	RIT	V
8.969	9.043	10.87	0.019	296	Sac	I_C
8.993	9.154	10.55	0.024	608	Kis	I_C
9.006	9.044	12.77	0.032	40	Sac	V
9.179	9.315	12.49	0.053	146	PZN	CR
9.224	9.229	12.59	0.149	5	OKU	V
9.239	9.300	10.84	0.020	152	OKU	I_C
9.382	9.620	10.40	0.002	643	Kai	I_C
9.414	9.595	10.24	0.003	428	NDJ	I_C
9.577	9.841	13.54	0.020	620	RIT	B
9.607	9.798	12.21	0.005	4709	LCO	V
9.635	9.828	10.13	0.010	1823	LCO	I_C
9.744	9.911	12.38	0.031	350	GFB	V
10.027	10.028	11.90	0.018	3	Kis	V
10.029	10.201	10.54	0.011	837	Kis	I_C
10.387	10.619	10.46	0.020	611	Kai	I_C
10.415	10.670	10.38	0.013	1389	deM	I_C
10.744	10.910	11.99	0.010	349	GFB	V
11.182	11.300	9.41	0.012	99	KU1	I_C
11.291	11.298	10.55	0.003	112	TAO	R
11.339	11.514	10.51	0.018	406	DPV	I_C
11.348	11.554	13.10	0.014	730	Trt	V
11.372	11.515	13.15	0.019	335	DPV	V
11.385	11.592	11.00	0.015	490	Kai	I_C
11.421	11.673	11.32	0.021	1314	deM	I_C
11.460	11.624	13.71	0.097	70	JSa	V
11.483	11.603	13.53	0.016	374	RJV	V
11.590	11.679	14.43	0.014	730	LCO	V
11.679	11.834	12.95	0.008	3859	LCO	I_C
12.228	12.232	15.49	0.139	5	OKU	V
12.234	12.271	12.95	0.028	177	TAO	R
12.302	12.334	13.81	0.011	311	TAO	R
12.386	12.611	13.89	0.025	484	Kai	I_C
12.405	12.670	14.08	0.022	640	deM	I_C
12.484	12.599	16.87	0.031	237	RJV	V
13.058	13.314	15.81	0.013	211	Mdy	R_C
13.199	13.334	15.97	0.048	1772	TAO	R
13.382	13.594	14.28	0.014	467	Kai	I_C
13.415	13.670	14.08	0.022	640	deM	I_C
13.438	13.473	13.91	0.040	93	NDJ	I_C
14.014	14.021	17.21	0.075	5	OKU	V
14.026	14.168	14.75	0.022	97	OKU	I_C
14.043	14.276	14.70	0.016	361	Kis	I_C
14.379	14.499	17.00	0.030	52	Trt	CV
14.421	14.565	14.85	0.012	152	RPc	I_C
14.422	14.614	14.56	0.007	248	NDJ	I_C
14.504	14.517	17.15	0.114	5	Trt	V
14.601	14.810	15.56	0.003	1830	LCO	CR
15.166	15.276	16.92	0.234	664	TAO	R
15.356	15.549	16.04	0.007	244	DPV	CR
15.364	15.550	17.41	0.024	42	DPV	V
15.434	15.559	14.84	0.017	81	RPc	I_C
15.694	15.762	14.45	0.008	166	SWI	I_C
16.092	16.142	14.60	0.397	5	TAO	R
16.302	16.377	16.07	0.013	26	PZN	CR
16.320	16.525	14.44	0.010	129	CRI	I_C
16.344	16.435	14.50	0.012	52	DPV	I_C
16.516	16.530	14.44	0.030	6	RPc	I_C
16.680	16.937	14.36	0.006	335	SWI	I_C
17.358	17.518	14.48	0.006	218	DPV	I_C
17.418	17.671	14.78	0.006	309	deM	I_C
17.440	17.575	14.62	0.014	43	RPc	I_C
18.297	18.336	17.37	0.254	470	TAO	R
19.328	19.332	16.45	0.258	68	TAO	R
19.403	19.451	14.82	0.011	33	DPV	I_C
19.423	19.498	14.79	0.026	17	RPc	I_C
19.712	19.761	16.61	0.008	60	GFB	CV
20.435	20.592	14.98	0.008	90	RPc	I_C
21.023	21.031	15.34	0.012	10	RPc	I_C

Start and end dates of observations, mean magnitudes, 1σ of mean magnitudes, numbers of observations, observers' codes, and filters are summarized. Note that observers for TAOS used custom made filters close to the union of standard R and V[34,79], but the magnitude reported in the present Letter was approximately calibrated to standard R.

*JD−2,457,189 (days).

†Mean magnitude.

‡1σ of mean magnitude.

§Number of observations.

‖Observer's code: PZN (IKI GRB follow up network), CRI (Crimean Observatory Team), deM (E. de Miguel), DPV (P. A. Dubovsky), Ter (Terskol Observatory), Kai (K. Kasai), NDJ (N. James), RPc (R. D. Pickard), Trt (T. Tordai), COO (L. Cook), Kis (S. Kiyota), KU1 (Kyoto Univ. Team), Mdy (Y. Maeda), LCO (C. Littlefield), RIT (M. Richmond), RJV (R. Javier), GFB (W. Goff), SWI (W. L. Stein), OKU (Osaka Kyoiku Univ. team), Sac (A. Miyashita), IMi (I. Miller), TAO (TAOS Team), KW2 (H. Maehara), Aka (H. Akazawa), Wnm (K. Hirosawa) and JSa (J. Lluis).

¶Filter. B, V, R_C, I_C are the standard Johnson-Cousins system. 'CR' and 'CV' mean unfiltered CCD photometry with zero point adjustment in R and V, respectively. 'cG' means green (G) channel output in a digital single-lens reflex camera, which gives an approximate response close to V (ref. 80).

Extended Data Table 2 | List of instruments for optical observations

CODE	Telescope (& CCD)	Observatory (or Observer)	Site
PZN	1m Zeiss-1000 Tien Shan +Apogee Alta	Astronomical Observatory	Almaty, Kazakhstan
	40cm ORI-40+FLI ML09000	ISON-Khureltogot	Mongolia
	70cm+FLI AS-32+FLI IMG6303E	Abastumani observatory	Georgia
CRI	1.25m AZT-11+FLI ProLine PL230	Crimean astrophysical observatory	Crimea
	38cm K-380+Apogee E47	Cremean astrophysical observatory	Crimea
deM	35cm SC+QSI-516wsg	Observatorio Astronomico del CIECEM	Huelva, Spain
DPV	28cm SC+MII G2-1600	Astronomical Observatory on Kolonica	Slovakia
	35cm SC+MII G2-1600	Astronomical Observatory on Kolonica	Slovakia
	VNT 1m+FLI PL1001E	Astronomical Observatory on Kolonica	Slovakia
Ter	Zeiss-600 60cm+SBIG STL-1001E	Terskol Observatory	Russia
	S2C 35cm	Terskol Observatory	Russia
Kai	28cm SC+ST7XME	Kiyoshi Kasai	Switzerland
NDJ	28cm SC+ST9XE	Nick James	UK
RPc	FTN 2.0m+E2V 42-40	LCOGT*	Hawaii, USA
	35cmSC+SXV-H9 CCD	Roger D. Pickard	UK
Trt	25cm ALCCD5.2 (QHY6)	Tamás Tordai	Budapest, Hungary
COO	T07† 43cm+STL-1100M	AstroCamp Observatory	Nerpio, Spain
	T21† 43cm+FLI-PL6303E	iTelescope.Net Mayhill	New Mexico, USA
	T11† 50cm+FLI ProLine PL11002M	iTelescope.Net Mayhill	New Mexico, USA
Kis	25cm SC+Alta F47	Seiichiro Kiyota	Kamagaya, Japan
	T18† 32cm+STXL-6303E	AstroCamp Observatory	Nerpio, Spain
	T5† 25cm+ST-10XME	iTelescope.Net Mayhill	New Mexico, USA
	T24† 61cm+FLI-PL09000	Sierra Remote Observatoy	California, USA
KU1	40cm SC+ST-9XEI	Kyoto U. Team	Kyoto, Japan
Mdy	35cm SC+ST10XME	Yutaka Maeda	Nagasaki, Japan
LCO	60cm+Apogee Alta U42 CCD	Van Vleck Observatory	Connecticut, USA
	40cm+SBIG STL-6303	Van Vleck Observatory	Connecticut, USA
RIT	30cm+ST-9E	RIT Observatory	New York, USA
RJV	LX200R 40cm+ST8 XME	Observatorio de Cantabria	Spain
GFB	CDK 50cm+Apogee U6	William Goff	California, USA
SWI	C14 35cmSC+ST10XME	William L. Stein	New Mexico, USA
OKU	51cm+Andor DW936N-BV	OKU Astronomical Observatory	Osaka, Japan
Sac	20cmL+ST-7XMEi	Atsushi Miyashita	Tokyo, Japan
IMi	35cm SC+SXVR-H16	Furzehill Observatory	UK
TAO	TAOS-B‡ 50cm+SI800 E2V47-20	Lulin Observatory	Taiwan
	TAOS-D‡ 50cm+SI800 E2V47-20	Lulin Observatory	Taiwan

Observers' codes (see Extended Data Table 1), names of telescopes and CCD cameras, observatory (or observer) and sites are summarized.
*Las Cumbres Observatory Global Telescope Network.
†itelescope.net.
‡The Taiwanese-American Occultation Survey (TAOS)[34,81,82].

Extended Data Table 3 | Basic information on objects showing violent short-term variations in outbursts

	V404 Cyg	GRS 1915+105	IGR J17091-3624	Rapid Burster	V4641 Sgr
Orbital period [d]	6.47129(7) (ref. 83)	33.85(16) (ref. 20)	>4 (ref. 84)	–	2.81678 (ref. 23)
Compact object	BH	BH	BH	NS	BH
Spectrum of the secondary	K3III (ref. 7)	K–M (ref. 20)	–	–	B9III (ref. 23)
M_1 ($M_\odot$)	9.0(0.6) (ref. 7)	10.1(0.6) (ref. 85)	11.8–13.7 (ref.86)	1.1(0.3) (ref. 87)	7.1(0.3) (ref. 88)
$q = M_2/M_1$ (Mass ratio)	0.06 (ref. 7)	0.042(0.024) (ref. 20)	–	–	0.45(0.05) (ref. 88)
***i* [deg] (Inclination angle)**	67(3) (ref. 7)	66(2) (ref. 89)	50–70 (ref. 90)	–	72.3(4.1) (ref. 88)
***V* magnitude minimum**	18.4 (ref. 91)	–	–	–	13.8 (ref. 88)
***V* magnitude maximum**	10.9 (This work)	–	–	–	8.8 (ref. 41)

Shown are orbital period, nature of the compact object, spectrum of the secondary, mass of the central object (M_1), mass ratio (q), inclination angle (i), minimum magnitude (V band), and maximum magnitude (V band) on V404 Cyg, GRS 1915+105, IGR 17091−3624, the Rapid Burster, and V4641 Sgr. M_2, mass of the secondary star. References are cited as follows: 7, 20, 23, 41, 83–91.

Publ. Astron. Soc. Japan (2016) 68 (6), 107 (1–14)
doi: 10.1093/pasj/psw101
Advance Access Publication Date: 2016 October 27

RZ Leonis Minoris bridging between ER Ursae Majoris-type dwarf nova and nova-like system

Taichi Kato,[1,*] Ryoko Ishioka,[2] Keisuke Isogai,[1] Mariko Kimura,[1] Akira Imada,[3] Ian Miller,[4] Kazunari Masumoto,[5] Hirochika Nishino,[5] Naoto Kojiguchi,[5] Miho Kawabata,[5] Daisuke Sakai,[5] Yuki Sugiura,[5] Hisami Furukawa,[5] Kenta Yamamura,[5] Hiroshi Kobayashi,[5] Katsura Matsumoto,[5] Shiang-Yu Wang,[2] Yi Chou,[6] Chow-Choong Ngeow,[6] Wen-Ping Chen,[6] Neelam Panwar,[6] Chi-Sheng Lin,[6] Hsiang-Yao Hsiao,[6] Jhen-Kuei Guo,[6] Chien-Cheng Lin,[6] Chingis Omarov,[7] Anatoly Kusakin,[7] Maxim Krugov,[7] Donn R. Starkey,[8] Elena P. Pavlenko,[9] Kirill A. Antonyuk,[9] Aleksei A. Sosnjvskij,[9] Oksana I. Antonyuk,[9] Nikolai V. Pit,[9] Alex V. Baklanov,[9] Julia V. Babina,[9] Hiroshi Itoh,[10] Stefano Padovan,[11] Hidehiko Akazawa,[12] Stella Kafka,[11] Enrique de Miguel,[13,14] Roger D. Pickard,[15,16] Seiichiro Kiyota,[17] Sergey Yu. Shugarov,[18,19] Drahomir Chochol,[19] Viktoriia Krushevska,[20] Matej Sekeráš,[19] Olga Pikalova,[21] Richard Sabo,[22] Pavol A. Dubovsky,[23] Igor Kudzej,[23] Joseph Ulowetz,[24] Shawn Dvorak,[25] Geoff Stone,[11] Tamás Tordai,[26] Franky Dubois,[27] Ludwig Logie,[27] Steve Rau,[27] Siegfried Vanaverbeke,[27] Tonny Vanmunster,[28] Arto Oksanen,[29] Yutaka Maeda,[30] Kiyoshi Kasai,[31] Natalia Katysheva,[18] Etienne Morelle,[32] Vitaly V. Neustroev,[33,34] and George Sjoberg[11,35]

[1]Department of Astronomy, Kyoto University, Kitashirakawa-Oiwake-cho, Sakyo-ku, Kyoto, Kyoto 606-8502, Japan
[2]Institute of Astronomy and Astrophysics, Academia Sinica, 11F of Astronomy-Mathematics Building, National Taiwan University, No. 1, Sec. 4, Roosevelt Rd, Taipei 10617, Taiwan
[3]Kwasan and Hida Observatories, Kyoto University, 17 Ohmine-cho Kita Kazan, Yamashina-ku, Kyoto, Kyoto 607-8471, Japan
[4]Furzehill House, Ilston, Swansea, SA2 7LE, UK
[5]Osaka Kyoiku University, 4-698-1 Asahigaoka, Kashiwara, Osaka 582-8582, Japan
[6]Graduate Institute of Astronomy, National Central University, Jhongli 32001, Taiwan
[7]Fessenkov Astrophysical Institute, Observatory 23, Almaty 050020, Kazakhstan
[8]DeKalb Observatory, H63, 2507 County Road 60, Auburn, IN 46706, USA
[9]Federal State Budget Scientific Institution "Crimean Astrophysical Observatory of RAS", Nauchny 298409, Republic of Crimea
[10]Variable Star Observers League in Japan (VSOLJ), 1001-105 Nishiterakata, Hachioji, Tokyo 192-0153, Japan
[11]American Association of Variable Star Observers, 49 Bay State Rd., Cambridge, MA 02138, USA

[12]Department of Biosphere-Geosphere System Science, Faculty of Informatics, Okayama University of Science, 1-1 Ridai-cho, Okayama, Okayama 700-0005, Japan
[13]Departamento de Ciencias Integradas, Facultad de Ciencias Experimentales, Universidad de Huelva, 21071 Huelva, Spain
[14]Center for Backyard Astrophysics, Observatorio del CIECEM, Parque Dunar, Matalascañas, 21760 Almonte, Huelva, Spain
[15]The British Astronomical Association, Variable Star Section (BAA VSS), Burlington House, Piccadilly, London, W1J 0DU, UK
[16]3 The Birches, Shobdon, Leominster, Herefordshire, HR6 9NG, UK
[17]VSOLJ, 7-1 Kitahatsutomi, Kamagaya, Chiba 273-0126, Japan
[18]Sternberg Astronomical Institute, Lomonosov Moscow State University, Universitetsky Ave., 13, Moscow 119992, Russia
[19]Astronomical Institute of the Slovak Academy of Sciences, 05960 Tatranska Lomnica, Slovakia
[20]Main Astronomical Observatory of the National Academy of Sciences of Ukraine, 27 Akademika Zabolotnoho ave., 03680 Kyiv, Ukraine
[21]Faculty of Physics, Lomonosov Moscow State University, Leninskie Gory, Moscow 119991, Russia
[22]2336 Trailcrest Dr., Bozeman, MT 59718, USA
[23]Vihorlat Observatory, Mierova 4, 06601 Humenne, Slovakia
[24]Center for Backyard Astrophysics Illinois, Northbrook Meadow Observatory, 855 Fair Ln, Northbrook, IL 60062, USA
[25]Rolling Hills Observatory, 1643 Nightfall Drive, Clermont, FL 34711, USA
[26]Polaris Observatory, Hungarian Astronomical Association, Laborc utca 2/c, 1037 Budapest, Hungary
[27]Public Observatory Astrolab Iris, Verbrandemolenstraat 5, B 8901 Zillebeke, Belgium
[28]Center for Backyard Astrophysics Belgium, Walhostraat 1A, B-3401 Landen, Belgium
[29]Hankasalmi Observatory, Vertaalantie 116, FIN-40500 Hankasalmi, Finland
[30]Kaminishiyamamachi 12-14, Nagasaki, Nagasaki 850-0006, Japan
[31]Baselstrasse 133D, CH-4132 Muttenz, Switzerland
[32]9 rue Vasco de GAMA, 59553 Lauwin Planque, France
[33]Finnish Centre for Astronomy with ESO (FINCA), University of Turku, Väisäläntie 20, FIN-21500 Piikkiö, Finland
[34]Astronomy Research Unit, PO Box 3000, FIN-90014 University of Oulu, Finland
[35]The George-Elma Observatory, 9 Contentment Crest, #182, Mayhill, NM 88339, USA

*E-mail: tkato@kusastro.kyoto-u.ac.jp

Received 2016 September 5; Accepted 2016 September 20

Abstract

We observed RZ LMi, which is renowned for its extremely short (∼19 d) supercycle and is a member of a small, unusual class of cataclysmic variables called ER UMa-type dwarf novae, in 2013 and 2016. In 2016, the supercycles of this object substantially lengthened in comparison to the previous measurements to 35, 32, and 60 d for three consecutive superoutbursts. We consider that the object virtually experienced a transition to the nova-like state (permanent superhumper). This observed behavior reproduced the prediction of the thermal-tidal instability model extremely well. We detected a precursor in the 2016 superoutburst and detected growing (stage A) superhumps with a mean period of 0.0602(1) d in 2016 and in 2013. Combined with the period of superhumps immediately after the superoutburst, the mass ratio is not as small as in WZ Sge-type dwarf novae, having orbital periods similar to RZ LMi. By using least absolute shrinkage and selection operator (Lasso) two-dimensional power spectra, we detected possible negative superhumps with a period of 0.05710(1) d. We estimated an orbital period of 0.05792 d, which suggests a mass ratio of 0.105(5). This relatively large mass ratio is even above that of

ordinary SU UMa-type dwarf novae, and it is also possible that the exceptionally high mass-transfer rate in RZ LMi may be a result of a stripped secondary with an evolved core in a system evolving toward an AM CVn-type object.

Key words: accretion, accretion disks — novae, cataclysmic variables — stars: dwarf novae — stars: individual (RZ Leonis Minoris)

1 Introduction

SU UMa-type dwarf novae (DNe) are a class of cataclysmic variables (CVs) which are close binary systems transferring matter from a red dwarf secondary to a white dwarf, forming an accretion disk. In SU UMa-type DNe, two types of outbursts are seen: normal outbursts and superoutbursts. Superoutbursts are defined by the presence of (positive) superhumps, which are humps with a period that is a few percent longer than the orbital period [for general information on CVs, DNe, SU UMa-type DNe, and superhumps, see e.g., Warner (1995)].

RZ LMi is one of the most enigmatic SU UMa-type DNe. This object was originally discovered as an ultraviolet-excess variable star [Lipovetskii & Stepanyan 1981; it was later given a designation of FBS 0948+344 (Abrahamian & Mickaelian 1993)]. Lipovetskii and Stepanyan (1981) reported that the object had a spectral energy distribution of spectral classes O–B at maximum. When the object was fading or rising, strong emission lines appeared. Lipovetskii and Stepanyan (1981) studied 16 objective prism plates and seven direct imaging plates and recorded a strong variation with a range of 14–17 mag. The object was recorded at 17 mag on the Palomar Obervatory Sky Survey (POSS). Based on the colors and rapid variation in a time-scale of a few days, Lipovetskii and Stepanyan (1981) suggested a dwarf nova-type classification. Green et al. (1982) also selected it as an ultraviolet-excess object (PG 0948+344) and confirmed it spectroscopically as a CV. They gave a variability range of $B = 14.4$–16.8 without details (the minimum likely referred to the magnitude in POSS). Despite the finding by Lipovetskii and Stepanyan (1981), Kholopov et al. (1985) designated RZ LMi as a nova-like (NL) variable by referring to Green et al. (1982). Kondo, Noguchi, and Maehara (1984) also selected RZ LMi as an ultraviolet-excess object.

The nature of the variability of this object remained unclear. Knowing the dwarf nova-type classification, one of the authors of this paper (TK) visually observed this object in 1987–1988 and found relatively stable ~20 d cycle lengths with additional short outbursts. This result was reported in the domestic variable star bulletin "Henkousei" (in Japanese). This report was probably the first to document the unusual cyclic variation of RZ LMi. Two teams observed this object photometrically: Robertson, Honeycutt, and Turner (1994) reported an unusual long-term repetitive light curve with a stable period (it is now known as the supercycle) of 19.2 d. Pikalova and Shugarov (1995) reported that the behavior was different from a typical dwarf nova in that it showed short fading and brightening. They also reported a possible period of 21.167 d or 23.313 d, and classified it as a VY Scl-type NL.

A clue to understanding the unusual behavior of RZ LMi came from the discovery of the SU UMa-type dwarf nova ER UMa with an ultrashort supercycle (interval between superoutbursts) of 43 d in 1994 (Kato & Kunjaya 1995). As presented orally in the conference held in Abano Terme, Italy, 1994 June 20–24, Robertson's team originally considered that the recurring NL-type bright state and the dwarf nova-type state in ER UMa and RZ LMi were the best examples to show the consequences of recurring mass-transfer bursts from the secondary. In the same conference, however, after Robertson's presentation, Y. Osaki introduced Kato and Kunjaya's detection of superhumps in ER UMa (Osaki 1995c) and showed that the unusual behavior of ER UMa could be understood within the framework of the thermal-tidal instability (TTI) model (Osaki 1989) if one can allow an exceptionally high mass-transfer rate (cf. Osaki 1995a). After this conference, Robertson's team published a paper following the interpretation by Kato and Kunjaya introduced by Y. Osaki (Robertson et al. 1994, 1995).[1] After the discovery of superhumps in ER UMa and the recognition of the similarity between ER UMa and RZ LMi, superhumps were naturally sought. The competition was intense: both Robertson, Honeycutt, and Turner (1995) and Nogami et al. (1995) observed the same superoutburst in 1995 and detected superhumps. These observations confirmed that RZ LMi does indeed belong to the SU UMa-type DNe. These objects, together with V1159 Ori, are usually called ER UMa-type stars (cf. Kato et al. 1999).

The mechanism of the ultrashort (19 d) supercycle and the unusually regular outburst pattern remained a mystery. Robertson, Honeycutt, and Turner (1994) suspected a mechanism outside the disk in addition to the one in the

[1] The dwarf nova-type nature was first clarified by Iida (1994). Misselt and Shafter (1995) also observed ER UMa in 1993–1994 and finally reached the same conclusion as Kato and Kunjaya (1995).

disk. A later publication by Olech et al. (2008) followed the former possibility and suggested a third body. In the standard TTI model, this short supercycle is difficult to reproduce, and Osaki (1995b) presented a working hypothesis that in RZ LMi the disk becomes thermally unstable during the superoutburst earlier than in other SU UMa-type DNe. Hellier (2001) suggested, following the interpretation in Osaki (1995b), that in systems with very small mass ratios (q), the tidal torque is too small to maintain the superoutburst, and that there occurs a decoupling between the thermal and tidal instabilities. Hellier (2001) suggested that one of the consequences of this decoupling can be found as the persistent superhumps after superoutbursts.

According to the working hypotheses by Osaki (1995b) and Hellier (2001), it is strongly predicted that the q is small in RZ LMi and that the disk radius after the superoutburst is larger than in other SU UMa-type DNe. RZ LMi, however, has defied every attempt to determine the orbital period, since it mostly stays in the "outburst" state and it is difficult to make a radial-velocity study in short quiescence. The almost continuous presence of superhumps also made it difficult to detect potential orbital variations by photometric methods. Without the orbital period or a radial-velocity study, it remained impossible to observationally determine q, and the evolutionary status of RZ LMi remained unclear despite its unusual outburst properties.

The situation dramatically changed after the detection of a possible change in the outburst pattern in the AAVSO observations (vsnet-alert 19524). We have conducted a world-wide campaign to observe RZ LMi during the 2016 season. The new development has also been helped by the classification of superhumps stage (A, B, and C: Kato et al. 2009) and identification of stage A superhumps representing the growing phase of superhumps at the radius of the 3 : 1 resonance (Osaki & Kato 2013b; Kato & Osaki 2013).

In this paper, key information and results are given in the main paper. The results not directly related to the conclusion of the paper, such as the variation of superhump periods and variation of the profile of superhumps, are given in the Supplementary Information, as they will provide useful information to expert readers.

2 Observations

The data were obtained under campaigns led by the VSNET Collaboration (Kato et al. 2004) in 2016. We also used the public data from the AAVSO International Database.[2] Time-resolved photometric observations were obtained on 75 nights (nights with more than 100 observations) between February 25 and June 10. Some snapshot observations were obtained on some other nights. We also performed time-resolved photometric observations during the period of 2013 March 5–April 29 at nine sites. We also obtained snapshot observations (several observations typically ~20 min apart) on 47 nights between 2014 March 8 and May 22. The logs of observations are given in the e-tables.[3] Alphabetical abbreviated codes in the log are observer codes of AAVSO and they mean that the data were taken from the AAVSO database. We also used historical photographic data reported by Pikalova and Shugarov (1995) (listed as "Shugarov," as he finally compiled all the data, in this paper).

The data were analyzed in the same way as described in Kato et al. (2009) and Kato et al. (2014b). We mainly used R software[4] for data analysis. In de-trending the data, we divided the data into four segments in relation to the outburst phase and used locally-weighted polynomial regression (LOWESS: Cleveland 1979). The times of superhumps maxima were determined by the template-fitting method as described in Kato et al. (2009). The times of all observations are expressed in barycentric Julian Days (BJD).

3 Results and discussion

3.1 Outburst light-curve and emergence of superhumps

Figure 1 illustrates the three consecutive superoutbursts in 2016 during which we obtained time-resolved photometric observations. The initial part of the light curve (upper panel) was the final fading part of the preceding superoutburst. There was only one normal outburst between the first and second superoutbursts. Although the initial part of the first superoutburst was not well sampled, we found that the superoutburst lasted for 26 d.

There were two normal outbursts between the second and the third superoutburst. The duration of the second superoutburst was 48 d, even longer than the first one. The intervals (supercycles) between the three superoutbursts were 32 d and 60 d. These values were 2–3 times longer than the historical supercycle (19 d) of this object (Robertson et al. 1994; Nogami et al. 1995).

During the best-observed second superoutburst, there was a shoulder (precursor outburst). Figure 2 shows the initial part of this superoutburst. The precursor part is clearly seen between BJD 2457483 and 2457484. During this phase, superhumps rapidly grew to the maximum amplitude and they started to decay slowly (lower panel; see

[2] ⟨http://www.aavso.org/data-download⟩.

[3] E-tables are available in the online edition as Supporting Information.

[4] The R Foundation for Statistical Computing ⟨http://cran.r-project.org/⟩.

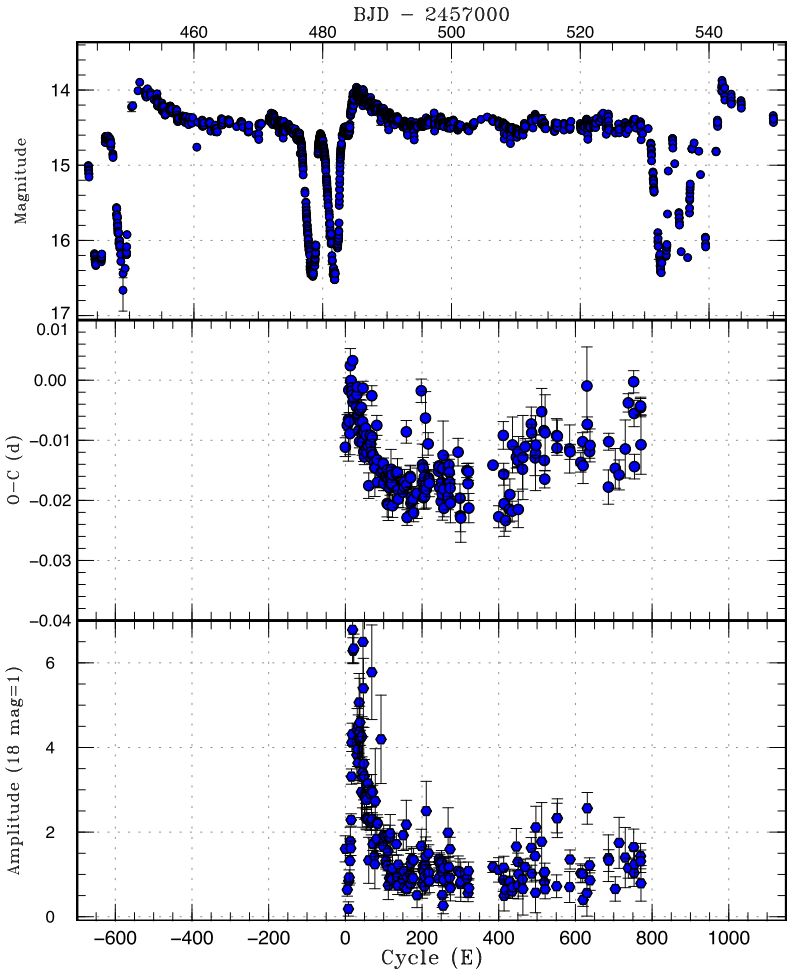

Fig. 1. Light-curve and $O-C$ diagram of superhumps in RZ LMi (2016). Upper: Light curve. The data were binned to 0.0023 d. In this figure, we show three consecutive superoutbursts which we observed. Middle: $O-C$ diagram for the second superoutburst (filled circles). We used a period of 0.05955 d for calculating the $O-C$ residuals. Lower: Amplitudes of superhumps. The scale is linear and the pulsed flux is shown in a unit corresponding to 18 mag = 1. (Color online)

also figure 3 for an enlargement). This behavior is the same as in ordinary SU UMa-type DNe [see e.g., figure 19 in Kato et al. (2013a) for one of the best-known SU UMa-type DNe VW Hyi; see also figure 4 in Osaki and Kato (2013a) for the corresponding part of the Kepler data of V1504 Cyg]. Similar precursors were also recorded in snapshot observations of the first superoutburst and less markedly (fewer observations) during the third superoutburst. These observations indicate that RZ LMi shows a sequence of a precursor and the main superoutburst as in ordinary SU UMa-type DNe at least in this season.

The variable supercycles now safely exclude the existence of a stable clock (such as an orbiting third body) which was supposed to work to produce regular superoutbursts (Robertson et al. 1994; Olech et al. 2008). Furthermore, Osaki (1995a) already showed that the supercycle length reaches the minimum as the mass-transfer rate ($\dot{M}$) increases, but that it lengthens again as $\dot{M}$ further increases. As $\dot{M}$ increases, the system eventually reaches the "permanent outburst" state (see figure 2 in Osaki 1995a), bridging ER UMa-type objects and what is called permanent superhumpers (Skillman & Patterson 1993; Patterson 1999). The current state of RZ LMi reproduced this prediction exactly, providing strong support to the explanation of the unusual short supercycles in ER UMa-type objects.

Osaki (1995b) formulated the duration of a superoutburst ($t_{\rm supermax}$) as below:

$$t_{\rm supermax} \sim t_{\rm vis}[f_M/(1-1/e)][1-(\dot{M}/\dot{M}_{\rm crit})]^{-1/2}, \quad (1)$$

where $t_{\rm vis}$ is the viscous depletion timescale and $\dot{M}_{\rm crit}$ is the critical $\dot{M}$ required to produce a hot, stable disk, respectively. The factor f_M is the fraction of the disk mass accreted during a superoutburst. It is given by

$$f_M \simeq 1-(R_0/R_{\rm d,crit})^{3.0}, \quad (2)$$

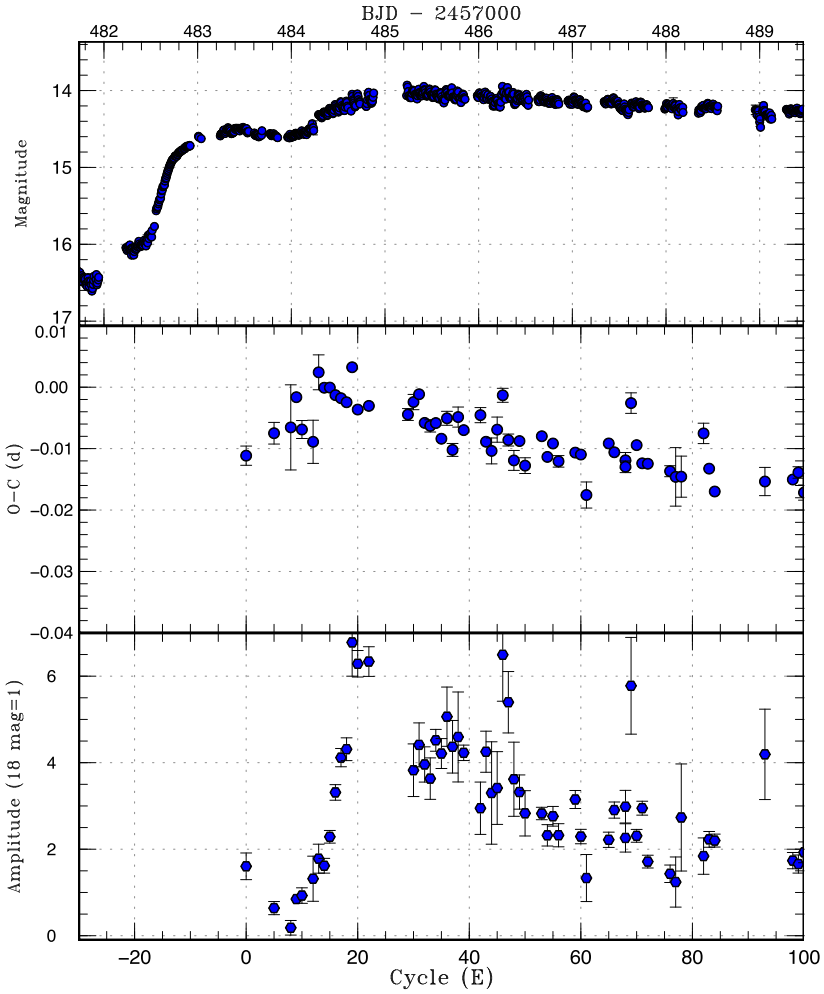

Fig. 2. Light-curve and $O-C$ diagram of superhumps in RZ LMi (2016). This figure is an enlargement of figure 1. Upper: Light curve. The data were binned to 0.0023 d. The precursor part is clearly seen between BJD 2457483 and 2457484. During this phase, superhumps rapidly grew. Middle: $O-C$ diagram for the second superoutburst (filled circles). We used a period of 0.05955 d for calculating the $O-C$ residuals. Lower: Amplitudes of superhumps. The scale is linear and the pulsed flux is shown in a unit corresponding to 18 mag = 1. (Color online)

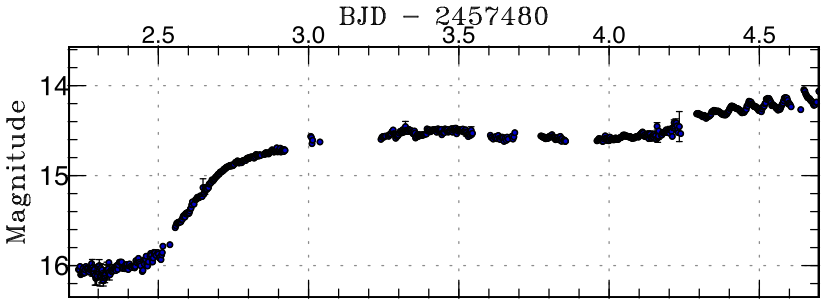

Fig. 3. Growing superhumps and precursor at the start of the 2016 April superoutburst. The data were binned to 0.0023 d. Superhump grew between BJD 2457483 and 2457484. (Color online)

where R_0 and $R_{\mathrm{d,\,crit}}$ represent the disk radius at the end of a superoutburst and at the start of a superoutburst (assuming that the disk critically reaches the radius of the 3 : 1 resonance at the start of a superoutburst), respectively. If we consider that t_{vis} and R_0 are the same between different superoutbursts of RZ LMi, we can estimate $\dot{M}$ during the current state. Using the parameters in Osaki (1995b), $t_{\mathrm{vis}} = 11.2$ d and an assumption of a large disk radius at the end of a superoutburst $R_0 = 0.42a$, where a is the binary separation, the historical t_{supermax} of 6 d (Robertson et al. 1995) is reproduced with $\dot{M}/\dot{M}_{\mathrm{crit}} = 0.5$. The current t_{supermax} values of 26 and 48 d require

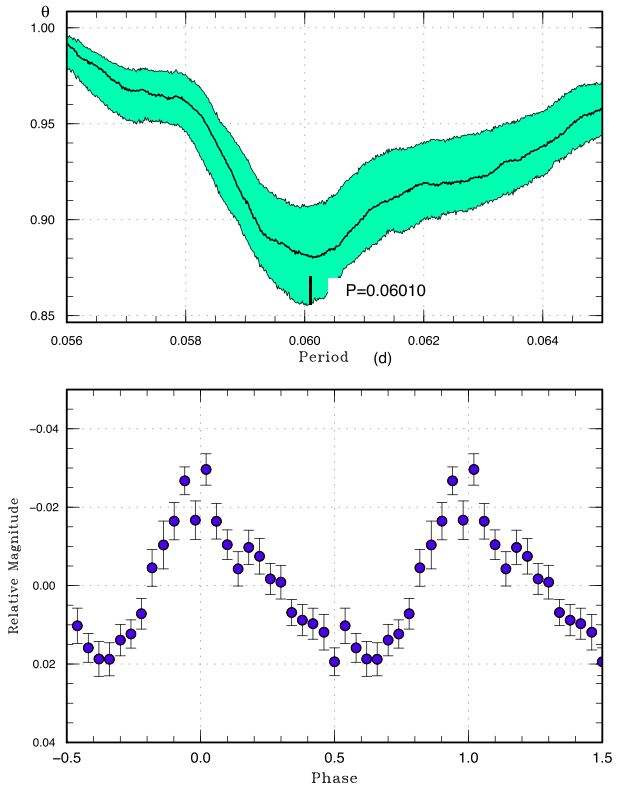

Fig. 4. Stage A superhumps in RZ LMi (2016). The data between BJD 2457483.01 and 2457484.40 were used. Upper: PDM analysis. We analyzed 100 samples which randomly contain 50% of observations, and performed PDM analysis for these samples. The bootstrap result is shown as a form of 90% confidence intervals in the resultant PDM θ statistics. Lower: Phase-averaged profile. (Color online)

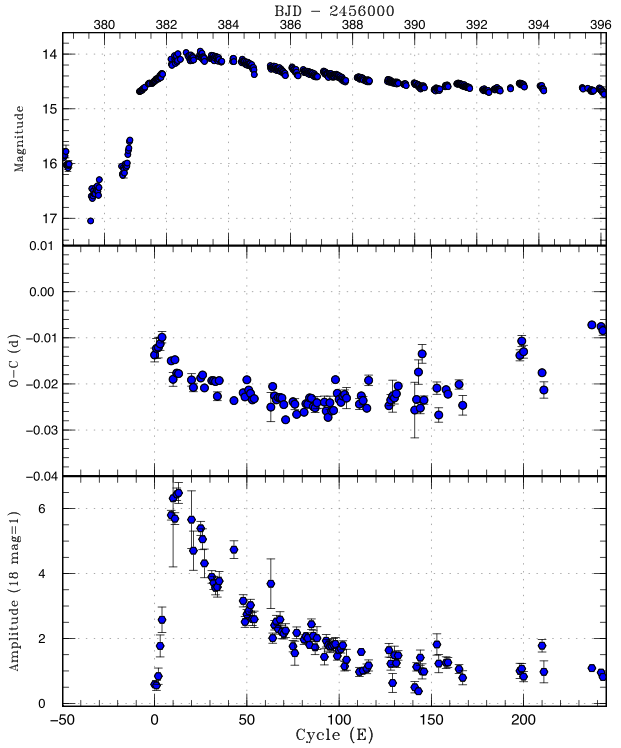

Fig. 5. $O-C$ diagram of superhumps in RZ LMi in 2013 April. Upper: Light curve. The data were binned to 0.0023 d. Middle: $O-C$ diagram (filled circles). We used a period of 0.05945 d for calculating the $O-C$ residuals. Lower: Amplitudes of superhumps. The scale is linear and the pulsed flux is shown in a unit corresponding to 18 mag = 1. (Color online)

$\dot{M}/\dot{M}_{\rm crit} = 0.97$ and 0.99, respectively. Although these estimates have uncertainties due to various assumptions, it is certain that the current state of RZ LMi is *critically* close to the stability border. If RZ LMi increases $\dot{M}$ further by 1%, the object should become a permanent superhumper. As judged from these estimates, we have seen an almost complete transition from an ER UMa-type object to a permanent superhumper. There has been at least one case (BK Lyn) in which a permanent superhumper became an ER UMa-type object and then returned back (Patterson et al. 2013; Kato et al. 2013a), and the case of RZ LMi may not be special.

3.2 Growing (stage A) superhumps and post-superoutburst superhumps

As is best seen in the lower panel of figure 2, the amplitudes of superhumps rapidly grew in ∼20 cycles. During the initial ∼13 cycles, the $O-C$ values (middle panel) were negative and a characteristic kink around $E = 13$ indicates that this object showed long-period (stage A) superhumps before entering the stable phase of stage B superhumps with a shorter period, as in other SU UMa-type DNe (see the e-tables for the full list of times of superhump maxima). This identification appears particularly confident since it has been recently demonstrated that ER UMa, the prototype of ER UMa-type objects, showed the same pattern with a precursor outburst (Ohshima et al. 2014). The period of stage A superhumps from the times of maxima ($E \leq 13$) is 0.0602(4) d. By using the data between BJD 2457483.01 and 2457484.40, we have obtained a period of 0.0601(1) d with the phase dispersion minimization (PDM: Stellingwerf 1978) method (figure 4). The errors are 1σ estimated by the methods of Fernie (1989) and Kato et al. (2010). We consider that the result by the PDM method is more reliable than that from superhump maxima, since it gives a smaller error, and adopted this period.

Although the second superoutburst was generally well observed, the observations were unfortunately relatively sparse around stage A. The 2013 April superoutburst of this object was relatively well observed in the same phase, although the brightness peak was missed and instead of a distinct precursor there was a stagnation in the rising phase, which was likely an embedded precursor (figures 5 and 6; see e-table for the full times of superhump maxima). During the observation in 2013, a continuous light curve

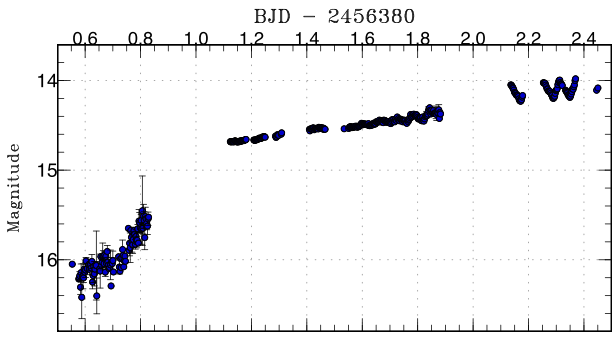

Fig. 6. Growing superhumps and stagnation (embedded precursor) at the start of the 2013 April superoutburst. The data were binned to 0.0023 d. Superhump grew between BJD 2456381.41 and 2456381.88. (Color online)

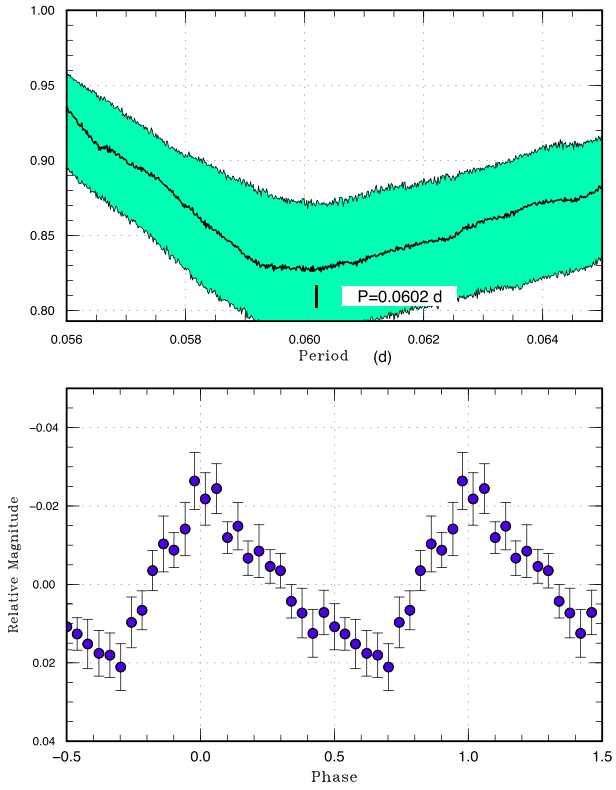

Fig. 7. Stage A superhumps in RZ LMi (2013 April). The data between BJD 2456381.41 and 2456381.88 were used. Upper: PDM analysis. Lower: phase-averaged profile. (Color online)

of growing superhumps ($0 \leq E \leq 4$) was well recorded. Using the data between BJD 2456381.41 and 2456381.88, we obtained a period of 0.0602(3) d with the PDM method (figure 7). Since this value is consistent with the 2016 one, we adopted an averaged value of 0.0602(1) d as the period of stage A superhumps.

The dynamical precession rate, $\omega_{\rm dyn}$, in the disk can be expressed by (see Hirose & Osaki 1990):

$$\omega_{\rm dyn}/\omega_{\rm orb} = Q(q)\,R(r), \tag{3}$$

where $\omega_{\rm orb}$ and r are the angular orbital frequency and the dimensionless radius measured in units of the binary separation a. The dependencies on q and r are

$$Q(q) = \frac{1}{2}\frac{q}{\sqrt{1+q}}, \tag{4}$$

and[5]

$$R(r) = \frac{1}{2}\sqrt{r}\,b^{(1)}_{3/2}(r), \tag{5}$$

where $\frac{1}{2}b^{(j)}_{s/2}$ is the Laplace coefficient;

$$\frac{1}{2}b^{(j)}_{s/2}(r) = \frac{1}{2\pi}\int_0^{2\pi}\frac{\cos(j\phi)d\phi}{(1+r^2-2r\cos\phi)^{s/2}}. \tag{6}$$

This $\omega_{\rm dyn}/\omega_{\rm orb}$ is equal to the fractional superhump excess in frequency: $\epsilon^* \equiv 1 - P_{\rm orb}/P_{\rm SH}$, where $P_{\rm orb}$ and $P_{\rm SH}$ are the orbital period and superhump period, respectively. If $P_{\rm orb}$ is known, we can directly determine q from the observed ϵ^* of stage A superhumps under the assumption that the period of stage A superhumps reflects the purely dynamical precession rate at the radius of the 3 : 1 resonance (Kato & Osaki 2013).

Since the orbital period of RZ LMi is not known, we cannot directly apply the method in Kato and Osaki (2013) to determine q dynamically. We can instead use the period of post-superoutburst superhumps to constrain q and the disk radius as introduced in Kato et al. (2013b):

$$\epsilon^*({\rm stageA}) = Q(q)\,R(r_{3:1}) \tag{7}$$

and

$$\epsilon^*({\rm post}) = Q(q)\,R(r_{\rm post}), \tag{8}$$

where $r_{3:1}$ is the radius of the 3 : 1 resonance;

$$r_{3:1} = 3^{(-2/3)}(1+q)^{-1/3}, \tag{9}$$

$\epsilon^*({\rm post})$ and $r_{\rm post}$ are the fractional superhump excess and disk radius immediately after the outburst, respectively. By solving equations (7) and (8) simultaneously, we can obtain the relation between $r_{\rm post}$ and q. If we have knowledge about $r_{\rm post}$, as determined in other systems in Kato and Osaki (2013), we have a more stringent constraint.

On 2013 March 20, the object was observed in quiescence closely following a superoutburst which started on

[5] There was a typographical error in the second line of equation (1) in Kato and Osaki (2013). The correct formula is $\frac{q}{\sqrt{1+q}}\left[\frac{1}{4}\sqrt{r}\,b^{(1)}_{3/2}\right]$. The results (including tables) in Kato and Osaki (2013) used the correct formula and the conclusions are unchanged. We used the correct formula in equation (5) in this paper. The same correction of the equation should be applied to Kato et al. (2013b), Nakata et al. (2013), and Kato (2015).

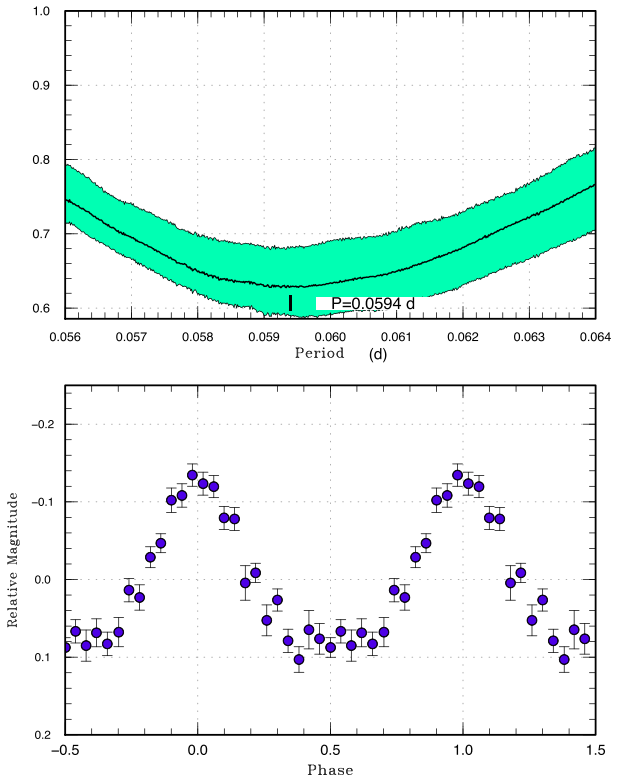

Fig. 8. Post-superoutburst superhumps in RZ LMi (2013 March 20). The data between BJD 2456371.5 and 2456371.9 were used. Upper: PDM analysis. Lower: Phase-averaged profile. (Color online)

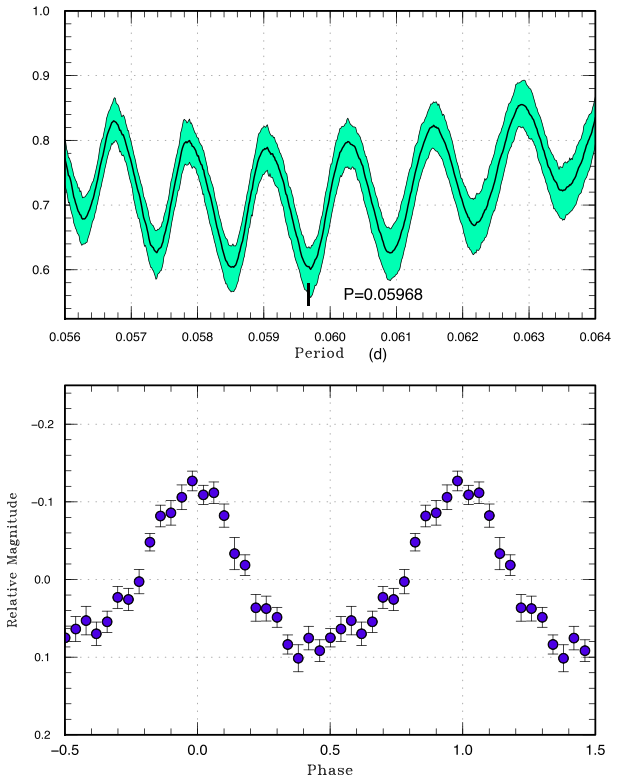

Fig. 9. Post-superoutburst superhumps in RZ LMi (2013 March 20 and 24). Upper: PDM analysis. Lower: Phase-averaged profile. (Color online)

March 6. The object displayed post-superoutburst superhumps and there was a continuous run covering six cycles. A PDM analysis of this continuous run yielded a period of 0.0594(2) d (figure 8). Since this variation was also present after one further normal outburst, and since the decaying amplitudes of this variation exclude the possibility of the orbital variation, we identified this period as that of post-superoutburst superhumps. We combined the quiescent data on March 20 and 24 and obtained a period of 0.05969(2) d (figure 9, assuming that the superhump phase and period did not change during a normal outburst). The shorter one-day alias (∼0.0584 d) is too close to the supposed orbital period (discussed later) and this alias is unlikely.

Using the periods of stage A superhumps and post-superoutburst superhumps, the relation between $r_{\rm post}$ and q is shown in figure 10. The measurements of $r_{\rm post}$ in SU UMa-type DNe using the same method are within the range of 0.30 and 0.38 (Kato & Osaki 2013). The smaller values represent the values for WZ Sge-type DNewith multiple rebrightenings (after such rebrightenings), and it is extremely unlikely to be the case for RZ LMi. If $r_{\rm post}$ is around 0.38, q is estimated to be 0.06(1). It would be noteworthy that Osaki (1995b) assumed $r_{\rm post} = 0.42$ for this particular object. If this is indeed the case, q needs to be as

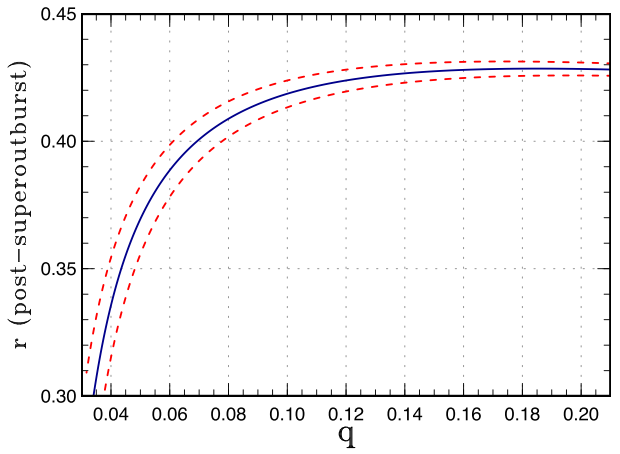

Fig. 10. Relation between q and $r_{\rm post}$ using the periods of stage A superhumps and post-superoutburst superhumps. Dashed curves represent the range of 1σ errors. (Color online)

large as 0.10(2). This consideration suggests that the expectations of Osaki (1995b) and Hellier (2001) that RZ LMi has a very small q and that the large disk radius immediately following a superoutburst are not true at the same time: either q is higher or the disk radius is smaller. This is the important conclusion from the present observation. Since stage A superhumps were not very ideally observed in the present study, further observations are needed to refine the result.

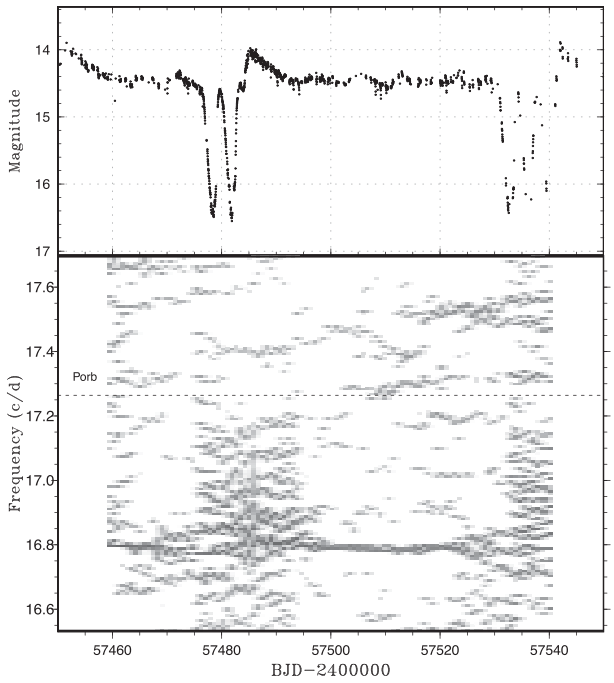

Fig. 11. Two-dimensional Lasso period analysis of RZ LMi (2016). Upper: Light curve. The data were binned to 0.02 d. Lower: Lasso period analysis. The strong persistent signal (disturbed during the starting phase of the superoutburst due to the non-sinusoidal profile and rapidly varying periods) around 16.8 c d^{-1} is superhumps. A weaker signal around 17.50–17.55 c d^{-1} between BJD 2457510 and 2457530 is possible negative superhumps. $\log\lambda = -6.4$ was used. Porb represents the orbital period we suggest. The widths of the sliding window and the time step used are 18 d and 0.8 d, respectively.

3.3 Possible negative superhumps and orbital period

We used the least absolute shrinkage and selection operator (Lasso) method (Tibshirani 1996; Kato & Uemura 2012), which has been proven to yield very sharp signals. We used the two-dimensional Lasso power spectra as introduced in the analysis of the Kepler data in such studies as Kato and Maehara (2013) and Osaki and Kato (2013b). These two-dimensional Lasso power spectra have been proven to be very effective in detecting signals in non-uniformly sampled ground-based data (see e.g., Ohshima et al. 2014) since Lasso-type period analysis is less affected by aliasing than traditional Fourier-type power spectra. This characteristic has enabled detection of negative superhumps in ground-based observations (e.g., Ohshima et al. 2014; Kato et al. 2014b). The result for RZ LMi in 2016 is shown in figure 11. The strong persistent signal around 16.8 cycles per day (c d^{-1}) is superhumps. A weaker signal around 17.50–17.55 c d^{-1} between BJD 2457510 and 2457530 is possible negative superhumps. Since the second superoutburst lasted for a very long time, it may have been possible that negative superhumps were excited during this long-lasting standstill-like phase, which gives a condition that is almost the same as that in permanent superhumpers (see subsection 3.1). A PDM analysis of the data between BJD 2457510 and 2457530 yielded a period of 0.05710(1) d. The superhump period in this interval was 0.059555(4) d.

It has been widely accepted that absolute fractional superhumps excesses (ϵ_+ for positive superhumps, and ϵ_- for negative superhumps, where $\epsilon \equiv P_{\rm SH}/P_{\rm orb} - 1$) are tightly correlated when both signals are simultaneously seen in NL CVs (e.g., Patterson et al. 1997; Montgomery 2009). The empirical relation is $\epsilon_+ \simeq 2|\epsilon_-|$. If it is also the case for RZ LMi, $P_{\rm orb}$ is expected to be around 0.05792 d. This period is labeled as Porb in figure 11. If this is indeed the orbital period, the consequence is important (cf. subsection 3.2). The measured period of stage A superhumps [0.0602(1) d] gives $\epsilon^* = 0.038(2)$, which is equivalent to $q = 0.105(5)$ [see table 1 in Kato and Osaki (2013). This value is higher than the typical ones for WZ Sge-type DNe, which have similar $P_{\rm orb}$ as RZ LMi (Kato & Osaki 2013; Kato 2015; Kato et al. 2016b). This q measurement invalidates the suggestion by Osaki (1995b) and Hellier (2001) that the unusual properties of RZ LMi is a result of the very low q. The q, however, is consistent with the relation derived from the period of stage A and post-superoutburst superhumps (subsection 3.2, figure 10) assuming the large disk radius at the end of a superoutburst. If this interpretation is correct, the disk radius at the end of a superoutburst is large, as required by Osaki (1995b), but the origin of the large disk (i.e., superoutbursts which terminate earlier than in ordinary SU UMa-type DNe) cannot be attributed to an exceptionally small q. In recent years, some SU UMa-type DNe show early termination of superoutbursts (such as V1006 Cyg, Kato et al. 2016a). In Kato et al. (2016a), the termination may be associated with the supposed appearance of stage C superhumps (late-stage superhumps with a shorter constant period). The origin of stage C superhumps is still poorly known, and the reason for the premature termination of superoutbursts, which may be related to the evolution of stage C superhumps, still needs to be clarified.

There is supporting evidence for a large q: the duration of stage A superhumps, which is considered to reflect the growth time of the 3 : 1 resonance, is very short (less than 1 d) in RZ LMi. From a theoretical standpoint, this growth time is expected to be proportional to $1/q^2$ (Lubow 1991), and this relation has been confirmed in WZ Sge-type DNe(Kato 2015). As judged from the rapid growth of superhumps in RZ LMi, it appears extremely unlikely that RZ LMi has as small a q as in WZ Sge-type DNe.

3.4 Evolutionary status

If the q derived from the possible negative superhumps and suggested by the rapid growth of superhumps (subsection 3.3) is correct, RZ LMi cannot be an object

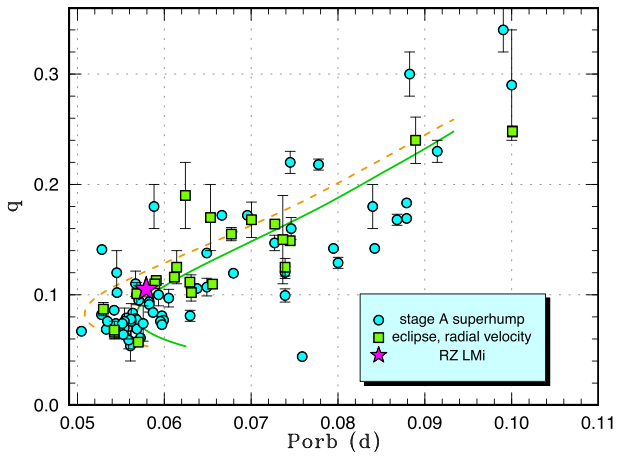

Fig. 12. Location of RZ LMi on the diagram of mass ratio versus orbital period. The dashed and solid curves represent the standard and optimal evolutionary tracks in Knigge, Baraffe, and Patterson (2011), respectively. The filled circles, filled squares, filled stars, and filled diamonds represent q values from a combination of the estimates from stage A superhumps published in six preceding sources (Kato & Osaki 2013; Nakata et al. 2013; Kato et al. 2014a, 2014b, 2015, 2016b), known q values from quiescent eclipses or radial-velocity study (see Kato & Osaki 2013 for the data source). In addition to the references listed in Kato et al. (2016b), we supplied the data for SDSS J143317.78+101123.3 in Hernández Santisteban et al. (2016). (Color online)

close to the period minimum or a period bouncer—Olech et al. (2008) conjectured that some ER UMa-type novae are period bouncers. The q we suggested is similar to or even larger than those of ordinary SU UMa-type DNe having similar $P_{\rm orb}$ (figure 12).

We know of at least one other object, GALEX J194419.33+491257.0 in the Kepler field, which has a very short $P_{\rm orb}$ of 0.0528164(4) d and very frequent outbursts (normal outbursts with intervals of 4–10 d) (Kato & Osaki 2014). This object has an unusually high $q = 0.141(2)$ measured using stage A superhumps. These properties are somewhat similar to those of RZ LMi. Kato and Osaki (2014) suggested the possibility that GALEX J194419.33+491257.0 may be a CV with a stripped core-evolved secondary and which is evolving toward an AM CVn-type CV. Such a condition might be a fascinating possibility to explain why RZ LMi has an exceptionally high $\dot{M}$ for its $P_{\rm orb}$.

3.5 Secular variation of supercycle

As discussed in subsection 3.1, it is likely that RZ LMi changed $\dot{M}$ by a factor of $\sim$2 in the last two decades. In recent years, a transition from the NL (permanent superhumper) state to the ER UMa-type state was discovered in BK Lyn (Patterson et al. 2013; Kato et al. 2013a). Patterson et al. (2013) proposed, based on the potential identification with an ancient classical nova in 101, that ER UMa stars are transitional objects during the cooling phase of post-eruption classical novae [the idea was not new and it was already proposed in Kato and Kunjaya (1995) and Osaki (1995a)]. Following this interpretation, Otulakowska-Hypka and Olech (2013) studied ER UMa-type objects and found a secular increase of the supercycle in most typical ER UMa-type objects. RZ LMi was included, and Otulakowska-Hypka and Olech (2013) gave a $\dot{P}$ of the supercycle of $(5.0 \pm 1.9) \times 10^{-4}$ in 18 yr. We should note that Zemko, Kato, and Shugarov (2013) also studied variation of supercycles in ER UMa and reported that supercycles vary in a range of 43.6–59.2 d with shorter time-scales of 300–1900 d. A secular increase of the supercycle was also statistically meaningful in that work (Zemko et al. 2013).

The conclusion of Otulakowska-Hypka and Olech (2013), however, was only based on the variation of supercycles, and they disregarded the possibility that the supercycle can also increase if $\dot{M}$ increases toward $\dot{M}_{\rm crit}$ since there is a minimum in the supercycle as $\dot{M}$ increases [cf. the right-hand branch of figure 1 in Osaki (1995a); see also subsection 3.1]. As this is apparently the case for RZ LMi, we studied the secular variation of supercycles in RZ LMi. We summarize the result in table 1 [the data in Kato et al. (2013a) also used AAVSO observations]. When raw data were not available, we measured the fraction of superoutburst and duty cycle by eye from the figures in the papers listed in the table. The data for 1986–1989 (Shugarov) were too sparse to determine the supercycle and only the duty cycle was estimated. The data for 1987–1988 (Kato) were visual observations. The supercycle was determined from seven well-defined bright outbursts. The duty cycle was probably underestimated due to the insufficient detection limit of visual observations. For AAVSO observations, the fraction of superoutbursts could be determined only to 0.05 since most of the data were randomly sampled snapshot observations.

It has became apparent that the supercycle was not stable as had been supposed in Robertson, Honeycutt, and Turner (1995) and Olech et al. (2008). The supercycle at the time of Robertson, Honeycutt, and Turner (1995) probably reached the historical minimum. It was likely the supercycle once lengthened to as much as $\sim$24 d before 2013, but it returned to 19–20 d. This behavior probably gave the impression that the supercycle is globally constant if seen in long time-scales, such as several years. The situation changed in 2016 when the supercycle strongly increased. This increase was associated with the increase of the fraction of superoutburst and the duty cycle, indicating that $\dot{M}$ increased despite the lengthening of the supercycle [contrary to the conclusion by Otulakowska-Hypka and Olech (2013)]. Although the situation before 2016 was less clear,

Table 1. Supercycles of RZ LMi.

Year	JD range*	Supercycle (d)	Fraction of superoutburst	Duty cycle†	Nights	Source
1984	45699–45851	19.6(1)	0.4	0.53	30	This work (Shugarov)
1984–1985	46019–46230	19.5–21.5	0.35:	0.39	31	This work (Shugarov)
1986–1989	46468–47682	—	—	0.6	7	This work (Shugarov)
1987–1988	47151–47318	22.5(9)	—	0.39	52	This work (Kato)
1992–1995	48896–49723	18.87	0.4	0.5	—	Robertson, Honeycutt, and Turner (1995)
2004–2005	53027–53519	19.07(4)	0.4	0.4	—	Olech et al. (2008)
2005–2006	53644–53884	19.7(1)	0.45	0.58	89	AAVSO
2006–2007	54041–54254	20.75(4)	0.40	0.55	113	AAVSO
2007–2008	54374–54626	21.3(1)	0.45	0.55	100	AAVSO
2008–2009	54749–54988	21.7(1)	0.40	0.31	96	AAVSO
2009–2010	55146–55334	24.3(1)	0.35	0.52	58	AAVSO
2012	55985–56070	21.61(2)	0.55	0.46	76	Kato et al. (2013a)
2012–2013	56273–56473	22.83(1)	0.50	0.62	149	This work
2013–2014	56563–56819	20.8(1)	0.40	0.48	151	This work (Neustroev), AAVSO
2014–2015	56930–57178	19.9(1)	0.45	0.55	96	AAVSO
2016	57416–57451	35	0.60	0.50	28	This work
2016	57451–57483	32	0.81	0.74	31	This work
2016	57483–57543	60	0.80	0.83	54	This work

*JD−2400000.
†Object brighter than 15.0 mag.

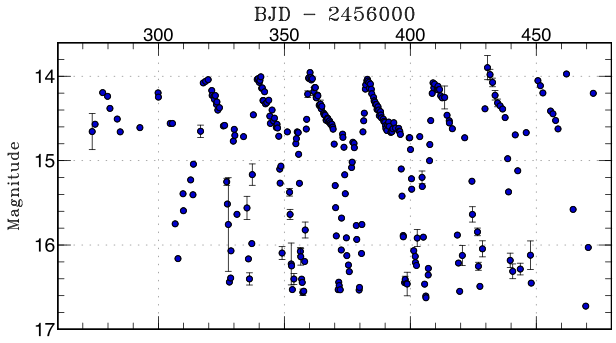

Fig. 13. Overall light-curve of RZ LMi in 2013. The data were binned to 0.03 d. (Color online)

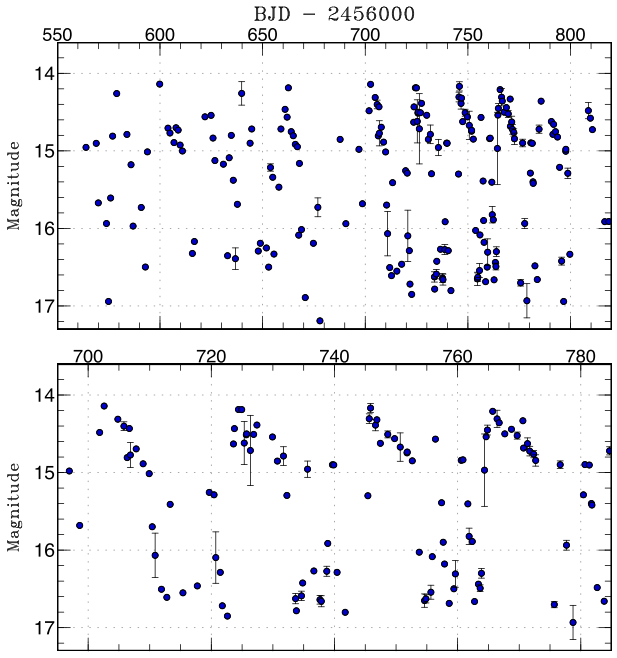

Fig. 14. Overall light-curve of RZ LMi in 2013–2014. The data were binned to 0.03 d. (Color online)

the changing supercycle suggests fluctuating $\dot{M}$ within time scales of a year or two. The outburst pattern was generally regular in the second best-observed season in 2013 (figure 13). The duration of the superoutburst was appreciably longer between BJD 2456380 and 2456400 (17 d, in contrast to 12–13 d in other superoutbursts in 2013; a mean value of supercycles in 2013 is given in table 1). It was likely that $\dot{M}$ temporarily increased also in 2013. In the 2013–2014 season, the durations of superoutbursts again decreased to shorter than 12 d (figure 14) while supercycle lengths remained short (∼21 d).

As far as RZ LMi is concerned, $\dot{M}$ is not secularly decreasing as in the scenario given by Patterson et al. (2013). Among other ER UMa-type objects, BK Lyn returned to its original NL state in late 2013 and the ER UMa-type state was only transiently present (Kato et al. 2013a). As discussed in Kato et al. (2013a), the hypothetical cooling sequence from NL objects → ER UMa-type DNe → ordinary SU UMa-type DNe after nova eruptions as proposed

by Patterson et al. (2013) is not very consistent with observational statistics, since such a cooling sequence would predict a large number of intermediate (having much more slowly cooling white dwarfs) objects between ER UMa-type DNeand ordinary SU UMa-type DNe, while observations could not confirm a large number of such objects. As seen in ER UMa, BK Lyn, and RZ LMi, the $\dot{M}$ variations look more irregular with time-scales of several years and it looks like that the majority of variations in outburst activities in these systems does not reflect the secular $\dot{M}$ variation as proposed by Patterson et al. (2013). As this paper has shown, the high activity of RZ LMi may be a result of a rare evolutionary condition with a relatively massive secondary. In such a case, we may not require a nova eruption to produce an object like RZ LMi.

4 Summary

We observed RZ LMi, which is renowned for the extremely (∼19 d) short supercycle and is a member of a small, unusual class of CV called ER UMa-type DNe, in 2013 and 2016. In 2016, the supercycles of this object substantially lengthened in comparison to the previous measurements to 35, 32, and 60 d for three consecutive superoutbursts. The durations of the superoutbursts also lengthened and they composed 60%–81% of the supercycle. Such long durations of superoutbursts have never been observed in this object, and we consider that the object virtually experienced a transition to the NL state (permanent superhumper). This observed behavior reproduced the prediction of the thermal-tidal instability model made by Osaki (1995a) extremely well. We estimated that in 2016, the mass-transfer rate of RZ LMi reached 97%–99% of the thermal stability limit, and that it was about two times larger than the value in the past.

We detected a precursor in the 2016 superoutburst and detected growing (stage A) superhumps in 2016 and in 2013. We estimated their period to be 0.0602(1) d. This makes the second case in which growing superhumps were confidently recorded in ER UMa-type DNe during the sequence of the precursor and the main superoutburst. We also detected post-superoutburst superhumps immediately after a superoutburst in 2013 with a period of 0.05969(2) d. Since both stage A superhumps and post-superoutburst superhumps can be considered to reflect the dynamical precession rates, we can derive the relation between the mass ratio and the radius of the post-superoutburst. The result suggests that the mass ratio is not as small as in WZ Sge-type DNe, having orbital periods similar to RZ LMi.

By using Lasso two-dimensional power spectra, we detected possible negative superhumps with a period of 0.05710(1) d. By combination with the period of ordinary superhumps, we estimated the orbital period of 0.05792 d. The period of stage A superhumps, combined with this orbital period, suggests a mass ratio of 0.105(5). This relatively large mass ratio is consistent with the rapid growth of superhumps. This mass ratio is even above ordinary SU UMa-type DNe, and it is also possible that the exceptionally high mass-transfer rate in RZ LMi may be a result of a stripped core evolved secondary in a system evolving toward an AM CVn-type object.

An analysis of historical records of supercycles in this system suggests that the variation of the outburst activity is sporadic with time-scales of years and it does not seem to reflect the secular variation caused by evolution.

Acknowledgement

This work was supported by the Grant-in-Aid "Initiative for High-Dimensional Data-Driven Science through Deepening of Sparse Modeling" (25120007) from the Ministry of Education, Culture, Sports, Science and Technology (MEXT) of Japan. CCN thanks the funding from National Science Council of Taiwan under the contract NSC101-2112-M-008-017-MY3. This work also was partially supported by RFBR grant 15-02-06178 (Crimean team, Shugarov and Katysheva) and Grant VEGA No. 2/0002/13 (Shugarov, Chochol, Sekeráš). This study was also supported by the Science Committee of the Science and Education Ministry of Kazakhstan (project No. 0075/GF4). The authors are grateful to observers of VSNET Collaboration and VSOLJ observers who supplied vital data. We acknowledge with thanks the variable star observations from the AAVSO International Database contributed by observers worldwide and used in this research. This research has made use of the SIMBAD database, operated at CDS, Strasbourg, France.

Supporting information

Supplementary data are available at *PASJAP* online.

E-tables 1–11 and e-figures 1–13.

References

Abrahamian, H. V., & Mickaelian, A. M. 1993, Astrofiz., 36, 109
Cleveland, W. S. 1979, J. Am. Statist. Assoc., 74, 829
Fernie, J. D. 1989, PASP, 101, 225
Green, R. F., Ferguson, D. H., Liebert, J., & Schmidt, M. 1982, PASP, 94, 560
Hellier, C. 2001, PASP, 113, 469
Hernández Santisteban, J. V., et al. 2016, Nature, 533, 366
Hirose, M., & Osaki, Y. 1990, PASJ, 42, 135
Iida, M. 1994, VSOLJ Variable Star Bull., 19, 2
Kato, T. 2015, PASJ, 67, 108
Kato, T., et al. 2009, PASJ, 61, S395
Kato, T., et al. 2010, PASJ, 62, 1525
Kato, T., et al. 2013a, PASJ, 65, 23
Kato, T., et al. 2014a, PASJ, 66, 30
Kato, T., et al. 2014b, PASJ, 66, 90

Kato, T., et al. 2015, PASJ, 67, 105
Kato, T., et al. 2016a, PASJ, 68, L4
Kato, T., et al. 2016b, PASJ, 68, 65
Kato, T., & Kunjaya, C. 1995, PASJ, 47, 163
Kato, T., & Maehara, H. 2013, PASJ, 65, 76
Kato, T., Monard, B., Hambsch, F.-J., Kiyota, S., & Maehara, H. 2013b, PASJ, 65, L11
Kato, T., Nogami, D., Baba, H., Masuda, S., Matsumoto, K., & Kunjaya, C. 1999, in Disk Instabilities in Close Binary Systems, ed. S. Mineshige & J. C. Wheeler (Tokyo: Universal Academy Press), 45
Kato, T., & Osaki, Y. 2013, PASJ, 65, 115
Kato, T., & Osaki, Y. 2014, PASJ, 66, L5
Kato, T., & Uemura, M. 2012, PASJ, 64, 122
Kato, T., Uemura, M., Ishioka, R., Nogami, D., Kunjaya, C., Baba, H., & Yamaoka, H. 2004, PASJ, 56, S1
Kholopov, P. N., Samus, N. N., Kazarovets, E. V., & Perova, N. B. 1985, IBVS, 2681
Knigge, C., Baraffe, I., & Patterson, J. 2011, ApJS, 194, 28
Kondo, M., Noguchi, T., & Maehara, H. 1984, Tokyo Astron. Obs. Ann., Sec. Ser., 20, 130
Lipovetskii, V. A., & Stepanyan, J. A. 1981, Astrofiz., 17, 573
Lubow, S. H. 1991, ApJ, 381, 259
Misselt, K. A., & Shafter, A. W. 1995, AJ, 109, 1757
Montgomery, M. M. 2009, ApJ, 705, 603
Nakata, C., et al. 2013, PASJ, 65, 117
Nogami, D., Kato, T., Masuda, S., Hirata, R., Matsumoto, K., Tanabe, K., & Yokoo, T. 1995, PASJ, 47, 897
Ohshima, T., et al. 2014, PASJ, 66, 67
Olech, A., Wisniewski, M., Zloczewski, K., Cook, L. M., Mularczyk, K., & Kedzierski, P. 2008, Acta Astron., 58, 131
Osaki, Y. 1989, PASJ, 41, 1005
Osaki, Y. 1995a, PASJ, 47, L11
Osaki, Y. 1995b, PASJ, 47, L25
Osaki, Y. 1995c, in Cataclysmic Variables, ed. A. Bianchini et al. (Dordrecht: Kluwer Academic Publishers), 307
Osaki, Y., & Kato, T. 2013a, PASJ, 65, 50
Osaki, Y., & Kato, T. 2013b, PASJ, 65, 95
Otulakowska-Hypka, M., & Olech, A. 2013, MNRAS, 433, 1338
Patterson, J. 1999, in Disk Instabilities in Close Binary Systems, ed. S. Mineshige & J. C. Wheeler (Tokyo: Universal Academy Press), 61
Patterson, J., Kemp, J., Saad, J., Skillman, D. R., Harvey, D., Fried, R., Thorstensen, J. R., & Ashley, R. 1997, PASP, 109, 468
Patterson, J., et al. 2013, MNRAS, 434, 1902
Pikalova, O. D., & Shugarov, S. Yu. 1995, in Cataclysmic Variables, ed. A. Bianchini et al. (Dordrecht: Kluwer Academic Publishers), 173
Robertson, J. W., Honeycutt, R. K., & Turner, G. W. 1994, in ASP Conf. Ser. 56, Interacting Binary Stars, ed. A. W. Shafter (San Francisco: ASP), 298
Robertson, J. W., Honeycutt, R. K., & Turner, G. W. 1995, PASP, 107, 443
Skillman, D. R., & Patterson, J. 1993, ApJ, 417, 298
Stellingwerf, R. F. 1978, ApJ, 224, 953
Tibshirani, R. 1996, J. R. Stat. Soc. Ser. B, 58, 267
Warner, B. 1995, Cataclysmic Variable Stars (Cambridge: Cambridge University Press)
Zemko, P., Kato, T., & Shugarov, S. 2013, PASJ, 65, 54

第 34 卷 增刊
2016 年 9 月

天 文 学 进 展
PROGRESS IN ASTRONOMY

Vol. 34, Sup.
Sept., 2016

doi: 10.3969/j.issn.1000-8349.2016.z1.02

鹿林天文台介绍

林宏钦，张明新，张光祥，张永欣，林启生，萧翔耀

(台湾“中央大学” 天文研究所，桃园 32001)

摘要： 台湾“中央大学”天文研究所鹿林天文台位于台湾中部玉山公园塔塔加地区的鹿林前山，海拔 2 862 m，目前有 7 台望远镜 (包括 1 m 望远镜)，是台湾最重要的光学天文基地。现正在筹建台湾最大的 2 m 望远镜。介绍了鹿林天文台的发展、现况与未来规划。

关 键 词： 天文台址；天文台；光学望远镜

中图分类号： P112 **文献标识码：** A

1 引 言

台湾“中央大学”天文研究所成立于 1992 年，为台湾最早的天文研究与教学单位，为学子提供接触宇宙科学的窗口，使其了解宇宙天体能量的本质、运行规律，以及演化的过程，藉以建立科学的宇宙观。并藉由观察宇宙的过程，了解自然并关怀自然。本所发展策略除了理论研究外，以光学与红外天文为主，利用鹿林天文台及国外大型望远镜进行课题研究，并参与多项国际合作研究计划，让卓越研究与教育并重为本所最大特色。在台湾教育和科技主管部门支持下，以“中央大学”天文研究所为首的数个大学单位，共同合作将鹿林天文台协办成可供台湾天文学术机构合用的天文研究设施与观测中心。

台湾“中央大学”在苗栗复校时期 (1958—1965) 就设有天文台，1977 年“中央大学”物理系成立物理与天文研究所。1981 年在旅美华人天文学家吕克华的协助下，于科学一馆顶楼设置了“中大”天文台，使用美国博精仪器公司 (Perkin-Elmer) 制造的 60 cm 盖赛格林 (Cassegrain) 反射式望远镜，该望远镜在启用后将近 20 年的时间是台湾最大的望远镜，肩负教育及研究的使命。“中大”天文台为台湾第一座具有天文研究用大型望远镜的天文台，以现代观测工具及技术研究天文现象。2013 年在李国鼎科技发展基金会的支持下，“中大”天文台进行全面整修，现作为开放参观及教学用途[1]。

由于中坜市区急遽发展，“中大”校内建筑大幅增加，光害污染日趋严重，“中大”天文台已不适合从事天文观测研究，必须另觅理想的观测地点。1990 年在台湾“国科会”支持

通讯作者： 林宏钦，hclin@astro.ncu.edu.tw

下，蔡文祥教授开始进行台湾天文台选址计划，于鹿林前山设置一个临时观测站进行选址研究及天文教学。历经 3 年的视宁度 (seeing)、气候、夜天光背景等条件调查后，确定玉山公园的鹿林前山为优良的天文台址。1997 年获得台湾“太空计划室”资助，兴建鹿林第一座天文台 SLT，1999 年完工，安装自行设计制造的 76 cm 超轻型望远镜 (SLT76)；2000 年开始进行观测，是鹿林天文台初期最重要的观测设备。在建造、调试与观测过程中，培养了许多使用与维护望远镜的人才，对日后鹿林天文台的运作提供了重要基础[2]。在台湾教育主管部门追求学术卓越发展计划的挹注下，2002 年建置台湾首座米级口径的鹿林 1 m 望远镜 (LOT)，同年冬季开始观测。目前正致力 2 m 望远镜建设。鹿林天文台鸟瞰图见图 1。

图 1 鹿林天文台鸟瞰图

2 鹿林天文台

鹿林天文台坐落于台湾中部玉山公园塔塔加地区的鹿林前山，海拔 2 862 m，地理位置为东经 120°52′25″ E，北纬 23°28′07″ N，是台湾最重要的光学天文基地。此台址较不受冬季东北季风或夏季西南气流和台风的影响；加上位处高山，空气污染和尘埃很少，大气透明度高，几乎没有光害，天光背景暗；由于海拔高，大气稀薄，消光较小，大气宁静度较好。多年的观测结果表明，该站的视宁度平均值约为 1.39″[2]，天光背景值为：$U = (21.78 \pm 0.30)$ mag/arcsec^2, $B = (22.01 \pm 0.08)$ mag/arcsec^2, $V = (21.28 \pm 0.06)$ mag/arcsec^2, $R = (20.91 \pm 0.05)$ mag/arcsec^2, $I = (19.40 \pm 0.06)$ mag/arcsec^2[3]，每年平均可观测 1 450 h (图 2)，约 180 夜 (以每晚 8 h 计)，较好的观测季节是每年的秋季与冬季 (见图 3)。

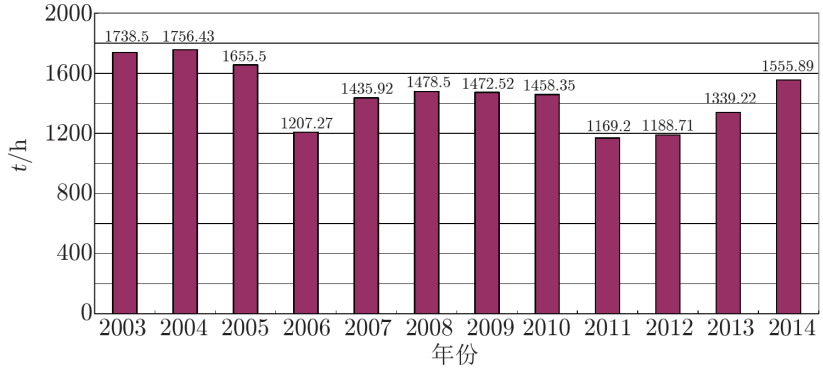

图 2　鹿林天文台年观测时数统计图 (2003—2014)

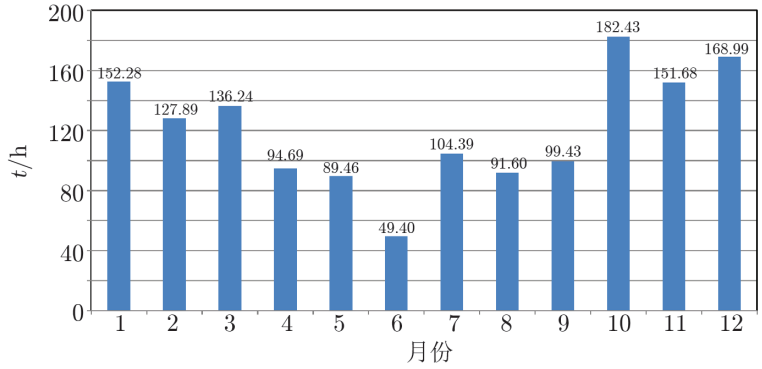

图 3　鹿林天文台月平均观测时数统计图 (2003—2014)

目前基地内有 1 m 望远镜 (LOT) 、TAOS 计划的 4 座 0.5 m 自动望远镜、 0.4 m 望远镜 (SLT40)、0.35 m 望远镜 (L35)，共 7 台光学望远镜。此外还有“成功大学”的红色精灵地面观测与极低频无线电波侦测系统 (ELF)、“中央大学”太空所的气晖全天相机、地科系土石流侦测预警系统及“环保署”鹿林山空气品质背景站 (LABS) 等地科、大气、太空相关的研究设施。

鹿林天文台主要策略是应用小型望远镜和台湾观测条件优势。因为小型望远镜的运作及时间分配，比中大型望远镜更具弹性；而台湾纬度较低，地理经度上与世界各主要天文台互补，因此可以观测较大的南天区，并针对瞬变的天文现象 (如超新星及伽玛射线暴)，与各大天文台合作协力观测，在全球天文观测网和太空与地面的联合观测中占据不可缺少的位置。例如 2006 年“中大”天文研究所参加夏威夷大学主导的泛星计划 (Pan-STARRS: the Panoramic Survey Telescope And Rapid Response System)。因为地理位置的关系，鹿林天文台是世界上能最早追踪泛星计划中各种瞬变现象的天文台。在台湾近百年的天文发展史上，鹿林天文台缔造了多项纪录：首度发现小行星、首度发现超新星、首度发现彗星、首度发现近地小行星及首度进行小行星命名。

2.1 鹿林 1 m 望远镜 (LOT)

鹿林 1 m 望远镜 (LOT) 是目前台湾口径最大的通用型光学望远镜 (见图 4)，为盖赛格林反射式光学系统，具备良好的光学成像、指向精度和追踪精度，配备有 CCD 相机、低分辨率光谱仪以及三色偏振成像仪 (TRIPOL2: Tri-range Imager and Polarimeter 2)。鹿林 1 m 望远镜以多波段成像及测光为观测手段，开展各项科学主题的研究。同时积极参与国际天文联测计划，如全球望远镜联合观测 (WET: The Whole Earth Telescope)、全球蝎虎 BL 类星体联合观测 (WEBT: The Whole Earth Blazar Telescope)、年轻系外行星掩星计划 YETI (Young Exoplanet Transit Initiative) 等。

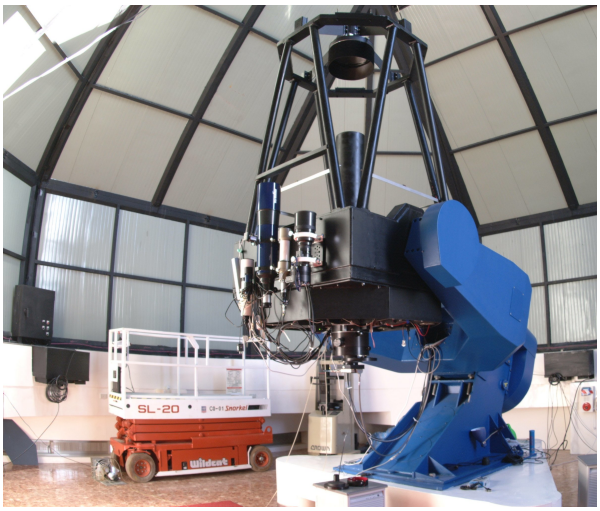

图 4 鹿林 1 m 望远镜 (LOT)

2003 年鹿林 1 m 望远镜加入伽玛射线暴 (gamma ray bursts, GRB) 光学余晖观测行列，并与东亚的一些天文台合作成立东亚伽玛射线暴观测网 (EAFON: East-Asia GRB Follow-up Observation Network)，3 年内成功观测 15 个光学余晖。2004—2007 年台湾超新星巡天计划 (Taiwan Supernovae Survey) 利用 LOT 进行超新星巡天工作，共发现了 15 颗超新星。每年通常约有十几个研究计划在 LOT 上进行，10 年来发表了近百篇研究论文 (见图 5)。在研究之外也支持各大学天文观测教学实习。

2.2 TAOS 计划

TAOS (The Taiwanese-American Occultation Survey) 计划由台湾“中央研究院”天文及天文物理研究所、“中央大学”天文研究所、美国哈佛史密松天文物理中心与韩国延世大学共同合作，目的在侦测包含柯伊伯带以及更远处的直径约 1 km 的小型天体。本计划藉由四部 0.5 m 自动望远镜，每晚监测数千颗恒星来搜寻位于柯伊伯带的太阳系天体对远方背景恒星造成的掩星现象。2005 年开始运转，6 年的观测结果显示，太阳系外围天体的数量比某些理论估计的数量少；对太阳系中直径大于 500 m 的柯伊伯带天体数量设下了严格的上限[4]。目前 TAOS 计划已暂告一段落，下一代的 TAOS II 计划 (Transneptunian Automated

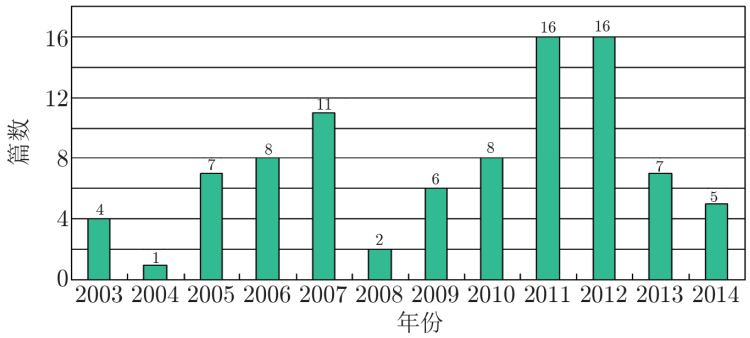

图 5 鹿林天文台 SCI 论文数统计

Occultation Survey) 将落脚墨西哥 Baja California 的 OAN 天文台[5]。

2.3 SLT40 望远镜

由于自制的 76 cm 望远镜 (SLT76) 存在许多难解问题。2005 年将 SLT76 望远镜拆除后在既有的圆顶内安装了一架 40 cm 望远镜，2006 年开始进行鹿林巡天计划 (LUSS) 搜寻太阳系小天体，3 年期间共发现 800 多颗小行星。其中有 300 多颗已获得永久编号，小行星发现数排名世界前 50。鹿林天文台发现的小行星目前已有 80 多颗得到永久命名，小行星名遍布全台湾，涵盖台湾的人物、团体、地理、山水及少数民族。2007 年 LUSS 首度发现彗星 (C/2007 N3) 与近地小行星 (2007 NL1)，该彗星后来命名为“鹿林彗星”(Comet Lulin)。LUSS 计划结束后，2010 年起 SLT40 专注于变星、彗星的长期监测工作[6]。

3 未来规划

当前“中大”天文研究所正致力于台湾最大的 2 m 望远镜建设，2 m 望远镜计划为“中央大学”“发展国际一流大学及顶尖研究中心计划”分项计划之一，由台湾教育主管部门补助。2 m 望远镜集光能力为 1 m 望远镜的 4 倍，预计配备四色同步成像仪，观测效率可比 LOT 提高一个数量级，另将配置近红外相机。鹿林 2 m 望远镜的建置，可望提升台湾本土的光学观测能力、拓展国际合作网络、促进天文仪器软硬件开发以及专业天文人才的养成[7]。

参考文献：

[1] http://www.astro.ncu.edu.tw/, 2016
[2] 蔡文祥. 物理双月刊, 1998, 20(4): 486
[3] Kinoshita D, Chen C W, Lin H C, et al. Chinese Journal of Astronomy and Astrophysics, 2005, 5(3): 315
[4] http://taos.asiaa.sinica.edu.tw/tw/index.php, 2016
[5] http://taos2.asiaa.sinica.edu.tw/tw/index.php, 2016
[6] http://nrch.culture.tw/twpedia.aspx?id=1161, 2016

[7] 黄崇源. 物理双月刊, 2009, 31(3): 252

An Introduction of the Lulin Observatory

LIN Hung-chin, CHANG Ming-hsin, CHANG Kuang-shiang,
CHANG Yung-hsin, LIN Chi-sheng, HSIAO Hsiang-yao

(Graduate Institute of Astronomy, "Central University", Taoyuan 320011)

Abstract: Graduate Institute of Astronomy, "Central University" (IANCU) is the first astronomy graduate program in Taiwan. The institute operates the Lulin Observatory, hosting a 1-m, a 0.4-m, a 0.35-m and a TAOS array of four 0.5-m telescopes. These facilities serve the faculty and students for education and basic research uses. Established in 1999, Lulin Observatory is the unique observatory in Taiwan dedicated to research and advanced education in astronomy. With an elevation of 2 862 m above sea level, Lulin observatory is located at the geometric center of the island. A 2-m telescope is being planned at Lulin.

Key words: astronomical site; observatory; telescope

工作報告

鹿林天文台觀測時數統計(2003-2016)

林宏欽、蕭翔耀、林啟生

鹿林天文台自 2002 年 9 月開始人員常駐，2003 年鹿林一米望遠鏡(LOT)上線，開始有正式觀測時數紀錄，可供瞭解鹿林長期的天氣狀況。依 2003-2016 共 14 年的統計結果，鹿林天文台年平均觀測時數為 1437 小時。一年可分為四個觀測季，

- 最佳觀測季：10-12 月。
- 次佳觀測季：1-3 月。
- 最差觀測季：4-6 月。4 月開始進入雨季，5-6 月受梅雨影響，天氣最差。
- 次差觀測季：7-9 月。主要受颱風及西南氣流影響，天氣變化大。此外夏季晝長夜短，每晚可觀測時間比冬季為短。

詳細統計資料及統計圖如下，

表 1 每月觀測時數統計 (2003-2016)

Month	2003	2004	2005	2006	2007	2008	2009	2010	2011	2012	2013	2014	2015	2016	Average
1	78.75	125	163.25	129	127.32	179	234.52	206.9	90.8	113.42	153.58	269.62	188.55	75.4	155.93
2	142.5	145.98	94.75	149	128.55	118.25	165.7	100.6	123.8	64.88	183.63	109.8	131.65	60.25	127.29
3	147.5	163	143	126.05	116.4	138.5	146.75	181.3	75.9	168.23	134.26	78.7	111.1	72.8	134.97
4	126.5	110.5	144.75	86.8	53.75	85.25	71.8	75.8	151.45	32.75	55.83	135.95	124	82.9	94.26
5	129.75	106.25	136.25	59.5	106.6	98.25	167.4	86.05	56.6	74.3	41.02	32.4	64.2	86.05	91.20
6	24	133	45	39.3	54	37	81.75	26.5	61.5	35.15	80.14	33.7	146.9	114.05	54.25
7	222.5	48	167.75	91.57	128.88	88.4	76.6	99.85	81.75	106.4	88.05	114.65	87.45	123.95	109.53
8	137.75	142	76	111.65	56.6	118.95	6.8	98.3	97.9	35.7	72.2	110.9	45.1	61	88.73
9	142	116	129.25	60.05	69.55	59.8	0	109.95	90.1	117.35	107.84	134.39	93.25	42.85	94.69
10	149.25	219.75	210.25	150.6	172.63	191.38	175.6	139.8	136.95	214.51	200.57	232.33	145.4	142.2	182.80
11	166.5	214.5	216.25	71.75	160.55	152.55	175.8	163.65	87.2	93.81	136.1	166.15	197.05	171.85	150.40
12	271.5	232.45	129	132	261.09	211.17	169.8	169.65	115.25	132.21	86	137.3	161.2	193.27	170.62
Total	1738.5	1756.43	1655.5	1207.27	1435.92	1478.5	1472.52	1458.35	1169.2	1188.71	1339.22	1555.89	1495.85	1226.57	1437.73

* 2009 年因受莫拉克颱風八八風災影響，自八月八日起至十月初約 2 個月期間道路中斷並停電，無法觀測。所以 2009 年之八、九月觀測時數很少，甚至為 0。
**Average 值為扣除最高及最低值後取平均。

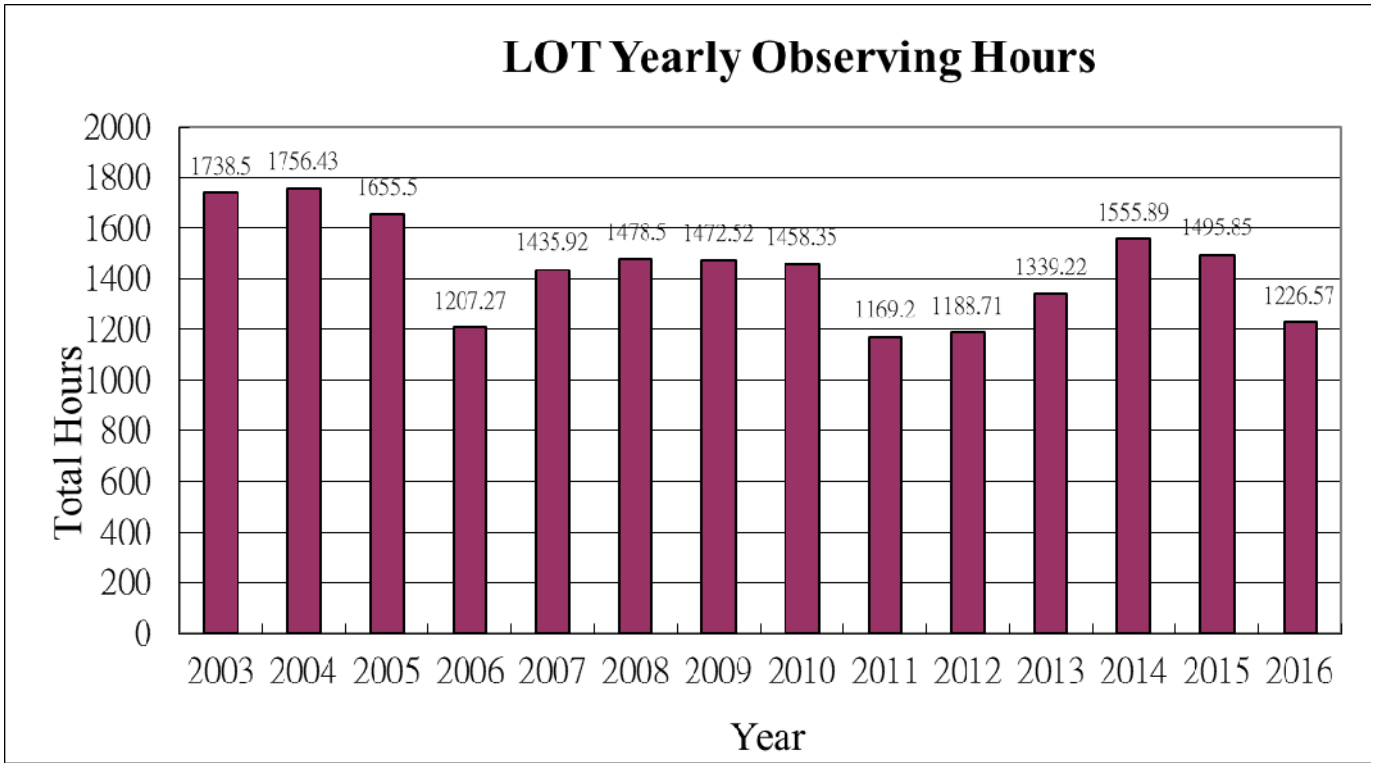

圖 1　鹿林天文台年平均觀測時數統計圖(2003-2016)

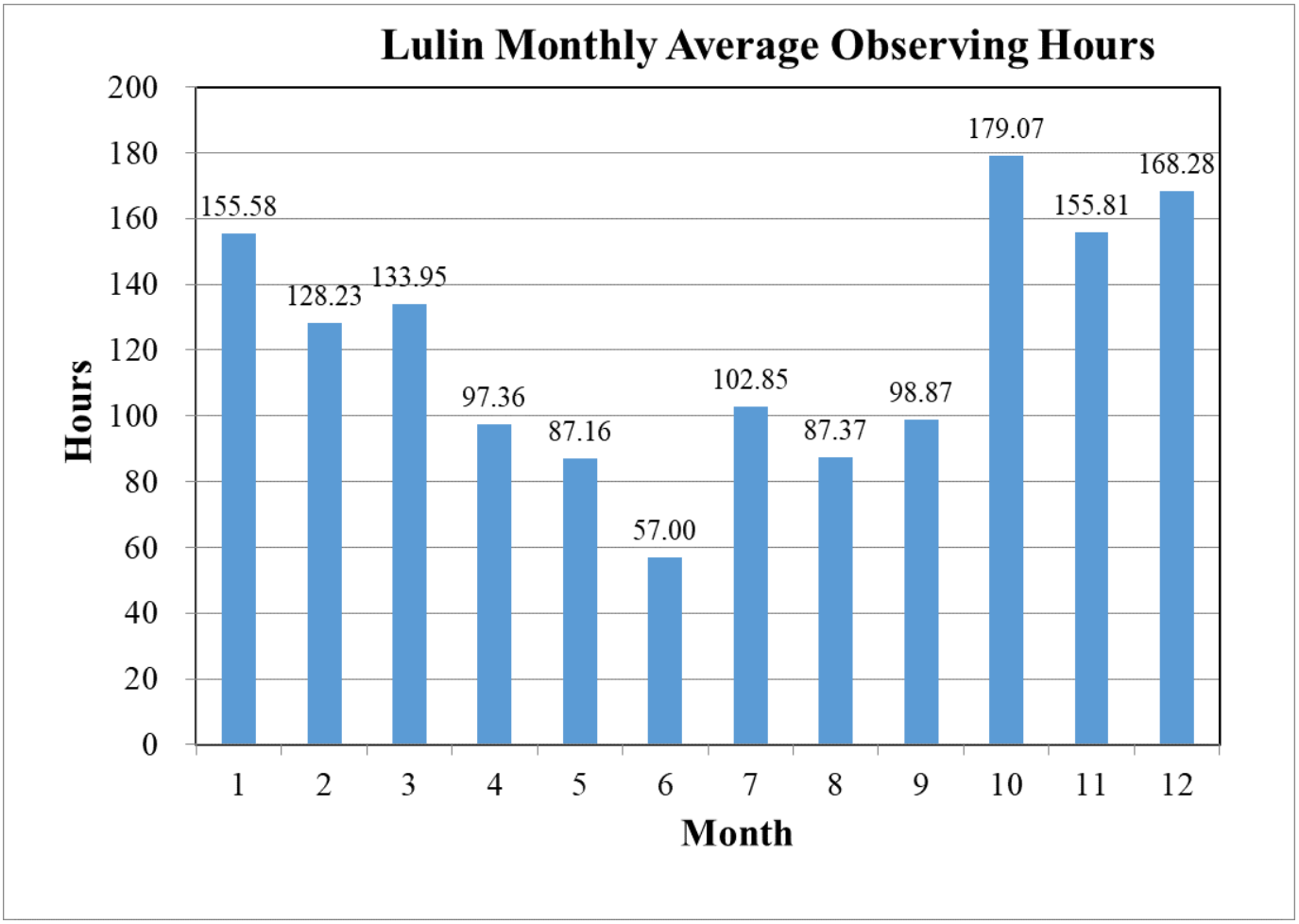

圖 2　鹿林天文台月平均觀測時數統計圖 (2003-2016)

鹿林天文台團體參觀教學2016

時間	單位	參觀人數
20160101	中大校友	2
20160102	福建天文學會秘書長	2
20160201	台南一中天文社	80
20160203	北一女中地科社	60
20160228	中原大學天文社	38
20160305	中山醫學大學天文社	18
20160320-21	NHK 攝影	4
20160409	復興實中	12
20160418	中央大學社區聯誼會	35
20160514	東海大學天文社	38
20160522	南瀛科學教育館志工	30
20160609-10	新竹中學教學觀測	9
20160610	台北天文館志工隊+銘傳大學天文社	23
20160616	清大教學觀測	16
20160628-29	中大天文營	18
20160704	SMILE 親子共學團	29
20160719	成大教學觀測	13
20160722	金門金城國中	3
20160727	新竹市南隘國小	16
20160729	高雄女中天文社	9
20160730	旺宏基金會	62
20160731	張光祥與成大蘇漢宗	24
20160805	中大電機系	12
20160806	清大物理 93 級校友會	41
20160813	鳳山高中天文社	30
20160814	群創光電	21
20160821	環保署署長	40
20160924	詹資能+群創光電	22
20161002	上海市上南中學(台北市文教協會)	20
20161105	群創光電	49
20161105	警察小隊	17
20161126	中山醫大天文社	10
20161219	澳門天文學會	4

TITLE: GCN CIRCULAR
NUMBER: 19575
SUBJECT: GRB 160624A: Lulin observation
DATE: 16/06/25 15:01:46 GMT
FROM: Albert Kong at NTHU <akhkong@gmail.com>

A.K.H. Kong (NTHU), M.Y. Lee, Y.-M. Lin (TFGHS), X. Hou (NTHU/YAO),
C.Y. Liu (NTHU)

We observed the field of GRB 160624A (D'Ai et al. GCN #19560) with the 1m telescope at the Lulin Observatory in Taiwan. We obtained a 600-s image with the SDSS r-band filter on 2016 June 24, 17:32 UT (~ 6 hours after the burst). Apart from the possible host galaxy that is also seen in SDSS (Cucchiara et al. GCN #19565), no new point source was detected at the enhanced XRT position (Beardmore et al. GCN #19566) with r > 22.2 mag.

利用顏色—星等圖中的造父變星位置尋找未發現的造父變星

—使用 SLT 資料

饒博士兆聰、駱世昌

摘要

造父變星是一種非常明亮的變星，其變光的光度和脈動週期有著非常強的直接關聯性，是建立銀河和河外星系距離標尺的可靠且重要的標準燭光。目前有至少一千個以上的星團在宇宙中，但已知在疏散星團中的造父變星大約只有三十顆，我們的目標是利用顏色—星等圖中的造父變星位置尋找未發現的造父變星。我們首先利用已知大約三十顆造父變星的 2 微米全天巡天(2MASS)中疏散星團資料來界定造父變星在顏色—星等圖中的位置，再分析 2MASS 中有可能存在造父變星的疏散星團。

關鍵字：造父變星、疏散星團、顏色—星等圖

介紹

根據恆星形成與演化的初始質量[分布]函數，我們預期在疏散星團的成員星有低質量也有高質量恆星生成，其中高質量恆星在演化會經歷不穩定階段而變成造父變星，但實際上在疏散星團中所發現的造父變星相當的稀少。

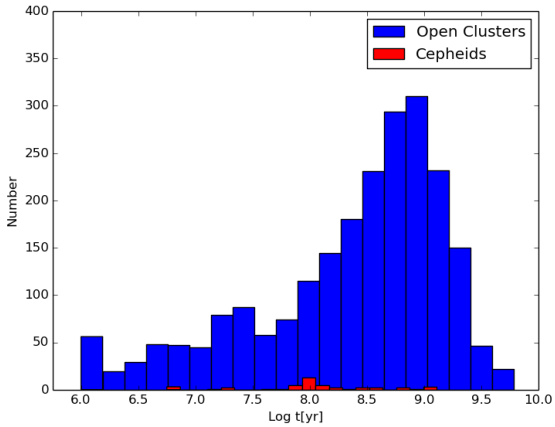

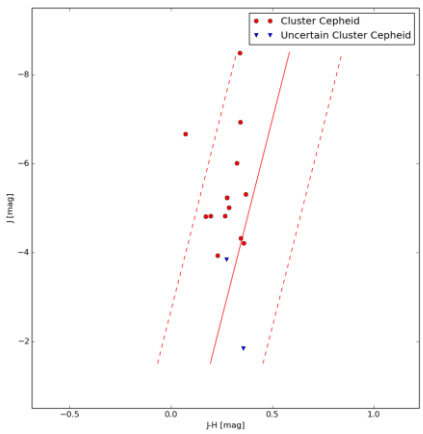

方法

利用 Chen 在 2014 年所發表的不穩定帶方程式代入已知在疏散星團的造父變星，界定已知造父變星在顏色—星等圖上確定的位置。左圖為十五顆已知為造父變星所畫出的顏色—星等圖。

將可能形成造父變星年齡為 $10^{7.8}$ 至 $10^{8.2}$ 年的疏散星團挑選出，使用 2MASS 中疏散星團資料畫出顏色—星等圖，其落於不穩定帶方程式範圍中的恆星即可能是造父變星。右圖為 Berkeley 60 的顏色—星等圖，其中有四顆恆星落於不穩定帶方程式範圍中。

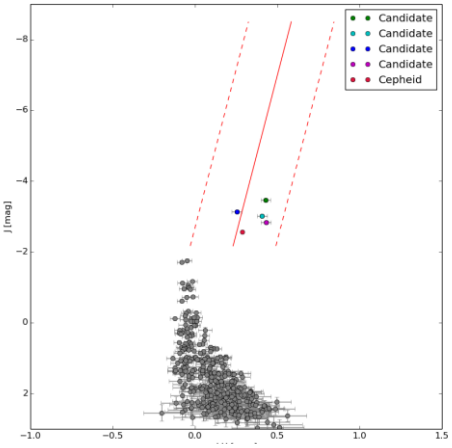

由國立中央大學天文所鹿林天文台 SLT 所拍攝的資料利用較差測光的方法分析其光變量。右圖為 Berkeley 60 的較差測光圖，四顆恆星均有光變量差，赤紅色的點為已知造父變星。

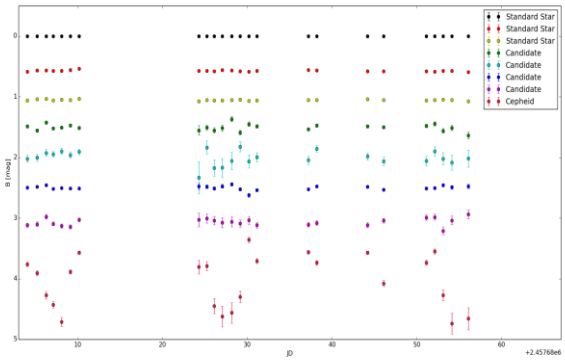

結果

我們分析了 Berkeley 60 中已知的造父變星，測得由國立中央大學天文所鹿林天文台 SLT 所拍攝的資料週期非常符合實際的週期（大約 6.7988 天），再分析 Berkeley 60 最有可能為造父變星的恆星，測得其週期約為 1.7393 天。左下角為 Berkeley 60 中已知的造父變星，右下角為 Berkeley 60 最有可能為造父變星的恆星。

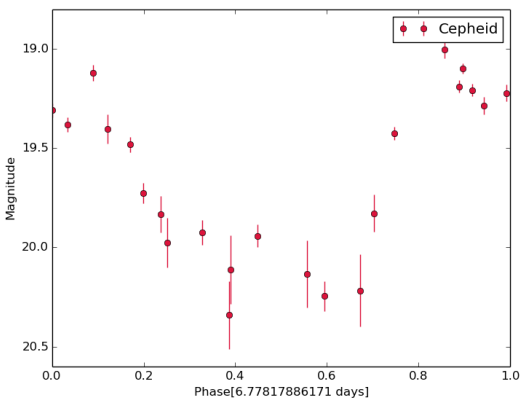

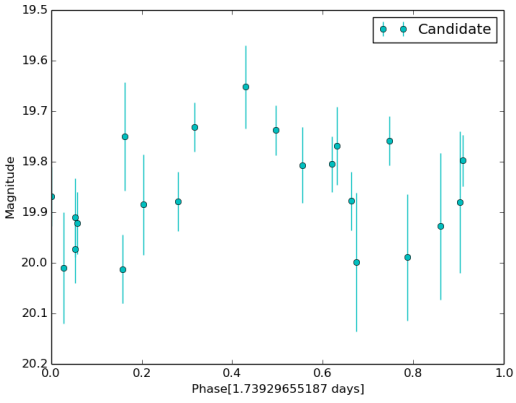

「宇宙學與粒子天文物理學」追求學術卓越發展計畫

黃偉彥
台大物理系

教育部追求學術卓越發展計畫，已於 2000 年一月一日開始執行；「宇宙學與粒子天文物理學」（Cosmology and Particle Astrophysics，以下簡稱 CosPA），以其主題明確，能充分掌握該領域國際現況而尋找學術發展之最佳切入點，而能幸運地獲致審查者之青睞，而得以在 26 件自然科學領域優秀計畫中脫穎而出，獲得全數通過之支助。

類似學術卓越計畫之推動，鄰近之中國大陸（以九七三計畫等方式）、南韓等，近年來皆不遺餘力，不惜巨資，以求取突破發展，國內為因應未來十年或二、三十年之可能激烈競爭，也無法踟躕不前。顯然已通過之計畫，受到 921 震災影響，幅度仍然太小，能否因應外來之挑戰，個人仍然覺得很不樂觀，但這次追求學術卓越發展計畫總算跨出了歷史性的第一步。

「宇宙學與粒子天文物理學」卓越發展計畫之通過，對我們這一群主持人、共同主持人而言，固然一則以喜，其實因期待而衍生之壓力其實更大，但也祇能戒慎恐懼，希望在國內物理界之支持下，可以在四年後交出一份差強人意之成績單。

以下謹將該計畫之內容，依總計畫及五項分項計畫之順序，向各位讀者依序摘錄，除了讓物理界同仁，包括年青後進，可以有大致之了解，日後可以提出建言，甚至參與我們努力之行列；當然也有拋磚引玉之意，讓物理界之一些先進，可以提出更突破性之追求學術卓越發展計畫。

宇宙學與粒子天文物理學（總計畫）

最近十年以來，天文與天文物理在台灣有了長足之進展。本計畫以台灣應該可以作出決定性貢獻之領域「宇宙學與粒子天文物理學」為主要研究大方向，希望藉以將天文與天文物理在大學之研究與教學提昇至國際一流水準。

在天文物理中許多領域裡，由於高科技帶來之觀測技術，其結果又衝擊前沿知識之快速進展，宇宙學成了近年最活躍之研究領域之一；最近的例子是 1998 年年底完成初步分析之超新星宇宙學計畫（Supernova Cosmology Project, Perlmutter, S. et al. Astro-ph/9812133），證明宇宙之膨脹速率其實仍在增加中，也可能表示另一種叫 Quintessence 之物質之存在[Steinhardt et al. Phys. Rev. Lett. 82, 896 (1999)]。

台大物理系(與電機系)目前在粒子物理，天文物理，及微波工程技術等方面之實力與專長，加上中研院 receivers 實驗室已經建立，正好提供了足夠之能力可以在實驗與理論宇宙學於最近未來作出意想不到之決定性貢獻。我們的計畫係建造一個極其特殊之宇宙背景輻射陣列望遠鏡(分項計畫一)，用以觀測宇宙背景輻射之 Sunyaev-Zel'dovich 效應；完成 CP 不守恆之實驗研究，及直接偵測冷黑暗物質之可行性研究(分項計畫二)；與以上兩方面實驗息息相關之理論宇宙學與粒子天文物理研究(分

項計畫三)；藉著這些全面性之推動，台大物理系應可吸引此一領域特別傑出之年青學者加入行列，也積極訓練資質優秀之學生，藉以建構一個卓越而活躍之天文物理研究群。

台大物理系集中在宇宙學與粒子天文物理學之積極研究，也將刺激台灣其他大學之進一步發展。這種刺激可以分為兩個方向，其一係初步由台大、中大、清大及中研院共同組成之台灣各大學天文聯盟(TUCA)，以 TUCA 之名義與國外光學及紅外線天文望遠鏡尋求進一步之合作，取得所需觀測時間，與前述 AMIBA 分項計畫可以達到相輔相成，健全發展台灣天文之正面效果(分項計畫四)；另一個方向，則是將中大在鹿林前山之計畫提昇為全國各大學共用之設施，也與各參與單位快速網路連線，甚至建構遠傳視訊之高科技研究與教學的大環境(分項計畫五)，在訓練學生與年青天文學者上可以跨出一大步。

在每一分項計畫裡，我們希望藉著微波工程、偵測器、冷凍術、高精準控制、高速計算、資訊管理、影像處理、光電等(當代及下一代)天文觀測所需高科技之研發，訓練出下一個階段高科技之年青人力，讓天文與天文物理研究，在台灣可以繼續更上層樓，維持永續之健全發展。

本計畫係基礎於既有之科學卓越以及已被充分證實之發展途徑，我們相信藉著本計畫將可以把大學裡天文與天文物理相關研究與教學提昇至國際上真正一流之境界。

分項計畫一：宇宙背景輻射陣列望遠鏡之建造與操作，及數據擷取與分析

自從 1990 年初起，COBE 衛星的觀測結果將宇宙學推進一個嶄新的境界，不同的理論模型得以用最先進的科技來檢驗。由於最近幾年台灣科學界及工程技術界的全面進展，也讓台灣能適時進入宇宙學這個蓬勃發展的領域。台大物理系結合台大電機系及中研院天文所因此提出了一個別具匠心的實驗計畫，AMIBA。此實驗為特別設計專以微波背景輻射為光源的毫米波干涉儀實驗，大大不同於現有的電波干涉望遠鏡實驗，也因此已經得到國際學界的注意。

AMIBA 實驗的科學目標為：(1) 決定哈伯常數，宇宙物質密度，並設宇宙常數的上下限；(2) 瞭解宇宙在紅位移 $100 < Z < 5$ 空窗期的演化；(3) 檢驗宇宙缺陷的存在與否；(4) 設暴漲宇宙期的能量下限。

AMIBA 實驗為毫米波干涉陣列，由 19 個一米大小的接收碟所構成，操作頻率為 90GHz，頻寬 15GHz，並座在 8 米的旋轉平台上。AMIBA 將置於夏威夷的莫納基山上，但設計為可移動式。此干涉實驗的電波放大器(HEMT)為台大電機系負責，硬體機械裝置由中研院航發研究所負責，控制及資料分析軟體由台大物理系負責，而訊號相關器由中研院天文所負責。澳洲的國家天文台也被邀請加入 AMIBA 的製造及技術研發。

此計畫的施工期預計為三年，第四年將正式開始觀測。

分項計畫二：「早期宇宙、黑暗物質、宇宙膨脹」之實驗粒子物理相關研究

本計畫在未來四年中從事下列三個相關方向之研究

1. BELLE 矽頂點偵測器（SVD 2）升級。這與 CP

破壞研究非常相關。

2. JLC 束管量能器（BPC）研發。這在 SUSY 粒子偵測上十分重要。
3. 以晶體偵測器搜尋『冷暗物質』（CDM）之可行性研究。

這三個工作在時間上形成一個很好的組合。SVD 的工作，預期兩年達成，工作內容為 SVD1.1 系統測試，SVD 2 之抗輻射性、可彎印刷電路板製作、頂點測定軟體、再發器以及 EFC 前之矽軌跡平面。這些工作在後兩年自然延伸到 JLC BPC 之研發與原型製作，而在 2003 年成為 JLC 的 TDR 的一部份。在本地從事 CDM 搜尋很吸引人，但必須先行研究低背景系統之可能性及適當地點之尋找。

CP 破壞、SUSY 粒子及 CDM 搜尋與初期宇宙（如重子不對稱問題）、暗物質及膨脹等問題直接相關。而這個以硬體研發為主的分項計畫將使台大高能組從現有之 EFC 經驗擴展至 BELLE 之核心，預備我們參與 JLC 製作另一個重要子系統，並且或許建立國內之 CDM 偵測計畫。在我們的物理分析團隊投入 B 物理與 CP 破壞之競爭性研究的同時，本計畫讓我們保持並擴展已建立之硬體研發競爭力，並提升台大高能實驗室之研究與教育基礎結構（infrastructure）。台大物理系在本計畫執行第一年將遷入新館，此舉在時間上與本計畫的配合更是巧妙之至。

[本組負責興建之 Partial EFC 已於 KEKB 加速器啟動過程中，分別於 1999 年 3/26 及 4/17 之束流對撞中偵測到約 10 個 Bhabha 事例，確証對撞成功，並提供亮度資訊！]

分項計畫三：「宇宙學與粒子天文物理學」理論整合研究

我們擬對各種非平衡與非線性現象在早期宇宙所扮演之角色進行深入而廣泛之研究與分析，從而建立早期宇宙之精準宇宙學模型。與 AMIBA 分項計畫及超新星宇宙學計畫相關之理論將是我們強調之重點。研究題材將包括(1)相變之非平衡效應，(2)拓撲模型，(3)宇宙背景輻射之原始與引致之異向性，(4)大尺度結構之重力模型，(5)黑暗物質之研究，(6)超弦理論所引致之重力理論修正。本計畫將強化 AMIBA 分項計畫之執行與分析，同時也將提供有關熱膨脹模型之起始條件及黑暗物質之進一步系統性之理解，以及其他背景對宇宙背景輻射引致之異向性。

分項計畫四：尖端光學與紅外線天文觀測

台灣大學，中央大學，清華大學，和中央研究院，將聯合組成一個協會。這個協會將以透過投資合作發展新儀器的方式，獲取使用大型光學紅外線望遠鏡的管道。最適合的合作對象是加拿大-法國-夏威夷-望遠鏡（CFHT），他的後端裝有許多先進而易使用的儀器。它的調適光學系統和極佳的大氣寧靜度,使其在紅外線波段的角分析力,比太空望遠鏡還好,在研究宇宙論,觀測星系團上,CFHT可以在許多工作上與AMIBA互補。利用S-Z效應偵測到的星系團、其紅位移Z如果小於0.8,可以用CFHT多天體光譜儀來測量。經由小心的校正和濾光鏡選擇,CFHT紅位移測量的極限可以延伸到Z=1.4。這種數據對於宇宙論參數的測定，和宇宙大尺度結構演化模式的檢驗。都非常重要。另外一個例子是應用將要完成(視野達到一平方度)的廣角攝影機,來研究鄰近星系團外緣區域,對背景星系造成的微弱重力透鏡效應。其

結果對於探討星系團的黑暗物質的分佈，非常有價值。由此可見,本計劃所提之紅外線與光學觀測,和子計劃一與二中提出的宇宙論電波及理論研究,正可相輔相成。何況我們更不可忽視,CFHT對現代天文學中其他的重要課題,例如:研究太陽系外側的彗星新故鄉古伯帶。以及對分子雲之濃密核心中星球誕生區域紅外線成像等,都可以發揮極大的威力。另外三個可能的對象為英國在夏威夷的UKIRT望遠鏡,以及亞利桑那大學Steward天文台或夏威夷大學天文研究所擁有的各種望遠鏡。

本計劃對於台灣光學紅外線天文學的研究架構之改進也很重要。臺灣電波天文學的成功發展，證明了下面這個三段式的發展策略的正確性:(1)Berkeley-Illinois-Maryland-Association毫米波觀測管道的獲得，為臺灣吸引了一隊活躍的電波天文觀測工作者。(2)與 SAO 合作,依照美方的設計，建造世界第一臺次毫米波陣列之努力，建立了我國電波天文儀器研發製造的能力。(3)本總計畫中的重點，設計建造具有高度競爭力的專用陣列-AMIBA，則表現了台灣在此一領域中不管科學或技術上，均已逐漸成熟。本子計畫提議獲取大型光學紅外線望遠鏡的使用權,和設計後端儀器(例如CFHT紅外線廣角相機),正是模仿電波天文利用國際合作成長之三步驟策略，在台灣發展光學紅外線天文學的步驟(1)和(2)。為了建立研究的大架構，ASIAA將要利用他的技術能力來支援儀器的發展，而中央大學則將改善玉山國家公園鹿林山的光學天文台(子計畫五)，供協會中所有成員訓練和測試使用。在促成國際合作上，主持人將利用他在發展臺灣電波天文上所累積的經驗，而兩位共同主持人則將發揮他們進出世界舞台的能力。我們另外還有諮詢小組，由數位活躍於宇宙論研究和儀器製作之世界級華裔天文學組成，他們已經決心透過提供諮詢，共同合作研究，協助評估，來臺教學，開放實驗室訓練我方人員等途徑來幫忙。如果本計畫能順利執行，這裡所提的步驟，一定能夠在下世紀初讓台灣透過重要的紅外線光學窗,來進行突破性天文研究。

分項計畫五：國內天文研究大環境軟硬體系統之建立

為配合教育部與國科會對國內大學研教之架構作大步革新，提昇在世界舞臺的科技競爭力，追求卓越的大前提下，以中央大學天文所為首的數個大學單位，計畫將位於玉山國家公園管理區內之鹿林前山天文台，協力開發成可供全國天文學術機構合用的天文研究設施。本分項計畫中申請之經費主要將用於改善鹿林前山天文台的聯外道路、水電設施及建立遠距通訊環境，提供未來進行遠距天文觀測等必須之軟硬體，將鹿林前山天文台建設成為國內完善的遠距天文觀測中心；並配合適切的科學專題研究，與總計畫及其他分項計畫互相呼應。

除了中短期的基礎架構工作,我們較長遠的(中長期）構想和企圖心是要利用這個千載難逢的機會，把台灣建設成中小型天文望遠鏡的一個國際中心，儘量發展本土的優勢，用以切入天文學前沿的計劃。這包括 2-m 之 NEO（近地物體）望遠鏡之推動，小型望遠鏡之區域性及全球性之規劃和落實。本項計劃陸續將會舉辦數個極具科學前瞻性的國際研討會，其中包括與 Princeton 及華沙之天文學家（及其他天文單位）合作之 IAU Colloquium (Small Telescope Astronomy on Global Scales)之籌劃。

為改善國內天文研究大環境，本計劃將與其他

分項計劃特別是有關 CFHT 等可能之國際合作密切配合，使得國內天文研究所之師生能有利用最新型觀察儀器之機會。除此之外，亦將極力爭取其他校際合作之管道（如討論中之中大及亞利桑那大學之合作協議），以增加台灣天文工作者之國際合作交流。

目前參與本計畫的大學單位為中央大學、清華大學及台灣大學，這些大學均各有重要的天文研究課題進行中，也是國內推廣天文教育的重鎮。未來我們將把合作對象擴大到其他國立及私立大學，以本土天文架構配合台灣的獨特經度條件（longitudinal coverage），提供給國內的天文學工作者一個優越的追求卓越環境和發揮條件。

結　語

Taiwan CosPA Project 提供了國內天文界、高能物理界、以及相關理論物理界，一個絕佳發展之契機；只是能否真正跨出重要的一步，其實仍待參與人員（含尚待加入陣容者）長期的努力，藉以建立起來之團隊，也必需有其素質上之基本要求，而各項會計與人事之措施，也必需有足夠彈性因應，追求世界一流，並非一蹴可幾的，更不應該是曇花一現的。

◎林試所／林朝欽｜中央大學／張光祥．張明新．林宏欽

鹿林天文臺的森林火災威脅

一九九三年一月六日玉山國家公園塔塔加登山口附近的麟趾山發生森林火燒，那年我剛從林務局轉任到林業試驗所成立森林火研究室，當時目睹了一場被林業單位認為相當嚴重的森林火災，一九九三年開始，我在火燒跡地的研究讓我有機會探訪鹿林天文臺，那是二〇〇一年我接到中央大學天文研究所的電話，中大天文所邀請我去鹿林天文臺協助他們的森林防火工作，才認識到鹿林天文臺。

鹿林天文臺於設立於一九九九年，選海拔2,862 公尺的鹿林前山，是因為較不受東北季風、西南氣流以及颱風的影響；加上地處高山，透明度及天空條件較佳，它是臺灣最重要的光學天文基地。鹿林天文臺的研究工作始於一九九〇年，於鹿林前山設置一個臨時觀測站，除進行正式臺的選址研究外也進行天文教學。將近三年的視相研究終於選得臺址，此臺址平均視相為 1.39 角秒，天空背景極暗，幾無光害，可觀測天數約 180 天，

↑圖1. 左邊影像是一九九一年所拍攝的麟趾山，右邊影像則是一九九三年的森林火災後的麟趾山，可以想像森林火災的影響力是巨大的

↑圖2. 從鹿林天文臺遠看麟趾山，火災後 23 年森林演替正進行著

↑圖3. 晨曦中的鹿林天文臺

較好的觀測季節是每年的秋季與初冬。一九九七年獲得太空計畫室 (今國家太空中心) 補助，正式開工興建第一座天文臺建築，一九九九年完工，安裝 76 公分超輕型望遠鏡。在教育部追求學術卓越發展計畫「國內天文研究大環境軟硬體系統之建立」的挹注下，二〇〇一年完成水電建設，二〇〇二年再安裝臺灣首座突破一公尺口徑的鹿林一米望遠鏡。二〇〇二年鹿林天文臺基礎建設完成以後，短短六年，已發表相關國際期刊論文 10 餘篇、會議論文 30 餘篇及快報 70 餘則。二〇〇三年七月開始，鹿林一米望遠鏡加入伽瑪射線爆 (gamma ray bursts, GRB)光學餘暉觀測行列，並與日本、大陸以及韓國的天文臺合作成立東亞伽瑪射線爆觀測網 (East-Asia GRB Follow-up Observation Network, EAFON)。在三年的觀測時間內成功觀測 15 個光學餘暉。此外，二〇〇四至二〇〇七年共發現了 15 顆超新星，所以這個天文臺可以說是臺灣的驕傲與珍貴的資產。

然而二〇〇一年七月第一次去鹿林天文臺時，就發現它其實面臨著森林火燒發生時被波及的威脅，於是同年我帶研究室同仁又去了一次，並作了燃料量調查，建議鹿林天文臺應該處理設施周邊的森林燃料。十餘年過去，我在二〇一六年八月再次造訪鹿林天文臺，設施周邊的森林燃料依舊存在 (不止天文臺，後來增加的環保署的空氣品質背景測站也一樣)，令人憂心，除了再次建議天文臺注意 (環保署也須要注意)，也希望森林管理單位的林務局、玉山國家公園管理處及臺灣大學實驗林管理處能加以重視，讓這個臺灣的珍貴的資產能免於被森林火燒波及的威脅。

森林火的一些基本概念

要說明鹿林天文臺為什

麼有被森林火燒波及的威脅之前，先得解釋一下森林火燒的基本理論，在臺灣森林發生火燒不論林務局或國家公園管理處，甚至帶有學術研究性質的臺灣大學實驗林管理處，都把它當成災害加以控制、撲滅。表面上理由充分，各機關也認為自己認真與勇於任事，但事實上因為不了解「火環境」，這個觀念與作法並不是很正確。例如二〇一六年四月武陵農場附近發生森林火，那裡也是櫻花鉤吻鮭保留區，林務局把它當經濟林看待積極滅火，國家公園管理處則配合林務局執行滅火計畫，二〇一六年的火燒點在二〇〇二年就發生過一次了，未來也很確定還會再發生的。同樣的鹿林天文臺周邊的森林也類似，現在看到的森林是一九六三年火燒後，一九九三年再次發生時積極滅火未波及的區域，不論現在看到的森林是人工造林還是自然更新的，它都是森林火生態學裡討論的干擾演替中的森林，這個區域像高麗菜一樣有國家公園、野生動物保護區、試驗林、國有林一層一層互相重疊與多重管理措施，然而這個區域森林是火燒敏感地，火燒記錄很清楚的記載一九三三年、一九六三年、一九九三年有過三次火燒。我個人目睹了一九九三年的火燒，之後開始對這個區域的火生態進行長達 15 年的監測，依森林火生態理論這個區域早晚是會發生火燒的，不論森林管理單位相信與否，這是一個事實，因為森林容不容易發生火燒依據森林燃料、地形與氣候三個條件，稱之為「火環境」，森林在什麼時候會真正發生燃燒則根據燃料濕度、空氣濕度與火原三個條件，稱之為「火三角」，根

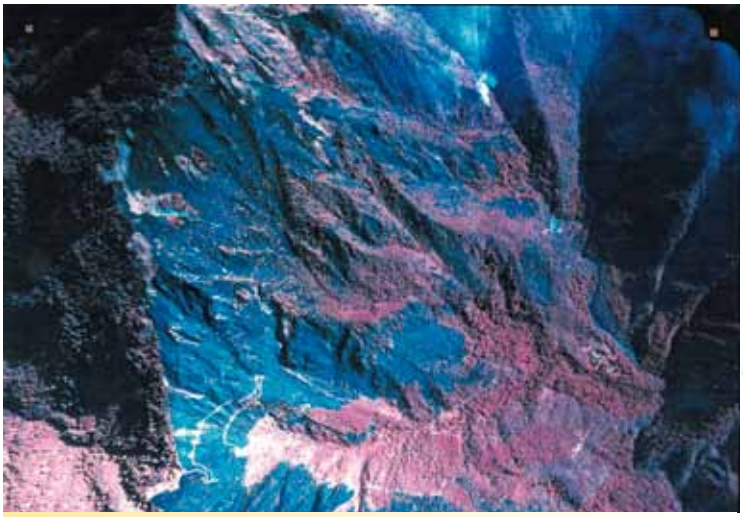

↑圖4. 一九九三年距鹿林天文臺不遠的玉山國家公園塔塔加的火燒範圍，黑色的火燒跡地接近 300 公頃，共撲救六天七小時

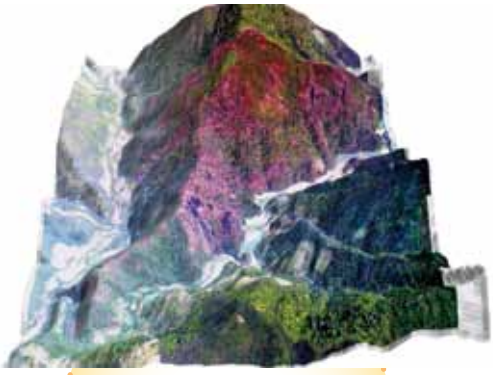

圖5. 二〇〇二年武陵森林火災範圍的立體圖，圖左側的溪流是櫻花鉤吻鮭保留區，二〇一六年在同一地區再發生一次森林火災

據火環境雖然無法準確預測何時會發生，卻可以很確定這個區域是火燒的敏感區。

讓我們回顧一下一九九三年一月六日起火點在玉山國家公園塔塔加登山口附近的鱗趾山的這場火，在火環境的有利條件一臺灣二葉松密林、南向坡 (鱗趾山) 及箱型谷、乾季，及一月六日那天正好有那不慎的火原出現，林務局雖未調查出火首，但確定是人為引起，六天七小時及 299.30 公頃森林被波及就是這場火燒的結果。

二〇〇二年五月的母親節，武陵農場在完全類似的狀況下，五天 10 小時及 300 公頃森林波及，相同地點二〇一六年四月又再發生。

同樣的故事在臺灣的中高海拔國有林裡不斷的上演，林務局談火色變，更怕媒體報導，這是視火為災害的後遺症。如果林務局能視火為生態，他們不會如此害怕森林火燒，因為火燒的敏感區是很容易判定出來的，什麼時候可能發生也有火災危險度在預測，這些監測等於是森林在告訴他們森林火的訊息，只要他們應用專業加以分析、了解就可以完全掌握森林火燒的防治工作。

可惜因為長期以來研究森林火生態的人太少，所以可參考的結果有限，我雖然不斷呼籲不要有火就滅，森林經營要考慮火的因素，甚至要把火當成生態系管理的工具，但在大眾尚無森林火生態的基本認知下，管理單位只能不分森林種類積極執行滅火，並以依法行政為最高準則，無法考慮我所論述的學理，以法令為依循的概念其實不容易當成自然資源管理專業。

鹿林天文臺被火燒波及的潛在危險

鹿林天文臺在鹿林前山的陵線上，阿里山公路在其北側下方，其東北邊是塔塔加鞍部的玉山登山口，一九九三年火燒跡地可以很明顯看到，火燒後所開設的森林防火線沿麟趾山陵經塔塔加鞍部，也很清楚的可以辨認出來。鹿林天文臺確實是一個好的觀測位置，但從森林火環境而言，它也是很容易在火燒發生時被波及的位置，從空中的鳥瞰圖 (圖6) 來說明為什麼很容易在火燒發生時被波及。

一、地形上

鹿林天文臺在山頂 (圖6)，圖6 左側的兩幢白色建築是天文臺主體、右下角的建築則是環保署的空氣品質背景測站，東方 (圖6 右側) 朝玉山、西側 (圖6 左側) 向嘉義縣，北邊 (圖6 上端) 往水里，南邊 (圖6 下端) 向著高雄縣。從地形上看，它的西南邊是明顯的箱型谷，如果火從這邊來，正好是煙囪效應的地點，這邊來的火如果達到樹冠火程度，除了鹿林天文臺受威脅，可能造成團火飛越嶺線，在東或北邊形成新火場，這兩邊是陡坡必然再向上延燒，鹿林天文臺就成了被火包圍的建築物。如果火從東或北來，雖然不是箱型谷，卻是陡坡，火在白天在山風的助長下必然向上延燒，如果達到樹冠火程度，也可能造成團火飛越嶺線，在西南邊的箱型谷裡必然很快形成新火場。如果火真的從東南邊的箱型谷地來，我預測它將與一九九三年塔塔加那場火的結果一樣焦黑一

↑圖6. 鹿林天文臺空中的鳥瞰，兩幢白色建築是天文臺主體，圖右下角的建築則是環保署的空氣品質背景測站，這三幢建築與松樹幾乎沒有距離

片。火會不會從北邊來？可能會，北邊是嶺線向沙里仙溪下降，雖沒有箱型谷形成煙囪效應與團火的威脅較低，但北邊是已達樹冠鬱閉的密林，形成樹冠火的機會大。所以在地形上鹿林天文臺面臨的火燒威脅是大的，不幸的是這兩向的臺灣二葉松、華山松如此接近建築物。

二、從燃料上

鹿林天文臺周邊的樹以針葉樹為主 (臺灣二葉松或臺灣五葉松)，地被的草生地是玉山箭竹或其他禾本科草本植物，針葉樹是與火密切的樹種，為什麼會密切？這是演化生態學理論

↑圖7. 鹿林天文臺周邊森林的地被植物是生長極濃密的玉山箭竹

探討的，不在此多說。簡單的說就是容易引燃的樹種，松針在這個區域也比較不會快速分解，所以可以用處於火藥庫來比擬鹿林天文臺的位置，就像你的鄰居是爆竹工廠，如果發生火災，你家被波及的危險性比別人要高些。鹿林天文臺除了西邊的森林不是完全的鬱閉密林，其他方向的森林基本上已是密林，而且很接近鹿林天文臺。

三、從氣候上

鹿林天文臺位於海拔 2,862 公尺的地方，雖然在亞熱帶的臺灣，但卻因為海拔高形成了近於溫帶的特性，也就是有乾濕季比較明顯的氣候，它的乾季大約是每年的十月到次年的二月，從林務局一九六三至二〇一三年的森林火災記錄，可以清楚看出來這個區域的火燒較高季節在這個期間，一九九三年塔塔加火燒就在一月。所以每年鹿林天文臺有五個月是在所謂的火季當中，這跟宜蘭縣棲蘭山雲霧帶的檜木

林完全不同，宜蘭縣山區的森林火燒很少，是因為氣候上乾濕季不是很明顯，縱使宜蘭縣山區也有箱型谷也有針葉樹燃料，但從火環境來說，這個區域的火燒敏感就降低了。

鹿林天文臺合理的防火措施

從上面火環境的分析，鹿林天文臺無法處理地形與氣候因子，但可以處理燃料因子，如果要真正達到安全的地步，它的主體建築 15 公尺範圍內應該要淨空，地被只能保持 30 公分以下長度。以這樣的觀點，現在生長在周邊 15 公尺內的樹必須砍除，尤其是已與主體建築接觸的松樹，這一點恐怕林務局、國家公園管理處、臺大實驗林管理處是難以接受的。其實松林是疏林狀態的林型，演替初期的密林是透過火燒調整，逐漸在演替後期達到疏林型態，如果過密導至燃料過多一次火燒可能讓演替在回到初其期狀態，高聳優美的松樹出現的森林可代表演替進行到中後期，這是森林火生態講的火的情境 (fire regime，regime 這個英文字無法找到適當的中文來表達)。總之就是有些森林與火是長週期互動，有些是短週期的互動，因為週期不同就形塑出不同的森林樣貌，鹿林天文臺附近的森林不該是現在這樣子，大自然會用火燒的方式來調整這裡的森林，如果從過去玉山地區三次的火燒記錄，鹿林天文臺附近的森林應該是屬於中長週期的 30～70 年的火情境。或許林務局、國家公園及臺大實驗林管理處不理解學理所解釋的現象，但火歷史卻清楚的紀錄著。

他山之石

鹿林天文臺不是世界上唯一有森林火燒威脅的天文臺，二〇〇三年一場森林火災毀掉距坎培拉 10 公里的 Mount Stromlo 天文臺六支天文望遠鏡，可說損失慘重，之後有了防範。二〇一三年位於 Wambelong 國家公園內桉樹林山頂的澳洲國家天文臺，也遭到大火的威脅 (圖8)，但因為週邊是燃料淨空的，加上火燒發生後森林救火隊強力的保護措失，才讓主體建築與儀器幸免於難。如果鹿林山一帶發生森林火燒，鹿林天文臺會不會如此幸運？在它目前沒有與森林燃料隔離的狀態下，它受森林火燒波及的威脅是存在的。我希望鹿林天文臺能夠儘快的關注這個威脅，也希望林務局、玉山國家公園管理處，及臺灣大學實驗林管理處能夠協助鹿林天文臺免於威脅，讓這個臺灣最重要的天文研究場發揮它的功能。

↑圖8. 澳洲的國家天文臺在二〇一三年遭遇的火燒威脅 (原載 University Today 同意使用 http://www.universetoday.com/248/contact-me/)

臺灣流星觀測網的建置與研究構想

文／楊義清

由於光電元件的進步，1990 年代開始出現使用感光耦合元件（charge coupled device，CCD）來記錄流星的觀測。除了直接分析流星的視訊紀錄以獲得流星軌跡資訊外，在感光耦合元件前加裝光柵還可以取得流星光譜資訊，因而豐富了流星研究的內容性。接下來在全球各地開始出現了許多的流星觀測網絡，而臺灣也在 2012 年開始有研究人員進行流星觀測網絡的建置。

當我們試著將整個地球當作一個系統來看，系統本身除了依循著動力學機制變遷之外，也會受到地球系統外的太陽系環境產生之干擾而有所影響。這些來自太陽系環境的干擾有兩大成因：一是來自太陽的風暴，二是進入大氣層的流星體。因此進一步地瞭解太陽系環境，對於生存在地球系統內的我們而言是很重要的資訊。在太陽系環境中，彗星與小行星能夠提供許多有關於太陽系的重要資訊，因此 2005 年時，美國 NASA 深擊號太空船（Deep Impact）於 9 月藉由釋放撞擊器來撞擊週期彗星譚普一號（9P/Tempel 1），並透過對所噴發灰塵的光譜觀測得到成分組成。日本 JAXA 的隼鳥號（Hayabusa）則是在 11 月接觸編號第 25143 糸川小行星（Itokawa），並採集了小行星的樣本返回地球。

相較於使用太空船的昂貴方式，藉由觀測流星體進入地球的過程則是便宜許多的方法。流星和隕石是直接將樣本帶進地球提供我們分析，預估每天約有 40 公噸重的流星體掉落至地球，相當於一顆直徑 1.4 公尺的小行星（以球粒隕石的密度估算）。由於流星體通常被認定為是彗星與小行星的碎片，所以關於流星或隕石的資訊仍有助於我們瞭解彗星與小行星。因此，研究者開始嘗試著紀錄每天在天空中發生的流星事件。1969 年美國 Bell 實驗室的 Willard Boyle 和 George Smith 發明了感光耦合元件後，迅速獲得天文學家的大量採用，當然也包含研究流星的天文學家。本文主要在介紹如何以感光耦合元件紀錄流星的視訊資料及臺灣成立的「臺灣流星觀測網」（Taiwan Elegant Meteor and TLE Network，TWEET）。

流星發光機制

在介紹本文主題前，先約略地介紹流星發光的機制及相關名詞。當流星還未被地球「捕獲」前，它會以顆粒狀碎片的形式漫遊於繞日軌道上。由國際天文學聯合會制定的流星體定義是**「運行在行星際空間的固體顆粒，體積比小行星小但比原子或分子還大」**。而英國的皇家天文學會則提出較明確的新定義**「流星體是直徑介於 100 微米至 10 公尺之間的固態天體」**。

大多數流星體在進入大氣層之後可分成三個階段：預熱期（preheating）、消融期（ablation）、無光飛行期（dark flight）。預熱期是發生在距地表 400 ～ 120 公里的大氣稀薄處，大氣分子很難能夠與流星體產生碰撞，因此幾乎沒有發光現象。消融期是指流星體抵達距地表 130 ～ 120 公里的高度，流星體會高速地撞擊大氣中的氣體分子而升溫。此時流星體會開始產生消融現象，也就是流星體會開始經歷短暫熔化、汽化過程而發光，同時大氣中的氣體分子也因為受到流星體撞擊與消融氣體的摩擦等因素亦開始發光。流星體在消融期的發光現象即為天文學上的流星現象，也是流星研究中所要觀測紀錄的部分。最後流星體的速度因為大氣阻力的作用會維持於終端速度，此時便無法再發光，直到撞擊地面的這段時間便稱為無光飛行期。

由於流星體在消融期間會有數秒左右的發光現象，這個發光現象也就是我們所熟知的「流星」。流星的亮度主要是取決於流星體顆粒的大小，而通常比綠豆大一點的流星體進入大氣層就能形成肉眼可見亮度的流星，因此使用感光耦合元件便足以紀錄下夜空中的流星影像，這個方法被稱為視訊觀測法（video observation）。1986 年起日本與荷蘭的研究者就開始使用這個方法觀測流星，到了 1999 年德國的研究者則開始以自動視頻系統定期觀測流星雨。在流星觀測上首要獲得的資訊便是流星體的軌道資訊，關於這點就需要利用三角定位法來進行，因此對單一個流星事件的多點觀測就成了唯一的途徑。藉由分析多點觀測所獲得的資料就可以得出流星體在太陽系裡運行的軌道，而且越多點的觀測資料會提高流星體軌道的精確度，所以流星觀測網絡的建置對於流星研究上非常有用。

基於對流星體軌道的研究，2008 年任職於中央大學天文所的阿部新助 (Shinsuke Abe) 助理教授便著手在中央大學校區內及鹿林天文臺上架設自動觀測系統。臺東及高雄兩地的自動觀測系統（圖 1），則是由筆者與曹俊傑同學於 2011 年完成架設

圖 1　自動觀測系統，左圖為監視攝影器材，右圖為放置電腦的機櫃。

的。2012 年起，科博館的林志隆副研究員與臺中大里高中的林士超老師於臺灣大學梅峰農場處架設一套自動觀測系統（現已撤離）、臺中惠文高中的吳秉勳老師也在惠文高中校內架設自動觀測系統。接著金門金城國中蔡松輝老師及彰化福興國中的吳炳連老師也分別協助在其校內架設自動觀測系統。最後東華大學物理系的紀信昌副教授也加入團隊，至此團隊雛型已成。所以大家覺得應該幫整個團隊取上一個容易上口又好記的名稱，最後大家同意採用「TaiWan Elegant mEteor and TLE Network」（TWEET），中文名稱則用「臺灣流星觀測網」（圖 2）。

流星自動化觀測設施

接著介紹流星自動化觀測所需的軟硬體設施。首先在監視攝影器材方面，包含有鏡頭、影像感應裝置及影像擷取卡；再加上一臺具有超大容量硬碟及網路的普通等級個人電腦，通常電腦上要安裝有監控軟體 UFOCapture 和校時軟體 NTPClock。所謂自動化觀測就是藉由電腦監控軟體，來拍攝紀錄影像感應裝置所觀測到的每一顆流星事件。影像感應裝置為包含有感光耦合元件（CCD）、前端處理器與數位信號處理器的複合系統。另外，有關於監控軟體 UFOCapture 的操作與設定，建議大家

圖 2　臺灣流星觀測網。

可以參閱《臺北星空》第 66 期關於臺灣流星觀測網專題介紹中〈流星監視錄影軟體 UFOCapture 操作介紹〉與〈流星自動觀測與分析軟體介紹〉兩篇文章，文中有較為詳盡的介紹。

在此筆者分享一個小經驗，依照目前個人電腦上處理器的等級是足以應付來自兩套影像感應裝置的訊號，但是 UFOCapture 在設計時應該沒有認真地考慮這個問題。所以當使用者購買兩套相同型號的影像擷取卡來安裝，UFOCapture 便會發生無法顯現影像的情況，這是因為電腦會將來自型號相同的影像擷取卡之訊號丟向同一個位址處理，因此勢必會出錯。所以只要使用者購買不同型號的影像擷取卡來安裝，就可以只使用一臺個人電腦來裝配多臺影像感應裝置。至於安裝校時軟體 NTPClock 的用處，則是為了給予每一個觀測到的流星事件精確的起迄時間。由於從流星體產生消融發光開始，光訊號傳達到 TWEET 不同觀測站的時間差異並不大，所以精確的時間紀錄有助於後續的分析。在 UFOCapture 的設定中，「Profile File」內容的設定對後續分析是極為重要的，因為其中包含有觀測站位置的經度、緯度及高度等資訊。後續關於流星軌道或流星體繞日軌道的分析，便需使用 UFOAnalyzer 與 UFOOrbit 兩套軟體，同樣地可以參閱在《臺北星空》中的〈流星自動觀測與分析軟體介紹〉一文。這些軟硬體的介紹也可另行參考曹俊傑碩士論文《自動化流星觀測網絡系統建置》（圖 3 ～ 5）。

經由 UFOAnalyzer 與 UFOOrbit 分析後，便可以獲得流星體在地球大氣層中消融發光的軌跡與流星體繞日的軌道（參閱圖 4 ～ 5）等兩類資訊。流星體繞日軌道的資料通常是用於研究流星雨母體上，特別是尋找小行星、彗星或新的流星雨，比較偏向於天文學的領域。相關研究討論可以參考《臺北星空》的〈流星體與母體軌道相關性研究〉文中介紹。

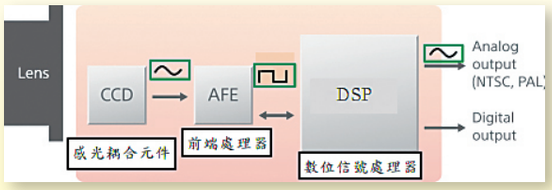

圖 3　鏡頭（lens）與影像感應裝置的示意圖。（擷取自自曹俊傑所撰《自動化流星觀測網絡系統建置》（未出版之碩士論文））

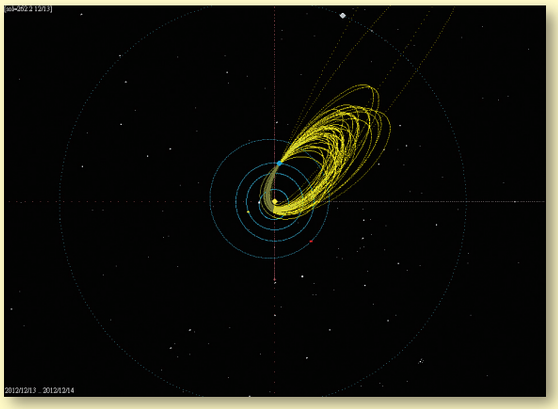

圖 4　TWEET 觀測站雙子座流星群俯視軌道圖。（圖片取自曹俊傑所撰《自動化流星觀測網絡系統建置》（未出版之碩士論文））

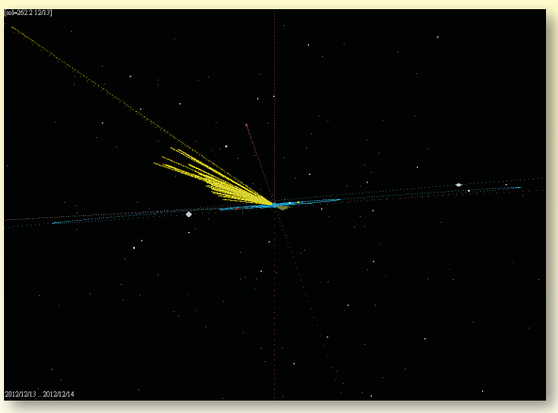

圖 5　TWEET 觀測站雙子座流星群側視軌道圖。（圖片擷取自曹俊傑所撰《自動化流星觀測網絡系統建置》（未出版之碩士論文））

此外，由於流星體消融現象多發生在地面上 100 公里左右的高空處。從圖 6 看來，探空氣球能夠探測的高度僅達 60 公里；太空梭無法在低於 400 公里的高度進行探測。因此，如果我們能夠藉由流星體的消融現象反推高空大氣的資訊，那將會是非常有意思的題目。

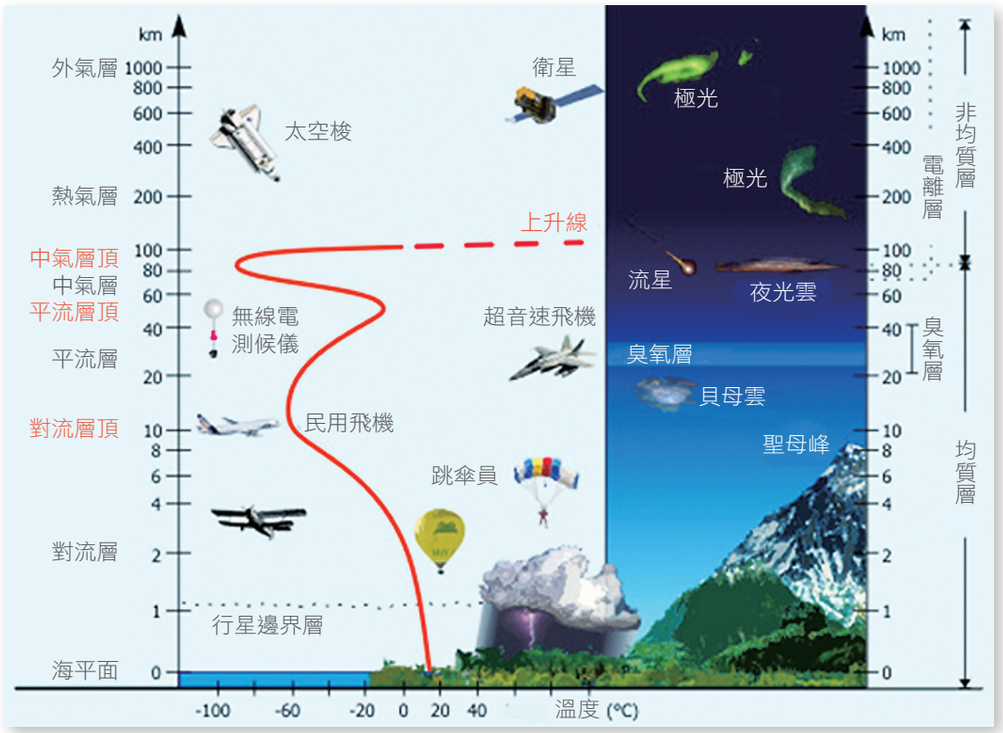

圖 6　大氣層分層示意圖。（原圖片取自 http://www.theozonehole.com/atmosphere.htm）（copyright: The Ozone Hole website，並參採「國家教育研究院雙語語彙、學術名詞暨辭書資訊網」檢索結果，予以中文翻譯。）

註：本文感謝吳秉勳與曹俊傑協助提供圖片資料。

參考資料

1. M. Beech and D. Steel, On the definition of the term “meteoroid”, Quarterly Journal of the Royal Astronomical Society, 36: 281-284 (1995).
2. 楊義清，臺灣流星觀測網（Taiwan Elegant Meteor and TLE Network）介紹，臺北星空，第 66 期，第 10-11 頁（2014）。
3. 賴楷翔，流星監視錄影軟體 UFOCapture 操作介紹，臺北星空，第 66 期，第 17-21 頁（2014）。
4. 吳秉勳，流星自動觀測與分析軟體介紹，臺北星空，第 66 期，第 22-27 頁（2014）。
5. 曹俊傑，自動化流星觀測網絡系統建置（未出版之碩士論文），國立高雄師範大學物理系，高雄市。
6. 林士超等人，鎏金歲月～流星體與母體軌道相關性研究，臺北星空，第 66 期，第 31-38 頁（2014）。

楊義清　國立臺東大學應用科學系教授

鹿林觀測與心得報告 20160708

報告者：劉致廷、賴詠丰、王傳耘、黃教峻

I. 原觀測計畫

A. **武仙座星系團**：觀察星系團結構了解宇宙網的基本構造，也可就各星團的類型與光度分布做比對。

B. **NGC 6210**：觀測行星狀星雲，周圍不同顏色暗示這顆恆星的基本元素，可推測當時此恆星生成時的環境。

C. **M19 球狀星團**：觀測星團內恆星取得光度資訊，畫出星色-星等圖與星色-星色圖，並觀測其中的短週期變星，如 V37。

天體	赤經（J2000）	赤緯（J2000）	視星等	欄 1
NGC-6210	$16^h44^m29.5^s$	+23°47’ 59.7〃	8.8	
M19	$17^h02^m37.69^s$	-26°16’ 04.6〃	7.47	
V37	$16^h41^m42.45^s$	+36°28’ 21.8〃	8-11	週期：1.176hr

II. 天文台導覽學習紀錄

鹿林山天文台包含：1 個 1m 望遠鏡（LOT）、1 個 40cm 望遠鏡（SLT）、1 個 35cm 望遠鏡（L35，未來可作為申請目標）、4 個 50cm（TAOS 計畫）。以下做為詳細紀錄。

A.LOT

ACE 濾鏡系統可放最多 14 個濾鏡。上下各有 8 個插槽但要各空出 1 個。例如：氧濾鏡，若有觀測到目標則代表該天體可能存在氧元素。但因為溫度或其他因素影響，用該濾鏡拍攝出的影像不一定會與真實情況符合，可能會有所誤差。U、B、V、R、I，U 偏向紫外線、B 偏藍、V 偏綠、R 偏紅、I 偏紅外線 。CCD 工作溫度-30° C，只能拍攝單色的影像。

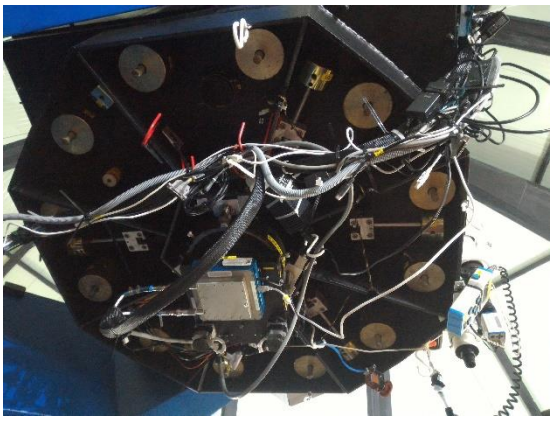

▲圖一：LOT 底部

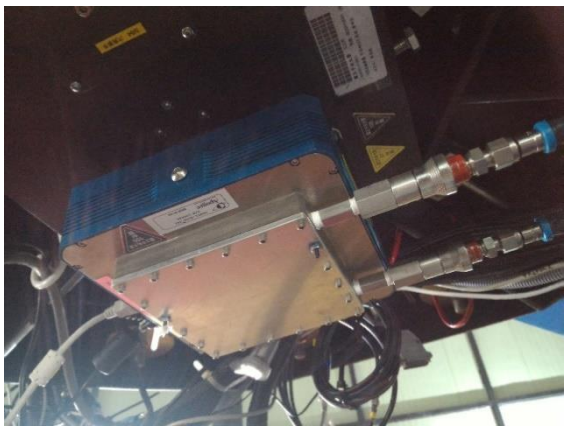

▲圖二：LOT 的 CCD

鏡身形式為「蓋賽格林反射式望遠鏡」，鏡筒下有 12 具重槌環狀排列，僅靠物理性平衡，不須機械操作。

赤道儀為音叉式赤道儀，因為機械結構不宜觀測北極星以下及赤緯-40° 以下天區。

天文台內有三具監視器，第一具監視整架望遠鏡的安全，第二具設在支架上面，觀測圓頂的開口是否對到望遠鏡，第三具則是設在尋星鏡上，不過因為有壞點在螢幕上因此幾乎沒有使用。

B. CCD 的影像修正

i. 暗電流（Dark Current）校正：

因為使用 CCD 拍攝影像時，需要持續的供電，而電流的持續供應則會產生熱，拍攝越久產生的熱越多， CCD 產生的雜訊也越多。最基本解決雜訊的方法就是使溫度降低，因此 LOT 的 CCD 溫度接控制在-30° C 上下。而如果我們可以在無光的環境下以相同的溫度與曝光時間再次拍攝 CCD 影像，所得到的就是純粹由 CCD 溫度所產生的雜訊，所以這樣的影像也稱為暗電流影像（dark current frame），也就是 CCD 本身在無光的環境下所產生的訊號。

ii. 偏壓雜訊（BIAS）校正：

一般天文 CCD 上有很多個像素，而從 CCD 讀出影像的過程中，每個像素的影像信號依序傳輸時會產生雜訊，這些雜訊同樣會加入拍攝的天體影像中，需要加以排除。這種校正影像稱為 BIAS（偏壓雜訊），等同曝光時間零秒。

iii. 平場校正（Flat Field）：

光線從望遠鏡直到被 CCD 的像素感應之前，都會經過望遠鏡的鏡片或玻璃、濾鏡、CCD 前方的保護玻璃等等，每個光線經過的地方如果有灰塵或污漬，或是透光率不同，就會造成到達像素的光線不均勻。此外望遠鏡雖然可以將光線集中聚焦，但是光線在出口處的中央越亮，會造成越旁邊的光線越弱，稱為周邊減光效應。如果不做校正，將會出現星星在 CCD 的位置不同，其亮度就會產生不同的錯誤。解決方式就是將整個系統對向均勻的光源拍攝影像，這樣就可以知道光量不均的狀況。這樣的校正影像稱為平場影像（Flat Field image）。

C. 變星資料的處理與分析

當我們獲得望遠鏡觀測後的原始資料，通常充斥著大量的雜訊。這時就需要將前述的校正用影像與原始資料做影像淨化，得到實際可用的資料。

i. 平場校正：

但校正用資料的品質也需符合標準，尤其是「平場校正」更需要檢查。每一個像素點可儲存的光電效應的量值範圍是 0~65535 單位，所以需要確定這張影像中每個像素平均所接收到光子的量值大約在 8000~60000 單位內，就可以讓資料所顯示的量值呈現線性關係。

ii. 暗電流校正：

而暗電流校正的影像需要檢查的有「曝光時間」與「CCD 的溫度」要與原始資料一致。

iii. 影像對齊：

原始資料本身拍攝過程中，若望遠鏡有過中天，赤道儀從新定位後翻轉，所得影像方向也會轉向，需校正以便利比對。我們利用軟體中的光子量值過濾功能將不必要資料排除後，就能得到肉眼能辨識的星點資料，經比對過後就可以將被翻轉的影像方向修正回來。翻轉修正回來後，因為望遠鏡拍攝時會有誤差，每個星點在不同的圖中位置可能會不同，所以要將所有的星點全部對齊（Align）。

iv. 光度分析：

當影像全部修正完畢之後，我們便可用修正後的正確影像進行光度分析。在軟體中的光度分析（Photometry）功能中，辨識（Identify）出目標星（Object）和參考星（Reference Star）後，就可以做出光度比較的圖表。

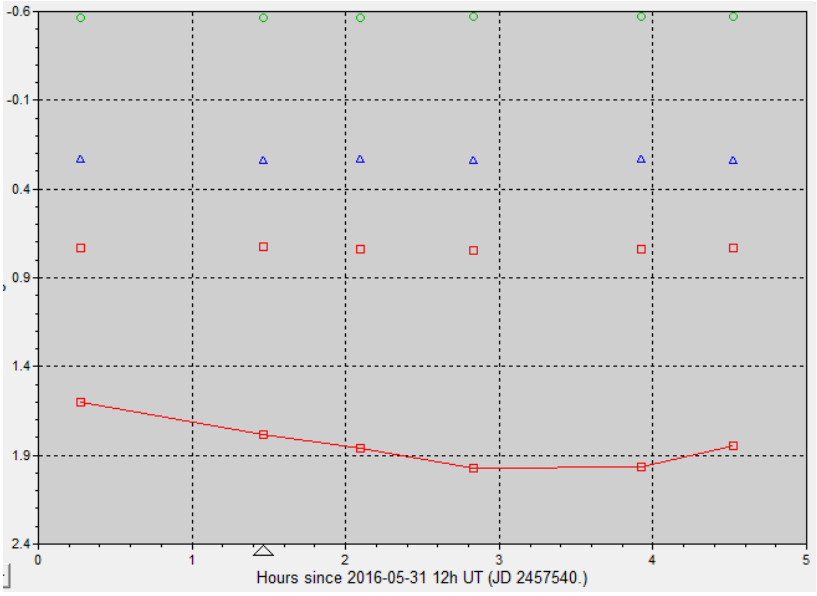

▲圖壹：變星分析圖表範例

III. 未來申請計畫

由於氣候不佳，我們借用了原有的資料，學會了 BVR 的疊圖技巧，加上親自操作，更加了解了軟體的使用方式，並且取得了恆星的光度變化資料，同時和我們原本計畫觀測的行星狀星雲做結合，同時學到了光度分析的方法以及 Excel 的文書處理技巧。未來如果有幸再次申請的話，希望能夠成功使用到 L35，並且分析自己所拍攝下來的資料。

IV. 心得

在下山的前一天，偶然發現了夕陽的餘暉打在濃厚的雲霧之中，彷彿置身於仙境之中，就算沒有看到星空，這美麗的景色似乎也值得了。下山時，雖然下著大雨，但途中仍然巧遇了台灣的國鳥，帝雉。或許沒有達到原本的目標，不過途中卻有很多小確幸，而這次的參訪，更讓我們對下次申請該做甚麼準備更有概念，希望還有下一次能夠探索這高深莫測的宇宙。

鹿林觀測報告 20160707

組員：呂沛儒，杜昱成，李彥霆，莊士毅

指導老師：黃晟庭

壹、 觀測計劃

一、觀測動機

希望能親眼目睹相隔天涯另一端的天體，記錄其光度與顏色變化解析其物理意義，再將這些資料及照片彙整起來，為社團留下珍貴資料並可作為研究報告使用。

二、觀測目標：

(一)復興新星蛇夫座 RS

這顆質量極大，接近錢卓極限的復興新星，我們想藉由鹿林的 CCD 觀測它的光度變化，藉此看出它接下來可能產生的大規模爆炸。

A. 座標位置：赤經：$17^h50^m30.2^s$##赤緯：- 06°42’ 28”

B. 視星等：12.5

(二)行星狀星雲

利用不同波段濾鏡觀測星雲內元素差異

A. 目標資料

NGC number	赤經(J2000)	赤緯(J2000)	視星等	
6543	$17^h58^m33.4^s$	+66°38’ 00”	9.8	天龍座-貓眼星雲
6826	$19^h44^m48.2^s$	+50°31’ 30”	10.2	天鵝座-眨眼星雲
6751	$19^h05^m55.6^s$	－05°59’ 33”	15.8	天鷹座-亮眼星雲
6369	$17^h29^m20.4^s$	－23°45’ 34”	16.6	蛇夫座-小鬼星雲
M2-9	$17^h05^m37.952^s$	-10°08’ 34.58”	14.7	蛇夫座-蝴蝶星雲
IC3568	$12^h33^m06^s$	+82°34'00"	12.3	鹿豹座-檸檬片星雲

三、觀測儀器：望遠鏡 STL35、鏡採（B、V、R、OIII、SII），使用 B、V、R、OIII、SII 濾鏡，分辨行星狀星雲的特徵與顏色間的關係，進而嘗試推出行星狀星雲結構與元素分布。

四、觀測時間：2016/6/9 至 2016/6/11，為期三天兩夜

觀測優先排序：小鬼星雲、蝴蝶星雲、蛇夫座 RS、亮眼星雲、眨眼星雲、貓眼星雲、檸檬片星雲

貳、 課程紀錄與實際觀測狀況

一、LOT 儀器簡介

(一)最多可以放 14 種濾鏡，上下各有 8 個插槽但要各空出 1 個，像是紅外線濾鏡 I。可以觀測到紅外線波段的物體。

(二)其赤道儀為音叉式結構（不適合觀測北極星以下天區和南緯 40 度以下天區）

(三)因為 LOT 十分巨大，為防止其鏡筒變形，其擁有十二個物理平衡的重錘。

(四)有三具監視器，第一具監視整架望遠鏡，第二具設在支架上面，觀測圓頂的開口，第三具則是設在尋星鏡上，不過因為有壞點在螢幕上因此幾乎沒有使用。

二、軟體

(一)The sky 星圖軟體的一種，可以直接設定觀測目標，望遠鏡的移動會配合軟體追蹤目標。

三、資料處理

(一)暗電流 在拍攝時，電流通過會產生熱源，熱源影響感光元件，產生雜訊，拍攝越久雜訊越多，所以最後修圖時，需做雜訊去除處理。

(二)平場 望遠鏡上有灰塵，直接拍攝會影響照片，且不同感光元件的性能不同，接收到的光線也不一樣，因此須先校正誤差，以求能取得最正確的畫面。

(三)偏壓 接收到的影像訊號為負值時，感光元件會無法顯示，所以需要加壓在 CCD 上，將數值提高為正，因此在最後修圖時，需要再將此增加的電壓數值去除，以求的最精確的照片。

(四)光譜資料處理取得光譜資料後，先將譜狹縫資料使用 EXCEL 軟體做出散佈圖，接著取出譜燈資料，做成散布圖，之後一一比對譜燈波長（對照組），盡量做多筆資料，以求資料的準確性，接著算出公式，讓系統自動算出恆星波長（實驗組），最後發現仍有誤差，表示輸入譜燈波長時可能不夠精確，如果數值誤差不大，代表成功完成光譜分析。

四、光譜資料分析程序

(一)藉由 MaxIm DL 軟體由 HR7314 光譜影像取得水平方向光度數值分布圖(profile)，轉出數值資料後，以 Excel 開啟。如圖 1。

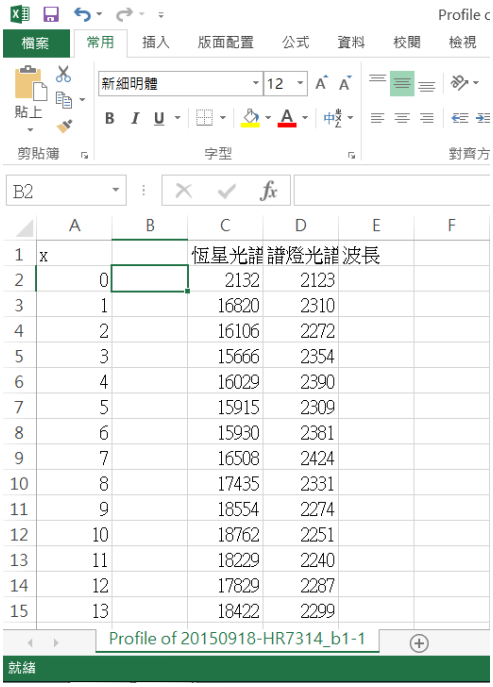

	A	B	C	D	E	F
1	x		恆星光譜	譜燈光譜	波長	
2	0		2132	2123		
3	1		16820	2310		
4	2		16106	2272		
5	3		15666	2354		
6	4		16029	2390		
7	5		15915	2309		
8	6		15930	2381		
9	7		16508	2424		
10	8		17435	2331		
11	9		18554	2274		
12	10		18762	2251		
13	11		18229	2240		
14	12		17829	2287		
15	13		18422	2299		

圖 1 光譜數值資料

(二)如同步驟(一)，開啟已知元素譜燈光譜，讀取數值後，將兩筆資料數值畫在同一張光度數值分布圖上。如圖 2。

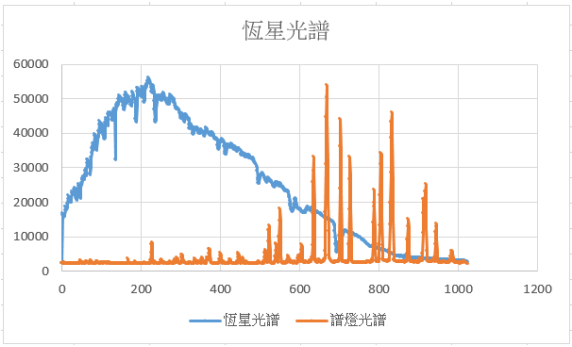

圖 2 恆星與標準譜燈光譜，藍色資料線為 HR7314 光譜，黃色資料線為譜燈光譜。

(三)藉由查詢已知光譜與波長值，如圖 3 資料，比對上述的譜燈光譜位置做線性回歸，求得 轉換波長 = $-10^{-04}x^2 + 3.833x + 4989.2$，X 為圖檔中的 X 座標值，如圖 4。

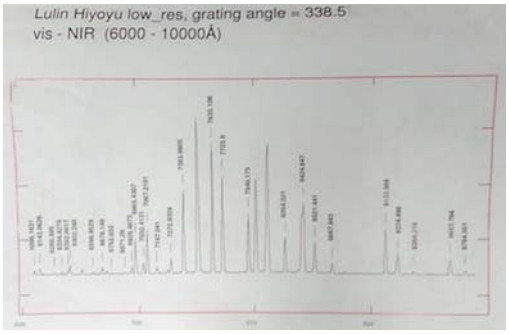

圖 3 已知譜燈譜線波長對照表#

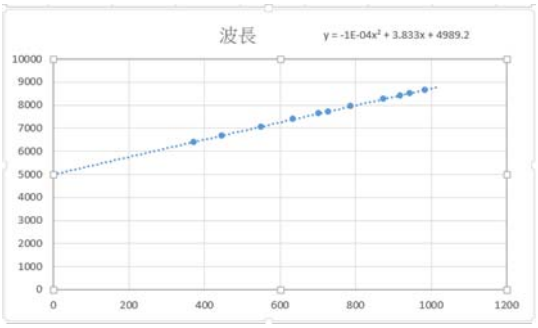

圖 4 X 座標值與實際譜線對照關係#

(四) 得到轉換關係後，再將所譜線位置轉成比對波長數值，如圖 5。再將轉換後的波長作圖，如圖 6，就能夠從圖表中找出明顯的吸收與發射光譜的波長。如此能進一步做光譜分析，得知元素、速度、恆星光譜型等物理參數。

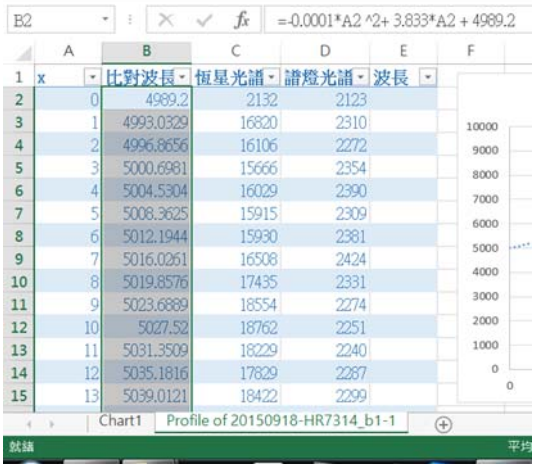

圖 5 轉換為比對波長#

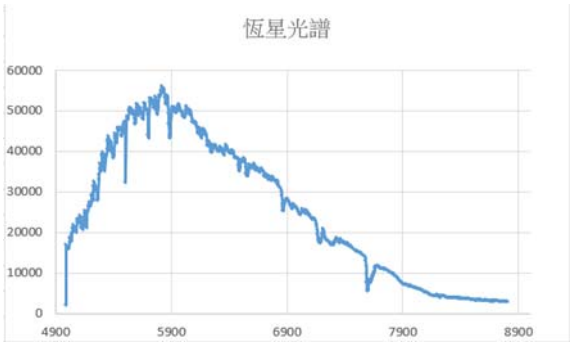

圖 6 比對波長轉換後的譜線#

參、未來計畫

這次上山後學到了光譜的分析，下次如果還有機會上山，希望能觀測恆星或星雲，因為已經熟悉了軟體的操作，所以下次可以進行更快更完整的分析，未來期望學弟也能夠上鹿林天文台體驗天文人的生活。

肆、上山心得

一、 杜昱成

這次的鹿林觀測計畫因為西南氣流影響，所以沒有了觀星的行程，但取而代之的，我們借用原有的資料，學會了 BVR 的疊圖技巧，因為親自操作，更加了解了軟體的使用方式，並且取得了譜燈跟恆星的光度變化資料，和我們原本計畫觀測的行星狀星雲做結合，也借此學到了光度分析的方法，和 Excel 的文書處理技巧。在最後一天的傍晚我們還看到了鹿林獨有的夕陽餘暉，金黃色光暈照在我們身旁，更顯得自己像是處在世外桃源，算是天氣欠佳中的小確幸。往後如果還有機會上山，相信經過了這次的訓練，先打好基礎，便能更快的上手，提升學習的效率，期望之後的觀測者，能從中獲得許多的知識，更加了解天文的廣大世界。

二、 呂沛儒

對於這次的上山我一直都十分期待，但在看到了關於天氣的資訊後。心中卻也萌生了不想去的念頭。因為這次上山的目的就是觀測，如果說天氣壞到讓你看不到任何東西時。那為什麼還要上去呢。這樣真的可以學到東西嗎。但是我仍然抱持著也許會還是能觀測的心態上山了。結果天氣仍然是十分不好。但出乎我意料，儘管不能觀星了。但我仍可以使用之前的資料來進行分析，我學到了像是 Excel 的使用技巧以及疊圖。雖然說並沒有進行觀測，但也真的是學到非常多事物。不過，在下雨時下山真的十分痛苦，鞋子都全溼啦。也是真的期望還有下次，能有個好天氣。進行一次完整的觀測。

新聞報導

2016/12/20 【大成報】

共享星空奧秘　我國參與的泛星計畫首批數據正式對全球公開

【大成報記者羅蔚舟／桃園報導】

國立中央大學天文所宣布，我國參與之「泛星計畫（Panoramic Survey Telescope And Rapid Response System，簡稱 Pan-STARRS）」，經過四年對夜空循環觀測，累積針對天體位置與亮度的巨量測量結果，特於台灣時間 12/19 晚上 9 點與歐美同步對全球公開首批資料，是有史以來規模最大的宇宙天文數據。

國立中央大學天文所所長陳文屏教授表示，「泛星計畫」是人類首次大規模巡邏夜空，以口徑 1.8 公尺的超廣角望遠鏡執行巡天任務，該望遠鏡建置於美國夏威夷毛伊島的哈雷阿卡拉（Haleakala）火山頂。從夏威夷整年可以觀看全天空四分之三的天空，泛星望遠鏡從 2010 年 5 月起在可見光到紅外線 5 個波段拍攝，每個天區都觀測了起碼 12 次，不同波段的數據用於研究天體性質，而重複觀測則能夠指認出位置產生變化（例如：彗星），或是亮度發生變化（例如：爆發死亡的超新星）的天體或現象。

陳文屏教授表示，首批公開數據包括數十億顆恆星與星系的精確位置與亮度，經過數年的處理與校正，12 月 19 日由位於美國馬利蘭州的「太空望遠鏡科學所（(Space Telescope Science Institute, STScI）」公布。

泛星天文台台長錢伯斯（Ken Chambers）說：「泛星有很多重要發現，包括大批近地小行星、太陽系外圍小天體、銀河系的三維塵埃分布，以及爆發恆星等。這批數據公開後，全世界的科學家將有更多新的，以及意料之外的發現。」

陳文屏教授表示，泛星計畫是目前發現近地小天體最多的計畫，清點可能撞擊地球的天體，對於保護人類文明做出貢獻。台灣泛星計畫主持人、中央大學天文所所長陳文屏說：「以往觀察宇宙像是拍照片，泛星則是幫夜空拍電影，我們得以從時間的觀點探討宇宙現象。」

泛星計畫由美國、德國、英國、台灣的研究團隊營運，其中台灣是亞洲唯一成員。陳文屏教授表示，泛星巡天的挑戰不僅止於天文觀測的軟硬體，在資訊工程方面，像是分析、處理、儲存也是創舉，整個數據量達 2 千兆位元（petabyte），換算成一般文件量，需要 1 億 6 千萬個抽屜才能存放。

陳文屏教授表示，有些爆發現象必須及時偵測以便後續研究，有些則必須仔細校正，達到最佳精確度以及全天空一致性。從望遠鏡獲得的數據由夏威夷天文中心利用高速電腦處理，然後分送科學團隊。首批公布「靜態」數據，也就是天體的平均數值，預計明（2017）年將發布第二批數據，包括每個天體在不同時期所測量的位置、亮度、影像等。即日起，任何人都可以利用泛星數據庫查詢從地球附近的小天體到遙遠的星系，赤緯負 30 度以北任何天體在不同波段的位置與亮度。

中央大學天文所受科技部補助，結合校內資訊工程專家，建立了泛星大數據中心，提供所內師生，以及中研院、台大、清大等學者使用，過去幾年在高紅移星系、星系團的質量分布、星團的瓦解過程、發現太陽系外圍冰冷天體等課題取得優良成果，也讓我國高中生參與搜尋小行星活動。

同為台灣泛星計畫主持人、中央大學天文所葉永烜教授說：「時變現象是未來天文學的重要領域之一，我們藉由參與泛星奠立了好的基礎，未來應該朝這方向專精。」中央大學正在鹿林天文台建立兩公尺口徑望遠鏡，秉持位於西太平洋、低緯度、高海拔的地理優勢，將對泛星計畫作出更大貢獻，持續探討靜態與動態宇宙天體的本質。

原文轉載自【2016-12-20/大成報】

相關連結 /
http://www.greatnews.com.tw/home/news_pagein.php?iType=1009&n_id=129660

2016/12/20 【勁報】

共享星空奧秘我國參與的泛星計畫首批數據正式對全球公開

記者 羅蔚舟／桃園報導

國立中央大學天文所宣布，我國參與之「泛星計畫（Panoramic Survey Telescope And Rapid Response System，簡稱 Pan-STARRS）」，經過四年對夜空循環觀測，累積針對天體位置與亮度的巨量測量結果，特於台灣時間 12/19 晚上 9 點與歐美同步對全球公開首批資料，是有史以來規模最大的宇宙天文數據。

國立中央大學天文所所長陳文屏教授表示，「泛星計畫」是人類首次大規模巡邏夜空，以口徑 1.8 公尺的超廣角望遠鏡執行巡天任務，該望遠鏡建置於美國夏威夷毛伊島的哈雷阿卡拉（Haleakala）火山頂。從夏威夷整年可以觀看全天空四分之三的天空，泛星望遠鏡從 2010 年 5 月起在可見光到紅外線 5 個波段拍攝，每個天區都觀測了起碼 12 次，不同波段的數據用於研究天體性質，而重複觀測則能夠指認出位置產生變化（例如：彗星），或是亮度發生變化（例如：爆發死亡的超新星）的天體或現象。

陳文屏教授表示，首批公開數據包括數十億顆恆星與星系的精確位置與亮度，經過數年的處理與校正，12 月 19 日由位於美國馬利蘭州的「太空望遠鏡科學所（(Space Telescope Science Institute, STScI）」公布。

泛星天文台台長錢伯斯（Ken Chambers）說：「泛星有很多重要發現，包括大批近地小行星、太陽系外圍小天體、銀河系的三維塵埃分布，以及爆發恆星等。這批數據公開後，全世界的科學家將有更多新的，以及意料之外的發現。」

陳文屏教授表示，泛星計畫是目前發現近地小天體最多的計畫，清點可能撞擊地球的天體，對於保護人類文明做出貢獻。台灣泛星計畫主持人、中央大學天文所所長陳文屏說：「以往觀察宇宙像是拍照片，泛星則是幫夜空拍電影，我們得以從時間的觀點探討

宇宙現象。」

泛星計畫由美國、德國、英國、台灣的研究團隊營運，其中台灣是亞洲唯一成員。陳文屏教授表示，泛星巡天的挑戰不僅止於天文觀測的軟硬體，在資訊工程方面，像是分析、處理、儲存也是創舉，整個數據量達 2 千兆位元（petabyte），換算成一般文件量，需要 1 億 6 千萬個抽屜才能存放。

陳文屏教授表示，有些爆發現象必須及時偵測以便後續研究，有些則必須仔細校正，達到最佳精確度以及全天空一致性。從望遠鏡獲得的數據由夏威夷天文中心利用高速電腦處理，然後分送科學團隊。首批公布「靜態」數據，也就是天體的平均數值，預計明（2017）年將發布第二批數據，包括每個天體在不同時期所測量的位置、亮度、影像等。即日起，任何人都可以利用泛星數據庫查詢從地球附近的小天體到遙遠的星系，赤緯負 30 度以北任何天體在不同波段的位置與亮度。

中央大學天文所受科技部補助，結合校內資訊工程專家，建立了泛星大數據中心，提供所內師生，以及中研院、台大、清大等學者使用，過去幾年在高紅移星系、星系團的質量分布、星團的瓦解過程、發現太陽系外圍冰冷天體等課題取得優良成果，也讓我國高中生參與搜尋小行星活動。

同為台灣泛星計畫主持人、中央大學天文所葉永烜教授說：「時變現象是未來天文學的重要領域之一，我們藉由參與泛星奠立了好的基礎，未來應該朝這方向專精。」中央大學正在鹿林天文台建立兩公尺口徑望遠鏡，秉持位於西太平洋、低緯度、高海拔的地理優勢，將對泛星計畫作出更大貢獻，持續探討靜態與動態宇宙天體的本質。

原文轉載自【2016-12-20 /勁報】

相關連結 / http://times.hinet.net/news/19833398

2016/12/20 【中時電子報 Campus】

中央大學泛星計畫天文數據全球首度公開

記者/廖育婉

國立中央大學天文所發布，參與「泛星計畫（Panoramic Survey Telescope And Rapid Response System，簡稱 Pan-STARRS）」，經過四年對夜空循環觀測，累積針對天體位置與亮度的巨量測量結果，於台灣時間昨日晚上 9 點與歐美同步對全球公開首批資料，是有史以來規模最大的宇宙天文數據。

「泛星計畫」是人類首次大規模巡邏夜空，以口徑 1.8 公尺的超廣角望遠鏡執行巡天任務，該望遠鏡建置於美國夏威夷毛伊島的哈雷阿卡拉（Haleakala）火山頂。從夏威夷整年可以觀看全天空四分之三的天空，泛星望遠鏡從 2010 年 5 月起在可見光到紅外線 5 個波段拍攝，每個天區都觀測了起碼 12 次，不同波段的數據用於研究天體性質，而重複觀測則能夠指認出位置產生變化。

首批公開數據包括數十億顆恆星與星系的精確位置與亮度，經過數年的處理與校正，12 月 19 日由位於美國馬利蘭州的「太空望遠鏡科學所（(Space Telescope Science Institute, STScI）」公布。

泛星天文台台長錢伯斯（Ken Chambers）說：「泛星有很多重要發現，包括大批近地小行星、太陽系外圍小天體、銀河系的三維塵埃分布，以及爆發恆星等。這批數據公開後，全世界的科學家將有更多新的，以及意料之外的發現。」

中央大學天文所教授葉永烜說：「時變現象是未來天文學的重要領域之一，我們藉由參與泛星奠立了好的基礎，未來應該朝這方向專精。」中央大學正在鹿林天文台建立兩公尺口徑望遠鏡，秉持位於西太平洋、低緯度、高海拔的地理優勢，將對泛星計畫作出更大貢獻，持續探討靜態與動態宇宙天體的本質。天文所所長陳文屏說：「以往觀察宇宙像是拍照片，泛星則是幫夜空拍電影，我們得以從時間的觀點探討宇宙現象。」

泛星計畫由美國、德國、英國、台灣的研究團隊營運，其中台灣是亞洲唯一成員。泛星巡天的挑戰不僅止於天文觀測的軟硬體，在資訊工程方面，像是分析、處理、儲存也是創舉，整個數據量達 2 千兆位元（petabyte），換算成一般文件量，需要 1 億 6 千萬個抽屜才能存放。

首批公布「靜態」數據，預計明年將發布第二批數據，包括每個天體在不同時期所測量的位置、亮度、影像等。即日起，任何人都可以利用泛星數據庫查詢從地球附近的小天體到遙遠的星系，赤緯負 30 度以北任何天體在不同波段的位置與亮度。

中央大學天文所受科技部補助，結合校內資訊工程專家，建立了泛星大數據中心，提供所內師生，以及中研院、台大、清大等學者使用，過去幾年在高紅移星系、星系團的質量分布、星團的瓦解過程、發現太陽系外圍冰冷天體等課題取得優良成果，也讓我國高中生參與搜尋小行星活動。

原文轉載自【2016-12-20/中時電子報 Campus】

相關連結 / http://campus.chinatimes.com/20161220002290-262301

2016/12/19 【中時電子報】

泛星計畫首批資料公開揭露史上最大天文數據

記者 林志成 / 報導

中央大學宣布，我國參與之「泛星計畫（Pan-STARRS）」，經過 4 年對夜空循環觀測，累積針對天體位置與亮度的巨量測量結果，於台灣時間今天晚上 9 時與歐美同步對全球公開首批資料，是有史以來規模最大的宇宙天文數據。

「泛星計畫」是人類首次大規模巡邏夜空，以口徑 1.8 公尺的超廣角望遠鏡執行巡天任務，該望遠鏡建置於美國夏威夷毛伊島的哈雷阿卡拉（Haleakala）火山頂。

「泛星計畫」由美國、德國、英國、台灣的研究團隊營運，其中台灣是亞洲唯一成員。泛星巡天的挑戰不僅止於天文觀測的軟硬體，在資訊工程方面，像是分析、處理、儲存也是創舉，整個數據量達 2 千兆位元（petabyte），換算成一般文件量，需要 1 億 6 千萬個抽屜才能存放。

中央大學表示，經由這個計畫，從夏威夷整年可以觀看 3/4 的天空，泛星望遠鏡從 2010 年 5 月起在可見光到紅外線 5 個波段拍攝，每個天區都觀測了起碼 12 次，不同波段的數據用於研究天體性質，而重複觀測則能夠指認出位置產生變化（例如：彗星），或是亮度發生變化（例如：爆發死亡的超新星）的天體或現象。

泛星天文台台長錢伯斯（Ken Chambers）說：「泛星計畫有很多重要發現，包括大批近地小行星、太陽系外圍小天體、銀河系的三維塵埃分布，以及爆發恆星等。這批數據公開後，全世界的科學家將有更多新的，以及意料之外的發現。」

「泛星計畫」是目前發現近地小天體最多的計畫，清點可能撞擊地球的天體，對於保護人類文明做出貢獻。台灣泛星計畫主持人、中央大學天文所所長陳文屏說：「以往觀察宇宙像是拍照片，

泛星則是幫夜空拍電影，我們得以從時間的觀點探討宇宙現象。」

中央大學指出，今晚首批公布「靜態」數據，包括數十億顆恆星與星系的精確位置與亮度；預計明年將發布第二批數據，包括每個天體在不同時期所測量的位置、亮度、影像等。即日起，任何人都可以利用泛星數據庫查詢從地球附近的小天體到遙遠的星系，赤緯負 30 度以北任何天體在不同波段的位置與亮度。

原文轉載自【2016-12-19 /中時電子報】

相關連結 / http://www.chinatimes.com/realtimenews/20161219005042-260405

2016/10/02 【大紀元日報】

「年輕天文學者獎」得主劉繼峰訪台窺視黑洞奧秘

【大紀元 2016 年 10 月 02 日訊】（大紀元記者徐乃義台灣桃園報導）「黑洞」和行星、恆星、星系迥然不同，不但是重要的科學課題，在小說與電影中尤其光怪離奇，可以讓太空船掉進去出不來，或是掉進去可以穿越時空，黑 洞是什麼？太空中真的有黑洞嗎？中央大學與台達電子文教基金會共同頒發的「年輕天文學者講座」，2016 年秋季獲獎者為中國科學院國家天文台的劉繼峰教授 來台訪問，接受頒獎並發表科學演講，訴說黑洞的故事。

中央大學天文所所長陳文屏解釋，當某個空間內塞進了過多物質，若沒有任何力量抵擋龐大的引力，這些物質內縮到無限小的體積內，便成為「黑洞」。這樣的質能狀態不僅隨著大小不同，而有特殊性質；我們熟悉的大千世界，甚至時間與空間的概念在黑洞附近也完全不管用。

研究黑洞吸積與噴流的交互作用的劉繼峰教授，榮膺今年秋季「年輕天文學者講座」，由台達電子文教基金會頒與講座獎金，中央大學天文所邀請來台學術訪 問。在台期間，除了將與天文所師生交流，另有 2 場科普演講訂於台中一中、台達電子台北總公司舉行，讓喜愛天文的民眾與學生得以與講者互動，認識黑洞。

原文轉載自【2016-10-02/大紀元日報】

相關連結 / http://www.epochtimes.com/b5/16/10/2/n8358368.htm

2016/09/30 【大成報】

2016 年秋季「年輕天文學者獎」得主　劉繼峰教授訪台發表黑洞奧秘

【大成報記者羅蔚舟／桃園報導】

「黑洞」大概是最吸引人的天體了，它和行星、恆星、星系迥然不同，不但是重要的科學課題，在小說與電影中尤其光怪離奇，可以讓太空船掉進去出不來，或是掉進去可以穿越時空，這是怎麼回事？黑洞是什麼？太空中真的有黑洞嗎？

由國立中央大學與台達電子文教基金會共同頒發的「年輕天文學者講座」，2016 年秋季獲獎者為中國科學院國家天文台的劉繼峰教授，自 9 月 28 日起來台訪問，接受頒獎並發表科學演講，訴說黑洞的故事。

劉繼峰教授研究太空物理，畢業於北京大學，2005 年取得美國密西根大學天文物理博士學位，之後在美國哈佛大學擔任愛因斯坦學者（Einstein Fellow）博士後研究與錢卓學者（Chandra Fellow）。自 2010 年起任職於中國科學院，並於 2015 年擔任中國科學院大學「天文與空間科學學院」副院長。

中央大學天文所所長陳文屏解釋，當某個空間內塞進了過多物質，若沒有任何力量抵擋龐大的引力，這些物質內縮到無限小的體積內，便成為「黑洞」。這樣的質能狀態不僅隨著大小不同，而有特殊性質；我們熟悉的大千世界，甚至時間與空間的概念在黑洞附近也完全不管用。

研究黑洞吸積與噴流的交互作用具有傑出成果的劉繼峰教授，經國際甄選委員會推薦候選，榮膺今年秋季「年輕天文學者講座」，由台達電子文教基金會頒與講座獎金，中央大學天文所邀請來台學術訪問。在台期間，除了將與天文所師生交流，另有兩場科普演講訂於台中一中、台達電子台北總公司舉行，讓喜愛天文的民眾與學生得以與講者互動，認識黑洞。

公開演講包含一場學術演講：9 月 30 日（週五）下午 2 點於中央

大學天文所（健雄館 1013 室），講題為「Ultraluminous Supersoft X-ray Sources as Super-critical Accretion onto Stellar Black Holes」，以及兩場中文科普演講「遇見黑洞」，分別於 10 月 1 日（週六）上午 9 點在台中一中（台中市育才街 2 號）、10 月 3 日（週一）下午 2 點在台達電子台北總公司（台北市內湖路陽光街 256 號）登場。

原文轉載自【2016-09-30/大成報】

相關連結 /
http://www.greatnews.com.tw/home/news_pagein.php?iType1009&n_id125082

2016/09/30 【勁報】

我要分享

2016 年秋季「年輕天文學者獎」得主　劉繼峰教授訪台發表黑洞奧秘

【勁報記者羅蔚舟／桃園報導】

「黑洞」大概是最吸引人的天體了，它和行星、恆星、星系迥然不同，不但是重要的科學課題，在小說與電影中尤其光怪離奇，可以讓太空船掉進去出不來，或是掉進去可以穿越時空，這是怎麼回事？黑洞是什麼？太空中真的有黑洞嗎？

由國立中央大學與台達電子文教基金會共同頒發的「年輕天文學者講座」，2016 年秋季獲獎者為中國科學院國家天文台的劉繼峰教授，自 9 月 28 日起來台訪問，接受頒獎並發表科學演講，訴說黑洞的故事。

劉繼峰教授研究太空物理，畢業於北京大學，2005 年取得美國密西根大學天文物理博士學位，之後在美國哈佛大學擔任愛因斯坦學者（Einstein Fellow）博士後研究與錢卓學者（Chandra Fellow）。自 2010 年起任職於中國科學院，並於 2015 年擔任中國科學院大學「天文與空間科學學院」副院長。

中央大學天文所所長陳文屏解釋，當某個空間內塞進了過多物質，若沒有任何力量抵擋龐大的引力，這些物質內縮到無限小的體積內，便成為「黑洞」。這樣的質能狀態不僅隨著大小不同，而有特殊性質；我們熟悉的大千世界，甚至時間與空間的概念在黑洞附近也完全不管用。

研究黑洞吸積與噴流的交互作用具有傑出成果的劉繼峰教授，經國際甄選委員會推薦候選，榮膺今年秋季「年輕天文學者講座」，由台達電子文教基金會頒與講座獎金，中央大學天文所邀請來台學術訪問。在台期間，除了將與天文所師生交流，另有兩場科普演講訂於台中一中、台達電子台北總公司舉行，讓喜愛天文的民眾與學生得以與講者互動，認識黑洞。

公開演講包含一場學術演講：9 月 30 日（週五）下午 2 點於中央

大學天文所（健雄館 1013 室），講題為「Ultraluminous Supersoft X-ray Sources as Super-critical Accretion onto Stellar Black Holes」，以及兩場中文科普演講「遇見黑洞」，分別於 10 月 1 日（週六）上午 9 點在台中一中（台中市育才街 2 號）、10 月 3 日（週一）下午 2 點在台達電子台北總公司（台北市內湖路陽光街 256 號）登場。

原文轉載自【2016-09-30/勁報】

相關連結 /
http://www.twpowernews.com/home/news_pagein.php?iType1009&n_id110737

2016/09/29 【民眾日報】

劉繼峰教授訪台　窺視黑洞奧秘

（記者鍾春蘭桃園報導）由國立中央大學與台達電子文教基金會共同頒發的「年輕天文學者講座」，2016 年秋季獲獎者為中國科學院國家天文台的劉繼峰教授，自本（9）月 28 日起來台訪問，接受頒獎並發表科學演講，訴說黑洞的故事。

中央大學天文所所長陳文屏解釋，當某個空間內塞進了過多物質，若沒有任何力量抵擋龐大的引力，這些物質內縮到無限小的體積內，便成為「黑洞」。這樣的質能狀態不僅隨著大小不同，而有特殊性質；我們熟悉的大千世界，甚至時間與空間的概念在黑洞附近也完全不管用。

研究黑洞吸積與噴流的交互作用具有傑出成果的劉繼峰教授，經國際甄選委員會推薦候選，榮膺今年秋季「年輕天文學者講座」，由台達電子文教基金會頒與講座獎金，中央大學天文所邀請來台學術訪問。在台期間，除了將與天文所師生交流，另有兩場科普演講訂於台中一中、台達電子台北總公司舉行，讓喜愛天文的民眾與學生得以與講者互動，認識黑洞。

公開演講包含一場學術演講：9 月 30 日（週五）下午 2 點於中央大學天文所（健雄館 1013 室），講題為「Ultraluminous Supersoft X-ray Sources as Super-critical Accretion onto Stellar Black Holes」，以及兩場中文科普演講「遇見黑洞」，分別於 10 月 1 日（週六）上午 9 點在台中一中（台中市育才街 2 號）、10 月 3 日（週一）下午 2 點在台達電子台北總公司（台北市內湖路陽光街 256 號）登場。

劉繼峰教授研究太空物理，畢業於北京大學，2005 年取得美國密西根大學天文物理博士學位，之後在美國哈佛大學擔任愛因斯坦學者（Einstein Fellow）博士後研究與錢卓學者（Chandra Fellow）。自 2010 年起任職於中國科學院，並於 2015 年擔任中國科學院大學「天文與空間科學學院」副院長。

原文轉載自【2016-09-29/民眾日報】

相關連結 / http://www.mypeople.tw/article.php?id1316506

2016/09/29 【皇家時報】

2016 年秋季「年輕天文學者獎」得主劉繼峰教授訪台　窺視黑洞奧秘

「黑洞」大概是最吸引人的天體了，它和行星、恆星、星系迥然不同，不但是重要的科學課題，在小說與電影中尤其光怪離奇，可以讓太空船掉進去出不來，或是掉進去可以穿越時空，這是怎麼回事？黑洞是什麼？太空中真的有黑洞嗎？

由國立中央大學 與台達電子文教基金會共同頒發的「年輕天文學者講座」，2016 年秋季獲獎者為中國科學院國家天文台的劉繼峰教授，自本（9）月 28 日起來台訪問，接受頒獎並發表科學演講，訴說黑洞的故事。

劉繼峰教授研究太空物理，畢業於北京大學，2005 年取得美國密西根大學天文物理博士學位，之後在美國哈佛大學擔任愛因斯坦學者（Einstein Fellow）博士後研究與錢卓學者（Chandra Fellow）。自 2010 年起任職於中國科學院，並於 2015 年擔任中國科學院大學「天文與空間科學學院」副院長。

中央大學 天文所所長陳文屏解釋，當某個空間內塞進了過多物質，若沒有任何力量抵擋龐大的引力，這些物質內縮到無限小的體積內，便成為「黑洞」。這樣的質能狀態不僅隨著大小不同，而有特殊性質；我們熟悉的大千世界，甚至時間與空間的概念在黑洞附近也完全不管用。

研究黑洞吸積與噴流的交互作用具有傑出成果的劉繼峰教授，經國際甄選委員會推薦候選，榮膺今年秋季「年輕天文學者講座」，由台達電子文教基金會頒與講座獎金，中央大學 天文所邀請來台學術訪問。在台期間，除了將與天文所師生交流，另有兩場科普演講訂於台中一中、台達電子台北總公司舉行，讓喜愛天文的民眾與學生得以與講者互動，認識黑洞。

公開演講包含一場學術演講：9 月 30 日（週五）下午 2 點於中央大學 天文所（健雄館 1013 室），講題為「Ultraluminous Supersoft

X-ray Sources as Super-critical Accretion onto Stellar Black Holes」，以及兩場中文科普演講「遇見黑洞」，分別於 10 月 1 日（週六）上午 9 點在台中一中（台中市育才街 2 號）、10 月 3 日（週一）下午 2 點在台達電子台北總公司（台北市內湖路陽光街 256 號）登場。

原文轉載自【2016-09-29/皇家時報】

相關連結 / http://blog.xuite.net/royaltimes98/wretch1/454487467

2016/09/29 【聯合財經網】

年輕天文學者獎劉繼峰窺視黑洞奧秘

記者 曹松清 / 報導

由國立中央大學與台達電子文教基金會共同頒發的「年輕天文學者講座」，2016 年秋季獲獎者為中國科學院國家天文台的劉繼峰教授，9 月 28 日起來台訪問，接受頒獎並發表科學演講，訴說黑洞的故事。

劉繼峰研究太空物理，畢業於北京大學，2005 年取得美國密西根大學天文物理博士學位，之後在美國哈佛大學擔任愛因斯坦學者（Einstein Fellow）博士後研究與錢卓學者（Chandra Fellow）。自 2010 年起任職於中國科學院，並於 2015 年擔任中國科學院大學「天文與空間科學學院」副院長。

中央大學天文所所長陳文屏解釋，當某個空間內塞進了過多物質，若沒有任何力量抵擋龐大的引力，這些物質內縮到無限小的體積內，便成為「黑洞」。這樣的質能狀態不僅隨著大小不同，而有特殊性質；我們熟悉的大千世界，甚至時間與空間的概念在黑洞附近也完全不管用。

研究黑洞吸積與噴流的交互作用具有傑出成果的劉繼峰，經國際甄選委員會推薦候選，榮膺今年秋季「年輕天文學者講座」，由台達電子文教基金會頒與講座獎金，中央大學天文所邀請來台學術訪問。在台期間，除了將與天文所師生交流，另有兩場科普演講訂於台中一中、台達電子台北總公司舉行，讓喜愛天文的民眾與學生得以與講者互動，認識黑洞。

公開演講包含一場學術演講：9 月 30 日（週五）下午 2 點於中央大學天文所（健雄館 1013 室），講題為「Ultraluminous Supersoft X-ray Sources as Super-critical Accretion onto Stellar Black Holes」，以及兩場中文科普演講「遇見黑洞」，分別於 10 月 1 日（週六）上午 9 點在台中一中（台中市育才街 2 號）、10 月 3 日（週一）下午 2 點

在台達電子台北總公司（台北市內湖路陽光街 256 號）登場。

原文轉載自【2016-09-29 /聯合財經網】

相關連結 / http://money.udn.com/money/story/5723/1992196

2016/09/29 【大紀元】

「年輕天文學者獎」得主劉繼峰教授訪台窺視黑洞奧秘

記者 徐乃義／桃園 報導

「黑洞」和行星、恆星、星系迥然不同，不但是重要的科學課題，在小說與電影中尤其光怪離奇，可以讓太空船掉進去出不來，或是掉進去可以穿越時空，黑洞是什麼？太空中真的有黑洞嗎？中大與台達電子文教基金會共同頒發的「年輕天文學者講座」，2016 年秋季獲獎者為中國科學院國家天文台的劉繼峰教授來台訪問，接受頒獎並發表科學演講，訴說黑洞的故事。

中大學天文所所長陳文屏解釋，當某個空間內塞進了過多物質，若沒有任何力量抵擋龐大的引力，這些物質內縮到無限小的體積內，便成為「黑洞」。這樣的質能狀態不僅隨著大小不同，而有特殊性質；我們熟悉的大千世界，甚至時間與空間的概念在黑洞附近也完全不管用。

研究黑洞吸積與噴流的交互作用的劉繼峰教授，榮膺今年秋季「年輕天文學者講座」，由台達電子文教基金會頒與講座獎金，中大天文所邀請來台學術訪問。在台期間，除了將與天文所師生交流，另有兩場科普演講訂於台中一中、台達電子台北總公司舉行，讓喜愛天文的民眾與學生得以與講者互動，認識黑洞。

原文轉載自【2016-09-29 /大紀元】

相關連結 / http://www.epochtimes.com.tw/n183518/

2016/09/29 【中時電子報 Campus】

天文學者獎得主劉繼峰訪台 窺視黑洞奧秘

記者 廖育婉 / 報導

「黑洞」大概是最吸引人的天體了，它和行星、恆星、星系迥然不同，不但是重要的科學課題，在小說與電影中尤其光怪離奇，可以讓太空船掉進去出不來，或是掉進去可以穿越時空，這是怎麼回事？黑洞是什麼？太空中真的有黑洞嗎？

由國立中央大學與台達電子文教基金會共同頒發的「年輕天文學者講座」，2016 年秋季獲獎者為中國科學院國家天文台的劉繼峰教授，自本（9）月 28 日起來台訪問，接受頒獎並發表科學演講，訴說黑洞的故事。

劉繼峰教授研究太空物理，畢業於北京大學，2005 年取得美國密西根大學天文物理博士學位，之後在美國哈佛大學擔任愛因斯坦學者（Einstein Fellow）博士後研究與錢卓學者（Chandra Fellow）。自 2010 年起任職於中國科學院，並於 2015 年擔任中國科學院大學「天文與空間科學學院」副院長。

中央大學天文所所長陳文屏解釋，當某個空間內塞進了過多物質，若沒有任何力量抵擋龐大的引力，這些物質內縮到無限小的體積內，便成為「黑洞」。這樣的質能狀態不僅隨著大小不同，而有特殊性質；我們熟悉的大千世界，甚至時間與空間的概念在黑洞附近也完全不管用。

研究黑洞吸積與噴流的交互作用具有傑出成果的劉繼峰教授，經國際甄選委員會推薦候選，榮膺今年秋季「年輕天文學者講座」，由台達電子文教基金會頒與講座獎金，中央大學天文所邀請來台學術訪問。在台期間，除了將與天文所師生交流，另有兩場科普演講訂於台中一中、台達電子台北總公司舉行，讓喜愛天文的民眾與學生得以與講者互動，認識黑洞。

公開演講包含一場學術演講：9 月 30 日（週五）下午 2 點於中央大學天文所（健雄館 1013 室），講題為「Ultraluminous Supersoft X-ray Sources as Super-critical Accretion onto Stellar Black Holes」，以及兩場中文科普演講「遇見黑洞」，分別於 10 月 1 日（週六）上午 9 點在台中一中（台中市育才街 2 號）、10 月 3 日（週一）下午 2 點在台達電子台北總公司（台北市內湖路陽光街 256 號）登場。

原文轉載自【2016-09-29 /中時電子報 Campus】

相關連結 / http://campus.chinatimes.com/20160929004187-262306

2016/07/25 【聯合財經網】

我要分享

中央大學矮柱路燈讓星空再現

記者 曹松清/報導

台灣多山，雖然造成平地面積狹小，但是山中的各種資源卻成為一大珍寶。而其中遠離城市，在中橫附近的幾段高山公路因幾無城市光害，是東亞的觀星聖地。

然而台灣的高山公路卻因坡度陡峭與轉彎處多，路燈的裝設往往因行車安全而不可或缺，但是其光害卻是觀星的最大殺手。日前武嶺的路燈因眩光與光害的影響造成觀星網友的韃伐而導致緊急拆除，道路安全與星空觀測形成魚與熊掌不可得兼的現象。

中央大學光電中心主任孫慶成教授表示，一個防眩光與低光害的路燈設計重點在於燈頭看起來要暗，發射的光線要能收斂在道路區域，亦即從光源發射的光線藉由燈具的設計，能夠將絕大多數光的能量集中在照射區域，而不是往天空照射，這樣燈頭看起來就會暗，而非明亮。

孫慶成的研究團隊在 2012 年即在頂尖期刊「光學快遞」中發表一款新的 LED 路燈，不但從遠處看其燈頭幾乎是暗的，路燈照在特定區域的光學能量效率也達到 81%，遠遠超過一般的 40%水準。該路燈受到包括華爾街日報在內的 30 多個國際媒體的報導。

孫慶成進一步表示，高掛的路燈，不管如何設計，還是會對附近使用者在觀望星空時產生影響，理想的燈應該是接近腰部高的路燈。由於中央大學專長於太空與大氣科學，如何降低天空的光害一直是團隊的研究課題，因此研究團隊早已進行防光害的路燈設計。中央大學已經設計出一款可用於高山觀星的營地道路照明路燈，該路燈高度低於一公尺，具有光線上揚角度的截止線，在一米高度以上的光線非常稀少，同時幾乎所有光線皆能柔和地分布於六十平方米的長方形地面上，光學設計相當巧妙。

孫慶成表示，該矮柱式路燈是全球第一款具廣域地面照明且有上揚光線截止線的燈具，完全是為防止光害而設計，相較於一般路燈如汽車的遠光燈般眩眼，中大的設計使用汽車近光燈的防眩設計，具有光線仰角的抑制。其實一般汽車近光頭燈的高對比截止線就是為了避免對路人造成眩光，而中大的矮柱路燈不但具有相同的防眩功能，還可以減少光害並對路面進行柔和的照明，可以兼具道路照明與星空再現，會是觀星者的最愛。

原文轉載自【2016-07-25 / 聯合財經網】

相關連結 / http://money.udn.com/money/sty/5735/1850764

2016/07/15 【聯合財經網】

葉永烜榮膺院士感念父母手足慷慨付出

經濟日報 曹松清

國立中央大學 13 日舉辦「葉永烜教授榮膺中央研究院院士慶祝茶會暨畫作捐贈儀式」，校長周景揚、中大學術基金會董事長劉兆漢、台聯大系統副校長綦振瀛、台達電子副總裁蔡榮騰、天文所所長陳文屏及教職員同仁等多位嘉賓齊聚賀喜。問及葉永烜的感想，他幽默比喻：「猶如老來得子。」

周景揚開場介紹新科院士，天文所葉永烜教授專長行星科學、太空物理及天文物理，1998 年起在中大任教，曾任理學院院長、副校長、台聯大系統副校長等職，具 15 年以上的豐富行政資歷。他的研究成就卓然耀眼，去年有 10 篇論文發表於國際兩大知名期刊《自然（Nature）》、《科學（Science）》，而迄今共計 60 篇論文刊載於此，其中 12 篇為葉永烜專文。

葉永烜也參與多項國際太空計畫，包含推動探測土星的「卡西尼計畫」、研究彗星的「羅賽塔計畫」等等。周景揚感謝葉永烜對學校貢獻良多，中央大學在國際合作表現相當優異，據《美國新聞與世界報導（U.S. News & World Report）》分析統計，中大於「國際合作」項目排名全球第 18 名，大幅領先國內多所大學。

他對天文及太空研究的貢獻，曾獲頒美國太空總署「特殊公共服務」榮譽勳章、卡西尼土星計畫團隊成就獎、伽利略木星計畫團隊成就獎等殊榮。2015 年也二度獲得教育部國家講座，今年榮膺中央研究院第 31 屆數理科學組院士，堪稱實至名歸。

同為院士的劉兆漢說，上週公布新科院士名單後，不少院士紛紛說：「早該得了」，突顯葉永烜的學術研究早已獲得相當的成就和敬重。劉兆漢說，38 年前，他在德國的馬克斯蒲朗克研究院第一次與葉永烜見面，談的是客家人的貢獻；兩人認識後，他很欣賞葉永烜，也於日後邀請他到中央大學任教。

劉兆漢表示，得知葉永烜榮膺中研院院士他很高興，這表示其在科學上的貢獻獲得大家的肯定。他也為中央大學高興，相信中大會記著葉永烜的貢獻並深懷感謝。

慶祝茶會上，葉永烜難得地公開表達他對父母、家人的感謝之意。他說，他的父母那一代在戰亂苦難中度過，他的父親可能從來沒有想過大兒子有一天會成為中央研究院院士，今日，他為自己的父母感到高興。

他說，他個人做研究看似無所顧慮，但其實背後是家人的犧牲和扶持，幾十年來弟妹照顧父母、照顧家人，這才是他有所成就最重要的因素。

他分享哲學家紀伯倫的話，「慷慨」不是給對方想要的東西，而是把你想要的東西給對方。葉永烜感恩他的父母、兄弟姊妹的付出，讓他成就了他自己；他也感謝中央大學的教職員同仁，也是盡心盡力，慷慨付出，成就他人。

閒暇時喜愛繪畫的葉永烜，上月起在中大校內舉辦油畫創作個展。其中有六幅以教務處等一級行政單位為主題發想的畫作，他也在茶會上特別贈與中大，留下一方最美麗動人的校園人文風景。

相關連結 / http://money.udn.com/money/sty/5723/1830493-%E8%91%89%E6%B0%B8%E7%83%9C%E6%A6%AE%E8%86%BA%E9%99%A2%E5%A3%AB-%E6%84%9F%E5%BF%B5%E7%88%B6%E6%AF%8D%E6%89%8B%E8%B6%B3%E6%85%B7%E6%85%A8%E4%BB%98%E5%87%BA

2016/07/14 【中國時報】

當選中研院士 葉永烜：像老來得子

記者 楊明峰／桃園報導

國際知名天文學家、國立中央大學教授葉永烜，上周獲選第 31 屆中研院士，他表示，感謝父母、兄弟姊妹的付出，讓他無後顧之憂，專心在學術研究。被問到獲選中研院士感想？葉永烜認為，「像老來得子」，不知高興與否？心情難以言喻。

69 歲德國籍華裔葉永烜，專長行星科學、太空物理及天文物理，曾提出探測土星的「卡西尼計畫」、參加羅賽塔號等太空探測任務，至今有 60 篇論文刊載於國際知名期刊 Nature（自然）、Science（科學），1998 年起在中大任教，曾任理學院院長、副校長、台聯大系統副校長等職。

因天文、太空的研究貢獻，葉永烜獲頒美國太空總署「特殊公共服務」榮譽勳章、卡西尼土星計畫團隊成就獎、伽利略木星計畫團隊成就獎，更二度獲得台灣教育部國家講座，今年獲選中研院數理科學組院士。

幼年歷經國共內戰的顛沛流離，葉永烜感謝家人的犧牲、奉獻，讓他得以留學歐美，專心做科學研究。

葉永烜指出，中研院院士是種榮譽，可鼓勵年輕人投入基礎科學研究，可能 100 個研究中大多沒有用處，純粹是研究者的對科學的好奇，但其中有一個若是成功、有用，就很不得了。

「只要有一個愛因斯坦就夠了！」葉永烜說，社會若要進步，要培養這樣的人，投資 100 個有 99 個沒用，但至少沒有害，就像是做生意投資，盼望有一個有用處，帶給社會很大的進步。

校方昨為葉永烜舉行獲選院士慶祝茶會，葉會中捐出 6 幅畫作給學校。

原文轉載自【2016-07-14/中國時報】

相關連結 / http://www.chinatimes.com/newspapers/20160714000616-260107

2016/07/13 【客家電視台】

客籍天文教授葉永烜獲選中研院院士

【羅安達 桃園】

中央研究院，日前選出 20 名新院士，數理科學組 6 人中，其中一位是中央大學，天文所的客籍教授葉永烜，葉永烜教授的研究專長是彗星，太陽系與行星形成、電漿物理等，葉教授說，中研院士是台灣最高的學術榮譽，他很榮幸也很感謝，未來會繼續努力，讓台灣天文科學有更長遠的發展。

「在 a 是它的半徑，半徑是 a 的小行星。」

黑板上密密麻麻的運算公式，在新任中研院院士，葉永烜教授的解說下，像是穿透的冷冷神秘感，新科院士葉永烜教授，是國立中央大學天文研究所，與太空科學研究所講座教授，並於澳門科技大學出任特聘教授，身為新院士，希望提出的建，政府可以傾聽，只要政府的態度正確，對台灣還是會有很好的發展。

新任中研院院士 葉永烜：「過去希望，現在也是一樣，就是政府會多多傾聽，他們(院士)的想法，因為到底他們院士，他們就是大概他們也看事情比較，怎麼說廣一點。」

而在台灣天文發展，葉教授卻提出「少子化」的危機感，他認為任何一項研究，沒有人來學習，對於任何發展都沒有幫助。

新任中研院院士 葉永烜：「少子化就是有很多複雜的後果，因為不是一個人，多生一個小孩就夠了是吧，其它就是時間不夠時間不夠，以後的 10 年、20 年，這樣的情況之下，我們要怎麼發展。」

長期專注研究天文的葉永烜，其實深受青光眼所苦，現在幾近半盲，但他說獲選為中研院院士是個責任，他會努力去完成院士該有的任務，而對於未來宇宙天文，葉教授則說，他希望有更多台

灣年輕人，願意投入天文學和太空科學研究，讓這門看似冰冷的科學，能夠更加發光發熱。

原文轉載自【2016-7-13/客家電視台】

相關連結 / http://www.hakkatv.g.tw/news/141360

2016/07/13 【中廣新聞網】

我要分享

中大教授葉永烜榮膺院士感謝家人犧牲扶持

國立中央大學葉永烜教授榮膺中央研究院院士，今天校方舉辦慶祝茶會及畫作捐贈儀式，會中，葉永烜教授表達對父母、家人的感謝之意，他在研究看似無所顧慮，但其實背後是家人的犧牲和扶持，才是他有所成就最重要的因素。

中大表示，葉永烜教授正在校內舉辦油畫創作個展，其中有六幅畫作是以教務處等一級行政單位為主題發想，在茶會上將這 6 幅贈送給中大，留下最美麗動人的校園人文風景。

中央大學校長周景揚表示，天文所葉永烜教授專長行星科學、太空物理及天文物理，1998 年起在中大任教，具 15 年以上的豐富行政資歷，他的研究成就卓然耀眼，去年有 10 篇論文發表在國際兩大知名期刊自然（Nature）、科學（Science），迄今共計 60 篇論文刊載，其中 12 篇為葉永烜專文。

中大表示，葉永烜教授也參與多項國際太空計畫，包含推動探測土星的「卡西尼計畫」、研究彗星的「羅賽塔計畫」等等，對學校貢獻良多。

原文轉載自【2016-7-13/中廣新聞網】

相關連結 / http://www.bcc.com.tw/newsView.2849809

2016/07/13 【自由時報】

新科中研院士葉永烜 獲選心情「猶如老來得子」

記者 李容萍／桃園報導

知名德國籍華人天文學家、現任國立中央大學天文所及太空科學所教授葉永烜，獲選中央研究院第 31 屆院士，中大今天為他舉辦慶祝茶會，校長周景揚率教職員蒞會祝賀，喜歡繪畫的葉永烜趁著在中大展出油畫之際，把其中 6 幅各自以中大行政單位為主題發想的畫作捐贈給中大。

69 歲的葉永烜，雖選擇科學研究做為一生的志業，但並未忘記從小對畫畫的喜愛，小學時曾幫同學畫一張坦克車或飛機，賺到兩張圖畫紙，但之後卻沒有繼續畫，直到 40 歲在德國大學研究所工作，住在什麼都沒有的小鎮，週末沒事做，每週開車送妻小到市中心購物時，總被一家賣畫筆的小店吸引，直到有一天鼓起勇氣推開那扇門。由於德國的畫筆價格高，剛開始他拿孩子的蠟筆作畫，因深愛油畫，曾為了省錢，拿燭火燒蠟筆，靠蠟滴作畫。

由於之前也曾獲得中研院院士提名，如今他以「猶如老來得子」來比喻自己當選院士的心情 ，並表達對父母、家人的謝意，投入研究看似無所顧慮，其實背後是家人的犧牲和扶持。

葉永烜說，研究基礎科學的人，常因喜歡、好奇常做很多研究，很多研究結果都沒有用處，但 100 個研究中如果有 1 個是成功、有意思的就不得了，現在能有多少愛因斯坦？有一個就夠了，他認為社會要進步的話，就要培養這樣的人，就像做生意有投資才有回收。

會中，同為中研院院士的中大學術基金會董事長劉兆漢也說，新科院士名單公布後，不少院士都說：「葉永烜早該得了」。

原文轉載自【2016-07-13 /自由時報】

相關連結 / http://news.ltn.com.tw/news/life/breakingnews/1762030

2016/07/08 【聯合報】

數理科學組／葉永烜激勵了天文學者

記者嚴文廷／台北報導

中研院數理科學組昨天選出六位新科院士，其中鑽研全球大規模造山運動的台大地質系教授、中研院地球所特聘研究員鍾孫霖是一路從台大地質系學士、碩士、博士，台灣土生土長培養出的院士，他得知獲選時，有點激動地說：「很高興這次能和前輩葉永烜一起當選，對於能有兩位地球科學領域獲選院士感到很開心。」

中央大學天文所及太空科學所教授葉永烜，受訪時自嘲說：「滿高興的，但你知道其實我已經入選為候選人好幾次了！」他強調，地球科學是基礎科學，只是研究的內容對社會有應用性，像颱風、地震等，這能讓兩位地球科學學者獲選，表達了這個學科對台灣的需求，是有其特色存在，也希望自己的獲選，能讓從事天文和地球科學研究學者是一種激勵。

原文轉載自【2016-07-08/聯合報】

相關連結 / http://udn.com/news/sty/9804/1814981

2016/06/23 【自由時報】

從地球觀測恆星塵埃 中研院 ALMA 研發獲認可

記者黃邦平／台北報導

探索天空的秘密一直是人類最大的夢想之一，國際合作在智利打造阿塔卡瑪大型毫米及次毫米波陣列（ALMA），中央研究院主導開發「第一頻段接收機」已獲認可、即將量產，可觀測鄰近恆星附近「公分尺度」的星際塵埃顆粒生成過程，見證行星誕生。

ALMA 共有 66 座天線，每座配備靈敏 10 組不同的的接收機，偵測、接收來自宇宙的 10 個頻段（Band）毫米電波，目前還剩第一、二、五頻段還在發展中。
中研院天文所研發的第一頻段接收機具有「低雜訊、高靈敏度、高動態範圍」特性，含備用共將製作 73 套，預計 2019 年底前安裝完成。

中研院天文及天文物理研究所副研究員黃裕津說，第一頻段接收機安裝後，ALMA 可觀測範圍的波長將延展至目前的 2 倍，即可偵測到紅移更高的遙遠天體，可觀測的宇宙空間也能擴展為目前的 8 倍，可偵測遙遠的宇宙早期恆星誕生雲氣團，並可觀測鄰近恆星的行星系統形成初始階段，台灣提供實物製作，也確保台灣所有天文學家以觀測計畫競投即可取得世界最先進天文儀器 ALMA 的使用權。

望遠鏡是看宇宙用的人造眼，ALMA 設計以 66 座天線形成干涉儀，透過天線不同方式排列，可看到不同細節，視力相當於直徑 16 公里的望遠鏡，靈敏度極高、清晰度也非常好，是哈伯太空望遠鏡的 10 倍。
第一頻段接收機計畫研發經理黃耀德表示，由於第一頻段的物理特性，技術要求遠比現有任何接收機系統更嚴苛，ALMA 望遠鏡採用，也是肯定台灣的電波天文儀器研發居世界領導地位。

這批接收機將由天文所與國家中山科學研究院航空研究所合作製造及整合測試，從零組件到系統的研製歷經 10 年，8 年前天文所

與日本國立天文台、智利大學、美國國家電波天文台、加拿大赫茲堡天文物理研究所及國家中山科學研究院組成國際合作團隊，並與國立台灣大學、國立中央大學、國立中正大學、國立台北大學合作開發接收機內部使用的毫米波電子積體電路與濾波器元件。計畫經費由本院與科技部支持。

ALMA 計畫是有史以來最大規模的地面型天文望遠鏡，建置在智利北部海拔 5000 公尺阿塔卡瑪沙漠中，由東亞、歐洲南天天文台會員國、北美等 3 組區域團隊及地主國智利等 22 國合作，自 2013 年 3 月啟用，將運轉至少 50 年。

原文轉載自【2016-06-23/自由時報】

相關連結 / http://news.ltn.com.tw/news/life/breakingnews/1739053

2016/05/30 【聯合新聞網】

澳洲天文學家柯莉莉 中央大學科普演講

記者鄭國樑／即時報導

人類每人平均 1 年需吸進 1 公噸氧氣，但是地球誕生之初卻沒有氧元素，氧氣究竟從何而來？國立中央大學、台達電子文教基金會邀請澳洲天文學者柯莉莉（Lisa Kewley）教授來台學術交流並發表科普演講，她專研究氧原子及星系演化，藉由氧氣的來龍去脈訴說宇宙天體演化的故事。

柯莉莉教授 6 月 3 日下午 2 點於中央大學天文所發表學術演講「星系組成和演化」，另以「氧氣：宇宙氣息」為題發表兩場公開科普演講，現場提供中文講解。

中大天文所所長陳文屏說，星系由千億顆恆星組成，是宇宙的基本結構，它的演化過程令人好奇。當初宇宙誕生大霹靂產生了氫與氦，其他元素幾乎都是恆星核融合的產物，隨著星系當中代代恆星的生老病死，拋回太空，豐富了星際物質的複雜元素，而我們生活的大千世界，包括人類身上的氧、磷、鐵、鈣，也都來自恆星。

他闡述，檢驗農田的土壤可以得知歷年來曾經種植的作物、噴施過的肥料等等，同樣的道理，若藉由分析星系的化學組成，則可解讀該星系的演化過程。

我們平常呼吸的氧氣，也存在於太空，由於氧原子對溫度很靈敏，柯莉莉用氧原子來追蹤星系當中複雜元素的含量以及性質，並利用尖端設備與巧妙的手段，觀測宇宙不同時期的星系，探討複雜元素的化學演化史，提升我們對星系演化的認知。

柯莉莉教授目前任職於澳洲國立大學天文與天文物理研究所，2004 年獲選哈伯學者，2014 年當選澳洲科學院院士、2016 年成為澳洲研究委員會會士。榮膺 2016 年春季「年輕天文學者講座」，該講座表彰國際上在天文學領域有卓越表現的年輕學者。

原文轉載自【2016-05-30/聯合新聞網】

相關連結 / http://udn.com/news/story/9/1729334-%E6%BE%B3%E6%B4%B2%E5%A4%A9%E6%96%87%E5%AD%B8%E5%AE%B6%E6%9F%AF%E8%8E%89%E8%8E%89-%E4%B8%AD%E5%A4%AE%E5%A4%A7%E5%AD%B8%E5%AD%B8%E8%A1%93%E6%BC%94%E8%AC%9B

2016/04/28 【聯合報】

「屏東」小行星 高高掛天空

記者翁禎霞／屏東報導

屏東縣政府與中央大學昨天正式宣布，現在起，有 1 顆叫「Pingtung」（屏東）的小行星就掛在天空！
中央大學鹿林天文台是於 2006 年發現這顆第 175583 號小行星，經過至少 4 次的鑑定，並送請國際天文學聯合會審查，今年 3 月通過命名為「Pingtung」。

這顆名為「屏東」的小行星，直徑粗估約 3-6 公里，大小約如小琉球，繞行太陽 1 圈約 5.55 年，離太陽最近時約 4.3 億公里，離太陽最遠時約 5.1 億公里，距離地球最近距離約為 2.8 億公里。

2006 年 10 月 15 日，鹿林天文台觀測員林啟生是在比對電腦資料時，發現有顆在金牛座附近的天體正在移動，經當時還是高中生的葉泉志比對，再通報國際小行星中心確認，之後經過至少 4 次在回歸中被觀測到，又能精準地測定軌道，終於獲得小行星的永久編號，並取得命名權。

為讓台灣也登上宇宙，近年團隊以台灣縣市為小行星命名，這顆「Pingtung」是台灣第十三個以縣市命名的小行星。

另外，屏東唐榮國小成立尋星小隊，今年也獲錄取「國際天文搜尋聯盟」全球天文月小行星搜尋活動，為東亞地區唯一獲選隊伍，更是全台灣唯一獲選的團隊。

唐榮國小校長施世治表示，尋星小隊師生們迄今已發現 8 顆可能為小行星的資料數據，已立刻向 IASC 回報，期待能為屏東天文教育創下劃時代的紀錄。

原文轉載自【2016-04-28/聯合報】

相關連結 / http://udn.com/news/story/7314/1658497-%E3%80%8C%E5%B1%8F%E6%9D%B1%E3%80%8D%E5%B0%8F%E8%A1%8C%E6%98%9F-%E9%AB%98%E9%AB%98%E6%8E%9B%E5%A4%A9%E7%A9%BA

2016/04/28 【中國時報】

以中央大學天文所長故鄉為名 小行星命名屏東

記者林和生／屏東報導

2006 年中央大學鹿林天文台在太陽系火星及木星間的小行星帶上，發現編號第 175583 號小行星，經送請國際天文學聯合會審查，近期通過以中央大學天文所所長陳文屏故鄉「Pingtung（屏東）」為名，成為全台第 13 個以縣市命名的小行星，也讓屏東登上宇宙星際。

屏東登上宇宙星際

縣長潘孟安、中央大學校長周景揚及小行星發現者林啟生，昨共同發表這項天文好消息，正式介紹 Pingtung 小行星誕生。中央大學國家講座教授葉永烜指出，屏東小行星大小粗估約 3 至 6 公里，繞行太陽 1 圈約 5.55 年（軌道週期），距地球約 2.8 億公里。

小行星是目前各類天體唯一能由發現者命名並得到世界公認的天體，當 1 顆小行星至少 4 次在回歸中被觀測到，軌道又能非常精確測定時，它就會得到一個永久編號。

一旦小行星取得永久編號，發現者擁有該小行星永久命名權，提出名稱必須經過國際天文學聯合會（IAU）小天體命名委員會審查通過並公告，就可成為該小行星的正式永久名稱，從發現到命名確認往往需數年觀測。

發展天文教育重點

潘孟安興奮表示，雖然屏東小行星距離遙遠，到底穹蒼之下的狀況如何不得而知，但兩者從此刻擦出火花，將是屏東縣日後發展天文教育重點。

原文轉載自【2016-04-28/中國時報】

相關連結 / http://www.chinatimes.com/newspapers/20160428000569-260107

2016/04/27 【中廣新聞網】

央大發現小行星 獲國際通過命名為「屏東」

國立中央大學鹿林天文台 2006 年在太陽系火星與木星之間的小行星帶上，發現「第 175583 號」小行星，經送請國際天文學會聯合會審查，上個月通過命名為「Pingtung(屏東)」，讓屏東登上宇宙星際；中央大學這幾年以台灣的縣市為鹿林天文台發現的小行星命名，這顆「Pingtung(屏東)」是台灣第 13 個以縣市命名的小行星。（溫蘭魁報導）

發現這顆小行星的是鹿林天文台觀測員林啟生，屏東縣長潘孟安今天(27 日)中午和中央大學校長周景揚一起發表這項天文好消息，並且和發現者林啟生共同點亮小行星，正式介紹「Pingtung(屏東)」小行星誕生。

中央大學國家講座教授葉永烜表示，小行星是目前各類天體中唯一可以由發現者進行命名，並得到世界公認的天體「天文國際聯盟有個中心，告訴他們說，我們發現有一個新的東西，就是我們跟國際天文聯盟說，我們為什麼要命名屏東小行星，他們就很高興的接受了。」

發現屏東小行星的觀測員林啟生表示，屏東小行星的大小粗估約 3 到 6 公里，相當於屏東市區或是離島小琉球的大小，繞行太陽一圈大約 5.55 年（軌道週期），距離太陽最近的時候大約 4.3 億公里，離太陽最遠時大約 5.1 億公里，距離地球 2.8 億公里左右，這顆「Pingtung(屏東)」小行星是 2006 年 10 月 15 號被發現，當時是在金牛座附近，現在、2016 年 4 月的位置則在魔羯座。（攝影：溫蘭魁）

原文轉載自【2016-04-27/中廣新聞網】

相關連結 / http://www.bcc.com.tw/newsView.2798250

2016/03/04 【自由時報】

〈北部〉小行星、植物 也以苗栗命名

記者鄭鴻達／苗栗報導

首艘以苗栗命名的巡防救難艦「苗栗艦」，將在四月底成軍，捍衛我國漁權。除了巡防艦，中央大學發現的小行星也以苗栗的英文「Miaoli」命名，另，「苗栗冬青」更是台灣唯一以地名為名的植物。

首艘以苗栗命名的海洋巡防救難艦「苗栗艦」，將在四月底正式成軍，駐紮於台中港，巡守苗栗、台中、彰化等中部海岸線，擔負守護漁權、民眾生命安全的重任。

中央大學天文所觀測助理蕭翔耀和廣州中山大學葉泉志同學，於九十七年共同發現編號二四六六四三小行星，並申請命名為「苗栗小行星」，以感念民國五十一年，中央大學來到台灣，於苗栗縣復校時，縣府與地方人士捐地的熱心協助。

而別名「刺葉冬青」的「苗栗冬青」，多分布在台灣海拔二千六百到三千二百公尺的山區，在民間常被用來作為園藝景觀植栽、盆景，是唯一用台灣地名命名的植物，如此命名方式，就是要宣告它屬於台灣原生植物之一。

原文轉載自【2016-03-04/自由時報】

相關連結 / http://news.ltn.com.tw/news/local/paper/964628

2016/09/26 【大紀元】

天文奇事多 海王星周圍新添 5 顆神秘星體

記者 張秉開 / 編譯報導

宇宙太空有很多意想不到的現象。在太陽系中，除九大行星之外，還有其它類型的星球，如各種小行星。科學家近日發現海王星的周圍又新添 5 顆怪異的星體——特洛伊小行星（Trojan asteroids），但未查明其來源。

據今日宇宙（universetoday.com）報導，主持這項研究的台灣國立中央大學天文學家林省文（Hsing-Wen Lin）表示，研究者使用夏威夷的全景巡天望遠鏡和快速反應系統（Pan-STARRS，簡稱「泛星望遠鏡」）發現並確認這些小行星。

研究者從 2010 年 5 月開始觀測，歷經四年直到 2014 年 5 月方鑑別出 5 顆直徑 100～200 公里的海王星-特洛伊族小行星。其中 4 顆特洛伊小行星和 1 顆特洛伊小行星分別位於兩種不同的不穩定軌道，因此推測它們可能是臨時被海王星擄獲的小行星。但是，研究者不清楚這 5 顆特洛伊小行星的來源。

特洛伊小行星是指軌道與太陽系的某顆大行星交疊的一類小型天體，它們都位於天文學所定義的「拉格朗日點」位置。

截至目前，天文學家發現海王星有 17 顆特洛伊小行星。而太陽系中的特洛伊小行星主要位於木星軌道，它們的數量超過 10 萬顆。也就是說，木星有 10 萬顆以上特洛伊小行星。

而且，天文學家發現火星等星球也有特洛伊小行星，甚至地球也有。

地球的特洛伊小行星命名為 2010 TK7，是美國航空航天局於 2010 年 10 月使用紅外線空間望遠鏡廣域紅外線巡天探測衛星（WISE）發現。

地球的特洛伊小行星和月亮不同，不僅距離非常遙遠，為地月之距的 50 倍，而且並不像月亮那樣圍繞地球旋轉，而是其軌道與地球軌道有周期性的交疊而已。

原文轉載自【2016-09-26 /大紀元】

相關連結 / http://www.epochtimes.com/b5/16/9/26/n8338572.htm

2016.07.13　中大新聞

天文所葉永烜榮膺中研院院士

感念父母家人「慷慨」付出

文 / 朱韻璇

中央大學天文所教授葉永烜榮膺中央研究院第 31 屆院士，他難得公開表達對父母及手足的感恩、感謝之情。朱韻璇攝

國立中央大學今（13）日舉辦「葉永烜教授榮膺中央研究院院士慶祝茶會暨畫作捐贈儀式」，校長周景揚、中大學術基金會董事長劉兆漢、台聯大系統副校長綦振瀛、台達電子副總裁蔡榮騰、天文所所長陳文屏及教職員同仁等多位嘉賓齊聚賀喜。問及葉永烜的感想，他幽默比喻：「猶如老來得子。」

中央大學校長周景揚開場介紹新科院士，天文所葉永烜教授專長行星科學、太空物理及天文物理，1998 年起在中大任教，曾任理學院院長、副校長、台聯大系統副校長等職，具 15 年以上的豐富行政資歷。他的研究成就卓然耀眼，去年有 10 篇論文發表於國際兩大知名期刊《自然（Nature）》、《科學（Science）》，而迄今共計 60 篇論文刊載於此，其中 12 篇為葉永烜專文。

葉永烜也參與多項國際太空計畫，包含推動探測土星的「卡西尼計畫」、研究彗星的「羅賽塔計畫」等等。周校長感謝葉永烜教授對學校貢獻良多，中央大學在國際合作表現相當優異，據《美國新聞與世界報導（U.S. News & World Report）》分析統計，中大於「國際合作」項目排名全球第 18 名，大幅領先國內多所大學。

他對天文及太空研究的貢獻，曾獲頒美國太空總署「特殊公共服務」榮譽勳章、卡西尼土星計畫團隊成就獎、伽利略木星計畫團隊成就獎等殊榮。2015 年也二度獲得教育部國家講座，今年榮膺中央研究院第 31 屆數理科學組院士，堪稱實至名歸。

同為院士的中大學術基金會董事長劉兆漢說，上週公布新科院士名單後，不少院士紛紛說：「早該得了」，突顯葉永烜的學術研究早已獲得相當的成就和敬重。劉兆漢說，38 年前，他在德國的馬克斯蒲朗克研究院第一次與葉永烜見面，談的是客家人的貢獻；兩人認識後，他很欣賞葉永烜，也於日後邀請他到中央大學任教。

劉兆漢表示，得知葉永烜榮膺中研院院士他很高興，這表示其在科學上的貢獻獲得大家的肯定。他也為中央大學高興，相信中大會記著葉永烜的貢獻並深懷感謝。

慶祝茶會上，葉永烜難得地公開表達他對父母、家人的感謝之意。他說，他的父母那一代在戰亂苦難中度過，他的父親可能從來沒有想過大兒子有一天會成為中央研究院院士，今日，他為自己的父母感到高興。

他說，他個人做研究看似無所顧慮，但其實背後是家人的犧牲和扶持，幾十年來弟妹照顧父母、照顧家人，這才是他有所成就最重要的因素。

他引述哲學家紀伯倫的話，「慷慨」不是給對方想要的東西，而是把你想要的東西給對方。葉永烜感恩他的父母、兄弟姊妹的付出，讓他成就了他自己；他也感謝中央大學的教職員同仁，也是盡心盡力，慷慨付出，成就他人。

閒暇時喜愛繪畫的葉永烜，上月起在中大校內舉辦油畫創作個展。其中有六幅以行政單位教務處、學務處、總務處、研發處、國際處、圖書館為主題發想的畫作，他也在茶會上特別贈與中大，留下一方最美麗動人的校園人文風景。

中央大學舉辦「葉永烜教授榮膺中研院院士慶祝茶會」，教職員同仁齊聚賀喜。前排左至右：中大副校長李光華、台達電子副總裁蔡榮騰、天文所教授葉永烜、校長周景揚、中大學術基金會董事長劉兆漢、台聯大系統副校長蓔振瀛。朱韻璇攝

一日鹿林

MEI-YING LEE · 2016年5月10日

我不是谷阿莫，不過給我8分鐘，我可以給你鹿林一日東西南北日夜天空的變化！請一定要看完啊，你鐵定感動萬分的。
https://www.youtube.com/watch?v=Kuu……

從日出到日出，東西南北連天頂都不放過，第一天結束觀測後，雖整夜未曾闔眼，但實在捨不得上床，於是捕捉到了日出時東方霞光、宛如一隻火鳥的火燒雲華麗出場，各式各樣高中低雲層各方飄移，令人目不暇給，哪是凡夫俗子所能想像？還有玉山上狀似飛碟的夾狀雲生成又散去，模樣神秘又可愛！此時朝向西方天空拍攝的縮時攝影機也不惶多讓，看到了地球影子的西沉，逆霞光光芒四射！

之後因為晚上還要工作，不得不去睡覺，於是縮時攝影機接手整個白天的工作。白天光影幻化，雲影飄移，午後對流雲生成活力旺盛，雲霧翻騰千變萬化，下午一點多火彩虹(環地平弧)亮麗現身，雖短暫卻令人驚艷，可惜當時睡眠中，未曾目睹精彩天象！之後雲層對流依然旺盛瘋狂，直到黃昏時夕陽西下才再見藍天，雲瀑由南向北翻山越嶺，實在壯觀！太陽下山20分鐘後，竟然在雲層間又一"太陽"現身，大氣光學神奇奧妙，令人嘖嘖稱奇！回首東方，夕陽餘暉在玉山上撒下一片金黃，太陽與雲彩的把戲結束，星空大戲接著上演。

因為LOT的觀測工作同時展開，於是兩部單眼各就各位，開始不同方向的固定攝影與捕捉，讓我在室內能專心工作！首先是獵戶天狼在美麗的黃昏天色中緩緩西沉，果然美不勝收，架在窗台上的相機同時獵取東方玉山上的星空，夏季銀河在玉山上緩緩昇起，老天加碼閃電大作，偶而甚至照亮整個天空，只有驚呼連連！再來當然是南方的熒惑守心囉！火星(就是熒惑啦)實在是亮到不行，與土星、心宿二形成的直角三角形，明亮小巧可愛！再來當然要看北方了，北極星不動如山，北斗與仙后一左一右、一落一昇，彷彿守護著鹿林天文台！觀星的人進進出出，留下了一道一道紅的、白的手電筒光跡，當然天頂橫跨南北的壯觀銀河與工作中的天文台是一定不能放過的，偶有流星劃過，令人開心不已。之後東方魚肚白，在玉山後的太陽光線射向北方山巒，隨著太陽上升，光線緩緩下降，鹿林一日最後在搖曳的蘆葦與光芒萬丈的日出中畫下句點，觀測工作也同時完美順利地結束。

中央大學新聞網 **News Network**

鹿林天文台發現小行星　命名「屏東」高掛天際文／屏東縣政府、國立中央大學

中央大學校長周景揚（右）致贈「屏東小行星銘板」給屏東縣長潘孟安（左）。中大鹿林天文台所發現的第175583號小行星，經國際天文學聯合會審查通過命名為「Pingtung（屏東）」。朱韻璇攝

2006年國立中央大學鹿林天文台在太陽系火星及木星之間的小行星帶上發現第175583號小行星，經送請國際天文學聯合會（IAU/CSBN）審查，近期通過命名為「Pingtung（屏東）」，讓屏東登上宇宙星際！

屏東縣長潘孟安27日與國立中央大學校長周景揚共同發表此項天文好消息，並共同點亮小行星，正式介紹Pingtung小行星誕生；雖然屏東小行星距離遙遠，到底小行星是什麼狀況不得而知，但屏東縣政府特別仿世界經典名著「小王子」，想像屏東小行星上有類似像屏東一般的城鎮，有一群可愛的人們快樂生活著，充滿童趣。

潘縣長表示，屏東縣近年積極推廣天文教育及觀星露營活動，像今年屏東彩稻生活節就規劃「稻浪星空」，讓民眾徜徉在稻香和滿天星斗間，恆春貓鼻頭公園更是全台觀賞南十字星最佳地區，縣府每年舉辦「南十字星吶」觀星活動，都吸引數千名親子參與，如今在浩瀚星河裡出現一顆與屏東同名的小行星，更振奮屏東的天文迷。

周景揚校長指出，鹿林天文台創設於1999年，位處玉山國家公園塔塔加地區海拔2862公尺的鹿林前山，是台灣本土最重要的光學天文基地。2006年鹿林天文台啟動「鹿林巡天計畫（LUlin Sky Survey，LUSS）」，2006-2009三年間共發現800多顆小行星、1顆近地小行星及1顆彗星，成效卓著。近年中央大學以台灣所有縣市為鹿林天文台發現的小行星命名，這顆「Pingtung」是台灣第13個以縣市命名的小行星。

中央大學國家講座教授葉永烜、鹿林天文台台長林宏欽及「Pingtung」小行星發現者林啟生也出席發表會說明。屏東小行星的大小粗估約3-6公里，繞行太陽一圈約5.55年（軌道週期），離太陽最近時(近日點)約4.3億公里，離太陽最遠時(遠日點)約5.1億公里。這顆「Pingtung」是2006年10月15日被發現，當時是在金牛座附近，2016年4月位置則在魔羯座。

葉永烜說，小行星是目前各類天體中唯一可以由發現者進行命名並得到世界公認的天體，小行星剛發現並通報國際小行星中心（Minor Planet Center，MPC），經初步確認後，MPC會按發現時的年與順序予以暫時編號；當一顆小行星至少4次在回歸中被觀測到，軌道又可以非常精確地測定時，它就會得到一個永久編號；一旦小行星取得永久編號後，發現者擁有該小行星的永久命名權，提出的名稱必須經過國際天文學聯合會（IAU）的小天體命名委員會（CSBN）審查通過並公告後，才可成為該小行星的正式永久名稱。從發現到命名確認往往需數年的觀測，屏東小行星175583 Pingtung就是歷經如此程序才獲得名稱。

其實不只中央大學鹿林天文台在尋找小行星，屏東縣唐榮國小亦在學校成立尋星小隊，獲得錄取「國際天文搜尋聯盟(IASC)」全球天文月小行星搜尋活動，為東亞地區唯一獲選隊伍，也是全台灣唯一獲選的團隊。

唐榮國小校長施世治表示，尋星小隊師生們利用早自修或是中午時間將IASC所拍攝得的星空圖片，以小行星辨識軟體做數據確認，據以判斷宇宙中移動的物體是否為小行星，若有新發現時，透過網際網路回報分析成果，與全球15所大學、高中學校競爭。現已收到三次資料、15筆數據，經過仔細比對分析發現2顆可能為小行星的資料數據，已立刻向IASC回報，期待能為屏東天文教育創下劃時代的紀錄。

為了慶祝天文盛事，縣府大廳特別佈置成小型天文展，自即日起展出至5月18日，除了介紹屏東小行星，還有太陽星系八大行星及觀星裝備，讓縣府變成美麗星海，還可以體驗躺在地上觀星的感覺，潘縣長歡迎民眾親子或學校老師帶著小朋友來認識天文，縣府貼心準備DIY小品贈送，啟發孩子們對天文的興趣。

中央大學校長周景揚（右四）、天文所教授葉永烜（右三）、鹿林天文台站長林宏欽（右二）、小行星發現者林啟生（右一）與屏東縣長潘孟安（左四）縣府團隊等人正式發表「屏東小行星」高掛天際。朱韻璇攝瀏覽人數：43

快樂教師電子報第77期

文・圖／國立中央大學天文研究所鹿林天文臺觀測員　林啟生

鹿林巡天介紹

中央大學天文研究所鹿林天文臺在西元2006 年3月開始執行鹿林巡天的計畫，簡稱 L.U.S.S.，這個計畫是以發現太陽系小天體為目的。成員包括天文臺的林宏欽臺長和觀測員 林啟生、楊庭彰、張敏悌、施佳佑以及蕭翔耀等人以及中國廣州的大學生葉泉志同學。器材方面則使用直徑40 公分的高精度RC型反射望遠鏡配合超高感度的冷卻CCD相機搭載在追蹤精度很高的中型赤道儀上做整體的攝影任務。

截至今年3月，也是計畫滿三周年，鹿林巡天計畫的成績不凡，總共發現新的小行星將近800 顆，其中已經被命名的有10多顆、彗星1 顆、近地小行星1 顆，73P 彗星分裂的小團塊數顆 。

鹿林彗星發現紀實

鹿林彗星是臺灣本土望遠鏡發現的第一顆彗星。西元2007 年7 月11日晚上7 時，晚餐後天氣還是烏雲密布，看來是一個很典型的夏季午後多雲的天氣，那天筆者值晚班，用餐後就進入觀測室等待天空放晴。直到子夜時分烏雲退散了，溼度也降了下來，立即打開天窗，進行拍攝的任務。當玉山已出現曙光，筆者也一如往常的把天文臺的圓頂天窗關上、望遠鏡放置好，然後回到到宿舍補眠 。這只是一個很普通的夜晚，卻是臺灣天文界使用本土望遠鏡發現第一顆彗星的夜晚。

某日，鹿林天文臺臺長林宏欽傳來一份震撼性的電郵 ，信中這樣敘述著：「 Hi all，We probably discover a new comet Best， HcLin 」（ 中譯：各位，我們可能發現一顆
新的彗星。）

之後在同年7月14日經由美國的天文學家James Young 以Table Mountain天文臺61 公分望遠鏡觀測證實具有彗星特徵，這一顆小行星搖身一變成為一顆彗星。

彗星剛發現時，距離地球大約9 億公里，位在寶瓶座內的黃道附近，亮度約19 等。7月17日天文快報IAUC第8857 期正式公告命名為「鹿林」彗星。

鹿林彗星的重要紀事

1. .回歸周期：當鹿林彗星剛剛被發現後，初步的軌道顯示它的離心率（ e）在1 左右，並沒辦法定的很精細。這是因為在它繞行太陽的軌道中，天文學家在短短幾天中只觀測到極長軌道中很小的一段而已。到了西元2008年年底，小行星中心給的數值是e=0.999987，表示它的周期是2,850萬年，更後來公布的資料是e=0.999991，周期是5,000萬年左右，但根據N A S A 的J P L 最新資料，e=1.000201000134273，這個數據顯示它是一顆軌道屬於雙曲線的非周期彗星。不管離心率到底要採用哪一組數字，都表
明它的家鄉是在太陽系外圍的歐特雲區(Oort cloud) ，我們就只能看它這麼一次而已。

2. 軌道面特性：鹿林彗星的軌道面和地球繞太陽的黃道面交叉角度很小，有如一臺筆記型電腦的螢幕與鍵盤快合起來的模樣，不同於西元1996年的百武、1997年的HALL-BOPP及2007年1月的McNaught等彗星，後者與黃道面都有著比較近於90 度的交叉角度。因為鹿林彗星的軌道面特性之故，所以在今年1 到3月是適合觀察的期間，而且它在天空的路徑都是貼近在黃道旁。

此外， 鹿林彗星的運行軌道標示著它跟著名的哈雷彗星一樣，用句通俗的話就是逆向開車。眾所皆知，太陽系的各大行星與大多數的小天體都以同一個方向繞行太陽，有如 在單行道上同向駕駛的方式，但鹿林彗星卻是向我們迎面而來，是一個比較少見的彗星軌道。

3.重要的節點：鹿林彗星已經慢慢遠離地球及太陽，要回到非常遙遠的故鄉。在它運行到太陽系內層時，最靠近太陽的時候是1月10日，那時離太陽還有1億8,000多萬公里，還位在地球軌道外側，不巧這時地球還在差不多一樣遠的一方，不能看見它最壯觀的一面；等它繞過近日點之後，要遠離太陽了，地球才在2月24日卡位到離它最近的地方，這時只距離6000 多萬公里，大約有著5 等左右的亮度，雖然不算完美，但這個亮度已經是彗星中少見的了。

此外還有一個有趣的節點，那就是鹿林彗星在2月26日到達類似「行星衝」的位置。
簡單的說「衝」就是太陽、地球、行星呈一直線的狀態。鹿林彗星衝有兩個層面可探討，其一就是讓彗星幾乎整夜可見，因此在子夜12 時都可以毫無困難地在頭頂的天空觀測到它，這個現象與一般人印象中彗星大都出現在黃昏西方低空或天亮前東方低空有相當的落差。其次彗星的離子尾都是以彗頭為準背對著太陽，鹿林彗星衝使得那一陣子我們看不到它的離子尾，因為離子尾跑到大大彗頭的後方去了；塵埃尾反而因為前些日子通過近日點，急轉彎甩尾的動作加上地球以及彗星軌道特性等關係，罕見的成為朝向太陽的逆向彗尾， 在觀測上實屬少見的彗星。

4. 簡要的鹿林彗星觀測與拍攝日記：今年2月下旬，鹿林彗星成為新聞媒體注目的焦點，那段時間是一般民眾最容易觀看到它的日子，但對天文界來說，鹿林彗星早在西元2008 年夏天就可以被天文同好以10 多公分的天文望遠鏡拍到它的蹤跡，不過那時它離太陽很遙遠，光度還是暗，拍不出壯觀的影像來。

西元2008 年12月中旬，彗星離近日點的日子已經很近了，不過那一陣子都無法觀測
到彗星，因為它在太陽的視線後方，要到12月下旬才會出現在快天亮前的東南方低空。今年的元旦假期凌晨2 時左右， 筆者開車到大雪山林道17公里處，苦等彗星爬過山
頭，直到凌晨4：30 分左右拍到它。這時的彗星有著白霧般的彗頭，彗尾不明顯。

接下來的日子，月亮逐漸影響到觀測與拍攝彗星，農曆過年前彗星早已過近日點，不過它因為逐漸接近地球而顯得更亮更大。拍攝到的影像中，有著短短向西的離子尾，塵埃尾也有，但是不很明顯。

過完年禁不住誘惑又跑上山拍攝，彗星已經提早東升，拍出的影像中，彗星包裹著綠色的氣體，使它有別於一般的彗星。

在2 月5日的影像中，彗頭往東西兩端各有一條彗尾，西邊帶點噴射狀的是離子尾，
往東邊是塵埃尾 。就一般常識來說，彗星尾巴不是都應該在同一邊嗎？真是一顆奇怪的掃把星！

2 月9日的月亮不僅影響彗星觀測， 還發生了半影月食，在明亮月光下，筆者還是使用望遠鏡看到了彗星。

2月16~17日，鹿林彗星觀測相關的網路上，已經有同好高興的宣布用肉眼直接看到了彗星，但筆者仍無法看見。用肉眼看到代表什麼呢？代表彗星至少比6 等還要亮了。

之後好幾天天氣都不太好， 20日凌晨，自動氣象站顯示天氣好了，筆者抬頭看一下，那個淡淡一團的，不就是彗星嗎？用了雙筒望遠鏡再確認了一次，沒錯，是我發現的鹿林彗星！它已經亮到成為肉眼可見的彗星了。

21日開始我成為臺灣最忙的一個飛人，有時配合電視臺錄影，經常要接記者電話。前一天在臺南辦活動，隔天在臺中辦，再隔天晚上，馬上出現在新竹的山上帶活動；每天的活動一結束，就馬上開著老爺車即刻上山拍攝鹿林彗星，天亮就睡在車上，締造了一連8個晚上連拍彗星的紀錄；直到3 月2 日壞天氣終於來臨，追星的日子就暫時告一段落。

在這段瘋狂追彗星的日子裡，曾拍到了彗星離子尾噴發的現象、離子尾逐漸變成看不著、往東指逆向的塵埃尾越來越明顯，越來越亮、越來越長的過程以及彗星經過明亮的土星旁的倩影等等；每天晚上看著天空中那一團朦朧光芒——我的彗星，就別有一番不同的滋味在心頭。

▲鹿林彗星最初形成時，亮度只有19等， 到最後亮度直逼5等，且出現彗尾，算是亮度很高的一顆彗星。

結語

當你展閱此文的此刻， 對一般人來說，鹿林彗星已經走了，他們再也看不到它的蹤影了；但是對天文學家來說，鹿林彗星仍然是一顆明亮的彗星，天文同好可以一直拍到5月分為止。

觀看一張印刷的彗星照片， 不會比親眼目睹來得感動，尤其是臺灣人發現的鹿林彗星。別嘆息！明亮的大彗星也許很快就要出現在天空中，撥出時間到山上去看看什麼是拖著90度尾巴的大彗星吧！

＜本文摘自 康軒【國小自然通訊5月號】＞

耕雲小行星 安祥禪弟子 星子

凡云整理

一個值得記住的日子，2016 年 5 月 31 日

跟往常 10 年來的生活規律一樣，大約中午將近一點我才睡醒來，盥洗後到大學旁的便當街吃早餐，回來打開電腦看郵件 。 看到一封由鹿林天文台林站長寄出給我的電子郵件：

標題爲 『恭喜 181670 KengYun (2008 BO 15) 終於通過了 ！ 』

電郵內文倒是只有附上網址：
http://ssd。jpl。nasa。gov/sbdb。cgi?sstr=181670&orb=1。

當我看到之時，在第一時間並沒搞清楚內容，後來定眼一看，真的是『終於通過了』！ 當天我即向簡師姐和曾師兄都告知了這個消息 。 雖然真正核準公佈的日期不是是 5 月 31 日，但我收到通知是 5 月 31 日，這天對安祥禪的所有同修們，確實是一個大日子 ：以 耕雲導師爲名的小行星終於通過命名了，也就說天空中有一顆人類編號爲 181670，大小有幾公里的小行星，被稱做『 耕雲 』。

安祥禪與我

說到這個部分， 總離不了要順便提及我與安祥禪的緣分!

大約在１９８４～８５年，那時我已經在大學讀書， 先前就時常索讀儒釋道之類的書, 現在回想，想必都是瞑瞑中的安排！那時我對瓊瑤阿姨的愛情小說跟金庸大叔的武俠小說可是一點都沒興趣！ 當時許多宗教書籍都是從慈雲雜誌內看到然後去函索取回來看， 現在早忘了我是不是也經由這條管道， 我只記得是從普門文庫收到當時與 耕雲導師相關的書本， 並經常閱讀 。 隨後就去函禪學會， 開始收到１６開本黃色封面的禪季刊和以後的中華禪學及安祥季刊，也曾到當時住在台南一中附近的何師兄住處去請回自性歌的錄音帶和書本等， 後來我是很喜歡聽自性歌這卷錄音帶的 。 雖然在１９８０年代後半期， 我就接觸耕雲導師的法， 也從雜誌內看到 耕雲導師在那邊有說法集會的消息， 但那時有兩年在當兵，心智未開年紀也小對這世界來來往往不熟悉，竟然都沒參加過任何一次 耕雲導師的法會，最終也沒見過 導師本人這一切都是因緣 。

１９９２年２月我離開台南老家到台中住及工作，幾年之間也只是都收到禪刊閱讀而已； 我已忘記是那一年第一次到台中道場， 也許是１９９７年也許更早個幾年， 剛來時對道場的人、事和佛法是很陌生的，然後斷斷續續會到道場與師兄姊們共修， 對師兄姊們說的許多修行情況， 基上是有聽沒懂 。２０００年後， 我比較常到道場與師兄姊們共修， 往後差不多是共修日有空都會前來共修 。

２００９年的８８水災那時，因爲這次天災關係， 我有差不多 2 個月不必到山上工作； ８月中某天傍晚吃飯時我突然中暑， 身體狀況不好， 除了看醫生調養， 並常常持誦 觀世音菩薩的聖號， 祈請菩薩幫忙渡過難關，身體部分直到２０１０年１月才基本上復原；而８８天災、生病之後一段長時間，我很容易『受驚不安』『膽怯害怕』等，也是常持佛號，不安等的心才慢慢復原過來 。 往後 1~2 年間， 每當到道場共修， 都能感覺到背部大椎脖子一帶溫溫的，現在當然知道爲何如此， 頂禮並感謝 耕雲導師的加持；在參加共修時對於師兄姐們談的， 也慢慢能聽懂並能體悟在心 。 從８８水災以來，自己的身心起了不少的變化， 目前來說對於平常的應機接物，都會試著去注意心態的變化， 保持著光明磊落的心來過日子 。

命名緣由

以上交待完畢， 要來談到爲何要命名 耕雲小行星 。 我本身的興趣單純些， 就喜歡天文地理跟宗教 。 我是一位天文愛好者， 因緣際會在２００５年１２月１日到中央大學天文研究所的鹿林天文台擔任晚間觀測員。 該天文台在２００６年到２００９年共三年期間執行一個稱做 LUSS 的巡天計劃， 發現了約８００顆小行星， 因著工作關係，我就這個因緣與合作夥伴共同發現了數百顆小行星 。 天文所這邊大約每年釋出一顆小行星給我自由命名，之前已經將故鄉歸仁以及台南和常居地台中都送上了天堂 。

要命名 耕雲小行星，早就在我的計劃之中，要命名導師的緣由也是很簡單 。 我們每個人肉身都是父母所生及照顧養大，在修行的層次上，都是要靠師父來喚醒法身及指導修行的方向 。 耕雲導師在他這輩子，歷經我們現在師兄姊都沒處過的戰亂 ， 在佛天的安排下來到了台灣 ， 當 他完成了生命的進化 ， 證得我即宇宙 ， 宇宙即我之後 ， 並不是只想著享清福 ， 還孜孜不倦的付出 ， 接引有志的行人 ， 舉辦法會 ， 不辭辛勞回覆弟子們的修行問題…等等 。 我剛好有這個可以命名小行星的機緣 ， 爲 耕雲導師 命名一顆小行星是應該而且也是必然的 ， 以答謝師恩 ！

鹿林天文台介紹

粗看之下 ， 天文科學跟修行沒有相關 ， 但佛法涵蓋世法 ， 世法能彰顯佛法 。 鹿林天文台位在玉山國家公園的塔塔加地區 ， 蓋在鹿林前山的山頭上 ， 海拔 2860 公尺 ， 隸屬於中央大學天文研究所 。 這是一處做天文科學研究的天文機關 。 目前設有全台灣口徑最大的 1 公尺望遠鏡一台 ， 口徑 50 公分四台 ， 40 公分一台和 35 公分一台 。 每當夜晚天氣晴朗就會開啓天文台圓頂做科學性的觀測研究 。 發現 耕雲小行星的望遠鏡是 40 公分這一台 ， 稱做 SLT 望遠鏡 。 它搭配有高靈敏度的相機 ， 又位在沒有光害汙染的高山上 ， 因此能拍到很暗的星體 ， 而在 2008 年執行巡天任務時 ， 才能有機會拍到當時大約 20 等亮度的 2008 BO 15 小行星 。 其餘請自行搜索 鹿林天文台 或 鹿林天文台 + 小行星 以及 星等 來參看相關資料 。

小行星是環繞太陽的小天體 ， 多數位在火星和木星的軌道之間公轉 ， 大的有數百公里 ， 小的可小至幾百公尺到幾公里大小 。 自 200 多年前人類發現第一顆小行星到現在至少已經發現 100 萬顆以上的小行星 。 多數路人甲跟路人乙都搞不清楚 ， 以爲發現小行星可以用發現者的名字命名 ， 實則不然 。 目前只有新發現的彗星以發現者的姓氏或機關來命名 ， 而小行星的發現者並不能命名自己 ， 只能命名他人或地名等 ， 請自行搜索 華人小行星 ， 行星、矮行星跟小行星 ， 來參看相關資料 。

發現跟命名小行星可以算做是兩件事 。 當使用大的望遠鏡拍攝星空 ， 比對出會移動的光點 ， 就知道它是太陽系的天體 。 此時要去核對小行星資料庫 ， 若是這個小光點是沒被紀錄過的 ， 要盡快將相關資料送到一個稱做國際天文學聯合會的小行星中心 ; 他們確認之後 ， 這顆就是新發現的小行星 ， 會給一個臨時編號 ， 而這位觀測者就是該顆小行星的發現者 。 在往後幾年間 ， 這顆小行星若是一再的被拍到 ， 它的軌道就會更加精確 ， 在一定規則之下 ， 就會給它一個正式編號 ， 有了正式編號 ， 發現者就可以加以命名 。

當發現者拿到小行星命名權並要命名小行星之時 ， 並不是自己命名昭告天下就算完成 ， 而是需要先寫一段命名文 ， 然後送到小行星中心底下的小行星命名審核委員會 ， 經過這些委員 / 天文學者 通過之後 ， 這顆大石頭才能稱做某某小行星 ， 而且是世界公認的 。

耕雲小行星介紹，此段分兩部分敘述 。

在 2012 年 3 月 ， 我跟時任理事長的曾師兄提及打算命名以導師爲名小的行星 ， 並獲得認同 ; 然後大家草擬了中文的命名文 ， 再商請比較熟悉英文

的香港羅師兄幫忙改寫成英文 ， 當時中文草稿及決定後的英文如下 ：

耕雲
耕雲先生(1924~ 2000)是一位禪的開悟者和大智慧家 ， 人類心靈的救濟者 。 他教導我們如何認識自己 ， 認清宇宙的法則和實相 ， 進而幫助他人 ， 完成自己和人類的進化 ， 過著幸福快樂的生活 。

KengYun
Mr。 Keng-Yun (1924 ~ 2000) was an enlightened Ch'an Master and intellectual， the spiritual savior of mankind。He teaches us how to understand ourselves， recognizes the laws of universe and reality。 Helping others accomplish their completeness and human evolution towards the bliss of lives。

師兄姊們都熟知 耕雲導師眾多偉大的事蹟 ， 但這些事蹟是沒辦法寫進去的 ， 主要是命名文只限定在 50 個英文字以下 ， 此外有權利審核的天文專家 ， 並不是宗教 / 修行界的人士 ， 送件的目的是希望能通過審核 ， 不是在講說耕雲導師多麼的偉大 。

一般小行星命名的審核 ， 快則半年慢則一年大致上就可以通過並發佈出來 。 2012 年 8 月送件之後等了一年多 ， 我都沒收到告知 國際上的小行星中心審核委員會那邊 ， 通過命名就會公佈 ， 沒通過的話也不會主動通知送件單位 。

到了 2014 年 7 月 ， 我又將命名文小改寫 ， 並請香港一位發現約 2000 顆小行星的楊先生幫忙看看內容是否有不妥之處 ， 然後又重新送件一次 ， 這次內容如下 ：

Keng-Yun
Mr。 Keng-Yun (1924 ~ 2000) was a master of Zen 。 He teaches us how to understand ourselves， recognizes the laws of universe and reality。 Helping others accomplish their completeness and human evolution toward the bliss of lives 。

往後 ， 有時我會在導師的法像前告訴 他說 ， 大意是 ： 耕雲導師啊 ， 要命名一顆以你爲名的小行星 ， 你在天上界是不可能不知道的呀 ， 雖然你早已經證得全宇宙就是你 ， 老早就不欠不缺什麼 ， 也不會去執著這個名號 ， 但也請你能體諒一下 ， 還是得要按照地球人的規矩來辦事 ， 可不要阻擋命名通過喔 ！

一笑！

之後 ， 就也不太抱著通過的希望 ， 只能等待 。 在小行星的命名申請上 ， 以地名跟機關名稱來命名是很容易獲得通過的 ， 但人名就很難說 ， 因爲要判斷一個人的是非功過 ， 三張嘴巴會有三種講法！譬如政治人物就必須在離世100年以後才能有機會被命名__像現在就沒有蔣介石跟毛澤東的小行星 ， 而跟科學性質有關的學者及演藝明星反而容易被通過命名 。 請參見 華人小行星 。 曾師兄就曾跟我說過 ， 大意是 耕雲導師那麼偉大 ， 怎麼會通過不了 ？ 其實很簡單 ， 審核專家並不是宗教人士 。

2016年5月31日 ， 終於通過命名了！

以下來說明 耕雲小行星的科學性質的內容 。

在進入以下網址就會有 耕雲小行星的相關資料 。 或查閱『181670 JPL ssd』http://ssd。jpl。nasa。gov/sbdb。cgi?sstr=181670&orb=1 。 其中主要的資料是

1. 181670 Kengyun (2008 BO15) 。 2008BO15是指小行星的臨時編號 ， 而181670是指正式編號 ， 以上兩個編號都是小行星中心給的 ， 而Kengyun就是這顆小行星的名稱 。 以上3個名稱都是相通 ， 指的是這顆大石頭 。
2. Classification: Main-belt Asteroid ， 是指該顆小行星爲主序帶的小行星 ， 軌道位在火星和木星之間 ， 爲一顆軌道很普通的小行星 。
3. 在表格之中 ， e是指離心率 ， 181670小行星離心率小 ， 只有0.03 ， 近似圓形軌道；而a跟q是指離太陽最近和最遠的距離 ， 數字是以天文單位算（au）， 一個au是１億５千萬公里 ， 所以１８１６７０號小行星離太陽約４億５千多萬公里 ， 離地球最近約３億公里多些 。
4. period是指繞太陽的周期 ，１８１６７０號小行星繞太陽一圈約需時5年8個月(5.68年) ， 而每跟地球接近一次約需時１.７５年 。
5. 網頁下方是命名文 ， 說明１８１６７０號小行星是在２００８年１月２８日 ， 由 C.-S. Lin and Q.-z. Ye（葉泉志__當時是就讀於中國大陸廣州中山大學）於鹿林天文台發現 。 而命名文則是依據２０１４年７月第二次送件做了些修改而成 。

KengYun (1924-2000) was a master of Zen， who taught others how to understand themselves， and to recognize the laws of universe and reality。 He

helped others accomplish their completeness and human evolution toward the bliss of lives。

6. 諸位師兄姊會很好奇這顆小行星能否使用望遠鏡看到？ 在2016年9月到10月之間， 181670號小行星亮度約在20等(星等是星星亮度表示方法)，使用一般10幾公分的天文望遠鏡是永遠看不到的， 即使使用鹿林天文台一米的大砲望遠鏡加上沒近視的眼睛也看不到 !!!! 必須使用口徑至少 40公分的望遠鏡在台灣高山上搭配高靈敏度的相機， 拍個幾分鐘才能有機會拍出光影來。 也就是說， 透過望遠鏡是看不到但夠大的望遠鏡有機會拍到 。

這顆小行星的大小只有幾公里大，估計3到6公里之間！形狀並不是像地球般接近球形， 而是不規則狀！耕雲小行星2016年10月初位在天空中的摩羯座方向上 。

181670號小行星2016年10月初在太陽系位置請見下圖 。

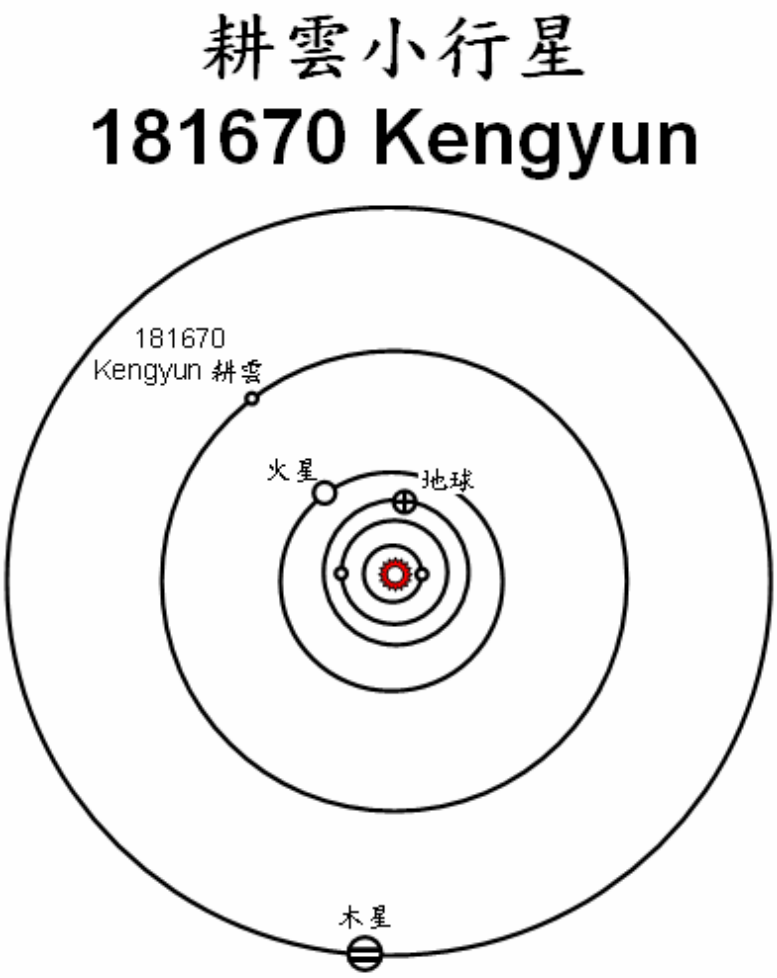

使用鹿林天文台 1 公尺望遠鏡拍出的影像 ， 只見這麼微弱的小光點在群星之間移動 ， 上圖及下圖正中心帶點狀的小光點即是 耕雲小行星 ， 而其它恆星呈拉線狀 。

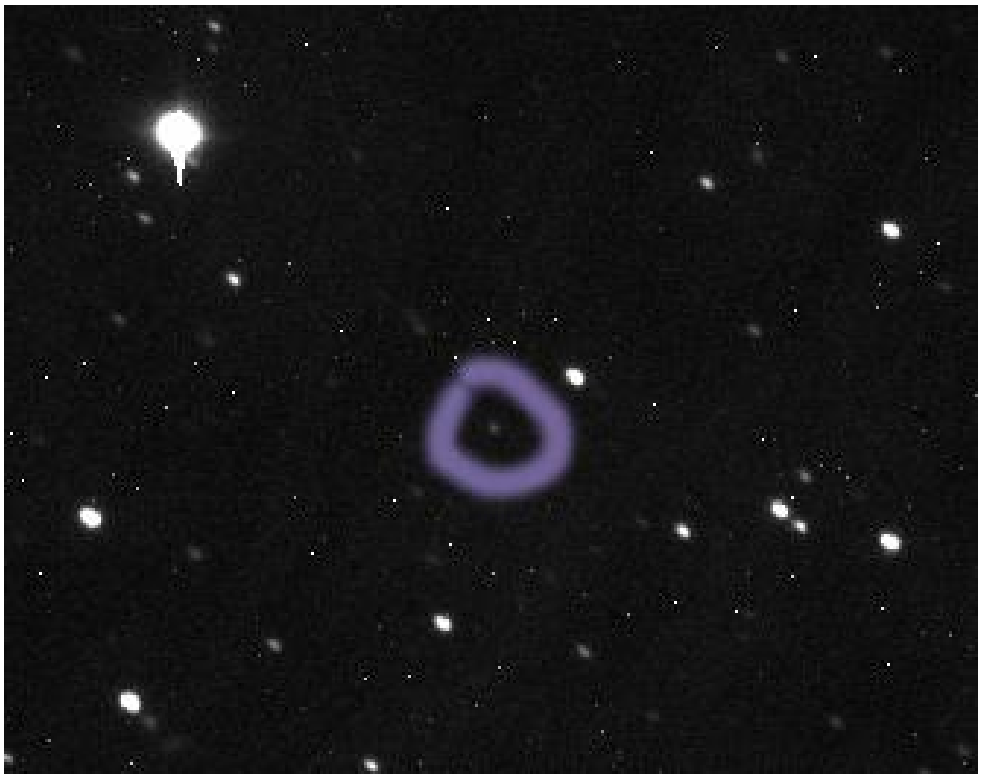

這支望遠鏡即是發現 耕雲小行星的大砲 .

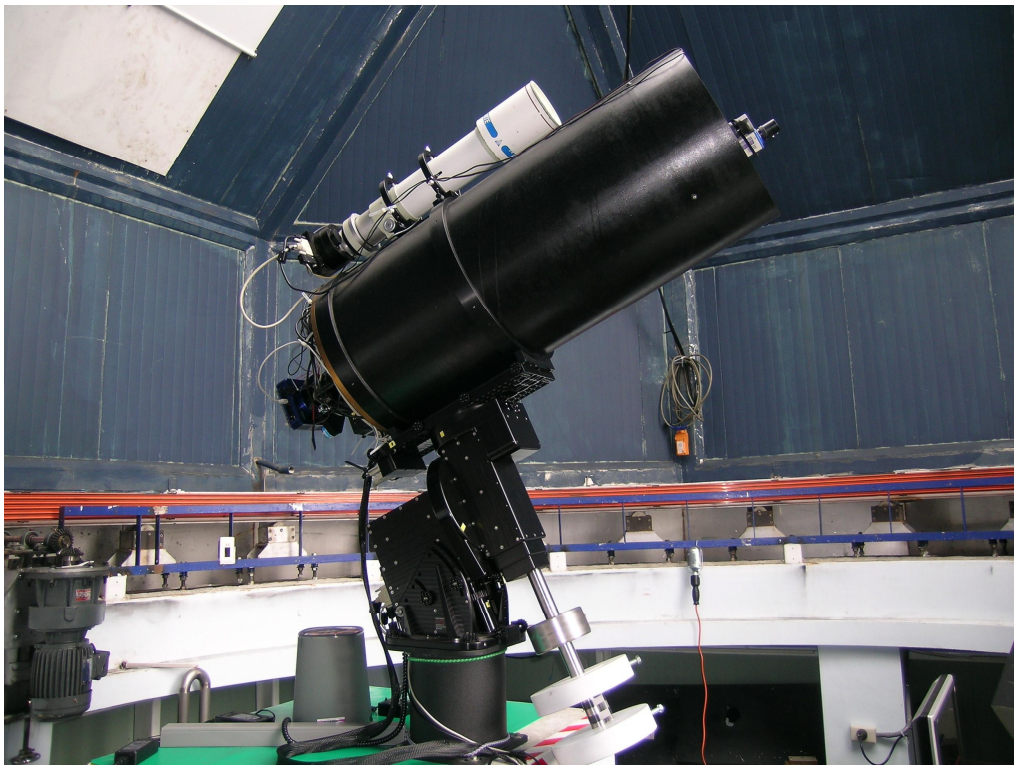

期盼

本文之目的在於向師兄姊們 / 安祥禪友介紹導師 耕雲小行星命名的前後因緣和經過 ， 同時也不能忘本 ， 兼談點發現的天文台和相關的天文知識 。 文末期盼已入安祥法門的師兄姊們 ， 能道業日進，其實應該說爲道日損 ， 秒秒心安 ， 六時本心現前 ; 現在正在尋覓以及未來會接觸安祥禪法門的朋友 ， 不再尋尋覓覓 ， 能安止於 耕雲導師的安祥禪門內 ， 上求佛道下化法界眾生 ， 他日於 耕雲導師的淨土 / 大圓覺海內相逢團圓。